U.S.NRC
United States Nuclear Regulatory Commission
Protecting People and the Environment

Technical Report-XXXX

Dynamic Response of Soil under Multidirectional Loading: Experimental Investigation and Modeling

[Comments]

Office of Nuclear Regulatory Research

AVAILABILITY OF REFERENCE MATERIALS IN NRC PUBLICATIONS

NRC Reference Material

As of November 1999, you may electronically access NUREG-series publications and other NRC records at the NRC's Public Electronic Reading Room at http://www.nrc.gov/reading-rm.html. Publicly released records include, to name a few, NUREG-series publications; *Federal Register* notices; applicant, licensee, and vendor documents and correspondence; NRC correspondence and internal memoranda; bulletins and information notices; inspection and investigative reports; licensee event reports; and Commission papers and their attachments.

NRC publications in the NUREG series, NRC regulations, and Title 10, "Energy," in the *Code of Federal Regulations* may also be purchased from one of these two sources.

1. **The Superintendent of Documents**
   U.S. Government Publishing Office
   Mail Stop SSOP
   Washington, DC 20402-0001
   Internet: http://bookstore.gpo.gov
   Telephone: 1-866-512-1800
   Fax: (202) 512-2104

2. **The National Technical Information Service**
   5301 Shawnee Road
   Alexandria, VA 22161-0002
   http://www.ntis.gov
   1-800-553-6847 or, locally, (703) 605-6000

A single copy of each NRC draft report for comment is available free, to the extent of supply, upon written request as follows:

U.S. Nuclear Regulatory Commission
Office of Administration
Publications Branch
Washington, DC 20555-0001
E-mail: distribution.resource@nrc.gov
Facsimile: (301) 415-2289

Some publications in the NUREG series that are posted at the NRC's Web site address http://www.nrc.gov/reading-rm/doc-collections/nuregs are updated periodically and may differ from the last printed version. Although references to material found on a Web site bear the date the material was accessed, the material available on the date cited may subsequently be removed from the site.

Non-NRC Reference Material

Documents available from public and special technical libraries include all open literature items, such as books, journal articles, transactions, *Federal Register* notices, Federal and State legislation, and congressional reports. Such documents as theses, dissertations, foreign reports and translations, and non-NRC conference proceedings may be purchased from their sponsoring organization.

Copies of industry codes and standards used in a substantive manner in the NRC regulatory process are maintained at—

The NRC Technical Library
Two White Flint North
11545 Rockville Pike
Rockville, MD 20852-2738

These standards are available in the library for reference use by the public. Codes and standards are usually copyrighted and may be purchased from the originating organization or, if they are American National Standards, from—

American National Standards Institute
11 West 42nd Street
New York, NY 10036-8002
http://www.ansi.org
(212) 642-4900

Legally binding regulatory requirements are stated only in laws; NRC regulations; licenses, including technical specifications; or orders, not in NUREG-series publications. The views expressed in contractor-prepared publications in this series are not necessarily those of the NRC.

The NUREG series comprises (1) technical and administrative reports and books prepared by the staff (NUREG-XXXX) or agency contractors (NUREG/CR-XXXX), (2) proceedings of conferences (NUREG/CP-XXXX), (3) reports resulting from international agreements (NUREG/IA-XXXX), (4) brochures (NUREG/BR-XXXX), and (5) compilations of legal decisions and orders of the Commission and Atomic and Safety Licensing Boards and of Directors' decisions under Section 2.206 of NRC's regulations (NUREG-0750).

U.S.NRC
United States Nuclear Regulatory Commission
Protecting People and the Environment

TECHNICAL REPORT-XXXX

Dynamic Response of Soil under Multidirectional Loading: Experimental Investigation and Modeling

[Comments]

Manuscript Completed: June 2019
Date Published:

Prepared by:
S. Olson
C. Rutherford
Y. Hashash
L. Bhaumik
A. Cerna Diaz
O. Numanoglu

University of Illinois at Urbana-Champaign
205 N Mathews Ave Urbana IL 61801

Dr. Thomas Weaver, NRC Project Manager

Office of Nuclear Regulatory Research

ABSTRACT

The seismic performance of nuclear power plant (NPP) structures constructed on compacted, coarse-grained soil depends on the soil's cyclic shear stress – shear strain – volumetric strain response. NPPs founded on a thick deposit of dense coarse-grained soil may experience nontrivial settlements due to small, but accumulated volumetric strains during an earthquake. Studies that have investigated the seismic response of coarse-grained soils are primarily limited to unidirectional loading. However, since seismic events are multidirectional in nature, design based on unidirectional studies may lead to underestimation of volumetric strains, and nontrivial settlements that can impact structures.

This report presents a broad study conducted to characterize dense coarse-grained soil behavior under multidirectional cyclic loading conditions. The study included three main components: (1) element-level testing; (2) centrifuge testing; and (3) numerical model development. The element tests involved multidirectional cyclic direct simple shear (mcDSS) laboratory experiments to characterize soil behavior under varying initial states, load paths, and boundary conditions. The initial state conditions included variations in relative density (D_R = 55 – 95 %), sample preparation method (dry pluviation with and without vibrations, and cyclic shearing) and consolidation stress (50 – 400kPa); loading conditions ranged from unidirectional cyclic to bidirectional circular, figure-8 and broadband at frequencies of 0.1 to 1 Hz and shear strains of 0.1 to 7 %; boundary conditions included drained and undrained (or constant volume) shearing. The test soils included a clean poorly-graded Ottawa sand; a well-graded mixture of sand, fine gravel, and silt; a non-plastic Mississippi River silty sand; and a Mississippi River clayey sand with low plasticity. Dynamic centrifuge tests were performed on thick (up to 20 m) layers of saturated dense Ottawa sand (D_R = 95 %) with models representing both free-field and a soil-structure system excited using unidirectional and bidirectional historical broadband motions. Lastly, a new constitutive model, I-soil, was developed to characterize soil behavior in three-dimensional stress space considering effective stress dependency, small-strain nonlinearity and proper hysteretic damping formulation, as well as shear volumetric coupling. The I-soil model was validated using the laboratory element tests and used to simulate the dynamic centrifuge tests in a 3-D finite element formulation.

This study forms a unique database of multidirectional element tests and dynamic centrifuge "case-histories" that provide new insight into the shear and volumetric response of dense coarse-grained soils under unidirectional and bidirectional loading. Free-field centrifuge experiments highlight that shear response in each orthogonal direction is not affected by bidirectionality. Thus, site amplification factors can be estimated for use in one-dimensional site response analysis. In contrast, the element and centrifuge tests illustrated that volumetric strains (ε_v) and excess porewater pressures (evaluated in terms of excess porewater pressure ratio, r_u) are affected by multidirectionality, with the ratios of bidirectional to unidirectional ε_v and r_u ranging from 1 to 4. Semi-empirical, simplified models based on dissipated energy and ground motion intensity parameters (e.g., Arias intensity) are proposed to estimate volumetric strains in dense coarse-grained soils. Estimates from the models are in good agreement with measurements. Finite element simulations show that the I-soil constitutive model calibrated using laboratory test results is able to capture reasonably the soil response observed in the dynamic centrifuge tests. Compared to other constitutive models, I-soil is efficient and mathematically simple and utilizes relatively few input parameters. When combined with an optimized computational platform, I-soil can reduce run times several-fold for large-scale, 3-D solid-fluid coupled simulations.

FOREWORD

The Fukushima nuclear power plant (NPP) disaster resulting from the 2011 Tohoku earthquake and tsunami has led to a global effort towards seismic safety re-evaluation of NPPs. During this process, the U.S. Nuclear Regulatory Comission (NRC) identified a potential gap in the seismic deformation analysis of NPPs. Specifically, present design procedures do not explicitly evaluate settlements in dense coarse-grained soils, which constitutes the foundation for a number of NPPs.

This NUREG/CR, prepared by a project team at the University of Illinois at Urbana-Champaign, culminates a four-year effort to combine laboratory multidirectional cyclic direct simple shear tests, multidirectional cyclic centrifuge tests with and without a heavy bearing pressure structure, and numerical modeling to develop semi-empirical and analytical design tools to estimate settlements in dense coarse-grained soils induced by multidirectional seismic loads. In addition, the experimental program provided a unique dataset to calibrate a new stress-shear strain-strength-volumetric strain constitutive model, I-soil. The model is capable of capturing: (1) small-strain nonlinearity; (2) hysteretic damping; (3) shear-induced volumetric strain (contraction-dilation); and (4) modulus degradation due to excess porewater pressure generation. This new model can be used to evaluate reliably both static and dynamic, three-dimensional geotechnical engineering problems.

TABLE OF CONTENT

LIST OF FIGURES

LIST OF TABLES

EXECUTIVE SUMMARY

Nuclear power plant (NPP) structures may be founded on dense (or compacted) coarse-grained soils to mitigate liquefaction-related issues. Seismic settlements of these dense sands generally are expected to be within tolerable structural limits, and are not incorporated in standard dynamic soil-structure interaction analyses of NPPs. However, even dense sands can undergo nontrivial volumetric contraction under multidirectional cyclic loads. Currently, seismic deformations in sands are primarily determined based on the cyclic shear stress – shear strain – volumetric strain response of clean sands defined from unidirectional cyclic laboratory tests, not accounting for the presence of fines or multidirectional seismic loads. State-of-practice methods multiply volumetric strains measured in unidirectional cyclic loading tests by a factor of two to account for multidirectional loading effects solely based on the bidirectional shake table tests conducted by Pyke et al. (1975) on a uniform, medium dense clean sand (relative density, D_R 60%). To enhance the understanding of the behavior of dense coarse-grained soil and to develop a numerical model to capture shear stress – shear strain – volumetric strain response, this report summarizes in three-parts a research program funded by the the U.S. Nuclear Regulatory Commission (NRC). The three parts include Part A: Element Testing; Part B: Centrifuge Testing; and Part C: Numerical Modeling.

Part A: Element Testing. A new unique database consisting of more than 500 drained and undrained (or constant volume) multidirectional cyclic direct simple shear tests is presented. The cyclic tests include unidirectional, circular, figure-8 and broadband strain paths. Drained tests using broadband motions were also conducted. Testing was conducted on medium dense to very dense (D_R 55 – 100 %) clean, silty, and clayey sands at varying consolidation stresses (50 – 400 kPa). Drained and reconsolidation volumetric strain under both unidirectional and bidirectional loading was found to be independent of the loading frequency for the clean sand and sand with silty fines. Well graded sands at the same relative density exhibited more volumetric strain than the poorly graded sand. The volumetric response of the low plasticity clayey sand was comparable to the silty sand at the same relative compaction. During drained loading, a limiting shear strain was observed, after which further increase of the shear strain does not increase the volumetric strain for the same number of loading cycles. For bidirectional tests, the limiting shear strain is about 5 %, while for unidirectional cyclic tests, it is about 10 %. The number of strain reversals in a loading path also influences volumetric strain. Volumetric strain in figure-8 loading paths is greater than that of the circular or oval loading path because of the greater degree of strain reversal in the “8”.

The effect of specimen preparation (dry funnel deposition, dry funnel deposition followed by table vibrations, and dry funnel deposition followed by small amplitude cyclic shearing) on drained, cyclic shear-induced volumetric strain was clarified for the clean sand. It was observed that for medium dense sands (D_R 60 %), preshearing the specimen (by table vibrations or small amplitude cyclic shearing) resulted in smaller volumetric strains than that of dry funnel deposited specimens. In contrast, for very dense sands (D_R 95 %), the difference in volumetric response using the three specimen preparation methods was negligible. Unidirectional and bidirectional broadband loading DSS tests corroborate the findings of the uniform cyclic tests.

The higher the porewater pressure (PWP) dissipation during reconsolidation, the higher the reconsolidation volumetric strain, for both unidirectional and bidirectional loading. Thus, for the same PWP ratio at two different depths, the soil at the lower depth will undergo more reconsolidation volumetric strain. For the same depth and same PWP, higher shear strain causes higher reconsolidation volumetric strain. Multidirectionality factors for volumetric strain varied from 1 to 4 for clean and non-plastic silty sand for various loading intensities, consolidation stresses, and densities, and can be used in conjunction with any method for settlement or PWP estimation, e.g.,

the Tokimatsu and Seed (1987) empirical method or with the GMP porewater pressure generation model (Green 2001).

Part B: Centrifuge Testing. A new database of dynamic centrifuge tests of a dense sand (D_R 95 %) subjected to unidirectional and multidirectional earthquake loads is presented. The experiments included free-field tests and tests with a high bearing pressure structure (380 kPa and 190 kPa). Prototype soil thicknesses were 20.5 m (60g tests) and 10.25 m (30g tests). The input motions included historical motions obtained from the Pacific Earthquake Engineering Research (PEER) Center and Chilean strong motion databases. To further complement the data from this study, centrifuge tests performed by others (Montoya 2012; Adalier 1996) on dense sands (D_R 70-85 %) were included in the analysis. The broadband and sinusoidal motions used in these studies exhibited Arias intensities that ranged from 0.1 to 30 m/s.

The free-field centrifuge experiments illustrated that dynamic shear response in each orthogonal direction (represented as response spectra) is not affected significantly by multidirectional shaking, as mean residuals computed between 1D and 2D response spectra were less than ±0.125 for periods up to 10 seconds. Also, comparing the recorded response with the response computed in a suite of 1D nonlinear effective and total stress site response analyses illustrates that site amplification factors can be estimated reasonably irrespective of multidirectionality (residuals < ~0.25). Site amplification factors computed from the centrifuge tests exhibited considerable scatter, and only marginally agreed with code-based amplification factors. In contrast, energy-based (e.g., Arias and Housner intensities) site amplification factors showed significantly less scatter and more consistent trends than amplification factors based on spectral accelerations. Centrifuge test multidirectionality factors for both excess PWP and volumetric strains (ε_v) ranged from 1 to 4, and approached unity as the soil approached liquefaction. On average, a multidirectional factor of 2 was reasonable for dense saturated sands. Energy-based intensity measures (Arias and Housner intensities) provided nearly unique estimates of excess PWP and ε_v for both 1D and 2D motions, indicating that they capture multi-directionality effects, while vectored peak accelerations and velocities (PGA and PGV) yielded different relationships for 1D and 2D motions.

A semi-empirical model to estimate shaking-induced volumetric strains of dense sands was developed from the centrifuge test results. The proposed model can be used with several ground motion measures (PGA, PGV, Arias and Housner intensity) in conjunction with shear wave velocity, standard penetration test blow count, and cone penetration test tip resistance.

Part C: Numerical Modeling. A new constitutive model, I-soil, was developed to characterize soil behavior. I-soil uses a physically motivated constitutive modeling framework and extends mathematically simple formulations to represent shear behavior. The model also uses a non-associative flow rule to represent shear-induced volumetric behavior. The model simulates pressure-independent and pressure-dependent soil behavior, small strain nonlinearity, and hysteretic damping characteristics. The formulation is three-dimensional and the model currently is available in LS-DYNA in effective stress space as a user-defined material model. Thus, any solid-fluid coupling formulation available within the software can be used with I-soil to simulate saturated drained-undrained-partially drained conditions with excess porewater pressure generation and dissipation.

Three-dimensional finite element analyses were utilized to simulate the dynamic centrifuge tests described in Part B. Both free-field and soil-structure interaction (SSI) simulations were conducted. The SSI simulations were conducted using a direct analysis method whereby the soil and structure were modeled together in a given simulation without any separate consideration for soil or structure. The results showed that I-soil captures most of the shear and volumetric behavior measured in the

dynamic centrifuge tests. Also, the efficiency of the constitutive modeling framework adopted in the I-soil formulation and the optimized explicit dynamic finite element analysis software LS-DYNA can perform a full 3D partially drained (solid-fluid coupled) SSI analysis within a couple of hours.

ACKNOWLEDGMENTS

The research described in this NUREG/CR was sponsored by the United States Nuclear Regulatory Commission (U.S. NRC), Office of Research. This NUREG report was considerably enhanced by the contributions of others. The guidance and review provided by Dr. Thomas Weaver during the project and preparation of the NUREG is gratefully acknowledged. Several undergraduate students at the University of Illinois at Urbana-Champaign contributed to the laboratory characterization of the sands used in this research. In particular, we would like to thank undergraduate students Kenya Mercado, Grant Wu, Hannah Blomberg, and Angela Wu. The staff in the U.S. Nuclear Regulatory Commission's Office of Research provided a detailed review of a draft of this report. Their review and comments were invaluable in improving the report, and their efforts are highly appreciated.

ABBREVIATIONS AND ACRONYMS

DEP	Ditributed element plasticity
DFD + CS	Dry Funnel Deposition + Cyclic Shearing
DFD + TV	Dry Funnel Deposition + Table Vibration
DFD	Dry Funnel Deposition
D_{Rc}	Relative density at the end of consolidation
D_{Rf}	Final relative density
D_{Ro}	Initial relative density
e_{max}	Maximum void ratio
e_{min}	Minimum void ratio
f	Loading frequency
F_a	Amplification site factor at 0.3 sec
FEM	Finite element method
FF	Free-field
F_v	Amplification site factor at 1.0 sec
GQ/H	General quadratic/hyperbolic
GQ/H-ε_v	General quadratic/hyperbolic volumetric model
G_s	Specific gravity
HI	Housner intensity
I_a	Arias intensity
IM	Intensity measure
MDF	Multidirectional Factor
MKZ	Modified Kondner – Zelasko
N_c	Number of loading cycles
NEHRP	National Earthquake Hazards Reduction Program
PDMY	Pressure dependent multi-yield
PGA	Peak ground acceleration
PGV	Peak ground velocity
PIMY	Pressure independent multi-yield
PM4Sand	Plasticity model for sand
PWP	Pore water pressure
r_u	Excess porewater pressure ratio = $\Delta u/\sigma'_{vo}$
S_a	Spectral acceleration

SSI	Soil-structure interaction
UBC	University of British Columbia
V_s	Shear wave velocity
$V_{s,30}$	average shear wave velocity in the upper 30m
$Vs_{,HH}$	Shear wave velocity horizontally propagated horizontally polarized
$Vs_{,HV}$	Shear wave velocity horizontally propagated vertically polarized
γ_{cs}	Cyclic shear strain amplitude
γ_{max}	Maximum shear strain
ε_v	Volumetric strain
ε_{vcyc}	Volumetric strain under drained cyclic loading
$\varepsilon_{vcyc,N=15}$	Volumetric strain at the end of 15 cycles of drained loading
ε_{vr}	Post undrained loading reconsolidation volumetric strain
Δu	Excess porewater pressure
ϕ'	Friction angle (degree)
σ'_{vo}	Initial effective vertical stress
σ_{vo}	Initial total vertical stress

1 INTRODUCTION

1.1 Background and Problem Statement

The devastating effects of the 2011 Fukushima nuclear power plant accident in Japan renewed the world's interest in the seismic safety of existing nuclear power plants (NPPs). In July 2011, the U.S. Nuclear Regulatory Commission (NRC) provided recommendations to enhance the safety of all U.S. nuclear reactors against geologic hazards. Thus, seismic design re-evaluations for 101 operating NPPs using up-to-date seismic hazard information for the central and eastern United States (CEUS) and western United States (WUS), became a NRC priority.

Seismic design for critical structures like NPPs often involves evaluating the potential for ground failure (e.g., liquefaction/strain softening) and its effects. However, liquefaction at NPP sites is not typically a concern because soil deposits underlying the foundation of power plant structures are dense and compacted. Such soils generally will not generate sufficient shear strains and excess porewater pressure (PWP) to trigger liquefaction. However, modest volumetric (contractive) strains can accumulate when dense sand is sheared cyclically (Youd 1972a). Therefore, when the soil deposit is thick, these volumetric strains can produce nontrivial settlements, which can, in turn, affect NPPs. This accumulation often is neglected or underestimated in current engineering practice. Seismic deformation analyses, commonly performed at NPP facilities, generally do not account for settlements in such dense coarse-grained compacted or natural soils. This may be due to existing semi-empirical and constitutive models not being well-calibrated to forecast volumetric strains in dense coarse-grained soils.

The cyclic shear stress-shear strain-volumetric strain behavior of dense sands is derived largely from unidirectional (1D) element tests that may underestimate accumulated volumetric strains (Pyke et al. 1975). Using shaking table tests, Pyke et al. (1975) conducted one of the first studies evaluating the effect of bidirectional (2D) shaking on dry coarse-grained Monterey No. 0 sand. The study suggested that settlements from bidirectional shaking could be approximated by summing the volumetric strains induced separately by shaking in two orthogonal horizontal directions. As a result, 2D shaking-induced settlements in medium dense sands typically are assumed to be about twice as large as unidirectional shaking-induced settlements. Seed el al. (1978) combined the results of Pyke et al. (1975) with the excess PWP generation model proposed by Martin et al. (1975) and concluded that the shear stresses required to trigger liquefaction in multidirectional shaking are approximately 10 to 20% smaller than those required to trigger liquefaction under unidirectional shaking. Later, Ishihara and Yamazaki (1980) also observed that to induce the same shear strain in a sand specimen, a bidirectional cyclic shear stress only 70 % that of the unidirectional cyclic shear stress is required.

Recent comparative unidirectional and bidirectional cyclic direct simple shear (DSS) tests (e.g., Kammerer 2002; Wu et al. 2003) have examined the effect of multidirectional loading on excess PWP generation. Similarly, using dynamic centrifuge testing Su and Li (2003) and Su Dong (2005) investigated multidirectional shaking effects on loose to medium sands and concluded that excess PWP and settlements generally increase under bidirectional shaking. These studies all suggest that volumetric strains based on unidirectional DSS and centrifuge testing underestimate those induced during multidirectional seismic shaking. However, most of these tests were performed on loose to medium dense sand specimens. In comparison, considerably fewer data are available to assess the performance of dense sands. Thus, there is a need to better quantify volumetric strains induced by multidirectional shaking of dense, coarse-grained soils in free-field and near-field (i.e., close to a structure) conditions.

1.2 Research Objectives

The primary objectives of this research project are as follows.

1. Develop a testing database of unidirectional and bidirectional DSS element tests to study compression (drained loading) and reconsolidation (undrained or constant volume loading) volumetric strains in medium dense to dense sands.
2. Develop unidirectional and bidirectional centrifuge case histories in dense sands with and without a structure to investigate and quantify dynamic soil response in the field.
3. Recommend multidirectionality factors for volumetric strains and porewater pressure generation to be used in practice.
4. Develop new or improved semi-empirical correlations for the estimation of bidirectional volumetric strains and porewater pressures under partially drained conditions.
5. Develop a new soil constitutive model to characterize 3D cyclic sand behavior.
6. Estimate the settlements of NPP structures during earthquake events via soil-structure interaction analyses.

1.3 Organization of Report

The report is organized as follows.

Chapter 1: This chapter introduces the research problem and briefly lists the objectives of the project, along with the organization of the report.

Chapter 2: This chapter describes all the previous work pertaining to unidirectional and bidirectional laboratory and centrifuge studies on granular material, and enumerates the factors that influence volumetric strain. Then, this chapter presents currently available semi-empirical models to estimate volumetric strain under drained and undrained conditions. Finally, prevalent numerical models and their advantages and disadvantages in terms of capturing volumetric response are described.

Chapter 3: This chapter presents the element and centrifuge testing programs, including instrumentation, soil type, density, saturation, load paths, boundary conditions, and specimen preparation techniques. The Illinois multidirectional direct simple shear device and the centrifuge used for the present study are detailed. Index testing results and oedometer data for the tested material also are described.

Chapter 4: This chapter presents the results of the element and centrifuge testing. The effect of various factors like frequency, shear strain, loading duration, confinement, soil type, plasticity, and specimen preparation on volumetric strain is described. The bidirectional deviatoric and volumetric response from the centrifuge tests are presented.

Chapter 5: This chapter includes the formulation of a semi-empirical volumetric strain model for dense sands based on the centrifuge testing database described in the previous chapters.

Chapter 6: This chapter presents the constitutive model developed to characterize the cyclic behavior of sands. The constitutive framework is introduced and element simulations are conducted to demonstrate the model capabilities.

Chapter 7: This chapter describes numerical issues and procedures related to soil-structure interaction (SSI) analysis using the finite element method. The details of modeling free-field and SSI problems are presented. In addition, details of handling input motions and initial stress conditions are presented.

Chapter 8: This chapter presents the finite element analyses conducted to simulate the dynamic centrifuge tests described in Chapter 4. The simulations results are compared to test measurements, and the performance of I-soil and the numerical model are evaluated.

Chapter 9: This chapter presents key conclusions and recommendations.

2 LITERATURE REVIEW

This chapter presents previous element and centrifuge tests conducted on medium dense to dense coarse-grained soils under unidirectional and bidirectional loading. First, the relevance of simple shear testing in capturing seismic stresses is highlighted briefly. Unidirectional and bidirectional simple shear tests are described. Factors affecting volumetric strain in coarse-grained soils, based on the element testing literature, are enumerated. Free-field and near-field unidirectional and bidirectional centrifuge tests that are available are described next. Available semi-empirical models to estimate volumetric strain under drained and undrained loading conditions are described, and their respective shortcomings discussed. Both simplified semi-empirical models and models that require site response analysis are summarized. Then, a review of existing constitutive models for sand including 1D cyclic nonlinear models and advanced models requiring the definition of a yield surface, as well as hardening and flow rules is presented.

2.1 Relevance of Simple Shear Testing

Most naturally occurring or artificially placed soil deposits have increasing stiffness with depth. Seismic shaking in such soil deposits of can be idealized as vertically-propagating, horizontally-polarized (VH) shear waves (Kramer 1996). Seismic VH shear waves subject the soil column to: (1) cyclic simple shear of rapidly fluctuating magnitude and direction on the horizontal plane; (2) multidirectional (three dimensional) loading; and (3) a smooth and continuous rotation of the principal stress directions. Figure 2-1 depicts the stress conditions in the free-field and under a structure prior to and during seismic loading. In the presence of a structure or a slope, the soil is subjected to an initial static shear stress in addition to the overburden stress (Figure 2-1b and d).

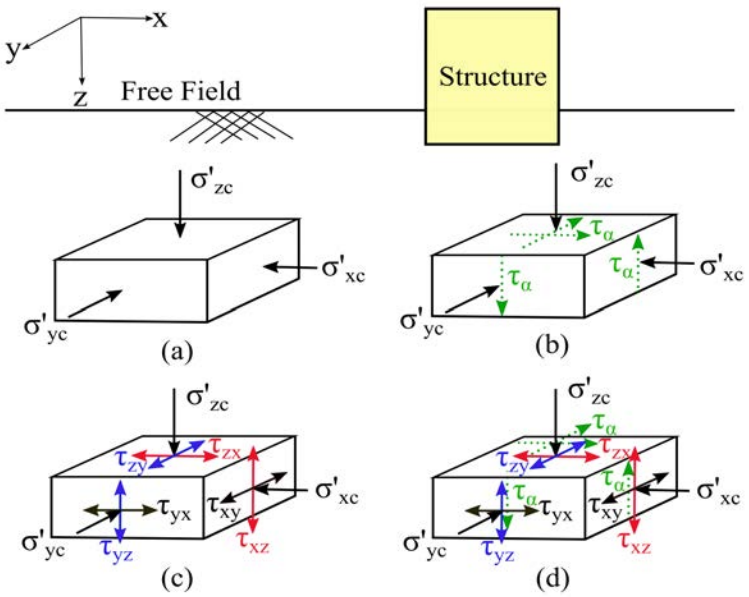

Figure 2-1 Normal and shear stresses on a soil element: (a) in free-field; (b) under or near a structure; (c) in free-field during cyclic loading; and (d) under or near a structure during cyclic loading. (Note: σ'_{zc}, σ'_{xc}, σ'_{yc} = consolidation normal stress on horizontal (z) and vertical (x and y) planes, respectively. Stress σ'_{zc} also denoted as σ'_{vc} in the text and figures. τ_α (or τ_c) = consolidation (static) shear stress on horizontal plane; τ_{ij} = cyclic shear stress on the i-plane acting in the j-direction, e.g., τ_{xy} = cyclic shear stress acting on the vertical x-plane in the y- direction).

To obtain reliable results for seismic design or in developing soil constitutive models, a laboratory shear device should be able to replicate the in-situ state of stress prior to and during shear, including the initial static shear applied in any required direction. Three devices are commonly used for element level testing of soils under cyclic loads in the laboratory: (1) cyclic triaxial; (2) direct simple shear (DSS); and (3) torsional shear (TS). The cyclic triaxial device is widely available and has established testing procedures and a large testing database; however, it causes an unrealistic, abrupt 90° change in the direction of principal stresses during shear. In contrast, the direct simple shear (DSS) or torsional shear (TS) devices can apply realistic in situ cyclic simple shear with a gradual rotation of principal stress directions.

In this study, the DSS was selected over the TS device primarily because the DSS specimen geometry easily accommodates bidirectional loading (Kammerer 2002). The DSS loading also simulates stress conditions under an embankment (Terzaghi et al. 1996), traffic loading (Shaw and Brown 1986), offshore structures subjected to wave loading (Franke et al. 1979; DeGroot et al. 1993) and next to an axially loaded pile (Randolph and Wroth 1981). The DSS device has been used extensively in geotechnical engineering to characterize dynamic soil behavior including stress-strain relationships, cyclic shear strength, porewater pressure (PWP) generation, volumetric strains and deformation patterns under unidirectional (e.g., Silver and Seed 1971; Youd 1972a; DeGroot et al. 1993; Duku et al. 2008; Yee et al. 2013; Lasley 2016; Vucetic and Mortezaie 2015) and bidirectional shear (e.g., Ishihara and Yamazaki 1980; Ishihara and Yoshimine 1992; Boulanger et al. 1993; DeGroot et al. 1993; Kammerer 2002; Rutherford 2012; Rudolph et al. 2014).

2.2 Previous Element Testing of Coarse-grained Soil under Cyclic Simple Shear

Naturally deposited or fill sands can experience considerable volumetric compression when subjected to repeated loading cycles (Youd 1972a; Ishihara and Yoshimine 1992; Duku et al. 2008). Depending on the permeability, saturation, and drainage boundary conditions of the deposit, the volume change has been attributed to: (1) vibration-induced compression in dry sands subjected to drained shaking (Silver and Seed 1971; Youd 1972a); or (2) reconsolidation due to post-cyclic dissipation of excess PWP in saturated sands subjected to undrained shaking (Ishihara and Yoshimine 1992; Wu 2002). However, in the field, sands may be partially drained or partially saturated, in which case a combination of compression and reconsolidation settlement occurs during seismic loading (Shahien 1998). The following section summarizes available element tests in the literature for assessing volumetric strain under unidirectional and multidirectional loading. The primary aim is to identify the parameters that govern volumetric strain during cyclic shear.

2.2.1 Unidirectional cyclic direct simple shear tests

Whitman and Ortigosa (1969) conducted shaking table tests on sands under varying vertical accelerations. It was observed that vertical accelerations less than 1g do not cause appreciable soil settlement. Assuming the field vertical acceleration is unlikely to exceed 1g, it was concluded that the effect of the vertical component of seismic loads can be neglected in deformation analysis.

Silver and Seed (1969, 1971) used an NGI-type DSS apparatus to conduct strain-controlled tests on a dry silica no. 20 sand, commercially available from Silica Sand Co. Cyclic shear strains (γ_c) ranging from 0.01 - 0.50 % were applied at a frequency of 1.0 Hz for 300 cycles. Medium dense to dense sands of relative densities (D_R) 45 - 80 % were tested at consolidation vertical stresses (σ'_{vo}) of 24 kPa - 192 kPa. Volumetric strain was found to increase with γ_c and number of cycles, and decrease with increasing D_R (Figure 2-2). The ε_v - γ_c relationship was observed to be independent of σ'_{vo} at γ_c > 0.05 %. However, it was observed that the threshold shear strain (minimum shear stain required to induce volumetric strain), increased with increasing σ'_{vo}.

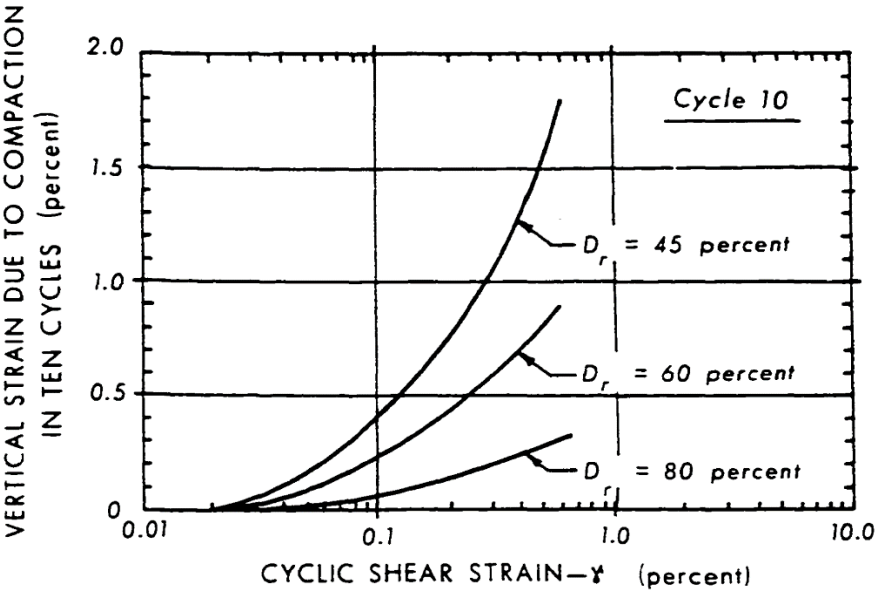

Figure 2-2 Effect of relative density and cyclic shear strain amplitude on volumetric strain at the end of 10 drained loading cycles (from Silver and Seed 1969, 1971).

Youd (1972a) conducted drained strain-controlled cyclic simple shear tests on saturated specimens of Ottawa sand (G_s = 2:65; e_{min} = 0:484; e_{max} = 0:752; ASTM D2049-69). An NGI-type simple shear apparatus was used to apply cyclic shear strains of 0.1 % to 9.0 % for up to 150,000 cycles, and σ'_{vo} ranged from 4.8 kPa to 192 kPa. The sample caps had porous discs to allow testing of saturated specimens. The specimens were prepared by dry pluviation into a wire-reinforced latex membrane. Youd (1972a) stated that specimens confined with wire reinforced membranes might have irregular deformation at the boundaries. To check this, Youd (1972a) plotted profiles of the boundaries and illustrated that the deformed boundary shapes closely approximate a true simple shear condition.

Each specimen underwent contraction followed by dilation in each loading cycle. The contraction – dilation cycles resulted in a net contractive response of the sand (Figure 2-3). The investigation by Youd (1972a) confirmed the findings by Silver and Seed (1971), additionally demonstrating that the settlements recorded in drained simple shear tests are: (1) identical for dry and saturated sands; and (2) frequency independent (for a frequency range of 0.17 - 1.92Hz; see Figure 2-4).

Youd (1972b) studied the effect of sample preparation on Ottawa C -109 sand using two different methods: (1) dry pluviation followed by table vibrations with the handle of a screwdriver; and (2) dry pluviation followed by tapping and drained shearing in an NGI-type DSS apparatus. Sand specimens were prepared to void ratios (e) of 0.51 using these two methods. Cyclic shear strains of 0.03 – 1 % were applied at σ'_{vo} = 50 kPa. It was observed that the volumetric strain in the soil was markedly influenced by the applied number of drained pre-straining (i.e., manual table vibration) cycles. For instance, despite being at the same void ratio (or density), the specimen with no pre-shearing accumulated about two orders of magnitude larger volumetric compression than the specimen with 5000 cycles of drained pre-straining history.

Pyke et al. (1975) conducted drained unidirectional strain-controlled cyclic DSS tests on well-graded clayey sand (SC) specimens in the device previously used by Silver and Seed (1969, 1971). The SC specimens were obtained from the Jensen Filtration Plant site and subjected to shear strains ranging from 0.1 to 0.4 % and σ'_{vo} = 40 – 180 kPa. The specimens were confined using wire

reinforced membranes and tested at the average field dry density and water content. Similar to the results from the clean sand tested by Silver and Seed (1969, 1971), the vertical settlement of the SC at a given loading cycle was independent of σ'_{vo}, inversely related to relative density, and directly related to shear strain amplitude. Pyke et al. (1975) also noted that the settlements computed using the results of the unidirectional simple shear tests were approximately 1/3 of the observed field settlement of 10 cm (4 in) induced at the Jensen Filtration Plant site by the San Fernando 1971 earthquake. The difference between the laboratory and field deformations was attributed to the effect of multi-directional shaking. To investigate the effect of multidirectional loads on volumetric compression, Pyke et al. (1975) conducted a series of stress-controlled shake table tests, described in the following section on multidirectional simple shear tests.

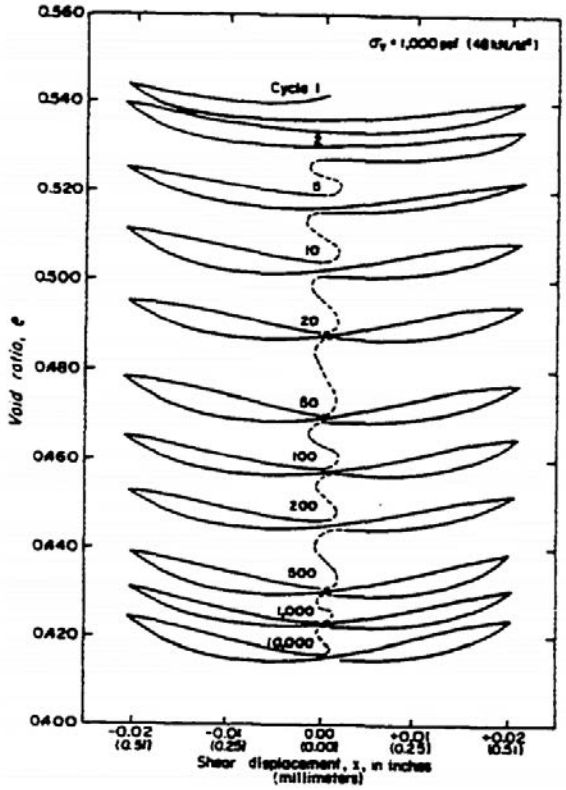

Figure 2-3 Void ratio versus shear displacement showing contraction – dilation cycles in dense (D_R 78 %) Ottawa C – 109 sand (from Youd 1972a).

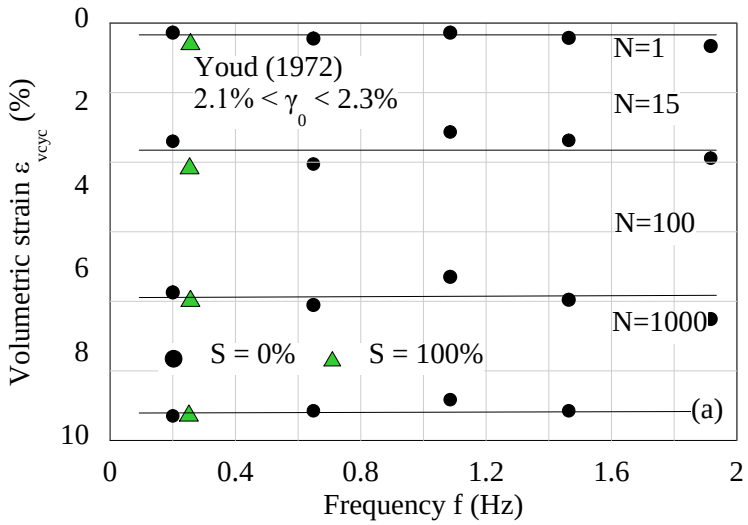

Figure 2-4 Results showing negligible effect of saturation and cyclic loading frequency (0.17 - 1.92 Hz) on volumetric strain of dense (D_R 78 %) Ottawa C – 109 sand (after Youd 1972a).

In the previously described research (see Figure 2-2), there exists a shear strain below which vertical compression does not occur. This threshold shear strain (γ_{tv}) was first clearly defined by Dobry et al. (1981, 1982) as the cyclic shear strain amplitude below which there is no appreciable change in soil structure and thus no permanent volumetric compression or PWP development. To characterize γ_{tv}, Vucetic (1994) examined available laboratory volumetric strain (Silver and Seed 1971; Youd 1972a; Pyke et al. 1975) and PWP data. It was observed that γ_{tv} increases as particle size decreases and as plasticity index increases. The threshold shear strain for volumetric compression in coarse-grained soil was found to vary from 0.01 – 0.03 %. Later, Hsu and Vucetic (2004) conducted multi-stage cyclic strain-controlled DSS tests on seven clean sands and clays to characterize γ_{tv} for different soils. The results of these tests corroborate the earlier observation of Vucetic (1994), namely that below the threshold strain there is negligible inelastic change in the soil fabric. No definite trend was found between γ_{tv} and saturation or effective vertical stress.

Wu (2002) conducted an extensive series of unidirectional, saturated, undrained, stress-controlled cyclic DSS tests on Monterey No. 0/30 sand of D_R ranging from 35 – 80 %, consolidated to an effective vertical stress of 40 – 180 kPa, with or without the presence of a static shear stress. In the analysis of reconsolidation volumetric strain, data from a bidirectional study by Kammerer (2002) also was considered. It was observed that the reconsolidation volumetric strain is primarily a function of relative density, effective vertical stress, and the cyclic stress ratio. Based on 36 field case histories of liquefaction induced lateral displacements, Wu (2002) interpreted that, for sloping ground, settlements were affected only when the lateral displacement was greater than 0.3 m. Based on the framework by Tokimatsu and Seed (1987) and Shamoto et al. (1998) (both described later), Wu (2002) proposed an updated method to estimate shaking-induced settlement.

Whang et al. (2004) conducted drained, strain-controlled cyclic simple shear tests on cylindrical specimens with D/H (diameter/height) ratios of 4.43, confined with a wire reinforced membrane. The study focused on compacted fills, thus specimens were prepared by compacting with a Harvard mini-compactor in two lifts. All the samples were subjected to an effective vertical stress of 101.3 kPa, and sheared with a cyclic shear strain varying from 0.1 - 1 % at a frequency of 1.0 Hz. Four different soils classified (using the Unified Soil Classification System, USCS) as CL (PI = 15; LL = 33; FC = 54 %), SC (PI = 14; LL = 35; FC = 40 %), SC (PI = 9; LL = 20; FC = 48 %) and SM (PI =

2; LL = 27; FC = 44 %) were tested. The soils in the study by Whang et al. (2004) have fines contents above the threshold value defined by Thevanayagam and Mohan (2000), such that the fines influence the mechanical response of the soil. Increasing relative compaction of the soil was observed to produce smaller volumetric strains, consistent with the observations of Pyke et al. (1975).

Whang et al. (2004) observed that the soil behavior was influenced by the degree of saturation only when the soil had plastic fines, with lower saturation causing higher volumetric strains in soils of relative compaction (RC) 88 to 92 %. Whang et al. (2004) hypothesized that this was the effect of void spaces in clods of the plastic fines in soils. In the presence of plastic fines at low saturation, the fines were said to form lumps or clods in the soil structure. These "clods" had high inter-clod void ratios and resisted compaction, leading to a looser soil and consequently more settlements. Higher saturation and compaction energy were thought to break down this clod structure, leading to lower overall void spaces and thus causing lower settlements, at the same relative compaction. Soils with non-plastic fines were reported to be negligibly influenced by saturation. Whang et al. (2004) suggested compacting plastic fills at wetter side of optimum moisture content to at least 90 % modified Proctor relative compaction to limit clod formation. Volumetric strains in the silty and clayey sand specimens were found to be lower than that of clean sands at the same RC.

Whang et al. (2005) studied the effect of density, saturation, and fines content on the drained volumetric strain of non-plastic silty sands. The silt-sized particles used was a non-plastic rock flour. In contrast to the finding for natural silty sands with plastic fines (Whang et al. 2004), it was observed that the volumetric compression of the silty sands was higher than that of the clean sand at the same relative compaction. Dry specimens and specimens with saturation ratio S_r = 60 % yielded more volumetric compression than specimens at S_r = 30 %. The authors attributed this to the presence of high matric suction at intermediate saturation levels.

To quantify the effect of post-compaction aging on volumetric compression, Duku et al. (2006) tested four soils with FC varying from 31 – 75 %, PL from 0 – 32, and LL from 28 – 58. Experiments were conducted in the UCLA DSS device, and the consolidation stress was applied for varying amounts of time. The non-plastic silty sand was found to be unaffected by the seating time. In contrast, for the low to moderate plasticity fine-grained soils, volumetric compression was observed to decrease by 50 – 70 % with a seating load time of 2 minutes to 2 hours.

Duku et al. (2008) studied the volumetric strains of sixteen clean sands under cyclic loads by conducting strain-controlled cyclic DSS with shear strains of 0.05 % to 1.0 %. Most of the tests were conducted at a frequency of 1.0 Hz, except for a smaller number of tests at 0.1 and 10 Hz, conducted to clarify the effect of frequency on volumetric compression. Samples were prepared by dry pluviation with vibratory compaction, tamping and kneading to relative densities of 45 – 80 %. The specimens were consolidated to effective vertical stresses of 50 – 400 kPa. It was assumed that the wire reinforced membrane used for lateral restraint exhibited negligible distortion. Supporting the observations of Youd (1972a), it was found that volumetric strain was independent of the loading frequency for a range of 0.1 – 10 Hz (Figure 2-5).

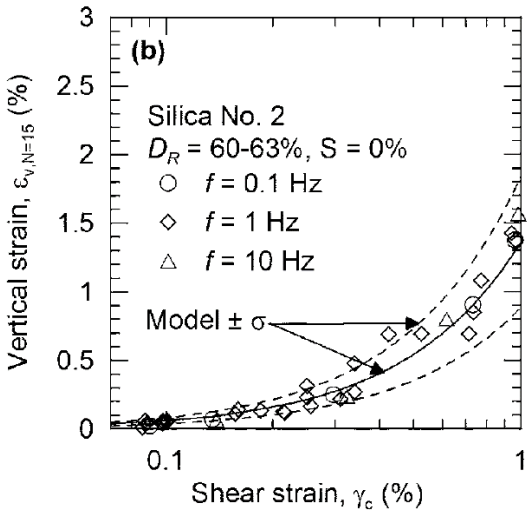

Figure 2-5 Results showing negligible effect of loading frequency (0.1 – 10 Hz) on volumetric strain at 15 loading cycles of medium dense (D_R 60 - 63 %) Silica No. 2 sand (from Duku et al. 2008).

It was observed that D_R and γ_c are the primary factors that affect seismic compression, similar to the aforementioned observations. Compositional factors like median particle size, uniformity coefficient, particle shape or angularity, fabric, mineralogy, void ratio breadth ($e - e_{min}$), and environmental factors including age and saturation were found to have negligible impact on the volumetric strains. Sands with overconsolidation ratios (OCR) of 1 to 4 were also tested by Duku et al. (2008). It was found that specimens with higher OCR exhibited lower volumetric compression at vertical stress of 100 kPa. However, at low overburden (50 kPa), OCR was observed to have negligible impact on volumetric strains. Duncan et al. (1991) observed that compacted fills are usually overconsolidated at 3 to 6 m depth owing to compaction-induced stresses, and normally consolidated at greater depths (Duku et al. 2008). Thus, Duku et al. (2008) concluded that the effect of stress history (OCR) is inconsequential for compacted sand fills. Higher effective vertical stress caused lower volumetric strains. Duku et al. (2008) proposed a new semi-empirical material model for estimation of volumetric strain that will be discussed in a later section.

Yee et al. (2013) supplemented the volumetric strain model developed by Duku et al. (2008) to include the effect of low plasticity fines (PI < 10) in the prediction of seismic compressibility of sands. To expand the Duku et al. (2008) database, Yee et al. (2013) conducted strain-controlled cyclic simple shear tests on three natural sands, separated from and then mixed with their natural fines to have fines content varying from 0 - 100 %. Seismic compression was found to increase with γ_c and number of cycles. Fines content greater than 10 % was observed to reduce volumetric strains. As previously observed by Pyke et al. (1975) and Whang (2004), an increase in relative compaction decreased volumetric compression. A modified form of the Duku et al. (2008) volumetric strain model, proposed by Yee et al. (2013), is presented later.

The most recent experimental study for characterizing volumetric compression in dry sands was conducted by Lasley et al. (2016). Specimens were tested in unidirectional DSS under both cyclic loads and earthquake time histories simulating the strain time histories at various layers in a soil column obtained from site response analysis. The tested D_R ranged from 30 % - 80 %, consolidated inside stacked rings to effective vertical stress of 50 – 250 kPa, and cyclically sheared at strains of 0.2 – 1.0 %. A new semi-empirical model, discussed later, was proposed based on these tests.

2.2.2 Summary observations from previous unidirectional DSS studies

This section summarizes observations from the previously described unidirectional DSS testing literature. These observations primarily pertain to clean sands or sands with less than 48 % plastic or non-plastic fines.

1. Volumetric strain, drained and reconsolidation, increases with increases in shear strain amplitude and number of loading cycles.
2. There exists a threshold shear strain, typically 0.01 – 0.03 %, below which, drained volumetric strain or porewater pressure generation does not occur.
3. Volumetric strain, drained and reconsolidation, decreases with increases in soil density.
4. Loading frequency in the range of 0.1 – 10 Hz does not affect drained volumetric strain of clean sands.
5. Drained pre-shearing reduces the drained volumetric strain of sand.
6. Drained volumetric strain decreases with increases in overburden and overconsolidation.
7. Vertical acceleration of less than 1g has a negligible impact on volumetric strain.
8. Volumetric strain in clean coarse-grained soil is independent of the saturation as indicated by drained tests by Youd (1972a) and Duku et al. (2008). Whang et al. (2004) reported that saturation affects the volumetric strain in the presence of plastic fines. However, as later described under the empirical methods section, Ghayoomi et al. (2013) conducted centrifuge tests on clean sands and observed that matric suction in partially saturated coarse-grained soil decreases the volumetric strain.
9. At the same relative compaction, fines content of greater than 10% reduces volumetric strain.

These points are further discussed in Section 2.3.

2.2.3 Multidirectional cyclic direct simple shear tests

Pyke et al. (1975) pioneered the study of the effect of multi-directional loading on the behavior of clean sands. Pyke et al. (1975) conducted both uni- and bi-directional stress-controlled tests on dry samples of Monterey No. 0 sand (D_{50} - 0.4mm) using two shaking tables, one mounted on top of the other. Dry pluviation from a spreader box was used for sample preparation. The circular sand samples, confined with a latex membrane under an internally applied vacuum, were 76 mm (3 in) thick and had sloping slides, with a diameter of 0.91 m (3 ft) at the top and 1.22 m (4 ft) at the base. A fully frictional base was created by gluing sand particles to the top of the table under the sample. Circular motions with randomly generated irregularities were used. It was observed that the settlement due to bidirectional shaking was approximately equal to the sum of the settlements caused by each of the components when applied separately (Figure 2-6; Figure 2-7a). While vertical table accelerations alone produced negligible settlements for less than 1g shaking (0.8g) up to 60 cycles, when combined with the horizontal accelerations (0.8g vertical table acceleration), they resulted in roughly 50 % greater deformation than that caused by the horizontal loads alone [e.g., settlements at cyclic stress ratio of 0.3; Figure 2-7b].

The first work that tested saturated sand under multi-directional cyclic simple shear was the experimental program conducted by Ishihara and Yamazaki (1980) at the University of Tokyo. They observed that to induce the same shear strain in a sand sample, a bidirectional cyclic shear stress of about 70 % of the unidirectional cyclic shear stress is required. Later, Nagase and Ishihara (1988), using the same simple shear device as Ishihara and Yamazaki (1980), conducted both unidirectional and multidirectional undrained stress-controlled simple shear tests on saturated specimens of Fuji river sand (G_s = 2.73; D_{50} = 0.40 mm; C_u = 3.16; e_{min} = 0.529; e_{max} = 1.064). The samples were prepared by water pluviation into a rubber membrane surrounded by teflon coated

stacked plates at D_R = 47 %, 73 % and 93 %, and then sheared using broadband motions. It was observed that the reconsolidation volumetric strain was a function of the maximum shear strain amplitude and D_R. Multidirectional loading was not observed to have an impact on reconsolidation volumetric strain as illustrated in Figure 2-8. Ishihara and Yoshimine (1992) proposed a graphical estimate for reconsolidation volumetric strain based on the experiments conducted by Nagase and Ishihara (1988). This semi-empirical model is discussed later.

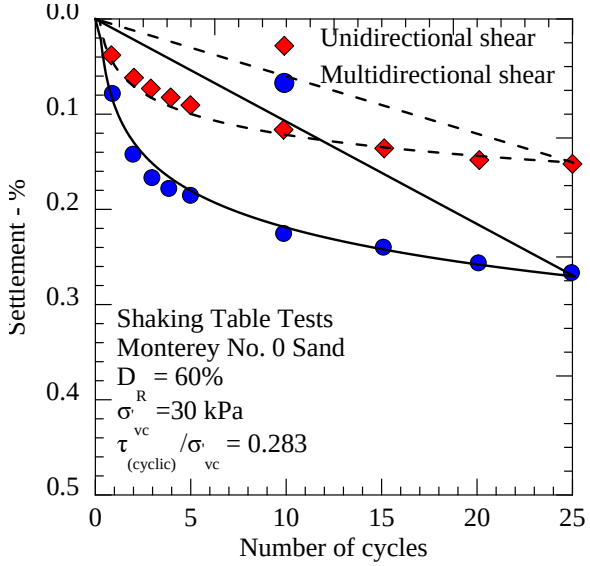

Figure 2-6 Settlement of Monterey No. 0 sand under unidirectional and multidirectional shake table tests (after Pyke et al. 1975).

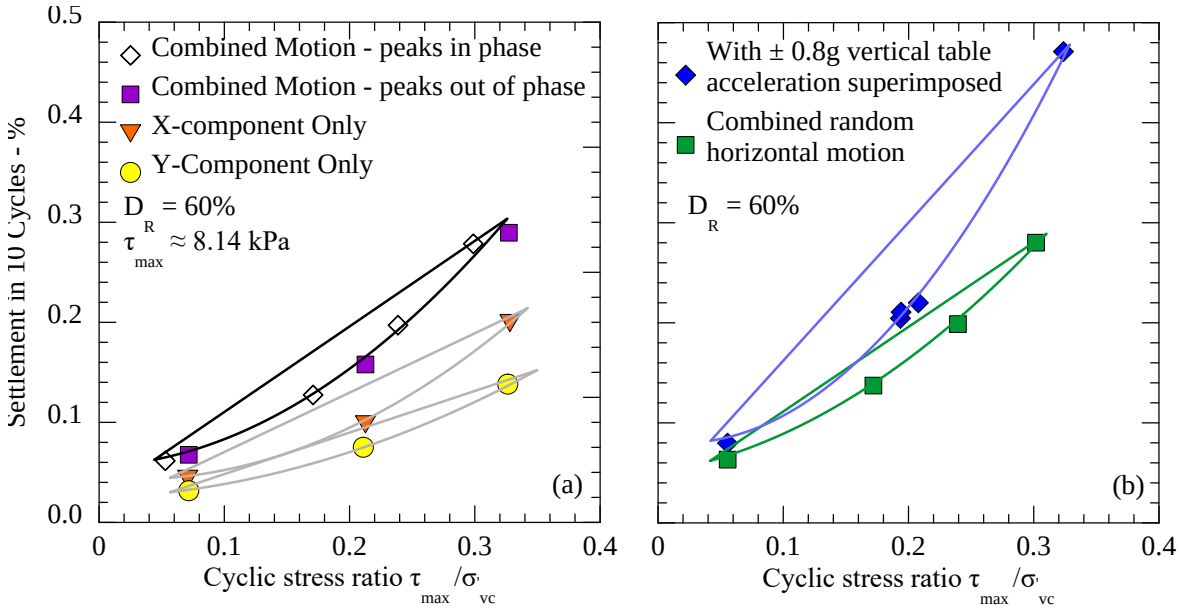

Figure 2-7 Settlement of Monterey No. 0 sand in shake table tests as a function of cyclic stress ratio: (a) unidirectional and multidirectional tests; (b) bidirectional tests with and without vertical acceleration (after Pyke et al. 1975).

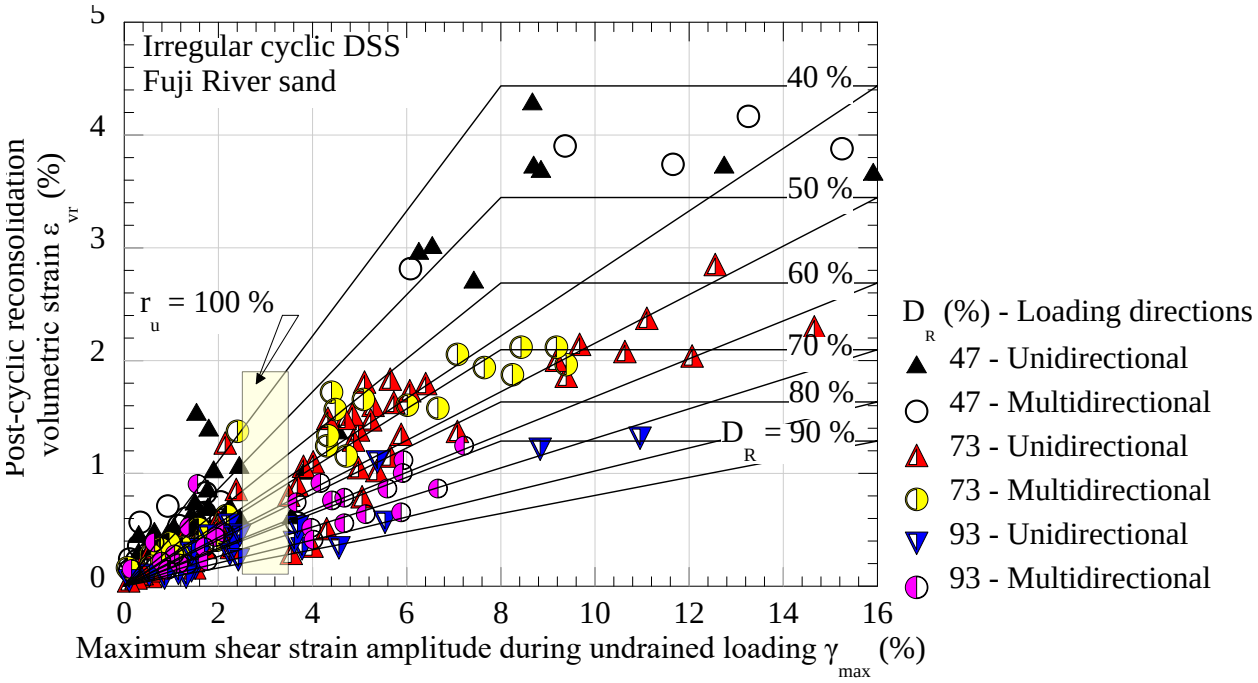

Figure 2-8 Post-cyclic (reconsolidation) volumetric strain of clean Fuji River sand for different maximum induced shear strains and relative densities from unidirectional and bidirectional undrained stress-controlled cyclic simple shear tests using irregular time histories (after Ishihara and Yoshimine 1992).

Fukutake and Matsuoka (1989) conducted multidirectional drained simple shear tests on Toyoura sand and observed a distinctive relationship between cumulative shear strain and volumetric strain. Resultant shear strain (Γ) and cumulative shear strain (G^*) were defined by Eqn. (2-1) and (2-2), respectively (Fukutake and Matsuoka 1989).

$$\Gamma = \sqrt{\gamma^2{}_x + \gamma^2{}_y} \tag{2-1}$$

$$G^* = \sum \Delta G^* = \sum \sqrt{\Delta\gamma^2{}_x + \Delta\gamma^2{}_y} \tag{2-2}$$

where γ_x and γ_y are shear strains in the horizontal, mutually perpendicular x and y directions. Together, Γ and G^* can be used to completely define a circular strain path. The relation among Γ, G^*, and drained volumetric strain (denoted as ε^s_z) obtained by Fukutake and Matsuoka (1989) is illustrated in Figure 2-9. As illustrated in the figure, longer strain paths (indicated by G^*) result in larger volumetric strains.

Kammerer (2002) conducted a series of bidirectional cyclic DSS tests on saturated specimens of Monterey No. 0 sand at D_R = 45 - 85 % and consolidated to an effective vertical stress of 80 kPa. Kammerer (2002) provided insight into the effects of stress reversal and stress rotation that occur during multidirectional loading on saturated undrained sand behavior and porewater pressure generation. Kammerer (2002) also used Eqn. (2-1) to define shear strain in multidirectional simple shear tests. Some reconsolidation volumetric strain measurements by Kammerer (2002) were used by Wu and Seed (2004) for comparing unidirectional and bidirectional reconsolidation volumetric strain.

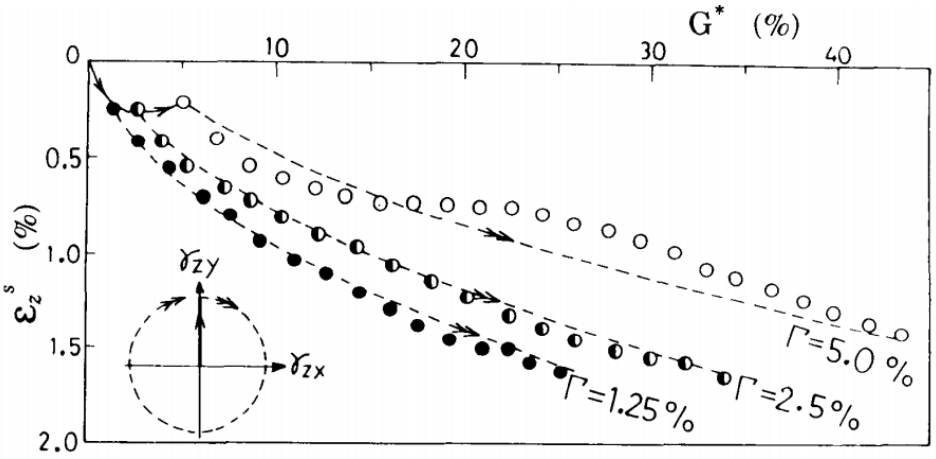

Figure 2-9 Drained volumetric strain of clean Toyoura sand for different resultant shear strains (Γ) as a function of cumulative shear strain (G*) from bidirectional circular drained strain-controlled cyclic simple shear tests (from Fukutake and Matsuoka 1989).

Matsuda et al. (2011) conducted strain controlled constant volume multidirectional simple shear tests on Toyoura sand with different cyclic shear directions (varying phase angle θ between the x and y strain cycle inputs). Specimens were tested at relative densities of 70 and 90 % and consolidated to an effective vertical stress of 49 kPa. It was again concluded that the shear strain amplitude was the governing factor in porewater pressure generation and reconsolidation vertical strain. It was also observed that higher phase angles generated higher porewater pressures.

The studies described here demonstrate the importance of the effect of multidirectional loading. The majority of the research on multidirectional testing has focused on clean sands or sands that are susceptible to liquefaction. Relevant multidirectional data on dense dry sands or sands with plastic and non-plastic fines are limited.

2.2.4 Summary observations from previous multidirectional DSS studies

This section summarizes observations from the described bidirectional DSS testing literature. These observations pertain to clean sands or sands with less than 48% plastic or non-plastic fines.

1. As with unidirectional tests, higher the shear strain amplitude and lower the density, higher the volumetric strain.
2. Drained bidirectional volumetric strain is approximately equal to twice the unidirectional volumetric strain.
3. To induce the same shear strain in a sand specimen, a bidirectional cyclic shear stress only 70 % of the unidirectional cyclic shear stress is required.
4. An upper limit of shear strain of about 8 % was observed by Ishihara and Yoshimine (1992), for which further increases in cyclic shear strain caused no further increase in reconsolidation volumetric strain.
5. Higher the phase difference between mutually perpendicular horizontal motions, higher the porewater pressure generation, and subsequently, higher the reconsolidation volumetric strain.
6. Stress rotation and reversal plays a significant role in the development of porewater pressure and volumetric strain.

7. While vertical acceleration alone does not significantly affect volumetric strain below 1g, when it is superimposed with horizontal accelerations, it can cause 50% increase in the volumetric strain.
8. Bidirectional loading possibly can be quantified by the vector sum or stresses and strains, and cumulative shear strain.

These points are further discussed under the factors affecting volumetric strain section.

2.3 Summary of Factors Affecting Volumetric Strain in Coarse-grained Soil

Based on existing laboratory element tests, the factors that affect volumetric strain under cyclic loading are summarized here for drained, undrained, and partially drained loading. The factors are divided into: (1) grain characteristics (represented by median particle size, uniformity coefficient and angularity); (2) state characteristics (represented by soil fabric or sample preparation, relative density, shear wave velocity, saturation, effective vertical stress, overconsolidation ratio and initial static shear); and (3) load characteristics (represented by number of loading directions, frequency, intensity – shear strain or cyclic stress ratio, and duration).

2.3.1 Drained loading

2.3.1.1 Grain characteristics

Compiling the data from Silver and Seed (1969, 1971) and Pyke et al. (1975), Shahien (1998) noted that sub-angular sands are about 1.5 times more compressible than sub-rounded ones when prepared to the same relative density (Figure 2-10). In contrast, Duku et al. (2008) observed that grain and state characteristics like median particle size, uniformity coefficient, particle shape, fabric, mineralogy, void ratio breadth ($e - e_{min}$), and environmental factors including age and saturation have negligible impact on the volumetric strains for 16 different sands. Duku et al. (2006) observed that non-plastic silty sand is unaffected by the vertical stress seating time. In contrast, for sands with moderately plastic fines, volumetric strain was observed to decrease by 50 – 70 % with an increment in seating time of 2 minutes to 2 hours. Thus, aged sands with plastic fines appear to be less compressible than unaged sands with plastic fines. Since seating time is a load factor, it is also included under the load characteristics subsection.

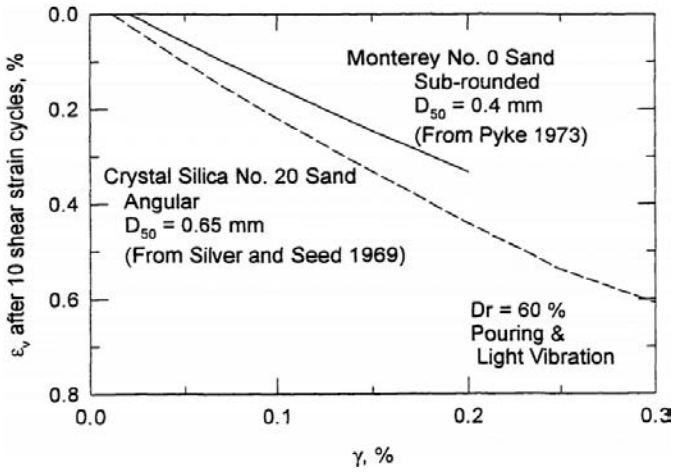

Figure 2-10 Effect of grain characteristics: angularity and median particle size on volumetric strain of dry sands (from Shahien 1998).

2.3.1.2 State characteristics

Numerous laboratory studies have shown that soil fabric can significantly affect the static and dynamic response of sands including stress-strain relationships, porewater pressure generation, cyclic shear strength and volumetric strain (Oda 1972; Ladd 1974; Mulilis et al. 1977; Tatsuoka 1979; Tatsuoka et al. 1986; Vaid and Negusey 1988; Vaid et al. 1999; Amini and Qi 2000; Yamamuro and Wood 2004; Wood et al. 2008; Sadrekarimi and Olson 2012; Sze and Yang 2014). Results from Seed et al. (1977) and Mulilis et al. (1977) illustrating the effect of soil fabric on the liquefaction resistance of Monterey No. 0 sand are shown in Figure 2-11. Drained pre-shaking or application of vibrations alters the soil fabric to increase liquefaction resistance or soil stiffness. Similarly, for a sand at relative density of 58 to 65 %, Yee et al. (2013) noted that volumetric strain from drained simple shear tests is lower in specimens that have prior cyclic loading history, as compared to freshly reconstituted "virgin" specimens prepared by vibratory methods or compaction (Figure 2-12). While there have been no systematic studies on the effect of specimen preparation on volumetric strain, liquefaction-related studies indicate that specimens prepared by vibratory methods are stiffer than specimens prepared by pluviation (air or water), and thus settlements in the latter can be expected to be larger than the former.

It was consistently observed in all previous experimental research that higher density, higher relative compaction, or higher shear wave velocity in clean, silty and clayey sands yielded lower volumetric strain. An example of this behavior is presented in Figure 2-2 based on Silver and Seed (1969, 1971). Saturation was found to have a negligible effect on the volumetric compression of clean and non-plastic silty sands by Youd (1972a; Figure 2-4), Duku et al. (2008) and Yee et al. (2013). However, for sands with low plasticity fines (PI < 10 and FC > 10 %), both Whang et al. (2005) and Yee et al. (2013) observed that volumetric strains at intermediate saturations (S_r = 30 %) were lower due to matric suction, while no distinct saturation effect was observed for S_r less than 10 % or greater than 60 %.

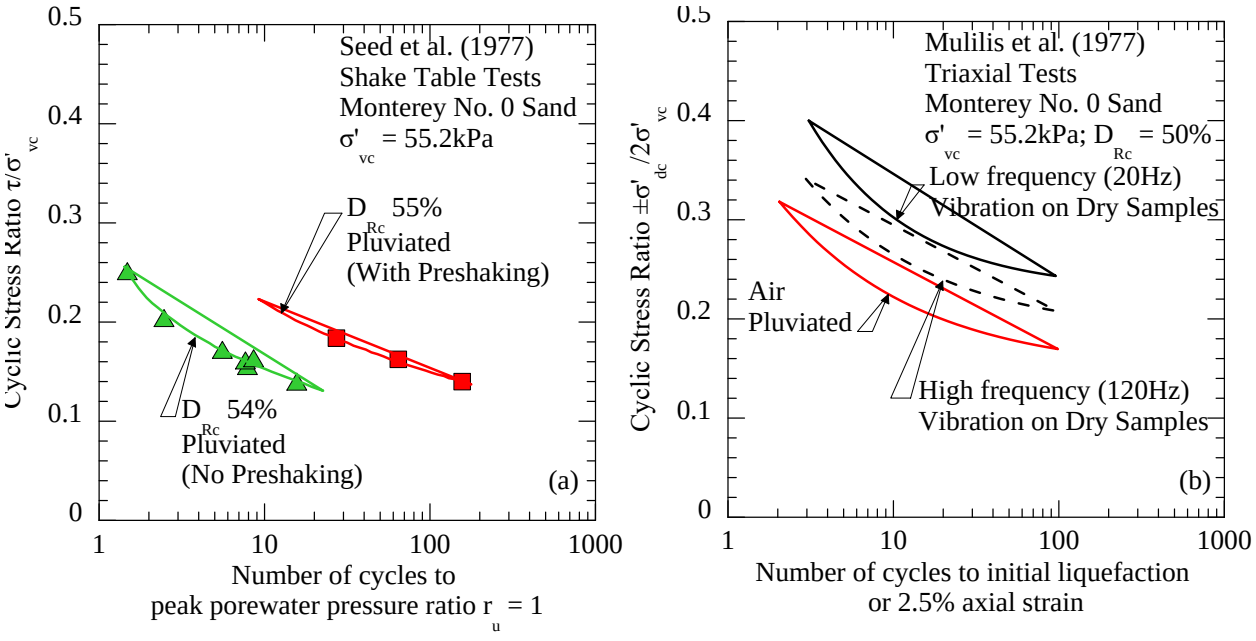

Figure 2-11 Effect of (a) pre-shaking (after Seed et al. 1977) and (b) specimen preparation method on liquefaction resistance (after Mulilis et al. 1977).

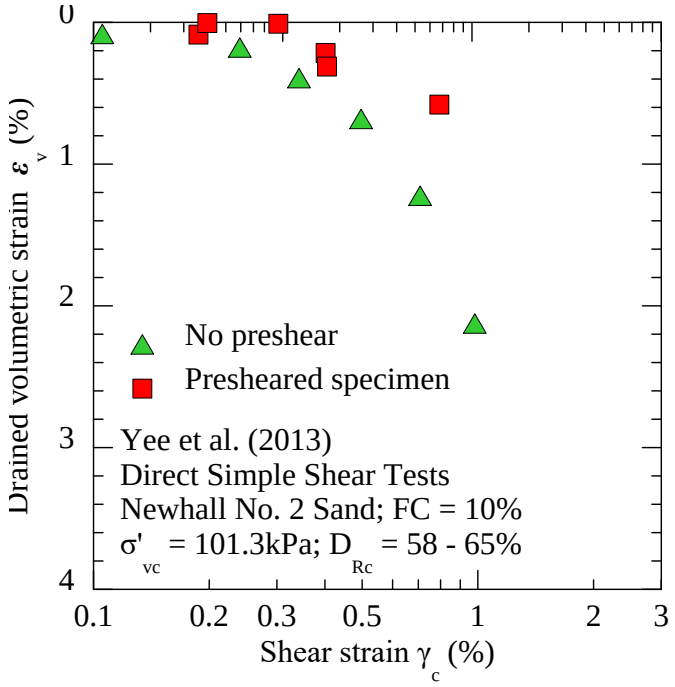

Figure 2-12 Effect of specimen preparation method (and preshearing) on drained volumetric strain (after Yee et al. 2013).

It is interesting to note that the effects of effective vertical stress were considered negligible by Silver and Seed (1969, 1971), Youd (1972) and Pyke et al. (1975), while research by Duku et al. (2008), Yee et al. (2013) and Lasley et al. (2016) illustrated the strong effect of effective vertical stress on volumetric strains induced by cyclic loading. Higher OCR and higher effective vertical stress was observed to decrease volumetric strain. There has been no explicit study examining the effect of initial static shear on drained volumetric strain; however, based on the work of Wu (2002) and Kammerer (2002), it can be concluded that permanent lateral deformations of sloping ground due to cyclic loading will probably increase volumetric strain.

2.3.1.3 Load characteristics

Loading frequency was found to have a negligible effect on volumetric strain by Youd (1972a) and Duku et al. (2008) for a frequency range of 0.17 - 10 Hz (Figure 2-4; Figure 2-5). It was consistently observed that higher shear strain amplitude and number of loading cycles generated larger volumetric strain (Figure 2-2; Figure 2-3), although the change in volumetric strain decreases as the number of cycles increases. Pyke et al. (1975) observed that settlements under bidirectional shaking is equal to the sum of settlements due to each unidirectional shaking component. Whitman and Ortigosa (1969) and Pyke et al. (1975) observed that vertical accelerations of less than 1g alone produced negligible settlements for shaking up to 60 cycles. However, Pyke et al. (1975) noted that when combined with the horizontal accelerations, vertical table accelerations of 0.8g resulted in roughly 50 % greater deformation than that caused by the horizontal loads alone. Increased seating time (i.e., aging due to secondary compression) was found to decrease drained volumetric strains in sands with plastic fines (Duku et al. 2006).

2.3.2 Undrained loading

Reconsolidation volumetric strain that follows undrained (or constant volume) loading is affected by most of the same parameters as drained loading. The primary factors found to affect reconsolidation

volumetric strain are relative density or shear wave velocity, the cyclic shear stress ratio and the maximum shear strain induced during undrained loading. Bidirectional loads were found to have a negligible impact on post-cyclic reconsolidation (Figure 2-8). In other words, reconsolidation settlements under unidirectional and bidirectional loads that induce the same shear strain are comparable; however, the cyclic stress required to cause the same strain level in bidirectional tests was observed to be 10 – 30 % less than that by unidirectional loads (Ishihara and Yamazaki 1980). This reduction was observed to be a function of relative density, and is further discussed in the section related to empirical models for volumetric strain. Increase in the phase difference between applied horizontal loads increase the porewater pressure developed, which then increases the post-cyclic settlement (Matsuda et al. 2011). Initial static shear stress was observed to increase settlement by 10 – 20 % when seismic loads caused more than 0.3 m of permanent lateral deformation based on 36 liquefaction-induced lateral displacement case histories (Wu 2002).

2.4 Free-field and near-field centrifuge tests of sands under unidirectional and multidirectional shaking

Centrifuge testing has been used to study static and dynamic geotechnical problems since the 1970s due to its better repeatability and lower costs compared to full-scale field tests. Similar to element tests, only a few free-field unidirectional centrifuge tests in which settlements were measured have been performed on saturated, dense sands (Adalier 1996; Elgamal et al. 2005; Montoya 2012) and only one series of free-field multidirectional tests have been performed on loose sands (Su 2005). These investigations provide insight into the volumetric strain response of coarse-grained soils to earthquake shaking. Similarly, soil-structure interaction induced volumetric strains have been increasingly studied in the last twenty years using only a limited number of unidirectional dynamic centrifuge tests (e.g., Liu and Dobry 1997; Dashti 2010), primarily performed on loose liquefiable sands and even fewer unidirectional tests on dense sands (e.g., Montoya 2012). All aforementioned centrifuge tests are summarized in Table 1 and tests description are given below.

2.4.1 Adalier (1996)

Adalier (1996), using centrifuge tests on a saturated 2-m thick Nevada sand on loose and dense models (e.g. D_R = 35 – 70 %), studied the effect of overconsolidation (OCR) on the liquefaction potential on level sand deposits. All models were subjected to a series of sinusoidal motions. Settlements were measured after each shaking event. For the normally consolidated dense model, D_R ~ 70% (OCR ~ 1), excess PWP ratios ranged from 0.35 to 0.96 through the profile, associated with an increase in average D_R from 70% to about 90% after three shaking events. Increasing OCR was shown to decrease settlements for all D_R tested in these experiments (Figure 2-13).

2.4.2 Elgamal et al. (2005)

Elgamal et al. (2005) summarized the dynamic response of a saturated very dense Nevada sand (D_R ~ 100%) performed on different model thickness varying from 5 to 20 m with PGA varying from 0.03 to 1.7g. One-dimensional (1D) shear-beam column numerical simulations were performed and showed good agreement with experiments results. Although this series of tests do not provide information on volumetric strains, it provides information on the shear behavior of dense sands that was used in this research to evaluate computed site response.

Table 2.1 Summary of available free-field (FF) and near-field (NF) centrifuge tests

Centrifuge Test	Sand	Dr(%)	Type	g level	References
Mitigation of Earthquake Induced Liquefaction Hazards	Nevada	70	FF	25	Adalier, K., (1996)
Seismic Response of Shallow Foundations on Liquefiable Saturated Sand	Nevada	52	NF	50	Liu, L., and Dobry, R., (1997)
Comprehensive Investigation of Nonlinear Site Response	Nevada	100	FF	9,18, 25, 37	T. Lai, A. Elgamal, Z. Yang, D. W. Wilson, and B. L. Kutter (2004)
Centrifuge Investigation on Sand Deposit and Sand Pile System under Multidirectional Earthquake Loading	Toyoura	40,50	FF	40	Su (2005)
Mechanisms of Seismically-Induced Settlement of Buildings with Shallow Foundations on Liquefiable Soil	Nevada	30 to 90	FF NF	55	J. Bray, S. Dashti (2010)
Bio-Mediated Soil Improvement and the Effect of Cementation on the Behavior, Improvement, and Performance of Sand	Ottawa	85	FF NF	50	Montoya (2012)

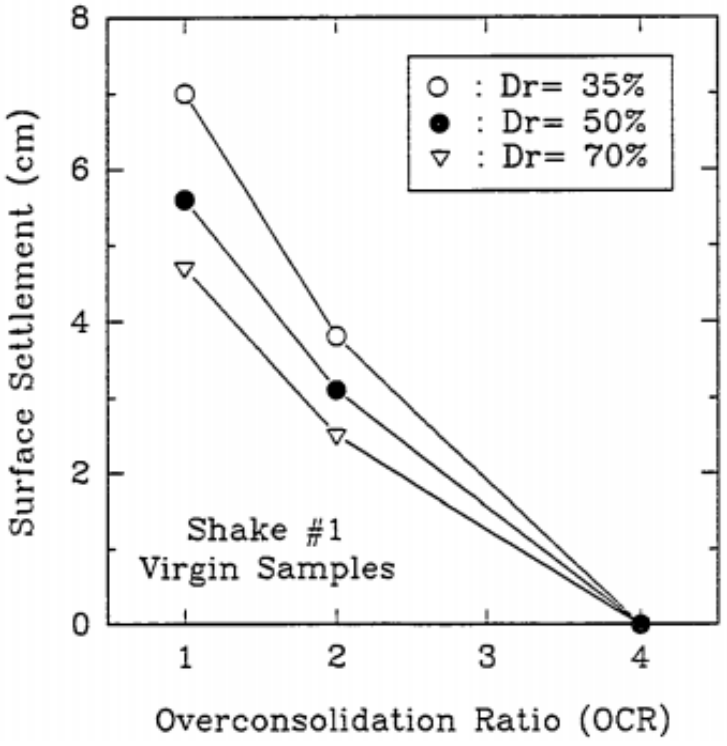

Figure 2-13 Surface settlements after first shaking events versus OCR (from Adalier 1996).

2.4.3 Su (2005)

Su (2005) studied the effect of multidirectional sinusoidal cyclic loading on PWP generation and settlements of a 16-m thick (prototype scale) uniform Toyoura sand (D_R ~ 40%). Su (2005) used both 1D and 2D cyclic loading to illustrate the importance of multidirectional loading on both excess PWP (Figure 2-14) and settlements. His results showed up to approximately 20% increase in Δu_{max} and 12% larger settlements under multidirectional shaking. This increase in excess PWP and settlements were much smaller than the values obtained by Pyke et al (1975).

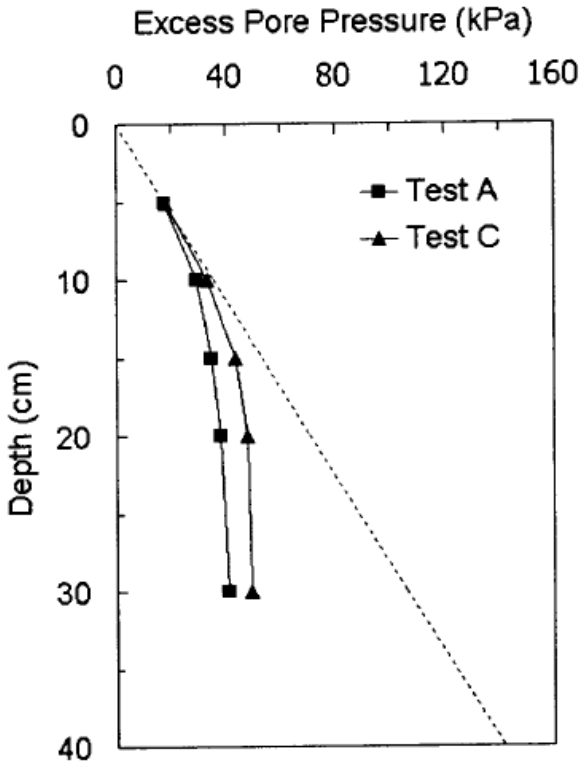

Figure 2-14 Maximum excess pore water pressures of a 16m (prototype scale) thick Toyoura sand (Dr~40%) under 1D (Test A) and 2D (Test C) loading (from Su 2005).

2.4.4 Dashti et al. (2010)

Dashti et al. (2010) performed a series of centrifuge tests on loose Nevada sand and proposed volumetric strain mechanisms in liquefiable soils. Dashti et al. (2010) showed that the normalization of building settlements by liquefiable soil thickness, which was based on Yoshimi and Tokimatsu (1977) and further developed in centrifuge tests by Liu and Dobry (1997) (Figure 2-15a), is not appropriate for thin liquefiable layers, as shown in Figure 2-15(b). Dashti et al. argued that the major source of building settlement resulted from ratcheting of the structure rather than solely volumetric strains of the soil. Dashti et al. (2010) describes this ratcheting as deviatoric strain, and suggested that dynamic rocking of the structure increased volumetric settlements. The building vertical settlements were three to eight times larger than the free-field settlements.

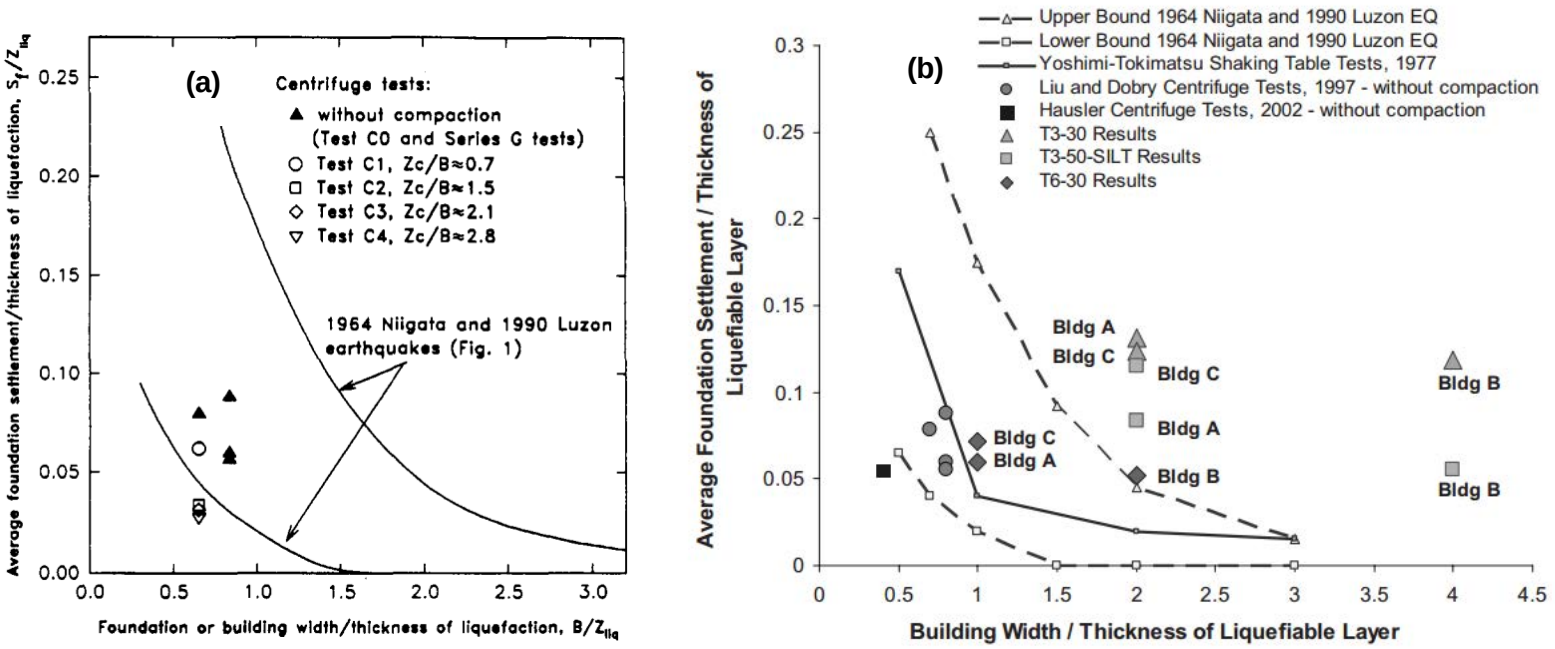

Figure 2-15 (a) Comparison between foundation/building width and foundation/building settlement, both normalized by thickness of liquefied layer, observed in centrifuge test series with field observations made following 1964 Niigata, Japan and 1990 Luzon Philippines earthquakes (from Liu and Dobry 1997); and (b) comparison of same parameters measured in another, more recent centrifuge test series with field observations (from Dashti et al. 2010).

2.4.5 Montoya (2012)

Montoya (2012) used centrifuge tests to study the effect of bio-mediated soil improvement for liquefaction mitigation purposes on the dynamic response of sands. The experimental program included free-field and near-field arrays on loose and dense non-treated sands (e.g., saturated Ottawa 50-70 sand with D_{Ro} ~ 85%). The near-field array included a single degree of freedom structure with a bearing pressure of ~100kPa. Building settlements were 30% to 100% greater than free-field settlements (Figure 2-16). Data from these series of tests are used in this research for developing both free-field and building semi-empirical volumetric strain models.

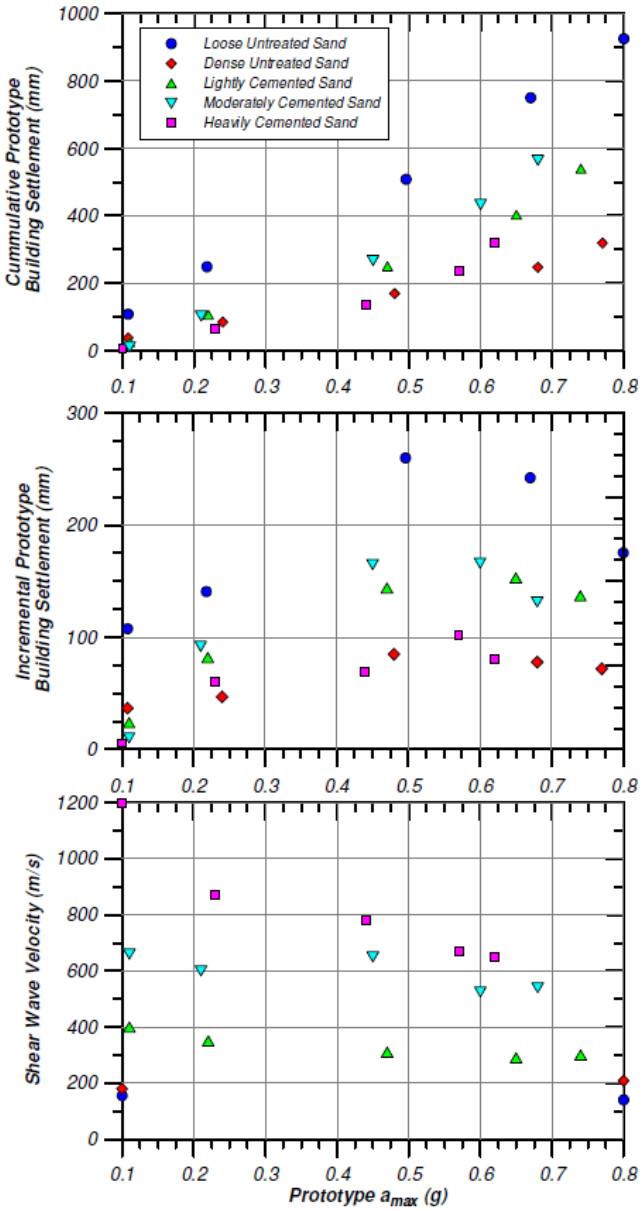

Figure 2-16 Incremental and cumulative building settlement with shear wave velocity of the soil model beneath the structure versus base acceleration (from Montoya 2012).

2.4.6 Kim (2017) database

Kim (2017) collected data from several centrifuge tests on loose to medium dense clean sands to estimate volumetric strains. The database includes VELACS (Verification of Liquefaction Analyses by Centrifuge Studies), Dashti (2010), and Montoya (2012) experiments. Further details on this database can be found in Kim (2017).

2.4.7 Summary of centrifuge tests

In summary, few dynamic centrifuge tests have been conducted for dense sand deposits, both under multidirectional earthquake loading and with a presence of a high-bearing pressure structure (i.e., q_b > 350kPa). In addition, the tests described above measured settlements only at the ground surface, making it impossible to define volumetric strain profiles. The proposed set of centrifuge tests address these shortcomings.

2.5 Available Semi-Empirical Methods to Estimate Seismic Volumetric Strain

Surface settlement, S, resulting from a shaking event is computed as the sum of volumetric strains of each of the soil sublayers:

$$S = \sum_{l=1}^{n} \varepsilon_{vl} h_l \tag{2-3}$$

where n = number of soil sublayers; ε_{vi} and h_i = volumetric strain and thickness respectively of the i^{th} sublayer. Eqn. (2-3) assumes that volumetric strain is equal to the vertical strain, which is applicable to a one or two-dimensional soil column with constant area. This is also the frequently adopted boundary condition in element tests where the soil specimen is confined with stacked rings or wire reinforced membranes to maintain a constant plan-view area. As previously discussed, this volumetric strain ε_v can be a result of vibration induced strain, ε_{vcyc}, or post-cyclic reconsolidation strain, ε_{vr}, or a combination of the two. All available semi-empirical models for estimating volumetric strain due to seismic loading are strain-amplitude or cyclic stress ratio based. The major drawback of such methods is that the loading time history must be converted to an equivalent number of cycles N_{eq} and a shear strain amplitude (γ) or average cyclic shear stress. This section summarizes the available semi-empirical models for estimating earthquake-induced volumetric strain.

2.5.1 Volumetric Strain (Drained Cyclic Shearing)

2.5.1.1 Seed and Silver (1972)

The semi-empirical method proposed by Seed and Silver (1972) assumes vertically propagating shear waves and consists of the following steps: (1) perform a seismic response analysis of the soil profile to determine the average shear strain γ at various depths in the profile; (2) test a representative soil specimen from the profile at the in situ effective vertical stress to an equivalent number of shear strain cycles that represent the design earthquake magnitude; and (3) integrate the volumetric strain determined for each layer to obtain the total settlement of the deposit (Eqn. 2-3). This method was used to estimate settlement of shake table tests on dry sand with less than a 50 % error. The method was applied to a field case history of a 15.2-m (50-ft) thick deposit of sand at a D_R of 45 % subjected to a maximum surface acceleration of 0.45g during the 1971 San Fernando earthquake. The computed settlement of 6.35 cm (2.5 in) agreed reasonably well with

measured settlements (Tokimatsu and Seed 1987). The drawback of this method is that it is not simplified; it requires a site response analysis.

2.5.1.2 Tokimatsu and Seed (1987)

Tokimatsu and Seed (1987) presented a simplified version of the Seed and Silver (1972) method for computing seismic volumetric strain based on unidirectional DSS tests conducted by Silver and Seed (1971) on clean sand. Unlike the Seed and Silver (1972) procedure, the Tokimatsu and Seed (1987) method does not require a site response analysis. The method is strain based and consists of the following steps: (1) graphically determine the shear strain γ in the soil profile [Figure 2-17 or Eqn. (2-4) and Eqn. (2-5), where Eqn. (2-4) is based on the form of CSR used in the simplified liquefaction evaluation procedure by Seed and Idriss (1971)]; (2) estimate the volumetric strain for 15 loading cycles (earthquake of magnitude, M 7.5) using Figure 2-18; (3) correct the volumetric strain for the design earthquake magnitude or number of cycles using Figure 2-19; and (4) apply a factor of 2 as recommended by Pyke et al. (1975) to account for multidirectional loading.

$$\gamma \frac{G_{eff}}{G_{\max}} = \frac{0.65 a_{\max} \sigma_{v0} r_d}{g G_{\max}} \tag{2-4}$$

$$G_{\max} = 20000 (N_1)^{1/3} (\sigma'_m)^{1/2} psf \tag{2-5}$$

where G_{eff} = effective shear modulus at the induced strain level; G_{max} = small-strain shear modulus; a_{max} = maximum horizontal ground surface acceleration; σ_{vo} = total vertical stress; r_d = depth reduction factor (Youd et al. 2001); g = acceleration due to gravity; N_1 = effective stress-corrected SPT blow count; σ'_m = effective mean stress which can be computed from the coefficient of earth pressure at rest (K_0) and effective vertical stress (σ'_{vo}) as:

$$\sigma'_m = \frac{\sigma'_{v0}}{3}(1 + 2K_0) \tag{2-6}$$

K_0 for normally consolidated soils can be computed respectively from the soil friction angle ϕ' and the Jaky (1948) equation (Eqn. 2-7). The later update by Mayne and Kulhawy (1982) can be used for overconsolidated soils (Eqn. 2-8).

$$K_0 = 1 - \sin\phi' \tag{2-7}$$

$$K_0 = (1 - \sin\phi') OCR^{\sin\phi'} \tag{2-8}$$

This method was applied to the field case history used by Seed and Silver (1972), and a settlement of 8.64 cm (3.4 in) was obtained, close to the value of 6.35 cm (2.5 in) determined by Seed and Silver (1972). It also was shown that the simplified estimate of shear strain agreed closely with the average shear strain profile obtained by site response analysis by Seed and Silver (1972). Since this method was based on charts and simple equations, did not require site response analysis, and provided good estimates of volumetric strain, it was readily adopted in geotechnical engineering practice. However, this method applies to clean sands only.

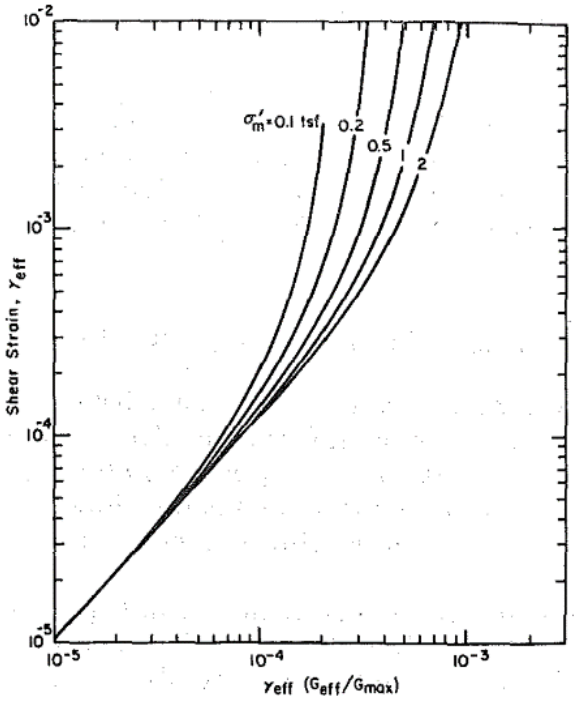

Figure 2-17 Chart for determination of shear strain induced in the field (from Tokimatsu and Seed 1987).

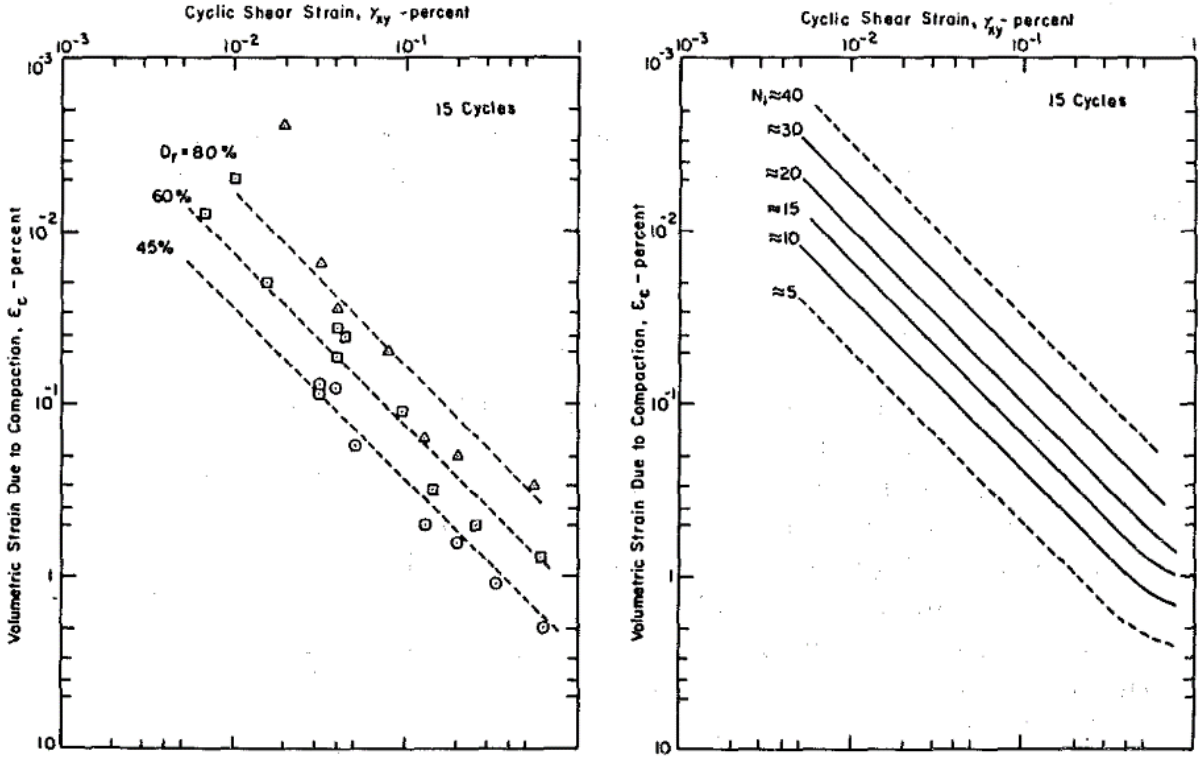

Figure 2-18 Volumetric strain at the end of 15 loading cycles as a function of shear strain and (a) relative density (D_R) or (b) SPT blow count (after Tokimatsu and Seed 1987).

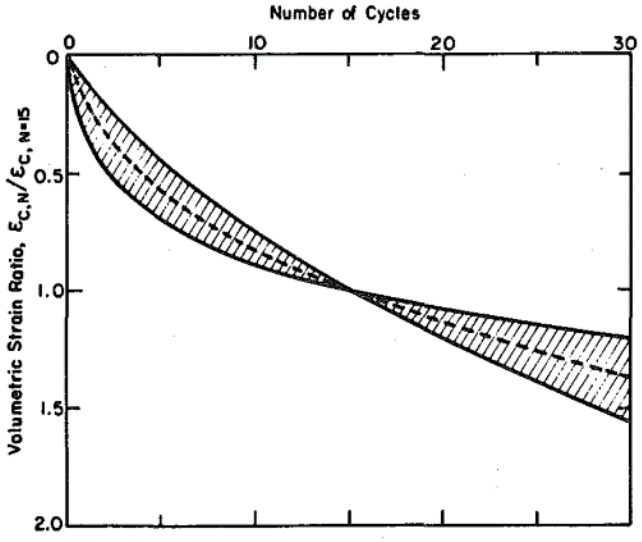

Figure 2-19 Effect of number of cycles on volumetric strain (from Tokimatsu and Seed 1987; based on the tests by Silver and Seed 1971).

2.5.1.3 Byrne (1991)

Byrne (1991) proposed an incremental volumetric strain model, based on the shear strain – volumetric strain coupling equation originally proposed by Martin et al. (1975). The volumetric strain for coarse-grained soil for a random pattern of strain cycles can be estimated as:

$$\varepsilon_{vcyc} = \sum_{i} (\Delta\varepsilon_{vcyc,1/2cycle})_i \tag{2-9}$$

where ε_{vcyc} is the total volumetric strain and $(\Delta\varepsilon_{vcyc,1/2cycle})_i$ is the incremental volumetric strain in the i^{th} half shear strain cycle of amplitude γ_i computed as:

$$(\Delta\varepsilon_{vcyc,1/2cycle})_i = 0.5\gamma_i C_1 \exp\left(-C_2 \frac{\varepsilon_{vcyci}}{\gamma_i}\right) \tag{2-10}$$

Here, C_1 and C_2 are soil-related parameters which can be estimated using:

$$C_1 = 7600 D_R^{-2.5} = 8.7 (N_1)_{60}^{-1.25} \tag{2-11}$$

$$C_2 = 0.4 / C_1 \tag{2-12}$$

where $(N_1)_{60}$ = effective stress and energy corrected SPT blow count. The model directly accounts for the effect of number loading cycles in the estimation of volumetric strain. However, this model requires the definition of a half loading cycle for seismic loads and does not consider the influence of fines.

2.5.1.4 Pradel et al. (1998)

Pradel et al. (1998) proposed a set of equations based on the graphical method of Tokimatsu and Seed (1987) to estimate drained volumetric compression. These equations, used in lieu of the iterations, graphs, and tables in the Tokimatsu and Seed (1987) method, made computation of volumetric strain easier to implement in a spreadsheet. Pradel et al. (1998) proposed the following for estimation of the equivalent shear strain γ based on the shear modulus – shear strain relation experimentally determined by Iwasaki et al. (1978):

$$\gamma = \frac{1 + a\left[\exp(b)\right]\left(\frac{\tau_{av}}{G_{max}}\right)}{1 + a} \tag{2-13}$$

$$a = 0.0389\left(\frac{\sigma'_m}{P_a}\right) + 0.124 \tag{2-14}$$

$$b = 6400\left(\frac{\sigma'_m}{P_a}\right)^{-0.6} \tag{2-15}$$

where τ_{av} = average uniform cyclic shear stress (Seed and Idriss 1971) and P_a = atmospheric pressure. The volumetric strain, based on fitting the data of Silver and Seed (1969, 1971) was:

$$\varepsilon_{vcyc,Nc=15} = \gamma\left(\frac{N_1}{20}\right) \tag{2-16}$$

where $\varepsilon_{vcyc,N=15}$ = volumetric strain at the end of 15 loading cycles of shear strain amplitude γ. The volumetric strain at the end of N_c loading cycles corresponding to an earthquake of magnitude M can be determined by:

$$\varepsilon_{vcycNc} = \varepsilon_{vcyc,Nc=15}\left(\frac{N_c}{15}\right)^{0.45} \tag{2-17}$$

$$N_c = (M - 4)^{2.17} \tag{2-18}$$

This method showed good agreement with the Tokimatsu and Seed (1987) and Seed and Silver (1972) method for the Jensen Filtration Plant (1971 San Fernando earthquake) and Santa Monica Mountains (1994 Northridge earthquake) case histories. However, this method is still solely applicable to clean sands and requires a seismic time history to be converted to an equivalent shear strain and number of cycles.

2.5.1.5 Shahien (1998)

Based on the laboratory data from Silver and Seed (1969, 1971), Shahien (1998) proposed the following general equation for estimation of drained level ground volumetric strain:

$$\varepsilon_{vcyc} = a\gamma^{b} \tag{2-19}$$

The parameters a and b were evaluated by Shahien (1998) based on a database of level ground drained volumetric strain laboratory tests (Silver and Seed 1969; Youd 1972a; among others), leading to the following expression for drained volumetric strain at the end of N_c loading cycles:

$$\varepsilon_{vcyc} = \frac{7N_c^{0.3}}{(N_1)_{60}^{0.75}}\gamma^{1.15} \tag{2-20}$$

Shahien (1998), based on analysis of published laboratory data, and Ohta and Goto (1978) recommended the following sets of relations for estimating γ for a given shear stress τ and earthquake magnitude M:

$$G_{\max} = 335\left[(N_1)_{60}\right]^{1/3} P_a^{0.5}\sigma'^{0.5}_{vo} \tag{2-21}$$

$$\tau_{\max} = \sigma'_{v0}\tan\phi'_s \tag{2-22}$$

$$G = F_{G-M}G_{\max}\left(1-\frac{\tau}{\tau_{\max}}\right)^{2.5} \tag{2-23}$$

$$\gamma = \frac{\tau}{G} \tag{2-24}$$

where τ_{max} = maximum shear stress, ϕ'_s = secant friction angle estimated from Figure 2-20, G = secant shear modulus and F_{G-M} = a correction factor for earthquake magnitude (see Table 2.8 in Shahien 1998). For a given earthquake, τ can be calculated using (Seed and Idriss 1971):

$$\frac{\tau}{\sigma'_{v0}} = 0.65\left(\frac{a_{\max}}{g}\right)\left(\frac{\sigma_{v0}}{\sigma'_{v0}}\right)r_d \tag{2-25}$$

Based on Eqns. (2-19) to (2-25), Shahien (1998) proposed a chart based solution for estimating ε_{vcyc} illustrated in Figure 2-21 for a magnitude 7.5 earthquake at σ'_{vo} = 100 kPa. When using the chart-based solution, corrections were proposed for earthquake magnitude (see Table 2.9 in Shahien 1998) and different effective vertical stresses (Figure 2-22). It is interesting to note from Figure 2-22 that volumetric strain seems to increase with increase in effective vertical stress, contrary to previously discusses observations from literature. This occurs for several reasons. Firstly, the correction is based on N_{60}. Eqn. (2-20) is used for estimating volumetric strain, which is inversely proportional to $(N_1)_{60}$. At σ'_{vo} > 100 kPa, $(N_1)_{60}$ is less than N_{60}, thus resulting in a higher volumetric strain than the one determined using N_{60}. Secondly, the strain-controlled tests on which this method is based (Silver and Seed 1969, 1971; and Youd 1972) indicate that σ'_{vo} does not influence volumetric strain. The effect of σ'_{vo} is accounted for in the shear stress and shear modulus, Eqns. (2-21) to (2-25), which contributes to the overburden correction factor in Figure 2-22. Shahien (1998) does not account for multidirectional loading citing the undrained tests from Ishihara and Yoshimine (1992), which showed negligible impact of bidirectional loading on reconsolidation volumetric strain.

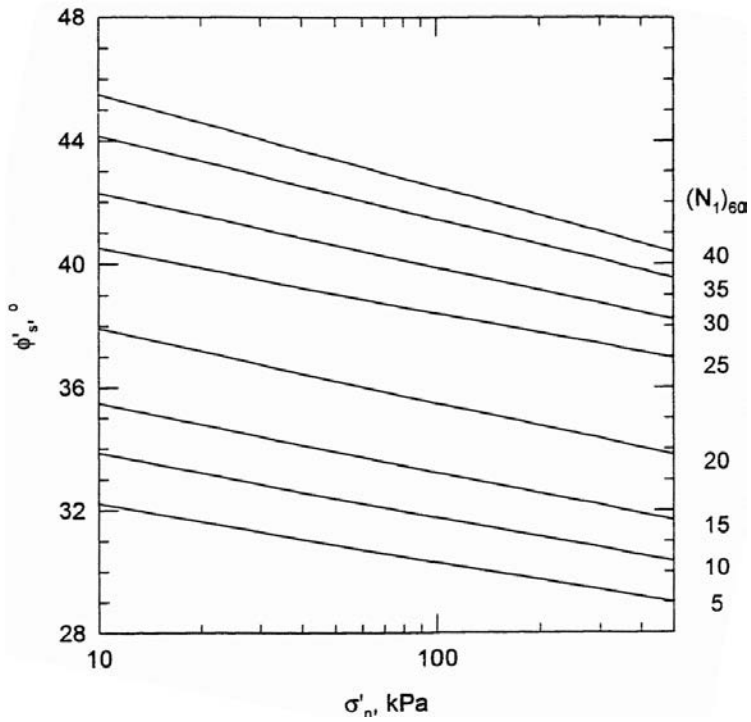

Figure 2-20 Chart for estimating secant friction angle from energy corrected SPT blow count and effective normal stress (from Shahien 1998).

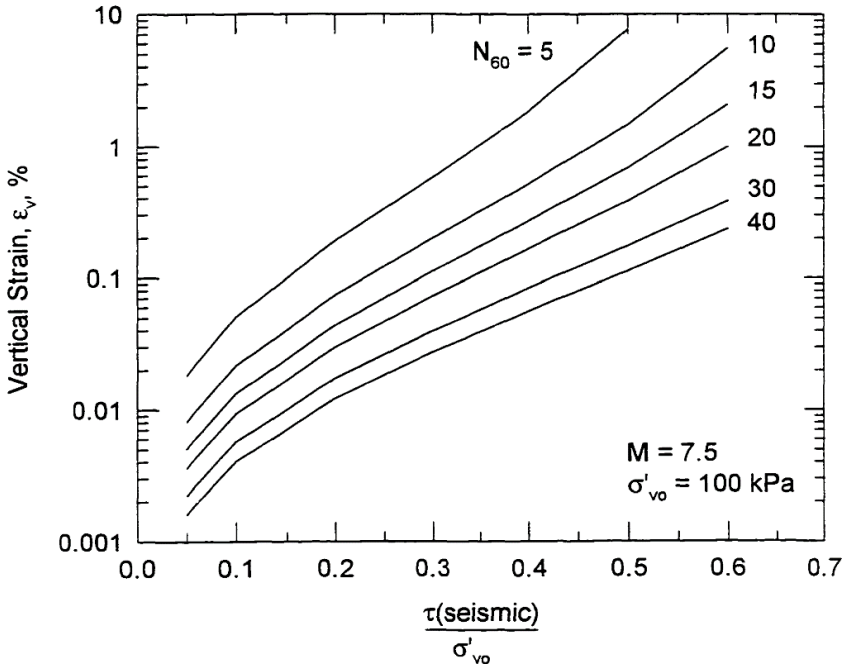

Figure 2-21 Chart for estimating level ground drained volumetric strain (from Shahien 1998).

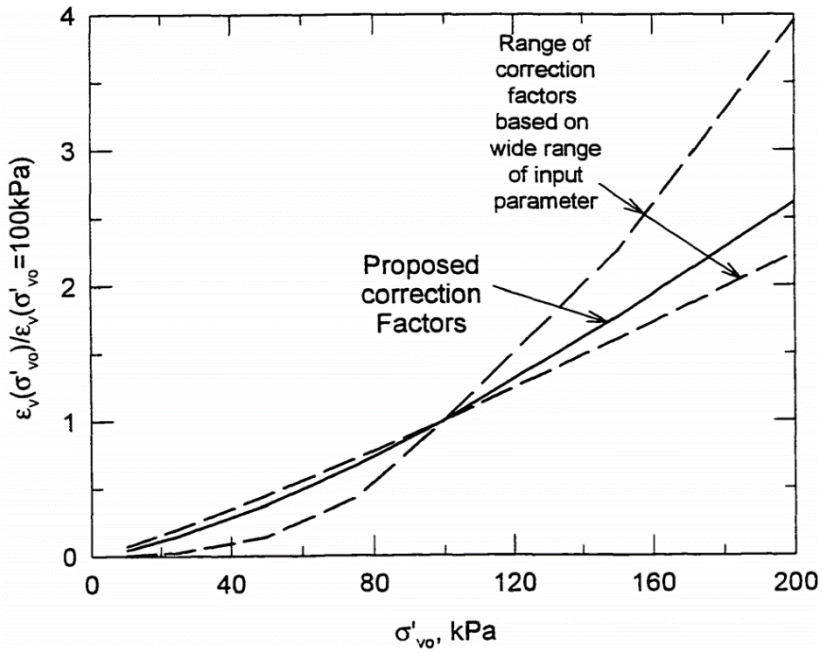

Figure 2-22 Chart for correcting volumetric strain for effective vertical stresses other than 100 kPa (from Shahien 1998).

2.5.1.6 Duku et al. (2008)

Duku et al. (2008) proposed a simple strain-based volumetric strain model for estimation of volumetric strain of clean sands based on strain-controlled unidirectional cyclic DSS tests. This model does not incorporate the effect of plastic or non-plastic fines, and applies to cyclic shear strains up to 1 %. No limiting value of volumetric strain is recommended.

$$(\varepsilon_{vcyc})_{Nc=15} = a[\gamma - \gamma_{th}]^b \tag{2-26}$$

$$a = 5.38\exp(-0.023\,D_R) \tag{2-27}$$

where a and b are soil-related factors. Duku et al. (2008) recommends b = 1.2, and threshold shear strain γ_{th} = 0.01 – 0.03 % based on Hsu and Vucetic (2004). Eqns. (2-28) and (2-29) were formulated for vertical stress and number of cycles correction, respectively. Although Duku et al. (2008) did not use effective vertical stress for Eqn. (2-28), because Eqn. (2-28) was based on drained tests, the vertical stresses are equal to the effective vertical stress.

$$\varepsilon_{vcyc,Nc=15,\sigma} = \varepsilon_{vcyc,Nc=15}\left(\frac{\sigma'_v}{P_a}\right)^{-0.29} \tag{2-28}$$

$$\varepsilon_{vcyc} = \varepsilon_{vcyc,Nc=15,\sigma}\left[\ln\left(\frac{N_c}{15}\right)^{0.29} + 1\right] \tag{2-29}$$

As with previous researchers, a factor of 2 was recommended to correct for multidirectional loads (Pyke at al. 1975). No recommendation was made to estimate equivalent shear strain and number of cycles. Although higher OCR was observed to lower the volumetric strain, it was not considered in the model, since compacted fills at low effective vertical stresses (near the surface), were relatively unaffected by OCR, as compared to the other parameters included in the model.

2.5.1.7 Yi (2010)

Drawing on the work of Silver and Seed (1969, 1971), Tokimatsu and Seed (1987) and Pradel (1998), Yi (2010) developed a method for estimation of volumetric strain using shear wave velocity. Yi (2010) used a published semi-empirical correlation between corrected SPT blow count and relative density (Mayne et al. 2002; Tokimatsu and Seed 1987) and corrected SPT blow count and effective stress corrected shear wave velocity of clean sands $(V_{s1})_{cs}$ (Andrus et al. 2004), to estimate D_R from V_s as shown in Eqn. (2-30). The remainder of the procedure is the same as Tokimatsu and Seed (1987; Figure 2-23).

$$D_R = 17.974[(V_{s1})_{cs} / 100]^{1.976} \tag{2-30}$$

In Figure 2-23, note that D_R 45 % corresponds to $(V_{s1})_{cs} \approx 159$ m/s using Eqn. (2-30), not 169 m/s as shown in the figure from Yi (2010).

A form for the theoretical maximum volumetric strain, called the ultimate volumetric strain, $\varepsilon_{v,ult}$ was determined by Yi (2010), using the laboratory defined bounds of void ratio, e_{max} and e_{min}:

$$\varepsilon_{v,ult} = \frac{(1-D_R)(e_{max}-e_{min})}{1+e_{max}-D_R(e_{max}-e_{min})} x100\% \tag{2-31}$$

However, this calculation assumes that the laboratory e_{max} and e_{min} (e.g., using ASTM D4254-06 and ASTM D4253-16 respectively) are the true maximum and minimum void ratio a soil can reach. Such an assumption may not hold true for soils that have been brought to a denser state by cyclic loading or for soils with greater than 15 % fines content.

A form for the limiting volumetric strain (Figure 2-24) was proposed based on the saturated stress-controlled unidirectional and bidirectional DSS experiments of Ishihara and Yoshimine (1992):

$$\varepsilon_{v,\lim} = 12\exp\left[-0.449\left(\frac{(V_{s1})_{cs}}{100}\right)^{1.976}\right] \tag{2-32}$$

The advantage of this method is that it uses V_s, a quantity directly measured in the field, and already includes the conversion to D_R. One other advantage is that a limiting volumetric strain is defined, to prevent overestimation of volumetric strains for strong shaking. However, this limiting value is based on post-cyclic reconsolidation volumetric strain and not drained volumetric strain (which the method computes). Moreover, the laboratory determined minimum void ratio e_{min} is the minimum that can be attained by a soil using the ASTM procedure; however, it is possible that the field void ratio can be lower than the ASTM e_{min}, especially for soils with fines.

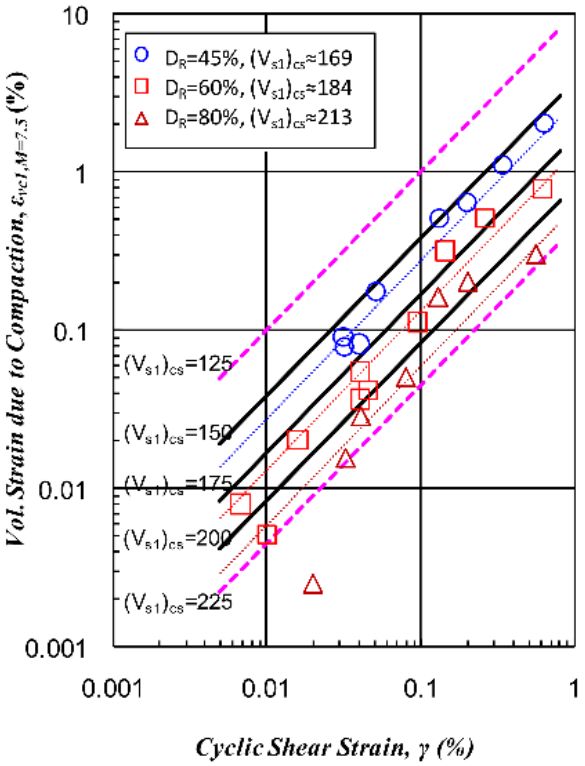

Figure 2-23 Volumetric strain based on cyclic shear strain and corrected shear wave velocity of dry sands based on Silver and Seed (1969, 1971) and Tokimatsu and Seed (1987) (from Yi 2010; Note: D_R 45 % corresponds to $(V_{s1})_{cs}$ ≈ 159 m/s using Eqn. (2-30), not 169 m/s as shown in the figure).

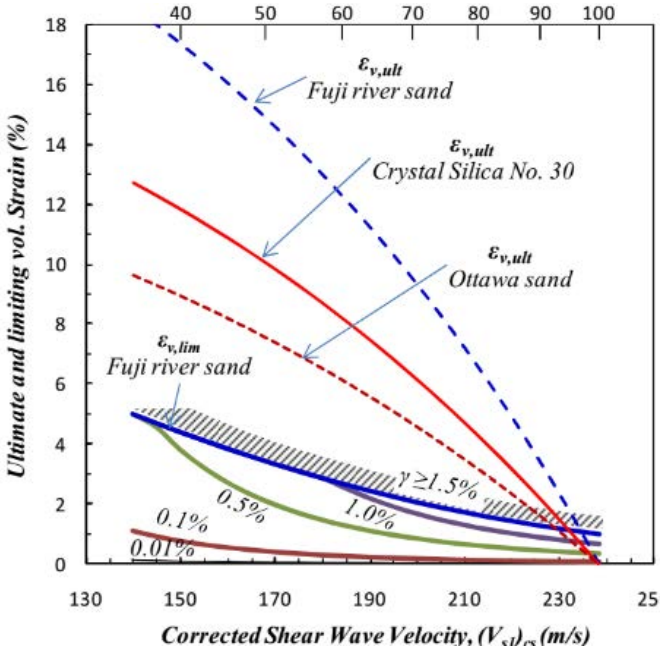

Figure 2-24 Ultimate and limiting volumetric strain for different sands as a function of shear strain, shear wave velocity and relative density (from Yi 2010).

2.5.1.8 Yee et al. (2013)

Yee et al. (2013) included parameters for sands with fines to the clean sand volumetric strain material model proposed by Duku et al. (2008). The following reduction factors were suggested for low plasticity (PI < 10) fines:

$$K_{FC} = 1 \qquad (\text{FC} < 10\ \%) \qquad (2\text{-}33)$$

$$K_{FC} = \exp\left[-0.042(\text{FC}-10)\right] \qquad (10 \le \text{FC} \le \text{FC}_L) \qquad (2\text{-}34)$$

$$K_{FC} = 0.35 \qquad (\text{FC} > \text{FC}_L) \qquad (2\text{-}35)$$

where FC_L is the threshold or limiting (as termed by Yee et al. 2013) fines content of ~ 35 % for most sand-silt mixes. The following corrections were recommended for low plasticity (PI <10), higher fines content (FC > 10 %) sands to account for the reduction in volumetric strains at intermediate saturation levels (S_r) caused by matric suction:

$$K_S = -0.017\,S_r + 1 \qquad (S_r < 30\ \%) \qquad (2.36)$$

$$K_S = 0.5 \qquad (30 \le S_r \le 50\ \%) \qquad (2\text{-}37)$$

$$K_S = 0.05\,S_r - 2 \qquad (50 \le S_r \le 60\ \%) \qquad (2\text{-}38)$$

$$K_S = 1 \qquad (S_r > 60\ \%) \qquad (2\text{-}39)$$

A modified form was proposed to account for the number of cycles, to which the correction factors for fines content and saturation could be multiplied to obtain the final volumetric strain:

$$\varepsilon_{vcyc} = \varepsilon_{vcyc,Nc=15,\sigma}\left(K_{FC}\right)\left(K_S\right)\left[\ln\left(\frac{N_c}{15}\right)^{-0.026\ln(\gamma-\gamma_{tv})+0.26}+1\right] \qquad (2\text{-}40)$$

The model presented by Yee et al. made a significant addition due to consideration of sands with fines. However, it has the aforementioned disadvantages of strain-based models and does not account for the presence of higher plasticity fines in the sand.

2.5.1.9 Lasley et al. (2016)

The most recent semi-empirical volumetric strain model was formulated by Lasley et al. (2016) based on the Seed and Silver (1972) method, the damage theory proposed by Richart and Newmark (1948), and about 450 cyclic and broadband loading strain-based DSS tests. Damage (D) = 100 % (failure) is arbitrarily defined as the accumulation of 1 % volumetric strain. The model for single amplitude loading condition is:

$$D = \left(R\right)^{0.1/R^{r0}+r0} \qquad (2\text{-}41)$$

$$R = \frac{N_c}{N} \tag{2-42}$$

$$r0 = 0.238 - 0.002D_R + 35.23\gamma - 0.0603\frac{\sigma'_{v0}}{P_a} + 7.093\gamma\frac{\sigma'_{v0}}{P_a} + \varepsilon_{r0} \tag{2-43}$$

$$\ln(N) = -13.5 - 2.94\ln(\gamma) + 0.232\frac{\sigma'_{v0}}{P_a} + 0.0254D_R + \varepsilon_N \tag{2-44}$$

where N = number of cycles for D = 100 %, ε_{r0} and ε_N are error terms with zero mean and standard deviation values of 0.048 and 0.62, respectively. Volumetric strain is proportional to the computed damage (with ε_v = 1 % for D = 100 %). The model can be used both via a simplified approach (not requiring site response analysis) and non-simplified approach (requiring site response analysis), and applies to non-uniform loading conditions as illustrated by Lasley (2015) via a case history and estimation of volumetric strain from irregular loading laboratory tests. The drawback of the model is that, as with other strain based methods, it requires estimation of the number of equivalent shear strain cycles or definition of a half cycle for seismic loads.

2.5.2 Post-cyclic reconsolidation volumetric strain (undrained shearing)

2.5.2.1 Tokimatsu and Seed (1987)

Based on cyclic triaxial and simple shear tests, Tokimatsu and Seed (1987) proposed a stress-based chart for the estimation of reconsolidation volumetric strain for an earthquake of magnitude 7.5, illustrated in Figure 2-25. The proposed chart was calibrated using case history data, and requires the use of energy, overburden and fines corrected SPT blow count, $(N_1)_{60,CS}$. The Seed and Idriss (1971) simplified equation was recommended to compute average CSR:

$$\frac{\tau_{av}}{\sigma'_0} = 0.65\left(\frac{a_{max}}{g}\right)\left(\frac{\sigma_0}{\sigma'_0}\right)r_d \tag{2-45}$$

Additional charts and tables were provided for correcting the reconsolidation volumetric strain for different earthquake magnitudes. This method, however, applies to clean sands only and does not apply a correction term to the computed CSR for multidirectional loading.

2.5.2.2 Ishihara and Yoshimine (1992)

Ishihara and Yoshimine (1992), based on the unidirectional and multidirectional irregular DSS experiments conducted by Nagase and Ishihara (1988), proposed a graphical solution for reconsolidation volumetric strain. This method does not require the computation of an equivalent shear strain, instead it uses the traditionally factor of safety against liquefaction (FS_{liq}; see Youd 2001; Cetin et al. 2004) as the demand parameter and relative density or effective stress-corrected SPT blow count N_1 as the capacity term. The chart is shown in Figure 2-26. FS_{liq} is defined by using the maximum shear stress required to cause 100 % pore pressure buildup or initial liquefaction ($\tau_{max,l}$) and the earthquake induced peak shear stress (τ_{max}):

$$FS_{liq} = \frac{\tau_{max,l} / \sigma'_v}{\tau_{max} / \sigma'_v} \qquad (2\text{-}46)$$

The procedure for determining FS_{liq} (denoted as F_l in Figure 2-26) incorporates earthquake magnitude and effective stress corrections; therefore, additional corrections for reconsolidation volumetric strain determination are not required. As with most of the previous methods, this was developed based on cyclic tests on clean sands, and thus is not validated for sands with plastic or non-plastic fines.

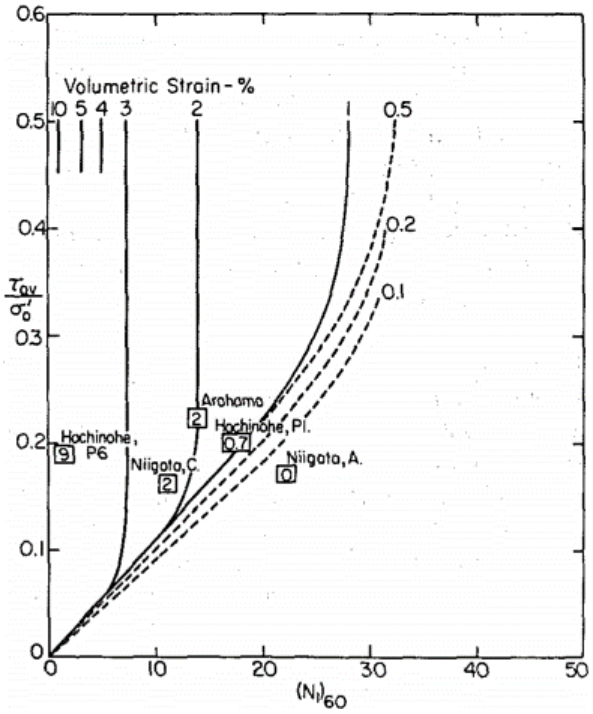

Figure 2-25 Chart for estimation of reconsolidation volumetric strain (from Tokimatsu and Seed 1987).

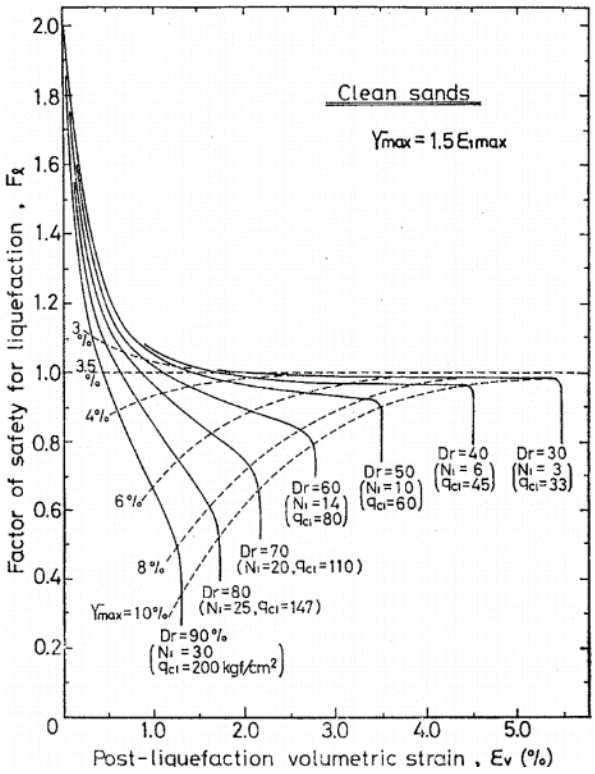

Figure 2-26 Chart for estimation of reconsolidation volumetric strain as a function of factor of safety against liquefaction (from Ishihara and Yoshimine 1992).

2.5.2.3 Shahien (1998)

Shahien (1998), based on various simple shear, triaxial, oedometer, and torsional shear laboratory tests (Lee and Albaisa 1974; Nagase and Ishihara 1988; Shamoto et al. 1996; among others), proposed Figure 2-27 to estimate earthquake-induced secant coefficient of volume compressibility $m_{v\text{-undrained}}$. The general form for $m_{v\text{-undrained}}$, given by Eqn. (2-47), was adopted from the Terzaghi et al. (1996) interpretation of the Burland and Burbridge (1985) method for settlement of footings under static loads. In Eqn. (2-47), constants a and b are functions of FS_{liq}.

$$m_{v-undrained} = \frac{a}{N_{60}^{b}} \tag{2-47}$$

The reconsolidation volumetric strain could then be estimated from:

$$\varepsilon_{vr} = m_{v-undrained} \Delta\sigma'_{v-undrained} \tag{2-48}$$

where $\Delta\sigma'_{v\text{-undrained}}$ is the change in effective vertical stress due to dissipation of porewater pressure following undrained loading. Based on the definition of FS_{liq}, undrained cyclic shear tests by Lee and Albaisa (1974), shaking table tests by DeAlba et al. (1975), and an empirical relation for excess porewater pressure Δu_{cyc} from Seed et al. (1975), Shahien (1998) suggested that for FS_{liq} greater than or equal to 1, Δu_{cyc} or $\Delta\sigma'_{v\text{-undrained}}$ for a granular soil deposit can be calculated as:

$$\frac{\Delta\sigma'_{v-undrained}}{\sigma'_{v0}} = \left(\frac{1}{FS_{liq}}\right)^5 \tag{2-49}$$

No corrections were suggested for multidirectional loading.

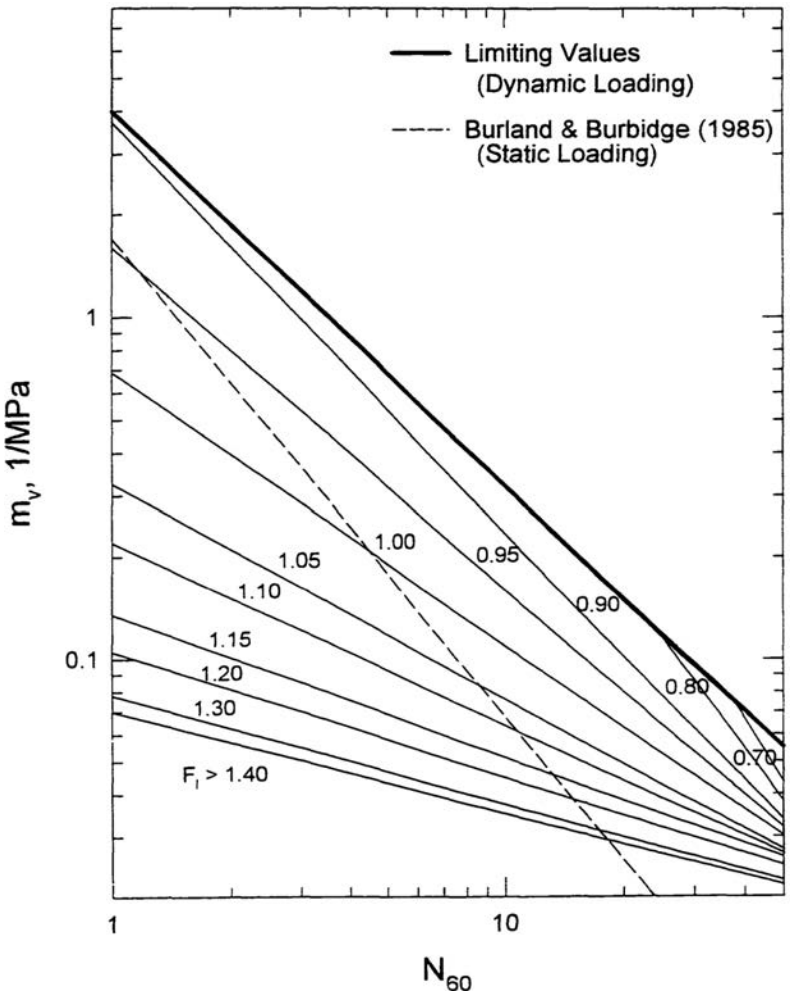

Figure 2-27 Correlation between $m_{v\text{-undrained}}$, energy-corrected SPT blow count N_{60} and factor of safety against liquefaction FS_{liq} (from Shahien 1998).

2.5.2.4 Shamoto et al. (1998)

Using the results of torsional shear tests, Shamoto et al. (1998) derived a set of relations for post-liquefaction horizontal and vertical ground deformation. Following the same approach as Tokimatsu and Seed (1987), Shamoto et al. (1998) proposed a series of charts for the computation of post-cyclic reconsolidation volumetric strain. These charts are presented in Figure 2-28 and require estimation of effective stress corrected CSR for a M7.5 earthquake and the SPT blow count corrected using the recommendations of Tokimatsu and Yoshimine (1992). The model was validated against cases from the 1995 Hyogoken-Nambu earthquake, based on which, Shamoto et al. (1998) suggested that field estimates of vertical strain should be $0.84\varepsilon_{v,charts}$. The major update of this semi-empirical model was that it applies to sands with fines content from 0 – 20 %.

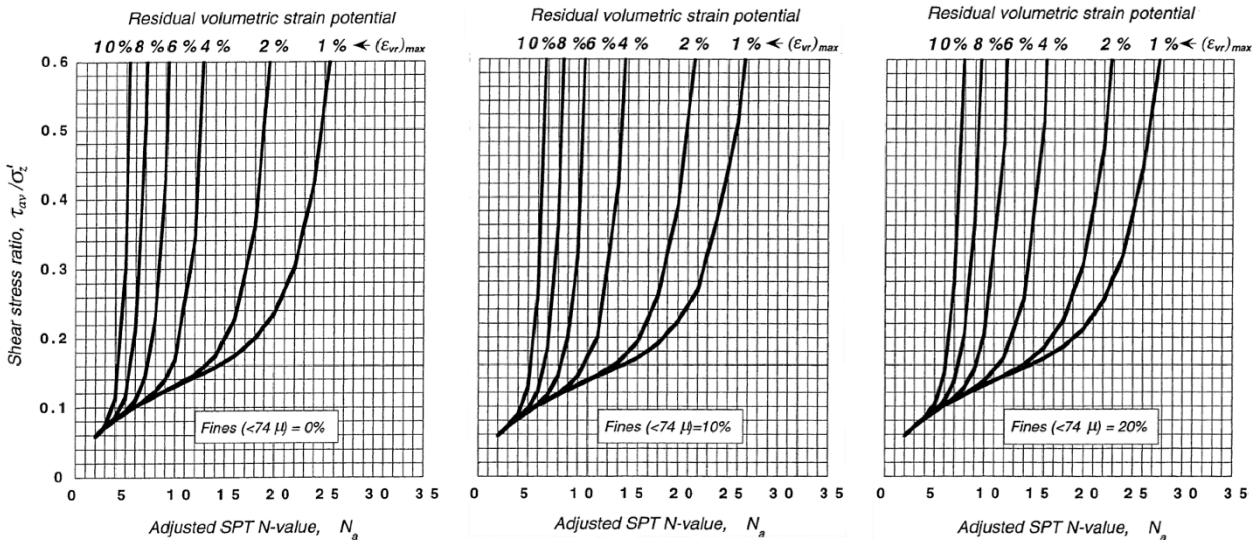

Figure 2-28 Chart for estimation of reconsolidation volumetric strain for sands with fines content from 0 to 20 % (after Shamoto et al. 1998).

2.5.2.5 Zhang et al. (2002)

Cone penetration tests (CPT) provide higher reliability and continuity in characterizing soil profiles compared to SPT (Zhang et al. 2002). Zhang et al. (2002) suggested a normalized equivalent clean sand cone tip resistance $(q_{c1N})_{cs}$ and FS_{liq} based method for estimating post-liquefaction free field settlements. Here, $(q_{c1N})_{cs}$ is determined based on the Robertson and Wride (1998) CPT data reduction method and FS_{liq} is computed as:

$$FS_{liq} = CRR / CSR \tag{2.50}$$

where CRR = cyclic resistance ratio determined from $(q_{c1N})_{cs}$ using Robertson and Wride (1998); and CSR = cyclic stress ratio calculated using Seed and Idriss (1971) Eqn. (2-25). The Robertson and Wride (1998) procedure was recommended because it is based on a single parameter, $(q_{c1N})_{cs}$, and additional data, e.g., median particle size and fines content is not required. Using $(q_{c1N})_{cs}$ and FS_{liq}, ε_{vr} is read from Figure 2-29. Zhang et al. (2002) developed Figure 2-29 using Ishihara and Yoshimine's (1992) chart for ε_{vr} (Figure 2-26); Tatsuoka et al. (1990) was used to empirically estimate q_c from D_R given in Figure 2-26, and the recommendation by Robertson and Wride (1998) used to determine $(q_{c1N})_{cs}$ to account for both clean and silty sands.

As shown by Zhang et al. (2002), field settlements estimated by this method was closer than the Tokimatsu and Seed (1987) SPT based method for the Marina District and Treasure Island case histories during the 1989 Loma Prieta earthquake. This method assumes that $(q_{c1N})_{cs}$ is sufficient to account for the presence of fines on ε_{vr}, which might prove erroneous, since the data used is based on simple shear tests on a single clean Fuji river sand. Zhang et al. (2002) comment that in the field, ε_{vr} will depend on the depth and lateral extent of the liquefiable layer; and if the layer is at 20m or more below the ground surface, there might not be any surface settlement. Engineering judgement is recommended for such cases.

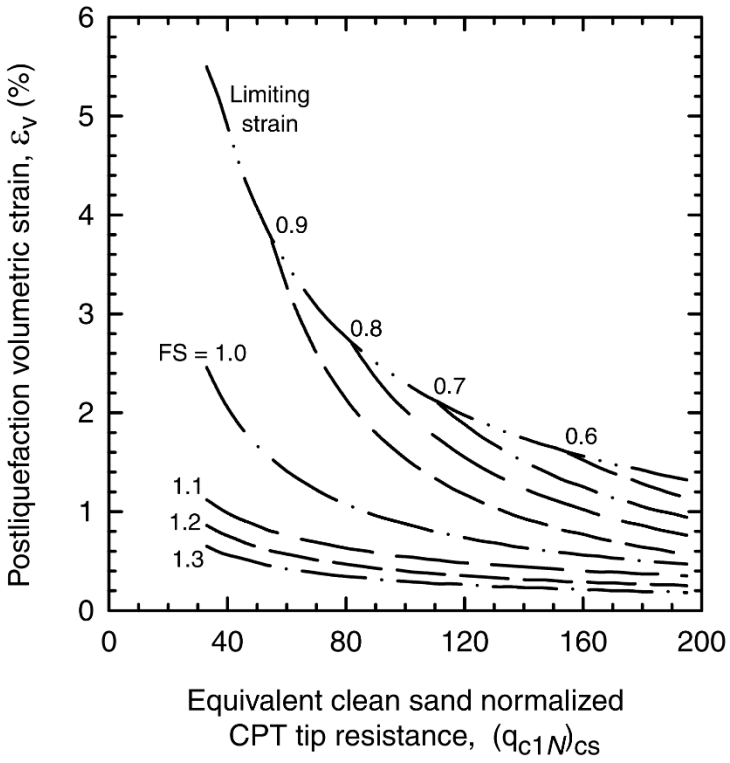

Figure 2-29 CPT (equivalent clean sand tip resistance) based method of estimating post-cylcic reconsolidation volumetric strain (from Zhang et al. 2002).

2.5.2.6 Wu and Seed (2004)

Wu and Seed (2004), using stress-controlled unidirectional and bidirectional DSS tests conducted by Wu (2002) and Kammerer (2002) respectively, proposed a correlation to estimate post-cyclic volumetric strain from corrected SPT blow count $(N_1)_{60,cs}$ and corrected $CSR_{eq,Mw=7.5}$ (Seed et al. 2001) The CSR also was corrected for multidirectional loading based on the results of Kammerer (2002). The graphical solution is illustrated in Figure 2-30, where the numbers above the upper horizontal axis (3 %, 5 %, 10 %, etc.) denote the reconsolidation volumetric strain. This method applies to both level and sloping or near-field soil layers that have an initial static shear. This method automatically accounts for magnitude corrections in the $CSR_{eq,Mw=7.5}$ value. An additional chart was made for application of effective stress correction to the estimated volumetric strain (Figure 2-31).

Two additional steps are proposed when calculating sloping ground settlements: (1) increase the settlement estimated from Figure 2-30 and Figure 2-31 by 10 – 20 % of the observed or estimated lateral ground deformation; and (2) if the estimated lateral ground movement is less than 0.3 m, the settlement due to presence of a slope can be neglected and if the lateral deformation is greater than 1.5 m, the method no longer applies, since the settlement mechanism at such large movements differs from laboratory data used for the method. The method was validated against some field case histories and applies to clean sands only. However, it incorporates initial static shear stress for estimating settlements on sloping ground, thus providing an improvement over previous models.

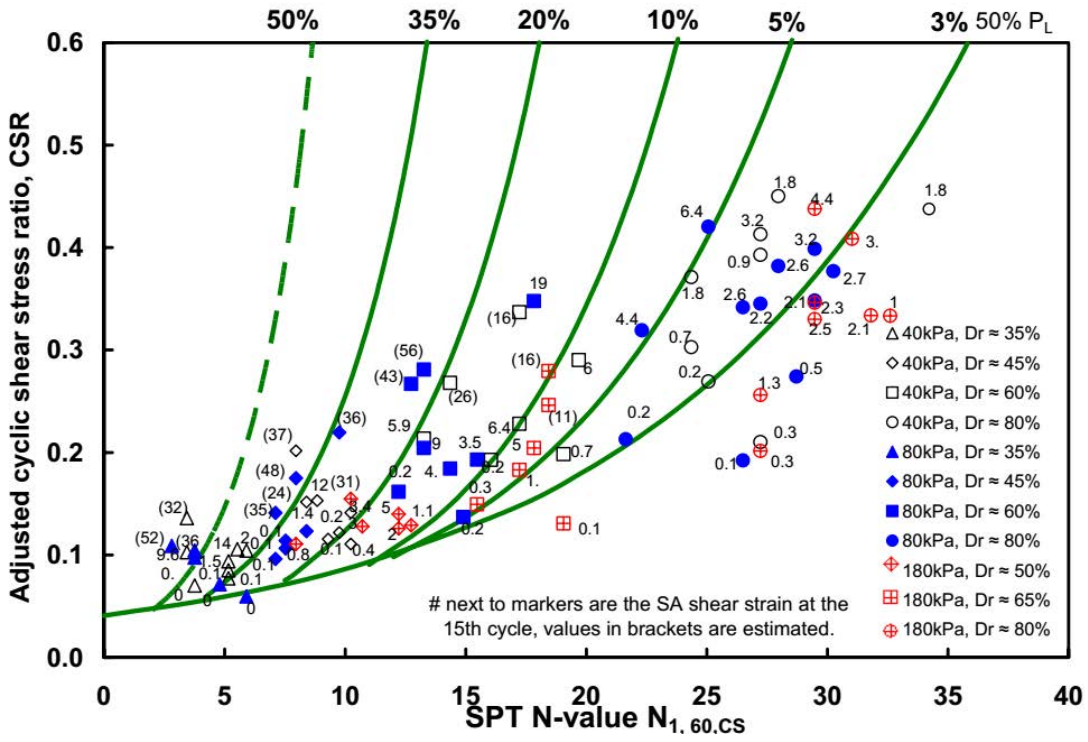

Figure 2-30 Chart for estimating post-cyclic reconsolidation volumetric strain (green lines with volumetric strain values denoted as a percentage on the top of the plot) based on stress-controlled unidirectional and bidirectional cyclic DSS tests (from Wu 2002; Wu and Seed 2004).

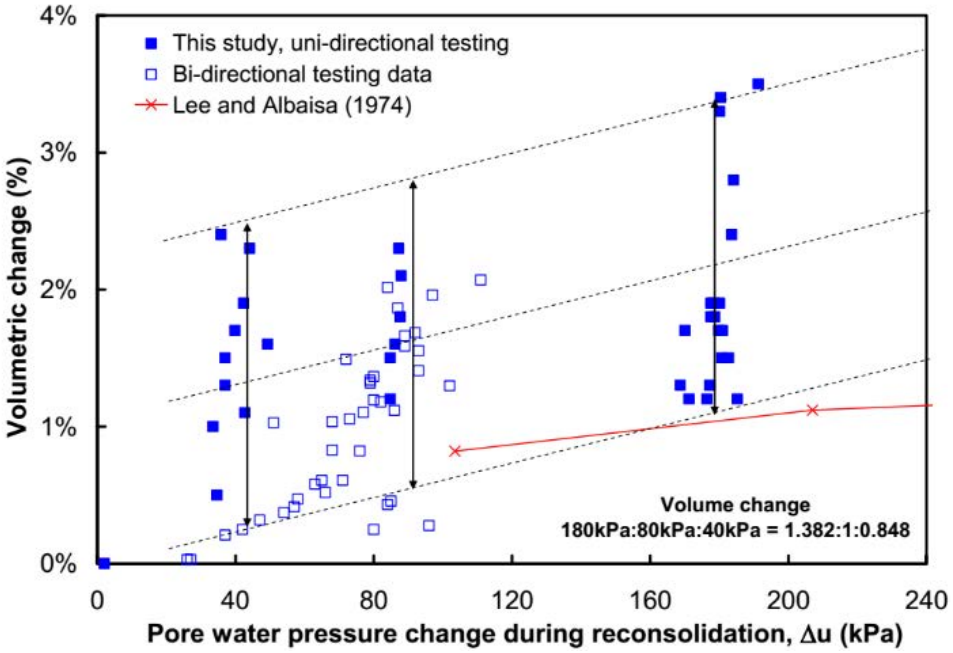

Figure 2-31 Chart for estimation of effective stress correction for reconsolidation volumetric strain (from Wu 2002).

2.5.2.7 Cetin et al. (2009)

Cetin et al. (2009) used published data on reconsolidation volumetric strain (Ishihara and Yoshimine 1992; Kammerer 2002; Wu 2002) to propose a semi-empirical stress-based probabilistic model for estimation of settlements in saturated coarse-grained soil:

$$\ln\left(\varepsilon_{vr}\right) = \ln\left[1.879\ln\left[\frac{780.416\ln(\mathrm{CSR}_{SS,20,1D,1atm}) - \mathrm{N}_{1,60,cs} + 2442.465}{636.613\mathrm{N}_{1,60,cs} + 306.732}\right] + 5.583\right] \pm 0.689$$

$$\textit{Limits}: 5 \le \mathrm{N}_{1,60,cs} \le 40, 0.05 \le \mathrm{CSR}_{SS,20,1D,1atm} \le 0.60 \tag{2-51}$$

The model uses effective stress corrected CSR for 1D laboratory DSS tests at 20 loading cycles as the demand term determined from the field CSR as:

$$\mathrm{CSR}_{SS,20,1D,1atm} = \frac{\mathrm{CSR}_{field}}{K_{md}K_{Mw}K_{\sigma}} \tag{2-52}$$

where corrections for multidirectionality, K_{md}, magnitude, K_{Mw} and effective stress, K_{σ} were recommended based on Wu (2002), Cetin et al. (2004) and Youd et al. (2001), respectively as:

$$K_{md} = 0.361\ln(D_R) - 0.579 \tag{2-53}$$

$$K_{Mw} = \frac{87.1}{M_w^{2.217}} \tag{2-54}$$

$$K_{\sigma} = \left(\frac{\sigma'_{v0}}{P_a}\right)^{-0.005D_R} \tag{2-55}$$

The model used a weighting factor that decreases linearly with depth based on recommendations of Iwasaki et al. (1982) to account for the effect of void redistribution due to upward seepage, reduced CSR in the deeper layers, and possible arching effects due to non-liquefied layers.

Cetin et al. (2009) proposed a threshold depth of 18m, below which soil layers do not contribute to surface settlements. The model was validated by estimating settlements for 49 high quality case histories, and due to its probabilistic nature, enables uncertainty characterization in the prediction of volumetric strain. The model is based on tests on clean sands only. Previous semi-empirical models for reconsolidation settlement, described above, were also evaluated by Cetin et al. (2009), with the following conclusions: (1) settlement estimates by the Tokimatsu and Seed (1987) and Shamoto et al. (1988) are lower than observed settlements, and have to be multiplied by a factor of 1.45 and 1.93 respectively; (2) Ishihara and Yoshimine (1992) and Wu and Seed (2004) predict higher settlements than the field and have to be reduced by factors of 0.90 and 0.98 respectively; and (3) although the Wu and Seed (2004) model gives excellent average settlement predictions, there is considerable scatter in the data.

2.5.3 Volumetric Strain under Partially-Drained Conditions

2.5.3.1 Shahien (1998)

Shahien (1998) considered settlements from drained and undrained response as the lower and upper limits for settlement, respectively, that occurs under more realistic partially drained conditions. The difference in the settlement computed considering drained and undrained analysis decreases as FS_{liq} increases, indicating that at FS_{liq} greater than or equal to 2, a partially drained analysis is not required (Figure 2-32). In this method, Eqns. (2-48) and (2-49) proposed by Shahien (1998) for undrained response, were combined and modified for estimating volumetric strain under partially drained condition $\varepsilon_{v\text{-}p.drained}$ as:

$$\varepsilon_{v-p.drained} = m_{v-p.drained}\left(\frac{1}{FS_{liq-p.drained}}\right)^{5}\sigma'_{v0} \tag{2-56}$$

Eqn. (2-56) is applicable for $FS_{liq\text{-}p.drained}$ greater than or equal to 1. The Mesri (1973) solution of Terzaghi's one dimensional consolidation for time dependent loading was modified to estimate pore pressure during partially drained response, and ultimately $FS_{liq\text{-}p.drained}$. A ten-step iterative solution is proposed for estimating $\varepsilon_{v\text{-}p.drained}$ based on the drainage boundary conditions of the soil deposit and time factor for earthquake duration (Section 4.11 of Shahien 1998). A modified formulation of Eqn. (2-56) for settlement estimation of granular soil deposits with gravel drains can be found in Shahien (1998). This procedure does not account for bidirectional loading.

2.5.4 Volumetric Strain under Partially-Saturated Conditions

The dynamic response of partially saturated soils may be different from that of dry or fully saturated soils due to (Ghayoomi et al. 2013): (1) different mechanism for compression of air-filled voids as opposed to water-filled voids; (2) resistance to volume change due to matric suction; and (3) changed method of generation and dissipation of excess porewater pressure, varying with the changing hydraulic conductivity of the soil at different levels of saturation.

2.5.4.1 Ghayoomi et al. (2013)

For partially saturated soil, using the principle of superposition, the total volumetric compression for each soil sublayer was calculated as the sum of the volumetric strain due to seismic compression ($\varepsilon_{vcyc\text{-}p.saturated}$) and post-cyclic reconsolidation ($\varepsilon_{vr\text{-}p.saturated}$) by Eqn. (2-57), where $\varepsilon_{vcyc\text{-}p.saturated}$ and $\varepsilon_{vr\text{-}p.saturated}$ are assumed to be uncoupled.

$$\varepsilon_{v-p.saturated} = \varepsilon_{vcyc-p.saturated} + \varepsilon_{vr-p.saturated} \tag{2-57}$$

Partially saturated conditions in estimating $\varepsilon_{vcyc\text{-}p.saturated}$ are incorporated by including saturation ratio (S_r) in the relations proposed by Tokimatsu and Seed (1987) and Pradel (1998):

$$\varepsilon_{vcyc-p.saturated} = \gamma\left[\frac{\left(\frac{D_R}{0.15}\right)^{2}}{20}\right]^{-1.2}\left(\frac{N}{15}\right)^{0.45}\left(1-S_r\right) \tag{2-58}$$

Eqn. (2-24) was recommended for calculating γ, where τ is determined using Eqn. (2-25) and modulus reduction relations from Menq (2003) was used to compute the shear modulus (G). Hardin and Richart (1963), Hardin and Drnevich (1972), and Ghayoomi and McCarthy (2011) were cited for estimation of G_{max}. Lu et al. (2010) was recommend for calculating the effective stress in partially saturated soil, which uses soil-water retention curve (SWRC) parameters and matric suction [defined as the difference between porewater (u) and pore air pressure (u_a)]:

$$\sigma' = \left(\sigma - u_a\right) + \frac{u_a - u}{\left\{1 + \left[\alpha_{vG}\left(u_a - u\right)\right]^{N_{vG}}\right\}^{(N_{vG}-1)/N_{vG}}} \tag{2-59}$$

where α_{vG} and N_{vG} are van Genuchten (1980) SWRC fitting parameters. Reconsolidation volumetric strain (ε_{vr}) is estimated using the following relation developed from Lee and Albaisa (1974) data:

$$\varepsilon_{vr-p.saturated} = \varepsilon_{vr-liq}\left(r_{u-sat}S^{n}\right)^{2.25} \tag{2-60}$$

where $\varepsilon_{vr\text{-}liq}$ = the volumetric strain for saturated soils estimated using Tokimatsu and Seed (1987) or Wu and Seed (2004); and $r_{u\text{-}sat}$ = PWP in a saturated soil, which can be estimated using Eqn. (2-61) from Kramer (1996) based on data from Seed and Lee (1965), where n = 3.5 was recommended based on partially saturated tests on sand by Yoshimi et al. (1989).

$$r_{u-sat} = \frac{1}{2} + \frac{1}{\pi}\sin^{-1}\left[2\left(\frac{N_c}{N_{liq}}\right)^{1/0.7} - 1\right] \tag{2-61}$$

where N_{liq} = number of cycles to liquefaction. An example settlement estimation by this method is presented in Figure 2-33. Parameters selected to evaluate G_{max}, modulus reduction, and porewater pressure had the largest impact on computed settlements. The method was validated against centrifuge tests with uniform saturation with depth. Minimum volumetric strain was predicted and measured at saturation ratios of 30 to 60 %. This model is based on very few experimental data on partially saturated sand, is highly dependent on the method selected to evaluate the required parameters, and includes the previously discussed uncertainties of the Tokimatsu and Seed (1987) method on which it is based.

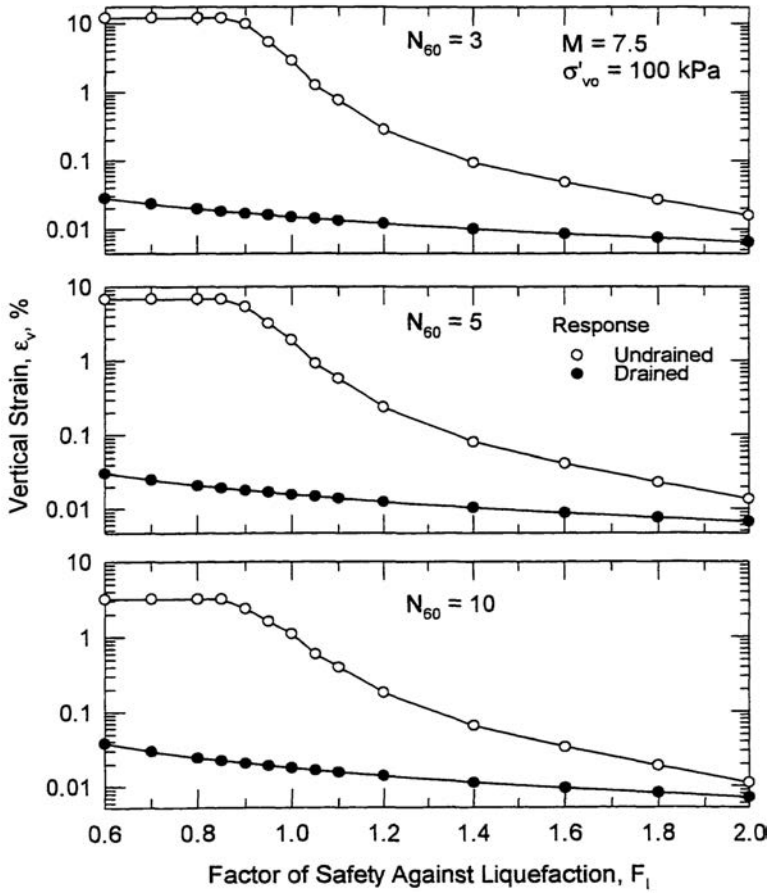

Figure 2-32 Volumetric strain due to drained and undrained loading as a function of factor of safety against liquefaction FS_{liq} for a M7.5 earthquake and different N_{60} values (from Shahien 1998).

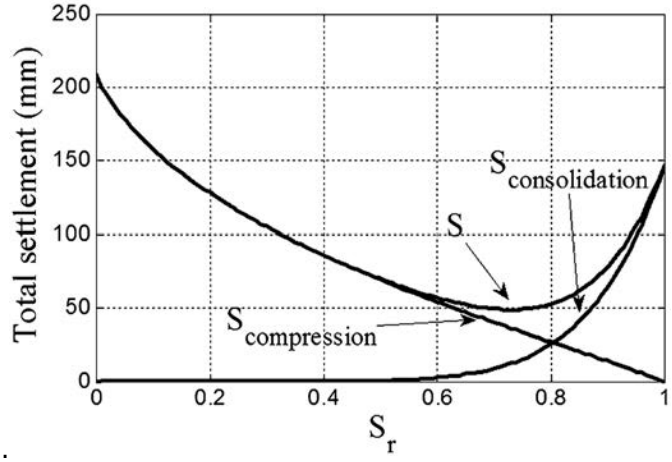

Figure 2-33 Estimated settlement in a D_R 45 %, F-75 Ottawa sand layer with different saturation ratios, illustrating the influence of cyclic compression and reconsolidation volumetric strain on the total settlement as a function of saturation ratio (from Ghayoomi et al. 2013).

2.6 Review of Selected Existing Constitutive Models for Sand

This section reviews existing constitutive models developed to simulate the dynamic behavior of sands under drained, undrained, and partially drained conditions. The models are broadly classified in two groups: 1D cyclic nonlinear models for nonlinear seismic site response and advanced constitutive models based on yield surface, hardening, and flow rule concepts to simulate boundary value problems in three-dimensional effective stress space.

2.6.1 1D cyclic nonlinear models for sand

Nonlinear 1D site response analysis is an essential prerequisite of 3D dynamic response analysis of complex systems (e.g., soil-structure systems, dams, etc.). The framework is established by solving the equation of motion and using a set of 1D constitutive equations defining the cyclic shear behavior of soil upon loading/unloading/reloading. DEEPSOIL (Hashash et al. 2015), a 1D site response analysis software that can perform equivalent linear and nonlinear analysis, is highly versatile and can be used in conjunction with 1D constitutive models to perform calibration studies based on free-field cases as an initial step to more complex 3D systems. D-MOD_2 (Matasovic 2006), an upgraded version of D-MOD (Matasovic and Vucetic, 1993), is another software to conduct 1D site response analysis. Both DEEPSOIL and D-MOD_2 solve the wave propagation problem assuming the shear waves propagate vertically through horizontally layered soil deposits. Both software packages utilize versions of the modified-Kondner-Zelasko (MKZ) constitutive model developed by Matasovic (1993). In addition, the General Quadratic/Hyperbolic (GQ/H) model developed by Groholski et al. (2016) is available in DEEPSOIL. These models along with variety of other 1D models are purely in shear space and are characterized by a backbone curve and a set of rules that defines the un/reloading behavior, stiffness degradation due to excess porewater pressure generation, and other effects. As a simple example, the backbone function $\mathrm{F}_{bb}(\gamma)$ for a 1D model can be described by a hyperbola:

$$\mathrm{F}_{bb}(\gamma) = \frac{\mathrm{G}_{max}\gamma}{1 + \left(\frac{\mathrm{G}_{max}}{\tau_{max}}\right)|\gamma|} \tag{2-62}$$

where G_{max} = maximum shear modulus; τ_{max} = shear strength at large shear strain; and γ = shear strain. Then, $\mathrm{F}_{bb}(\gamma)$ can be used with un/reloading rules to simulate cyclic behavior. These rules can be obtained from Masing (1926) rules known as Masing behavior, extended Masing rules (Kramer 1996), and/or non-Masing (Phillips et al. 2009) rules which better captures the hysteretic damping observed in laboratory tests.

2.6.1.1 Modified Kondner – Zelasko (MKZ) model

The MKZ hyperbolic model, a generic model for clays and sands, is based on the hyperbolic model developed by Kondner and Zelasko (1963). Modification was introduced by adding two additional parameters, β and s, that adjust the shape of backbone curve:

$$\tau = \frac{\mathrm{G}_{max}\gamma}{1 + \beta(\frac{\gamma}{\gamma_r})^s} \tag{2-63}$$

where τ = shear strength and β,γ_r and s are model parameters. This model defines the backbone curve without considering effective stress. Hashash and Park (2001) introduced effective stress dependency by making γ_r depend on effective stress, as:

$$\gamma_r = Reference\ Strain\ (\frac{\sigma_v'}{Reference\ Stress})^b \tag{2-64}$$

where σ_{ref} = reference effective vertical stress (0.18 MPa) at $\gamma_r = \tau_{max}/G_{max}$ = *reference strain*, and a and b are curve fitting parameters.

2.6.1.2 General Quadratic/Hyperbolic (GQ/H) model

The GQ/H model was developed to properly represent the shear strength mobilized at large shear strains. This was the main departure from other 1D hyperbolic constitutive models and is necessary because modulus reduction curves obtained from laboratory tests tend to over- or under-estimate the shear strength at large strains due to the extrapolation of curve fits to laboratory modulus reduction data. The GQ/H model allows the control of the shear strain – shear stress curve and asymptotically approaches the shear strength defined at large shear strain. The shear strain – shear stress curve is described as:

$$\frac{\tau}{\tau_{max}} = \frac{2(\frac{\gamma}{\gamma_r})}{1 + \left(\frac{\gamma}{\gamma_r}\right) + \sqrt{\left[1 + \left(\frac{\gamma}{\gamma_r}\right)\right]^2 - 4\theta_\tau(\frac{\gamma}{\gamma_r})}} \tag{2-65}$$

where θ_τ is defined as:

$$\theta_\tau = \theta_1 + \theta_2 \frac{\theta_4 \left(\frac{\gamma}{\gamma_r}\right)^{\theta_5}}{\theta_3^{\theta_5} + \theta_4 \left(\frac{\gamma}{\gamma_r}\right)^{\theta_5}} \leq 1 \tag{2-66}$$

where θ_1 through θ_5 are curve-fitting parameters used to obtain the best fit to the normalized modulus reduction curves over a specified strain range. This model can be utilized for both clays and sands and both Masing type and non-Masing type hysteretic behavior. Further information about the model can be found in Groholski et al. (2016).

2.6.2 Plasticity-based Constitutive Models for Sand

Hyperbolic models are useful to simulate the free-field 1D dynamic response of level or gently sloping ground. In addition, along with some excess porewater pressure models pseudo-coupled via empirical relations (i.e., no direct coupling in the constitutive equations) to the soil model at a constitutive level with a stiffness degradation rule, liquefaction studies potentially can be conducted. However, a more general method to represent soil behavior can be achieved using advanced constitutive modeling techniques that use basic principles of mechanics (Kramer 1996). Advanced constitutive models generally use plasticity concepts and require a yield surface (or function), hardening rules, and flow rules. The yield function determines the limit stress conditions for elastic response. The limit stress conditions depend on the effective stress state, σ, and a strength

parameter, k, that defines the boundaries of the yield surface. The simplest form of the yield condition is defined as:

$$f(\sigma, k) = 0 \tag{2-67}$$

In case of perfect plasticity response, the value of k is constant. However, if any hardening (or softening) laws are incorporated, depending on the plastic strains (or other state variables), the value of k can change linearly or nonlinearly. The numerical value of f determines the behavior of the material model. If f is negative, the material behaves elastically and no plastic straining (no yield condition) occurs. If f attempts to exceed zero, plastic behavior is triggered. Therefore, the stress state is immediately brought to the yield surface and f is set to zero by a special numerical technique [e.g., a radial return algorithm (Simo and Hughes 1998)]. This means that f cannot become positive in any case and the stress state cannot exceed the limits of the yield surface, which is presented schematically in Figure 2-34.

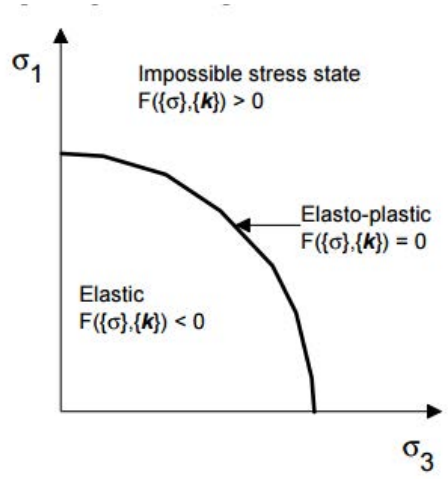

Figure 2-34 Schematic of yield surface in principal stress space (from Stewart et al. 2008).

Flow rules establish the relation between a stress increment and plastic strain increment. The simplest functional form in principal stress space can be expressed as:

$$\Delta\varepsilon_k^p = \lambda \frac{\partial g(\sigma, m)}{\partial \sigma_k}, k = 1,2,3 \tag{2-68}$$

where $\Delta\varepsilon_k^p$ is the plastic strain increment, λ is a positive scalar multiplier determined from a consistency condition, and g is the plastic potential function that is defined by the stress state and some state variable. There are two types of flow rules: (1) associative; and (2) non-associative. If the plastic potential function is the same as the yield function ($g = f$), the flow rule is associative and the plastic strain increment is perpendicular to the yield surface. The schematic of the flow rule is presented in Figure 2-35.

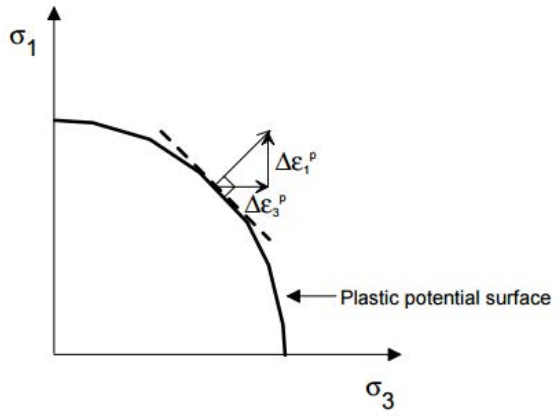

Figure 2-35 Schematic of plastic flow rule in principal stress space (from Stewart et al. 2008)

The change in the size and shape of the yield surface is described by hardening (or softening) laws. The size change (expansion or contraction of the yield surface) is provided by isotropic hardening during which the center of the yield surface remains the same while the size is expanding or contracting. The translation of the yield surface along the stress space is provided by kinematic hardening during which the yield surface moves in the stress space without any size change. Both isotropic and kinematic hardening are individually visualized in principal stress space in Figure 2-36.

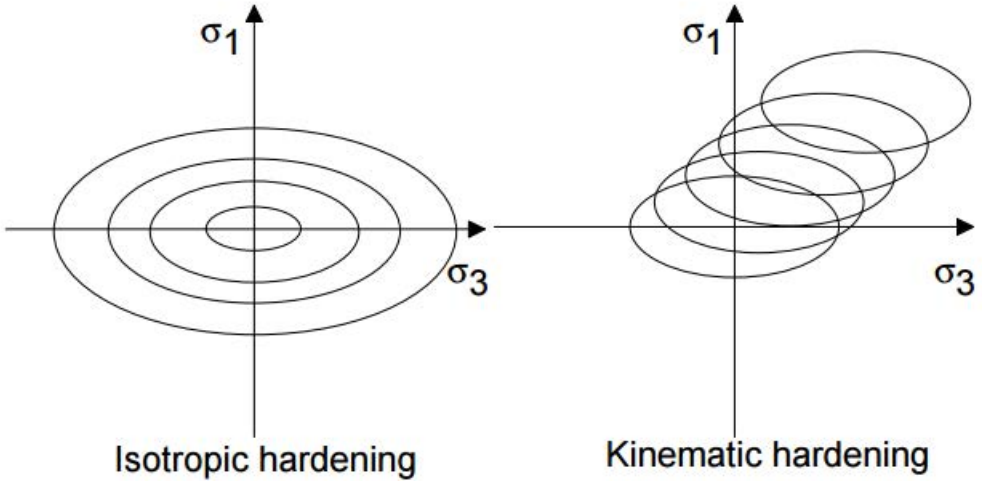

Figure 2-36 A schematic of isotropic and kinematic hardenings in principal stress space (from Stewart et al. 2008).

In the context of geotechnical engineering, different plasticity-based constitutive models have been developed and used to simulate the 3D nonlinear, cyclic behavior of sands. These models are typically established from two frameworks: (1) multi-yield surface plasticity (Mroz 1967; Iwan 1967); and (2) bounding surface plasticity (Dafalias and Popov 1975; Krieg 1975). Another framework, distributed element plasticity (or DEP) for cyclic loading, was based on Iwan (1967) and is used to simulate soil behavior. A 3D generalization of DEP type models was established by Chiang and Beck (1994) and used by researchers to model the nonlinear monotonic shear behavior of sands in three dimensional stress space. A DEP model does not require any kinematic hardening rule to achieve proper cyclic response. Einav and Collins (2008) demonstrated the physical meaning of

the DEP-type constitutive setup related to the statistical distribution of micromechanical yielding of a representative volume element. Table 1 summarizes the constitutive models that are extensively reviewed in the following subsections.

Table 2-2 Summary of Plasticity Models, Underlying Frameworks and Software

Model	Plasticity Framework	Computational Software
Prevost (1985) & PDMY	Multi-yield surface	OpenSees
NorSand	Cambridge type	FLAC
Dafalias Manzari	Bounding surface	OpenSees
PM4Sand	Bounding surface	FLAC
MIT-S1	Bounding surface	Plaxis (upon request)
Simplified MIT-S1	Bounding surface	Unknown
UBC Sand	Hyperbolic Hardening	Plaxis, FLAC

2.6.2.1 Prevost (1985) frictional coarse-grained (cohesionless) soil model

Prevost (1985) was one of the first examples of multi-yield surface plasticity used in constitutive modeling of frictional coarse-grained (cohesionless) soils. The model takes advantage of the simplicity and efficiency of J2 plasticity theory and applies a multi-yield surface concept to describe nonlinear shear behavior and shear induced anisotropy in a piecewise linear fashion. The yield surfaces used to define the model are conical (as shown in Figure 2-37) and f for each surface is computed as:

$$f = \frac{3}{2}(\boldsymbol{s} - p\boldsymbol{\alpha}) : (\boldsymbol{s} - p\boldsymbol{\alpha}) - k^2 p^2 \tag{2-69}$$

where $\boldsymbol{s}$ = the deviatoric stress tensor, $p = \frac{\sigma_{ii}}{3}$, the effective mean confining stress, $\boldsymbol{\alpha}$ = kinematic deviatoric tensor defining the coordinates of the yield surface center in principal stress space, and k is a soil strength parameter defined above.

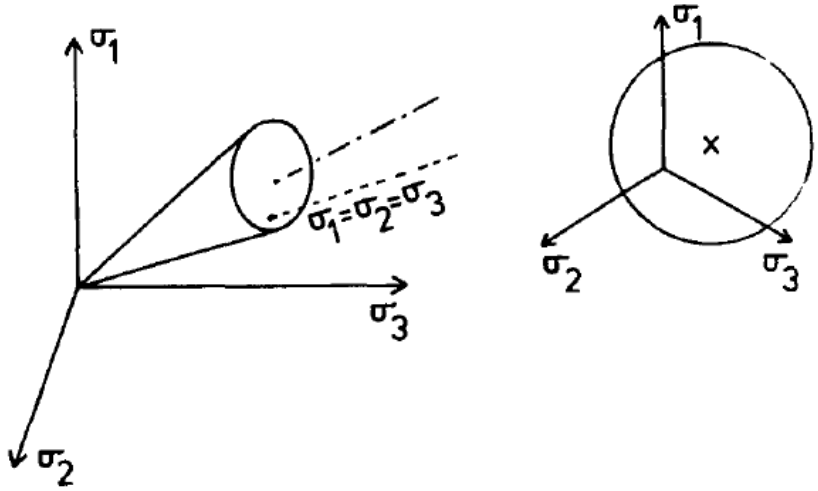

Figure 2-37 Yield surface in principal stress space (from Prevost 1985).

The purely deviatoric kinematic hardening rule used to develop the model is capable of handling general 3D nonlinear shear stress – shear strain behavior under cyclic loading. It allows the yield surfaces to move in 3D stress space and produces Masing type un/reloading behavior. Any experimental data obtained from laboratory tests such as direct simple shear or triaxial tests can be incorporated by adjusting the hardening modulus.

The flow rule for shear-induced volumetric behavior is non-associative and the direction of the plastic volumetric strains are related to the effective stress ratio as:

$$3P'' = \frac{\left(\frac{\eta}{\eta_{pt}}\right)^2 - 1}{\left(\frac{\eta}{\eta_{pt}}\right)^2 + 1} \tag{2-70}$$

where P'' is the volumetric component of the plastic strain directions, η_{pt} is the phase transformation stress ratio and η is the current effective stress ratio defined by:

$$\eta = \frac{\left(\frac{3}{2}\boldsymbol{s}:\boldsymbol{s}\right)^{\frac{1}{2}}}{p} \tag{2-71}$$

The model is able to represent stress ratio-dependent, shear-induced volumetric behavior and allow for volumetric deformations in both loading and un/reloading by a non-associative flow rule. The phase transformation stress ratio (η_{pt}) is used to define contractive and dilative stress states. This is achieved by the term η /η_{pt} in (2-70). If η < η_{pt}, contraction occurs, and if η >η_{pt}, dilation occurs. When η = η_{pt}, no plastic volumetric strain occurs. The general deviatoric behavior schematic of the multi-yield surface based model is presented in Figure 2-38.

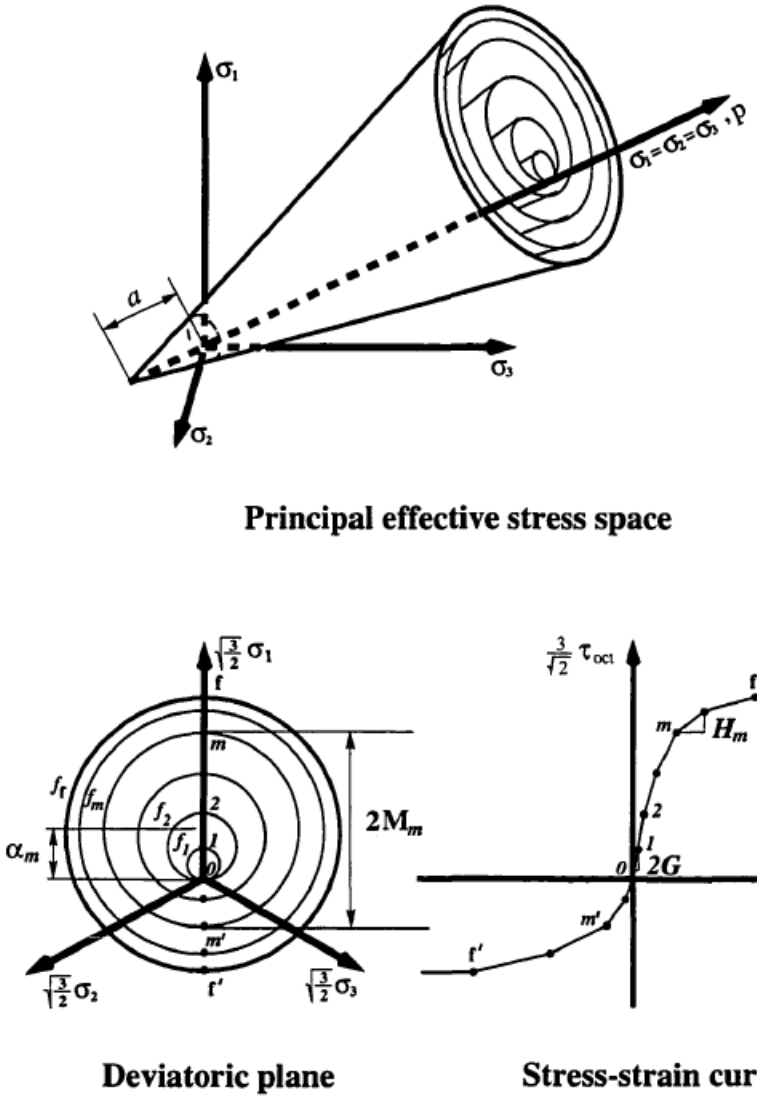

Figure 2-38 Multi-yield surface model general scheme (from Parra 1996).

Parra (1996) expanded the Prevost (1985) constitutive model, adding features to better represent dilative and contractive behavior and cyclic mobility, which is important to determine lateral deformations during dynamic loadings. Parra (1996) separated the non-associative flow rule into different functional forms for contraction and dilation behavior as follows:

$$3P'' = \frac{\left(\frac{\eta}{\eta_{pt}}\right)^2 - 1}{\left(\frac{\eta}{\eta_{pt}}\right)^2 + 1} \psi_c \ (during\ contraction\ phase) \tag{2-72}$$

$$3P'' = \frac{\left(\frac{\eta}{\eta_{pt}}\right)^2 - 1}{\left(\frac{\eta}{\eta_{pt}}\right)^2 + 1}\psi_d \ (during\ dilation\ phase) \tag{2-73}$$

where ψ_c and ψ_d are model contraction and dilation functions determined by η, η_{pt}, cumulative deviatoric strains, and effective mean stress. The parameters ψ_c and ψ_d can be calibrated based on experimental observations.

Parra's work provided flexibility for controlling the volumetric behavior and large shear strains observed during cyclic mobility by modifying the maximum octahedral shear strain reached at maximum mobilized shear strength. The ideal octahedral shear stress – octahedral shear strain and octahedral shear stress – effective mean stress for the model are shown in Figure 2-39.

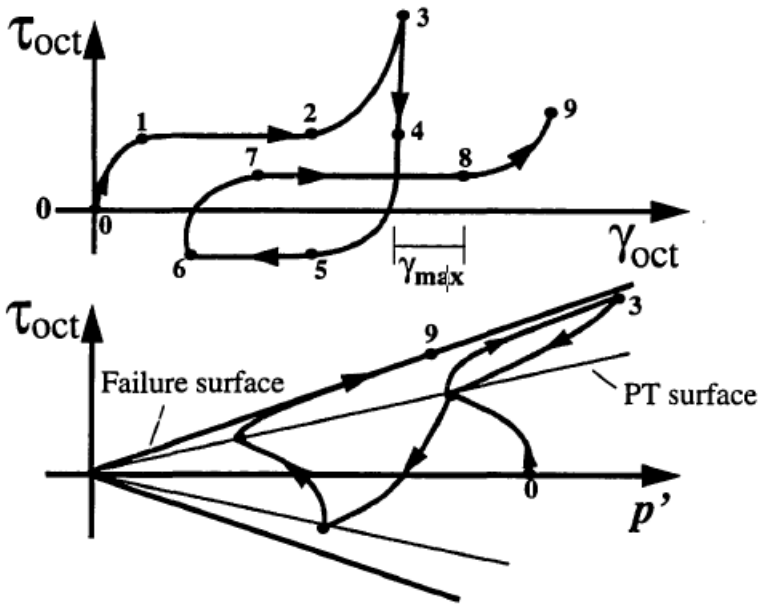

Figure 2-39 Basic response mechanism of Parra (1996) constitutive model in octahedral shear space and effective mean stress space (from Parra 1996).

The model was further extended by Yang (2000) to improve the behavioral performance by introducing a perfectly plastic slip strain modification which provides flexibility for the model to better represent cyclic mobility. The final form of the model has been implemented in OpenSees (Mazzoni et al. 2006) as the pressure-dependent, multi-yield (PDMY; PressDependMultiYield) model and has been utilized in 3D large-scale boundary value problems (e.g., Elgamal et al. 2002, 2005, 2008; Yang et al. 2003; Lai et al. 2004; and Karimi and Dashti 2015).

Although the PDMY model has been utilized in 3D boundary value problems, hysteretic behavior represented by the model is Masing type and overestimates damping at medium to large shear strain levels. In addition, the nature of the multi-yield surface concept causes memory/storage problems (Prevost 1982), even using modern computing methods. That is, the multi-yield surface

plasticity framework requires a significant amount of memory to solve large-scale problems because the model tracks individual variables associated with each yield surface. Fluid coupled problems and additional history variables for non-associative flow rules place more demand on memory usage and reduce computational efficiency. In addition, numerical implementation of kinematic rules for the multi-surfaces is demanding because of the necessity to prevent the potential intersection of the yield surfaces.

2.6.2.2 NorSand model

The NorSand model was developed by Jefferies (1993) for sands and is a generalized critical state (Roscoe et al. 1958; Schofield and Wroth 1968) compatible class of Cambridge type constitutive models. The model explicitly uses state parameter (ψ; Been and Jefferies 1985) as a state variable to control isotropic hardening and softening behavior. Ultimately after large shear strains, soil elements reach the critical state where continuous shear deformation occurs without further volume change. In addition, the use of ψ incorporates the effects of effective stress and void ratio on model behavior. Similar to Cam clay models, the plastic flow rule takes the following form:

$$D = \frac{(M - \eta)}{1 - N} \tag{2-74}$$

where $D = \dot{\epsilon}_p/\dot{\epsilon}_q$ is a "dilatancy function" that relates plastic deviatoric strains ($\dot{\epsilon}_q$) to plastic volumetric strains ($\dot{\epsilon}_p$), M is critical state stress ratio and N is a volumetric coupling coefficient.

The yield surface is derived from energy considerations stating that the rate of plastic work is always positive, and is related to the flow rule via normality rule (i.e., the associative flow rule), consistent with Drucker (1957), as:

$$\eta = M\left[1 + \ln\left(\frac{p_i}{p}\right)\right] \; if \; N = 0 \tag{2-75}$$

$$\eta = M\left[1 + (\mathrm{N} - 1)\left(\frac{p}{p_i}\right)^{\frac{N}{1-N}}\right] \; if \; N \neq 0 \tag{2-76}$$

where p = mean effective stress and p_i = effective mean stress that controls the yield surface via a hardening rule defined as image mean stress for NorSand. At the image mean stress, either the void ratio equals the critical state void ratio, or the shear stress ratio equals the shear stress ratio at critical state. The details of the derivation can be found in Davis and Selvadurai (2002).

The NorSand-M version was rigorously evaluated for different types of monotonic loading conditions and was implemented in the commercial software FLAC for plane strain boundary value problems. The "-M" stands for monotonically increasing loads where the effective mean stress and deviatoric stress increase monotonically and un/reloading are elastic. Recently, Jefferies et al. (2015) demonstrated the performance of the cyclic behavior obtained from the NorSand-PSR model by comparing the simulated results (obtained from constitutive driver) to cDSS tests. The "-PSR" stands for "principal stress rotation" and the study was intended to include the effects of principal stress rotation on the constitutive model by modifying the hardening rule to capture the observed

behavior in cDSS tests. Although the -PSR model still captures monotonic behavior reasonably well, the comparison plots presented in Jefferies et al. (2015) shows that the model still suffers from elastic un/reloading behavior and therefore produces stiffer response in small strains, neglecting the importance of small strain soil nonlinearity. This drawback is due to the fact that, in order to keep the formulation simple, the model does not involve any kinematic hardening.

2.6.2.3 MIT-S1 model

Pestana (1994) developed the MIT-S1 constitutive model, a unified effective stress soil model for clays and sands, to describe the rate independent behavior of normally and over-consolidated soils using incrementally linearized elasto-plasticity theory (Prevost 1978). The model consists of a single anisotropic "leminscate shape" bounding surface (Figure 2-40) that is a function of effective stress and current void ratio with density and rotational hardening rules to define shear behavior.

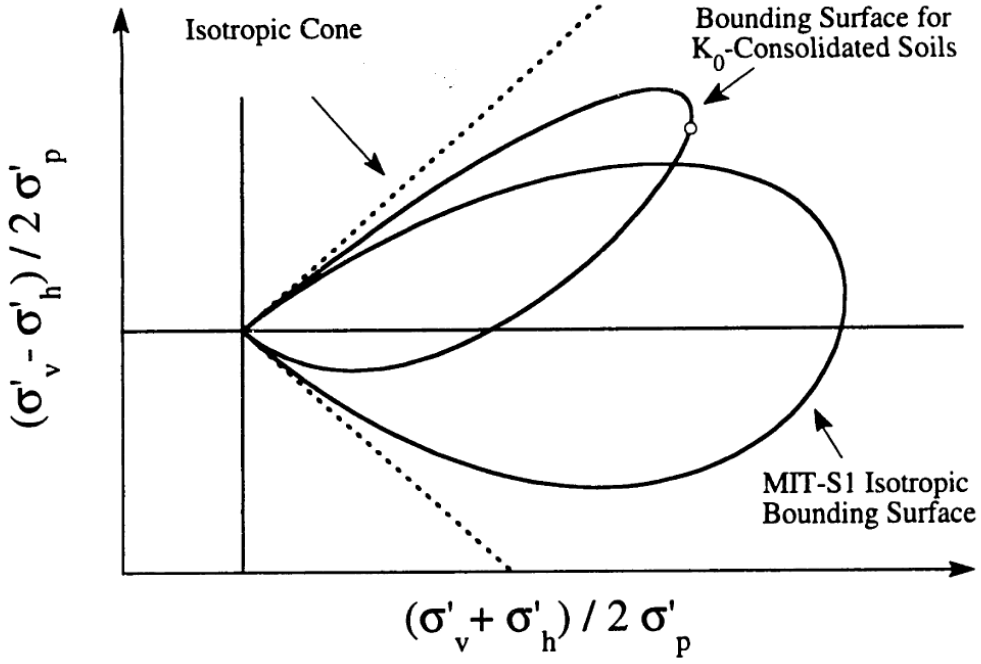

Figure 2-40 Schematic of anisotropic bounding surface used in MIT-S1 (from Pestana et al. 2002).

A critical state compatible non-associative flow rule is used to define plastic strains. The model can handle small strain nonlinearity, and simulations were in good agreement with drained and undrained monotonic triaxial tests on sands over wide ranges of effective mean stress and density (Pestana et al. 2002). Pestana et al. (2002) also presented "perfectly hysteretic" cyclic behavior obtained from the model, as shown in Figure 2-41. However, the authors of this report are not aware of any study that demonstrates that this model can reasonably simulate cyclic laboratory tests and/or solve large-scale boundary value problems where seismic loading is considered.

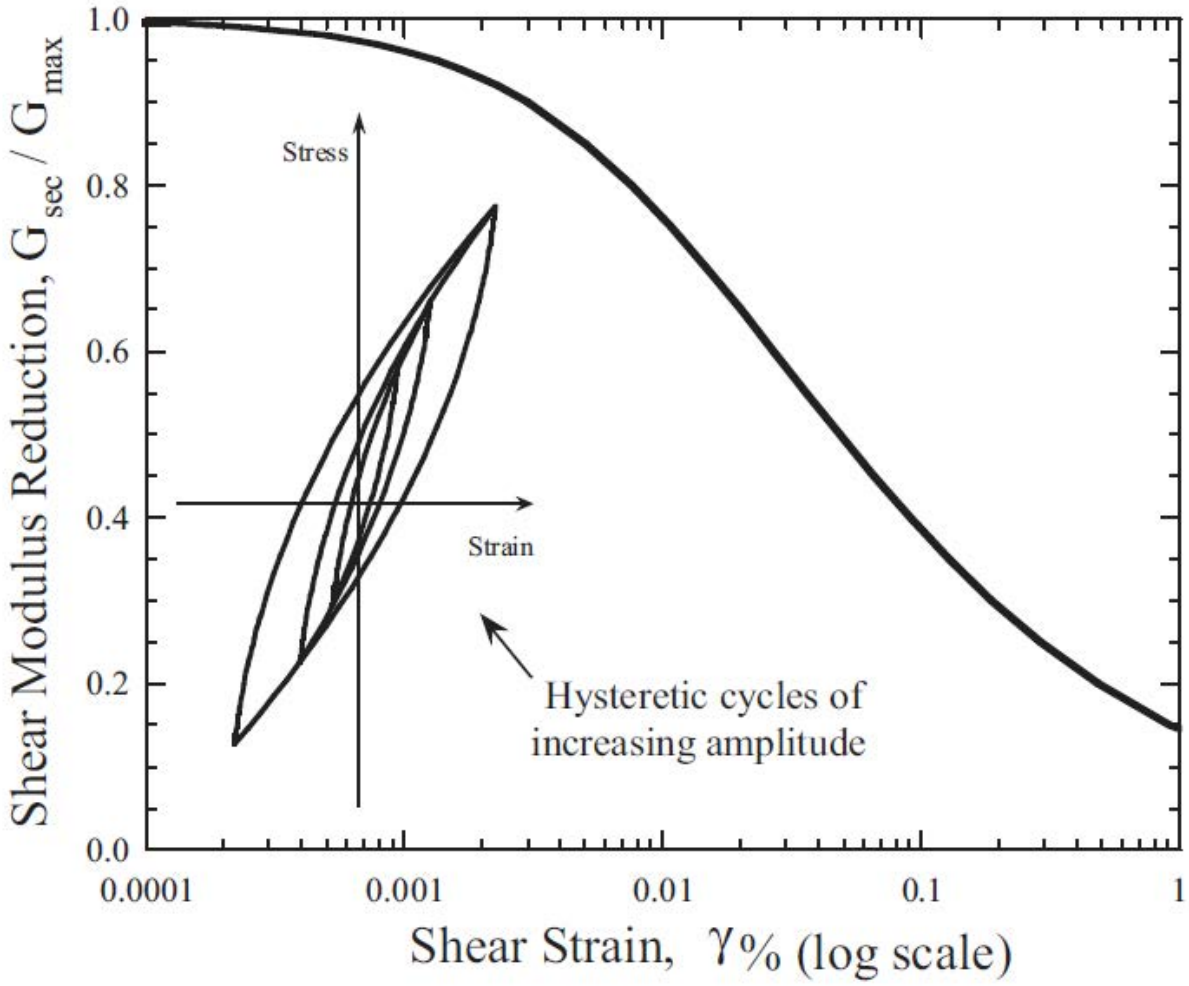

Figure 2-41 Hysteretic behavior and small strain nonlinearity in MIT-S1 (from Pestana et al. 2002).

Assimaki et al. (2000) reduced the generalized MIT-S1 model to a simplified form to describe the behavior of coarse-grained soils under cyclic loading via modulus reduction and damping curves. A primary focus was to describe the modulus reduction and damping curves analytically by extracting information from the original MIT-S1 model. A comparison of simplified MIT-S1 modulus reduction and damping curves with experimental data was presented in their study and demonstrated good agreement for small strains ($< 10^{-4}$). The modulus reduction and damping curves obtained from the simplified model were shown to apply to frequency domain 1D site response analysis. This simplified model is restricted to only 1D site response analysis.

2.6.2.4 Dafalias-Manzari model

Manzari and Dafalias (1997) is another example of a bounding surface plasticity concept applied to sand modeling within the critical state soil mechanics framework. The model is capable of working in both drained and undrained monotonic and cyclic loading conditions. Similar to multi-yield surface models, this model uses the same yield function presented in eqn. (2-69). The parameters M_c (critical state stress ratio), M_c^d (dilation stress ratio), and M_c^b (bounding stress ratio) shown in Figure 2-42 control the shear and volumetric behavior.

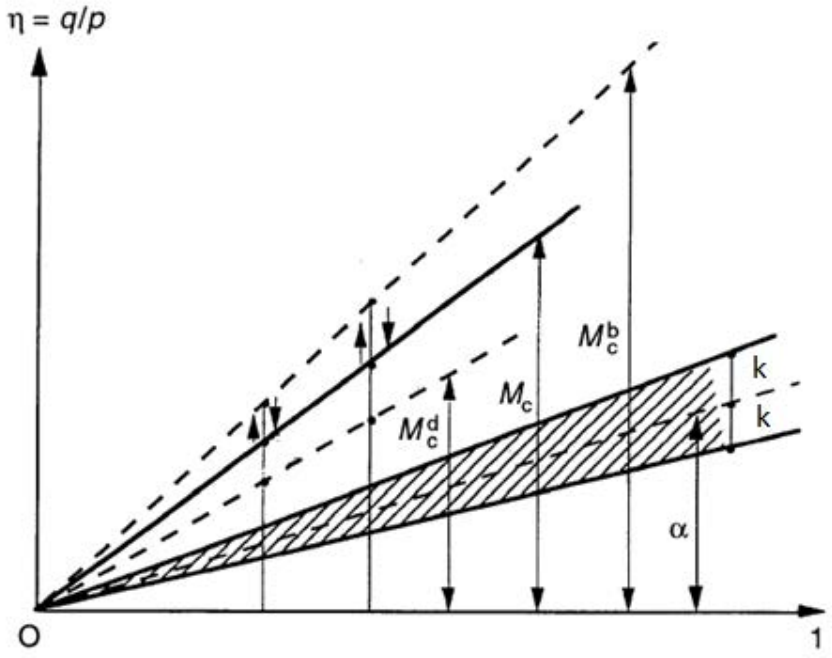

Figure 2-42 Schematic illustration in the η (effective stress ratio), 1 (p/p) space of the bounding (peak) stress ratio M_c^b, critical stress ratio M_c and dilatancy stress ratio M_c^d, the back-stress ratio (center of the yield surface) α defined by hardening law, the width 2k of the wedge-type yield surface (from Manzari and Dafalias 1997).

The incremental plastic volumetric strains $d\varepsilon_v^p$ are related to incremental plastic deviatoric strains $|d\varepsilon_q^p|$ by a non-associative flow rule as following:

$$d\varepsilon_v^p = D|d\varepsilon_q^p| \tag{2-77}$$

where D is the dilatancy function defined as:

$$D = A_d(M_c^d - \eta) \tag{2-78}$$

where A_d is a function of the soil state and similar to the (1-N) term introduced in the NorSand model. Eqn. (2-78) implies that when $\eta < M_c^d$, volumetric behavior is contractive and when $\eta > M_c^d$, volumetric behavior is dilative. This behavior is adapted from Rowe's (1962) dilatancy theory. In addition, in Dafalias and Manzari (2004), both M_c^d and M_c^b depend nonlinearly on M_c and the functions have the following form:

$$M_c^d = M_c * \ exp(n^d\psi) \tag{2-79}$$

$$M_c^b = M_c * \ exp(-n^b\psi) \tag{2-80}$$

where n^d and n^b are material parameters (that have values > 0) and ψ is the state parameter.

Eqns. (2-79) and (2-80) show that the general model behavior is state parameter (ψ) driven and critical state compatible, therefore it can capture post-peak strain softening, and when $\psi = 0$, $M_c^d = M_c$, and dilation is zero. Depending on the initial state, M_c^b can be greater or smaller than M_c and once $\psi = 0$, $M_c^b = M_c$ so that critical state stress ratio is achieved. Therefore, the model also can capture volumetric behavior. However, the Manzari and Dafalias (1997) model has a $p - q$ "locking" problem, which has a crucial effect on modeling liquefaction. Specifically, as illustrated in Figure 2-43, the $p - q$ response stabilizes after a small number of cycles and no further decrease in effective stress occurs.

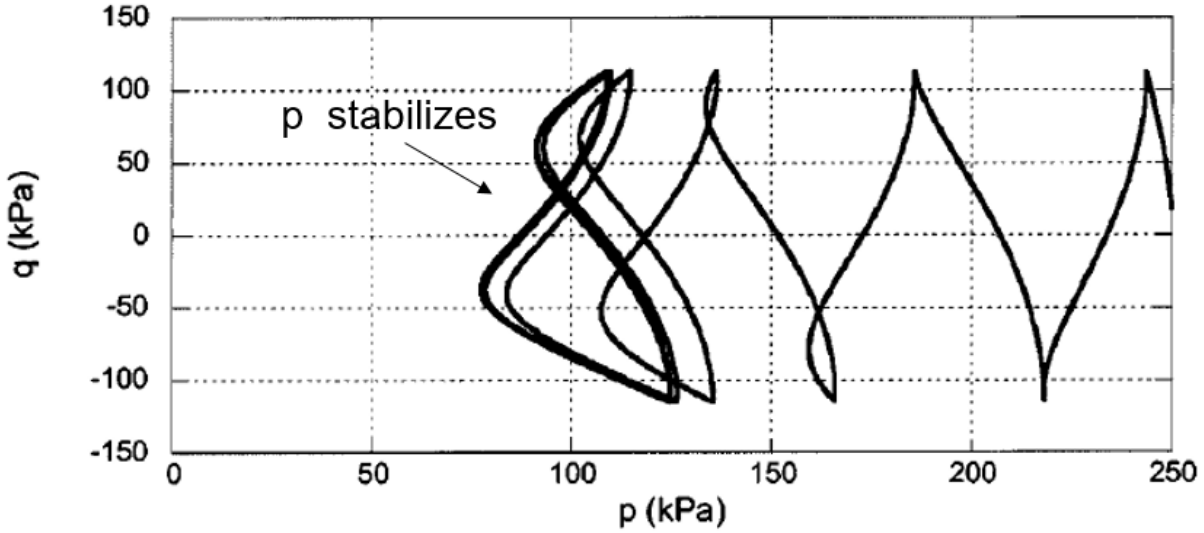

Figure 2-43 Stabilization of p on p-q path under cyclic loading (from Manzari and Dafalias 1997).

However, in a micro-mechanical context, Nemat-Nasser et al. (1982) showed that as the effective mean stress approaches zero during cyclic loading, a sand exhibits strong dilation during loading but undergoes stronger contraction during unloading due to destruction of the fabric. Based on this study, Dafalias and Manzari (2004) added fabric terms to their model to better represent sand behavior at low effective stresses. The fabric term is simply embedded in the A_d parameter as:

$$A_d = A_0(1+< \mathrm{sz} >) \tag{2-81}$$

where A_0 is initial constant, $s = \pm 1$ depending on the current stress ratio, and z represents the cumulative fabric dilatancy effects and is incrementally calculated as:

$$dz = -c_z < -d\varepsilon_v^p > (sz_{max} + z) \tag{2-82}$$

where c_z and z_{max} are fabric dilatancy related parameters and <> is MacCauley brackets (Dafalias and Manzari 2004). Upon including the fabric term, the z parameter evolves based on the accumulation of volumetric strains, and the $p - q$ locking problem vanishes (Figure 2-44).

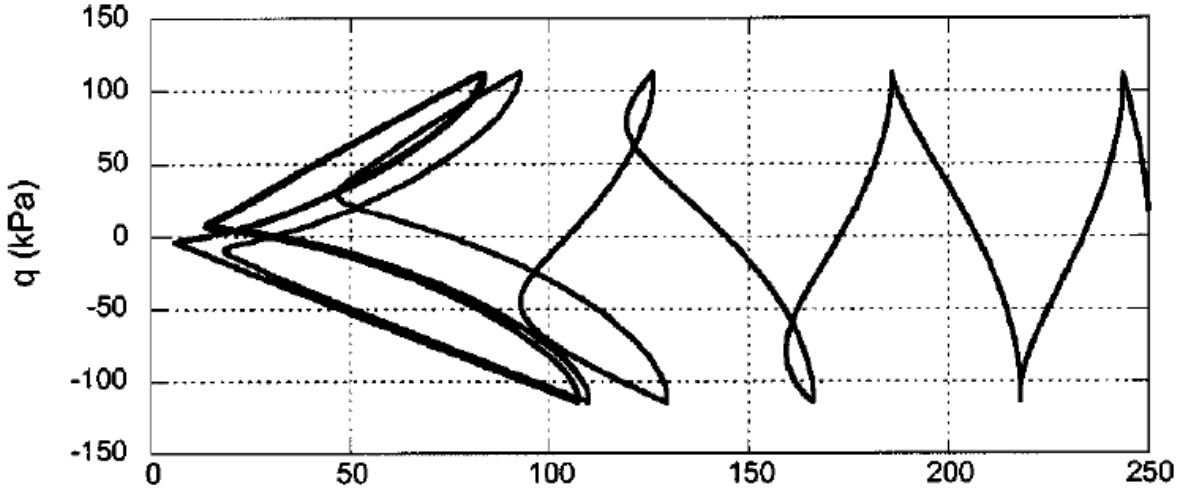

Figure 2-44 Stress path including fabric destruction term (from Dafalias and Manzari 2004).

Multi-dimensional generalization of the Dafalias-Manzari formulation was implemented in OpenSees and recently utilized in a plane strain numerical simulation (Ghofrani et al. 2017) to reproduce the results obtained from dynamic centrifuge tests performed in the "Liquefaction Experiments and Analysis Project" (LEAP). Even though the cycle by cycle behavior simulated in the model did not match the undrained cyclic triaxial tests, the overall behavior after a certain number of cycles was reproduced reasonably. In addition, plane strain numerical simulation worked reasonably well to simulate a gently sloping centrifuge sand model subjected to a ramped one-directional sinusoidal motion. However, Boulanger et al. (2012) demonstrated that the model still shows locking of hysteresis loops after a certain number of cycles which is not experimentally observed (Figure 2-45).

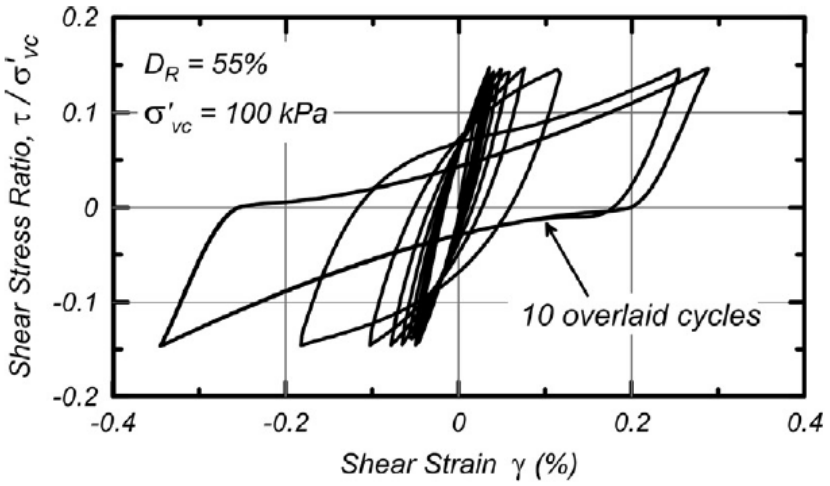

Figure 2-45 Overlaying hysteretic behavior after certain cycles of loading (from Boulanger et al. 2012).

In addition, Ghofrani et al. (2017) reported that the implemented model still suffers from the over-shooting problem during un/reloading (Figure 2-46) which is a typical problem for bounding surface plasticity-based constitutive models (Mojtaba et al. 2014).

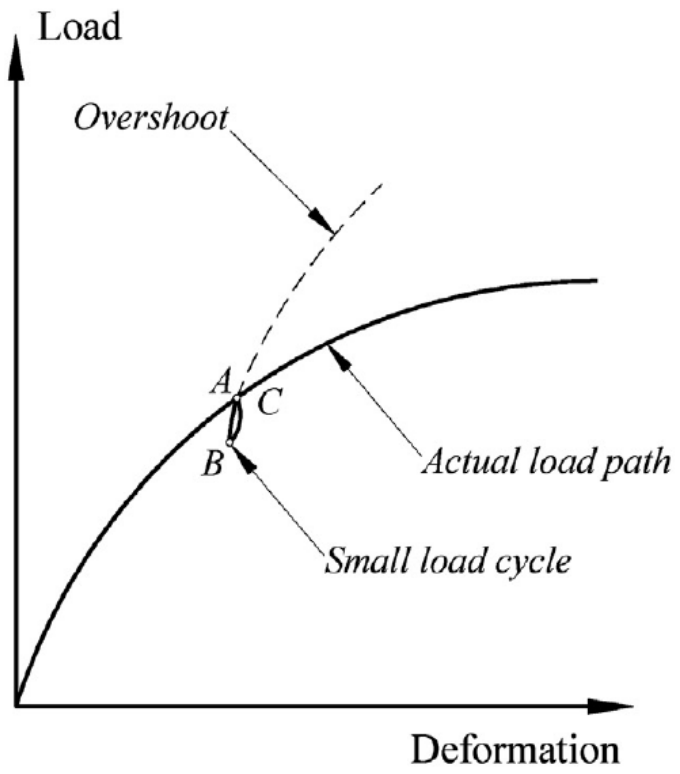

Figure 2-46 Demonstration of over-shooting problem on load-deformation curve due to small cycle of un/re-loading (from E-Kan et al. 2014).

2.6.2.5 UBCSand model

UBCSAND (Puebla et al. 1997), a relatively simple and practical effective stress plasticity model, was developed for sandy soils to study liquefaction phenomenon. The model uses a relation similar to the Duncan and Chang (1970) hyperbolic formula to define the hardening relation between an incremental plastic shear strain and incremental stress ratio increase:

$$d\gamma^p = \frac{1}{G^p/\sigma'} d\eta \tag{2-83}$$

where $d\gamma^p$ is incremental plastic shear strain and G^p is the plastic modulus, which is computed as:

$$G^p = G_i^p \left(1 - \frac{\eta}{\eta_f} R_f\right)^2 \tag{2-84}$$

where G_i^p the initial plastic modulus, η_f is the stress ratio at failure which is equal to sin ϕ', and R_f is the failure ratio used to truncate the best fit hyperbolic relationship that is asymptotic to a Mohr – Coulomb yield stress . The yield function has a Mohr-Coulomb yield criteria form and the plastic volumetric strain increments are calculated using a non-associated flow rule derived by Puebla et al. (1997), which essentially follows Rowe (1962), as:

$$d\varepsilon_v^p = d\gamma^p(\eta_{pt} - \eta) \tag{2-85}$$

where η is the current stress ratio and η_{pt} is phase transformation stress ratio.

Puebla et al. (1997) demonstrated that the model properly predicts monotonic loading laboratory tests as well as large scale boundary value problems related to static liquefaction. Model performance was validated against centrifuge test results, and good agreement was observed. In addition, Byrne et al. (2004) demonstrated the plane strain space applicability of the model by simulating dynamic centrifuge tests. Similarly, Armstrong et al. (2012) used the model to simulate dynamic centrifuge tests. Overall, the model has been shown to provide reasonable fidelity given its relative simplicity. However, there are certain drawbacks introduced with the model's simplicity, such as: (1) unloading is perfectly elastic and cannot simulate small strain nonlinearity during cyclic loading, thereby overestimating stiffness in stress-controlled loading (Figure 2-47 and Figure 2-48) and overestimating hysteretic damping in strain-controlled loading; and (2) in cyclic liquefaction problems, the model cannot properly simulate contractive behavior at low mean effective stresses due to the perfectly elastic response during the entire unloading path (Figure 2-48).

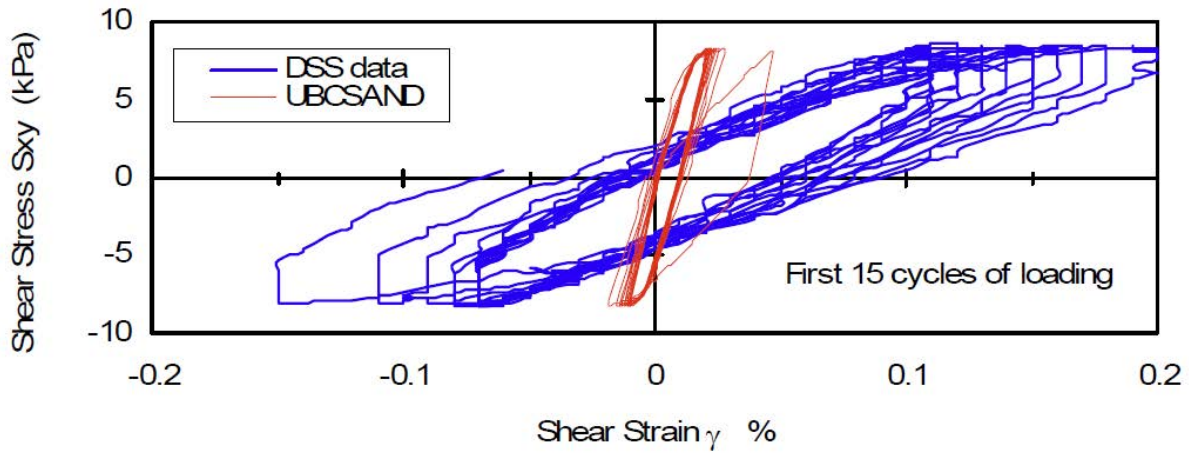

Figure 2-47 UBCSAND Simulated and DSS test measured hysteretic behavior in 15 cycles (from Itasca Consulting Group 2009).

Therefore, caution is needed when the model is utilized to study the accumulative effects of small to medium amplitude cyclic strains where small strain nonlinearity is important. Similarly, as explained above, caution is required when applying the model to cyclic liquefaction problems because the model does not properly capture soil response.

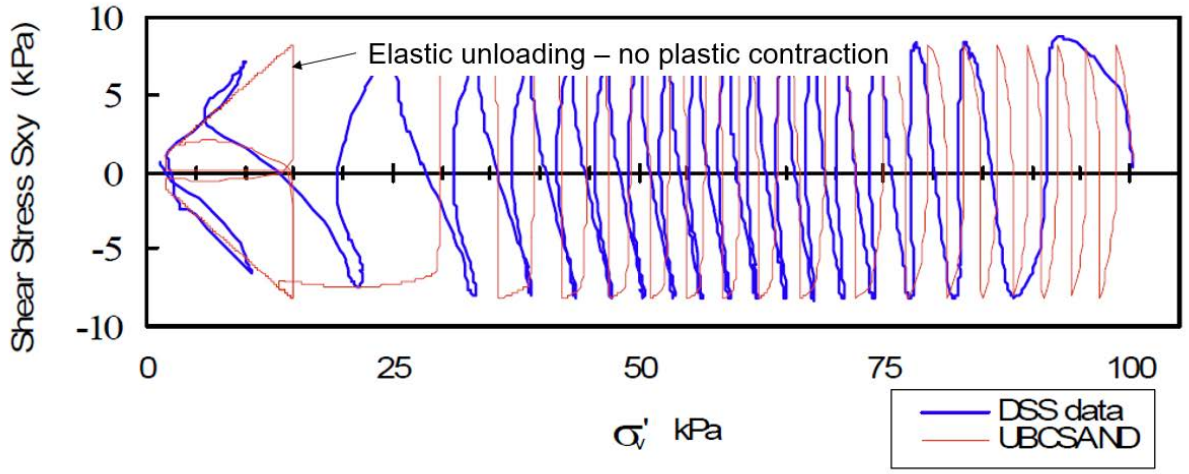

Figure 2-48 Measured vs simulated stress path from UBCSAND (from Itasca Consulting Group, 2009).

2.6.2.6 PM4Sand model

Based on the Dafalias and Manzari (2004) model, Boulanger and Ziotopoulou (2012, 2015) developed a sand plasticity model, PM4Sand, that attempts to improve the predictive capabilities of the model for seismic applications. Improvements are achieved through equation-level calibrations derived from experimental and case history data. The model replaces the state parameter with the relative state parameter index (Boulanger 2003) to capture critical state behavior. One of the main modifications is the revision of the fabric destruction formulation (z) to make it dependent on the plastic shear strain rather than the plastic volumetric strains, expressed as:

$$dz = -\frac{c_z}{1+<\frac{z_{cum}}{2z_{max}}-1>}\frac{<-d\varepsilon_v^p>}{D}(sz_{max}+z) \tag{2-86}$$

where dz is related to $<-d\varepsilon_v^p>/D$ which is, in turn, related to the incremental deviatoric strain since $D = d\varepsilon_v^p/d\varepsilon_q^p$ and z_{cum} is the cumulative value of absolute changes in z.

In addition, significant empirical improvements were introduced to the A_d parameter to better simulate cyclic contraction – dilation response of sands (especially relevant to simulating cyclic mobility and liquefaction) over wide ranges of initial effective stress and void ratio. The model separates the contractive volumetric strains and dilative volumetric strains and rigorously formulates A_d based on experimental observations. Figure 2-49 presents the element-level simulations of the model with two different sets of calibrated parameters that produce a significantly better cyclic response compared to the original Dafalias and Manzari (2004) model.

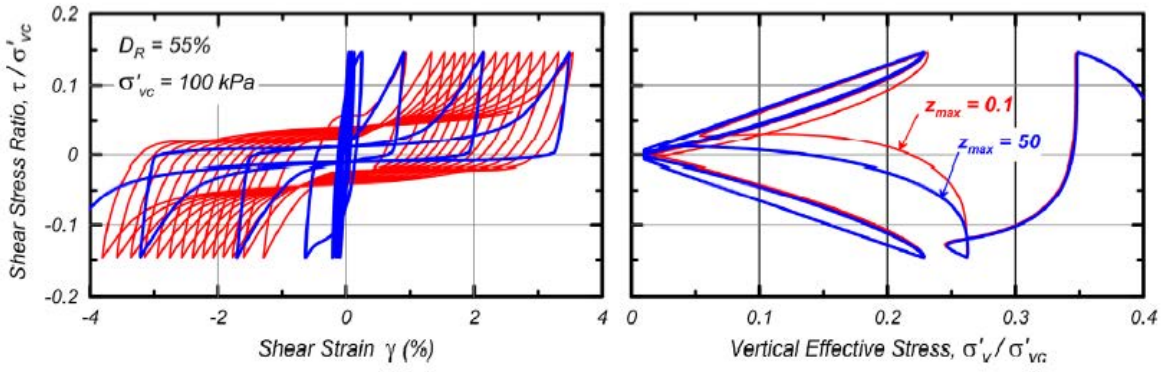

Figure 2-49 PM4Sand element level simulations with two different calibrated parameters z_{max} = 0.1, and z_{max} = 50 (from Boulanger et al. 2013)

Moreover, an empirical scheme outside of the plasticity formulation (empirically reducing the elastic shear strains) was introduced to calculate post-shaking reconsolidation strains. Armstrong et al. (2015) demonstrated the performance of the model in a dynamic centrifuge test simulation that involved pile pinning of a bridge abutment affected by cyclic liquefaction. The study showed that the model reasonably reproduces the measurements obtained from the dynamic centrifuge test assuming that a plane strain condition is applicable. The main drawback of the model is that the formulation is limited to plane strain conditions which prevents simulation of multi-directional loading conditions for 3D geometries and 3D stress space. In addition, the precision achieved by the model is tempered by the significant effort that is required to calibrate the model parameters for boundary value problems.

2.7 Summary

This chapter presents previous work on estimation of volumetric strains of sands under cyclic loading conditions. Element and centrifuge tests conducted on medium dense to dense coarse-grained soils under unidirectional and bidirectional loading and existing constitutive models for sand including 1D cyclic nonlinear models and advanced models requiring the definition of a yield surface, hardening and flow rule are evaluated. The following items summarize the main topics covered in this chapter:

1. The relevance, advantages, and limitations of simple shear testing in capturing seismic stresses.
2. Descriptions and limitations of the existing unidirectional and bidirectional simple shear testing databases.
3. Key factors affecting volumetric strain in coarse-grained soils, based on the element testing literature.
4. Description of available free-field and near-field unidirectional and bidirectional centrifuge tests on coarse-grained soils from literature.
5. Descriptions and limitations of available semi-empirical models for estimation of volumetric strain under drained, undrained, partially drained, and partially saturated conditions.
6. Review of existing constitutive models and related frameworks for sand, advantages and disadvantages of particular theories and models in the context of 1D, 2D, and 3D modeling.

3 EXPERIMENTAL TESTING PROGRAM

3.1 Introduction

This chapter describes the element and centrifuge testing programs conducted for the project. The element tests were primarily conducted in a multidirectional direct simple shear device under cyclic unidirectional, bidirectional circular, oval, figure-8, and broadband loading paths on four medium dense to very dense sands with varying fines content and plasticity. The centrifuge testing consisted of unidirectional and bidirectional tests conducted on very dense Ottawa sand, conducted under both free-field conditions and with a structure. The testing program had two primary objectives: (1) to develop semi-empirical correlations for estimating settlements and porewater pressure (PWP) generation under bidirectional shaking, with and without a structure; and (2) to provide a high-quality dataset for calibrating a new soil constitutive model that accurately captures bidirectional deviatoric and volumetric response under seismic loads. The laboratory testing database is presented first, including the index properties of the test soils, specimen preparation methods, and oedometer results and the direct simple shear test series. A description of the centrifuge testing program follows. These two unique testing programs afford new insights into the dynamic response of dense coarse-grained soils under realistic multidirectional seismic loads.

3.2 Soils Tested

Four different sands were tested in the element testing program. The sands were selected to represent naturally occurring deposits and common fill soils. These include: (1) a clean uniformly graded sand, Ottawa 40/70 (OT), commercially available from U.S. Silica (classified as SP); (2) a well-graded sand-silt mixture prepared by mixing portions of commercially obtained sands and natural silts sieved from a Mississippi River silty sand (with a final gradation classified as SW-SM); (3) a natural Mississippi River (MR) silty sand obtained from Cape Girardeau, Missouri (classified as SM); and (4) a Mississippi River – Gulf of Mexico (MR-GM) clayey sand mixture (classified as SC). The Gulf of Mexico clay was sampled from the Walker Ridge area, a deep-sea canyon in the Gulf of Mexico. The clean Ottawa sand was used for the dynamic centrifuge tests. The following section summarizes the index properties of the test sands.

3.3 Index Properties

3.3.1 Gradation and scanning electron microscope images

Figure 3-1 shows the grain size distributions of the Ottawa sand, sand-silt mixture, Mississippi River silty sand, and Mississippi River-Gulf of Mexico clayey sand. Throughout the rest of the document these sands are referred to as OT-SP, SW-SM, MR-SM, and MRGM-SC respectively. The index properties and composition of the sands are summarized in Table 3-1. The GEOL6060LV (Low Vacuum) Scanning Electron Microscope (SEM) was used to capture images of the sands at 50 times magnification. Figure 3-2 presents the SEM images of the OT-SP, SW-SM, and MR-SM. The Ottawa sand (OT-SP) has sub-rounded particles, the Lab Mix (SW-SM) consists of sub-rounded to sub-angular particles and the Mississippi river sand (MR-SM) has sub-rounded to sub-angular particles. Since the MRGM-SC is composed of 92.5 % MR-SM, it also consists of predominantly sub-rounded to sub-angular particles.

3.3.2 Limiting void ratios

The Japanese method equivalent to ASTM D4253 (ASTM 2016) was used to determine the minimum void ratio (e_{min}) of the OT-SP and SW-SM; the dry-tipping method equivalent to ASTM D4254 (ASTM 2006) was used for the maximum void ratio (e_{max}) of the OT-SP, SW-SM, MR-SM,

and MRGM-SC. In the Japanese method, a 101.6 mm (4 in) diameter standard Proctor mold is filled with 5 layers of sand, 200 blows being applied per layer with a metal hammer to reach the maximum density. The Japanese method for estimating e_{min} is applicable to sands with a maximum fines content of 15%, i.e. the OT-SP and SW-SM (see Table 3-1 for fines content).

A different method that allows for a higher fines content is required for determining the limiting densities of the MR-SM and the MRGM-SC. The method delineated by Yamamuro and Lade (1988) and Lade et al. (1998) for silty sands is used to measure the e_{min} of MR-SM and MRGM-SC. In this method, 822 gm of sand is first placed into a 2000 ml graduated cylinder with a spoon, and after each 3rd scoop (~ 50 gm) the cylinder is symmetrically tapped eight times with the rubber handle of a screwdriver. The entire sand was thus deposited to measure minimum void ratio, after which the same setup was used to apply the dry tipping method to measure the maximum void ratio. This last step for determining e_{max} is repeated until 5 repetitions result in the same volume.

Because relative density, $D_R = (e_{max} – e)/(e_{max} – e_{min})$ is used as a standard metric for representing the behavior of clean sands, it is important to get a standard measure of the limiting void ratios. Therefore, the limiting density tests for each sand were performed at least 5 times. The results obtained are presented in Table 3-1. The values of e_{max} and e_{min} for the OT-SP, SW-SM, and MR-SM fall within the range of values reported in literature (Table 3-2).

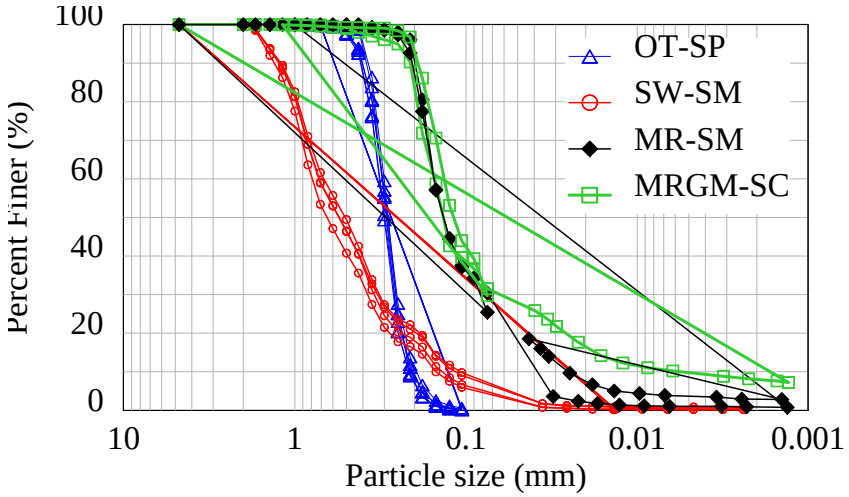

Figure 3-1 Particle size distributions of the test sands: Ottawa sand (OT-SP), Lab mixture (SW-SM), Mississippi River silty sand (MR-SM), and Mississippi River-Gulf of Mexico clayey sand (MRGM-SC).

Table 3-1 Average index properties and grain characteristics for the tested sands.

Sand		Ottawa 40/70	Lab Mix	Mississippi River	Mississippi River-Gulf of Mexico
Nomenclature		OT-SP	SW-SM	MR-SM	MRGM-SC
USCS[a]		SP	SW-SM	SM	SC
D_{10}[a]	(mm)	0.220	0.140	0.033	0.007
D_{30}[a]	(mm)	0.26	0.36	0.08	0.07
D_{50}[a]	(mm)	0.29	0.55	0.15	0.14
D_{60}[a]	(mm)	0.31	0.76	0.16	0.15
C_u[a]		1.41	5.43	4.81	22.73
C_C[a]		0.99	1.22	1.31	4.95
FC	(%)	0.0	7.2	26.1	30.9
CF	(%)	0.0	0.0	1.8	7.9
G_s[b]		2.655 ± 0.006	2.660 ± 0.006	2.653 ± 0.006	2.659 ± 0.009
e_{max}[c]		0.822 ± 0.012	0.631 ± 0.025	1.049 ± 0.006	0.922 ± 0.011
e_{min}[d]		0.504 ± 0.008	0.317 ± 0.021	0.597 ± 0.003	0.601 ± 0.016
$\gamma_{d,max}$[e]	(kN/m^3)	17.33	19.78	18.78	18.96
w_{opt}	(%)	-	-	8.8	11.1
Particle Shape		SR	SR-SA	SR-SA	SR-SA
Composition					
Quartz	(%)	100	85.2	70	64.75
Feldspar	(%)	-	4.2	21	19.425
Carbonates	(%)	-	1	5	4.625
GM		-	-	-	7.5

Note: MR – Mississippi River; USCS – Unified Soil Classification System; D_{50} – median particle size; C_U – coefficient of uniformity; C_C – coefficient of curvature; FC – fines content; G_s – specific gravity; e_{max} – maximum void ratio; e_{min} – minimum void ratio; at least five trials were conducted for the limiting void ratio determinations.

[a]ASTM D2487 (ASTM 2011)

[b]ASTM D854 (ASTM 2014)

[c]Dry tipping method equivalent to ASTM D4254 (ASTM 2006)

[d]Japanese method equivalent to ASTM D4253 (ASTM 2016) for Ottawa sand; Lade et al. (1998) method for MR sand

[e]ASTM D1557 (ASTM 2012)

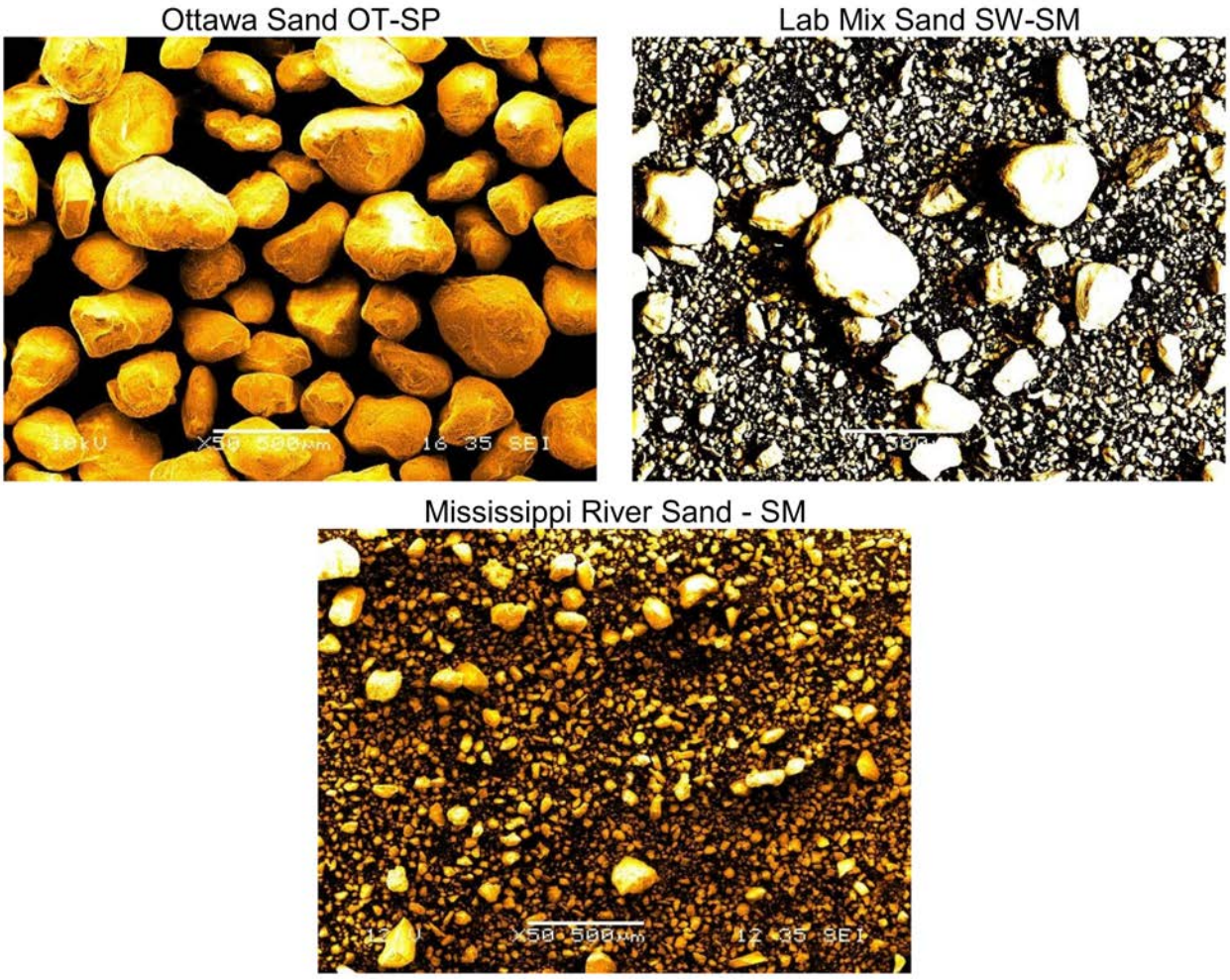

Figure 3-2 Scanning Electron Microscope images and particle shapes for the tested sands: (a) Ottawa sand (SR), (b) LabMix SW (SR – SA), (c) Mississippi River sand (SR – SA); a, b, and c x50. Note: SR – sub–rounded and SA – sub–angular.

3.3.3 Atterberg Limits

The silt portion of the SW-SM and the MR-SM are non-plastic. The fines portion of a natural clayey silty sand obtained from Cape Girardeau (MR-SM), falls at the boundary of a clay and silt in the ASTM D2487 (2011) plasticity chart, illustrated in Figure 3-3. To increase the plasticity of this MR-SC-SM fines (passing no. 200 sieve), so that an SC can be obtained, two mixtures were tried. The first trial mixture consisted of 75 % MR-SC-SM fines and 25 % GM, the second trial of 50 % MR-SM fines and 50 % GM. Since both the fine mixtures classified as CL (Figure 3-3), the 75/25 mixture was selected and 30% of it added to the coarse part of the MR-SC-SM (which was retained on no. 200 sieve). Thus, the final MRGM-SC mixture consists of 7.5 % of Gulf of Mexico clay.

3.4 Sample Preparation Methods in Element Tests

To produce high quality experimental data for developing empirical correlations and calibrating numerical models, it is critical that the sample preparation method and the consolidation stress path used in the laboratory replicate the natural in-situ soil as closely as possible. Several methods are available for reconstituting sand specimens in the laboratory for both element (e.g., cyclic triaxial,

direct simple shear, torsional shear) and large-scale (e.g., shake table, centrifuge) tests. The most popular method among these is pluviation (through water or air) with varying drop heights (Vaid et al. 1999; Elgamal et al. 2005; Sadrekarimi and Olson 2012; Olson et al. 2015). In the laboratory, pluviated sand reaches a terminal velocity and hence a limiting density that does not increase with further increase of drop height (Vaid and Negusey 1988). Thus, pluviation is used in conjunction with vibration techniques to reach higher target densities that cannot be achieved by pluviation alone. The different sample reconstitution methods, e.g., pluviation with or without vibration, can cause varying spatial arrangement of sand grains and related voids, called the soil "fabric" (Brewer 1964). Numerous laboratory studies have shown that the soil fabric can significantly affect the static and dynamic response of sands including stress-strain relationships, porewater pressure generation, cyclic shear strength and volumetric strain (Oda 1972a; Oda1972b; Ladd 1974; Ladd and Hernandez 1977; Mulilis et al. 1977; Tatsuoka 1979; Tatsuoka et al. 1986; Vaid and Negusey 1988; Vaid et al. 1999; Amini and Qi 2000; Yamamuro and Wood 2004; Wood et al. 2008; Sadrekarimi and Olson 2012; Sze and Yang 2014).

Table 3-2 Limiting void ratios of the tested sands determined in the present study compared to that of similar sands reported in literature.

Sand	Grain Shape	e_{max}	e_{min}	Reference	Procedure
Ottawa 40/70	SR	0.822± 0.012	0.504± 0.008	This Work	ASTM[a,b]
Ottawa	–	0.800	0.490	Lee and Seed 1967	–
Ottawa 35/60	SR	0.722	0.407	Youd 1973	ASTM[a], NS[d]
Ottawa	R	0.790	0.490	Been et al. 1987	–
Ottawa C 778	R – SR	0.780	0.480	Salgado et al. 2000	ASTM[a,b]
Ottawa C 778	R – SR	0.780	0.480	Murthy et al. 2007	ASTM[a,b]
Ottawa F75	–	0.805	0.486	Alshibli and Hasan 2008	ASTM[a,b]
Ottawa F55	R	0.800	0.608	Ganainy et al. 2012	–
Ottawa C 778	–	0.800	0.500	Eseller-Bayat et al. 2012	–
Lab Mix SW-SM	SR – SA	0.631± 0.025	0.317± 0.021	This Work	ASTM[a,b]
SW	SA	0.700	0.350	Sowers and Sowers 1951	–
Fine to Coarse SW	–	0.700	0.350	McCarthy 1977	–
MR-SM	SR – SA	1.049± 0.006	0.597± 0.003	This Work	R[f]
MR-SM	SR – SA	1.038	0.563	Sadrekarimi and Olson 2011	R[f]

Note: e_{max} – maximum void ratio; e_{min} – minimum void ratio; R – Rounded; SR – Sub–rounded; SA – Sub–angular; NS – Non-standard procedure; R – Yamamuro and Lade 1997

[a]Dry tipping method equivalent to ASTM D4254 for e_{max} (ASTM 2006)

[b]Japanese method equivalent to ASTM D4253 for e_{min} (ASTM 2016)

[c]for e_{max}

[d]for e_{min}

[f]for sands with fines content > 15% which precludes the use of the ASTM standard

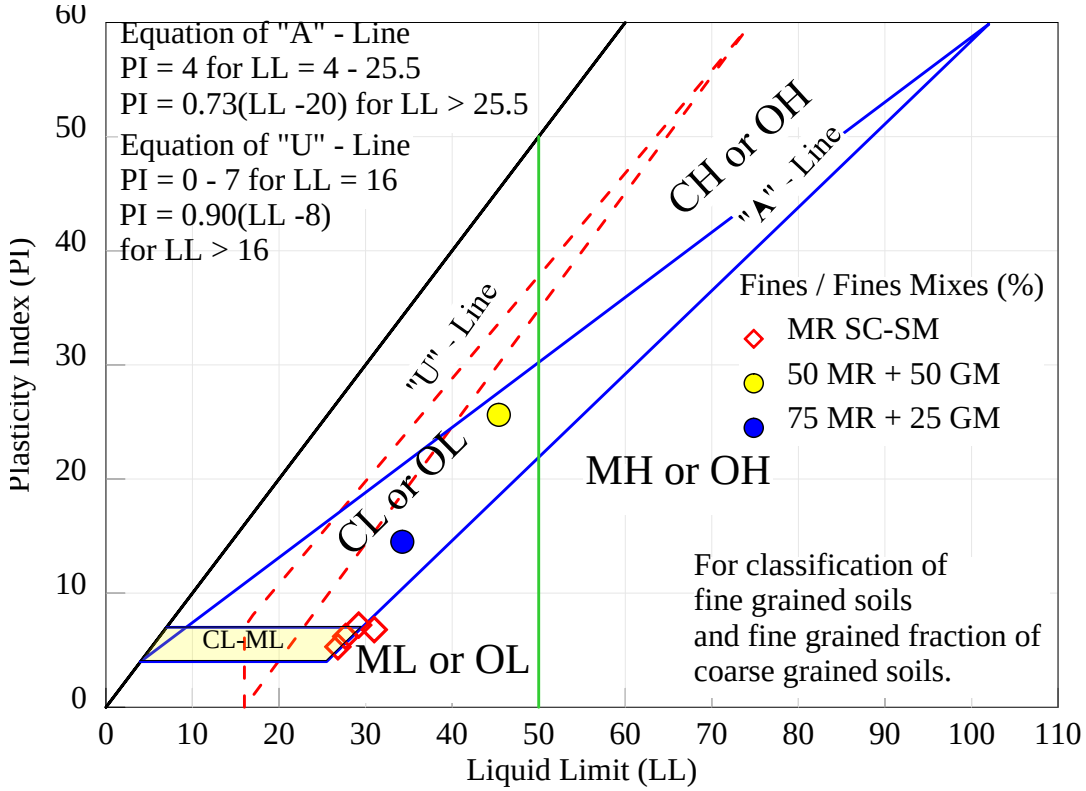

Figure 3-3 Location of the Mississippi River silty – clayey sand on the border of ML and CL on the ASTM D2487 (2011) plasticity chart.

The earliest studies to systematically investigate the effect of soil fabric on the cyclic behavior of sands was conducted by Ladd (1974), Ladd and Hernandez (1977) and Mulilis et al. (1977) through a series of stress-controlled cyclic triaxial tests. Ladd (1974) observed that the cyclic shear strength of silty sand (SP-SM) specimens (D_R = 63 – 84%) prepared by moist tamping was double that of specimens prepared by dry vibration. Mulilis et al. (1977) observed that the liquefaction resistance in moist vibrated specimens of Monterey No. 0 sand (D_R 50%) was almost twice that of dry pluviated specimens at the same density, the liquefaction resistance of moist tamped and dry vibrated specimens falling in between that of moist vibrated and dry pluviated specimens. Later, tests by Miura and Toki (1982) in triaxial compression and extension and experiments by Ibrahim and Kagawa (1991) in cyclic torsional shear confirmed these observations.

Mulilis et al. (1977) also noted that the effect of specimen preparation on the dynamic strength of a Mississippi River sand is much less than that of the Monterey No. 0 sand, indicating that soil type influences the magnitude of the effect of the specimen reconstitution technique on dynamic response of sand. Fabric and electrical conductivity studies by Mulilis et al. (1977) revealed that variation in the orientation of sand grain contact and packing due to different specimen preparation methods are possible causes of the disparities in cyclic behavior. Contrary to the observations of Mulilis et al. (1977) for a sand at D_R of 50%, Vaid and Negusey (1988) reported that specimens of ASTM C-109 Ottawa sand at D_R of 85%, formed by dry pluviation alone, and dry pluviation in a loose state followed by vibrations, resulted in identical stiffness, i.e., Young's modulus interpreted from resonant column tests. This indicates that the effect of specimen preparation on dynamic soil response might also be a function of the relative density of the soil.

From unidirectional shake table tests on Monterey No. 0 sand (D_R 55%), Seed et al. (1977) illustrated that low magnitude (M = 5) pre-shearing caused an insignificant change in relative density (54% to 54.7%), but a marked eight times increase in the number of cycles to liquefaction. Seed et al. (1977) attributed this heightened liquefaction resistance to increase in the lateral earth pressure coefficient (K_0) and change in the soil fabric induced by pre-shearing. Later, Yee et al. (2013) observed the same behavior in drained tests. For a sand at relative density of 58 to 65%, Yee et al. (2013) noted that volumetric strain from drained simple shear tests is lower in specimens that have prior cyclic loading history, as compared to freshly reconstituted "virgin" specimens prepared by vibratory methods or compaction.

Four specimen preparation methods were considered for the present study and are briefly described below. The methods are illustrated schematically in Figure 3-4. The first two methods involve deposition through air without any vibrations or cyclic loading. These methods were considered because air pluviation or raining: (1) produces the fabric of natural eolian and alluvial deposits (Vaid et al. 1999); and (2) is commonly used in centrifuge testing (e.g., Olson et al. 2015). Use of the same specimen preparation method for element and centrifuge testing affords unbiased comparison of results, in terms of the soil fabric. The specimen reconstitution methods used are:

1. *Dry Funnel Deposition (DFD):* A predetermined mass of dry sand was deposited into the specimen mold using a funnel. The drop height between the funnel and mold was varied depending on the target relative density (50 – 75%). The funnel in raised in a circular motion while preparing the specimen to maintain the drop height. This method is extensively used in laboratory testing of sands (Wood et al. 2008). To achieve relative densities lower than 55%, a hollow cylinder with a wire mesh attached to the base is placed in the mold, prior to DFD with zero drop height. After DFD, the screen is slowly raised to produce a uniform loose soil specimen (Kammerer 2002; Bernhardt 2013).

2. *Air Pluviation by Dry Soil Raining (DSR):* Sand is rained with a varying drop height from a large hollow cylindrical pluviator of diameter of 300 mm and height of 200 mm. The base of the pluviator is fitted with a plate with perforations (Rad and Tumay 1987) to allow the raining of sand to relative densities in the range of 70 to 86%. This pluviator is most commonly used for preparation of centrifuge sand beds (Olson et al. 2015). A schematic of this pluviator is shown in Figure 3-4.

3. *Dry Funnel Deposition followed by Table Vibrations (DFD + TV):* Specimens formed by DFD are first loaded with a surcharge of 35 lbs prior to application of table vibrations with a rubber mallet to obtain relative densities from 60% to 95%. Air or water pluviation followed by vibration is one of the most common methods used in geotechnical laboratory testing to achieve dense sand samples (Wu 2002; Kammerer 2002; Wood et al. 2008).

4. *Dry Funnel Deposition followed by Cyclic Shearing (DFD + CS):* A specimen is formed at a given initial density using DFD, and then subjecting the specimen to drained cyclic shearing under an effective vertical stress of 100kPa in the I-mcDSS until a target specimen height or relative density is reached. It has been shown in literature (e.g. Yee et al. 2013) that a "presheared" specimen thus formed yields a much stiffer stress-strain and deformation response (D_R 65%), and hence results from such specimen tests are usually discarded for studying the "virgin" response of the soil. However, in the following chapter, we present results to show that, for dense to very dense sands D_R > 80%, the volumetric strain of presheared specimens formed by DFD + CS is closer to an air pluviated specimen, whereas a "virgin" DFD + TV sample yields a somewhat stiffer response (~ 16% stiffer).

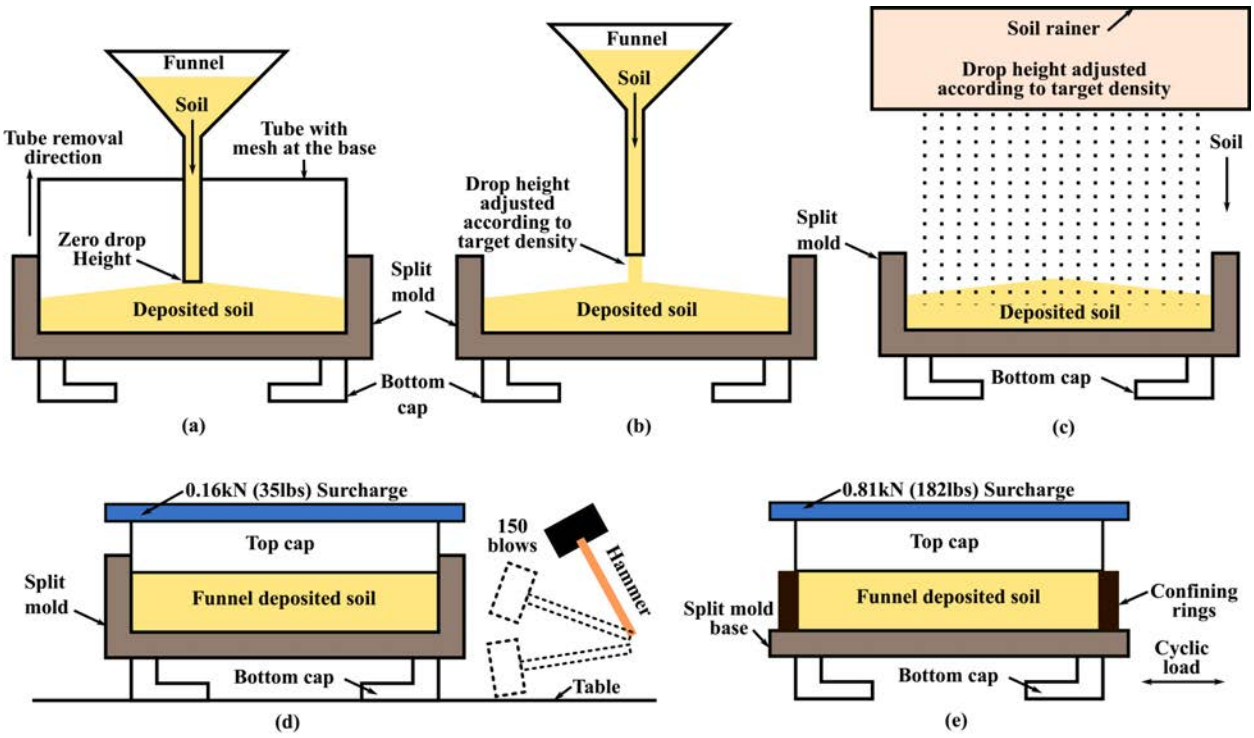

Figure 3-4 Schematic of sample reconstitution methods considered in this study. (a) Dry funnel deposition with zero drop height followed by raising a screen through the sample (D_R < 55%); (b) dry funnel deposition with varying drop height (D_R 60% - 75%); (c) deposition from a soil rainer with varying drop height (D_R 70% - 86%); (d) funnel deposition with drop height of 0.50 m followed by application of 0.16 kN (35 lbs) of surcharge and table vibrations applied with a hammer (D_R 75% - 96%); and (e) funnel deposition followed by cyclic shearing in the l-mcDSS (D_R > 55%).

3.5 Oedometer Tests

Incremental loading oedometer tests were conducted in a traditional Bishop frame on the different sand types following the ASTM-D2435-11 (2011) procedure. Figure 3-5 shows the compression behavior of the OT-SP and the MR-SM, each initially at varying D_R. Data from Mesri and Vardhanabhuti (2009) are included for comparison. The coefficient of volume compressibility (m_v) in oedometer tests is computed using (Terzaghi et al. 1996):

$$m_v = \frac{\Delta\varepsilon_v}{\Delta\sigma'_v} \tag{3-87}$$

The oedometer m_v decreases with increase in effective stress and relative density of the sand. This is illustrated in Figure 3-6 for the OT-SP sand.

However, during cyclic DSS tests, apart from the increase in density induced by cyclic shearing, K_0 also increases and the fabric of the soil changes (Seed et al. 1971). The last two effects are not captured by the incremental loading oedometer tests conducted on the sand specimens. Moreover, the field coefficient of volume compressibility ($\bar{m}_v$; Terzaghi et al. 1996) is always slightly higher than the oedometer m_v since in the field the soil is not confined with rigid steel boundaries, and some lateral deformation may occur.

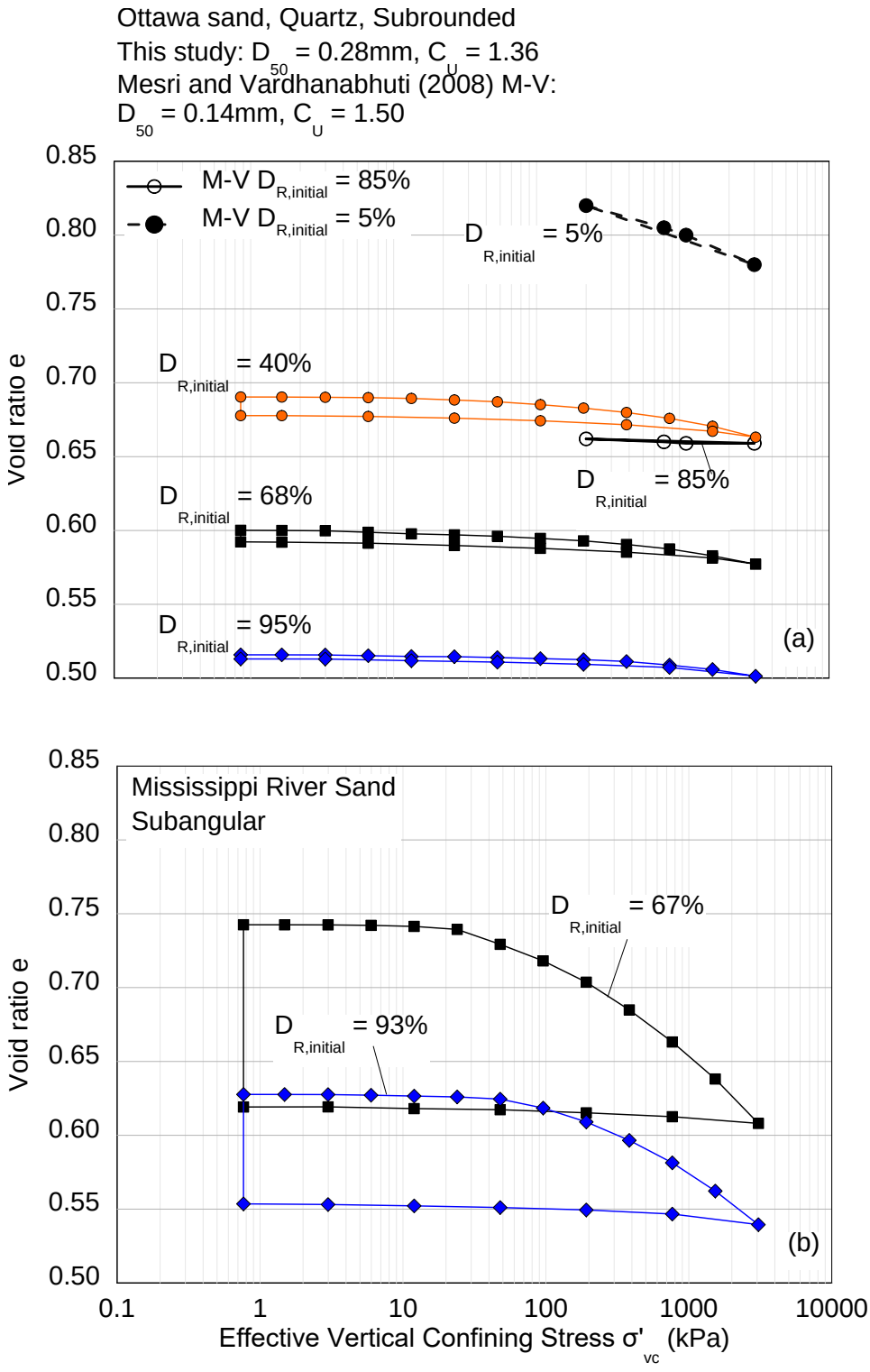

Figure 3-5 End-of-primary (EOP) e – log(σ'$_{vc}$) data from incremental loading oedometer test on: (a) Ottawa sand (OT-SP), compared to data from Mesri and Vardhanabhuti (2009); and (b) Mississippi River silty sand (MR-SM).

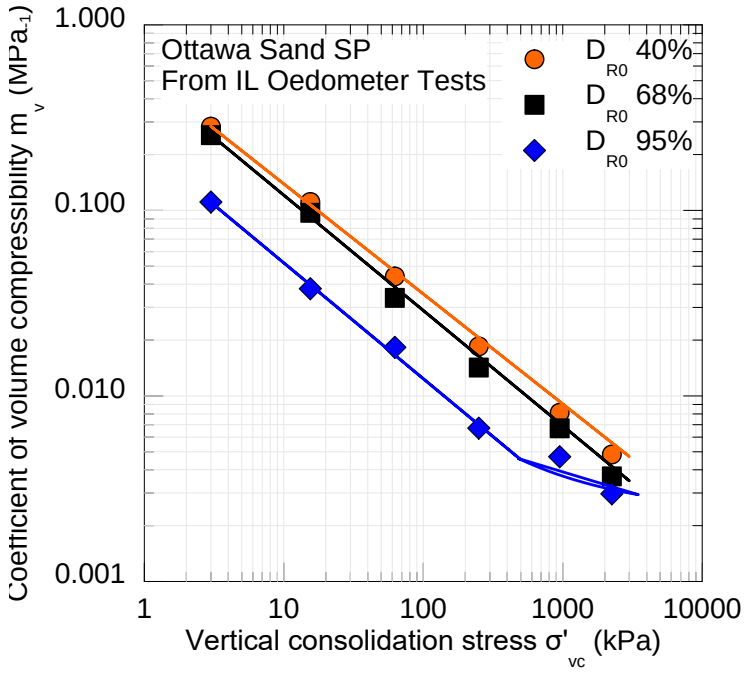

Figure 3-6 Coefficient of volume compressibility (m_v) of loose to very dense (D_{R0} 40 – 95%) Ottawa sand from incremental loading oedometer tests.

3.6 Direct Cyclic Simple Shear Testing

3.6.1 Illinois multidirectional direct simple shear (I-mcDSS) device

The mechanical components of the I-mcDSS were designed using the Rutherford and Biscontin (2013) device as a prototype. The I-mcDSS retains the main features of the multidirectional simple shear device described by Rutherford and Biscontin (2013) including: (1) application of loads or strains (monotonic, cyclic – sine wave, square wave, saw tooth wave) in three mutually perpendicular directions, in the vertical (z) direction and two mutually orthogonal horizontal (x and y) directions; (2) a chamber for cell pressure allowing back pressure saturation; (3) reduced mechanical compliance or "rocking" between the top and base platen by using a four column support frame with intermediate guide rods for the vertical assembly; (4) a multidirectional load cell to obtain post friction measurement of vertical and shear loads; (5) pressure transducers to measure excess porewater pressure; and (6) a low-energy, low-noise hydraulic power supply, with virtually constant heat generation, specifically designed for laboratory use. The I-mcDSS improves over the Rutherford and Biscontin (2013) device by incorporating these additional features: (1) a servo-hydraulic control system that allows arbitrary user defined loading in the x, y and z directions; (2) an improved control algorithm that permits high frequency broadband loading; (3) bender elements that allow measurement of shear wave velocity to estimate the small strain stiffness of the soil; and (4) automated regulation of back-pressure as opposed to the manual control used by Rutherford (2012).

The I-mcDSS device consists of five main components: (1) the I-mcDSS testing equipment; (2) a hydraulic power supply; (3) a panel for back pressure application; (4) a computer and data acquisition system; and (5) a bender element system (BE). The BE system has a separate computer and data acquisition console. Photographs of component (1) to (4) are presented in Figure 3-7. Figure 3-8 shows a schematic of the mechanical parts of component (1), and a typical specimen used in the I-mcDSS testing equipment.

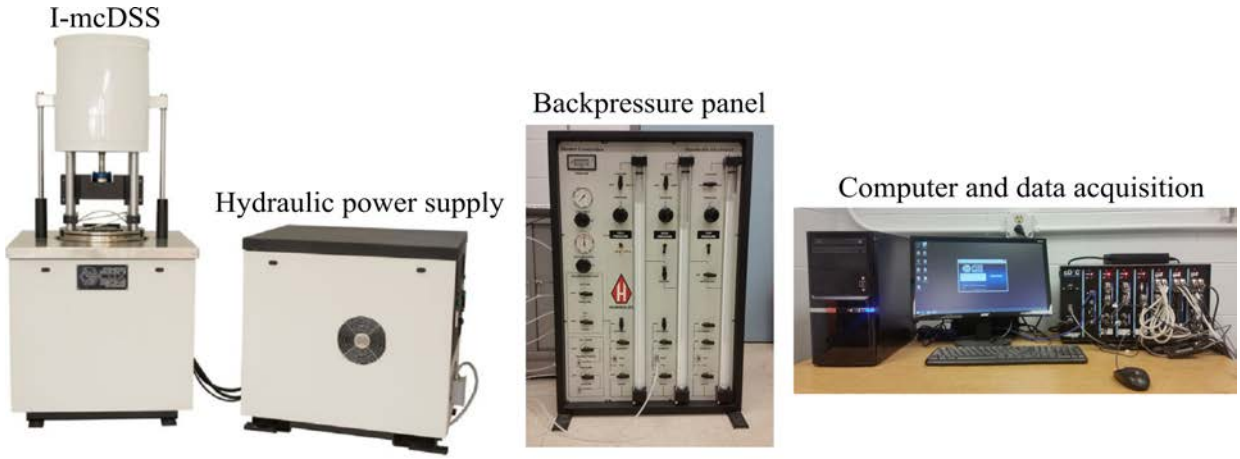

Figure 3-7 Photograph of the main components of the Illinois multidirectional cyclic direct simple shear device.

3.6.1.1 Application and Measurement of Vertical and Bidirectional Horizontal Loading and Displacement

Vertical loading is applied through an actuator fitted at the top of the main I-mcDSS unit forming part of the top assembly (Figure 3-8). A hydraulic servo valve (SV1) controls the vertical actuator. The top loading unit is mounted on a four-column support frame with intermediate guide rods with low friction bearing sleeves. The support frame and guide rods (Figure 3-9) do not allow lateral movements and increase the stiffness to minimize rocking prevalent in previous devices (e.g. Ishihara and Yamazaki 1980; Boulanger et al. 1993; Duku et al 2007). The top assembly can apply a total load of 25 kN (~ 5600 lbf) transmitted to the sample via a connector system shown in Figure 3-9. The vertical assembly is fitted with a load cell of capacity ±11.1 kN (~ 2500 lbf) with ±0.04% hysteresis and static band error, which corresponds to ±0.55 kPa (0.08 psi) for a 101.6 mm diameter specimen. The error is comparable to that reported by other investigators, e.g. ±0.43 kPa by Boulanger et al. (1993). The vertical actuator allows a maximum displacement of 100 mm.

Horizontal loads are applied through individual hydraulic actuators connected to the two horizontal tables (x and y). A single servo valve (SV2) controls the x and y actuator via its two outlet ports. The upper x table is mounted on the lower y table using low friction track bearing. The y table is mounted on tracks that are perpendicular to the tracks of the x table and are attached to the base of the device. The x and y tables can be servo-hydraulically controlled independently or in conjunction to create unidirectional and bidirectional loads respectively. This horizontal loading system forms the lower assembly of the I-mcDSS device. The x and y tables are fitted with horizontal load cells (Figure 3-8) that have a capacity of ±4.4 kN (~ 1000 lbf). The x and y load cells have an error range of ±0.55 kPa (0.08 psi) for a 101.6 mm diameter specimen. A total actuator displacement of ±10 mm is possible in the x and y directions. Due to friction in the device bearings, the actual load imparted to the sample is lower than the load recorded by the load cell. This frictional load is reduced by lubricating the track bearings of the x and y tables using Chevron ISO46 hydraulic oil. The oil is continuously applied via a custom built pneumatic system in the I-mcDSS device. The magnitude of the frictional load was measured to vary from 1 - 4 kPa for a 101.6 mm diameter specimen. Since the frictional load is greater than the device's accuracy for stress measurement (±0.55 kPa), the interpreted shear stress form x and y load cells recordings are corrected for device friction.

Apart from the x, y and z load cells, the I-mcDSS device can optionally be fitted with a multidirectional load cell which provides the measurement of force and torque in three mutually perpendicular directions (Figure 3-8). This specialized load cell is extremely sensitive and eliminates the effect of friction generated in the horizontal x and y tables. Displacements in the horizontal x, y and vertical z directions are monitored with individual linear variable differential transformers (LVDTs) that are mounted on the two horizontal tables and the vertical load frame respectively. The full range of the vertical LVDT is ±50 mm and the two horizontal LVDTs is ±10 mm. The reading resolution of the LVDTs is ±0.001 µm, which corresponds to volumetric strain and shear strain of $5x10^{-8}$ for a specimen of height 19.05 mm (0.75 in). Here, the volumetric strain is measured in terms of change in specimen height, since metal confining rings maintain a constant specimen cross-sectional area. Vertical deformation is currently measured with a single vertical LVDT mounted on the vertical loading unit and aligned with the center of the specimen. The I-mcDSS device configuration and the data acquisition system allows up to three vertical LVDTs. The additional LVDTs are recommended for higher accuracy in vertical deformation measurement, e.g., when testing specimens of diameter greater than 101.6mm.

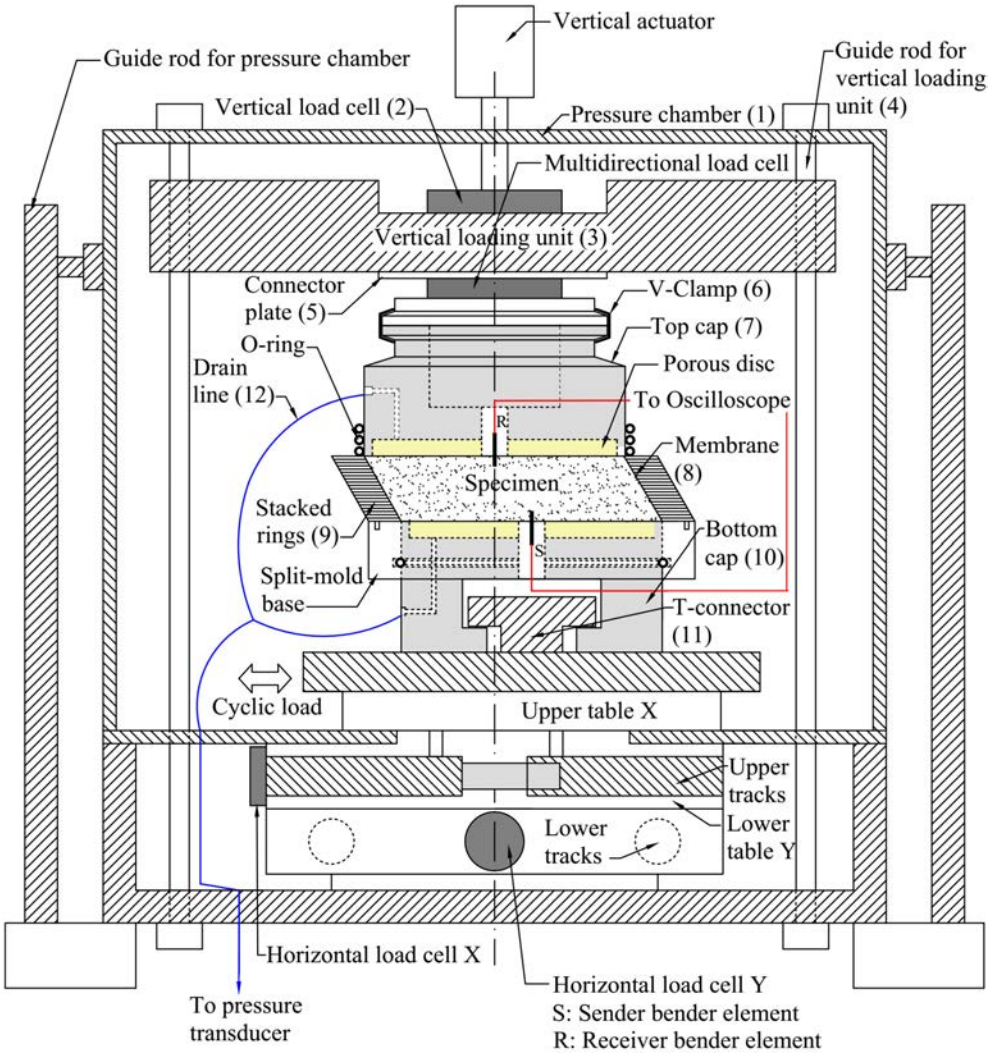

Figure 3-8 Schematic cross section of the Illinois multidirectional cyclic direct simple shear (I-mcDSS) device illustrating the main mechanical components and the specimen, with provision for measurement of shear wave velocity.

To check for cross-coupling between the x and y table, sine wave input amplitudes of 0.1 mm and 3 mm were applied at frequencies of 0.1Hz and 1.0Hz first to the x table (y table stationary) and then to the y table (x table stationary). LVDT reading of the stationary table was recorded in each case. The results showed negligible movement of the stationary table, thus indicating no cross-coupling between the two horizontal tables of the I-mcDSS device.

3.6.1.2 Application and measurement of backpressure and cell pressure

The I-mcDSS is equipped with a stainless-steel chamber that enables application of cell pressure using air via an electro/pneumatic convertor. The maximum air pressure that can be applied by the chamber is 861.8 kPa (125 psi). The chamber is currently fitted with a pressure transducer to monitor chamber pressure. A Humboldt pressure panel (HM-4150) is connected to a volume change electro/pneumatic convertor to regulate the back pressure applied to the sample via the I-mcDSS via the I-mcDSS control software. The back-pressuring system uses two pressure transducers [range of 500 kPa (72 psi)] to measure the porewater pressure in the specimen. This setup, illustrated in Figure 3-10, enables undrained testing of specimens, allows Skempton's B value check, and directly measures porewater pressure. Consolidation and reconsolidation volume change of saturated specimens are monitored in two ways: (1) vertical LVDT movement as previously discussed; and (2) volume change burette supplied with the Humboldt panel with a reading range of 10 cc. The burette resolution is 0.02 cc which corresponds to a volumetric strain of 0.013% for a 19.05 mm high and 101.6 mm (4 in) diameter specimen.

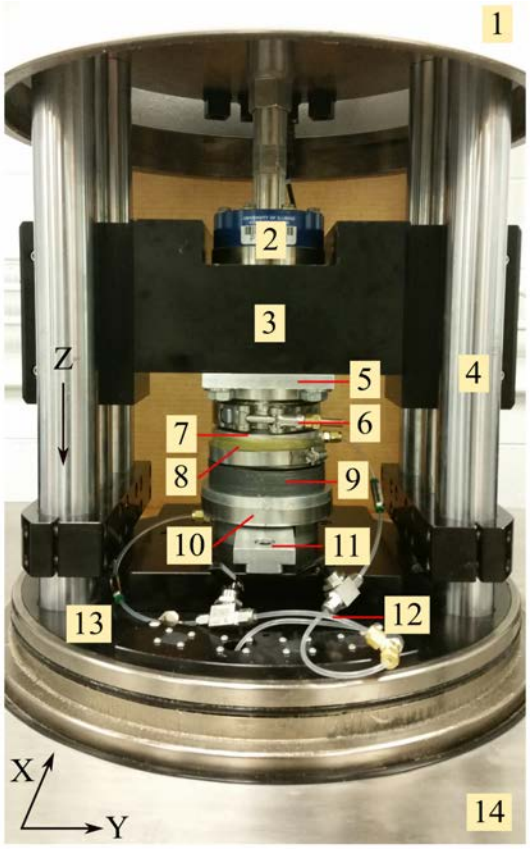

1 - Pressure Chamber
2 - Vertical Load Cell
3 - Vertical Loading Unit
4 - Guide Rods
5 - Connector Plate
6 - V-Clamp
7 - Top Cap
8 - Membrane
9 - Confining Rings
10 - Bottom Cap
11 - T-connector
12 - Drain Lines
13 - Bottom Assembly
14 - Bottom Housing

Figure 3-9 Specimen assembly and placement in the I-mcDSS.

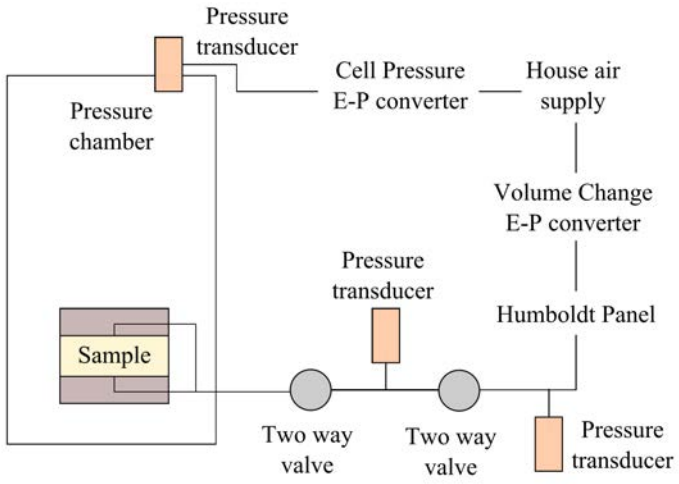

Figure 3-10 Simplified schematic of the cell pressure and back pressure saturation system used in the I-mcDSS (E-P – Electro-Pneumatic).

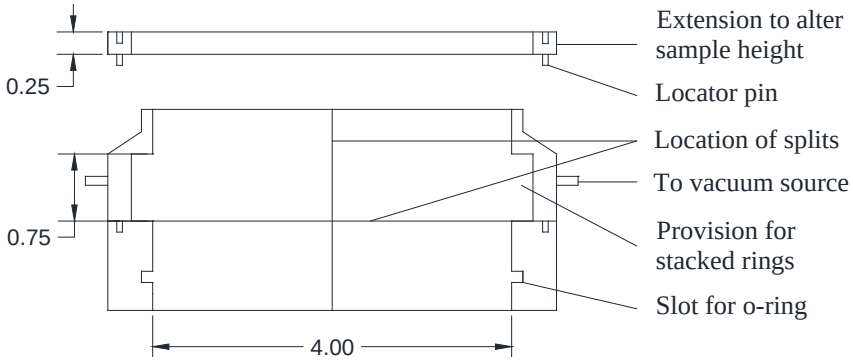

Figure 3-11 Schematic of the four-way split mold and extension designed after Bernhardt (2013) to house the stacked rings during sample preparation – all dimensions shown are in inches.

3.6.1.3 Specimen

The I-mcDSS device can test cylindrical soil specimens of diameter up to 152 mm (6 in). The specimen is located between the top and the bottom assembly (Figure 3-8). The specimen is connected to the top assembly through a rigid aluminum top cap using a steel V-clamp. The sample is attached to the bottom assembly by a T-shaped bracket via a T-slot in the rigid aluminum specimen base cap. The T-bracket is fixed to the bottom assembly with two bolts. Figure 3-8 and Figure 3-9 show these connections schematically and with a picture respectively.

A major drawback of simple shear devices is their inability to apply complementary shear stresses to the specimen, resulting in non-uniform shear and normal stresses on the boundary of the specimen. This has been evaluated both experimentally (Airey and Wood 1985, 1987; Amer et al. 1987; DeGroot et al. 1994) and through mathematical and numerical analysis (Roscoe 1953; Amer et al. 1987). Researchers have used samples of different diameter (D) to height (H) ratios to mitigate the effect of this non-uniform stress distribution. Franke et al. (1979) observed negligible effect of

the lack of complementary shear stress for saturated sand samples with D/H ranging from 3.75 to 7.5. Airey and Wood (1985) found that that a D/H ratio of 5 reduces the effect of the non-homogenous boundary stresses at the center of the sample. Amer et al. (1987) reported a more conservative value of D/H of 8 for the shear modulus and damping of the soil to remain independent of specimen size and for a uniform shear stress distribution over 85% of the sample cross-sectional area. To counter the issue of non-uniform boundary stresses, a sample D/H ratio greater than 4 was used for the present testing. This is comparable to the D/H used by Kammerer (2002) and Rutherford (2012) for bidirectional simple shear testing.

The top and bottom caps were specifically designed to conform to the diameter to height ratio (> 4) required to limit stress non-uniformity at the sample boundaries previously discussed. The present study tests specimens of diameter 101.6 mm (4 in) and height 19.05 mm (0.75 in). To minimize boundary effects, the specimen height is greater than 10 times the maximum particle diameter tested in this study (0.6 mm; OT-SP) as per ASTM-D6528-07 (2007). Cylindrical indentations were made on both caps to house porous stones and ports were provided to allow the measurement of porewater pressure and application of back pressure to the specimen. To prevent slip between the base of the specimen and bottom cap and to ensure a full transmission of shear stresses into the specimen, standard fully frictional ends (Pyke et al., 1975; Bernhardt, 2013) were created by attaching sand particles of the tested sand to the porous stones with quick setting epoxy. The caps were modified to house bender elements and are illustrated in Figure 3-8 and Figure 3-9.

3.6.1.4 Lateral confinement

ASTM-D6528-07 (2007) and ASTM-D2435-11 (2011) have standardized wire reinforced membranes and Teflon coated stacked rings for providing lateral confinement in direct simple shear tests to maintain simple shear conditions by allowing zero lateral deformation, i.e. maintaining a constant circular cross-sectional area (K_o conditions). However, wires can deform in the horizontal plane due to (1) non-uniform shear stresses developed in the vertical plane in a simple shear device; and (2) higher stiffness of dense sands (D_R = 60 – 95%) used in the present study. Therefore, in this work, a stack of thin metal rings (Figure 3-8 and Figure 3-9) with low friction was used for confining the sand specimen. The outer and inner diameter of the rings are 113.65 mm ± 0.39 mm (4.47 in ± 0.02 in) and 102.76 mm ± 0.39 mm (4.0455 in ± 0.02 in), and each ring is 0.635 mm (0.025 in) thick. The thickness of the rings is less than 1/10th the specimen height per ASTM-D6528-07 (2007) for maintaining uniform shear. The friction between the rings is minimized by spraying the rings on all sides with PermaSlikG (Bernhardt, 2013), an industrial lubricant from Everlube. The coefficient of friction between the rings after the application of the MoS_2 (molybdenum sulphide) coating is 0.04 per the ASTM D2714 procedure (ASTM-D2714-09, 2009). A thin [0.508 mm (~0.02 in)] latex membrane separates the sand specimens from these confining rings. Due to the presence of the rings, it was not feasible to measure horizontal normal stress on the I-mcDSS specimen. Thus, the complete stress state of the specimen in the I-mcDSS cannot be defined (Budhu 1985; Amer et al. 1987; Airey and Wood 1987; Budhu and Britto 1987; Boulanger et al. 1993).

3.6.1.5 Split-mold

A four-way split mold was machined following the design outlined by Bernhardt (2013) for testing chrome metal spheres under unidirectional simple shear loading. The top half of the split mold can accommodate the stacked rings and latex membrane. Vacuum can be applied from two opposite ends for sample preparation (Figure 3-11). After the top cap is securely in place, the upper section of the split mold is removed and the base is left in place, held with a pipe clamp, to provide a platform that keeps the stacked rings level during shear. A rubber O-ring placed in a groove in the bottom cap is used to keep the lower section of the split mold level (Figure 3-8 and Figure 3-11). The split

mold can be used to prepare a sample of diameter 101.6 mm (4 in) and height 19.05 mm (0.75 in) to 25.4 mm (1.0 in). The height of the sample can be varied by using an optional extension ring of height 6.35 mm (0.25 in) (Figure 3-11).

3.6.1.6 Computer control and data acquisition system

The control and data acquisition system (cDAQ) for the I-mcDSS was developed by Cooper Technology Ltd., UK along with James Cox and Sons. The control system uses a closed feedback loop proportional-integral-derivative (PID) gain servo-controller algorithm written in LabVIEW (Johnson 1997). The cDAQ has: (1) three factory fitted servo cards to connect to the three servo-hydraulic valves for control; and (2) three factory fitted data acquisition cards connected to all the transducers used in the I-mcDSS, except the bender elements. The software accepts feedback from the x, y and z loads cells and LVDTs fitted in the I-mcDSS for control. The layout of the I-mcDSS control system components is shown in Figure 3-12. The loads or displacements in the x, y and z directions and the cell pressure and back pressure can be controlled manually or automatically. The PID gains of load cells used in the I-mcDSS are sensitive to the stiffness of the tested sample, and were fine-tuned by trial and error for optimal control of the device for testing medium dense to dense sands (D_R > 50%).

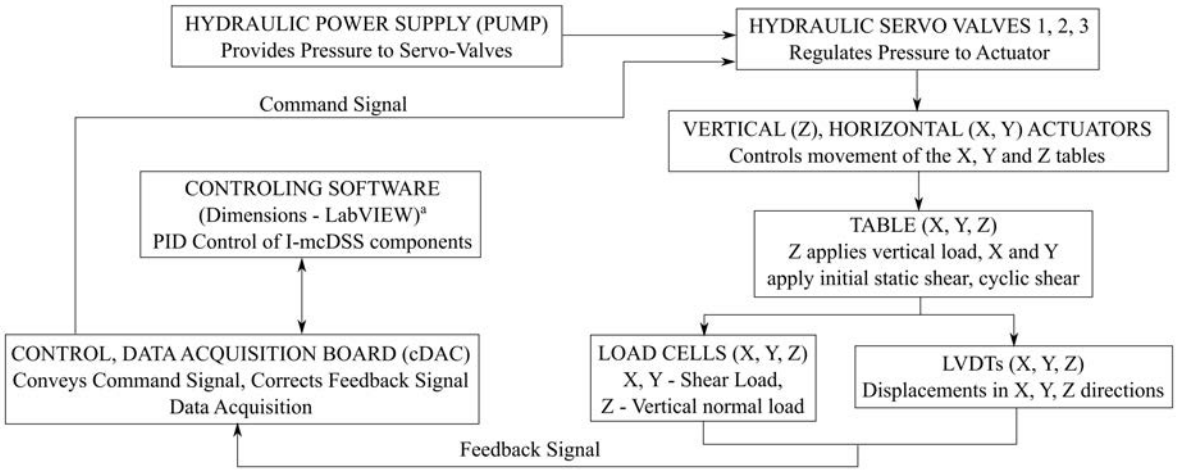

Figure 3-12 Layout of the control system components of the I-mcDSS ([a]Developed by Cooper Technology Ltd., UK).

3.6.2 Measurement of shear wave velocity in the I-mcDSS

Two transducers were initially considered for measurement of shear wave velocity in the I-mcDSS: (1) bender elements (BE); and (2) ultrasonic transducers (UST). Although BEs are intrusive while the USTs are not, the former was selected because of: (1) a large available testing database; and (2) shear waves generated by the flat USTs are too weak to obtain a proper signal for shear wave velocity measurement in coarse-grained soils (Cheng and Leong 2014).

Bender elements are piezoelectric transducers that are made of a central electrode consisting of a metal shim and two outer electrodes and two piezoceramic sheets in between (Figure 3-13). The electrically polar nature of crystals or crystal asymmetry results in piezoelectricity. When a mechanical load is applied to a piezoelectric element, its lattice deforms, altering the dipole moment and generating voltage (mechanism used in receiving BEs). Conversely, when a voltage is applied, the crystal lattice deforms generating a mechanical wave (mechanism used in transmitting BEs)

(Lee and Santamarina 2005). BEs have been commonly used in laboratory triaxial (Salgado et al. 2000; Jung et al. 2007; Karl et al. 2008) and oedometer testing (Lee and Santamarina 2005), but to a limited extent in a direct simple shear setup (Dyvik and Madshus 1985; Chang et al. 2014; Morales-Velez et al. 2015). This is because the very short distance between the transmitting and receiving BE in the DSS (height of samples typically being ~ 25.4mm or 1in): (1) increases the error in estimation of tip-to-tip distance between the BEs; and (2) complicates detection of shear wave velocity arrival in the presence of near-field effects. Coupling between the shear and compression waves generated by different lobes of the BE result in near-field effects (Viggiani and Atkinson 1995, Arulnathan et al. 1998 and Lee and Santamarina 2005).

In the present work, the specimen height used is 19.05 mm (0.75 in). To the authors' knowledge, BEs for such a short specimen has not been used. Therefore, to establish the feasibility of using BEs with the present I-mcDSS sample, BEs were first fabricated and tested in a sand bed (OT-SP) with a tip-to-tip distance of 11mm (3mm cantilever length of the sender and receiver). Strong received signals were recorded, and the estimated shear wave velocity agreed well with published correlations (Menq 2003). The feasibility test was followed by installing the BEs in the I-mcDSS specimen caps (Figure 3-13). The following sections describes the fabrication and installation of the BEs in the I-mcDSS and the corresponding control and data acquisition system.

3.6.2.1 Fabrication and installation of BEs in the I-mcDSS

Lead-zincronate-titanate (PZT) bender elements of dimension 12.7 mm x 8.0 mm x 0.6 mm (length x width x thickness), obtained from Piezo Systems, Inc. were used for fabrication of the bender elements. The following procedure was used for the fabrication of BEs: (1) electrical wires were soldered to the outer and inner electrodes of the BEs to obtain a series (receiver) or parallel (sender) type BE (see Figure 3-13 and see El-Sekelly 2011 for details); (2) five waterproofing coats of polyurethane were applied to the BEs; (3) the BEs were fixed inside a hollow nylon screw using Epo-Tek 301 epoxy [low viscosity (100 cP, 24 hr set time, high stiffness after curing, manufactured by Epoxy Technology Inc.]; (4) conductive silver metal paint was applied to the series type BE for electrical shielding that reduces electromagnetic coupling between the BEs (Lee and Santamarina 2005); and (5) the bender element were installed in the Ottawa sand bed (for feasibility testing) and later in the I-mcDSS (Figure 3-8). The top and bottom cap of the I-mcDSS were modified to accept the BEs. The I-mcDSS top cap with bender element is shown in Figure 3-13. The BE configuration in the I-mcDSS produces vertically-propagating, horizontally-polarized (VH) shear waves in the specimen. The entire BE setup consists of: (1) a random waveform generator for triggering a shear waves in the specimen; (2) the BEs – sender and receiver; (3) an oscilloscope to view the sent and received signals; and (4) a graphical user interphase connected to the oscilloscope for data viewing, acquisition, and interpretation. This setup is schematically shown in Figure 3-14.

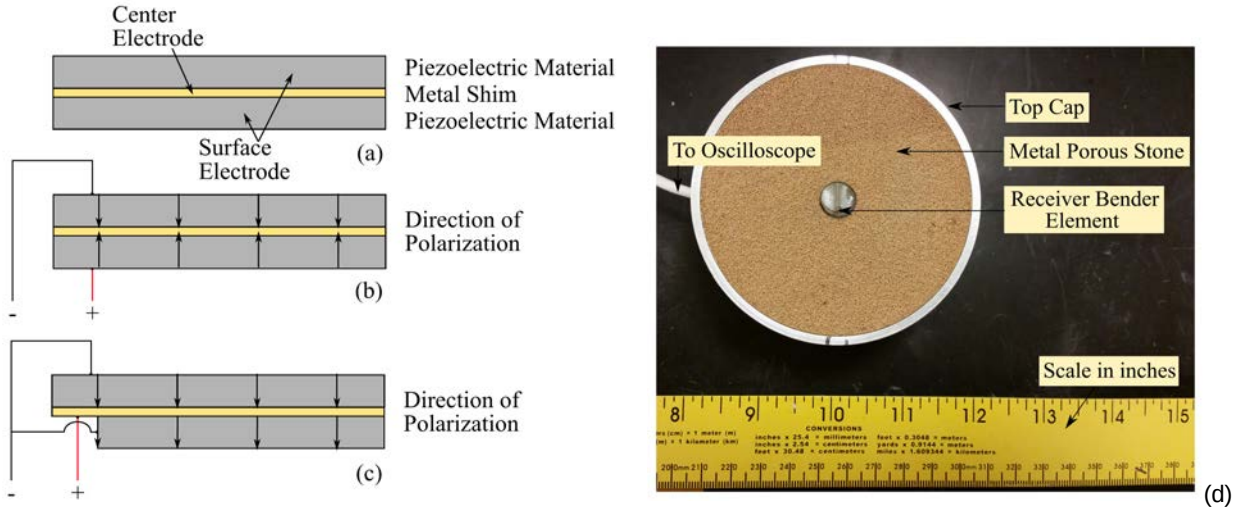

Figure 3-13 Schematic of Bender Element: (a) Components; (b) Series Type – Receiver; (c) Parallel Type – Sender; (d) Top cap of the l-mcDSS specimen with receiver bender element.

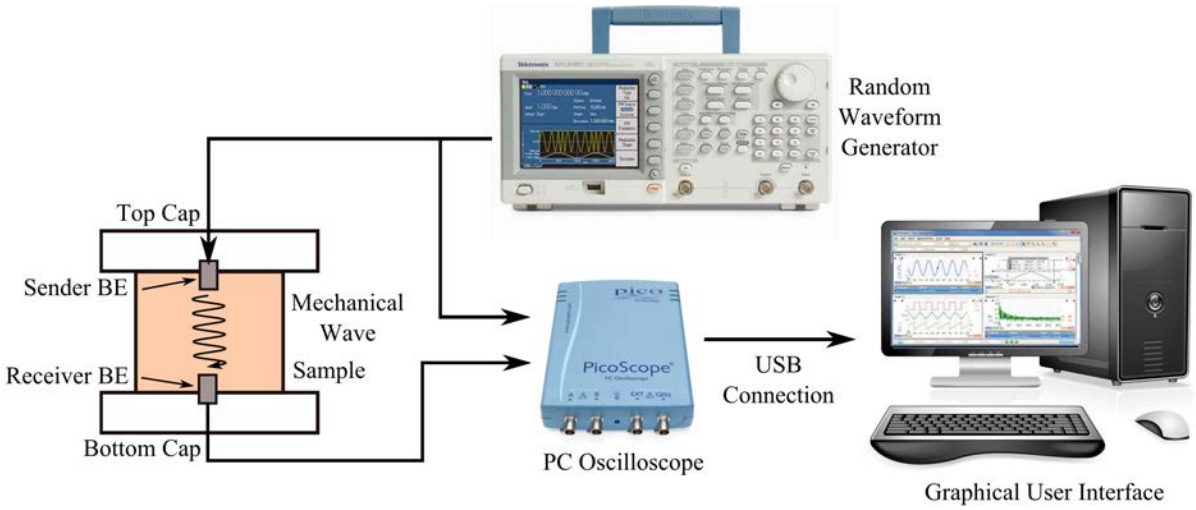

Figure 3-14 Schematic of Bender Setup in the l-mcDSS for measurement of shear wave velocity (pictures of the PC oscilloscope, random waveform generator and computer are obtained from www.google.com).

3.6.3 Summary of element testing

In the field, settlements under seismic loads typically occur under partially drained conditions, which can be replicated in dynamic centrifuge tests (Olson et al. 2015). However, for laboratory element tests, replicating the "partial drainage" of the field is complicated. Thus, traditionally, element tests have been conducted under drained (Silver and Seed 1971; Whang et al. 2004; Duku et al. 2008 among others) or undrained conditions (Wu 2002; Kammerer 2002; Rutherford 2012 among others). In this project, the direct simple shear experimental program focused on two aspects of the volumetric response of medium dense to dense sands (D_R 50 – 95%): (1) drained settlement due to particle rearrangement (Silver and Seed 1971); and (2) post-cyclic reconsolidation settlement

due to dissipation of excess porewater pressure (Ishihara and Yoshimine 1992). The effect of several factors on volumetric strain were evaluated: grain size distribution, relative density, soil fabric, loading intensity and duration, load reversal, preshearing, and effective stress.

Since the specimens were laterally confined, the measured vertical strain equals the volumetric strain. All specimens were K_0 consolidated under effective vertical stresses of 50 to 400 kPa prior to shearing. Most of the specimens have an overconsolidation ratio of 1, except for a few that were overconsolidated. All of the element tests presented in this report represent level-ground, free-field conditions, i.e., they have no initial static shear stress. When saturation was required, specimens were first flushed with carbon dioxide for thirty minutes (Mullilis et al. 1975), and then with deaired water of a volume at least three times the specimen volume. For the saturated I-mcDSS tests, the sample was flushed with water both from top to bottom and vice versa. Following this, back pressure saturation was done until a Skempton's B-value of 0.95 or greater was obtained. A back pressure of 100 kPa was used. The testing program is summarized below in terms of drainage and loading boundary conditions.

3.6.3.1 Drained direct simple shear tests

Unidirectional (sinusoidal, broadband) and bidirectional (circular, oval, figure-8 and broadband) strain controlled drained cyclic simple shear tests were conducted at shear strains of 0.1% to 7%. For comparison, cyclic shear strain amplitude in unidirectional tests is considered equivalent to the resultant shear strain amplitude in bidirectional tests. Loading frequencies for these tests were 0.1 and 1 Hz, 150 to 450 loading cycles were applied. Duku et al. (2008) and Yee et al. (2013) illustrated that volumetric strain in clean sands and sands with non-plastic fines are negligibly influenced by degree of saturation ranging from 0 to 90%. Thus, the OT-SP, SW-SM and MR-SM specimens in this study were tested dry. The MRGM-SC specimens were saturated before testing, since it was intended to study the effect of plastic fines on volumetric strains. Table 3-3 to Table 3-14 summarizes the drained direct simple shear test series for the OT-SP, SW-SM, MR-SM and MRGM-SC sands, including the sample preparation method used and volumetric strains measured after the 15 loading cycles.

3.6.3.2 Constant volume direct simple shear tests

Constant volume simple shear tests on dry specimens are commonly used for replicating undrained tests on saturated specimens because: (1) a shorter time is required; and (2) simpler experimental setup is required for preparing dry specimens. In constant volume simple shear testing, it is assumed that the change in the vertical stress during shear is equivalent to the porewater pressure generation in an undrained test with constant total vertical stress (Bjerrum and Landva 1966). Iversen (1977) reported identical shear stress and pore pressure response in height controlled and volume controlled monotonic direct simple shear tests on Drammen clay with overconsolidation ratio 1 and 4. Later, this assumption was verified for monotonic simple shear tests on normally consolidated Drammen clay by Dyvik et al. (1987). For this project, unidirectional (sinusoidal) and bidirectional (circular, figure-8) strain controlled constant volume cyclic simple shear tests were conducted at shear strains of 0.1% to 2%. The OT-SP, SW-SM and MR-SM sands were tested dry, while the MRGM-SC was tested fully saturated with Skempton's B coefficient greater than 0.95. Since, 15 undrained loading cycles are representative of an average earthquake (M = 7.5, Seed et al. 1971), 30 loading cycles were applied to obtain conservative values of reconsolidation volumetric strain. Table 3-15, Table 3-16, Table 3-17, and Table 3-18, summarizes the constant volume direct simple shear test series for the OT-SP, SW-SM, MR-SM, and MRGM-SC sands respectively, including the sample preparation method used and the reconsolidation volumetric strain whenever available. All laboratory test results are presented in Appendices A and B.

Table 3-3 Summary of unidirectional cyclic strain-controlled drained I-mcDSS tests on Ottawa sand (OT-SP).

Test Path	Test ID	Sample Prep.	OCR	S_r	D_{Rc}	σ'_{vc}	f	γ_{cs}	$\varepsilon_{vcyc,Nc=15}$
					(%)	(kPa)	(Hz)	(%)	(%)
Medium dense sand									
↔	cdss347sp	DFD	1	0	56.2	101	0.1	0.037	0.019
↔	cdss349sp	DFD	1	0	56.7	101	0.1	0.047	0.031
↔	cdss326sp	DFD + TV	1	0	64.8	101	0.1	0.078	0.064
↔	cdss27sp	DFD	1	0	57.3	98	1.0	0.293	0.205
↔	cdss246sp	DFD	1	0	64.1	51	0.1	0.367	0.607
↔	cdss23sp	DFD	1	0	58.2	94	1.0	0.372	0.265
↔	cdss35sp	DFD	1	0	57.3	94	1.0	0.375	0.165
↔	cdss107sp	DFD	1	0	54.2	94	0.1	0.376	0.264
↔	cdss108sp	DFD + CS	1	0	61.0	92	0.1	0.386	0.189
↔	cdss17sp	DFD	1	0	59.9	39	0.1	0.451	0.425
↔	cdss138sp	DFD	1	0	56.6	102	1.0	0.476	0.487
↔	cdss148sp	DFD + TV	1	0	61.1	101	0.1	0.531	0.590
↔	cdss39sp	DFD	1	0	57.5	94	1.0	0.550	0.513
↔	cdss151sp	DFD	1	0	56.6	101	1.0	0.657	0.039
↔	cdss129sp	DFD + TV	1	0	59.2	101	1.0	0.669	0.582
↔	cdss657sp	DFD	1	0	59.9	101	1.0	0.711	0.632
↔	cdss16sp	DFD	1	0	56.7	95	0.1	0.719	1.034
↔	cdss02sp	DFD	1	0	56.2	98	1.0	0.724	0.823
↔	cdss15sp	DFD	1	0	62.5	95	0.1	0.726	0.913
↔	cdss655sp	DFD	1	0	60.7	101	1.0	0.751	0.365
↔	cdss01sp	DFD	1	0	59.9	47	1.0	0.754	1.048
↔	cdss152sp	DFD	1	0	52.5	101	1.0	0.940	0.793
↔	cdss19sp	DFD	1	0	60.0	94	1.0	0.985	1.625
↔	cdss444sp	DFD	1	0	50.0	202	0.1	1.364	0.025
↔	cdss31sp	DFD	1	0	53.4	96	1.0	1.374	1.339
↔	cdss432sp	DFD	1	0	58.2	202	0.1	1.375	0.784
↔	cdss95sp	DFD	1	0	53.3	97	0.1	1.421	0.000
↔	cdss90sp	DFD	1	0	61.6	94	0.1	1.442	1.464
↔	cdss96sp	DFD + CS	1	0	62.3	96	0.1	1.444	0.518
↔	cdss147sp	DFD + TV	1	0	60.8	101	0.1	2.011	1.911
↔	cdss37sp	DFD	1	0	52.1	96	1.0	2.049	1.918
↔	cdss38sp	DFD	1	0	58.6	96	1.0	2.764	2.523
↔	cdss44sp	DFD	1	0	57.4	96	0.1	3.476	3.404
↔	cdss43sp	DFD	1	0	56.9	97	1.0	3.480	4.115
↔	cdss32sp	DFD	1	0	57.4	95	1.0	3.489	3.602

Note: ↔ = Unidirectional cyclic; DFD = dry funnel deposition; TV = table vibration; CS = cyclic shearing; OCR = overconsolidation ratio; S_r = saturation ratio; D_{Rc} = relative density after consolidation; σ'_{vc} = consolidation vertical stress; f = loading frequency; γ_{cs} = maximum single amplitude cyclic shear strain; and $\varepsilon_{vcyc,Nc=15}$ = volumetric strain at the end of 15 sinusoidal loading cycles.

Table 3-3 (cont.) Summary of unidirectional cyclic strain-controlled drained I-mcDSS tests on Ottawa sand (OT-SP).

Test Path	Test ID	Sample Prep.	OCR	S_r	D_{Rc}	σ'_{vc}	f	γ_{cs}	$\varepsilon_{vcyc,Nc=15}$
					(%)	(kPa)	(Hz)	(%)	(%)
Medium dense sand									
↔	cdss36sp	DFD	1	0	58.9	97	1.0	3.491	2.862
↔	cdss41sp	DFD	1	0	52.4	98	1.0	3.804	4.026
↔	cdss42sp	DFD	1	0	58.4	94	1.0	4.534	3.337
↔	cdss40sp	DFD	1	0	55.8	95	1.0	5.487	4.340
↔	cdss33sp	DFD	1	0	60.7	92	1.0	6.927	5.206
↔	cdss665sp	DFD	1	0	59.3	101	0.1	10.158	7.340
Dense sand									
↔	cdss336sp	CP	1	0	79.8	101	0.1	0.066	0.043
↔	cdss249sp	DFD	1	0	68.9	51	0.1	0.075	0.105
↔	cdss320sp	DFD + TV	1	0	82.8	101	0.1	0.076	0.012
↔	cdss348sp	DFD + CS	1	0	65.9	101	0.1	0.076	0.002
↔	cdss333sp	DFD + CS	1	0	83.0	101	0.1	0.078	0.052
↔	cdss220sp	DFD	1	0	68.3	101	0.1	0.084	0.056
↔	cdss25sp	DFD + CS	1	0	71.1	94	1.0	0.166	0.015
↔	cdss219sp	DFD	1	0	74.1	101	0.1	0.222	0.183
↔	cdss28sp	DFD + CS	1	0	69.7	93	1.0	0.303	0.221
↔	cdss29sp	DFD + CS	1	0	78.6	95	1.0	0.312	0.096
↔	cdss91sp	CP	1	0	72.3	93	0.1	0.336	0.261
↔	cdss93sp	DFD + CS	1	0	77.9	95	0.1	0.339	0.185
↔	cdss92sp	DFD + CS	1	0	75.6	96	0.1	0.340	0.243
↔	cdss335sp	CP	1	0	82.3	101	0.1	0.355	0.161
↔	cdss245sp	DFD	1	0	66.2	101	0.1	0.369	0.415
↔	cdss327sp	DFD + TV	1	0	66.0	101	0.1	0.371	0.198
↔	cdss34sp	DFD	1	0	66.3	91	1.0	0.393	0.141
↔	cdss18sp	DFD + CS	1	0	68.7	96	0.1	0.446	0.373
↔	cdss218sp	DFD	1	0	66.2	101	0.1	0.505	0.439
↔	cdss241sp	DFD + CS	1	0	82.7	101	0.1	0.510	0.380
↔	cdss54sp	DFD + TV	1	0	77.9	93	0.1	0.661	0.587
↔	cdss194sp	DFD	1	0	65.8	101	1.0	0.696	0.643
↔	cdss613sp	DFD	1	0	65.3	101	0.1	1.026	0.838
↔	cdss606sp	DFD	1	0	65.8	101	0.1	1.037	1.020
↔	cdss605sp	DFD	1	0	70.6	101	0.1	1.056	0.710
↔	cdss101sp	DFD	1	0	71.0	93	0.1	1.303	1.244
↔	cdss103sp	DFD + CS	1	0	83.8	92	0.1	1.334	0.483
↔	cdss117sp	CP	1	0	80.8	94	0.1	1.345	1.025

Note: ↔ = Unidirectional cyclic; DFD = dry funnel deposition; TV = table vibration; CS = cyclic shearing; OCR = overconsolidation ratio; S_r = saturation ratio; D_{Rc} = relative density after consolidation; σ'_{vc} = consolidation vertical stress; f = loading frequency; γ_{cs} = maximum single amplitude cyclic shear strain; and $\varepsilon_{vcyc,Nc=15}$ = volumetric strain at the end of 15 sinusoidal loading cycles.

Table 3-3 (cont.) Summary of unidirectional cyclic strain-controlled drained I-mcDSS tests on Ottawa sand (OT-SP).

Test Path	Test ID	Sample Prep.	OCR	S_r	D_{Rc}	σ'_{vc}	f	γ_{cs}	$\varepsilon_{vcyc,Nc=15}$
					(%)	(kPa)	(Hz)	(%)	(%)
Dense sand									
↔	cdss322sp	DFD + TV	1	0	84.6	101	0.1	1.382	0.614
↔	cdss328sp	DFD + TV	1	0	67.7	101	0.1	1.404	0.757
↔	cdss230sp	DFD	1	0	67.3	101	0.1	1.404	1.229
↔	cdss233sp	DFD	1	0	68.6	52	0.1	1.406	1.493
↔	cdss30sp	DFD	1	0	72.3	96	1.0	1.427	0.904
↔	cdss436sp	DFD	1	0	73.2	202	0.1	1.428	0.027
Very dense sand									
↔	cdss04sp	DFD + TV	1	0	88.8	101	0.1	0.074	0.004
↔	cdss482sp	DFD + CS	1	0	92.8	51	0.1	0.079	0.022
↔	cdss439sp	DFD + CS	1	0	89.6	202	0.1	0.080	0.033
↔	cdss440sp	DFD + CS	1	0	93.1	404	0.1	0.083	0.022
↔	cdss261sp	DFD + CS	1	0	98.6	101	0.1	0.086	0.031
↔	cdss08sp	DFD + TV	1	0	86.7	101	0.1	0.215	0.070
↔	cdss319sp	DFD + TV	1	0	92.5	101	0.1	0.218	0.047
↔	cdss259sp	DFD + CS	1	0	101.2	101	0.1	0.229	0.115
↔	cdss106sp	DFD + TV	1	0	88.0	96	0.1	0.355	0.076
↔	cdss116sp	DFD + CS	1	0	86.3	97	0.1	0.355	0.102
↔	cdss321sp	DFD + TV	1	0	86.1	101	0.1	0.365	0.146
↔	cdss484sp	DFD + CS	1	0	88.2	51	0.1	0.386	0.261
↔	cdss438sp	DFD + CS	1	0	87.0	202	0.1	0.388	0.080
↔	cdss441sp	DFD + CS	1	0	95.9	404	0.1	0.392	0.072
↔	cdss244sp	DFD + CS	1	0	93.1	101	0.1	0.521	0.257
↔	cdss59sp	DFD + TV	1	0	93.6	101	0.1	0.726	0.290
↔	cdss229sp	DFD + CS	1	0	95.7	101	0.1	0.786	0.262
↔	cdss55sp	DFD + TV	1	0	91.6	94	0.1	1.312	0.467
↔	cdss99sp	DFD + CS	1	0	89.1	143	0.1	1.334	0.290
↔	cdss115sp	DFD + CS	1	0	86.1	93	0.1	1.334	0.587
↔	cdss104sp	DFD + TV	1	0	92.2	94	0.1	1.352	0.401
↔	cdss58sp	DFD + TV	1	0	89.2	44	0.1	1.367	0.629
↔	cdss437sp	DFD + CS	1	0	93.5	202	0.1	1.475	0.523
↔	cdss442sp	DFD + CS	1	0	97.5	404	0.1	1.506	0.203

Note: ↔ = Unidirectional cyclic; DFD = dry funnel deposition; TV = table vibration; CS = cyclic shearing; OCR = overconsolidation ratio; S_r = saturation ratio; D_{Rc} = relative density after consolidation; σ'_{vc} = consolidation vertical stress; f = loading frequency; γ_{cs} = maximum single amplitude cyclic shear strain; and $\varepsilon_{vcyc,Nc=15}$ = volumetric strain at the end of 15 sinusoidal loading cycles.

Table 3-4 Summary of bidirectional oval / circular cyclic strain-controlled drained I-mcDSS tests on Ottawa sand (OT-SP).

Test Path	Test ID	Sample Prep.	OCR	S_r	D_{Rc}	σ'_{vc}	f	γ_{cs}	$\varepsilon_{vcyc,Nc=15}$
					(%)	(kPa)	(Hz)	(%)	(%)
Medium dense sand									
0	mcdss242sp	DFD	1	0	62.2	51	0.1	0.094	0.163
0	mcdss236sp	DFD	1	0	64.7	51	0.1	0.445	0.983
0	mcdss143sp	DFD	1	0	56.4	101	0.1	0.453	0.604
0	mcdss26sp	DFD	1	0	57.2	98	0.1	0.453	0.548
0	mcdss144sp	DFD + TV	1	0	61.7	101	0.1	0.458	0.453
0	mcdss109sp	DFD	1	0	52.0	96	0.1	0.466	0.964
0	mcdss110sp	DFD + CS	1	0	61.3	95	0.1	0.477	0.436
0	mcdss48sp	DFD	1	0	64.1	95	0.1	0.690	0.886
0	mcdss47sp	DFD	1	0	57.3	92	0.1	0.770	1.149
0	mcdss68sp	DFD	1	0	62.0	96	1.0	0.882	0.996
0	mcdss63sp	DFD	1	0	63.0	96	1.0	0.889	0.974
0	mcdss13sp	MT	1	10	-28.5	48	1.0	0.890	9.391
0	mcdss06sp	DFD	1	0	55.3	95	1.0	0.901	2.531
0	mcdss09sp	DFD	1	0	57.1	46	1.0	0.915	2.459
0	mcdss22sp	DFD	1	0	63.5	94	0.1	0.915	1.241
0	mcdss20sp	DFD	1	0	64.5	92	0.1	1.239	2.659
0	mcdss49sp	DFD	1	0	58.2	95	0.1	1.722	2.745
0	mcdss146sp	DFD + TV	1	0	60.3	101	0.1	1.729	3.026
0	mcdss71sp	DFD	1	0	63.2	96	0.1	1.737	2.504
0	mcdss330sp	DFD + TV	1	0	63.9	101	0.1	1.743	2.532
0	mcdss62sp	DFD	1	0	63.7	97	1.0	1.767	1.982
0	mcdss111sp	DFD	1	0	54.1	98	0.1	1.767	-
0	mcdss112sp	DFD + CS	1	0	62.3	95	0.1	1.797	1.842
0	mcdss46sp	DFD	1	0	57.0	94	0.1	2.539	3.464
0	mcdss50sp	DFD	1	0	58.7	94	0.1	2.590	3.873
0	mcdss445sp	DFD + CS	4	0	64.2	51	0.1	2.619	-
0	mcdss51sp	DFD	1	0	56.8	95	0.1	3.440	4.407
0	mcdss52sp	DFD	1	0	62.2	93	0.1	3.486	3.772
0	mcdss53sp	DFD	1	0	59.3	97	0.1	4.330	4.395
0	mcdss45sp	DFD	1	0	58.9	94	0.1	4.362	4.448
Dense sand									
0	mcdss329sp	DFD + TV	1	0	65.9	101	0.1	0.093	0.100
0	mcdss350sp	DFD + CS	1	0	69.2	101	0.1	0.096	0.064
0	mcdss217sp	DFD	1	0	70.0	101	0.1	0.096	0.113
0	mcdss216sp	DFD	1	0	67.5	101	0.1	0.292	0.367

Note: 0 = Bidirectional oval or circular; DFD = dry funnel deposition; TV = table vibration; CS = cyclic shearing; OCR = overconsolidation ratio; S_r = saturation ratio; D_{Rc} = relative density after consolidation; σ'_{vc} = consolidation vertical stress; f = loading frequency; γ_{cs} = maximum single amplitude cyclic shear strain; and $\varepsilon_{vcyc,Nc=15}$ = volumetric strain at the end of 15 sinusoidal loading cycles; * exception, very loose sand.

Table 3-4 (cont.) Summary of bidirectional oval / circular cyclic strain-controlled drained I-mcDSS tests on Ottawa sand (OT-SP).

Test Path	Test ID	Sample Prep.	OCR	S_r	D_{Rc}	σ'_{vc}	f	γ_{cs}	$\varepsilon_{vcyc,Nc=15}$
					(%)	(kPa)	(Hz)	(%)	(%)
Dense sand									
0	mcdss337sp	CP	1	0	81.0	101	0.1	0.106	0.077
0	mcdss94sp	DFD + CS	1	0	80.0	93	0.1	0.422	0.360
0	mcdss114sp	CP	1	0	83.9	94	0.1	0.437	0.410
0	mcdss24sp	DFD	1	0	65.5	91	0.1	0.459	0.364
0	mcdss332sp	DFD + TV	1	0	80.8	101	0.1	0.519	0.269
0	mcdss69sp	DFD	1	0	65.5	95	1.0	0.887	1.075
0	mcdss21sp	DFD	1	0	66.0	97	0.1	0.924	1.111
0	mcdss10sp	DFD	1	0	69.1	196	1.0	0.932	1.076
0	mcdss81sp	CP	1	0	79.5	97	0.1	1.500	2.248
0	mcdss98sp	CP	1	0	74.4	94	0.1	1.609	1.733
0	mcdss433sp	DFD + CS	2	0	65.6	202	1.0	1.746	1.250
0	mcdss228sp	DFD	1	0	65.8	51	0.1	1.747	2.922
0	mcdss247sp	DFD + CS	1	0	68.9	101	0.1	1.758	1.922
0	mcdss325sp	DFD + TV	1	0	84.8	101	0.1	1.778	1.284
0	mcdss72sp	DFD + CS	1	0	79.3	92	0.1	1.789	1.479
0	mcdss75sp	DFD + CS	1	0	80.5	92	0.1	1.792	1.696
0	mcdss231sp	DFD + CS	1	0	81.1	101	0.1	1.795	0.975
0	mcdss74sp	DFD + CS	1	0	83.7	94	0.1	1.805	1.303
0	mcdss73sp	DFD + CS	1	0	83.7	93	0.1	1.805	1.159
0	mcdss260sp	DFD	1	0	72.2	51	0.1	2.667	3.560
0	mcdss435sp	DFD + CS	4	0	71.2	51	1.0	2.673	2.089
Very dense sand									
0	mcdss323sp	DFD + TV	1	0	89.5	101	0.1	0.092	0.026
0	mcdss60sp	DFD + TV	1	0	90.5	101	0.1	0.098	0.030
0	mcdss334sp	DFD + CS	1	0	87.0	101	0.1	0.099	0.085
0	mcdss331sp	DFD + TV	1	0	87.7	101	0.1	0.099	0.051
0	mcdss257sp	DFD + CS	1	0	94.1	101	0.1	0.102	0.042
0	mcdss113sp	DFD + TV	1	0	91.9	101	0.1	0.274	0.174
0	mcdss251sp	DFD + CS	1	0	94.5	101	0.1	0.295	0.123
0	mcdss105sp	DFD + TV	1	0	89.7	93	0.1	0.441	0.239
0	mcdss87sp	DFD + CS	1	0	89.9	96	0.1	0.445	0.455
0	mcdss324sp	DFD + TV	1	0	90.6	101	0.1	0.461	0.349
0	mcdss235sp	DFD + CS	1	0	94.8	101	0.1	0.665	0.327
0	mcdss318sp	DFD + TV	1	0	91.8	101	0.1	0.904	0.429
0	mcdss227sp	DFD + CS	1	0	93.1	101	0.1	0.970	0.549

Note: 0 = Bidirectional oval or circular; DFD = dry funnel deposition; TV = table vibration; CS = cyclic shearing; OCR = overconsolidation ratio; S_r = saturation ratio; D_{Rc} = relative density after consolidation; σ'_{vc} = consolidation vertical stress; f = loading frequency; γ_{cs} = maximum single amplitude cyclic shear strain; and $\varepsilon_{vcyc,Nc=15}$ = volumetric strain at the end of 15 sinusoidal loading cycles.

Table 3-4 (cont.) Summary of bidirectional oval / circular cyclic strain-controlled drained l-mcDSS tests on Ottawa sand (OT-SP).

Test Path	Test ID	Sample Prep.	OCR	S_r	D_{Rc}	σ'_{vc}	f	γ_{cs}	$\varepsilon_{vcyc,Nc=15}$
					(%)	(kPa)	(Hz)	(%)	(%)
Very dense sand									
0	mcdss56sp	DFD + TV	1	0	93.3	92	0.1	1.636	0.378
0	mcdss82sp	CP	1	0	85.3	93	0.1	1.672	1.034
0	mcdss83sp	DFD + CS	1	0	90.2	94	0.1	1.690	0.741
0	mcdss86sp	DFD + CS	1	0	92.0	95	0.1	1.697	0.768
0	mcdss88sp	DFD + CS	1	0	93.6	95	0.1	1.701	0.647
0	mcdss89sp	DFD + CS	1	0	98.5	91	0.1	1.720	-
0	mcdss57sp	DFD + TV	1	0	89.8	94	0.1	1.722	0.392
0	mcdss145sp	DFD + TV	1	0	91.7	101	0.1	1.742	0.551
0	mcdss76sp	DFD + CS	1	0	91.1	93	0.1	1.833	0.644

Note: 0 = Bidirectional oval or circular; DFD = dry funnel deposition; TV = table vibration; CS = cyclic shearing; OCR = overconsolidation ratio; S_r = saturation ratio; D_{Rc} = relative density after consolidation; σ'_{vc} = consolidation vertical stress; f = loading frequency; γ_{cs} = maximum single amplitude cyclic shear strain; and $\varepsilon_{vcyc,Nc=15}$ = volumetric strain at the end of 15 sinusoidal loading cycles.

Table 3-5 Summary of bidirectional figure-8 cyclic strain-controlled drained I-mcDSS tests on Ottawa sand (OT-SP).

Test Path	Test ID	Sample Prep.	OCR	S_r	D_{Rc}	σ'_{vc}	f	γ_{cs}	$\varepsilon_{vcyc,Nc=15}$
					(%)	(kPa)	(Hz)	(%)	(%)
Medium dense sand									
8	mcdss494sp	DFD	1	0	60.7	51	0.1	0.045	0.064
8	mcdss485sp	DFD	1	0	64.0	51	0.1	0.608	0.221
8	mcdss11sp	DFD	1	0	55.0	45	0.5	0.902	4.023
8	mcdss12sp	DFD	1	0	61.6	95	0.5	0.910	2.001
8	mcdss666sp	DFD	1	0	56.0	101	0.1	1.013	2.192
8	mcdss608sp	DFD	1	0	62.8	101	0.1	1.041	1.757
8	mcdss607sp	DFD	1	0	63.1	101	0.1	1.047	1.563
8	mcdss499sp	DFD	1	0	56.7	51	0.1	1.354	3.479
8	mcdss354sp	DFD	1	0	53.5	101	0.1	1.709	2.990
8	mcdss471sp	DFD	1	0	58.6	202	0.1	1.719	2.386
8	mcdss353sp	DFD	1	0	57.0	101	0.1	1.721	3.436
8	mcdss560sp	DFD	1	0	56.5	51	1.0	1.722	3.764
8	mcdss569sp	DFD	1	0	58.0	51	1.0	1.725	3.535
8	mcdss562sp	DFD	1	0	57.0	51	1.0	1.727	3.941
8	mcdss544sp	DFD	1	0	59.4	51	1.0	1.732	4.142
8	mcdss65sp	DFD	1	0	56.3	93	1.0	1.738	3.543
8	mcdss226sp	DFD	1	0	63.6	51	0.1	1.739	3.757
8	mcdss522sp	DFD + CS	1	0	64.2	51	1.0	1.743	3.287
8	mcdss573sp	DFD	1	0	63.9	51	1.0	1.745	2.376
8	mcdss64sp	DFD	1	0	62.8	94	0.1	1.745	2.632
8	mcdss528sp	DFD + CS	1	0	63.2	51	1.0	1.749	3.334
8	mcdss567sp	DFD	1	0	64.2	25	1.0	1.749	3.201
8	mcdss61sp	DFD	1	0	57.8	93	0.1	1.790	3.335
8	mcdss479sp	DFD	1	0	59.1	202	0.1	2.605	0.024
8	mcdss660sp	DFD	1	0	59.7	101	0.1	5.104	7.904
8	mcdss659sp	DFD	1	0	63.6	101	0.1	7.189	7.821
Dense sand									
8	mcdss215sp	DFD	1	0	73.9	101	0.1	0.099	0.122
8	mcdss488sp	DFD + CS	1	0	66.6	51	0.1	0.276	0.074
8	mcdss214sp	DFD	1	0	67.8	101	0.1	0.277	0.360
8	mcdss447sp	DFD + CS	1	0	68.3	202	0.1	0.449	0.495
8	mcdss213sp	DFD	1	0	78.0	101	0.1	0.468	0.833
8	mcdss222sp	DFD	1	0	70.6	51	0.1	0.470	0.744
8	mcdss212sp	DFD	1	0	69.4	101	0.1	0.616	0.974
8	mcdss255sp	DFD	1	0	70.2	101	0.1	0.920	1.350

Note: 8 = Bidirectional figure-8; DFD = dry funnel deposition; TV = table vibration; CS = cyclic shearing; OCR = overconsolidation ratio; S_r = saturation ratio; D_{Rc} = relative density after consolidation; σ'_{vc} = consolidation vertical stress; f = loading frequency; γ_{cs} = maximum single amplitude cyclic shear strain; and $\varepsilon_{vcyc,Nc=15}$ = volumetric strain at the end of 15 sinusoidal loading cycles.

Table 3-5 (cont.) Summary of bidirectional figure-8 cyclic strain-controlled drained I-mcDSS tests on Ottawa sand (OT-SP).

Test Path	Test ID	Sample Prep.	OCR	S_r	D_{Rc}	σ'_{vc}	f	γ_{cs}	$\varepsilon_{vcyc,Nc=15}$
					(%)	(kPa)	(Hz)	(%)	(%)
Dense sand									
8	mcdss252sp	DFD	1	0	67.5	51	0.1	0.923	2.184
8	mcdss223sp	DFD + CS	1	0	78.7	101	0.1	0.945	0.768
8	mcdss549sp	DFD	1	0	77.7	51	0.1	1.084	0.318
8	mcdss102sp	DFD + CS	1	0	78.3	93	0.1	1.632	1.482
8	mcdss240sp	DFD + CS	1	0	70.2	101	0.1	1.740	3.147
8	mcdss551sp	DFD + CS	1	0	65.8	51	1.0	1.751	3.064
8	mcdss534sp	DFD + CS	1	0	67.1	51	1.0	1.756	3.297
8	mcdss537sp	DFD + CS	1	0	67.8	51	1.0	1.758	2.951
8	mcdss531sp	DFD + CS	1	0	66.9	51	1.0	1.759	3.052
8	mcdss243sp	DFD + CS	1	0	69.0	101	0.1	1.759	2.644
8	mcdss575sp	DFD	1	0	68.5	51	1.0	1.761	1.658
8	mcdss525sp	DFD + CS	1	0	68.3	51	1.0	1.765	2.822
8	mcdss449sp	DFD + CS	4	0	70.5	51	0.1	1.765	1.538
8	mcdss472sp	DFD + CS	1	0	72.0	51	1.0	1.781	1.812
8	mcdss237sp	DFD + CS	1	0	74.7	101	0.1	1.790	2.419
8	mcdss256sp	DFD + CS	1	0	80.1	101	0.1	1.794	1.520
8	mcdss97sp	DFD + CS	1	0	65.1	93	0.1	1.795	1.650
8	mcdss224sp	DFD + CS	1	0	79.7	101	0.1	1.796	1.692
8	mcdss481sp	DFD	1	0	76.3	41	0.1	1.797	0.286
8	mcdss234sp	DFD + CS	1	0	82.2	101	0.1	1.798	1.458
8	mcdss250sp	DFD + CS	1	0	78.7	101	0.1	1.799	2.368
8	mcdss541sp	DFD + CS	1	0	80.6	51	1.0	1.802	2.378
8	mcdss450sp	DFD + CS	4	0	77.8	51	0.1	1.804	-
8	mcdss258sp	DFD	1	0	72.8	51	0.1	2.665	4.003
8	mcdss221sp	DFD	1	0	80.2	102	0.1	2.699	3.955
8	mcdss474sp	DFD	1	0	76.2	202	0.1	2.700	0.012
8	mcdss664sp	DFD	1	0	66.5	101	0.1	3.105	5.181
Very dense sand									
8	mcdss476sp	DFD + CS	1	0	88.9	404	0.1	0.097	0.049
8	mcdss254sp	DFD + CS	1	0	95.2	101	0.1	0.098	0.079
8	mcdss446sp	DFD + CS	1	0	97.5	202	0.1	0.099	0.039
8	mcdss483sp	DFD + CS	1	0	93.3	51	0.1	0.102	0.014
8	mcdss248sp	DFD + CS	1	0	93.7	101	0.1	0.296	0.163
8	mcdss486sp	DFD + CS	1	0	93.2	51	0.1	0.485	0.323

Note: 8 = Bidirectional figure-8; DFD = dry funnel deposition; TV = table vibration; CS = cyclic shearing; OCR = overconsolidation ratio; S_r = saturation ratio; D_{Rc} = relative density after consolidation; σ'_{vc} = consolidation vertical stress; f = loading frequency; γ_{cs} = maximum single amplitude cyclic shear strain; and $\varepsilon_{vcyc,Nc=15}$ = volumetric strain at the end of 15 sinusoidal loading cycles.

Table 3-5 (cont.) Summary of bidirectional figure-8 cyclic strain-controlled drained I-mcDSS tests on Ottawa sand (OT-SP).

Test Path	Test ID	Sample Prep.	OCR	S_r	D_{Rc}	σ'_{vc}	f	γ_{cs}	$\varepsilon_{vcyc,Nc=15}$
					(%)	(kPa)	(Hz)	(%)	(%)
Very dense sand									
8	mcdss477sp	DFD + CS	1	0	92.5	404	0.1	0.487	0.143
8	mcdss475sp	DFD + CS	1	0	93.1	202	0.1	0.488	0.138
8	mcdss238sp	DFD + CS	1	0	93.9	101	0.1	0.493	0.256
8	mcdss232sp	DFD + CS	1	0	95.5	101	0.1	0.642	0.326
8	mcdss225sp	DFD + CS	1	0	94.2	101	0.1	0.976	0.326
8	mcdss253sp	DFD + CS	1	0	87.8	101	0.1	1.821	1.127
8	mcdss489sp	DFD + CS	1	0	91.0	51	0.1	1.840	0.355
8	mcdss478sp	DFD + CS	1	0	94.1	404	0.1	1.842	0.421
8	mcdss487sp	DFD + CS	1	0	91.5	51	0.1	1.843	0.542
8	mcdss473sp	DFD + CS	1	0	95.6	202	0.1	1.853	0.454

Note: 8 = Bidirectional figure-8; DFD = dry funnel deposition; TV = table vibration; CS = cyclic shearing; OCR = overconsolidation ratio; S_r = saturation ratio; D_{Rc} = relative density after consolidation; σ'_{vc} = consolidation vertical stress; f = loading frequency; γ_{cs} = maximum single amplitude cyclic shear strain; and $\varepsilon_{vcyc,Nc=15}$ = volumetric strain at the end of 15 sinusoidal loading cycles.

Table 3-6 Summary of unidirectional cyclic strain-controlled drained I-mcDSS tests on Lab Mix sand (SW-SM).

Test Path	Test ID	Sample Prep.	OCR	S_r	D_{Rc}	σ'_{vc}	f	γ_{cs}	$\varepsilon_{vcyc,Nc=15}$
					(%)	(kPa)	(Hz)	(%)	(%)
Medium dense sand									
↔	cdss422sw	DFD	1	0	44.8	202	0.1	0.072	0.013
↔	cdss373sw	DFD	1	0	57.5	51	0.1	0.074	0.072
↔	cdss421sw	DFD	1	0	45.2	202	0.1	0.353	0.151
↔	cdss424sw	DFD	1	0	46.5	404	0.1	0.353	0.104
↔	cdss372sw	DFD	1	0	57.2	51	0.1	0.361	0.500
↔	cdss173sw	DFD	1	0	61.1	101	0.1	0.725	1.202
↔	cdss420sw	DFD	1	0	48.8	202	0.1	1.339	1.246
↔	cdss398sw	DFD	4	0	47.7	101	0.1	1.340	1.023
↔	cdss423sw	DFD	1	0	57.2	404	0.1	1.359	0.665
↔	cdss371sw	DFD	1	0	59.7	51	0.1	1.373	2.611
↔	cdss162sw	DFD	1	0	64.0	101	1.0	1.390	2.917
↔	cdss192sw	DFD	1	0	60.8	101	0.1	2.071	2.873
↔	cdss195sw	DFD	1	0	54.2	101	0.1	3.413	4.073
↔	cdss203sw	DFD	1	0	50.0	101	0.1	6.709	6.233
Dense sand									
↔	cdss465sw	DFD + TV	1	0	82.4	404	0.1	0.072	-
↔	cdss425sw	DFD	1	0	66.8	404	0.1	0.075	0.017
↔	cdss190sw	DFD	1	0	76.2	101	0.1	0.216	0.191
↔	cdss467sw	DFD + TV	1	0	80.7	404	0.1	0.351	0.018
↔	cdss427sw	DFD + TV	1	0	84.2	202	0.1	0.360	0.017
↔	cdss166sw	DFD	1	0	69.3	101	0.1	0.372	0.307
↔	cdss191sw	DFD	1	0	78.9	101	0.1	0.504	0.615
↔	cdss469sw	DFD + TV	1	0	80.0	404	0.1	1.322	0.157
↔	cdss395sw	DFD + TV	1	0	84.8	51	0.1	1.340	1.093
↔	cdss174sw	DFD + CS	1	0	73.1	101	0.1	1.409	1.912
↔	cdss161sw	DFD	1	0	69.4	101	0.1	1.433	1.614
↔	cdss202sw	DFD	1	0	66.0	101	0.1	4.879	5.691
Very dense sand									
↔	cdss389sw	DFD + TV	1	0	94.7	51	0.1	0.075	0.026
↔	cdss426sw	DFD + TV	1	0	101.4	202	0.1	0.076	0.009
↔	cdss211sw	DFD + TV	1	0	101.0	101	0.1	0.080	0.013
↔	cdss210sw	DFD + TV	1	0	101.7	101	0.1	0.211	0.048
↔	cdss392sw	DFD + TV	1	0	89.6	51	0.1	0.358	0.239
↔	cdss156sw	DFD + TV	1	0	99.0	101	0.1	0.376	0.197
↔	cdss185sw	DFD + CS	1	0	94.2	101	0.1	0.391	0.174

Note: ↔ = Unidirectional cyclic; DFD = dry funnel deposition; TV = table vibration; CS = cyclic shearing; OCR = overconsolidation ratio; S_r = saturation ratio; D_{Rc} = relative density after consolidation; σ'_{vc} = consolidation vertical stress; f = loading frequency; γ_{cs} = maximum single amplitude cyclic shear strain; and $\varepsilon_{vcyc,Nc=15}$ = volumetric strain at the end of 15 sinusoidal loading cycles.

Table 3-6 (cont.) Summary of unidirectional cyclic strain-controlled drained I-mcDSS tests on Lab Mix sand (SW-SM).

Test Path	Test ID	Sample Prep.	OCR	S_r	D_{Rc}	σ'_{vc}	f	γ_{cs}	$\varepsilon_{vcyc,Nc=15}$
					(%)	(kPa)	(Hz)	(%)	(%)
Very dense sand									
↔	cdss209sw	DFD + TV	1	0	98.9	101	0.1	0.484	0.336
↔	cdss208sw	DFD + TV	1	0	95.8	101	0.1	0.726	0.696
↔	cdss408sw	DFD + TV	1	0	85.5	51	1.0	1.343	0.396
↔	cdss428sw	DFD + TV	1	0	86.6	202	0.1	1.344	0.167
↔	cdss167sw	DFD + TV	1	0	97.3	101	0.1	1.390	0.628
↔	cdss175sw	DFD + CS	1	0	93.0	101	0.1	1.471	0.495
↔	cdss176sw	DFD + CS	1	0	96.6	101	0.1	1.482	0.381

Note: ↔ = Unidirectional cyclic; DFD = dry funnel deposition; TV = table vibration; CS = cyclic shearing; OCR = overconsolidation ratio; S_r = saturation ratio; D_{Rc} = relative density after consolidation; σ'_{vc} = consolidation vertical stress; f = loading frequency; γ_{cs} = maximum single amplitude cyclic shear strain; and $\varepsilon_{vcyc,Nc=15}$ = volumetric strain at the end of 15 sinusoidal loading cycles.

Table 3-7 Summary of bidirectional oval / circular cyclic strain-controlled drained I-mcDSS tests on Lab Mix sand (SW-SM).

Test Path	Test ID	Sample Prep.	OCR	S_r	D_{Rc}	σ'_{vc}	f	γ_{cs}	$\varepsilon_{vcyc,Nc=15}$
					(%)	(kPa)	(Hz)	(%)	(%)
Medium dense sand									
0	mcdss164sw	DFD	1	0	63.0	101	0.1	0.092	0.096
0	mcdss374sw	DFD	1	0	52.8	51	0.1	0.093	0.120
0	mcdss165sw	DFD	1	0	60.5	102	0.1	0.272	0.539
0	mcdss266sw	DFD	1	0	59.2	51	0.1	0.452	1.282
0	mcdss204sw	DFD	1	0	63.0	56	0.1	1.729	3.087
0	mcdss188sw	DFD	1	0	61.1	101	0.1	4.317	5.398
Dense sand									
0	mcdss157sw	DFD	1	0	71.9	101	0.1	0.459	0.816
0	mcdss180sw	DFD + CS	1	0	71.0	101	0.1	0.462	0.479
0	mcdss178sw	DFD + CS	1	0	79.2	101	0.1	0.472	0.288
0	mcdss170sw	DFD	1	0	67.5	101	0.1	0.639	1.114
0	mcdss205sw	DFD	1	0	65.4	51	0.1	0.915	2.374
0	mcdss163sw	DFD	1	0	68.7	101	0.1	0.922	1.876
0	mcdss396sw	DFD + TV	1	0	84.5	51	0.1	1.674	1.135
0	mcdss67sw	DFD	1	0	65.1	95	0.1	1.766	3.519
0	mcdss181sw	DFD + CS	1	0	76.8	101	0.1	1.773	1.818
0	mcdss171sw	DFD + CS	1	0	79.8	101	0.1	1.792	1.492
0	mcdss66sw	DFD	1	0	67.4	96	1.0	1.796	4.087
0	mcdss187sw	DFD	1	0	73.2	101	0.1	2.656	4.685
Very dense sand									
0	mcdss390sw	DFD + TV	1	0	94.6	51	0.1	0.093	0.113
0	mcdss196sw	DFD + TV	1	0	91.5	101	0.1	0.100	0.113
0	mcdss197sw	DFD + TV	1	0	101.5	101	0.1	0.280	0.386
0	mcdss154sw	DFD + TV	1	0	96.6	101	0.1	0.447	0.283
0	mcdss393sw	DFD + TV	1	0	90.8	51	0.1	0.448	0.457
0	mcdss182sw	DFD + CS	1	0	100.8	101	0.1	0.499	0.260
0	mcdss198sw	DFD + TV	1	0	91.3	101	0.1	0.646	0.916
0	mcdss199sw	DFD + TV	1	0	107.0	101	0.1	0.949	0.915
0	mcdss168sw	DFD + TV	1	0	95.7	102	0.1	1.721	1.789
0	mcdss409sw	DFD + TV	1	0	101.6	51	0.1	1.768	1.032
0	mcdss184sw	DFD + CS	1	0	86.8	101	0.1	1.817	0.736
0	mcdss172sw	DFD + CS	1	0	94.9	101	0.1	1.854	0.390

Note: 0 = Bidirectional oval or circular; DFD = dry funnel deposition; TV = table vibration; CS = cyclic shearing; OCR = overconsolidation ratio; S_r = saturation ratio; D_{Rc} = relative density after consolidation; σ'_{vc} = consolidation vertical stress; f = loading frequency; γ_{cs} = maximum single amplitude cyclic shear strain; and $\varepsilon_{vcyc,Nc=15}$ = volumetric strain at the end of 15 sinusoidal loading cycles.

Table 3-8 Summary of bidirectional figure-8 cyclic strain-controlled drained I-mcDSS tests on Lab Mix sand (SW-SM).

Test Path	Test ID	Sample Prep.	OCR	S_r	D_{Rc}	σ'_{vc}	f	γ_{cs}	$\varepsilon_{vcyc,Nc=15}$
					(%)	(kPa)	(Hz)	(%)	(%)
Medium dense sand									
8	mcdss375sw	DFD	1	0	38.1	51	0.1	0.087	0.243
8	mcdss456sw	DFD	1	0	44.0	404	0.1	0.088	0.027
8	mcdss455sw	DFD	1	0	50.7	202	0.1	0.089	0.041
8	mcdss453sw	DFD	1	0	38.6	202	0.1	0.434	0.542
8	mcdss454sw	DFD	1	0	49.5	404	0.1	0.443	0.349
8	mcdss186sw	DFD	1	0	60.6	101	0.1	0.606	1.124
8	mcdss183sw	DFD	1	0	64.8	101	0.1	0.911	2.242
8	mcdss451sw	DFD	1	0	44.6	202	0.1	1.656	3.300
8	mcdss452sw	DFD	1	0	45.6	404	0.1	1.657	1.875
8	mcdss262sw	DFD	3.46	0	62.7	51	0.1	1.726	4.001
8	mcdss263sw	DFD	1	0	62.8	51	0.1	1.729	4.762
8	mcdss160sw	DFD	1	0	64.4	101	1.0	1.741	4.871
Dense sand									
8	mcdss462sw	DFD + TV	1	0	76.3	202	0.1	0.087	0.035
8	mcdss179sw	DFD	1	0	70.1	101	0.1	0.093	0.083
8	mcdss177sw	DFD	1	0	70.5	101	0.1	0.283	0.447
8	mcdss158sw	DFD	1	0	68.5	101	0.1	0.457	0.954
8	mcdss265sw	DFD	1	0	65.4	51	0.1	0.461	0.988
8	mcdss264sw	DFD	1	0	69.6	51	0.1	0.923	2.163
8	mcdss397sw	DFD + TV	1	0	81.7	51	0.1	1.663	1.701
8	mcdss464sw	DFD + TV	1	0	83.7	202	0.1	1.664	1.321
8	mcdss159sw	DFD	1	0	67.2	101	0.1	1.742	4.781
8	mcdss668sw	DFD	1	0	73.4	101	0.1	5.218	7.519
8	mcdss667sw	DFD	1	0	65.5	101	0.1	7.166	7.519
8	mcdss663sw	DFD + TV	1	0	67.1	101	0.1	7.187	4.477
Very dense sand									
8	mcdss466sw	DFD + TV	1	0	93.6	404	0.1	0.092	0.040
8	mcdss391sw	DFD + TV	1	0	100.1	51	0.1	0.094	0.082
8	mcdss207sw	DFD + TV	1	0	103.0	101	0.1	0.100	0.072
8	mcdss206sw	DFD + TV	1	0	98.9	101	0.1	0.273	0.485
8	mcdss155sw	DFD + TV	1	0	92.3	101	0.1	0.440	0.525
8	mcdss394sw	DFD + TV	1	0	90.9	51	0.1	0.447	0.552
8	mcdss468sw	DFD + TV	1	0	92.1	404	0.1	0.449	0.109
8	mcdss463sw	DFD + TV	1	0	93.6	202	0.1	0.450	0.252
8	mcdss201sw	DFD + TV	1	0	100.7	101	0.1	0.604	0.295

Note: 8 = Bidirectional figure-8; DFD = dry funnel deposition; TV = table vibration; CS = cyclic shearing; OCR = overconsolidation ratio; S_r = saturation ratio; D_{Rc} = relative density after consolidation; σ'_{vc} = consolidation vertical stress; f = loading frequency; γ_{cs} = maximum single amplitude cyclic shear strain; and $\varepsilon_{vcyc,Nc=15}$ = volumetric strain at the end of 15 sinusoidal loading cycles.

Table 3-8 (cont.) Summary of bidirectional figure-8 cyclic strain-controlled drained I-mcDSS tests on Lab Mix sand (SW-SM).

Test Path	Test ID	Sample Prep.	OCR	S_r	D_{Rc}	σ'_{vc}	f	γ_{cs}	$\varepsilon_{vcyc,Nc=15}$
					(%)	(kPa)	(Hz)	(%)	(%)
Very dense sand									
8	mcdss200sw	DFD + TV	1	0	94.2	101	0.1	0.893	0.821
8	mcdss470sw	DFD + TV	1	0	89.7	404	0.1	1.690	0.688
8	mcdss410sw	DFD + TV	1	0	92.9	51	0.1	1.706	1.518
8	mcdss169sw	DFD + TV	1	0	96.8	101	0.1	1.709	1.452

Note: 8 = Bidirectional figure-8; DFD = dry funnel deposition; TV = table vibration; CS = cyclic shearing; OCR = overconsolidation ratio; S_r = saturation ratio; D_{Rc} = relative density after consolidation; σ'_{vc} = consolidation vertical stress; f = loading frequency; γ_{cs} = maximum single amplitude cyclic shear strain; and $\varepsilon_{vcyc,Nc=15}$ = volumetric strain at the end of 15 sinusoidal loading cycles.

Table 3-9 Summary of unidirectional cyclic strain-controlled drained I-mcDSS tests on Mississippi River sand (MR-SM).

Test Path	Test ID	Sample Prep.	OCR	S_r	RC	σ'_{vc}	f	γ_{cs}	$\varepsilon_{vcyc,Nc=15}$
					(%)	(kPa)	(Hz)	(%)	(%)
Medium dense sand									
↔	cdss296sm	DFD	1	0	86.9	101	0.1	0.076	0.052
↔	cdss382sm	DFD	1	0	87.7	51	0.1	0.077	0.082
↔	cdss434sm	DFD	1	0	89.8	404	0.1	0.080	0.011
↔	cdss419sm	DFD	1	0	88.5	202	0.1	0.080	0.016
↔	cdss379sm	DFD	1	0	84.9	51	0.1	0.360	1.069
↔	cdss297sm	DFD	1	0	86.2	101	0.1	0.365	0.576
↔	cdss418sm	DFD	1	0	88.7	202	0.1	0.375	0.276
↔	cdss298sm	DFD	1	0	87.8	101	0.1	0.742	0.993
↔	cdss370sm	DFD	1	0	44.9	0	0.1	0.764	0.003
↔	cdss121sm	DFD	1	0	89.2	93	0.1	1.343	1.517
↔	cdss378sm	DFD	1	0	85.3	51	0.1	1.368	3.807
↔	cdss413sm	DFD	1	0	87.0	202	0.1	1.398	1.871
↔	cdss299sm	DFD	1	0	87.6	101	0.1	1.403	1.891
↔	cdss351sm	DFD + CS	1	0	88.0	101	0.1	1.407	-
↔	cdss414sm	DFD	1	0	88.8	404	0.1	1.419	1.095
↔	cdss417sm	DFD	1	0	88.7	202	0.1	1.424	1.676
↔	cdss352sm	DFD + CS	1	0	89.0	101	0.1	1.575	0.871
Dense sand									
↔	cdss272sm	DFD + TV	1	0	91.4	101	0.1	0.076	0.013
↔	cdss287sm	DFD + TV	1	0	92.2	101	0.1	0.223	0.088
↔	cdss269sm	DFD + TV	1	0	91.3	101	0.1	0.366	0.123
↔	cdss431sm	DFD	1	0	90.0	404	0.1	0.382	0.137
↔	cdss284sm	DFD + TV	1	0	90.4	101	0.1	0.476	0.493
↔	cdss275sm	DFD + TV	1	0	92.7	101	0.1	0.732	0.387
↔	cdss443sm	DFD + TV	1	0	92.4	202	0.1	1.384	1.078
↔	cdss416sm	DFD + CS	1	0	90.4	404	1.0	1.452	0.293
↔	cdss278sm	DFD + TV	1	0	91.8	101	0.1	2.078	1.628
↔	cdss279sm	DFD + TV	1	0	91.8	101	0.1	3.445	2.822
↔	cdss280sm	DFD + TV	1	0	90.7	101	0.1	4.792	4.092
↔	cdss281sm	DFD + TV	1	0	91.0	101	0.1	6.836	5.736
Very dense sand									
↔	cdss126sm	DFD + CS	1	0	98.3	101	0.1	0.388	0.078

Note: ↔ = Unidirectional cyclic; DFD = dry funnel deposition; TV = table vibration; CS = cyclic shearing; OCR = overconsolidation ratio; S_r = saturation ratio; RC = relative compaction after consolidation; σ'_{vc} = consolidation vertical stress; f = loading frequency; γ_{cs} = maximum single amplitude cyclic shear strain; and $\varepsilon_{vcyc,Nc=15}$ = volumetric strain at the end of 15 sinusoidal loading cycles.

Table 3-10 Summary of bidirectional oval / circular cyclic strain-controlled drained I-mcDSS tests on Mississippi River sand (MR-SM).

Test Path	Test ID	Sample Prep.	OCR	S_r	RC	σ'_{vc}	f	γ_{cs}	$\varepsilon_{vcyc,Nc=15}$
					(%)	(kPa)	(Hz)	(%)	(%)
Medium dense sand									
0	mcdss383sm	DFD	1	0	86.7	51	0.1	0.093	0.224
0	mcdss295sm	DFD	1	0	86.9	102	0.1	0.093	0.084
0	mcdss293sm	DFD	1	0	86.4	101	0.1	0.455	0.994
0	mcdss380sm	DFD	1	0	86.9	51	0.1	0.473	1.819
0	mcdss291sm	DFD	1	0	86.0	101	0.1	0.911	2.367
0	mcdss355sm	DFD	1	0	87.0	51	0.1	1.537	4.651
0	mcdss289sm	DFD	1	0	85.4	101	0.1	1.718	5.434
0	mcdss376sm	DFD	1	0	86.8	51	0.1	1.741	6.342
0	mcdss411sm	DFD	1	0	87.2	202	0.1	1.786	4.046
0	mcdss77sm	DFD	1	0	84.2	91	0.1	1.842	5.223
0	mcdss70sm	DFD	1	0	84.1	94	1.0	1.872	5.470
Dense sand									
0	mcdss271sm	DFD + TV	1	0	90.5	101	0.1	0.093	0.074
0	mcdss286sm	DFD + TV	1	0	91.8	101	0.1	0.280	0.259
0	mcdss268sm	DFD + TV	1	0	91.4	101	0.1	0.456	0.448
0	mcdss283sm	DFD + TV	1	0	92.2	101	0.1	0.608	0.675
0	mcdss274sm	DFD + TV	1	0	92.2	101	0.1	0.911	0.939
0	mcdss122sm	DFD	1	0	91.3	93	0.1	1.709	1.780
0	mcdss78sm	DFD + CS	1	0	93.5	93	0.1	2.044	0.612
0	mcdss79sm	DFD + CS	1	0	93.8	94	0.1	2.052	0.640
0	mcdss80sm	DFD + CS	1	0	94.7	93	0.1	2.070	0.617
0	mcdss276sm	DFD + TV	1	0	92.1	101	0.1	2.650	2.894
0	mcdss277sm	DFD + TV	1	0	92.0	101	0.1	4.352	4.300
Very dense sand									
0	mcdss127sm	DFD + CS	1	0	98.4	101	0.1	0.488	0.130

Note: 0 = Bidirectional oval or circular; DFD = dry funnel deposition; TV = table vibration; CS = cyclic shearing; OCR = overconsolidation ratio; S_r = saturation ratio; RC = relative compaction after consolidation; σ'_{vc} = consolidation vertical stress; f = loading frequency; γ_{cs} = maximum single amplitude cyclic shear strain; and $\varepsilon_{vcyc,Nc=15}$ = volumetric strain at the end of 15 sinusoidal loading cycles.

Table 3-11 Summary of bidirectional figure-8 cyclic strain-controlled drained I-mcDSS tests on Mississippi River sand (MR-SM).

Test Path	Test ID	Sample Prep.	OCR	S_r	RC	σ'_{vc}	f	γ_{cs}	$\varepsilon_{vcyc,Nc=15}$
					(%)	(kPa)	(Hz)	(%)	(%)
Medium dense sand									
8	mcdss384sm	DFD	1	0	86.6	51	0.1	0.092	0.182
8	mcdss460sm	DFD	1	0	87.8	202	0.1	0.094	0.054
8	mcdss294sm	DFD	1	0	87.1	101	0.1	0.094	0.145
8	mcdss292sm	DFD	1	0	86.0	101	0.1	0.454	1.364
8	mcdss381sm	DFD	1	0	86.9	52	0.1	0.458	2.051
8	mcdss458sm	DFD	1	0	88.8	202	0.1	0.472	0.698
8	mcdss459sm	DFD	1	0	89.6	404	0.1	0.473	0.384
8	mcdss290sm	DFD	1	0	86.8	102	0.1	0.917	2.642
8	mcdss377sm	DFD	1	0	86.0	51	0.1	1.721	7.510
8	mcdss412sm	DFD	1	0	87.7	202	0.1	1.757	4.722
8	mcdss288sm	DFD	1	0	88.3	101	0.1	1.767	4.393
8	mcdss457sm	DFD	1	0	89.2	404	0.1	1.784	2.962
Dense sand									
8	mcdss270sm	DFD + TV	1	0	90.5	101	0.1	0.094	0.103
8	mcdss285sm	DFD + TV	1	0	91.8	101	0.1	0.275	0.303
8	mcdss267sm	DFD + TV	1	0	92.0	101	0.1	0.461	0.635
8	mcdss282sm	DFD + TV	1	0	92.2	101	0.1	0.606	0.635
8	mcdss273sm	DFD + TV	1	0	92.1	101	0.1	0.901	1.313
8	mcdss123sm	DFD + TV	1	0	90.4	101	0.1	1.686	3.849
8	mcdss415sm	DFD + CS	2	0	90.3	202	0.1	1.803	2.594
Very dense sand									
8	mcdss124sm	DFD + CS	1	0	96.8	101	0.1	1.583	0.161
8	mcdss125sm	DFD + CS	1	0	96.1	101	0.1	1.779	-

Note: 8 = Bidirectional figure-8; DFD = dry funnel deposition; TV = table vibration; CS = cyclic shearing; OCR = overconsolidation ratio; S_r = saturation ratio; RC = relative compaction after consolidation; σ'_{vc} = consolidation vertical stress; f = loading frequency; γ_{cs} = maximum single amplitude cyclic shear strain; and $\varepsilon_{vcyc,Nc=15}$ = volumetric strain at the end of 15 sinusoidal loading cycles.

Table 3-12 Summary of strain-controlled unidirectional and bidirectional drained I-mcDSS tests on Mississippi River Gulf of Mexico sand (MRGM-SC).

Test Path	Test ID	Sample Prep.	OCR	S_r	RC	σ'_{vc}	f	γ_{cs}	$\varepsilon_{vcyc,Nc=15}$
					(%)	(kPa)	(Hz)	(%)	(%)
Medium dense sand									
↔	cdss674sc	DFD + TV	1	1	91.3	101	0.1	0.512	0.974
↔	cdss645sc	DFD + TV	1	1	89.4	101	0.1	1.959	1.770
8	mcdss647sc	DFD + TV	1	1	86.0	101	0.1	0.512	1.101
8	mcdss673sc	DFD + TV	1	1	92.0	101	0.1	1.097	2.453
8	mcdss646sc	DFD + TV	1	1	86.9	101	0.1	1.956	5.091

Note: ↔ = Unidirectional cyclic; 8 = bidirectional figure-8; DFD = dry funnel deposition; TV = table vibration; CS = cyclic shearing; OCR = overconsolidation ratio; S_r = saturation ratio; RC = relative compaction after consolidation; σ'_{vc} = consolidation vertical stress; f = loading frequency; γ_{cs} = maximum single amplitude cyclic shear strain; and $\varepsilon_{vcyc,Nc=15}$ = volumetric strain at the end of 15 sinusoidal loading cycles.

Table 3-13 Summary of strain-controlled broadband loading drained I-mcDSS tests on Ottawa sand (OT-SP) and Lab Mix sand (SW-SM).

Test Path	Test ID	Sample Prep.	OCR	S_r	D_{Rc}	σ'_{vc}	f	γ_s	ε_{vds}
					(%)	(kPa)	(Hz)	(%)	(%)
Ottawa sand (OT-SP)									
BB	bb361sp	DFD	1	0	57.8	101	0.01	0.690	0.629
BB	bb360sp	DFD	1	0	61.3	101	0.01	0.723	0.362
BB	bb610sp	DFD	1	0	65.5	101	0.01	1.016	0.464
BB	bb609sp	DFD	1	0	67.2	101	0.01	1.026	0.466
BB	bb495sp	DFD + CS	1	0	94.9	101	0.01	0.059	0.053
BB	bb496sp	DFD + CS	1	0	91.9	101	0.01	0.062	0.140
BB	bb497sp	DFD + CS	1	0	94.4	101	0.01	0.244	0.104
BB	bb498sp	DFD + CS	1	0	95.2	101	0.01	0.267	0.099
mBB	mbb362sp	DFD	1	0	60.2	101	0.01	0.176	0.125
mBB	mbb363sp	DFD	1	0	57.3	101	0.01	0.861	0.943
mBB	mbb611sp	DFD	1	0	63.6	101	0.01	1.024	0.709
mBB	mbb500sp	DFD + CS	1	0	90.4	101	0.01	0.055	0.095
mBB	mbb501sp	DFD + CS	1	0	89.7	101	0.01	0.313	0.114
Lab Mix sand (SW-SM)									
BB	bb400sw	DFD	1	0	61.1	101	0.01	0.656	0.657
BB	bb399sw	DFD	1	0	65.4	101	0.01	0.725	0.453
mBB	mbb401sw	DFD	1	0	63.6	101	0.01	0.848	1.264

Table 3-14 Summary of strain-controlled broadband loading drained I-mcDSS tests on Mississippi River sand (MR-SM).

Test Path	Test ID	Sample Prep.	OCR	S_r	RC	σ'_{vc}	f	γ_s	ε_{vds}
					(%)	(kPa)	(Hz)	(%)	(%)
Mississippi River sand (MR-SM)									
BB	bb403sm	DFD	1	0	87.7	101	0.01	0.680	0.817
BB	bb402sm	DFD	1	0	87.0	101	0.01	0.728	0.881
BB	bb406sm	DFD	1	0	86.7	101	0.01	1.327	2.007
BB	bb405sm	DFD	1	0	86.5	101	0.01	1.385	1.940
mBB	mbb404sm	DFD	1	0	86.4	101	0.01	0.856	1.764
mBB	mbb407sm	DFD	1	0	87.0	101	0.01	1.683	3.916

Note: BB = Unidirectional broadband; mBB = multidirectional broadband; DFD = dry funnel deposition; CS = cyclic shearing; OCR = overconsolidation ratio; S_r = saturation ratio; D_{Rc} = relative density after consolidation; RC = relative compaction after consolidation; σ'_{vc} = consolidation vertical stress; f = frequency of the entire time history (e.g., an earthquake time history = 100s implies f = 0.01Hz); γ_s = maximum shear strain; and ε_{vds}= volumetric strain at the end of drained shaking.

Table 3-15 Summary of unidirectional and bidirectional cyclic constant volume I-mcDSS tests on Ottawa sand (OT-SP).

Test Path	Test ID	Sample Prep.	OCR	S_r	D_{Rc}	σ'_{vc}	f	γ_{cs}	ε_{vr}
					(%)	(kPa)	(Hz)	(%)	(%)
Unidirectional cyclic tests									
↔	cdss656chsp	DFD	1	0	55.2	101	0.10	0.069	-
↔	cdss344chsp	DFD	1	0	54.9	100	0.10	0.073	0.327
↔	cdss658chsp	DFD	1	0	53.5	95	0.10	0.073	-
↔	cdss555chsp	DFD	1	0	61.2	202	0.10	0.075	-
↔	cdss513chsp	DFD	1	0	56.6	50	1.00	0.075	0.141
↔	cdss521chsp	DFD	1	0	57.7	51	1.00	0.142	0.179
↔	cdss512chsp	DFD	1	0	56.0	51	1.00	0.210	0.181
↔	cdss654chsp	DFD	1	0	51.9	52	0.10	0.302	0.997
↔	cdss556chsp	DFD	1	0	56.5	201	0.10	0.362	-
↔	cdss341chsp	DFD	1	0	54.1	103	0.10	0.362	0.791
↔	cdss516chsp	DFD	1	0	55.7	52	1.00	0.364	0.662
↔	cdss614chsp	DFD	1	0	64.3	160	0.10	0.484	-
↔	cdss517chsp	DFD	1	0	56.5	51	1.00	0.553	0.932
↔	cdss518chsp	DFD	1	0	56.1	51	1.00	0.688	1.561
↔	cdss533chsp	DFD	1	0	57.0	40	0.10	0.689	1.938
↔	cdss536chsp	DFD	1	0	58.7	50	0.10	0.691	0.995
↔	cdss524chsp	DFD	1	0	57.2	49	1.00	0.827	1.080
↔	cdss519chsp	DFD	1	0	57.0	54	1.00	1.035	1.049
↔	cdss520chsp	DFD	1	0	57.4	49	0.10	1.241	1.226
↔	cdss514chsp	DFD	1	0	57.0	49	1.00	1.374	1.216
↔	cdss338chsp	DFD	1	0	62.9	98	0.10	1.390	1.380
↔	cdss558chsp	DFD	1	0	62.4	204	0.10	1.394	-
↔	cdss662chsp	DFD + TV	1	0	70.3	103	0.10	0.502	-
↔	cdss669chsp	DFD + TV	1	0	69.9	101	0.10	0.503	-
↔	cdss661chsp	DFD + TV	1	0	69.6	76	0.10	0.503	-
↔	cdss653chsp	DFD + TV	1	0	71.7	73	0.10	0.504	0.234
↔	cdss652chsp	DFD + TV	1	0	72.1	105	0.10	0.507	0.181
↔	cdss515chsp	DFD	1	0	73.8	197	1.00	1.420	1.114
↔	cdss128chsp	DFD	1	0	67.8	182	0.10	30.915	-

Note: DFD = dry funnel deposition; TV = table vibration; CS = cyclic shearing; OCR = overconsolidation ratio; S_r = saturation ratio; D_{Rc} = relative density after consolidation; σ'_{vc} = consolidation vertical stress; f = loading frequency; γ_{cs} = maximum single amplitude cyclic shear strain; and ε_{vr} = reconsolidation volumetric strain.

Table 3-15 (cont.) Summary of unidirectional and bidirectional cyclic constant volume I-mcDSS tests on Ottawa sand (OT-SP).

Test Path	Test ID	Sample Prep.	OCR	S_r	D_{Rc}	σ'_{vc}	f	γ_{cs}	ε_{vr}
					(%)	(kPa)	(Hz)	(%)	(%)
Unidirectional cyclic tests									
↔	cdss542chsp	DFD + CS	1	0	96.1	104	0.10	0.079	-
↔	cdss545chsp	DFD + CS	1	0	94.0	51	0.10	0.079	-
↔	cdss552chsp	DFD + CS	1	0	94.7	201	0.10	0.081	-
↔	cdss527chsp	DFD	1	0	57.0	50	0.10	0.094	0.335
↔	cdss491chsp	DFD + CS	1	0	93.6	51	0.10	0.273	0.195
↔	cdss564chsp	DFD + CS	1	0	93.3	102	0.10	0.389	-
↔	cdss570chsp	DFD + CS	1	0	91.0	51	0.10	0.390	-
↔	cdss553chsp	DFD + CS	1	0	94.1	207	0.10	0.437	-
↔	cdss561chsp	DFD + CS	1	0	93.5	209	0.10	1.474	-
↔	cdss538chsp	DFD + CS	1	0	92.8	106	0.10	1.474	0.468
↔	cdss565chsp	DFD + CS	1	0	93.7	109	0.10	1.478	-
↔	cdss578chsp	DFD + CS	1	0	87.3	55	0.10	1.567	-
Circular / Oval cyclic tests									
0	mcdss345chsp	DFD	1	0	52.4	104	0.10	0.090	0.181
0	mcdss342chsp	DFD	1	0	57.4	94	0.10	0.455	1.159
0	mcdss339chsp	DFD	1	0	71.2	98	0.10	1.768	1.368
Figure-8 cyclic tests									
8	mcdss346chsp	DFD	1	0	57.6	100	0.10	0.092	0.198
8	mcdss530chsp	DFD	1	0	56.8	49	0.10	0.452	1.037
8	mcdss557chsp	DFD	1	0	58.6	199	0.10	0.455	-
8	mcdss343chsp	DFD	1	0	64.5	100	0.10	0.459	1.170
8	mcdss340chsp	DFD	1	0	54.1	92	0.10	1.698	2.081
8	mcdss540chsp	DFD	1	0	63.0	43	0.10	1.726	-
8	mcdss550chsp	DFD	1	0	65.6	203	0.10	0.089	-
8	mcdss576chsp	DFD + CS	1	0	83.4	54	0.10	0.477	-
8	mcdss559chsp	DFD	1	0	66.6	190	0.10	1.741	-
8	mcdss548chsp	DFD + CS	1	0	94.1	203	0.10	0.098	-
8	mcdss563chsp	DFD + CS	1	0	91.7	50	0.10	0.098	-
8	mcdss547chsp	DFD + CS	1	0	92.6	101	0.10	0.099	-
8	mcdss546chsp	DFD + CS	1	0	94.2	50	0.10	0.100	-
8	mcdss577chsp	DFD + CS	1	0	87.8	58	0.10	0.480	-
8	mcdss574chsp	DFD + CS	1	0	86.6	45	0.10	0.482	-
8	mcdss571chsp	DFD + CS	1	0	92.5	99	0.10	0.483	-

Note: DFD = dry funnel deposition; TV = table vibration; CS = cyclic shearing; OCR = overconsolidation ratio; S_r = saturation ratio; D_{Rc} = relative density after consolidation; σ'_{vc} = consolidation vertical stress; f = loading frequency; γ_{cs} = maximum single amplitude cyclic shear strain; and ε_{vr} = reconsolidation volumetric strain.

Table 3-15 (cont.) Summary of unidirectional and bidirectional cyclic constant volume I-mcDSS tests on Ottawa sand (OT-SP).

Test Path	Test ID	Sample Prep.	OCR	S_r	D_{Rc}	σ'_{vc}	f	γ_{cs}	ε_{vr}
					(%)	(kPa)	(Hz)	(%)	(%)
Figure-8 cyclic tests									
8	mcdss554chsp	DFD + CS	1	0	94.3	207	0.10	0.484	-
8	mcdss480chsp	DFD + CS	1	0	90.1	192	0.10	1.816	0.689
8	mcdss572chsp	DFD + CS	1	0	92.5	98	0.10	1.828	-
8	mcdss490chsp	DFD + CS	1	0	93.0	48	0.10	1.833	0.398
8	mcdss566chsp	DFD + CS	1	0	97.7	408	0.10	1.850	-

Note: DFD = dry funnel deposition; TV = table vibration; CS = cyclic shearing; OCR = overconsolidation ratio; S_r = saturation ratio; D_{Rc} = relative density after consolidation; σ'_{vc} = consolidation vertical stress; f = loading frequency; γ_{cs} = maximum single amplitude cyclic shear strain; and ε_{vr} = reconsolidation volumetric strain.

Table 3-16 Summary of strain-controlled unidirectional and bidirectional constant volume I-mcDSS tests on Lab Mix sand (SW-SM).

Test Path	Test ID	Sample Prep.	OCR	S_r	D_{Rc}	σ'_{vc}	f	γ_{cs}	ε_{vr}
					(%)	(kPa)	(Hz)	(%)	(%)
Unidirectional cyclic tests									
↔	cdss315chsw	DFD	1	0	59.6	102	0.10	0.073	0.131
↔	cdss312chsw	DFD	1	0	65.3	101	0.10	0.368	0.647
↔	cdss309chsw	DFD	1	0	67.2	100	0.10	1.400	1.400
↔	cdss639chsw	DFD + TV	1	0	87.8	106	0.10	0.099	-
Circular / Oval cyclic tests									
0	mcdss316chsw	DFD	1	0	62.3	102	0.10	0.091	0.127
0	mcdss313chsw	DFD	1	0	63.1	101	0.10	0.459	1.289
0	mcdss310chsw	DFD	1	0	66.9	101	0.10	1.750	1.625
Figure-8 cyclic tests									
8	mcdss317chsw	DFD	1	0	60.3	100	0.10	0.092	0.266
8	mcdss314chsw	DFD	1	0	65.2	101	0.10	0.459	1.282
8	mcdss311chsw	DFD	1	0	65.3	98	0.10	1.731	1.731
8	mcdss640chsw	DFD + TV	1	0	90.1	101	0.10	0.105	-

Note: DFD = dry funnel deposition; TV = table vibration; CS = cyclic shearing; OCR = overconsolidation ratio; S_r = saturation ratio; D_{Rc} = relative density after consolidation; σ'_{vc} = consolidation vertical stress; f = loading frequency; γ_{cs} = maximum single amplitude cyclic shear strain; and ε_{vr} = reconsolidation volumetric strain.

Table 3-17 Summary of strain-controlled unidirectional and bidirectional constant volume l-mcDSS tests on Mississippi River sand (MR-SM).

Test Path	Test ID	Sample Prep.	OCR	S_r	RC	σ'_{vc}	f	γ_{cs}	ε_{vr}
					(%)	(kPa)	(Hz)	(%)	(%)
Unidirectional cyclic tests									
↔	cdss306chsm	DFD	1	0	86.4	100	0.10	0.076	0.127
↔	cdss582chsm	DFD	1	0	86.6	206	0.10	0.076	-
↔	cdss581chsm	DFD	1	0	87.7	50	0.10	0.078	-
↔	cdss303chsm	DFD	1	0	87.0	101	0.10	0.368	0.629
↔	cdss586chsm	DFD	1	0	85.5	52	0.10	0.368	-
↔	cdss300chsm	DFD	1	0	86.7	96	0.10	1.393	3.354
↔	cdss621chsm	DFD	1	0	85.7	51	0.10	2.011	-
↔	cdss622chsm	DFD	1	0	86.0	197	0.10	2.018	-
↔	cdss580chsm	DFD + TV	1	0	92.5	52	0.10	0.076	-
↔	cdss625chsm	DFD + TV	1	0	94.6	98	0.10	0.105	-
↔	cdss630chsm	DFD + TV	1	0	91.7	49	0.10	0.509	-
↔	cdss631chsm	DFD + TV	1	0	92.1	100	0.10	0.510	-
↔	cdss632chsm	DFD + TV	1	0	93.5	203	0.10	0.517	-
↔	cdss634chsm	DFD + TV	1	0	92.6	99	0.10	2.033	-
↔	cdss633chsm	DFD + TV	1	0	92.6	42	0.10	2.033	-
↔	cdss635chsm	DFD + TV	1	0	94.7	202	0.10	2.079	-
Circular / Oval cyclic tests									
0	mcdss307chsm	DFD	1	0	86.3	96	0.10	0.092	0.135
0	mcdss304chsm	DFD	1	0	86.7	97	0.10	0.461	1.304
0	mcdss301chsm	DFD	1	0	86.6	101	0.10	1.740	2.475
Figure-8 cyclic tests									
8	mcdss584chsm	DFD	1	0	85.7	51	0.10	0.091	-
8	mcdss583chsm	DFD	1	0	86.1	53	0.10	0.093	-
8	mcdss308chsm	DFD	1	0	86.6	98	0.10	0.094	0.211
8	mcdss585chsm	DFD	1	0	87.6	203	0.10	0.098	-
8	mcdss305chsm	DFD	1	0	87.0	102	0.10	0.459	1.308
8	mcdss616chsm	DFD	1	0	85.6	52	0.10	0.513	1.730
8	mcdss302chsm	DFD	1	0	87.0	101	0.10	1.735	2.367
8	mcdss624chsm	DFD	1	0	84.8	50	0.10	1.965	-
8	mcdss623chsm	DFD	1	0	86.8	202	0.10	2.010	-
8	mcdss628chsm	DFD + TV	1	0	91.9	100	0.10	0.103	-
8	mcdss629chsm	DFD + TV	1	0	93.9	196	0.10	0.104	-
8	mcdss620chsm	DFD + TV	1	0	92.2	200	0.10	0.512	-
8	mcdss618chsm	DFD + TV	1	0	92.0	51	0.10	0.514	-
8	mcdss619chsm	DFD + TV	1	0	92.3	102	0.10	0.516	-

Note: DFD = dry funnel deposition; TV = table vibration; CS = cyclic shearing; OCR = overconsolidation ratio; S_r = saturation ratio; RC = relative compaction after consolidation; σ'_{vc} = consolidation vertical stress; f = loading frequency; γ_{cs} = maximum single amplitude cyclic shear strain; and ε_{vr} = reconsolidation volumetric strain.

Table 3-17 (cont.) Summary of strain-controlled unidirectional and bidirectional constant volume l-mcDSS tests on Mississippi River sand (MR-SM).

Test Path	Test ID	Sample Prep.	OCR	S_r	RC	σ'_{vc}	f	γ_{cs}	ε_{vr}
					(%)	(kPa)	(Hz)	(%)	(%)
Figure-8 cyclic tests									
8	mcdss637chsm	DFD + TV	1	0	92.7	92	0.10	2.012	-
8	mcdss638chsm	DFD + TV	1	0	92.9	202	0.10	2.014	-
8	mcdss636chsm	DFD + TV	1	0	93.0	50	0.10	2.017	-

Table 3-18 Summary of strain-controlled unidirectional and bidirectional constant volume l-mcDSS tests on Mississippi River Gulf of Mexico sand (MRGM-SC).

Test Path	Test ID	Sample Prep.	OCR	S_r	RC	σ'_{vc}	f	γ_{cs}	ε_{vr}
					(%)	(kPa)	(Hz)	(%)	(%)
Unidirectional cyclic tests									
↔	cdss672chsc	DFD + TV	1	1	91.8	104	0.10	0.105	0.012
↔	cdss671chsc	DFD + TV	1	1	90.9	101	0.10	0.504	0.558
↔	cdss649chsc	DFD + TV	1	1	89.3	104	0.10	1.938	1.143
Figure-8 cyclic tests									
8	mcdss651chsc	DFD + TV	1	1	92.8	101	0.10	0.106	0.018
8	mcdss650chsc	DFD + TV	1	1	92.0	101	0.10	0.514	0.897
8	mcdss648chsc	DFD + TV	1	1	89.3	104	0.10	1.938	2.586

Note: DFD = dry funnel deposition; TV = table vibration; CS = cyclic shearing; OCR = overconsolidation ratio; S_r = saturation ratio; RC = relative compaction after consolidation; σ'_{vc} = consolidation vertical stress; f = loading frequency; γ_{cs} = maximum single amplitude cyclic shear strain; and ε_{vr} = reconsolidation volumetric strain.

3.7 Dynamic Centrifuge Testing

Since the 1970s, centrifuge testing has been used in geotechnical engineering to characterize 'large-scale' soil behavior. Due to its better repeatability and lower costs compared to full-scale field tests, centrifuge testing has been used worldwide to study static and dynamic geotechnical problems. To achieve the similitude with large-scale models, scaling relationships are used to convert model to prototype physical factors including (e.g., Schofield 1980, 1981): force, length, mass, acceleration, and stress and time relationships for both static and dynamic problems (e.g. Table 3-19). For dynamic centrifuge problems involving saturated media, it has been long recognized the conflict in time scaling for dynamic and diffusion phenomena (Schofield 1981, Kutter 1995). To resolve this scaling issue, different experimental methods have been proposed (e.g. Ko 1994, Stewart et al. 1994) which typically involves the use of alternate viscous fluid to delay the time of consolidation in centrifuge testing. Other factors that may affect centrifuge modeling such as particle size (e.g., Kutter 1994) and strain rates also have been also studied (e.g., Sathialingam and Kutter 1994), along with recommendations to reduce their effects. Despite the apparent difficulty in implementing centrifuge physical models, this technique has been applied successfully in

liquefaction studies involving level ground and soil-structure models (e.g., Dobry and Liu 1994; Popescu and Prevost 1995).

Given the ability of centrifuge testing to simulate complex field soil-structure interaction problems, this technique was used in this study to generate “field” case histories that could be utilized to validate existing or newly proposed numerical models for both shear and volumetric response, in addition to developing semi-empirical correlations based on recorded centrifuge data. Four dynamic centrifuge tests that included free-field and near-field conditions were performed to study the effect of multidirectional shaking on the volumetric strain response of dense sands. The models consisted of a saturated, dense Ottawa sand with prototype depths of 20.5 m and 10.25 m at centrifugal accelerations of 60g and 30g, respectively. The models were built by dry pluviation from a drop height of ~50 cm to reach the target initial relative density (D_{Ro}) of 95%.

3.7.1 RPI NEES centrifuge facility

The NEES Centrifuge Facility at Rensselaer Polytechnic Institute (RPI) is located in Troy, New York. The geotechnical centrifuge has a capacity of 150g for 1D cyclic tests, and 2D cyclic tests limits the maximum operational centrifugal acceleration to 100g.

3.7.1.1 Centrifuge

The RPI NEES centrifuge machine components (Figure 3-15) include a swinging platform, balancing counterweight, an automatic internal balancing system, a hydraulic rotary joint, and optical and electrical slip rings. The nominal arm radius (in flight) is 2.7 m at which load capacity and acceleration are defined. The centrifuge operates safely up to its force limit (e.g., 100g or 150g) using a given pair of payload mass and acceleration. The connection between the centrifuge machine and the control monitoring room uses fiber optics, wireless network technology for data transmission.Table 3-20 and Table 3-21 describe its performance and component specifications.

3.7.1.2 2D shaker

The 2D shaker was used in conjunction with the 2D laminar container to replicate both unidirectional and bidirectional motions at centrifugal accelerations of 60g and 30g. The 2D shaker (Table 3-22) uses a servo-hydraulic, multi-actuator system formed by two hydraulic actuators, one in both the X- and Y-directions, that when used with control system software allows the convergence of target input motions (e.g. periodic, aperiodic, random or scale earthquake signals) in the frequency and time domains. Table 3-22 and Table 3-23 describe its performance and component specifications.

Table 3-19 Scaling factors for centrifuge physical modeling (after Taylor, 1995).

Parameter	Centrifuge Model Units	Full scale Prototype Units
Length	1/N	1
Area	$1/N^2$	1
Moment of Inertia	$1/N^4$	1
Stress	1	1
Strain	1	1
Displacement	1/N	1
Area	$1/N^2$	1
Volume	$1/N^3$	1
Density	1	1
Mass	$1/N^3$	1
Force	$1/N^2$	1
Time (dynamic event)	1/N	1
Time (viscous flow problems)	1	1
Time (diffusion event)	$1/N^2$	1
Acceleration	N	1
Frequency	N	1
Energy	$1/N^3$	1
Velocity	N	1
Elastic Modulus, E	1	1
Flexural Rigidity, EI	$1/N^4$	1
Strain Rate (dynamic event)	N	1
Strain Rate (diffusion event)	N^2	1

N: Scale Factor

Table 3-20 Centrifuge general specifications (http://www.nees. rpi.edu /equipment/ centrifuge/).

Component	Specification
General	
Manufacturer	Acutronic, France
Model	665-1
Capacity	150 g-ton
G-Range	1 to 160 Gs
Electrical Sliprings	
Signal (1 amp)	50
Power (10 amp)	12
Video	2
Fluid Joints	
Hydraulic (200 bars)	2
Air or Water (20 bars)	4
In-Flight Automatic Balancing System	
Imbalance Load Range:	± 4500 N
Max. Balancing Time	60 sec.
Data Acquisition Channels	128

Table 3-21 Centrifuge platform specifications (after http://www.nees.rpi.edu/equipment/centrifuge/).

Component	Specification
Centrifuge Platform	
Length, direction bucket swings	1000 mm
Length, tangential direction	1000 mm
Typical radius to soil container base while spinning	3.0 m
Radiusfrom centrifuge center to pivot point	2000 mm
Load	
Nominal maximum platform payload mass: 1500 kg	1500 kg
Nominal maximum mass of soil in a model: 800 kg	800 kg
Speed	
Maximum speed for nominal maximum payload mass	265.0 rpm
Time required to slow from maximum to zero speed	10 min
Time required to increase from zero to maximum speed	10 min

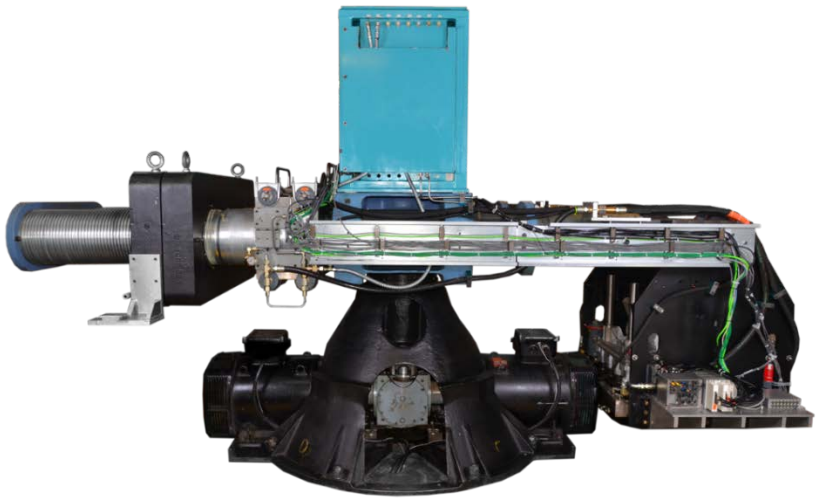

Figure 3-15 RPI NEES centrifuge including shaker basket (to the right), counterweight (to the left), motors (at the base) and control systems (at the top) (http://www.nees.rpi.edu/).

Table 3-22 2D shaker performance specifications (http://www.nees.rpi.edu/equipment/shakers/2d-shaker/).

Property	Specification
Method	Servo-hydraulic multi-actuator system
Shaking Type	Periodic or random, determined by input signal
Shaking Direction	Two prototype horizontal directions
Force	11,000 pounds (49kN) each axis
Max. shaking velocity	45 in/sec (1.1 m/s) each axis
Max. Table Displacement	0.50 in (12.2 mm) each axis
Max. Payload Dimensions	38 in × 26 in × 28 in
(L × W × H)	(965 mm × 660 mm × 711 mm)
Max. Payload Weight	550 pounds (250 kg)
Frequency	5–350 Hz
Max. Centrifugal Acceleration	100 g
Stroke	1.00″ peak to peak (25.4 mm)

Table 3-23 2D shaker component specifications (http://www.nees.rpi.edu/equipment/shakers/2d-shaker/).

Component	Specification
Table Size	
Length	965 mm
Width	900 mm
Overhead Clearance	10,000 mm
Payload Mass	
Maximum mass (reduced performance)	700 kg
Nominal max at maximum performance	300 kg
Shaker Characteristics	
Mounted on a centrifuge	Available
Maximum centrifugal acceleration	100 g
Peak-to-Peak Stroke	
X (horizontal axis)	25.4 mm
Y (2nd horizontal axis)	25.4 mm
Maximum Velocity of Table Surface Center	
X (horizontal axis)	1100 mm/s
Y (2nd horizontal axis)	1100 mm/s
Maximum Frequency of Table	
X (horizontal axis)	350 Hz
Y (2nd horizontal axis)	350 Hz
Maximum Actuator Capacity	
X (horizontal axis)	49,000 N
Y (2nd horizontal axis)	49,000 N

Figure 3-16 RPI NEES centrifuge 2D Shaker (http://www.nees.rpi.edu/).

3.7.1.3 2D laminar container

The 2D laminar container (Figure 3-17) [internal dimensions of 59.4 cm (D) × 40 cm (H)] can be mounted on the 2D shaker table. It consists of a stack of aluminum rings connected by 120 roller bearings that are designed to allow multi-directional motions while minimizing frictional boundary resistance. A vertically low friction adjustable restraint located at the top is used to keep the rings from rocking. The maximum allowable g-level when using the 2D laminar container is 100g. The design of this 2D laminar container was based on an existing 2D laminar container used by the centrifuge facility at the Hong Kong University of Science and Technology (HKUST), designed and manufactured by PVL Technologies. Table 3-24 and Table 3-25 describe its performance and component specifications.

Table 3-24 2D laminar container performance specifications (http://www.nees.rpi.edu/equipment/laminar-boxes/).

Property	Specification
Weight (empty)	129 lb (58 kg)
Weight (filled with saturated sand)	600 lb (212 kg)
Overall Height	21.5 inches (546 mm)
Overall Length	35 inches (890 mm)
Overall Width	27 inches (685 mm)
Min. Interior Diameter	23 inches (533 mm)
Max. Ineterior Diameter	23.8 inches (605 mm)
Mean Interior Diameter	23.4 inches (594 mm)
Max. Operating Centrifugal Acceleration	100 g

Table 3-25 2D laminar component specifications (http://www.nees.rpi.edu/equipment/laminar-boxes/).

Component	Specification
Container Type	Shear beam
Name	2D Laminar Box
Transparent walls?	Unavailable
Container mass	58.0 kg
Max. mass of soil that can be cotained	154.0 kg
Container spin on a centrifuge	Available
Max. g rating	100 g
Container space	Cylindrical
Interior Dimensions	
Diameter	594.0 mm
Height	546.0 mm
Top of thecontainer	Completely open

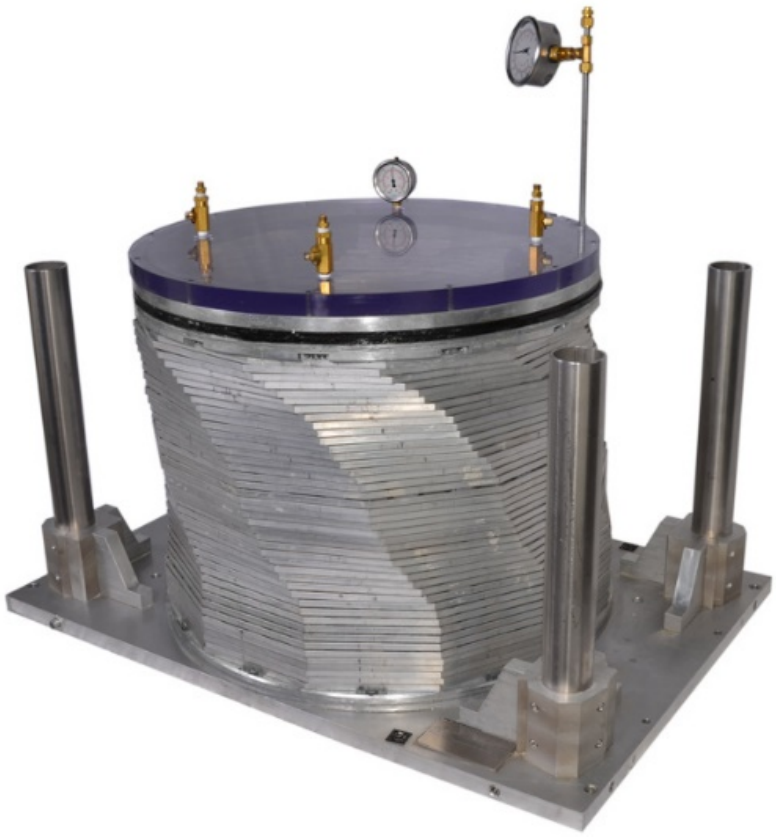

Figure 3-17 RPI NEES centrifuge 2D laminar container (http://www.nees.rpi.edu/).

3.7.1.4 Instrumentation

All centrifuge models were instrumented using accelerometers (ACC), porewater pressure transducers (PPT), and side and vertical linear voltage differential transformers (LVDT). Figure 3-18 presents a photograph of the instrumented soil model after construction. All the instruments were calibrated using RPI standards. Unique to these tests, vertical LVDT settlement plates were fabricated and placed within the model to measure vertical strain with depth (Figure 3-19). The settlements plates consist of a perforated aluminum disk to allow fluid flow without moving the plate. Vertical LVDT rods were covered with shrink tubing to reduce soil friction. The ACCs were PCB Piezotronics Model (Figure 3-20) 353B17. The PPTs were Model PDCR-81+ units manufactured by Druck, Inc (Figure 3-21). The LVDTs were MHR-500 (side LVDTs) and MHR-1000 (vertical LVDTs, Figure 3-22).

Pairs of bender elements were used to measure shear wave velocities at various test stages. Bender elements consist of piezoelectric transducers that use electrical excitation as a way to send shear and compression waves depending on the arranging of the bender pairs. All bender elements used in the experiments were fabricated at Illinois (Figure 3-23) following RPI standards, as described in Cerna-Diaz (2017). The bender elements data acquisition (BEDAQ) (Figure 3-24), developed by Tessari (2007), is used to control the properties of the signal in terms of type, frequency, and amplitude, as well used to determine arrival times during testing.

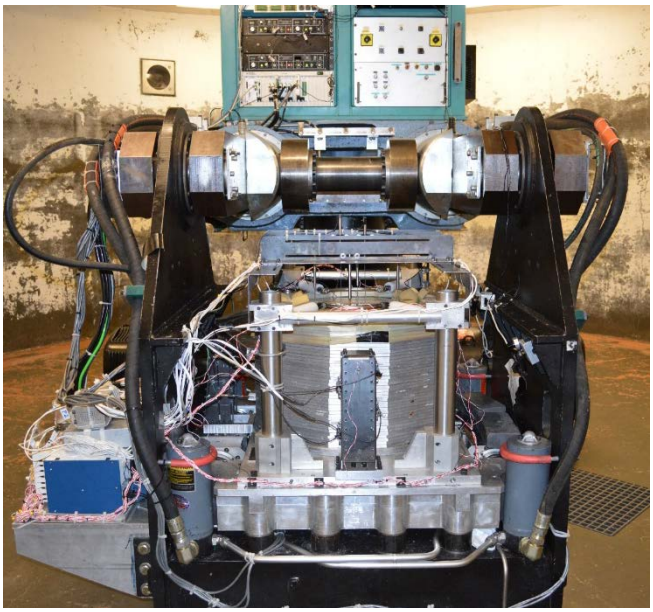

Figure 3-18 Instrumented soil model mounted on the 2D shaker unit on centrifuge arm.

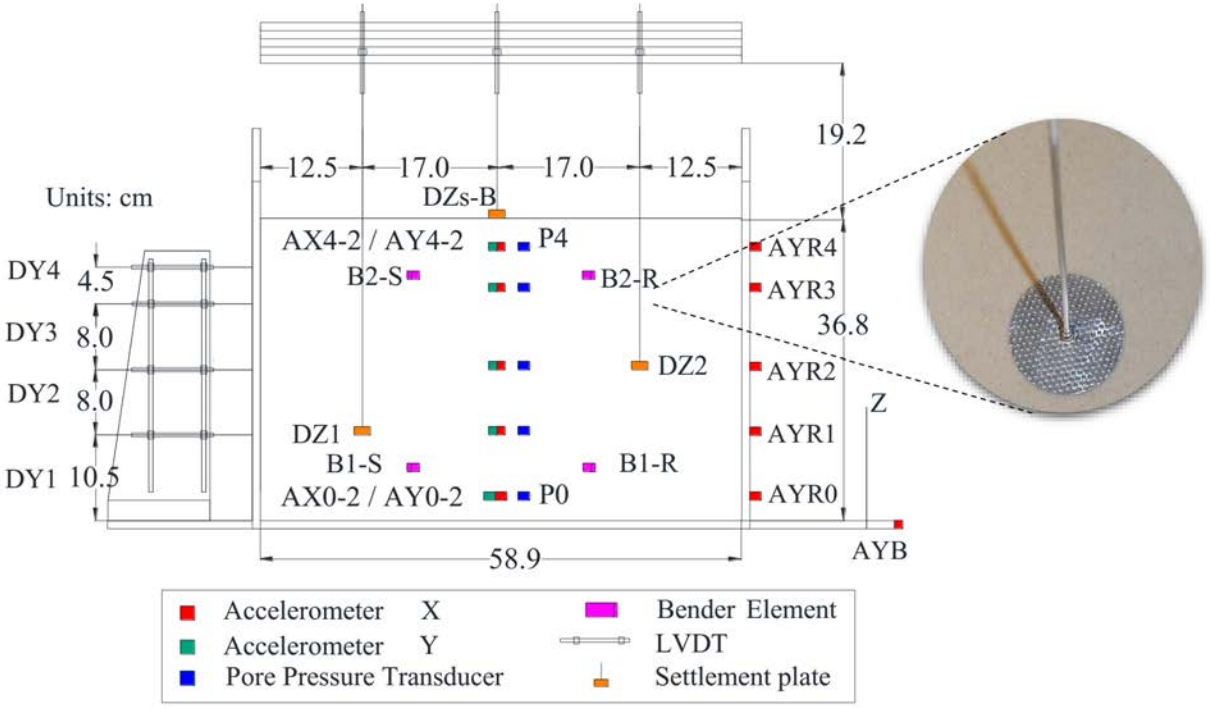

Figure 3-19 Instrumentation layout for test Dr95FF (Free Field D_{Ro}~95%) and settlement plate used to measure settlements along the models.

Figure 3-20 Accelerometers PCB Piezotronics Model 353B17 (http://www.nees.rpi.edu/).

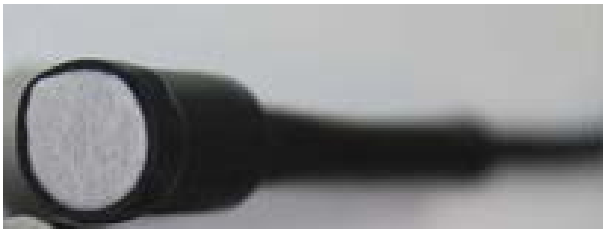

Figure 3-21 Pore water pressures transducers Model PDCR-81+ units manufactured by Druck, Inc (http://www.nees.rpi.edu/).

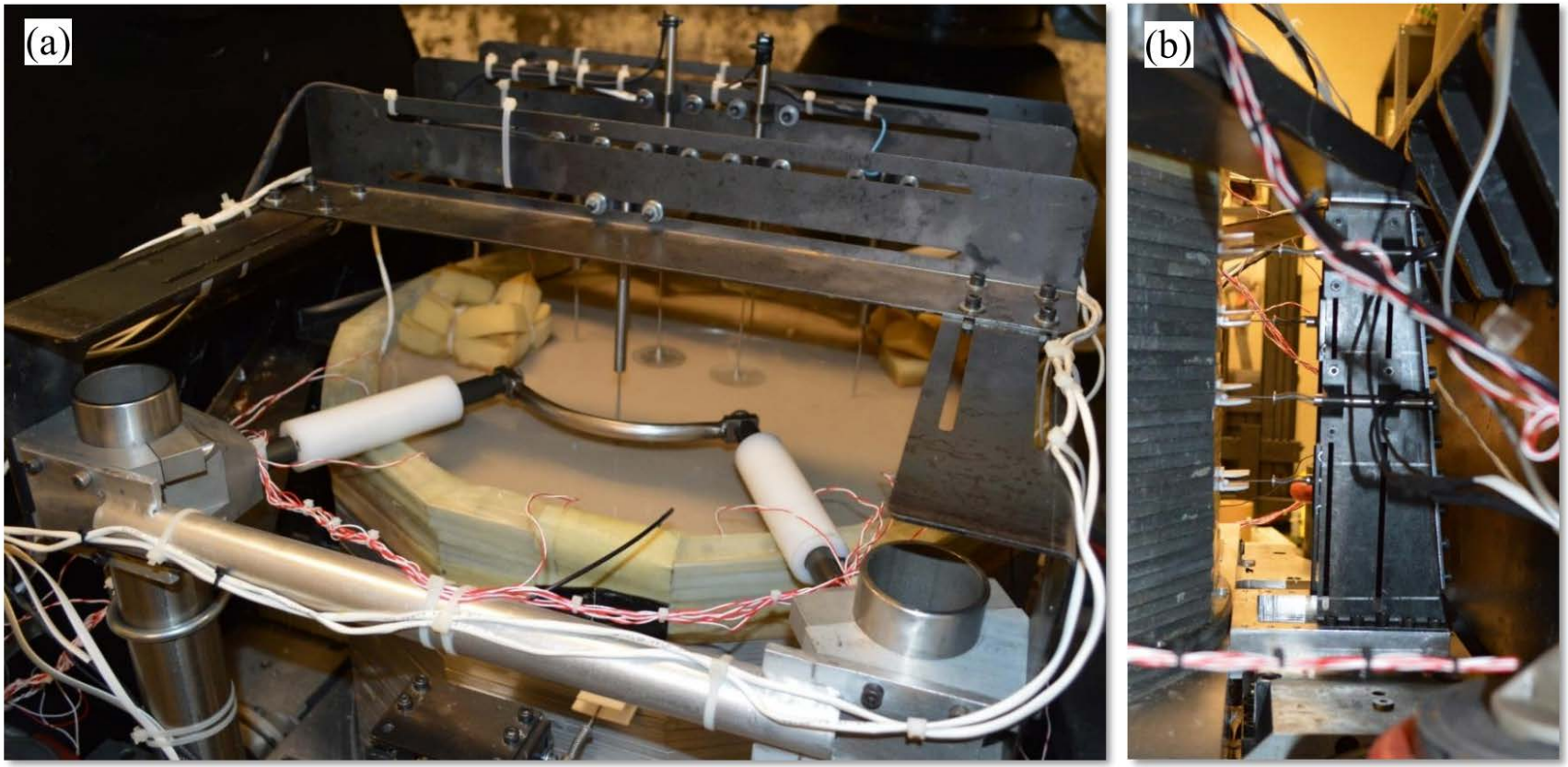

Figure 3-22 (a) Vertical LVDTs (MHR-1000 type); and (b) lateral LVDTs (MHR-500 type) used in centrifuge testing program.

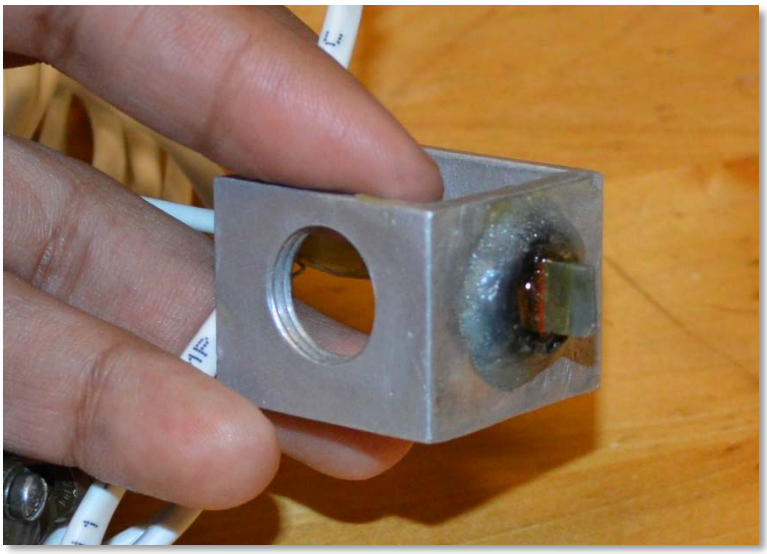

Figure 3-23 Bender element fabricated at Illinois.

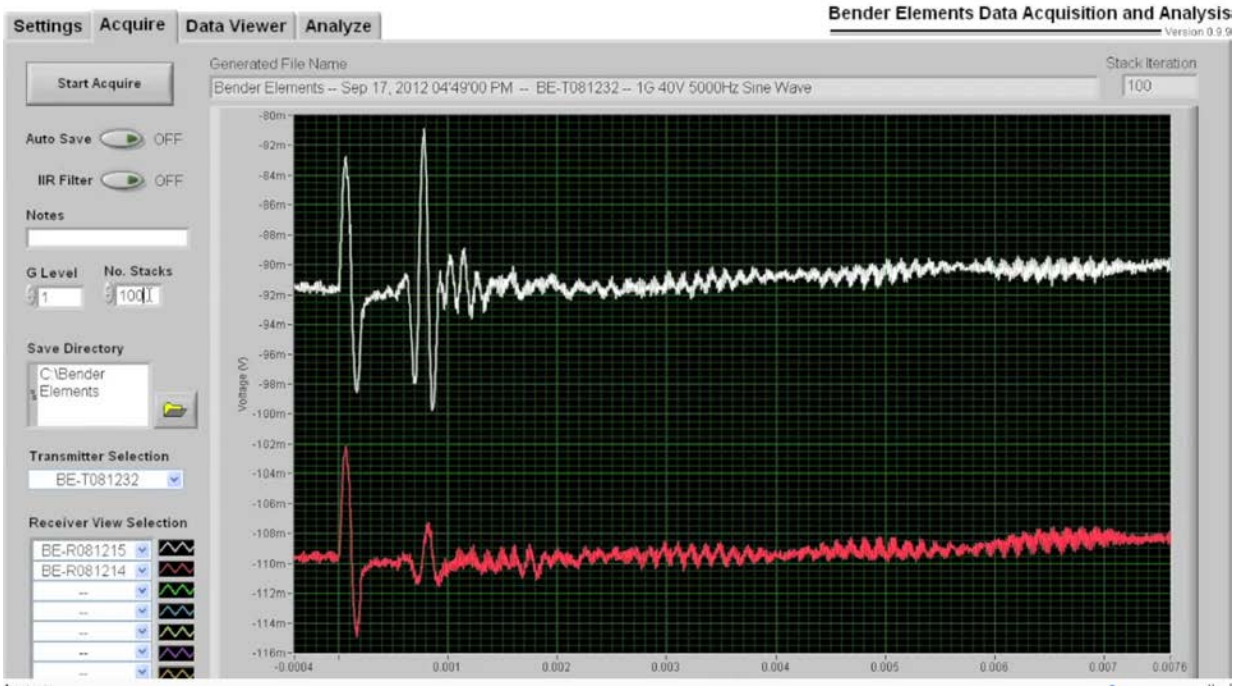

Figure 3-24 Bender element data acquisition and analysis (http://www.nees.rpi.edu/).

3.7.1.5 Centrifuge testing program

Four dynamic centrifuge tests (Table 3-26) that include free-field and near-field conditions (i.e., without and with a structure, respectively) were performed to study the effect of multidirectional shaking on the volumetric strain response of dense sands. The first two tests (CT1 and CT2) were used primarily to obtain broadband input motions imposed in subsequent production tests (PT1 or Dr95FF and PT2 or Dr95NF). All models consisted of a saturated, dense Ottawa sand with

prototype depths of 20.5 m and 10.25 m at centrifugal accelerations of 60g and 30g, respectively. The models were built by dry pluviation from a drop height of ~50 cm to reach the target initial relative density. All models' instrumentation layout are described in detail in Cerna-Diaz (2017).

Table 3-26 Summary of centrifuge tests performed for this research.

No.	Test type	Prototype Thickness (m)	Initial Relative Density D_{Ro} (%)	Centrifugal Acceleration (g)	Type of Loading	Purpose
1	Calibration Test 1 [CT1]	20.5, 10.25	95	60, 30	2D	Calibration of 6 motions with free-field mass
2	Calibration Test 2 [CT2]	20.5, 10.25	95	60, 30	1D, 2D	Calibration of 6 motions with structure mass
3	Production Test 95-FF-60g [PT1]	20.5, 10.25	95	60, 30	1D, 2D	30 motions free-field
4	Production Test 95-S-60g [PT2]	20.5, 10.25	95	60, 30	1D, 2D	30 motions with structure

3.7.2 Model preparation

The soil models for all four tests consisted of saturated dense Ottawa sand. For this purpose, model construction involved the use of a membrane to prevent leakage. The customized membranes were built during testing at RPI to be used with the 2D laminar container (Figure 3-25). Centrifuge models were built by placing dry soil by pluviation into the container. A customized pluviator built at Illinois (Figure 3-26) was used for the proposed models, and based on tests at Illinois, an initial relative density (D_{Ro}) of 95% by pluviation was achieved (at a drop height of 50 cm or higher). The placement of the sand was done by lifts (corresponding to instrumentation target levels for each specific test). During this process, instrumentation used at each level were sorted in different containers. The instruments were placed in vertical arrays within the model (specific locations and coordinates are given in Cerna-Diaz 2017).

The overall model construction process is summarized in Figure 3-27. At the top of each lift, accelerometers were placed first in (X, Y) pairs. A wax cover around the accelerometer was applied. This was done primarily for water protection. The X accelerometers were aligned (parallel) to the longer side of the table while the Y accelerometers were placed parallel to shorter side of the table. Each accelerometer cable was taped at the top and bottom of the remaining space of the laminar container to restrict movement of the instruments as others were being placed. The porewater pressure transducers then were placed at their specific locations without interfering with the rest of the instrumentation paths, followed by dry pluviation of the next lift of sand. Similarly, settlement plates and bender elements were placed at target elevations making sure that each instrument location (x, y, z) was recorded. During the building process, lifts were placed without any shaving or additional tamping to prevent non-homogenous soil densities from occurring. During construction, target relative density were verified at each horizontal lift.

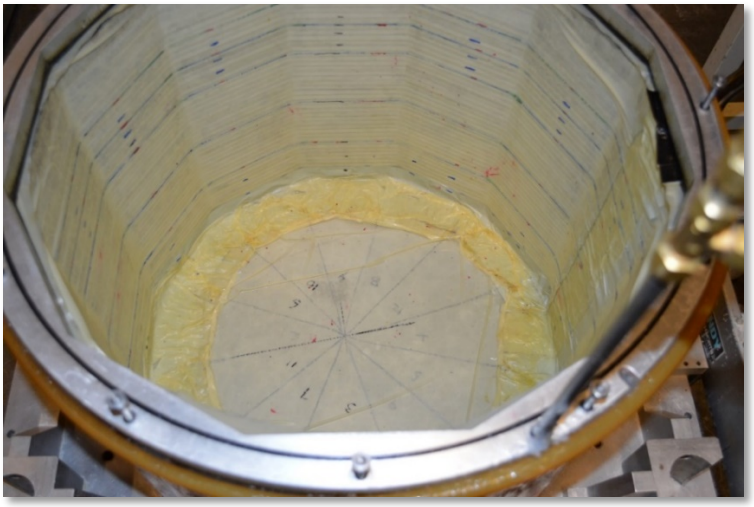

Figure 3-25 Latex membrane used in the 2D laminar container.

Figure 3-26 Pluviator fabricated at Illinois.

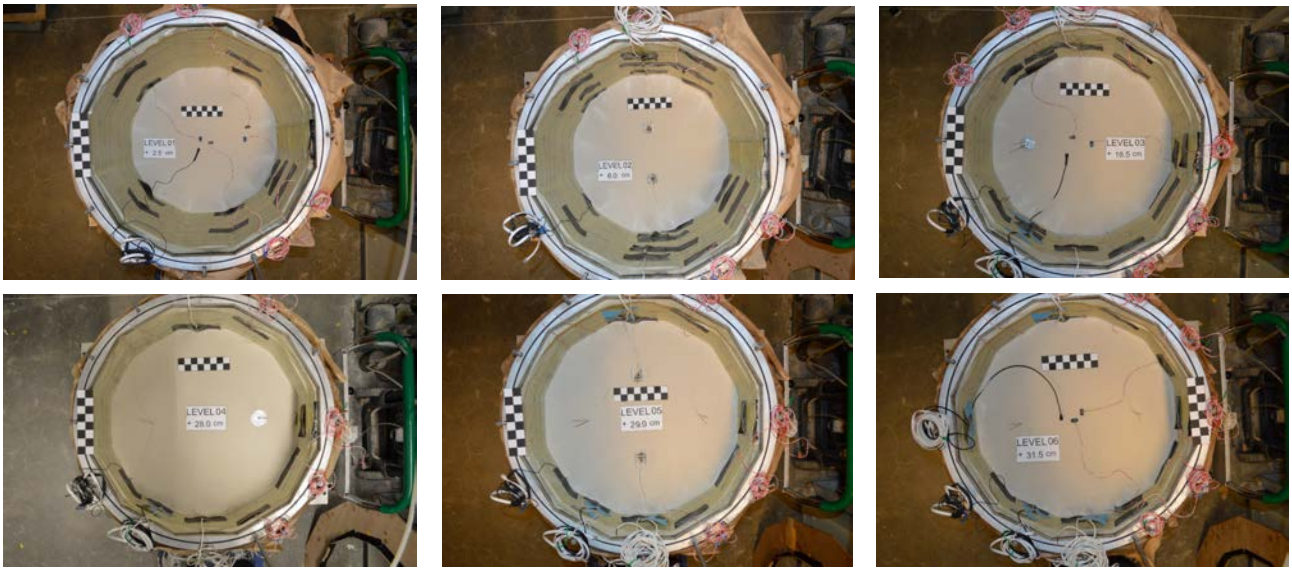

Figure 3-27 Overall building process of centrifuge free field models.

3.7.3 Model saturation

3.7.3.1 Viscous Fluid

All models were saturated using a viscous fluid prepared at RPI. The viscous fluid concentration was selected and tested according to the target centrifugal acceleration. For all tests, a ~2.0% hydroxypropyl methylcellulose (HPMC) solution was used to attain fluid viscosities of about 60 [60 cSt] times that of the pure water, in which the fluid concentration is expressed as the percent HPMC (by mass) of the entire solution. The exact percentage of HPMC was confirmed by trial and error during training at RPI, and agrees with that determined by Stewart et al. (1998) and that published on the RPI wiki (Figure 3-28). Furthermore, this concentration was verified every time the fluid was prepared at RPI.

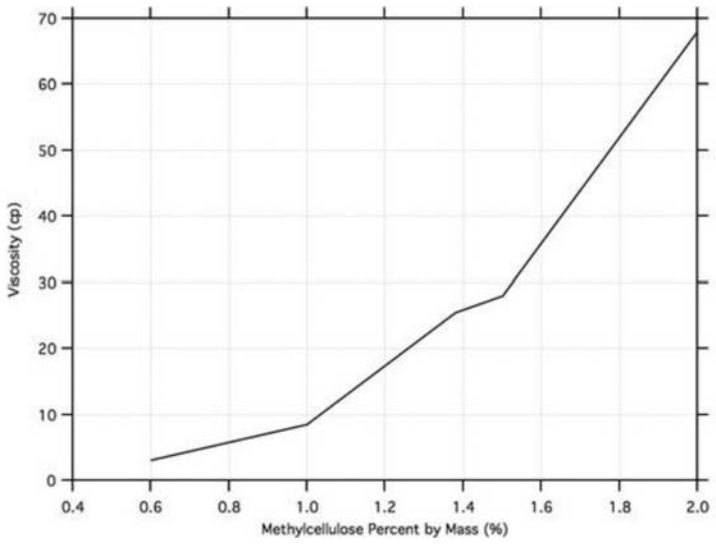

Figure 3-28 Methylcellulose percent by mass and fluid viscosity (in centiStokes, cSt, or centipoise, cp) relationship (http://www.nees.rpi.edu/).

3.7.3.2 Saturation procedure

In the centrifuge room, the model was saturated with CO_2 to expel trapped air from the model. The CO_2 was applied from two valves, both connected from the lid of the container to the CO_2 tank, as depicted in Figure 3-29. After observing that the outer membrane was engorged, the CO_2 tank was closed and the vacuum then was turned on again to release the remaining CO_2 and air. The target pressure on the container gages were kept under 25 kPa (indication of good vacuum). Then, the saturation process was started using the prepared viscous fluid at the target viscosity stored in two buckets connected via two tubes to the model. The pouring rate was controlled to about 1 to 2 drops per second to minimize erosion of the model. Furthermore, wet sponges were used to allow the falling fluid to spread smoothly to the rest of the model and avoid creating local erosion features (Figure 3-30).

Figure 3-29 Centrifuge model during saturation with CO_2 shown at right of photo.

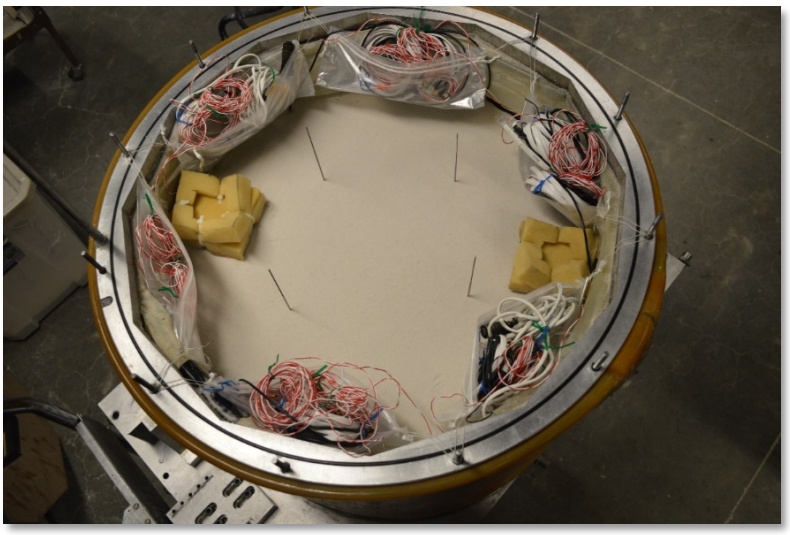

Figure 3-30 Sponges used for saturation of the model and storage of instrumentation to prevent model disturbance.

3.7.4 DAQ and centrifuge conditioning

After the model was saturated, LVDT top frames were secured and connected to the surface and buried settlements plates to measure vertical displacements. Similarly, external side LVDTs were placed directly onto the laminar container rings via a spring system so that lateral displacements were measured throughout the test. The centrifuge DAQ system was configured using a remotely connected laptop. In summary, the DAQ typically has four SCXI (modules numbered 1 to 4) available in which the accelerometers, PPTs, and LVDTs were connected through cards. Each card has 8 channels numbered from 0 to 7. The DAQ software was used to enter the name, calibration factor and serial number of all sensors. Then, each instrument calibration factor was assigned in the DAQ software. The filter value for accelerometers was set at 2.5 kHz, recommended for dynamic tests. Also, the name of each accelerometer was entered in the DAQ software and they were placed individually at the corresponding SCX. Likewise, the PPTs and LVDTs were mounted recording its serial number, calibration factor and name in the DAQ. Exterior vertical LVDTs were placed as vertical as possible. The LVDTs were attached to a steel connector aligned in the Y-direction of the model and connected to the main frame. Again, the sensors serial number, scaling factors and names were entered in the DAQ software.

After installing all the transducers, they were secured using cable ties. LVDTs were tested to assure that their full stroke was available. This was done first by controlling the LVDTs from the DAQ software and making sure that their reading was constant and close to a value of zero. If the reading values was nonzero, either positive or negative, it was changed by pushing or pulling the LVDT from the core, respectively. As a reference, the LVDTs have positive values when the core moves away from the LVDT and negative values when moving towards the LVDTs. After this, side LVDTs were tested by pushing/pulling (as required) so that their readings were ‘zero’. Due to the many LVDTs used in these experiments, it also was critical to assign different excitation frequencies to adjacent LVDTs to avoid crosstalk, yet ensure excitation frequencies were high enough to capture the range of frequencies expected during testing. Finally, five accelerometers were installed on the model table (X, Y and Z directions). These sensors, especially the ones for the X and Y direction were used to assess the input motions.

3.7.5 Input ground motions

Two dynamic centrifuge tests (CTDr95FF and CTDr95NF) were performed to calibrate the input motions that were used in the free-field production test (Dr95FF) and in a near-field production test (Dr95NF). The calibrated input motions consist of 30 1D and 2D recorded seismic events, including both crustal and subduction rupture mechanisms in which the two horizontal orthogonal components were available. Target motions were obtained from the PEER (Ancheta et al 2013) and Chilean (RENADIC; Boroschek et al 2010) strong motion databases, in which station Site Classes are B, C and D based on V_{s30} classifications (NEHRP 2009) (Table 3-27). The selected input motions exhibited a range of energy content (Arias intensity 0.1 to 11 m/s) to induce both nearly linear and nonlinear soil response. During test Dr95FF, each motion was filtered using a fourth-order Butterworth bandpass filter between frequencies of 0 to 350 Hz (model scale). The 30 broadband input motions are summarize in Table 3-28 and Table 3-29, and Figure 3-31 presents smoothed Fourier amplitude, response spectra, and input Arias and Housner intensities for the motions.

Table 3-27 NEHRP Site Classes

Site Class	Soil Profile Name	Average Properties in Top 30 meters (as per 2000 IBC section 1615.1.5) Soil Shear Wave Velocity, V_s	
		Feet/second	Meters/second
A	Hard Rock	$V_s > 5000$	$V_s > 1524$
B	Rock	$2500 < V_s \leq 5000$	$762 < V_s \leq 1524$
C	Very dense soil and soft rock	$1200 < V_s \leq 2500$	$366 < V_s \leq 762$
D	Stiff soil profile	$600 < V_s \leq 1200$	$183 < V_s \leq 366$
E	Soft soil profile	$V_s < 600$	$V_s < 183$

3.7.6 Conduct of centrifuge tests and post-test measurements

Once models were completed and safety inspections were performed, a first attempt to spin the model was executed. Before this safety spin, the DAQ system was initialized and all the instruments capabilities were tested prior to final spin up. The safety spin is performed to check the centrifuge balance and ensure secure instrument/cable connections. In some cases, it was necessary to spin down the model before or during the test to check issues related with the 2D shaker, securing instruments, and/or centrifuge balance. The final spin up to the target g levels then was carried out. For the experiments performed in this study, the target g levels were 60g and 30g, respectively.

During spin up to 60g, the DAQ recorded data at a sampling rate of 10 samples per second to observe general instrument trends. The rate of increase of g level was 2g/min. During spinning, shear wave velocities (Vs) were measured using bender elements every 10g up to the target 60g acceleration. Once the target g level stabilized, the sampling rate was set to a minimum of 5000 samples per second (depending on the number of instruments). Subsequently, Vs was measured before and after each input ground motion was imposed on the models. The time between each ground motion was estimated and selected during each test. Generally, this time included time to dissipate all the excess porewater pressures developed during shaking, time for checking key sensors, and time for bender elements measurements in between shaking events. After testing was completed, the model was spun down to 1g. During this process, shear wave velocity measurements were also carried out using bender elements.

After the experiments were completed, the model was disassembled by cutting the cable ties and disconnecting all instruments. Surface settlements then were measured manually at key locations. For near field tests, the final position and tilt of the structure also was measured. The model then was excavated using two small shovels. This process was carried out carefully to avoid damaging sensor cables. During this process, final coordinates (x, y, z) for all instruments were recorded (Figure 3-32). All of these measurements are documented in Cerna-Diaz (2017).

Table 3-28 60g (2D) ground motion recordings used for this study.

Sl. No.	Event	HypD (km)	V_{s30} (m/s)	Site Class*	Station	M_w	PGA (g)		Arias Intensity (m/s)			Average Significant Duration D_{savg} (s)
							x	y	I_x (m/s)	I_y (m/s)	I_{total} (m/s)	
M10	Kobe 1995/01/16	21.4	--	--	OSAJ	6.9	0.097	0.115	0.207	0.342	0.549	43.9
M11	Northridge1 994/01/17	64.4	322.0	D	0087	6.7	0.091	0.127	0.093	0.181	0.274	19.2
M1	Chi-Chi 1999/09/20	60.74	505.2	C	TCU-087	6.1	0.142	0.154	0.589	0.653	1.242	36.0
M12	Loma Prieta 1989/10/18	18.0	271	D	58393	6.9	0.109	0.201	0.216	0.435	0.651	16.02
M13	Lotung 1986/11/14	54.0	293.0	D	Smart1 006	7.3	0.238	0.328	0.663	1.558	2.221	15.5
M3	Landers 1992/06/28	15.36	379.3	C	Joshua Tree	7.3	0.234	0.259	1.532	1.812	3.344	27.9
M5	Chile 2010/02/27	100.0	500.7	C	Maipu	8.8	0.350	0.308	2.219	2.010	4.229	50.8

* NEHRP based on $V_{s,30}$

Table 3-29 30g (2D) ground motion recordings used for this study.

Sl. No.	Event	HypD (km)	V_{s30} (m/s)	Site Class*	Station	M_w	PGA (g)		Arias Intensity (m/s)			Average Significant Duration D_{savg} (s)
							x	**y**	**I_x (m/s)**	**I_y (m/s)**	**I_{total} (m/s)**	
M6	Loma Prieta 1989/10/18	32.25	370.8	C	Saratoga - Aloha Ave	6.9	0.440	0.535	0.984	1.388	2.372	6.08
M7	Kobe 1995/01/16	11.1	609	B	Nishi Akashi	6.9	0.437	0.455	2.235	2.318	2.276	11.4
M9	Landers 1992/06/28	15.36	379.3	C	Joshua Tree	7.3	0.407	0.437	5.090	6.170	11.26	28.3

* NEHRP based on $V_{s,30}$

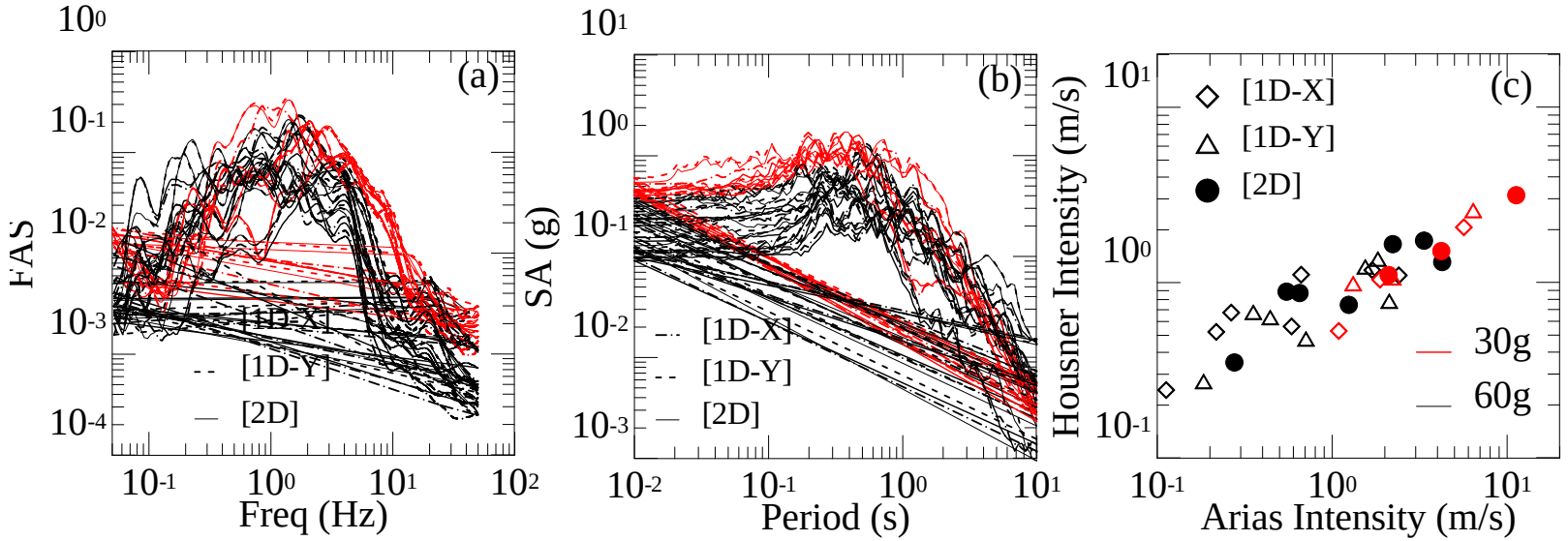

Figure 3-31 Input ground motions used in centrifuge tests (black lines and symbols are 60g motions, red lines and symbols are 30g motions). (a) Smoothed Fourier amplitude spectra (FAS); (b) response spectra; and (c) Arias and Housner intensities.

3.7.7 Instrument response

Acceleration time histories were obtained successfully for almost all accelerometers with few exceptions as noted in the Appendix C. These recordings were used to estimate seismic demand throughout the model. The seismic demand involved the computation of acceleration, velocity and displacement time histories as well as response spectra, Arias and Housner intensities. For near field experiments, acceleration time histories on the structure were used to compute relative acceleration with respect to the foundation soil. For both free field and near field experiments, displacements based on acceleration time histories were also used to compare with lateral LVDT displacement data. This was especially valuable for the LVDTs located in the X direction where mechanical vibration noise was induced by the LVDT frame. This was noted when comparing LVDTs and displacements based on acceleration time histories (Figure 3-33). This served as a basis to utilize a special filter to eliminate the noise in the lateral LVDT readings in the X direction.

Porewater pressure time histories were obtained successfully for almost all PPTs with few exceptions, noted in the Appendix C. These recordings were used to compute porewater pressure ratios ($r_u = \Delta u/\sigma'_{vo}$). During the free-field experiments, all recorded r_u values were less than 0.6. The maximum r_u of 0.6 corresponding to first motion at shallow depth. For the near-field tests, excess pore water pressures were computed throughout the model. Furthermore, for both free-field and near-field experiments dynamic porewater pressures were used to calculate head loss and hydraulic gradient time histories.

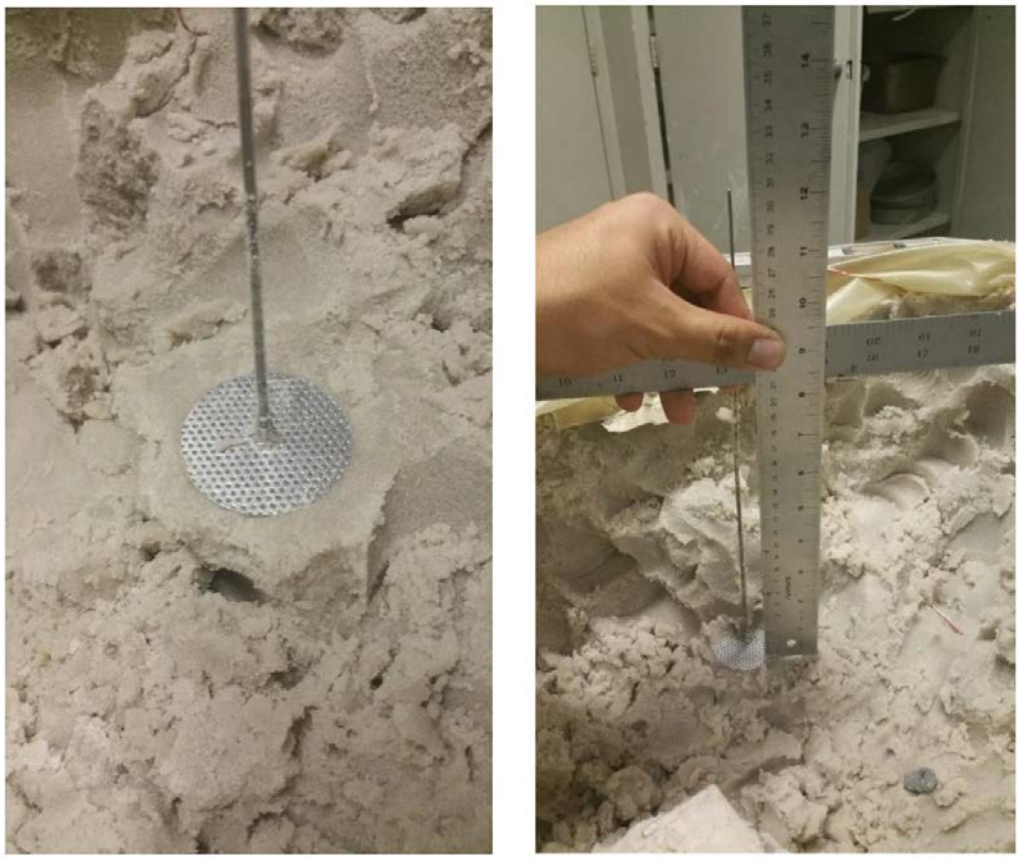

Figure 3-32 Excavation process and post-experiment measurements.

Displacements in the lateral and vertical directions were recorded successfully for all centrifuge tests with some exceptions, noted in the Appendix C. The vertical displacements along the model were used to track change in relative density for tributary sublayers and vertical strain induced by shaking. Lateral displacements were used to assess the shear response of the models.

Shear wave velocity also was recorded at specific test stages to capture shear stiffness (see Appendix C). This parameter was obtained by computing the arrival time (e.g., first arrival method) of the shear wave for a given distance between BEs. The Vs was important as it reflects both mean effective stress and relative density. Measurements of Vs were done for both horizontally propagated-vertically polarized (HV) and horizontally propagated-horizontally polarized (HH) waves. Measured values compared favorably to well-established correlations for Vs.

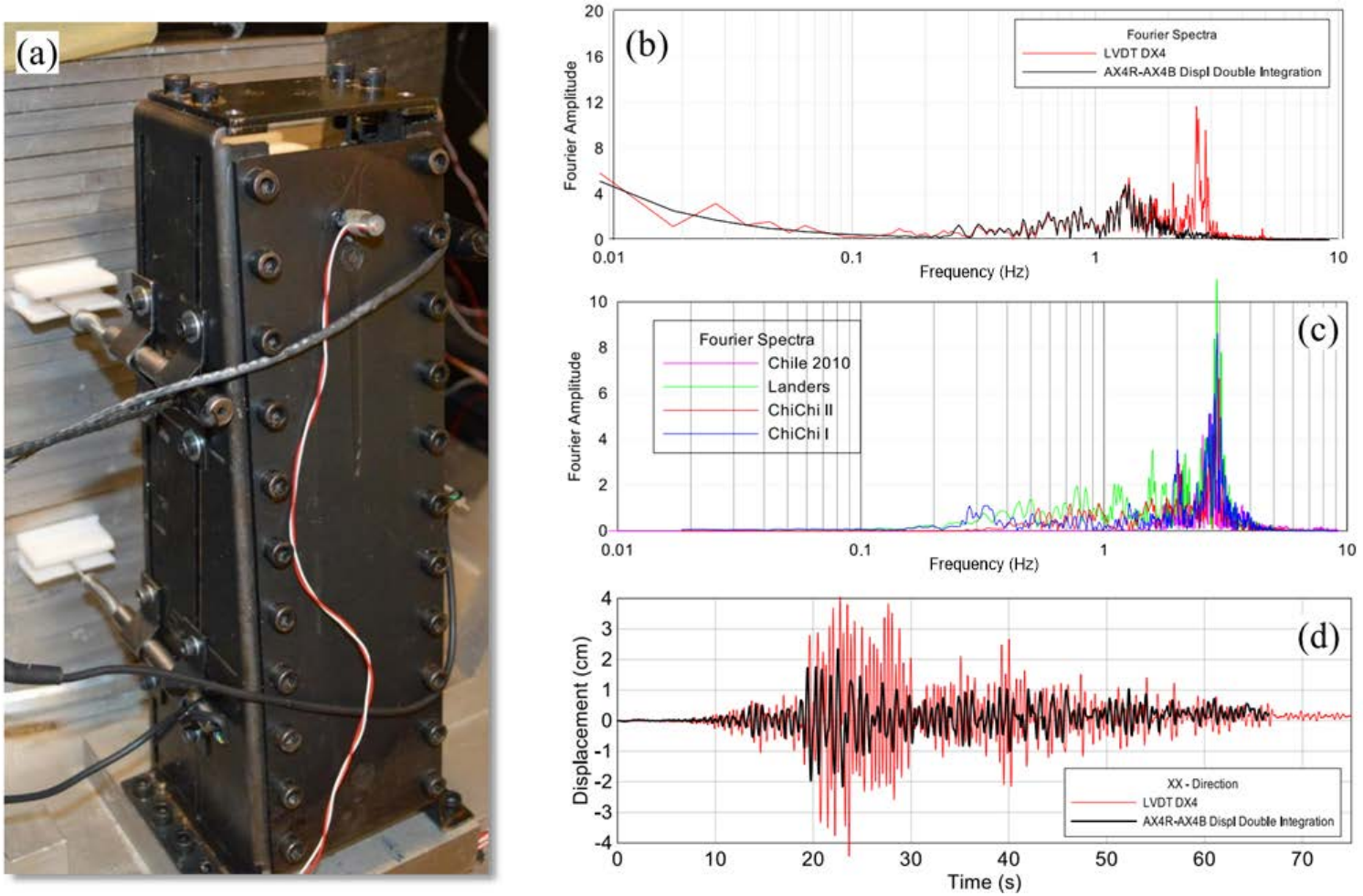

Figure 3-33 (a) Lateral LVDT frame system along with accelerometer for vibration identification; (b) Fourier amplitude spectrum of displacements from LVDTs and estimated using accelerometers in the X direction (observe difference for frequencies > 2 Hz); (c) Fourier amplitude spectrum of displacements from accelerometers located in the LVDT frame in the X direction (observe vibration with frequencies > 2 Hz) (d) Time histories of displacements from both LVDTs and estimated using accelerometers in the X direction.

4 RESPONSE OF DENSE SANDS TO UNIDIRECTIONAL AND BIDIRECTIONAL SHAKING

4.1 Introduction

This chapter describes results from the element and the centrifuge testing programs. The laboratory testing results are presented first, including drained and constant volume tests for investigating drained and reconsolidation volumetric strains, respectively. Following this, the results of the unidirectional and bidirectional centrifuge tests are discussed in terms of deviatoric response, site amplifications, settlements and porewater pressure generation. Finally, recommendations are made for multidirectionality factors for drained and reconsolidation volumetric strain and porewater pressure generation.

4.2 Volumetric strain from unidirectional and bidirectional element tests

Unidirectional strain-controlled tests were conducted for comparison of the response to multidirectional loading. In the unidirectional tests, sinusoidal cyclic shear strain γ_c was applied in one direction [$\gamma_{cx} = \gamma_c \sin(\omega t)$, $\gamma_{cy} = 0$]. Here, γ_{cx} and γ_{cy} are the cyclic shear strains in the x and y direction, respectively, and γ_c is the cyclic shear strain amplitude. The cyclic shear strain amplitude γ_c in each direction is defined as the ratio of the maximum horizontal displacement in that direction divided by the height of the specimen at the end of consolidation. Bidirectional strain controlled tests were conducted using oval, circular, and figure-8 strain paths to represent idealized seismic loading. For the bidirectional circular tests, equal shear strain amplitude γ_c was applied in the x and y direction. To obtain a circular path, a 90° phase difference (θ) was maintained between the x and y signals [$\gamma_{cx} = \gamma_c \sin(\omega t)$, $\gamma_{cy} = \gamma_c \sin(\omega t + \pi/2)$]. For a figure-8 path, the loading frequency in the y direction was kept half of that in the x direction [e.g. $\gamma_{cx} = \gamma_c \sin(\omega t)$, $\gamma_{cy} = \gamma_c \sin(0.5\omega t)$]. For most bidirectional tests, γ_c in the x and y direction are unequal to obtain an oval strain path or figure-8 of different widths in each horizontal direction. A historical earthquake displacement path and schematics of the shear strain time histories for unidirectional cyclic, circular, and figure-8 tests are shown in Figure 4-1. A limited number of tests were conducted using a historical broadband motion like the one illustrated in Figure 4-1(a).

In this study, γ_c ranges from 0.10 to 7 %. All specimens were K_0 consolidated to effective vertical stresses of 50, 100, 200 and 400 kPa. Tests on OT-SP and SW-SM were conducted with consolidated relative densities ranging from 55 to 95 %; tests on MR-SM and MRGM-SC were conducted with consolidated relative compaction ranging from 85 to 99 %. All tests reported here are on normally consolidated specimens unless otherwise indicated. All tests on the OT-SP, SW-SM, and MR-SM were conducted on dry specimens, and tests on MRGM-SC were conducted on fully saturated specimens. All tests represent level-ground free-field conditions, i.e., there is no initial static shear stress on the horizontal plane.

For γ_c of 0.10 to 7 %, 150 loading cycles are adequate to represent any realistic seismic loading (Seed et al. 1975, Liu et al. 2001, Green and Terri 2005, Lee 2009, Lasley 2015). Moreover, the rate of change of volumetric strain in medium to very dense sands, tested in this study, becomes negligible after 150 loading cycles, as illustrated later. Thus 150 to 300 uniform strain cycles were applied in the present testing series for the drained loading cases. For constant volume loading, a maximum of 30 uniform loading cycles are used. The shear stress – shear strain – volumetric strain response of dry clean sands was observed to be frequency independent for frequencies ranging from 0.1 – 10.0 Hz, based on Youd (1972a) and Duku et al. (2008). This is verified for all the sands and for bidirectional loading, as described later. Thus, most tests in this study were conducted at a

frequency of 0.1 Hz. This frequency also allowed better control of the I-mcDSS device, especially for bidirectional loading cases. A total of about 600 tests were performed. The volumetric strain values reported are the mean values measured in each cycle. 'Equivalent' tests indicate tests on sand specimens with similar relative densities, sample preparation method, consolidation stress, and cyclic shear strain amplitude. Unidirectional and bidirectional tests that are equivalent are compared in the subsequent sections to investigate the effect of bidirectional loading on volumetric strain. Results from drained tests are presented first, followed by constant volume tests.

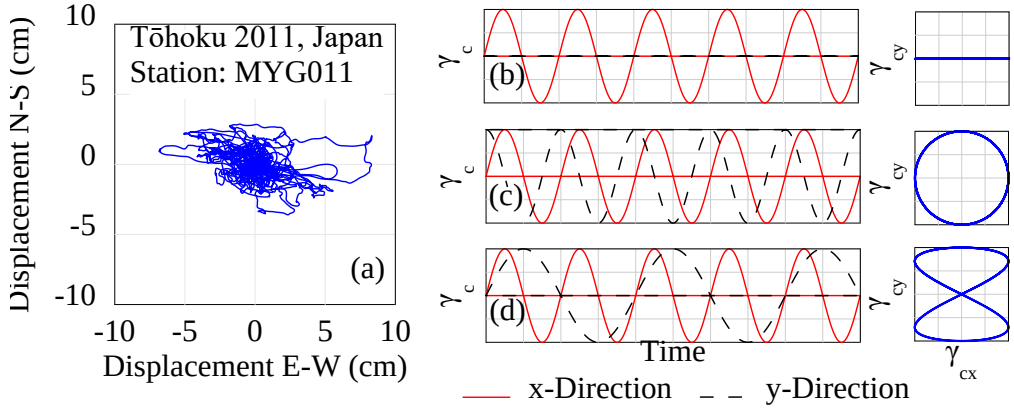

Figure 4-1 Illustration of an earthquake displacement as opposed to the idealized strain history applied in the laboratory: (a) Horizontal displacements during the Tōhoku 2011 earthquake in Japan recorded at station MYG011; Idealized horizontal strain paths applied in the testing program presented in this paper: (b) unidirectional, (c) bidirectional circular and (d) bidirectional figure-8.

4.3 Drained I-mcDSS Tests

Representative results from drained unidirectional and bidirectional cyclic direct simple shear tests on Ottawa sand are shown in Figure 4-2 and Figure 4-3, respectively. The application of cyclic strain controlled loading under drained conditions leads to an accumulation of volumetric strain, as evident from Figure 4-2(c, f) and Figure 4-3(e). This volumetric strain leads to gradual stiffening of the soil, and an increase in the shearing resistance (Figure 4-2b, e; Figure 4-3b, d, g). Figure 4-2(d) shows that in unidirectional shear, there is strain reversal along one direction, while in Figure 4-3(f), for a bidirectional test the shear strain direction gradually rotates. To quantify drained volumetric strain under multidirectional seismic loading, the effect of different loading, initial state and soil related parameters are interpreted separately. Except of the section that discusses the effect of different soil types on volumetric strain, relative density D_R represents density of the OT-SP and SW-SM; and relative compaction RC represents the density of the MR-SM and MRGM-SC. Further discussion of suitable parameters that may be used to quantify density across soils of different levels of fines content is presented later.

4.3.1 Loading frequency

To investigate the effect of loading frequency, tests were conducted on specimens of OT-SP and SW-SM sand prepared to a relative density of 60 %, and MR-SM sand at a relative compaction of 88%. All sands were consolidated to an effective vertical stress of 95kPa. Two frequencies were considered, 0.1 and 1 Hz. First, tests on the Ottawa sand were conducted at comparable relative density, frequency, overburden, and input shear strain to estimate the variability in the soil behavior. This was done to attribute the difference in soil response (e.g., volumetric strain) to a loading, soil,

or initial state related factor, and not to the inherent variability in the experimental data. Possible sources of experimental scatter can be equipment-related, procedure-related, or random (Duncan 2000; Phoon and Kulhawy 1999). For example: (1) difference in D_R after consolidation despite using the same method for specimen preparation, handling, and consolidation; (2) device control, e.g., applying a strain amplitude of 0.98 or 1.02 % instead of the specified 1 %; and (3) minor variations in sand specimens, e.g., gradation, especially for well graded soils.

In Figure 4-4(a), the unidirectional tests cdss43sp, cdss36sp, cdss32sp and cdss41sp are all conducted on D_R ~ 60 % specimens with σ'_{vc} of 95kPa, γ_c ~ 3.49 % and frequency 1.0 Hz. For the tests mentioned, maximum standard deviation (SD) of the volumetric strain is 0.81, and coefficient of variation (COV) is 0.23. The definitions for SD and COV follow Duncan (2000). The mean and variance of volumetric strain are calculated at each loading cycle, and the maximum values of SD and COV from the entire loading time history is reported here. Figure 4-4 shows the volumetric strain response with the number of cycles for both unidirectional and bidirectional oval loading. The volumetric strains at loading frequencies of 0.1 and 1.0 Hz for the unidirectional tests for any loading cycle are comparable. This is true for all the sands OT-SP (Figure 4-4a, b), SW-SM (Figure 4-4c), and MR-SM (Figure 4-4d). Volumetric strain at the end of 15 loading cycles summarized in Figure 4-5, clearly illustrates the frequency independency for the clean OT-SP sand for unidirectional and bidirectional loads. Published data from previous unidirectional experimental studies support this observation (Youd 1972a; Duku et al. 2008), and is also depicted in Figure 4-5(a).

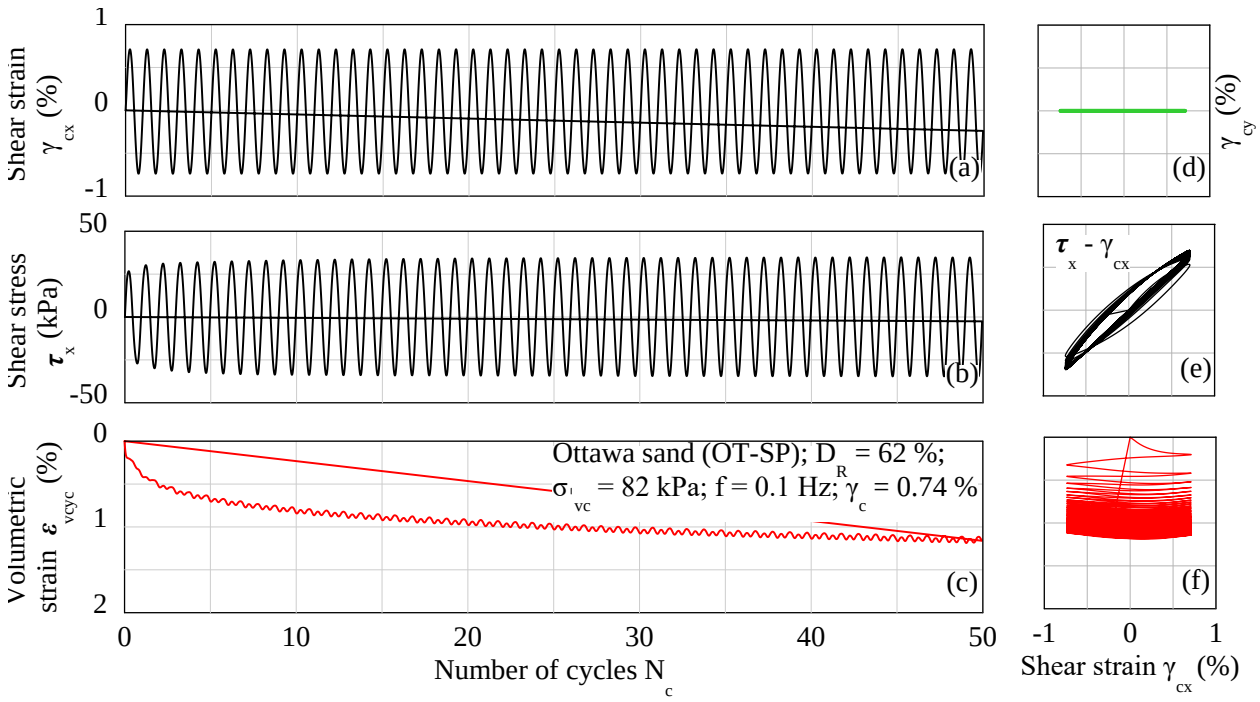

Figure 4-2 Cyclic strain-controlled response of dry medium dense Ottawa sand in drained unidirectional simple shear: (a), (b) and (c) shear strain, shear stress and volumetric strain respectively with number of cycles, (d) strain path, (e) and (f) shear stress and volumetric strain respectively with shear strain.

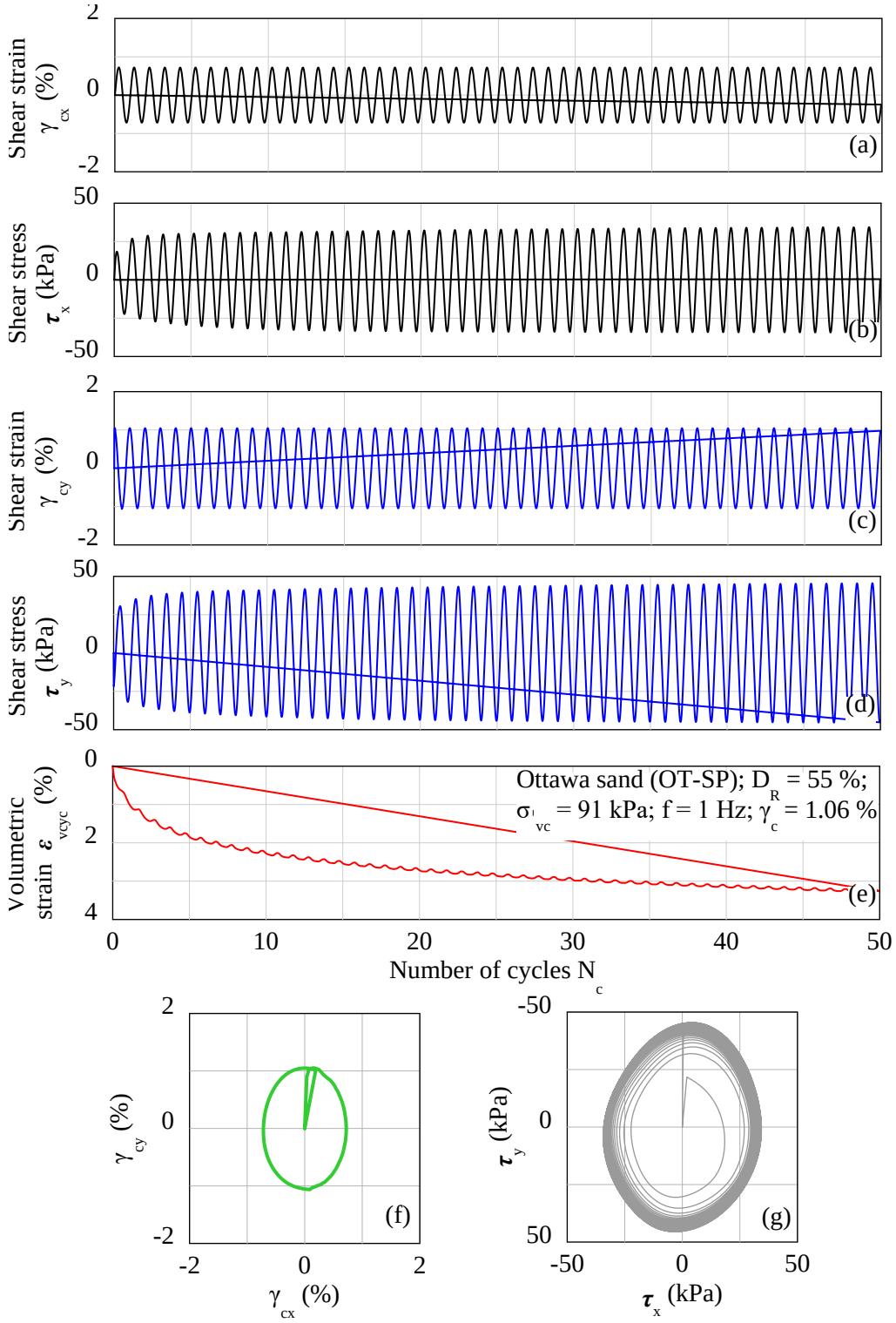

Figure 4-3 Cyclic strain-controlled response of dry medium dense Ottawa sand in drained bidirectional circular simple shear: (a), (b) shear strain, shear stress respectively in x direction, (c), (d) shear strain, shear stress respectively in y direction, and (e) volumetric strain with number of cycles, (f), (g) plan view of shear stress and shear strain respectively.

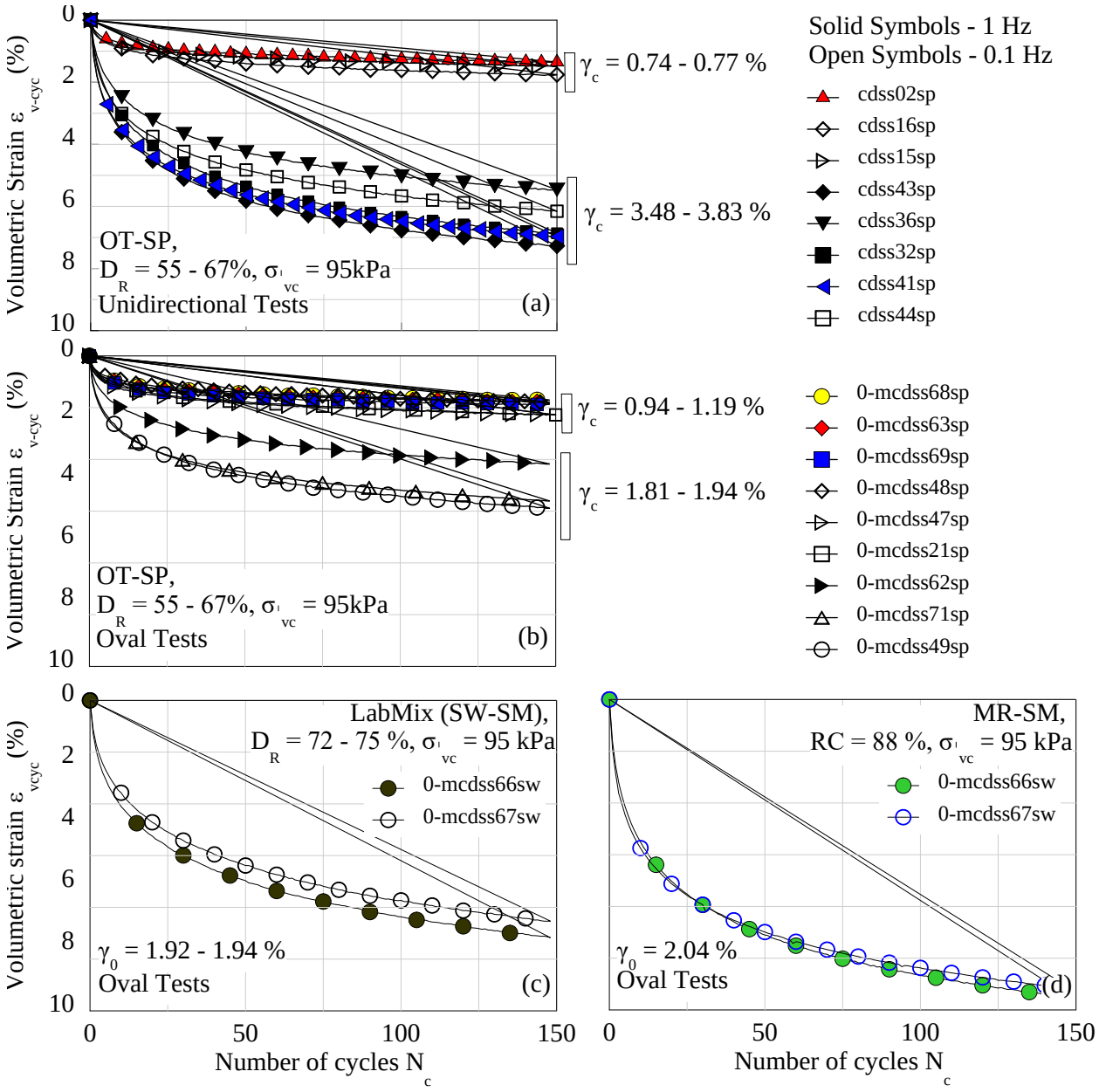

Figure 4-4 Volumetric strain from: (a) Unidirectional and (b) Bidirectional oval tests on Ottawa sand; Bidirectional oval tests on (c) SW-SM sand, and (d) MR-SM sand showing negligible effect of loading frequency on volumetric strain for frequencies 0.1 and 1.0 Hz.

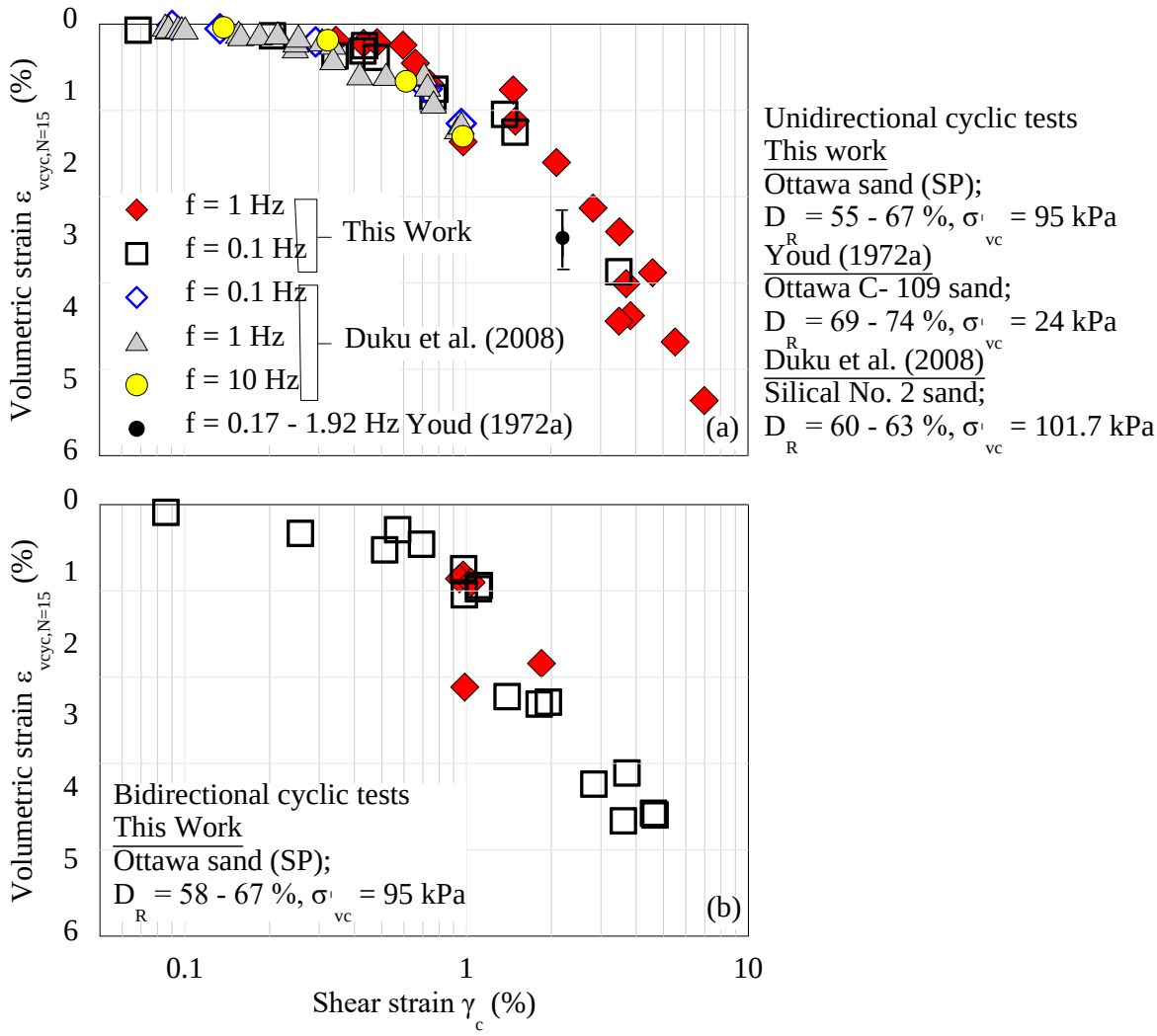

Figure 4-5 Negligible effect of loading frequency (0.1 – 10 Hz) on drained volumetric strain from strain-controlled cyclic simple shear tests: (a) Unidirectional tests on medium dense Ottawa sand from this work, also with data from Youd (1972a) and Duku et al. (2008); (b) Bidirectional tests on medium dense Ottawa sand.

4.3.2 Number of loading cycles

The majority (85 – 90 %) of soil stiffening, in terms of the shear modulus (G) of the soil, occurs in the first 10 to 15 cycles of drained loading, after which the rate of soil stiffening and accumulation of volumetric strain decreases. Shear modulus increases as the soil becomes stiffer, illustrated by the upward shift of the shear stress - shear strain plots Figure 4-2(e), and the outward shift of the shear stresses in the x and y-directions in Figure 4-3(g). Here, G rapidly increases for the first 15 cycles, after which its rate of increase decreases and levels off at about 100 cycles. Thus, it naturally follows that the volumetric strain increment per cycle of shear strain ($\Delta\varepsilon_{vcyc}$) in the soil is maximum within the first 10 to 15 loading cycles as illustrated in Figure 4-6 for unidirectional and bidirectional tests on OT-SP. This is consistent with the observation of previous unidirectional strain controlled simple shear research (Whang et al. 2004; Duku et al. 2008).

For estimation of drained seismic compression, traditionally, volumetric strain at 15 uniform loading cycles is reported along with a normalized volumetric shear strain as a function of the number of strain cycles, N_c (Tokimatsu and Seed 1987, Pradel 1998, Duku et al. 2008, Yee et al. 2013). We adopted this approach to illustrate the effect of the number of loading cycles on volumetric strain. Figure 4-7 shows $\varepsilon_{vcyc}/\varepsilon_{vcyc,N=15}$ versus the number of cycles for unidirectional and bidirectional loading. The average ratio $\varepsilon_{vcyc}/\varepsilon_{vcyc,N=15}$ has the same relation with the number of cycles for both unidirectional and bidirectional tests. The results are similar to those obtained by (Duku et al. 2008) in unidirectional simple shear tests on 16 sands. However, the Tokimatsu and Seed (1987) curve (Figure 4-7) for the effect of number of cycles on volumetric strain overestimates $\varepsilon_{vcyc}/\varepsilon_{vcyc,N=15}$ at cycles above 25.

The Tokimatsu and Seed (1987) method for determining the effect of the number of loading cycles on drained volumetric strain is calibrated based on simple shear tests with 30 loading cycles obtained from Silver and Seed (1971). The rate of increase of volumetric strain in the first 30 cycles is higher than the next 120 cycles (Figure 4-6). Thus, if a semi-empirical correlation, relating volumetric strain to number of cycles, is calibrated for the first 30 cycles, it will overestimate the volumetric strains for cycles above 30, which is why the Tokimatsu and Seed (1987) solution overestimates volumetric strain for loading cycles above 30. For seismic applications, this would be a concern for earthquakes of magnitude 8.5 or higher. However, for other dynamic loads with cycles much greater than 30, e.g. traffic or waves, the Tokimatsu and Seed (1987) method would overestimate the volumetric strain.

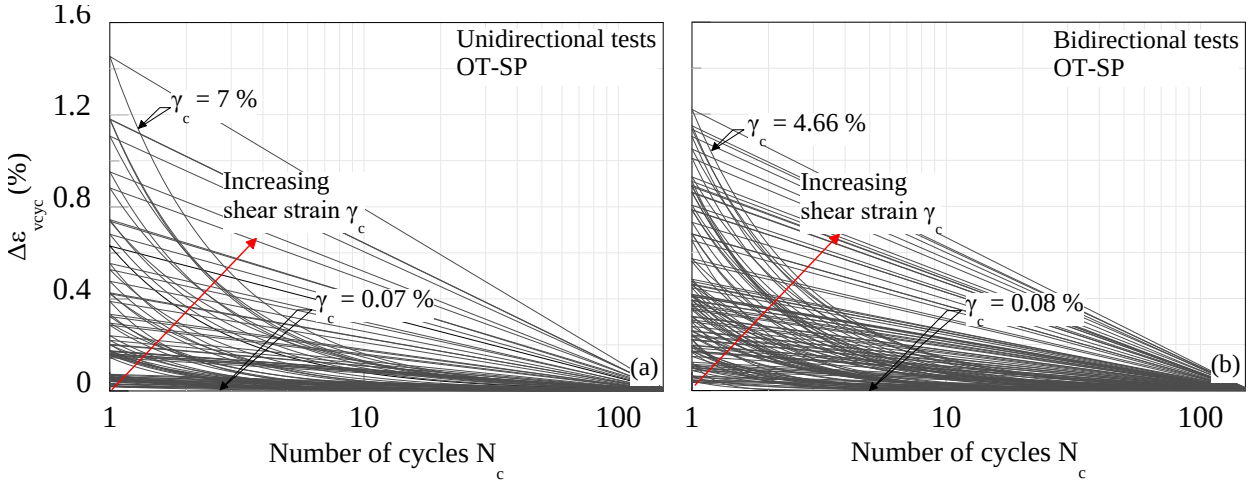

Figure 4-6 Incremental volumetric strain ($\Delta\varepsilon_{vcyc}$) per cycle of strain versus number of cycles for OT-SP sand under: (a) unidirectional; (b) bidirectional loading.

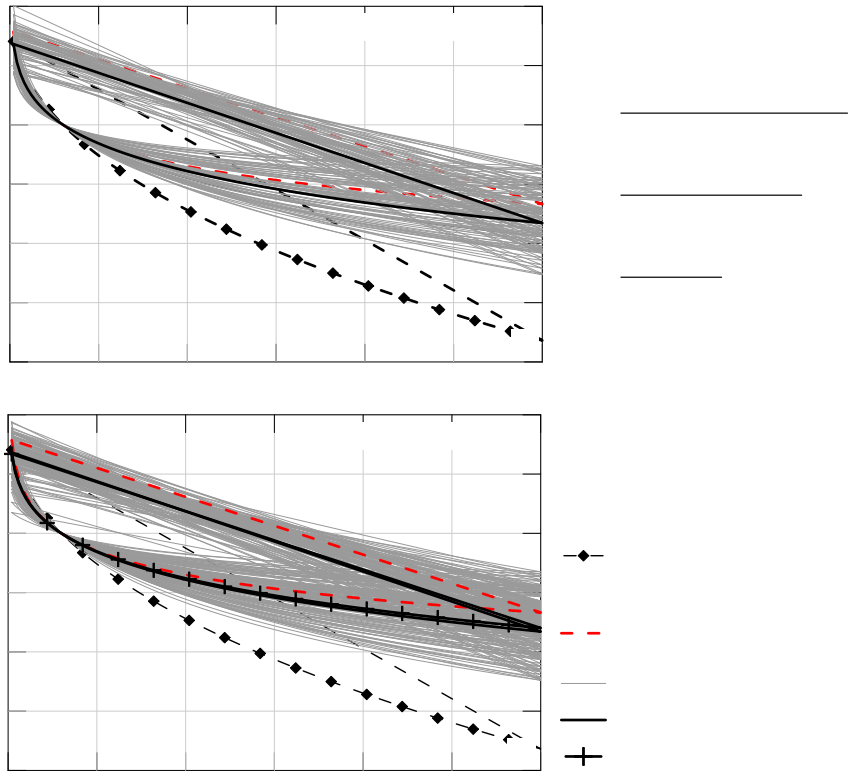

Figure 4-7 Results of (a) uni and (b) bidirectional tests showing effect of number of shear strain cycles on normalized volumetric strain, compared to literature.

4.3.3 Shear strain amplitude

Unidirectional and bidirectional I-mcDSS tests were conducted with γ_c ranging from 0.07 to 7 % and 0.07 to 4.7 % respectively. The range of shear strains considered in this work cover shear strains that might develop in dense granular soils under dynamic loads, as evidenced by the centrifuge test results discussed later. This strain range is not sufficient for the soil to reach a critical state. To illustrate the effect of shear strain amplitude, representative results from unidirectional cyclic tests on OT-SP are presented in Figure 4-8. For the tests presented, OT-SP specimens were consolidated to a relative density of about 60 % at an effective vertical stress of 95kPa prior to cyclic loading. Volumetric strain increases with an increase in shear strain amplitude, the rate of increase slowing down as the shear strain approaches 7%. The increase in volumetric strain $\Delta\varepsilon_{vcyc}$ for a γ_c increase of 3.45 to 7 % is only about 33 % of $\Delta\varepsilon_{vcyc}$ for a γ_c increase of 0.07 to 3.45 %. Bidirectional tests (oval and figure-8) were conducted with "equivalent" experimental parameters for comparison. Shear strain amplitudes for unidirectional tests are considered equivalent to the maximum vector sum of x and y shear strains for the bidirectional tests. Bidirectional test results are presented in Figure 4-9 for the OT-SP, MR-SM, SW-SM, and MRGM-SC. As with the unidirectional tests, as shear strain increases in oval and figure-8 tests, volumetric strain increases.

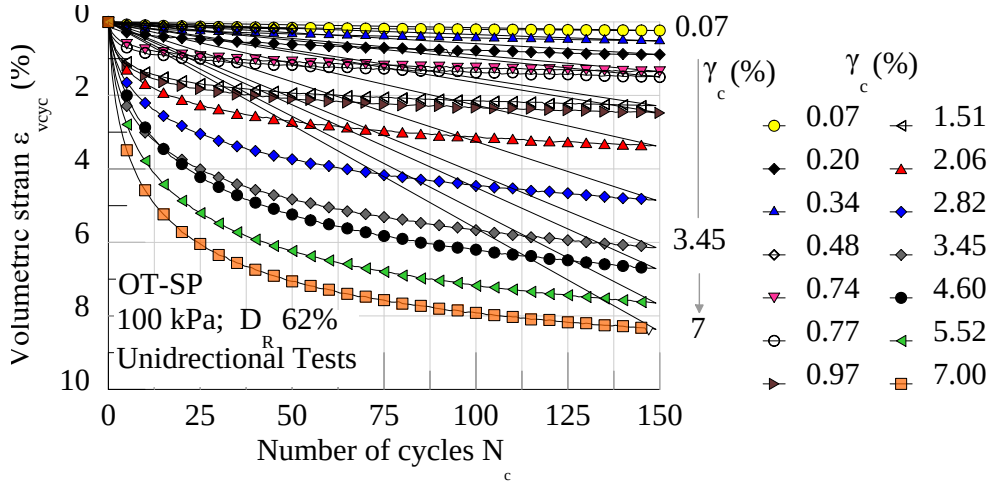

Figure 4-8 Unidirectional I-mcDSS tests results on Ottawa sand illustrating the effect of cyclic shear strain amplitude γ_c on volumetric strain.

A summary plot of the volumetric strain with shear strain amplitude for the OT-SP and the SW-SM is presented in Figure 4-10; and for MR-SM, and MRGM-SC in Figure 4-11. Tests with a relative density of about 60% for OT-SP and SW-SM and relative compaction of 89% for the MR-SM, and MRGM-SC, consolidated to about 95 kPa are shown. The rate of increase of volumetric strain reduces as the shear strain amplitude increase. A clear levelling off is evident in the bidirectional tests on the OT-SP (Figure 4-10b) and SW-SM (Figure 4-10d), and the unidirectional results on SW-SM (Figure 4-10c). Drained volumetric strains in the MR-SM and MRGM-SC are comparable. This may be due to the very similar gradation of both the sands, and the low-plasticity of the MRGM-SC fines. In Figure 4-12 the current results from the OT-SP are compared to the volumetric strain estimates based on experiments by Silver and Seed (1971) on silica no. 20 sand and Duku et al. (2008) on 16 different sands. The OT-SP is selected for the comparison since it is a clean sand, comparable to the sands used by the aforementioned researchers.

Overall, slightly lower to comparable vertical strains are recorded in the present study for shear strain up to 1 %, after which the current results show ε_{vcyc} gradual levelling off. At shear strains above 1 %, the previously published correlations highly overestimate the volumetric strains of the sands tested here. This is because Silver and Seed (1971) and Duku et al. (2008) used shear strains up to 0.5 % and 1.0 % for simple shear testing. In this shear strain range, the volumetric strain correlates linearly or with a small power (1.2, Duku et al. 2008) to shear strain. When extended to shear strains above 1 %, these models do not level off the volumetric strain or decrease the rate of development of volumetric strain. Additionally, these models do not recommend any limiting volumetric strain (see Yi et al. 2010 for definition of limiting volumetric strain). Therefore, at strains greater than 1 %, volumetric strains estimated by the published models shown in Figure 4-12 are higher than the recorded ones. At shear strains less than 1 %, slightly lower volumetric strains reported in this study might be due to the use of stacked metal rings for specimen confinement, which completely restricts lateral deformation. The wire reinforced membranes used by the previous researchers have lower stiffness than the metal rings, thus allowing greater compliance and compression of the specimens. Kammerer (2002) reported volumetric strains up to 1 % due to compliance of a wire reinforced membrane.

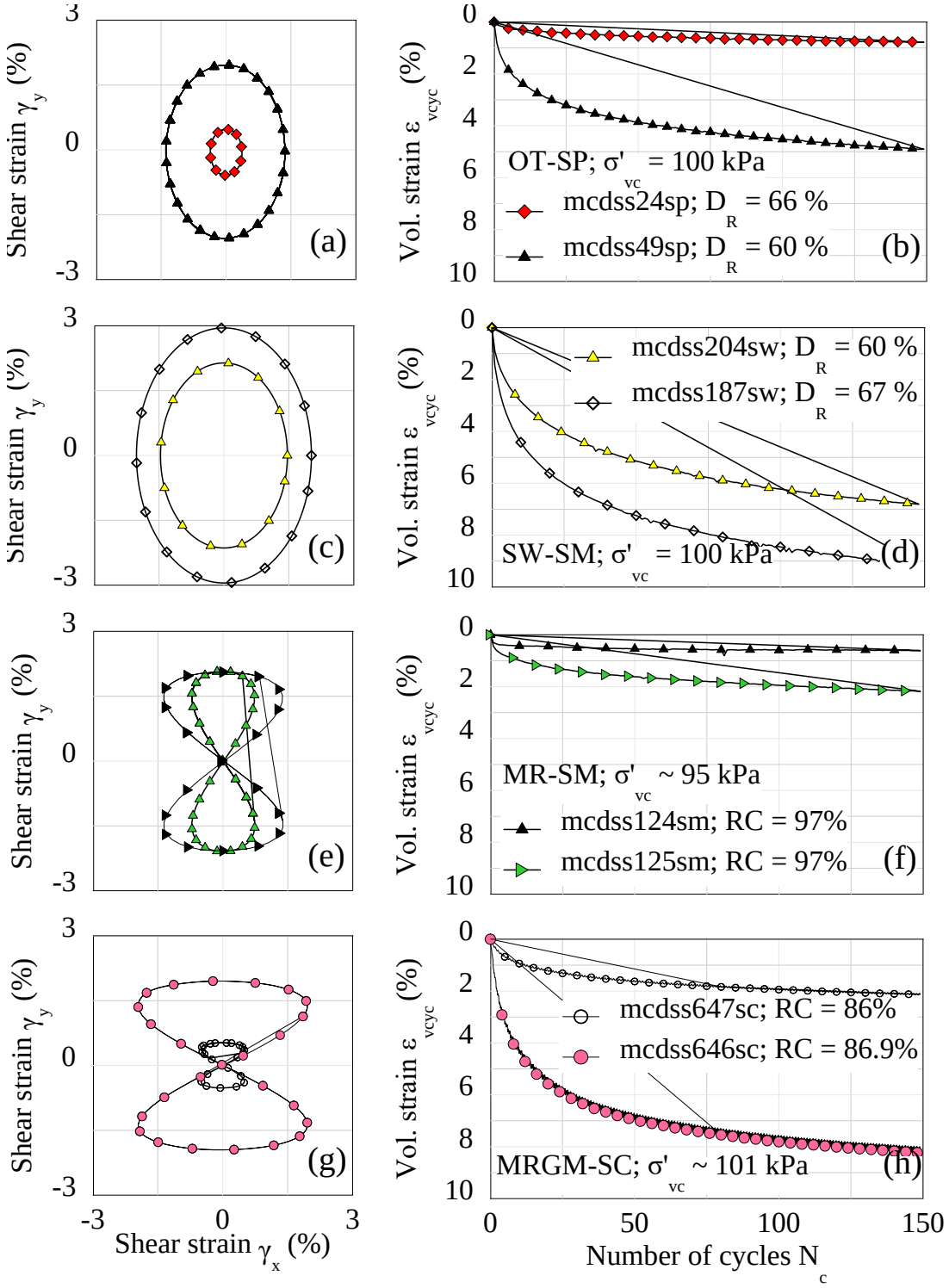

Figure 4-9 Bidirectional I-mcDSS tests results: (a), (c), (e), (g) strain path and (b), (d), (f), (h) volumetric strain on OT-SP, SW-SM, MR-SM, and MRGM-SC illustrating the effect of cyclic shear strain amplitude γ_c on volumetric strain.

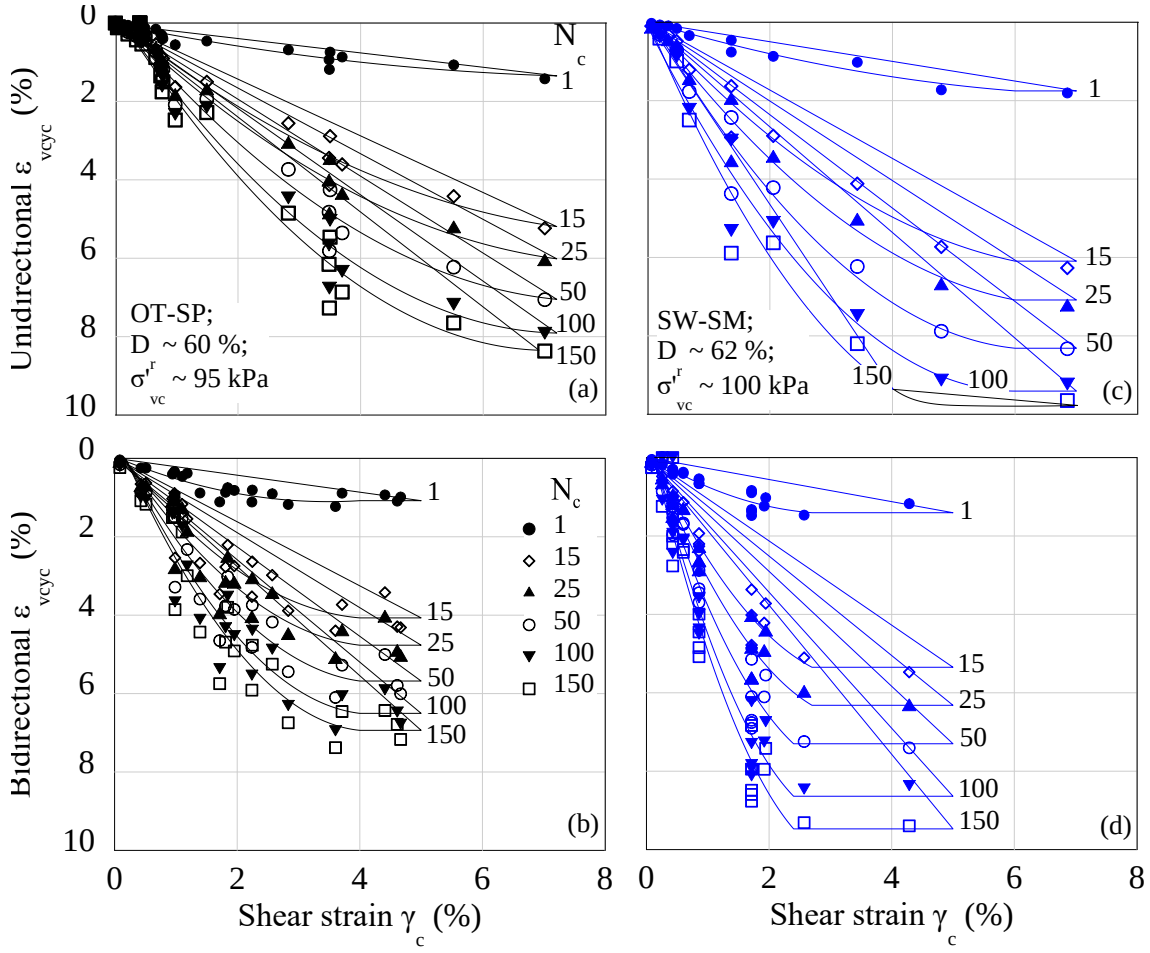

Figure 4-10 Volumetric strain from unidirectional and bidirectional I-mcDSS tests on: (a), (b) OT-SP (FC = 0 %) and (c), (d) SW-SM (FC = 9 %) illustrating the effect of cyclic shear strain amplitude and number of loading cycles.

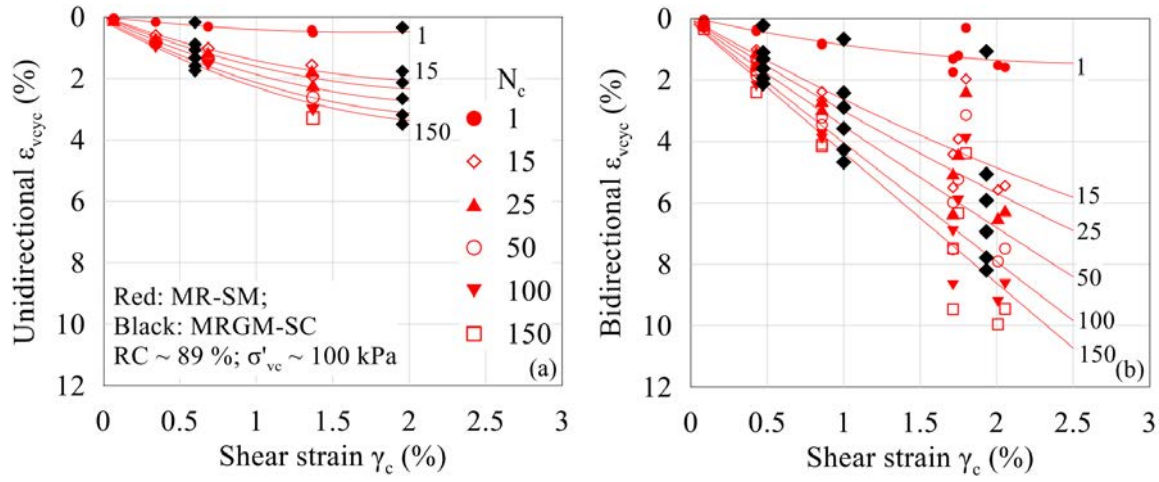

Figure 4-11 Volumetric strain from (a) unidirectional and (b) bidirectional I-mcDSS tests on MR-SM (red) and MRGM-SC (black) (FC ~ 30 %) illustrating the effect of cyclic shear strain amplitude and number of loading cycles.

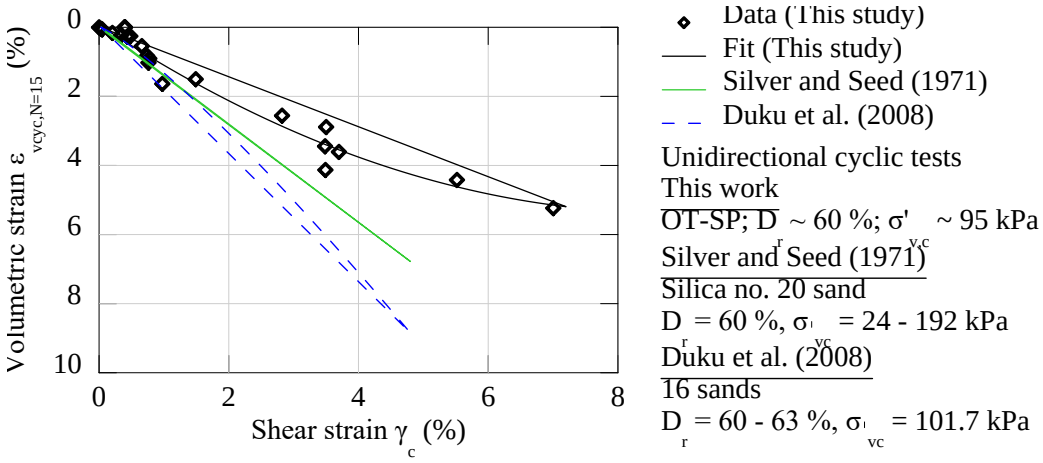

Figure 4-12 Volumetric strain at 15 cycles from l-mcDSS tests on Ottawa OT-SP sand (FC = 0 %) compared to empirical volumetric strain estimations from literature (Silver and Seed 1971; Duku et al. 2008).

4.3.4 Multidirectional loading and load path

The effects of multidirectional loading on volumetric strain is evident by comparing unidirectional and equivalent bidirectional tests shown in Figure 4-13 for the OT-SP, MR-SM, and MRGM-SC. Figure 4-13 (a) and (c) show that volumetric strain increases with the addition of a second loading direction for RC = 92 % to 98 % (clean sand D_R of 60 % to 91 %, respectively) and cyclic shear strain amplitudes of 0.45 % to 1.56 %. This increase occurs for all the soil types tested and can also be seen in Figure 4-10 and Figure 4-11. It is interesting to note from Figure 4-13(b) and (c) that figure-8 tests consistently result in higher volumetric strain than equivalent circular tests.

While considering the difference in drained soil response to unidirectional and bidirectional loading, it is important to understand the effect of the rotation and reversal of the imposed shear strain. Previous research has illustrated the influence of shear stress reversal and rotation on the cyclic porewater pressure response of saturated sands (Kammerer et al. 2002). In one-directional testing, strain is applied along the same unchanging line, without any rotation. The application of the shear strain will first cause the particles to move closer together and the specimen to contract. As the particles move into a denser packing, they will then start climbing over one another (dilate). Now, when the unidirectional cyclic strain changes direction and return to zero, the particles unlock sufficiently to allow further contraction. Continuing to strain (in this reverse direction) will result in dilation. This cycle is repeated in cyclic unidirectional shearing, resulting in gradual accumulation of settlement illustrated in the shear strain versus volumetric strain plot in Figure 4-14.

On the other hand, in bidirectional circular/oval loading, there is a continuous change in the direction of application of shear strain superimposed on either a constant (circular path) or a varying (oval path) initial shear strain applied to the specimens. The strains do not go back to the zero position at any time. Therefore, after the initial shear strain has been imposed in one direction, even if it is sufficient to initiate limited dilation, the reversal of the strain direction causes the particles to unlock and move into a denser configuration, which in turn, leads to dilation at larger strain. Thus, a dilation-contraction regime is established leading to a gradual increase of settlement (Figure 4-15). Within a certain initial strain range (insufficient to cause significant dilation), the higher the initial shear strain amplitude, the more contraction occurs. Thus, volumetric strain in oval tests are lower than

"equivalent" circular tests. This agrees with previous observations in liquefaction-related research that, the more circular the stress path, the more unlocking that occurs, the more contraction that occurs, and the quicker the onset of liquefaction (Ishihara and Yamazaki 1980).

Figure-8 tests are a combination of a high amount of strain rotation and release. This is illustrated in Figure 4-15. At the corners of the "8," a high degree of strain rotation occurs, and the direction of application of the shear strain changes. Moreover, there are approximately 540^0 of strain direction change or reversal in the figure-8 tests, as opposed to the 360^0 in the circular and 180^0 in the unidirectional tests Thus, in figure-8 tests, for comparable resultant shear strains, higher volumetric strains are observed.

For the bidirectional tests, volumetric strains eventually level off at shear strains of about 4 to 5 % (Figure 4-10b, d; Figure 4-16). The volumetric strains in unidirectional tests are found to approach the volumetric strains in bidirectional tests at a shear strain of about 10 %, as shown for medium dense OT-SP and SW-SM in Figure 4-16. The multidirectionality factor for volumetric strain (bidirectional test ε_{vcyc} / unidirectional test ε_{vcyc}) at shear strains varying from 3 % to 6 % is examined using oval and figure-8 tests. When the initial shear strain applied in circular loading exceeds about 3.5 %, the soil particles start to climb over adjacent particles, initiating dilation. At such high strains, the soil might be reaching a limiting void ratio for the current level of strains, and further contraction is simply not possible. Thus, the bidirectional volumetric strain starts levelling off quickly for a shear strain amplitude of 5 % (Figure 4-16). For unidirectional loading, higher shear strain is required to reach the maximum volumetric strain for specimens at the same density. Figure 4-16 shows that this shear strain is about 10 % for the medium dense OT-SP and SW-SM. Because of this, the volumetric strains recorded in unidirectional tests become comparable to the ones recorded in circular tests. Thus, the multidirectionality factor at a shear strain of 10 % approaches 1, and bidirectional loading effect seismic compression in a manner similar to that observed at lower γ_c.

Figure 4-16 also shows the ultimate volumetric strain computed using laboratory determined values of minimum void ratio e_{min} (ASTM D4253-16). The ultimate volumetric strain (ε_{vult}) is computed as: $(e-e_{min})/(1+e)$. For bidirectional loading with a shear strain of 5 % and higher, ε_{vult} is reached in about 15 cycles of drained loading, whereas it is reached at a shear strain of 10 % for unidirectional cyclic loading (Figure 4-16a, c). At a greater number of loading cycles, e.g., 50 loading cycles, bidirectional tests at 3 % shear strain start approaching ε_{vult}, and bidirectional tests at 5 % or higher shear strains exceed the laboratory ε_{vult} (Figure 4-16b, d). This implies that a relative density of greater than 100% has been reached by the soil. However, 50 loading cycles of 5 % shear strain amplitude is representative of an extremely high intensity earthquake. For instance, 26 cycles of shaking are considered equivalent to an earthquake M 8.5 (Tokimatsu and Seed 1987). Thus, for medium dense sand with fines content less than 15 %, for most practical applications, ε_{vult} can be used as an approximate upper limit of volumetric strain.

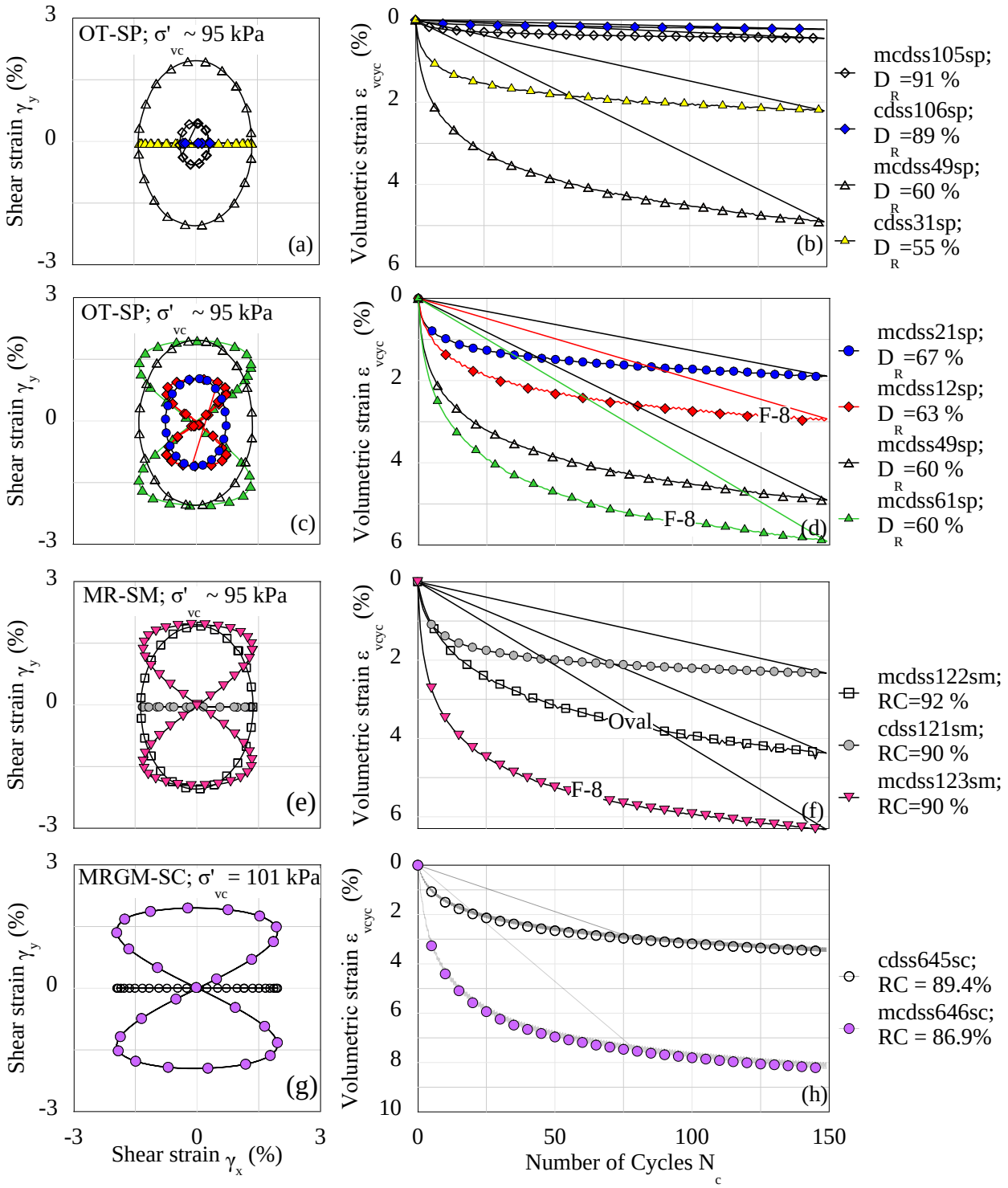

Figure 4-13 Strain path and volumetric strain history from I-mcDSS tests illustrating the effect of: (a) and (b) multidirectional loading on OT-SP; (c) and (d) load path on OT-SP; (e) and (f) multidirectional loading and load path on MR-SM; and (g) and (h) multidirectional loading on MRGM-SC.

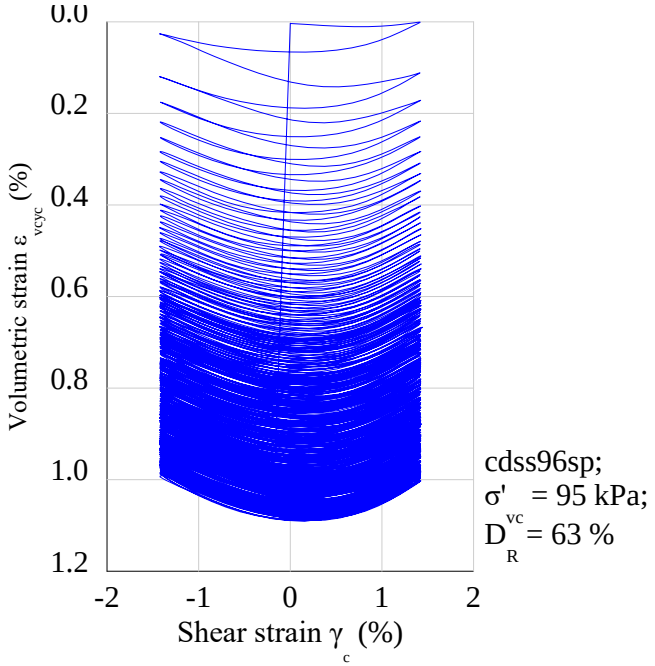

Figure 4-14 Volumetric strain versus shear strain from unidirectional I-mcDSS tests on OT-SP illustrating dilation-contraction cycles.

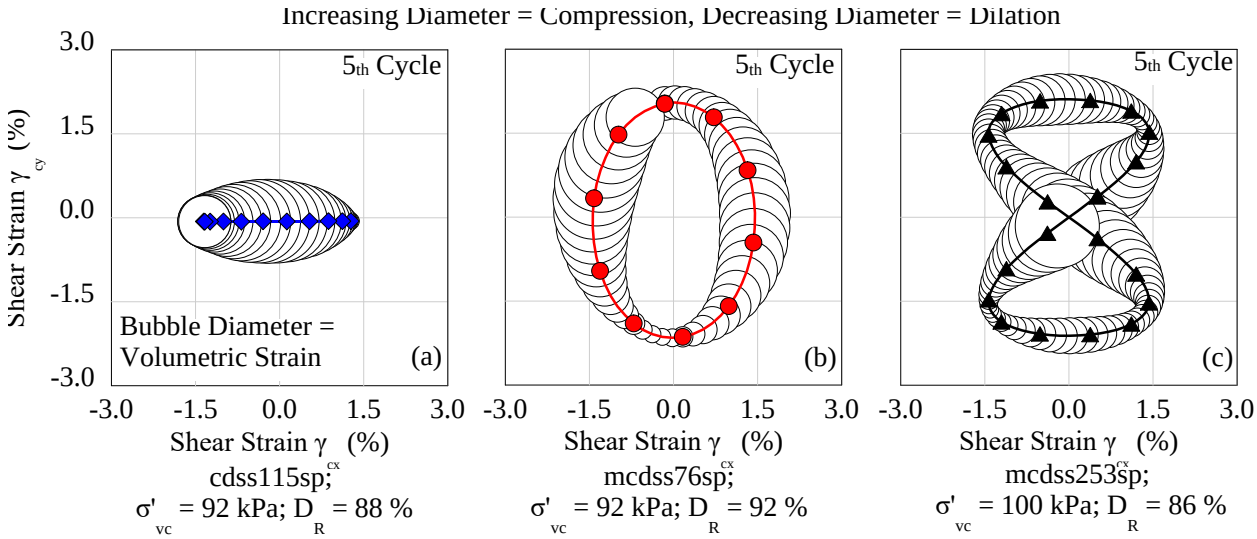

Figure 4-15 Comparison between the volumetric strain dilation-contraction cycles of the OT-SP in (a) unidirectional, (b) circular, and (c) figure-8 tests.

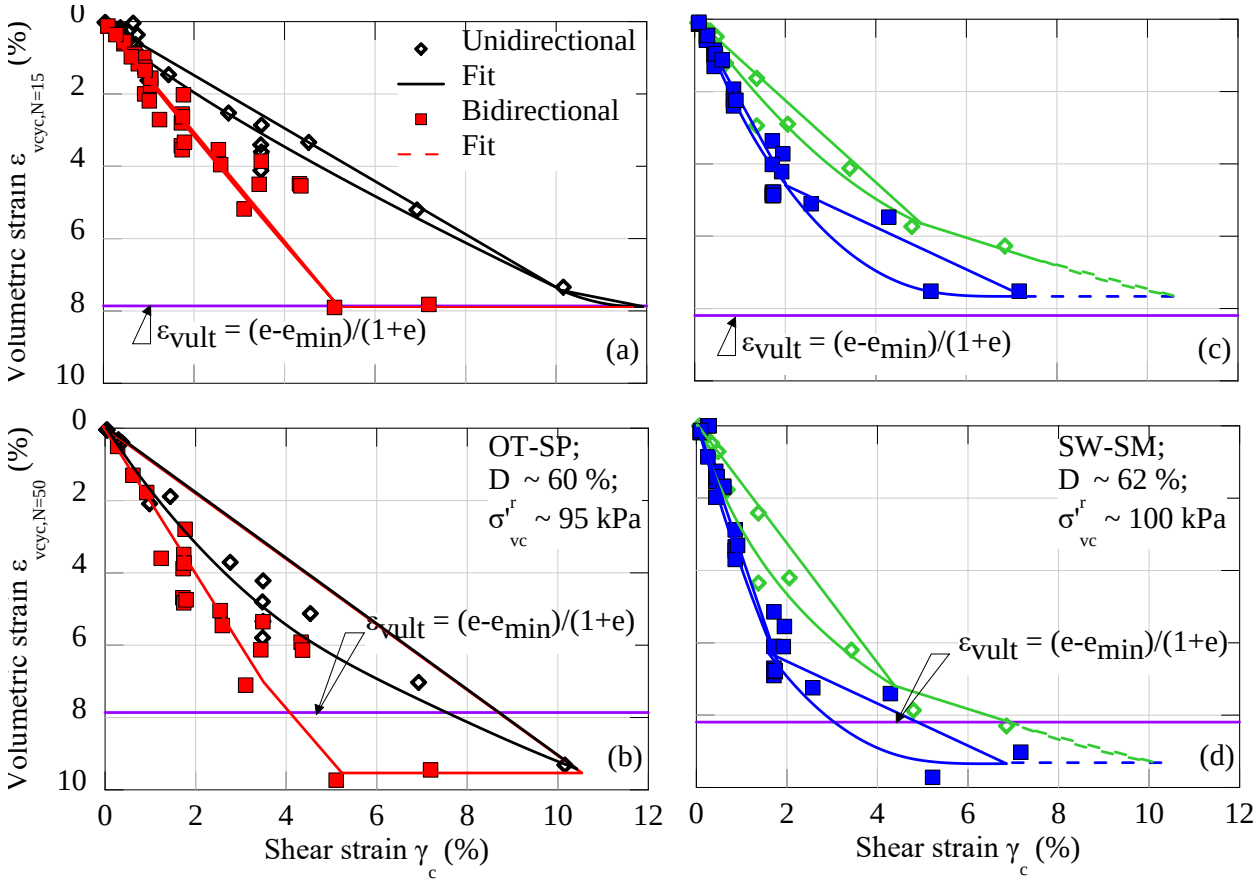

Figure 4-16 Effect of bidirectional loading on volumetric strain at 15 and 50 cycles respectively from I-mcDSS tests on: (a), (b) OT-SP and (c), (d) SW-SM, also illustrating the effect of cyclic shear strain and laboratory determined ultimate volumetric strain.

4.3.5 Confinement

Increasing the vertical consolidation stress resulted in a decrease of the drained volumetric strain for all the sands tested and for both unidirectional and bidirectional loads. Representative results from unidirectional tests are presented in Figure 4-17 for OT-SP, SW-SM, and MR-SM. The coefficient of volume compressibility m_v, see Eqn. (3-87) for definition, of the OT-SP from incremental loading oedometer tests is shown in Figure 4-18 (repeated here from Chapter 3 for convenience). As the effective stress increases, m_v decreases, thus the volume change potential of the soil decreases, similar to the decrease in volume change with increasing effective stress observed in the I-mcDSS tests. Other researchers, except for Silver and Seed (1971) and Youd (1972a), have also found that increasing effective confining stress corresponds to a decrease in drained volumetric strain from unidirectional cyclic tests (e.g., Duku et al. 2008). This is corroborated further by the centrifuge test results described later. It is unclear why Silver and Seed (1971) and Youd (1972a) did not observe a similar trend.

In the field, the combination of greater effective confining stress and lower shear strain at high depths (~18 m) typically leads to a drastic reduction in volumetric strain. A volumetric strain cutoff depth of 18 m (σ'_{vo} ~ 180 kPa for a watertable at the ground surface) was recommended for post-cyclic reconsolidation volumetric strain by Cetin et al. (2009). However, in this work, we observed up to 0.8 % volumetric strain at 400 kPa (~ 40 m depth) for the MR-SM (Figure 4-17c), at a shear

strain of 1.37 %. Thus, for instance in the case of a deep pocket of loose soil that develops shear strains greater than 1%, some centrifuge tests suggest that volumetric strain is possible at depths greater than 18 m (Kim 2017; Xuan 2017).

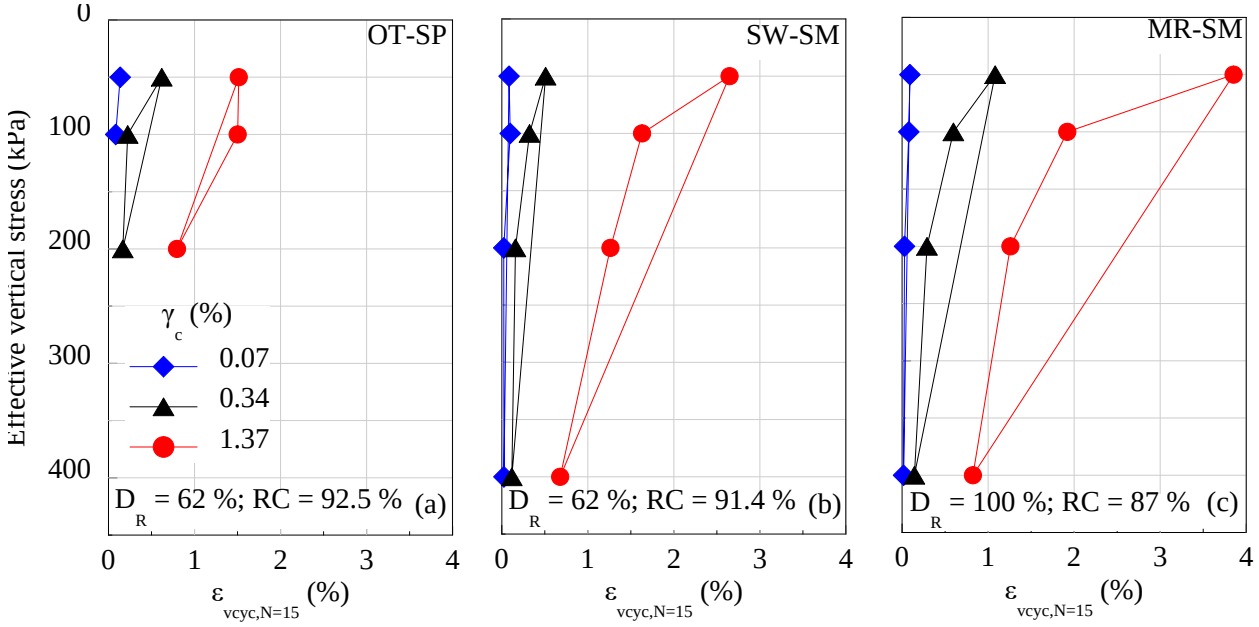

Figure 4-17 Effect of confinement on volumetric strain at 15 cycles from drained unidirectional I-mcDSS tests on: (a) OT-SP; (b) SW-SM; and (c) MR-SM, also illustrating the effect of shear strain.

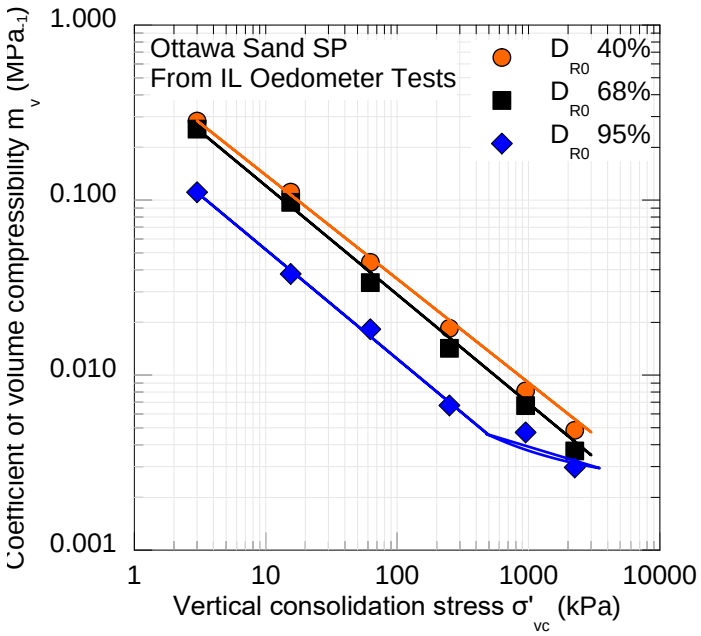

Figure 4-18 Coefficient of volume compressibility m_v of loose to very dense (D_{R0} 40 – 95%) OT-SP from incremental loading oedometer tests.

4.3.6 Density

To show the effect of relative density on volumetric strain representative unidirectional tests on OT-SP, and bidirectional tests on SW-SM are shown in Figure 4-19. Here, the OT-SP is consolidated to 95 kPa and the SW-SM to 100kPa. Specimens with relative density 95 % have lower volumetric strain than the specimens at 62 % relative density, the difference increasing with increase in the shear strain. This is also evident from the m_v data in Figure 4-18, which shows that denser specimens have lower volumetric compressibility. For instance, in Figure 4-19(d), at 1 % shear strain, ε_{vcyc} for D_R 60 % is about 3.4 times that for D_R 95 % specimens, at 2 % shear strain this factor increases to 5.8. The volumetric strain obtained from very dense OT-SP specimens (DR 93 %) is compared to data on D_R 80% Crystal Silica No. 20 from Silver and Seed (1971) in Figure 4-20. The data compares well, with ε_{vcyc} for D_R 80 % being only slightly higher than for D_R 93 %.

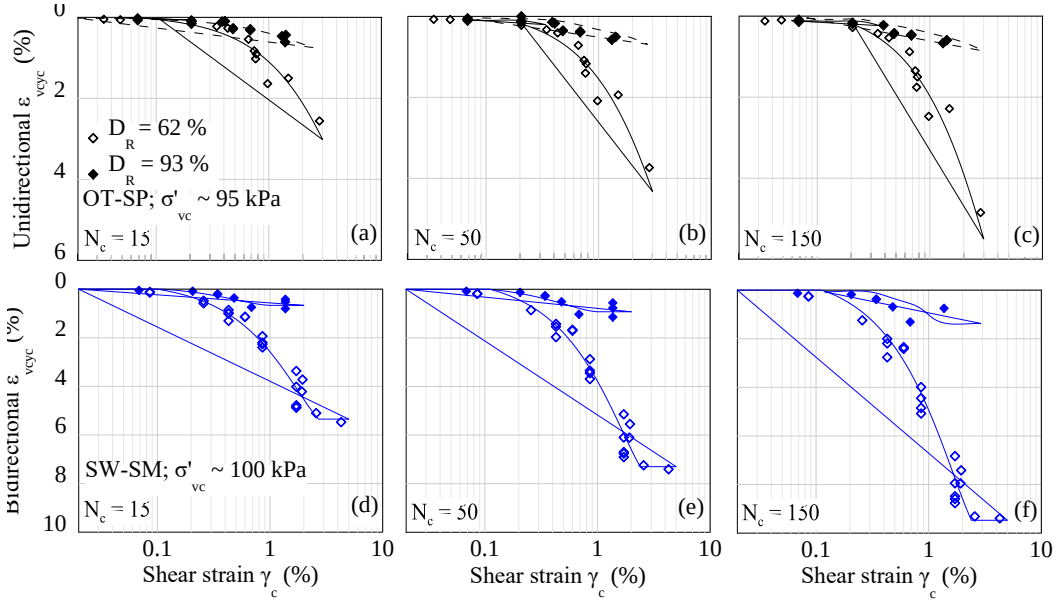

Figure 4-19 Effect of density on volumetric strain: (a), (b), (c) OT-SP at 15, 50 and 150 unidirectional cyclic loading cycles respectively; (d), (e), (f) SW-SM at 15, 50 and 150 bidirectional oval or figure-8 loading cycles respectively.

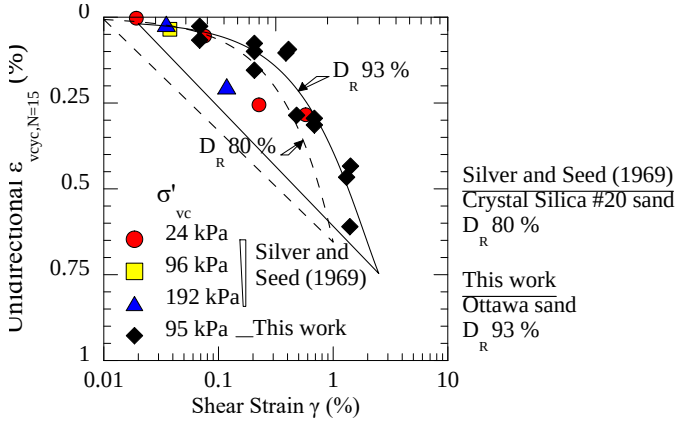

Figure 4-20 Effect of density on volumetric strain: data for D_R 80 % from Silver and Seed (1971), data for D_R 93 % from this work.

4.3.7 Non-plastic fines content and gradation

Figure 4-21 illustrates that the volumetric strain in the SW-SM is higher than volumetric strain in the OT-SP for unidirectional and bidirectional tests and for all loading cycles, when compared at the same relative density, confinement, and shear strain amplitude, before a limiting shear strain is reached. As previously discussed, there exists a shear strain, after which, on further increase in the shear strain, no further volumetric strain is accumulated for the same number of loading cycles. For bidirectional tests, this limiting shear strain is about 5%, whereas for unidirectional tests it is about 10 %, at which the volumetric strains level off (Figure 4-21). Before the volumetric strains level off, the SW-SM is more compressible than the OT-SP. This is also evident from a comparison of a unidirectional cyclic test on OT-SP and SW-SM presented in Figure 4-22.

The presence of non-plastic fines (9 %) in the SW-SM, in addition to the wider range of particle size with respect to the clean OT-SP, allows the SW-SM to be more contractive at the same relative density. In alluvial or aeolian sands, for identical depositional energy, sands with higher uniformity coefficient (C_U) or well-graded sands reach a higher relative density with respect to poorly-graded sands of low C_U. Because of this, when these soils are prepared to comparable relative densities, the well-graded sand is more compressible than the poorly-graded one (Mei et al. 2017). This observation is in good agreement to the findings of Belkhatir et al. (2014) for positive pore pressure generation in sands of relative density 20 to 91 %. For a sand of relative density 50 %, Singh (1994) also observed that increasing the low-plasticity (plasticity index equal to or less than 7.5) or non-plastic fines content results in higher positive porewater pressures. Singh (1994) tested soils with smooth gradations. Belkhatir et al. (2014) noted that sands with a higher content of low plasticity fines content and higher uniformity coefficient have higher volumetric strain when specimens are compared at the same relative density.

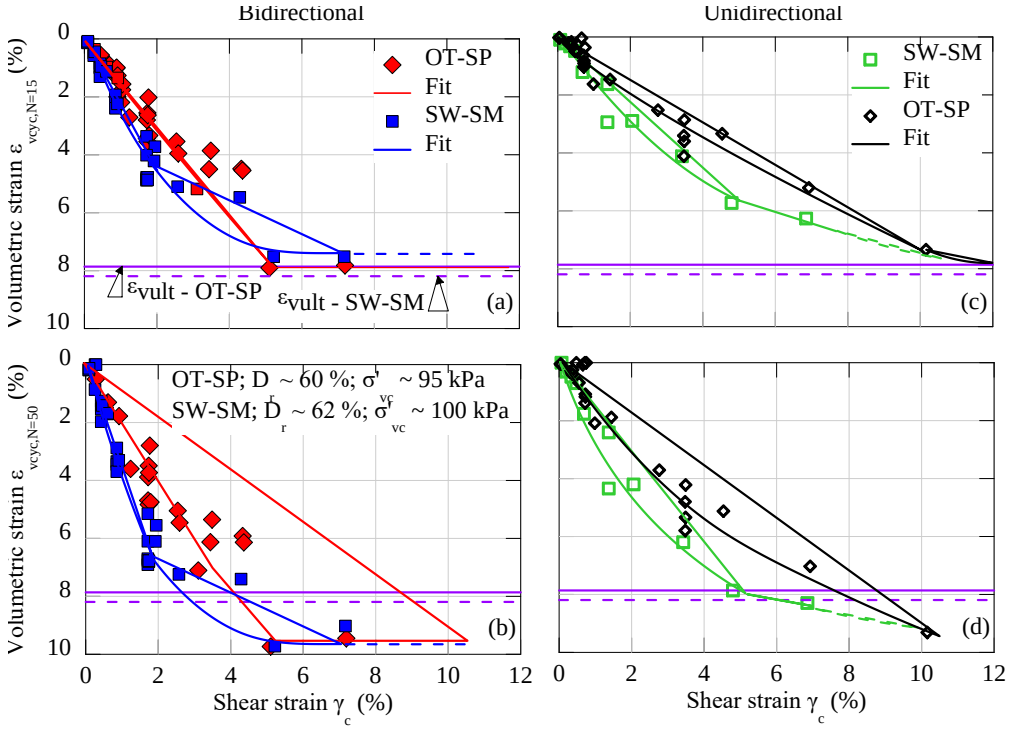

Figure 4-21 Volumetric strain versus shear strain compared for medium dense OT-SP and SW-SM under 15 and 50 loading cycles: (a), (b) bidirectional oval or figure-8; and (c), (b) unidirectional cyclic I-mcDSS tests.

However, above 5 % shear strain for bidirectional loads and 10 % shear strain for unidirectional loads, after the volumetric strain levels off, the OT-SP and SW-SM volumetric strains are comparable. This may be because the OT-SP and SW-SM have the same ($e_{max} - e_{min}$) of 0.32, or the same potential for compression, and comparable ultimate volumetric strains (Figure 4-21).

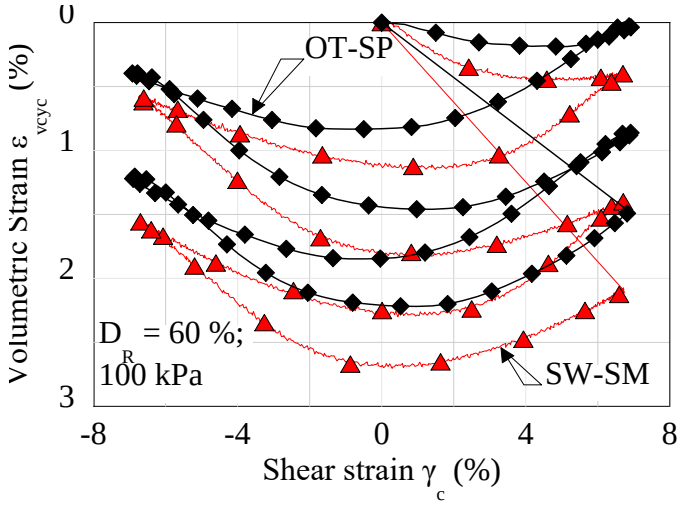

Figure 4-22 Volumetric strain versus shear strain from first 2 cycles of a unidirectional cyclic I-mcDSS tests on OT-SP (FC = 0 %) and SW-SM (FC = 9 %) illustrating dilation-contraction cycles.

4.3.8 Specimen preparation method

4.3.8.1 Repeatability

To verify whether consistent and repeatable results are obtained from OT-SP specimens that have been DFD and cyclically sheared to an identical relative density, starting from varying initial densities, specimens were prepared at relative densities ranging from 64 – 91 % and then cyclically sheared (unidirectional and circular paths) with a shear strain less than or equal to 2 %, to obtain a relative density of 91 – 95 %. Following this, cyclic circular strain paths were applied to these DFD + CS specimens at a shear strain amplitude of 2.1 %. Figure 4-23 illustrates the volumetric response from five such tests. The volumetric strains are in excellent agreement for all five tests, indicating that repeatable response can be obtained from specimens prepared by DFD + CS, regardless of the initial relative density prior to CS. One potential advantage of using DFD + CS specimens is that multiple tests can be conducted on the same specimen, if the cyclically sheared specimen has an identical response to specimens prepared by traditional methods (DFD, Raining, DFD + TV). The following sections examine the volumetric response of medium to very dense sands prepared by the different specimen preparation methods.

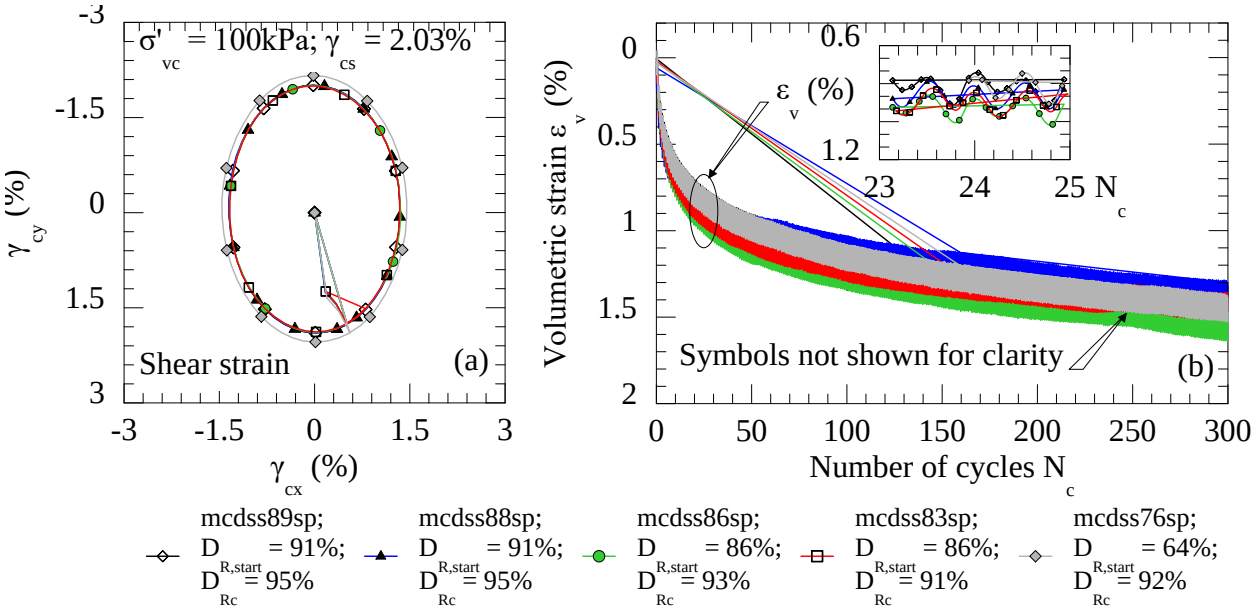

Figure 4-23. Very dense (D_{Rc} 91 - 95 %) OT-SP specimens prepared by DFD + CS from different initial densities ($D_{R,start}$) subjected to bidirectional oval loading: (a) Strain path – shear strain in x versus y direction; (b) volumetric strains versus number of cycles, with a magnified illustration of the contraction-dilation cycles.

4.3.8.2 Effect on medium dense sand

Figure 4-24(a) and Figure 4-25(a) compares the volumetric strain time histories from unidirectional and bidirectional oval tests respectively on medium dense OT-SP samples (D_R 60 – 67%). Peak shear strains for the unidirectional and oval tests shown are 1.4 % and 2.0 % respectively. It is consistently observed that specimens prepared by DFD + CS show lowest volumetric compression, specimens formed by DFD exhibit the highest compression and DFD + TV specimens lie in between. This observation is consistent with observations of Yee et al. (2013) discussed in the literature review chapter (Chapter 2). Figure 4-26 summarizes the results for all the I-mcDSS tests reported in Chapter 3. For the entire range of shear strain amplitudes tested (0.07 – 3.3 %), DFD specimens are most contractive and DFD + CS specimens are least so.

The reason for the higher stiffness of the CS specimen can be attributed to: (1) increase in K_0 during drained shearing, as postulated by previous researchers (Seed et al. 1971); and (2) the change in the soil fabric due to cyclic shearing. Unfortunately, the I-mcDSS does not afford measurement of the horizontal shear stress due to use of the stacked rings for confinement, thus no measurements for K_0 could be made. In terms of soil fabric, DFD specimens have their long axes oriented preferentially in the horizontal direction (Oda 1972). Under horizontal cyclic shearing, loading is applied along the bedding plane of the specimen, and this inherent fabric anisotropy leads to accumulation of higher volumetric strain. The DFD + TV sample of D_R 56 – 71 % were prepared by application of just 2 to 5 rubber hammer blows to the table after DFD, thus negligibly affecting the anisotropic fabric of the DFD specimen. However, when subjected to cyclic shearing, the specimen undergoes dilation-contraction cycles (Figure 4-23b). As the particles dilate, the preferred orientation formed by DFD is disrupted, leading to a more isotropic fabric, which is more resistant to some modes of shear. Hence, even at comparable relative densities, the DFD + CS specimens experience lower volumetric strains than the DFD or the DFD + TV specimens. This behavior is consistent for both unidirectional and bidirectional circular tests.

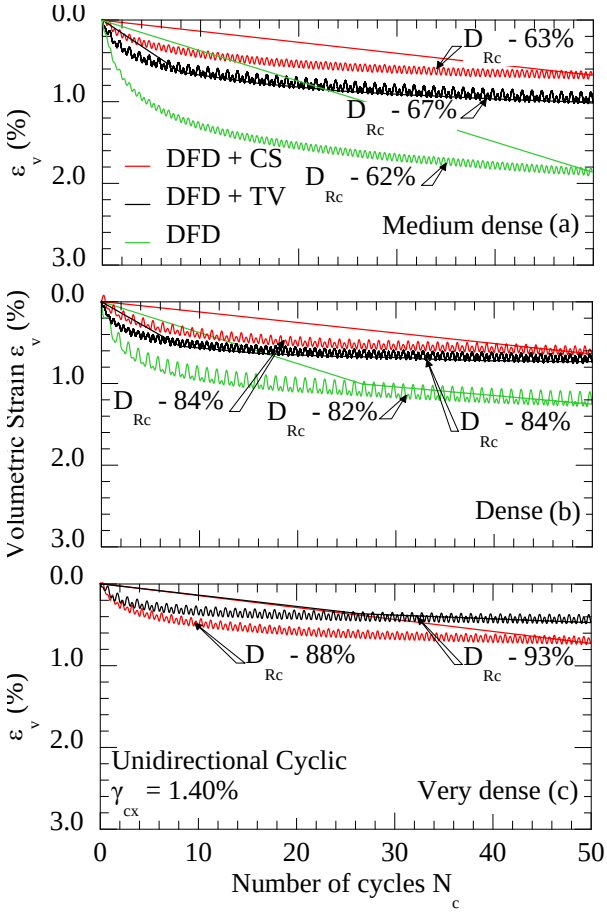

Figure 4-24 Representative results showing effect of sample preparation on volumetric strain in unidirectional cyclic tests for Ottawa sand: (a) medium dense (D_{Rc} 62 - 67%); (b) dense (D_{Rc} 82 - 84%); (c) very dense (D_{Rc} 88 - 93%).

4.3.8.3 Effect on Dense Sand

Figure 4-24(b) and Figure 4-25(b) compares the volumetric strain from unidirectional and bidirectional oval tests respectively of dense sand samples (D_{Rc} 80 – 85 %). Peak shear strains for the unidirectional and oval tests shown are 1.4 and 2.0 % respectively. Specimens prepared by raining (equivalent to DFD), exhibited slightly higher volumetric strain compared to those prepared by DFD + CS and DFD + TV in the unidirectional tests. In the bidirectional tests, the DFD specimen has the same volumetric compression as those prepared by the other methods. In the unidirectional test, the rained specimen (D_{Rc} 82%) is more compressible than the TV or CS specimens (D_R 84 %), due to the difference in relative density along with experimental scatter.

Figure 4-26 shows that the overall volumetric contraction of dense sands prepared by DFD, DFD + TV and DFD + CS are comparable. A single trend line thus represents the volumetric strain – shear strain response. When the soil is rained to a relative density of 80 – 85 %, the pluviator is held at a drop height of 50 cm. Thus, considerable energy is imparted to the sand particles as they deposit in the mold. It is possible that DFD followed by uniform cyclic shearing and table vibrations with 100 – 125 hammer strikes, imparts an equivalent energy to the soil mass. Thus, all three methods of specimen reconstitution result in comparable compressibility, and consequently in similar volumetric compression. This differs from the response of medium dense sands as reported by previous

researchers (Yee et al. 2013) and in this study, where DFD yielded the most compressible and DFD + CS the least compressible fabric. The difference may be because a medium dense sand (e.g., D_{Rc} 60 %) is funnel deposited with zero drop height, whereas consequent TV and CS imparts energy to the soil making it stiffer. However, as discussed, the dense sand(e.g., D_{Rc} 82 %) is rained with much higher energy, thus yield identical response to TV and CS specimens in terms of cyclic drained volumetric strain.

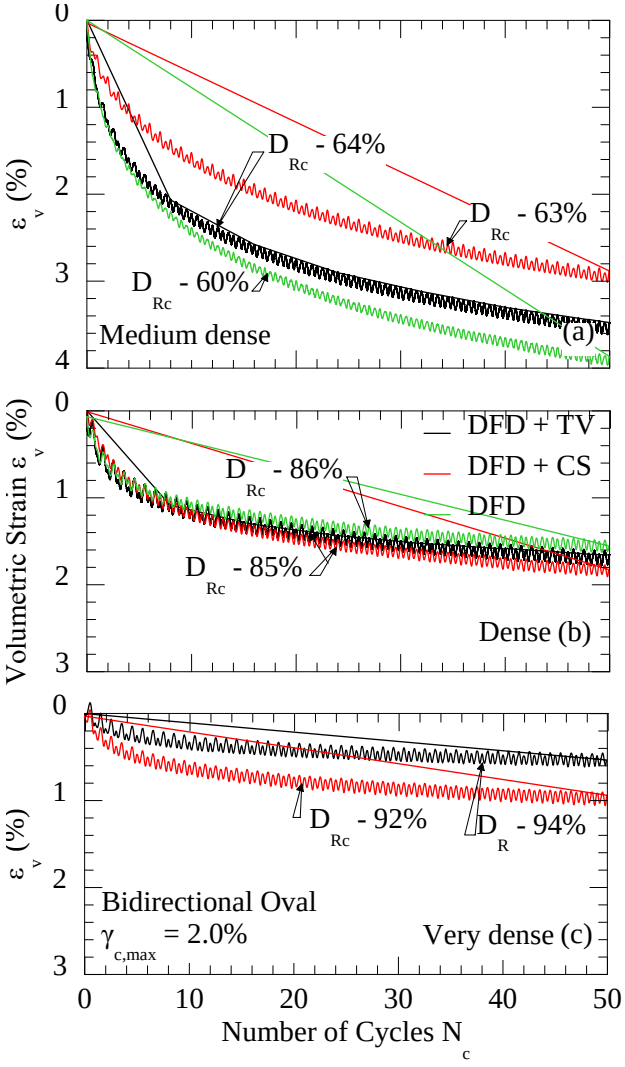

Figure 4-25 Representative results showing effect of sample preparation on volumetric strain in bidirectional oval tests for Ottawa sand: (a) medium dense (D_{Rc} 60 - 64%); (b) dense (D_{Rc} 85 - 86%); (c) very dense (D_{Rc} 92 - 94%).

4.3.8.4 Effect on Very Dense Sand

Figure 4-24(c) and Figure 4-25(c) illustrate the volumetric strain from unidirectional and bidirectional oval tests of very dense sand specimens (D_{Rc} 86 – 95 %). Peak shear strains for the unidirectional and oval tests shown are 1.4 and 2.0 % respectively. It was observed that specimens prepared by DFD + CS show somewhat higher volumetric compression than specimens formed by DFD + TV compared to the behavior of medium dense or dense sand samples (D_R < 86 %). Figure 4-26(c) summarizes the results for the very dense sands. Even though DFD + CS samples produce more

volumetric compression, the magnitude of this difference is less than 20 %. Moreover, very dense sands undergo less than 1 % volumetric compression (Figure 4-26c) for 15 loading cycles (equivalent to a M 7.5 earthquake; Seed et al. 1971). For such a small volumetric compression, the less than 20 % difference in the specimens prepared by CS or TV can be considered negligible. Thus, a single fit for all the very dense sand volumetric strain – shear strain data is shown in Figure 4-26. It is important to note that, in contrast to medium dense sands and observations by previous researchers (Yee et al. 2013), cyclically sheared specimens of very dense sands can produce repeatable and representative results for soil layers formed by densification to D_{Rc} greater than 86%.

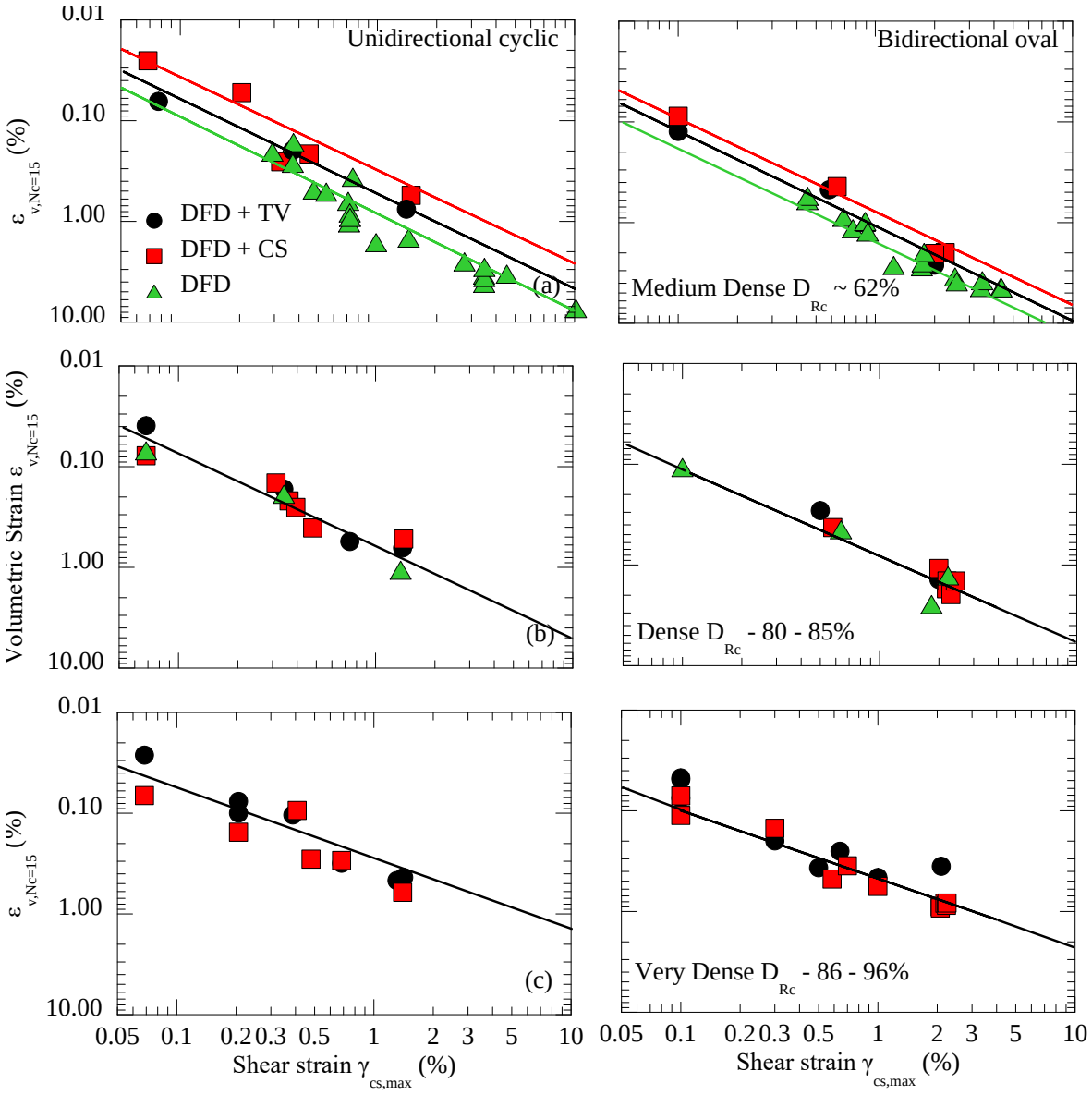

Figure 4-26 Summary of the effect of specimen preparation on compression volumetric strain (logarithmic scale) at the end of 15 strain cycles in unidirectional and bidirectional circular tests for Ottawa sand: (a) medium dense (D_R 60 - 67%); (b) dense (D_R 80 - 85%); (c) very dense (D_R 86 - 92%).

4.3.9 Broadband Loading Tests

To study the element response of the sands under broadband loads, strain-controlled unidirectional and bidirectional drained broadband loading tests were conducted on dry medium dense Ottawa sand (D_R ~ 64 %) prepared by dry funnel deposition (tests bdss360sp, bdss361sp and mbdss363sp). For direct simple shear tests using seismic loading, researchers have used: (1) scaled acceleration records for stress-controlled (Ishihara and Nagase 1985) and strain-controlled tests (Duku et al. 2007); and (2) scaled strain time histories obtained from equivalent-linear site response analysis (Lasley et al. 2016). The input loading used in the present work was the displacement time histories from the E-W and N-S components of the M = 7.62 Chi-Chi Taiwan 1999 earthquake (station TCU078; NEHRP site class C) obtained from the PEER NGA database.

Displacement time histories are used because they are directly related to the seismically induced shear strains in the soil. Each load path, scaled to induce a maximum shear strain of 0.68 and 1 %, was applied five consecutive times. Results from the unidirectional and bidirectional tests are shown in Figure 4-27 and Figure 4-28 respectively. The volumetric strain increases with increase in strain magnitude until the maximum shear strain occurs, leveling off thereafter, even though strain cycles of lower amplitude were being applied. This holds true for both unidirectional and bidirectional loads. The peak shear strain for the bidirectional load is defined as the maximum value of the resultant shear strain of the N-S and E-W components. For the unidirectional E-W and N-S loading tests, 90 % and 80 % of the total volumetric strain for each loading sequence develops respectively by the time the peak shear strain was reached; for the corresponding bidirectional test, 85 % volumetric strain had accumulated. These observations generally agree with the volumetric strain trends observed by Duku et al. (2007) and Lasley et al. (2016) and for porewater pressure generation by Ishihara and Nagase (1985) for irregular loading.

Figure 4-27 and Figure 4-28 also illustrates the gradual stiffening of the specimen during drained compression, similar to the previously discussed sinusoidal cyclic tests (see Figure 4-2 and Figure 4-3), by the: (1) increasing τ with number of loading time histories; and (2) decreasing ε_{vcyc} on application of each consecutive displacement time history. Furthermore, the ε_{vcyc} during bidirectional loading is approximately equal to the sum of ε_{vcyc} due to the unidirectional N-S and E-W load tests (Figure 4-28e). Pyke et al. (1975) observed the same behavior in bidirectional shake table tests on medium dense Monterey No. 0 sand (D_R ~ 60%). This result is consistent with the previously described unidirectional, oval, and figure-8 tests (Figure 4-13), where the volumetric strain in the bidirectional tests was about 2 times that of the unidirectional test.

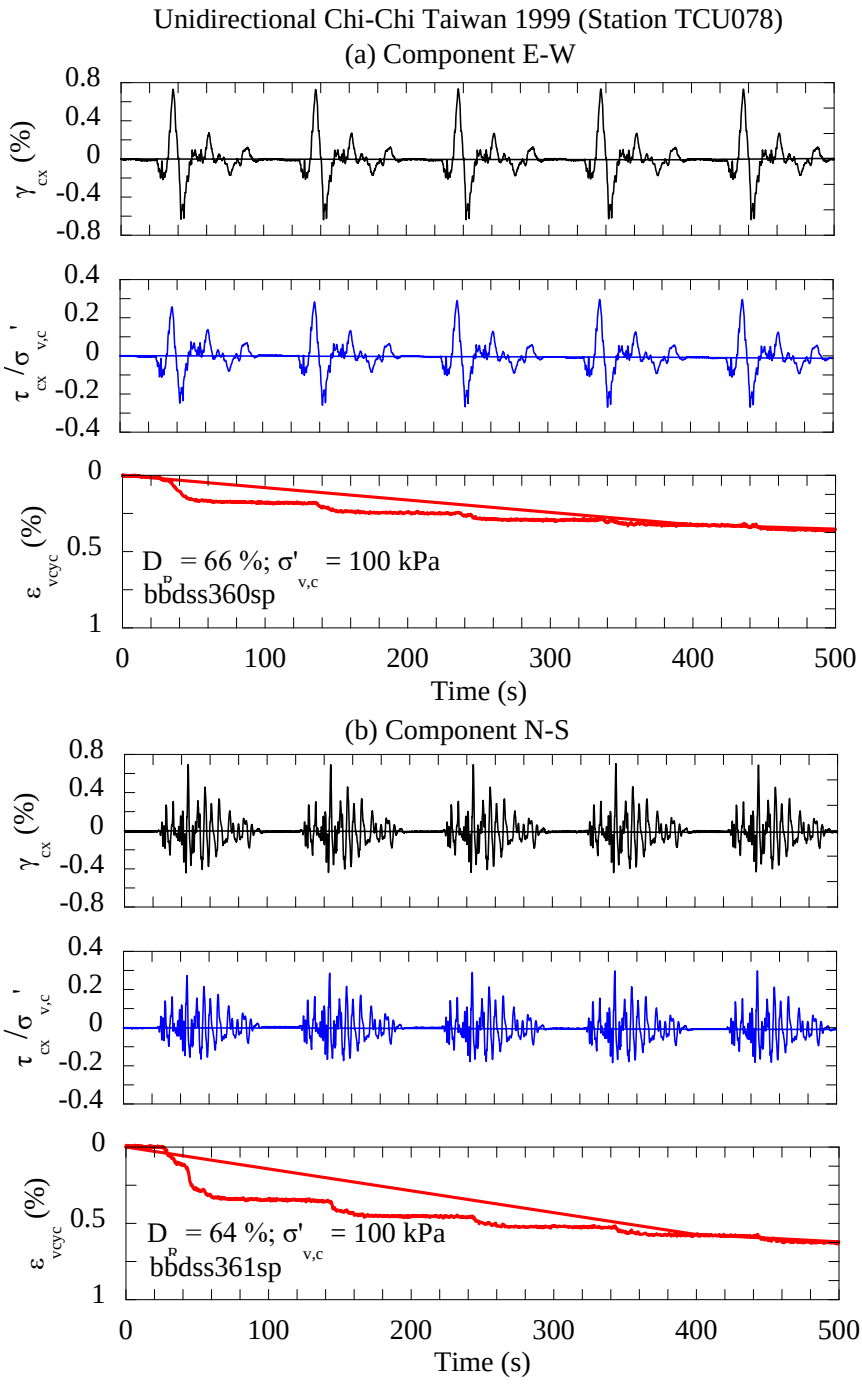

Figure 4-27 Unidirectional strain controlled test on medium dense Ottawa (D_R 64 – 66 %) sand using the displacement time histories of the: (a) E-W; and (b) N-S components of the Chi-Chi Taiwan 1999 earthquake in the I-mcDSS; five sequences of the entire time series was used.

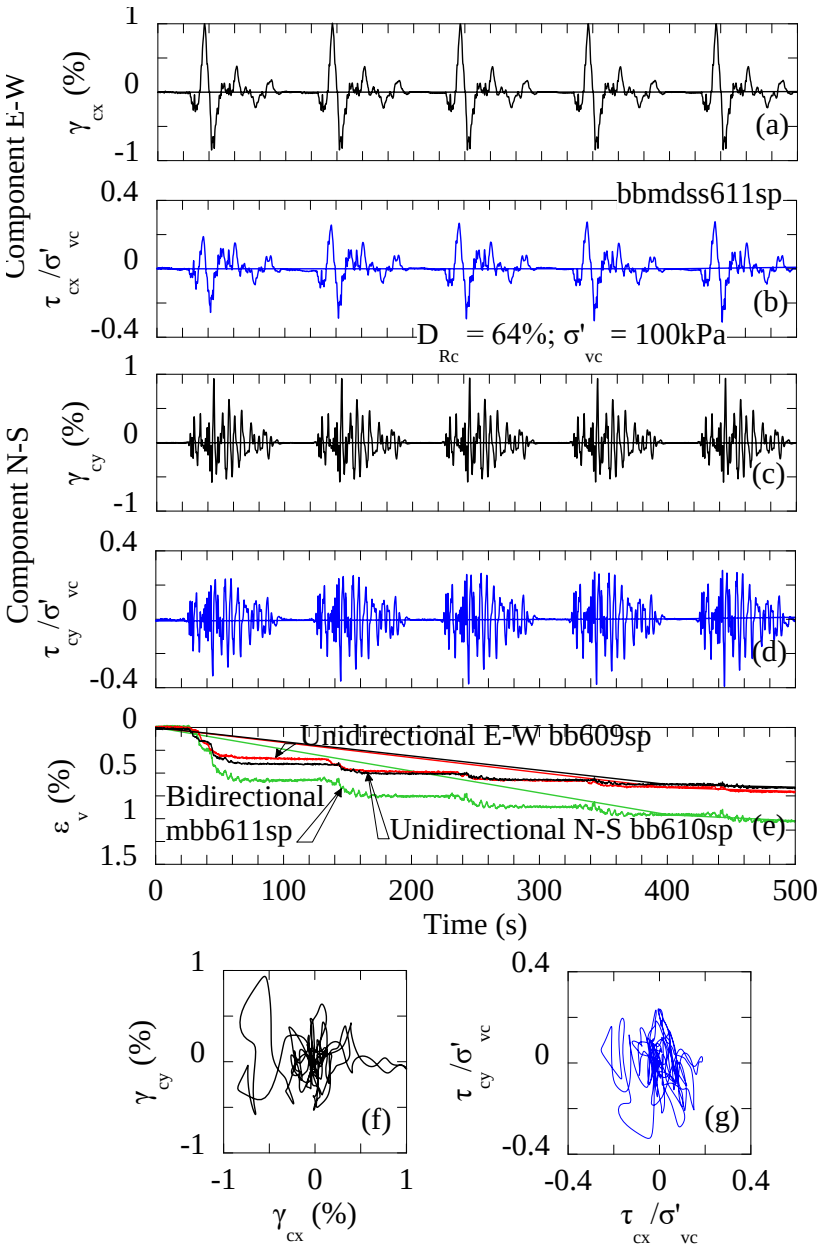

Figure 4-28 Bidirectional strain controlled test on medium dense Ottawa (D_{Rc} ~ 63%) sand using the displacement time histories of the E-W and N-S components of the Chi-Chi Taiwan 1999 earthquake (Station TCU078) in the I-mcDSS: (a) γ_{cx}, (b) τ_{cx}/σ'_{vc} time histories for the E-W component; (c) γ_{cy}, (d) τ_{cy}/σ'_{vc} time histories for the N-S component; (e) ε_v with time, also ε_v from equivalent unidirectional tests using each component individually (D_{Rc} ~ 64 – 66%); (f) and (g) Plan view of γ_c and τ_c/σ'_{vc} respectively; five sequences of the entire time series is used.

4.4 Conclusions from Drained Element Level Testing

The drained element testing series observations are summarized below:

1. Drained volumetric strain under both unidirectional and bidirectional loading is independent of the loading frequency (0.1 – 10Hz) for the poorly graded clean OT-SP, the well graded SW-SM, and the silty sand MR-SM.
2. The majority (85 – 90 %) of soil stiffening occurs in the first 10 to 15 cycles of drained loading, after which the rate of soil stiffening and accumulation of volumetric strain decreases. This is true for all the soils tested, and for both unidirectional and bidirectional loads.
3. Increase in shear strain increases the volumetric strain for both unidirectional and bidirectional loading. The rate of increase of volumetric strain with shear strain gradually decreases, and finally levels off at higher shear strains (5 % for bidirectional tests, 10 % for unidirectional tests).
4. During drained loading, there is a limiting shear strain, after which further increase of the shear strain does not increase the volumetric strain for the same number of loading cycles. For bidirectional tests, the shear strain at which the volumetric strain levels off is about 5 %, for unidirectional cyclic tests, it is about 10 %. The unidirectional and bidirectional tests level off at comparable values of volumetric strain.
5. Drained volumetric strain in bidirectional loading tests are generally greater than equivalent unidirectional loading tests by an average factor of 2.2, comparable to the factor of 2 from Pyke et al. (1975). However, when unidirectional tests reach a shear strain of 10 %, or reach the limiting shear strain described in point 4 above, the multidirectionality factor for volumetric strain becomes 1.
6. The number of total reversals in a loading path influences the volumetric strain. Volumetric strain in figure-8 loading paths is greater than that of the circular or oval loading path because of the greater degree of strain reversal in the “8”.
7. Increasing confinement and density decreases the drained volumetric strain. This is corroborated by the coefficient of volume compressibility data from oedometer tests.
8. For shear strains lower than the limiting values described in point 4, volumetric strain in the well graded SW-SM is higher than the poorly graded clean OT-SP, at the same relative density. This is probably a result of the OT-SP requiring more energy than the SW-SM to reach the same relative density.
9. The effect of specimen preparation depends on the relative density of the soil: medium dense samples (D_{Rc} 60 – 67%) formed by DFD are more compressible than DFD + CS soils, with the compressibility of DFD + TV soils being in between. Volumetric strain in dense sands (D_{Rc} 80 – 86%) is comparable across all the specimen preparation methods considered, and in very dense sands (D_{Rc} 86 – 101%), volumetric compression in TV specimens are comparable to CS specimens.
10. Volumetric strain in medium dense soils by DFD are higher than cyclically sheared sands (DFD + CS) at D_R 60 – 67%, which produce a much stiffer response. This is consistent with the findings of Yee et al. (2013) for medium dense sands in uni-directional DSS loading.
11. Cyclically sheared specimens can be used for characterizing volumetric contraction in dense to very dense sands (D_{Rc} > 80%) formed by sedimentation or by artificially applied vibratory compaction, since the fabrics have comparable stiffness. This is contrary to the behavior of medium dense specimens, as illustrated by the present work and the findings of previous researchers (Yee et al. 2013).
12. Unidirectional and bidirectional broadband loading DSS tests corroborate the findings of the uniform cyclic tests. Small-strain bidirectional loading leads to a volumetric strain about 1.5 to 2 times higher than unidirectional loading. Also, when a sequence of the same shaking is applied multiple times to the specimen, with each new shaking, the volumetric strain increment is lower. The authors believe that this is due partly to the increase in relative density and partly to increase in K_0 or the effect of pre-shaking.

4.5 Constant Volume I-mcDSS Tests

When coarse-grained soil deposits, at an initial overburden of σ'_{vo}, are subjected to undrained loading, there is a tendency for particle rearrangement and volume change. Since undrained loading occurs under constant volume conditions, this volume change tendency of the soil results in the generation of excess porewater pressure, leading to a decrease in the effective stress. At the end of undrained loading, the excess porewater pressure dissipates, and the effective stress of the soil returns to σ'_{vo}. This results in a decrease in the soil volume, termed the post-cyclic reconsolidation volumetric strain (Ishihara and Yoshimine 1992). The excess porewater pressure (PWP) is often represented in term of the ratio of excess PWP and σ'_{vo}, called the excess porewater pressure ratio, r_u. In the field, in loose to medium dense soil (D_R 15 – 65 %), the excess porewater pressure may cause liquefaction (defined here as $r_u = 1$, or $\gamma_c = 3.5$ %; Nagase and Ishihara 1988). Liquefaction is unlikely to occur in dense to very dense sands (D_R > 65 %). The centrifuge case histories presented in later sections of this chapter illustrate this behavior.

All tests presented here were conducted under constant volume (CV) conditions, as discussed in Chapter 3. In constant volume testing, it is assumed that the change in the vertical stress during shear is equivalent to the porewater pressure generation in an undrained test with constant total vertical stress (Bjerrum and Landva 1966). Iversen (1977) reported identical shear stress and pore pressure response in height controlled and volume controlled monotonic direct simple shear tests on Drammen clay with overconsolidation ratios of 1 and 4. Later, this assumption was verified for monotonic simple shear tests on normally consolidated Drammen clay by Dyvik et al. (1987).

Results from a constant volume strain-controlled DSS test conducted in the I-mcDSS is presented in Figure 4-29. The specimen was air pluviated using DFD and K_0 consolidated at 100 kPa to a relative density of 54 %. Smooth shear stress – shear strain – volumetric strain response is obtained. The decrease in shear stress amplitude with increase in porewater pressure ratio, and the rapidly flattening shear stress-shear strain hysteresis loop is in good qualitative agreement with the behavior of undrained, saturated contractive sand specimens, and strain-controlled constant volume DSS tests on Nevada sand presented by Vucetic and Mortezaie (2015). Representative results from a bidirectional oval direct simple shear test on OT-SP is presented in Figure 4-30. Similar to the unidirectional test, a rapid increase in the porewater pressure reduces the shear stress in both the x and y directions and the soil reaches $r_u = 1$ in about four loading cycles of 2 % shear strain amplitude. To quantify reconsolidation volumetric strain (ε_{vr}) under multidirectional constant volume loading, the effect of different loading paths, amplitudes and soil related parameters are investigated separately.

4.5.1 Loading frequency

The unidirectional drained volumetric strain ε_{vcyc} of granular material is frequency independent (present study; Youd 1972a; Duku et al. 2008) for a frequency range of 0.1 to 10 Hz. The same is true for bidirectional drained volumetric strains for a frequency of 0.1 and 1 Hz, as observed in the current study. To investigate the effect of loading frequency on reconsolidation volumetric strain ε_{vr}, tests were conducted on medium dense D_R ~ 60 % OT-SP consolidated to an effective vertical stress of 50 kPa. Two loading frequencies 0.1 and 1 Hz were considered, 30 loading cycles were applied for each test. The measured ε_{vr} is shown in Figure 4-31. The soil did not liquefy for shear strains below 0.3 %, whereas all the specimens liquefied for shear strain above 0.3 %. Similar to ε_{vcyc}, ε_{vr} is found to be independent of the loading frequency for a frequency of 0.1 and 1 Hz.

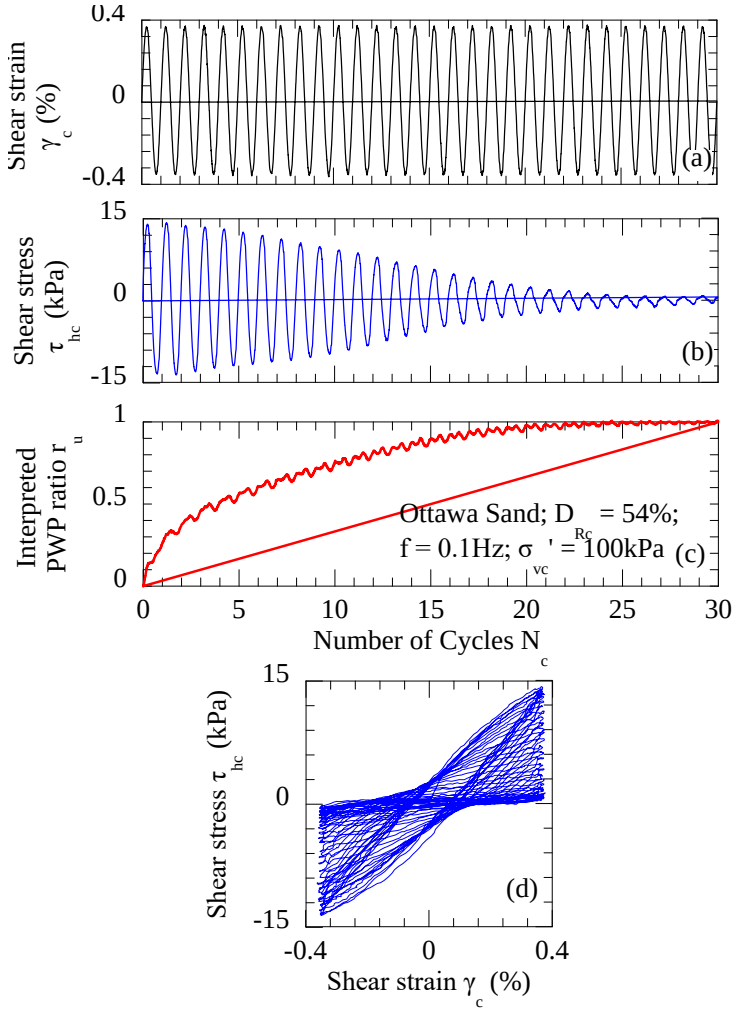

Figure 4-29 Shear stress – shear strain – porewater pressure response in constant volume unidirectional cyclic direct simple shear test for medium dense OT-SP (D_R 54 %).

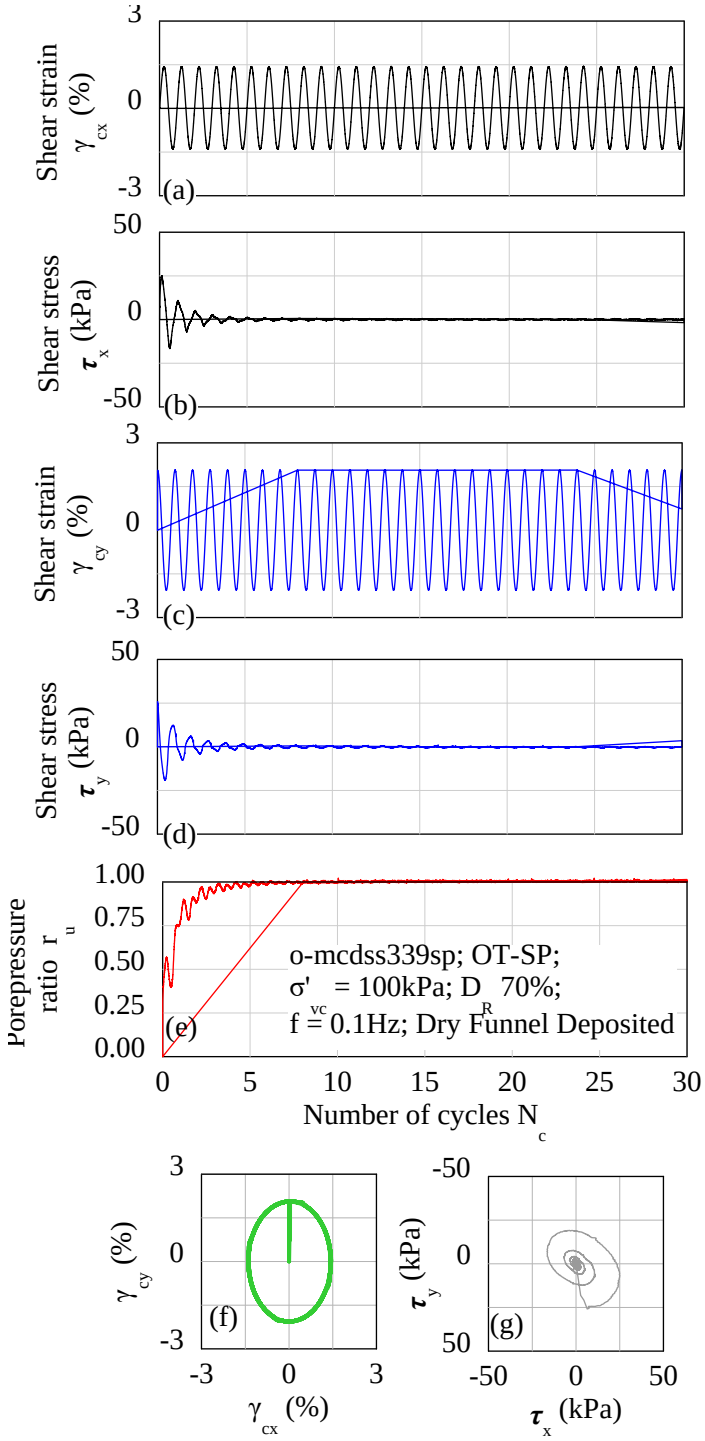

Figure 4-30 Shear stress – shear strain – porewater pressure response in constant volume bidirectional oval direct simple shear test for medium dense OT-SP (D_R 70 %).

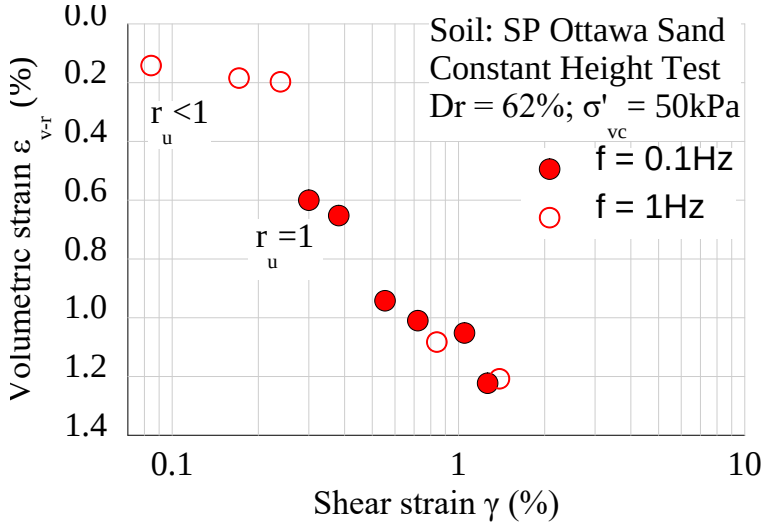

Figure 4-31 Results from unidirectional tests on medium dense OT-SP showing the negligible effect of loading frequency on post-cyclic reconsolidation volumetric strain for frequencies 0.1 and 1.0 Hz. Specimens with γ_c less than 0.3 % did not liquefy after 30 loading cycles, whereas all other specimens did.

4.5.2 Shear strain amplitude and multidirectional loading

The post-cyclic reconsolidation volumetric strain for the same soil, effective vertical stress, relative density and fabric is related to the excess porewater pressure generated during cyclic loading (Lee and Albaisa 1974; Nagase and Ishihara 1988; Wu 2002). This is because r_u indicates both the contractiveness of the soil and the loading magnitude. However, after initial liquefaction r_u ceases to be a useful parameter for quantifying ε_{vr}. Nagase and Ishihara (1988) and Ishihara and Yoshimine (1992) found that the maximum induced shear strain during cyclic loading was a better parameter to capture ε_{vr} since it works both before and after liquefaction has occurred. In this report, ε_{vr} is presented both in terms of the cyclic shear strain amplitude and porewater pressure dissipated following cyclic loading. The latter is beneficial in understanding ε_{vr} under different confinements, and the volumetric (contraction/dilation) tendencies of the soil during cyclic loading.

Figure 4-32 illustrates the effect of shear strain amplitude on the porewater pressure generation under cyclic loading for medium dense D_R 62 % OT-SP consolidated to an effective vertical stress of 100 kPa. Excess porewater pressure increases with increasing shear strain amplitude under unidirectional, oval, and figure-8 loading conditions. The higher degree of reversal in the figure-8 loading path results in higher porewater pressure with respect to the oval loading path for all shear strain amplitudes. This is consistent with the observations from drained volumetric strains previously discussed. Figure 4-32(c) shows that the porewater pressure under bidirectional loading is consistently higher than the unidirectional loading. This observation is corroborated by the centrifuge test results described in later sections.

Figure 4-33 is plotted to illustrate the effect of strain reversal on porewater pressure generation in bidirectional figure-8 loading. As the strain path moves from zone 1 to zone 2, a partial reversal of the strain direction leads to an increase in r_u (contractive behavior). As the strain almost monotonically increases along zone 2, the soil exhibits slightly dilative behavior, illustrated by the slight reduction in r_u. As the strain path reverses again from zone 2 to zone 3, r_u increases indicating that unlocking due to nearly complete strain reversal has increased the contractiveness of the soil.

Figure 4-34 and Figure 4-35 depict the porewater pressure ratios inferred from constant volume tests on the SW-SM and the MR-SM respectively. The response is consistent with that of the clean OT-SP: r_u increases with γ_c, r_u is higher for figure-8 loading with respect to oval loading for the same γ_c, and r_u for bidirectional loading is higher than that for unidirectional loading. Figure 4-36 illustrates the increase in porewater pressure, and reduction of shear stress, with increase in shear strain amplitude for dense MRGM-SC sand. A shear strain of 2 % results in a rapid increase of porewater pressure, and a corresponding sharp decrease in the shear stress of the soil, whereas a shear strain of 0.11 % causes negligible increase in the porewater pressure, and no decrease in the shear stress of the MRGM-SC.

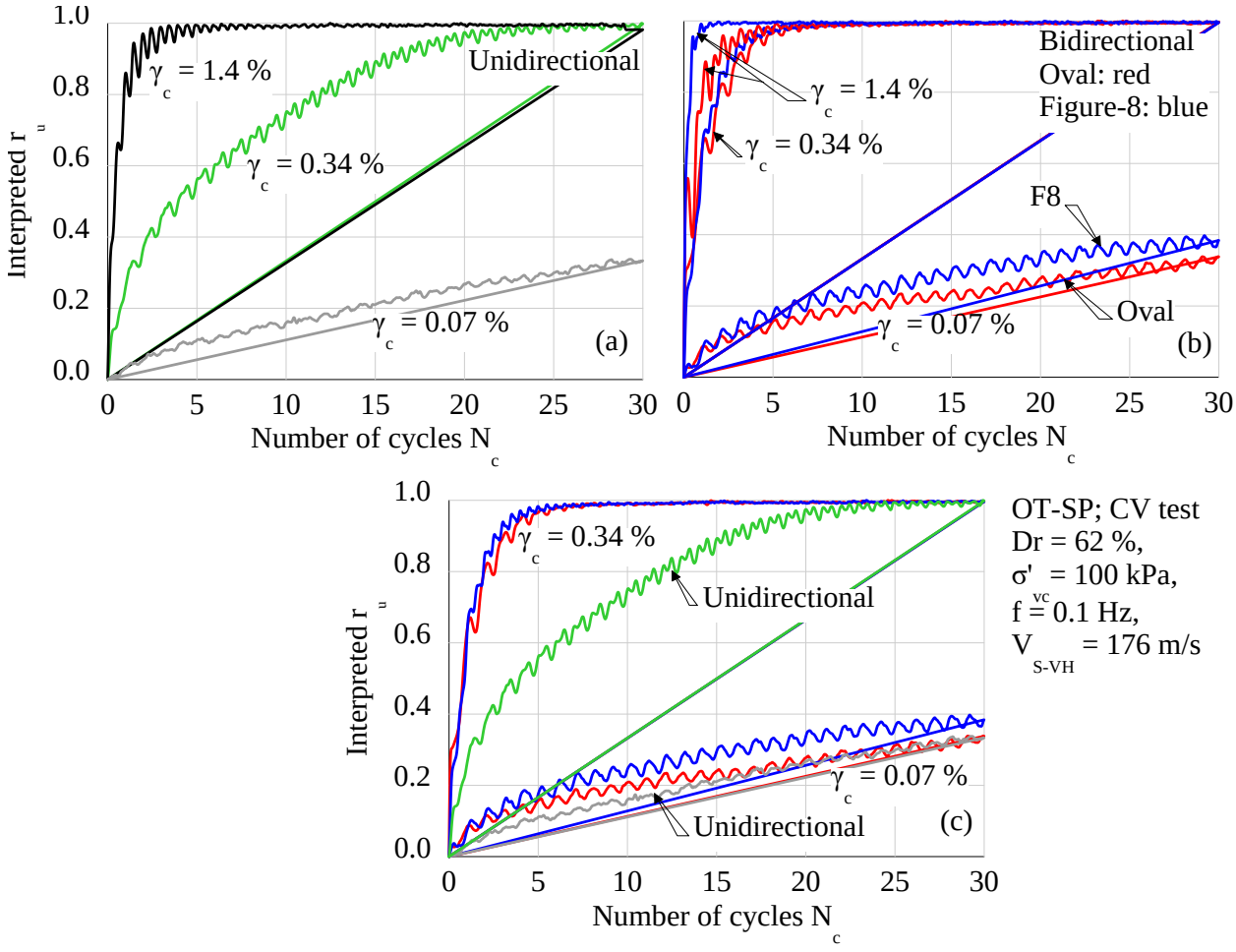

Figure 4-32 Interpreted porewater pressure ratio in medium dense Ottawa OT-SP sand under (a), (c) unidirectional, (b), (c) oval and figure-8 loading illustration the effect of shear strain amplitude and bidirectional loading.

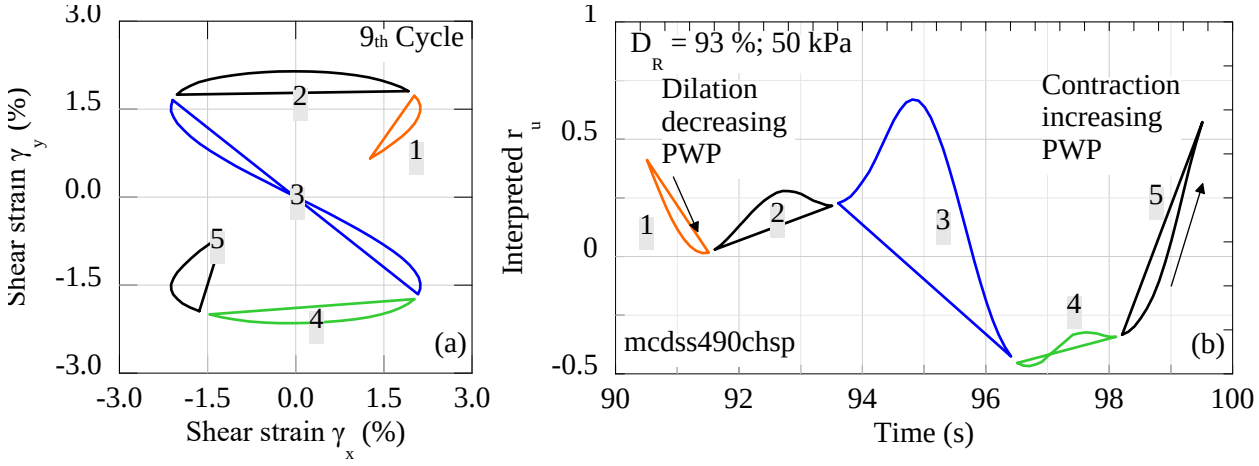

Figure 4-33 (a) Shear strain path and (b) interpreted porewater pressure ratio with time in very dense Ottawa OT-SP sand (D_R 93 %) illustrating contractive and dilative tendencies of the soil under bidirectional constant volume loading.

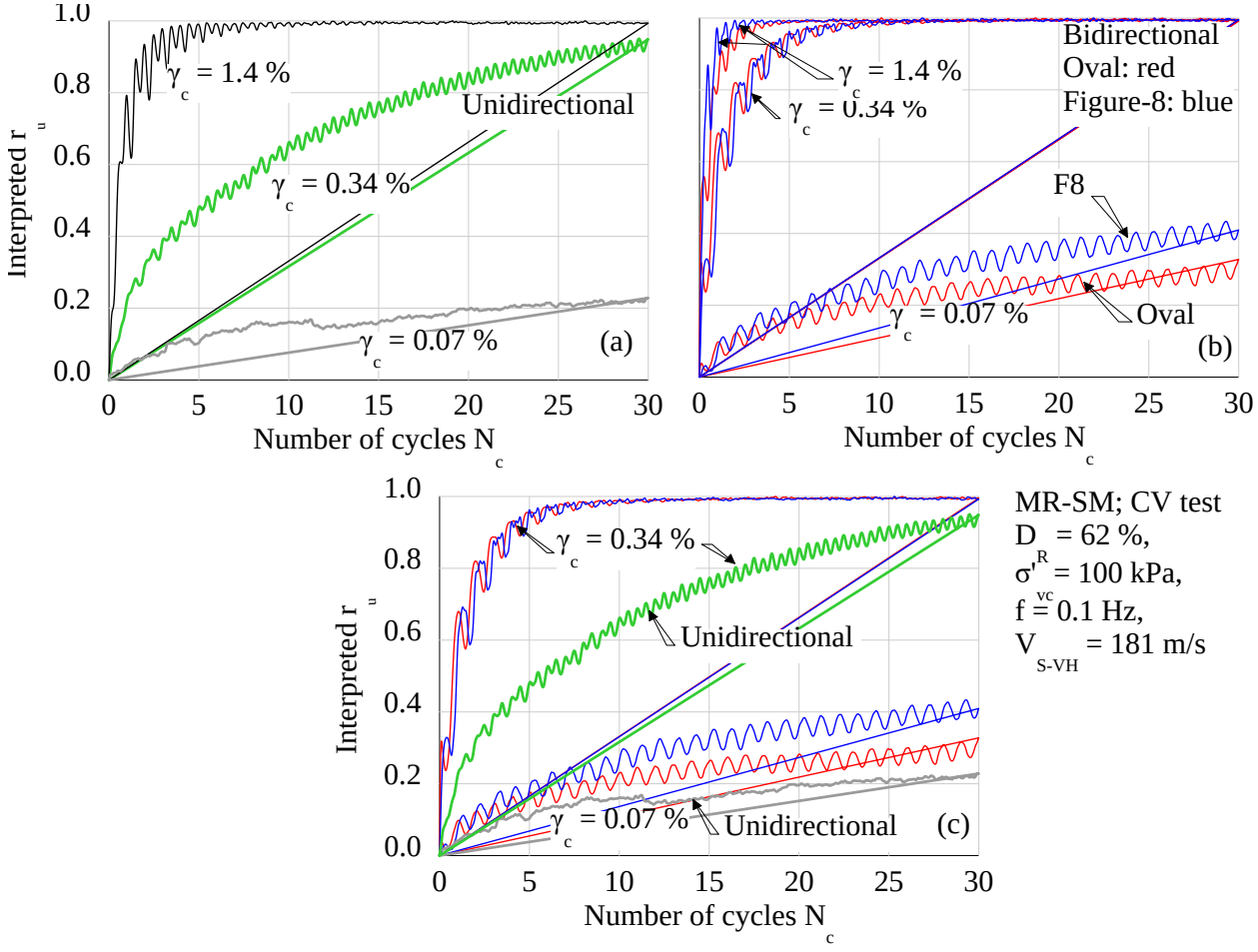

Figure 4-34 Interpreted porewater pressure ratio in medium dense LabMix SW-SM sand (FC = 9 %) under (a), (c) unidirectional, (b), (c) oval and figure-8 loading illustration the effect of shear strain amplitude and bidirectional loading.

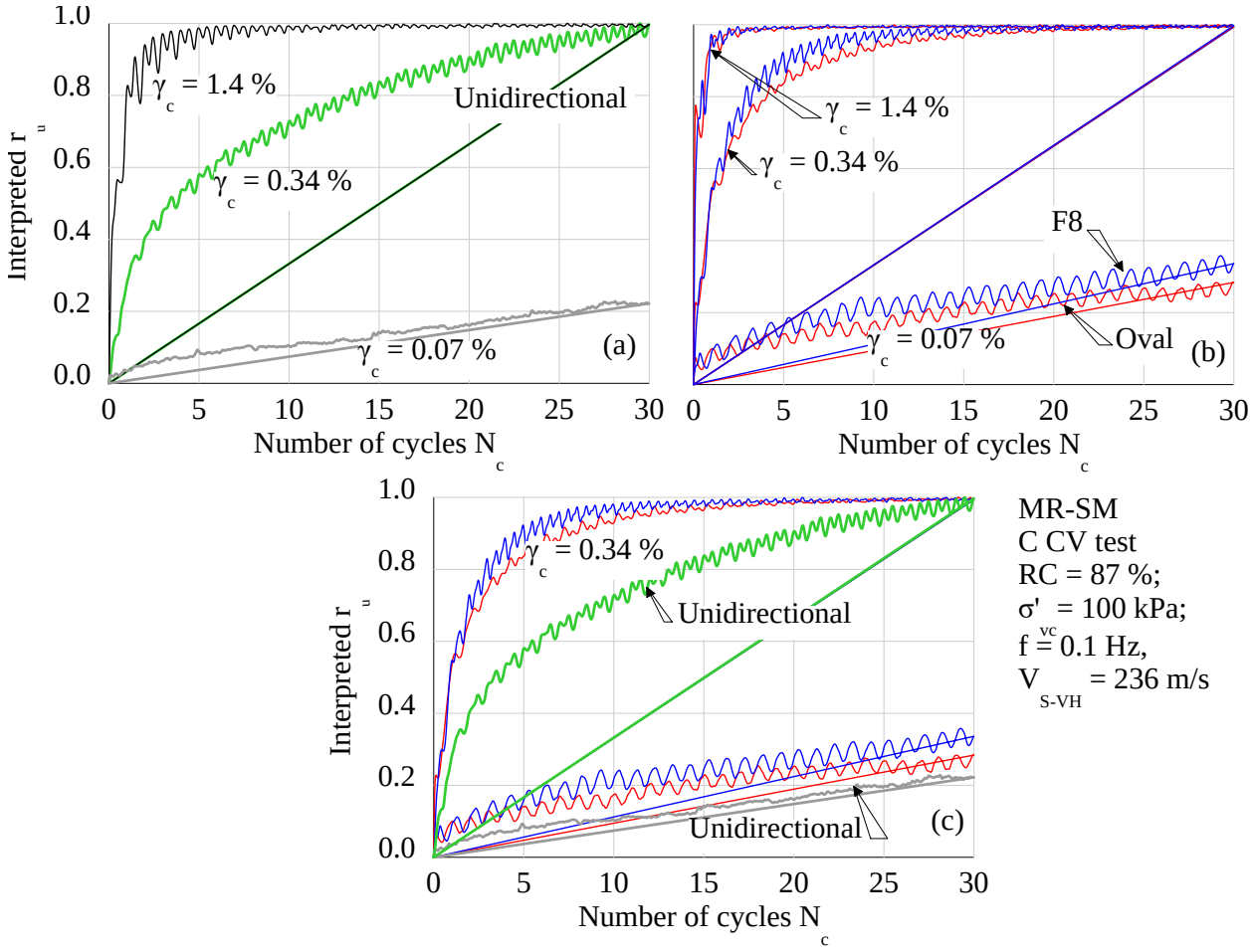

Figure 4-35 Interpreted porewater pressure ratio in medium dense Mississippi River MR-SM sand (FC = 30 %) under (a), (c) unidirectional, (b), (c) oval and figure-8 constant volume loading illustration the effect of shear strain amplitude and bidirectional loading.

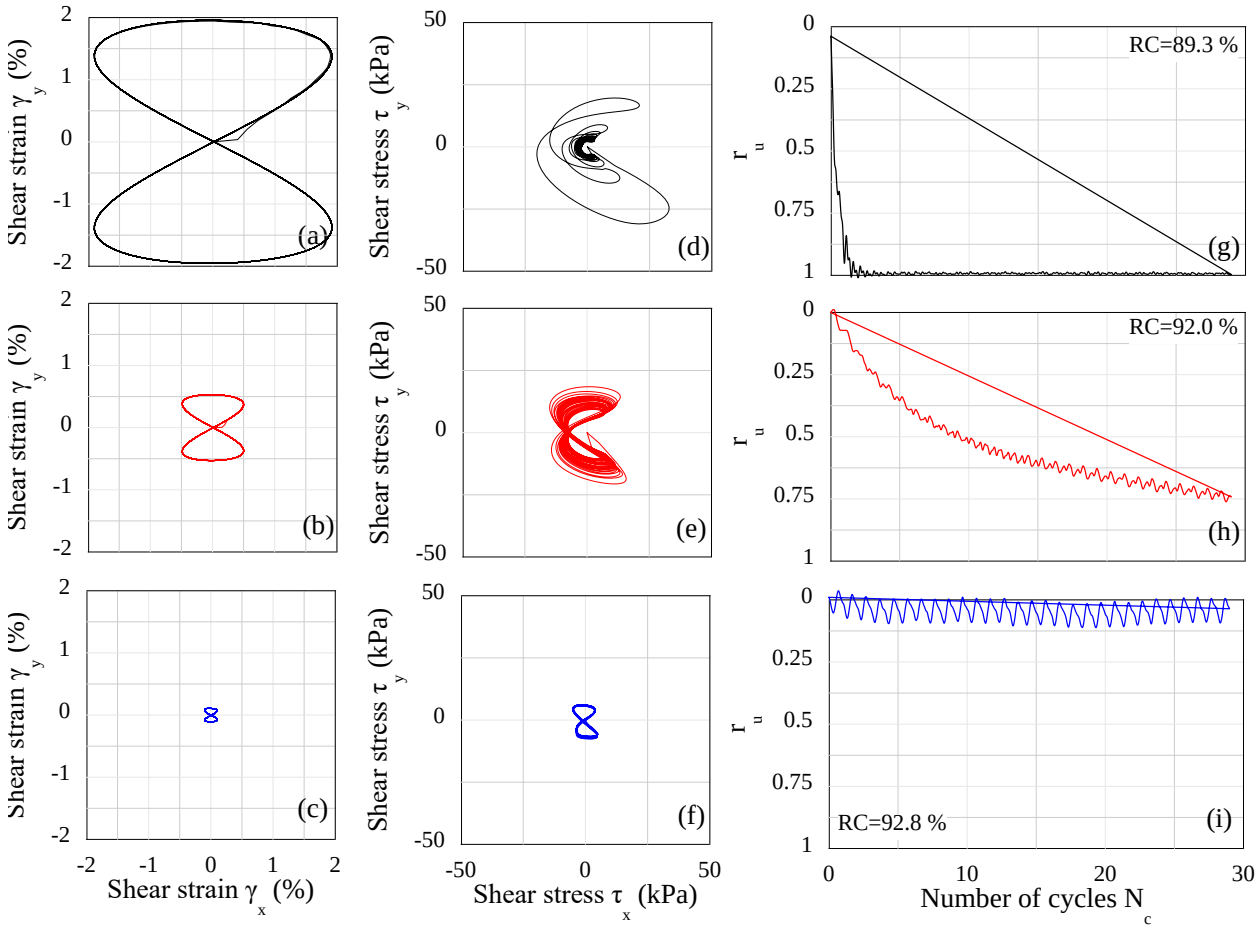

Figure 4-36 Figure-8 tests on medium dense Mississippi River Gulf of Mexico MRGM-SC sand illustrating the effect of shear strain amplitude: (a), (b), (c) shear strain; (d), (e), (f) shear stress; and (g), (h), (i) interpreted porewater pressure ratio.

To quantify the effect of bidirectional loading on excess porewater pressure, this report uses a multidirectionality factor (MDF r_u). Here, MDF r_u is the r_u under bidirectional loading normalized with the volumetric strain under equivalent unidirectional loading (comparable γ_c, density, overburden pressure, sample preparation method). MDF r_u varying with the number of cycles and average MDF r_u for 15 to 25 loading cycles is presented in Figure 4-37. The multidirectionality factor ranges from about 1 to 3 and decreases with increase in the number of cycles and increase in the shear strain amplitude. At a shear strain amplitude of 2 %, average MDF r_u is 1 for 15 to 25 loading cycles, because both the unidirectional and bidirectional loading liquefies (r_u = 1) the soil. This observation is discussed in greater detail under the centrifuge results section.

Since the excess porewater pressure reflects the volume change tendency of the soil, it follows that the reconsolidation volumetric strain should follow the same behavior. This is shown in Figure 4-38 which illustrates reconsolidation volumetric strain under unidirectional and bidirectional loading conditions for all the tested soils. Reconsolidation volumetric strain increases with the shear strain amplitude and is higher for bidirectional loading with respect to unidirectional cyclic loading. Here, ε_{vr} is higher for oval and figure-8 loading. Ishihara and Yamazaki (1980) observed that to induce the same shear strain in a sand sample, a bidirectional cyclic shear stress of about 0.7 times that of the unidirectional cyclic shear stress is required. Therefore, under equivalent cyclic shear stress, the

bidirectional loading would induce higher shear strain than unidirectional loading, and therefore result in higher volumetric strains.

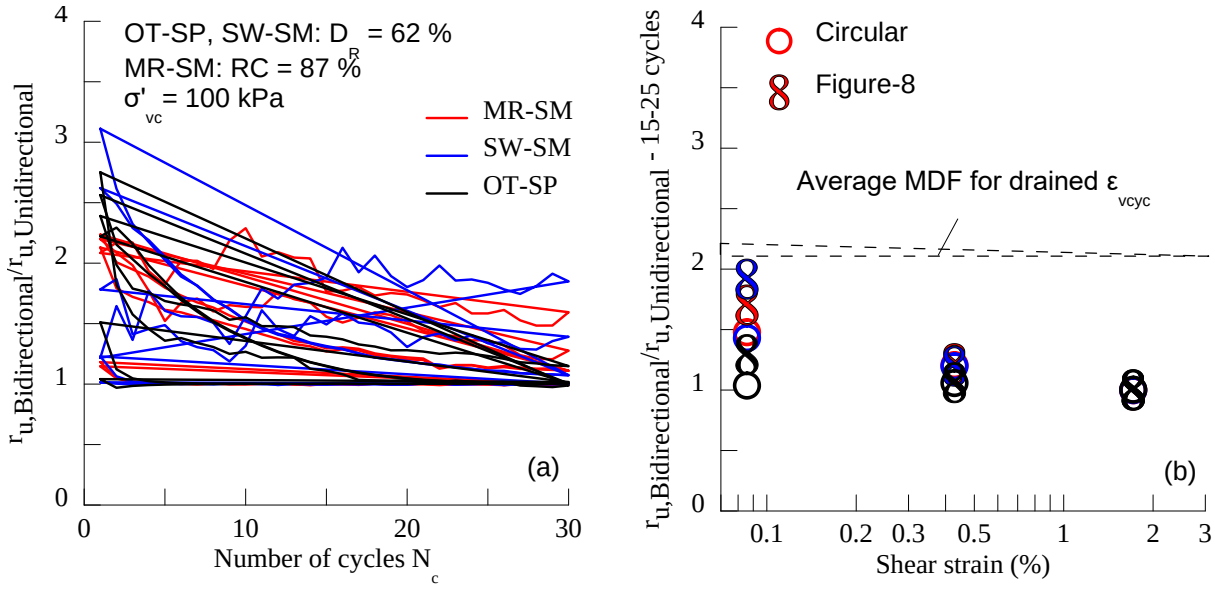

Figure 4-37 Multidirectionality factor for porewater pressure from the I-mcDSS constant volume tests on medium dense sands with (a) number of cycles, (b) shear strain amplitude.

4.5.3 Confinement

For the same relative density, soil and cyclic shear strain amplitude, the reconsolidation volumetric strain increases with an increase in confinement. This is illustrated in Figure 4-39 for unidirectional I-mcDSS constant volume tests on the Ottawa OT-SP sand. This observation might appear counter intuitive since it has been observed in the field that settlement reduces with depth (Cetin et al. 2009). This is because in the field the shear strain also generally decreases with greater depth. However, at the same shear strain amplitude and same density, at higher effective stress, higher porewater pressures are generated in the soil. Following cyclic loading, higher porewater pressure dissipation leads to higher volumetric strain accumulation. This was observed in unidirectional cyclic tests on granular material conducted by Lee and Albaisa (1974), Hussein and Stewart (1994), Wu (2002) and, Kammerer (2002).

4.6 Conclusions from Constant Volume Element Testing

The primary conclusions from constant volume element testing are summarized below:

1. Similar to drained volumetric strain, the reconsolidation volumetric strain is independent of the loading frequency for a range of 0.1 – 1 Hz for the OT-SP, SW-SM, and MR-SM.
2. The higher the porewater pressure dissipated during reconsolidation, higher the reconsolidation volumetric strain, for both unidirectional and bidirectional loading. Thus, for the same porewater pressure ratio at two different depths, the soil at the lower depth will undergo more reconsolidation volumetric strain. These findings are similar to observations by Wu (2002) from unidirectional direct simple shear tests on Monterey sand.
3. For the same depth, and same porewater pressure developed, higher shear strain causes higher reconsolidation volumetric strain.
4. Higher density causes lower reconsolidation volumetric strain.

5. Porewater pressure under bidirectional loading is about twice the porewater pressure under unidirectional loading for lower shear strains (< 0.3 %), when liquefaction does not occur. If shear strains are large enough to cause liquefaction for both the unidirectional and bidirectional loading cases (e.g. for shear strain about 2 %), the multidirectionality factor for porewater pressure becomes 1.
6. As observed under drained shearing, the loading path influences the volumetric response of the soil. Figure-8 loading paths with a greater degree of strain reversal with respect to the oval or circular loading path, results in slightly higher porewater pressure development.

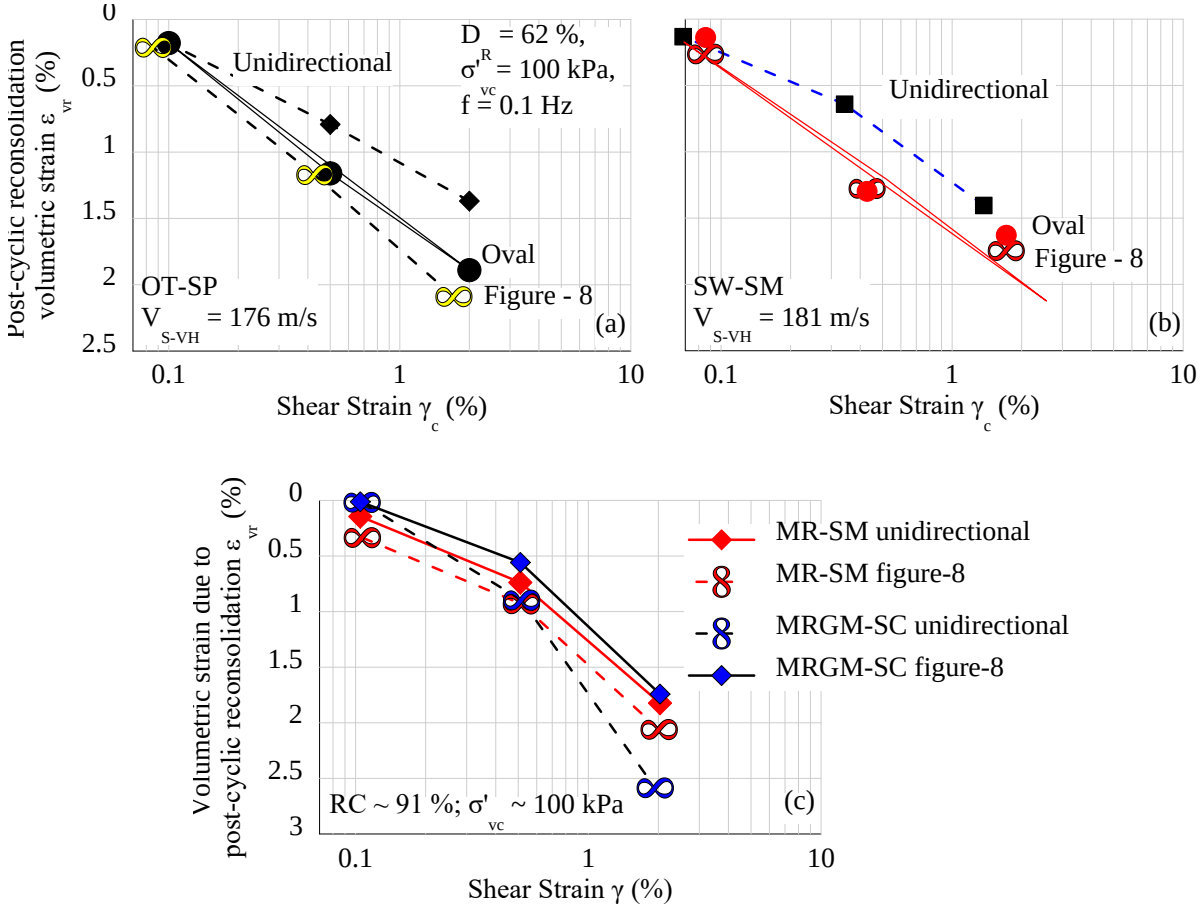

Figure 4-38 Post-cyclic reconsolidation volumetric strain under unidirectional and bidirectional oval and figure-8 loading from I-mcDSS constant volume tests on medium dense: (a) OT-SP; (b) SW-SM; (c) MR-SM and MRGM-SC.

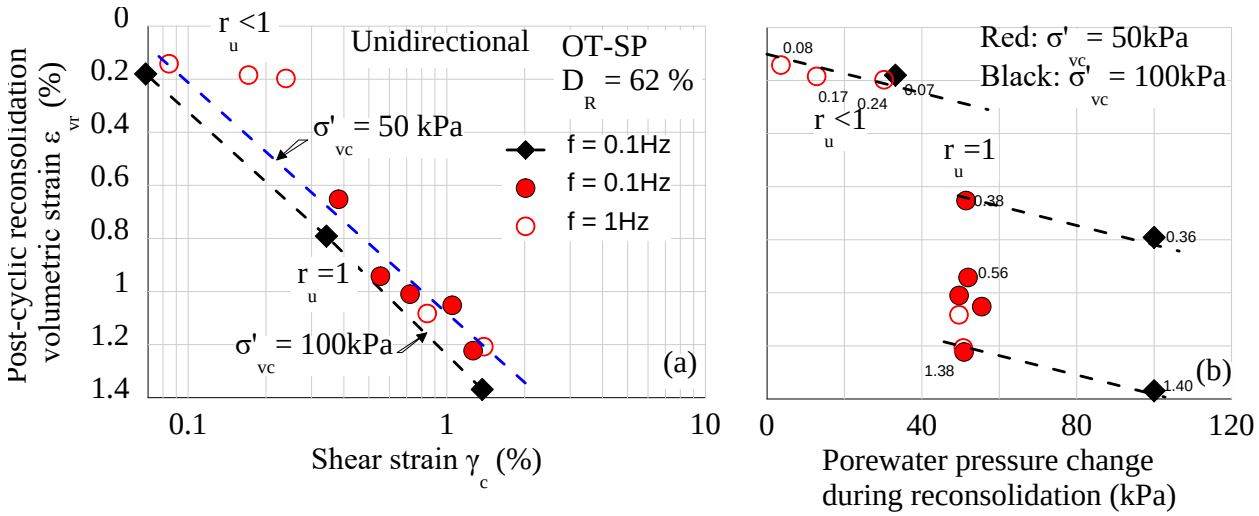

Figure 4-39 Post-cyclic reconsolidation volumetric strain under unidirectional loading at different confinements from I-mcDSS constant volume tests on medium dense OT-SP sand as a function of: (a) shear strain; and (b) porewater pressure change during reconsolidation. The numbers beside the symbols in (b) indicate shear strain.

4.7 Free-field volumetric strain under unidirectional and bidirectional centrifuge tests

Although a large database of drained and undrained cyclic element tests are available (including tests performed in this study), there are few dynamic centrifuge tests available to assess sand behavior under multi-directional loading, and available tests were performed on loose sands (Su and Li 2003; Su 2005). In this study, the authors describe the behavior of thick, saturated, dense sand profiles subjected to a unique set of unidirectional (1D) and bidirectional (2D) broadband motions of varying intensities to assess both shear and volumetric response under free-field conditions. Combined with 1D centrifuge tests on dense sands performed by others (Adalier 1996; Elgamal et al. 2001; Montoya 2012), we used the results from the 1D and 2D dynamic centrifuge tests to validate shear response from model amplification factors extracted from various centrifuge tests. Using data from the dynamic centrifuge tests and multi-directional cyclic simple shear tests, multi-directionality factors for excess porewater pressure (PWP) generation and volumetric strains were found to vary considerably with increasing maximum excess PWP. Additionally, we compare energy-based intensity measures (Arias and Housner intensities) with vector peak shaking parameters (e.g., PGA, PGV) to capture both volumetric and excess PWP generation under multidirectional earthquake loading.

Near-field and structure (i.e., soil-structure interaction) volumetric strains have been increasingly studied in the last twenty years using dynamic centrifuge tests. Based on Yoshimi and Tokimatsu (1977), Liu and Dobry (1997) normalized near-field settlements by liquefiable soil thickness from a centrifuge test series. While this normalization exhibited some trends with normalized building width, Dashti et al. (2010) later performed a series of centrifuge tests on loose Nevada sand and showed that this normalization is not appropriate for thin liquefiable layers. Dashti et al. (2010) argued that the major source of near-field settlement resulted from ratcheting of the structure rather than solely volumetric strains of the soil. Dashti et al. (2010) described this ratcheting as deviatoric strains, and suggested that dynamic rocking of the structure increased volumetric settlements.

In summary, few dynamic centrifuge tests have been conducted for dense sand deposits, both under multidirectional earthquake loading and with a presence of a high-bearing pressure structure (i.e., q_b > 350kPa). In addition, the tests described above measured settlements only at the ground surface, making it impossible to define volumetric strain profiles. As described below, the set of centrifuge tests performed in this study address these shortcomings.

4.7.1 Intensity measures (IM) for unidirectional and bidirectional centrifuge tests

Intensity measures (IM) have long been used to describe earthquake effects on structures. These IM include vector peak (e.g., PGA, PGV) and cumulative (e.g., Housner Intensity, Arias Intensity) shaking parameters. Pioneering work by Housner (1952) correlated spectral velocity intensity (Sv), also known as Housner intensity, to damage observed in structures for historical earthquakes in California. Housner intensity (HI) is defined as:

$$HI_{x,y} = \int_{0.1}^{2.5} S_{v_{x,y}}(\xi = 0.05, T)dT \tag{4-88}$$

where T = period (s). Arias (1970) proposed an IM as the sum of the energy released per unit of weight of a linear oscillator, now termed Arias intensity (Ia), defined as:

$$Ia_{x,y} = \frac{\pi}{2g}\int_{0}^{tmax} a(t)_{x,y}^{2}dt \tag{4-89}$$

where g = acceleration of gravity and a(t) is acceleration at time, t. These IMs are computed for both 1D and 2D motions so that total energy from multi-directional shaking can be correlated to both volumetric and excess PWP generation under multidirectional earthquake loading.

4.7.2 Dynamic shear response of saturated dense sand

4.7.2.1 Response spectra (1D and 2D motions)

Figure 4-40(a) and (b) shows soil response spectra for motion M12-2D, X, and Y (see Table 3-28) in Test Dr95FF. Ground motions were amplified in both the X- and Y-directions. In general, minor differences are observed between 1D and 2D response spectra for the X- and Y-directions. Figure 4-40(c) and (d) present residuals computed between the 1D and 2D response spectra (in log-log space) for each X- and Y-direction acceleration time history as:

$$Residual\ S_a = \log\left(\frac{\mathrm{Sa,\ 2Dx\ or\ y}}{\mathrm{Sa,\ 1Dx\ or\ y}}\right)) \tag{4-90}$$

where Sa is spectral acceleration. Positive residuals indicate that $Sa_{,1D}$ was less than $Sa_{,2D}$, while negative values indicate that $Sa_{,1D}$ was greater than $Sa_{,2D}$. Figure 4-40(c) and (d) also shows that the mean residuals for all motions at all depths are essentially zero for periods up to 10 seconds. This result indicates that the dynamic shear behavior is not affected significantly by multidirectional shaking. Note that two individual ground motion recordings exhibited residuals of slightly greater than +0.25 in the Y-direction (Figure 4-40d). These motions were recorded at near-surface accelerometers AX4-2 and AX3-2 during motion M9-2D (at 30g), and likely resulted from out-of-range acceleration readings that caused excessive high frequency components. Although these two recordings did not dramatically affect the mean residuals, they were excluded from the mean residual calculations.

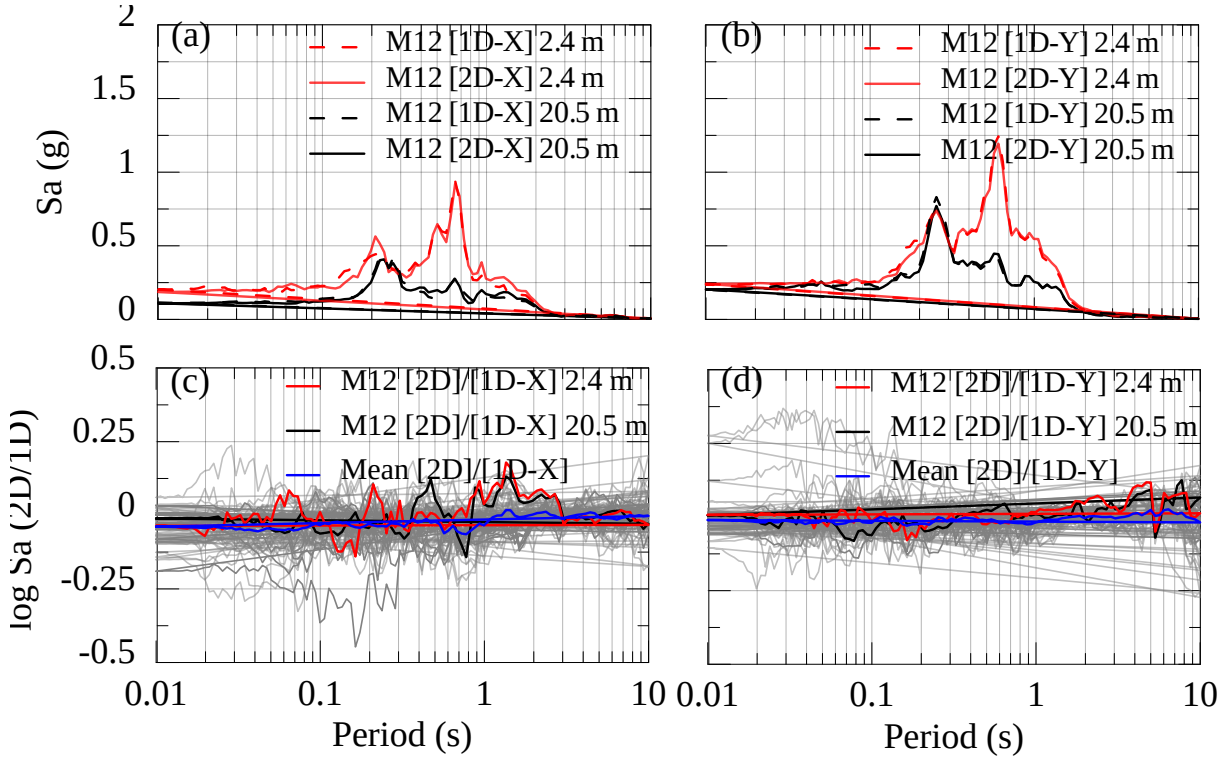

Figure 4-40. Response spectra comparisons for test Dr95FF. (a) Input and surface response motion M12, X-direction; (b) input and surface response motion M12, Y-direction; (c) ratio of spectral accelerations (2D to 1D, X-direction) for all 60g and 30g motions, highlighting motion M12, X-direction; and (d) ratio of spectral accelerations (2D to 1D, Y-direction) for all 60g and 30g motions, highlighting motion M12, Y-direction.

4.7.3 Ground Motion Amplification

Figure 4-41 summarizes the ground motion amplification that occurred between the base of the model to the near-surface accelerometer in terms of intensity measures PGA, PGV, Sa(T=0.3s), Sa(T=1.0s), Ia, and HI in test Dr95FF for all 1D and 2D ground motions at centrifuge accelerations of 60g and 30g. These measured values were supplemented with values measured in centrifuge tests performed by Adalier (1995), Elgamal et al. (2001), and Montoya (2012). Adalier (1995) studied liquefaction mitigation techniques of different soil improvement methods using centrifuge experiments that also included free-field experiments on a saturated dense Nevada sand (D_{Ro}~70%). Elgamal et al. (2001) summarized the seismic response of a 5 m to 20 m-thick saturated very dense Nevada sand (D_{Ro}~100%). Montoya (2012) studied the effect of bio-mediated soil improvement on the dynamic response of sands that included free-field centrifuge experiments on a dense (non-treated) saturated Ottawa 50-70 sand (D_{Ro}~85%).

As shown in Figure 4-41, amplification of acceleration-based intensity measures [PGA, Sa(T=0.3s), and Ia] generally was more variable than amplification of velocity-based intensity measures (PGV and HI). While acceleration-based intensity measures showed greater variance, computed amplification ratios still were relatively consistent, with 5th, 50th, and 95th percentile values (respectively) of 1.0, 1.5, and 3.6 for PGA; 0.9, 1.4, and 3.6 for Sa(T=0.3s); and 0.9, 3.8, and 7.6 for Ia. Computed amplification ratios for velocity-based intensity measures were quite consistent,

with 5th, 50th, and 95th percentile values (respectively) of 1.0, 1.7, and 2.9 for PGV; and 1.2, 1.7, and 2.6 for HI.

The acceleration-based intensity measures (Figure 4-41 a, c, and e) exhibited noticeable differences in amplification factors among the measured datasets, particularly in the Elgamal et al. (2001) dataset. Upon closer inspection, the velocity-based intensity measure amplification data suggest that input motions with low velocity-based intensities (e.g., low HI; Figure 4-41f) tended to generate higher acceleration-based intensity measure amplification factors.

4.7.4 Dynamic volumetric response of saturated dense sand

4.7.4.1 Excess PWP generation

Figure 4-42 presents acceleration in X- and Y-direction, excess PWP ratio and settlement time histories measured in test Dr95FF for input motion M12. Maximum excess PWP (Δu_{max}) measured during 2D shaking was 200% larger than Δu_{max} values measured during the corresponding 1D [X and Y] shaking events (Figure 4-42c). Su (2005) studied the effect of multidirectional sinusoidal cyclic loading on PWP generation and settlements of a 16-m thick (prototype scale) uniform Toyoura sand (D_{Ro} ~ 40%). His results showed up to approximately 20% increase in Δu_{max}. The PWP factor measured in this study for dense sands is consistently larger than that suggested by Su (2005) for loose sand (See Figure 4-43) because Δu_{max} in loose sand is limited by the triggering of liquefaction, thus relatively strong 2D shaking can produce only a limited increase over similar intensity 1D shaking. In contrast, Δu produced in dense sands commonly are significantly lower than that required for liquefaction.

Figure 4-46(a) shows multi-directional factors extracted from centrifuge test Dr95FF. Su (2005) and El-Shafee (2016) estimated ratios of 2D to 1D recorded excess PWP ratios ($r_u = \Delta u/\sigma'_{vo}$) as a function of 1D excess PWP ratios. Generally, multi-directional factors ranged from 1 to 4, increasing with decreasing $r_{u,1D}$. The scatter decreases as $r_{u,1D}$ approaches 1. Further, as Δu_{max} reaches a limiting value (i.e., the soil approaches level-ground liquefaction, $r_{u,1D}$ ~ 1), the ratio of $r_{u,2D}/r_{u,1D}$ approaches unity and becomes independent of multi-directional loading.

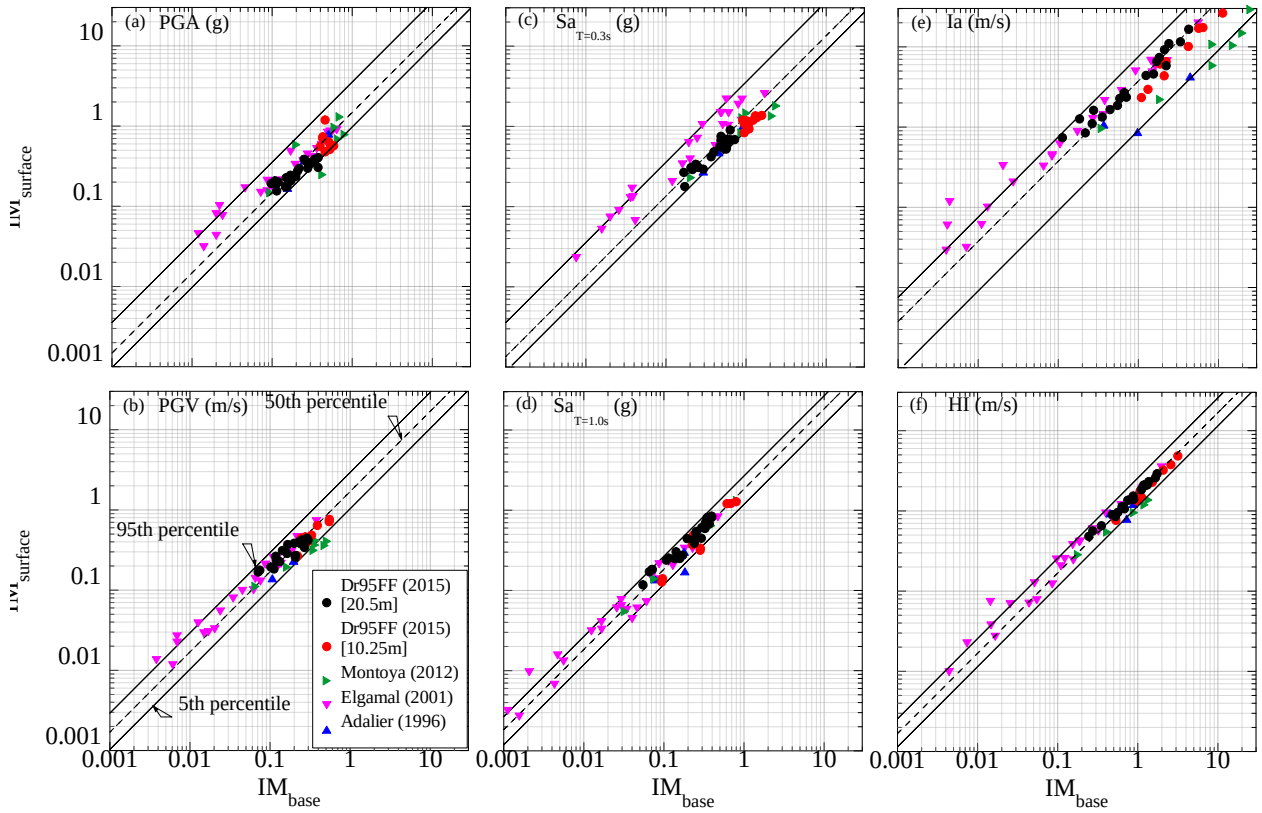

Figure 4-41. Comparison of input and near-surface intensity measurements in centrifuge tests. (a) PGA; (b) PGV; (c) Sa(T=0.3s); (d) Sa(T=1s); (e) Arias intensity; and (b) Housner intensity

This observed soil response was supported by incorporating $r_{u,2D}/r_{u,1D}$ time histories from unidirectional and bidirectional stress-controlled tests (Ishihara and Yoshimine 1992; Wu 2001; and Kammerer 2002) as well as strain-controlled (Section 4.4.2) undrained simple shear tests performed on Monterey sand (D_{Ro}~48-64 %) (e.g. Wu 2001; Kammerer 2002) , Fuji river sand (D_{Ro}~93 %) (Ishihara and Yoshimine, 1992) and Ottawa 40/70 (D_{Ro}~53-70 %) (Section 4.4.2), all poorly graded sands (SP). This also highlights that multi-directionality factors can approach unity in element tests on dense sand specimens if the cyclic loading is sufficiently intense to liquefy the soil. As observed in Figure 4-48, r_u values were less than 0.25 and decreased with depth, but were consistently larger in 2D events. Overall, r_u values in 2D events generally were less than 0.5, as shown in Figure 4-49(a).

From M12-2D, X and Y motions profile, as shown by Figure 4-48, a relationship between the initial shear wave velocity, seismic energy demand (e.g. Housner Intensity) and excess PWP ratio could be selected at various depth locations from 1D and 2D motions. This was done for all motions imposed on the 20.5 m thick profile. Results are shown as a cyclic response summary in Figure 4-49(a) for 1D and 2D motions from both the Dr95FF test and the Su (2005) test performed on Dr40% Toyoura sand in terms of layered-recorded maximum excess PWP ratio, both with respect to Vs. Although there are limited 2D data for loose sands, it appears that the difference between 1D and 2D maximum excess PWP ratios are more pronounced for dense sands compared to loose sands. It is also evident in Figure 4-49(a) that only a small level of energy is necessary to cause significant PWP generation in loose sands compared to dense sands, as illustrated by the Housner intensity isolines (i.e., equal HI values).

4.7.5 Settlements

Figure 4-48 (a) shows profiles of measured settlement plate displacements (with fitted settlement profiles), computed vertical strains, maximum r_u, Arias and Housner intensities, PGA, and PGV for input motion M12-1D-X, 1D-Y, and 2D. We note that nearly all of settlements occurred during shaking, and as expected, reconsolidation settlements in the dense sand were minor. Using this settlement profile, vertical strains (ε_v) were calculated as shown in (4-91) and (4-92) by estimating the post-shaking thickness of the "tributary" layer for each settlement plate as:

$$\varepsilon_v(\%) = \frac{Hpre_{,i} - Hpost_{,i}}{Hpre_i}.100 \tag{4-91}$$

$$Hpost_{,i} = Hpre_{,i} - \delta_i + \delta_{i+1} \tag{4-92}$$

where $Hpre_{,i}$ = pre-shaking layer i thickness; $Hpost_{,i}$ = post-shaking layer i thickness; δ_i = cumulative settlement of layer i (settlement plate reading); and δ_{i+1} = cumulative settlement of layer i+1 (settlement plate reading). For Su (2005), settlement was measured only at the surface, therefore, vertical strains with depth were estimated using the Kim (2017) model, which uses sublayer PWP recordings and compressibility estimates to compute settlements and vertical strains with depth.

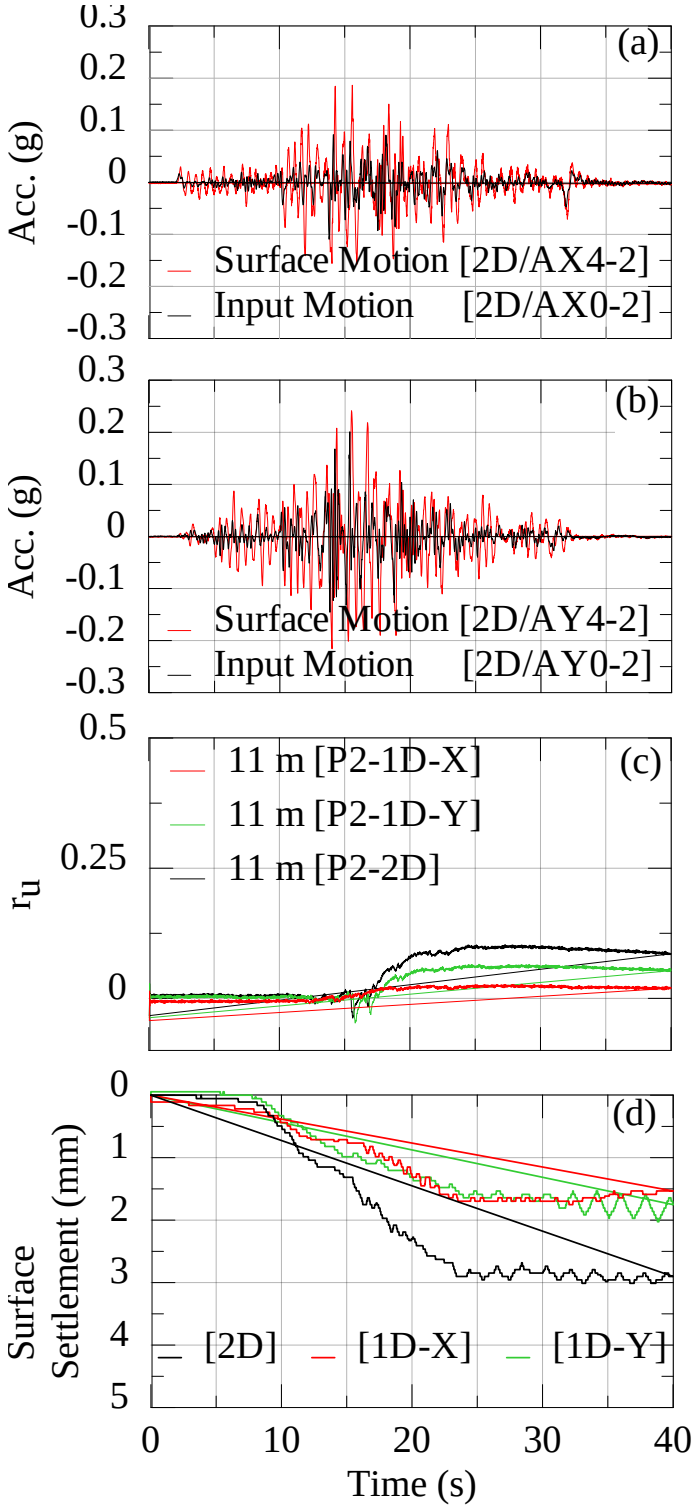

Figure 4-42. Instrument time histories for input motion M12-X, Y, and 2D from test Dr95FF. (a and b) recorded input and surface acceleration time histories; (c) excess PWP at 11m depth; and (d) free-field surface settlement.

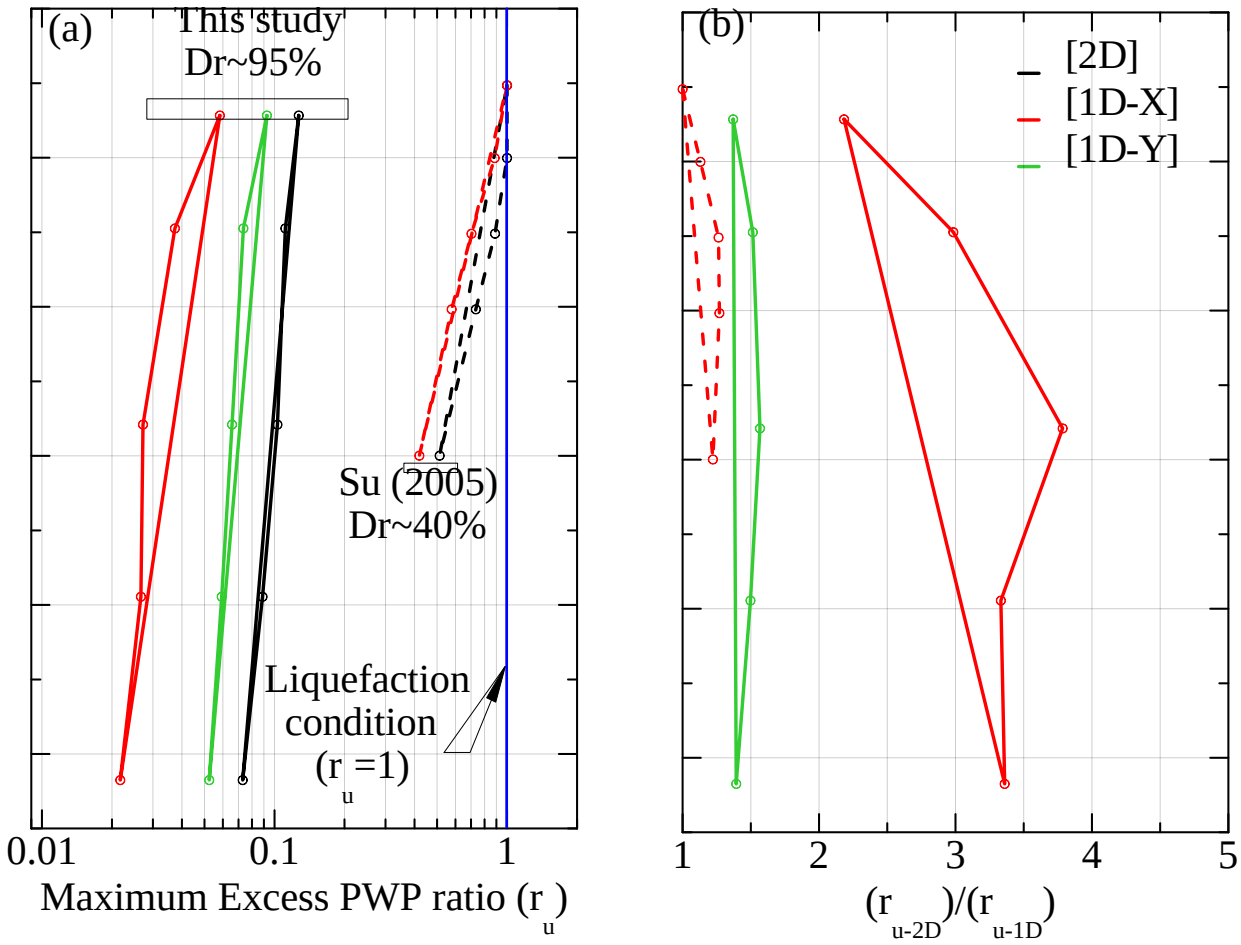

Figure 4-43. (a) Maximum excess PWP ratio versus depth M12-X, Y, and 2D from test Dr95FF and Su (2005). (b) Computed r_u multidirectional factors from Dr95FF and Su (2005).

As illustrated in Figure 4-48, estimated vertical strains were larger in the upper 10m, although all strains were small (<0.1%) during this motion. Similarly, as observed in Figure 4-42(d) and Figure 4-48(a), 2D shaking induced an increase in settlements up to 110% compared to 1D [X- and Y-direction] shaking. This factor is much larger than that reported by Su (2005) and El-Shafee (2016) for loose sands, where 2D shaking caused about 12% to 20% larger settlement than 1D shaking. Lastly, we note that nearly all of settlements occurred during shaking, and as expected reconsolidation settlements in the dense sand were minor.

4.7.6 Relative Density and Shear Wave Velocity

All 30 motions were applied sequentially during test Dr95FF, with 21 motions imposed first at 60g and followed by the remaining 9 imposed at 30g. At 60g, the model was excited using 1D motions (X then Y), followed by 2D motions listed in Table 3-28. After spinning down to 30g, the model was shaken with X, Y, and 2D motions listed in Table 3-29. After each shaking event, excess PWP was allowed to dissipate, bender element readings were obtained, and the next motion was input. The average relative density at the beginning of each shaking event (starting from D_{Ro}~95%) was computed via settlements measured by two vertical LVDTs placed at the surface (Figure 4-44) which yielded a final average relative density of 102% at the end of the 30g shaking series.

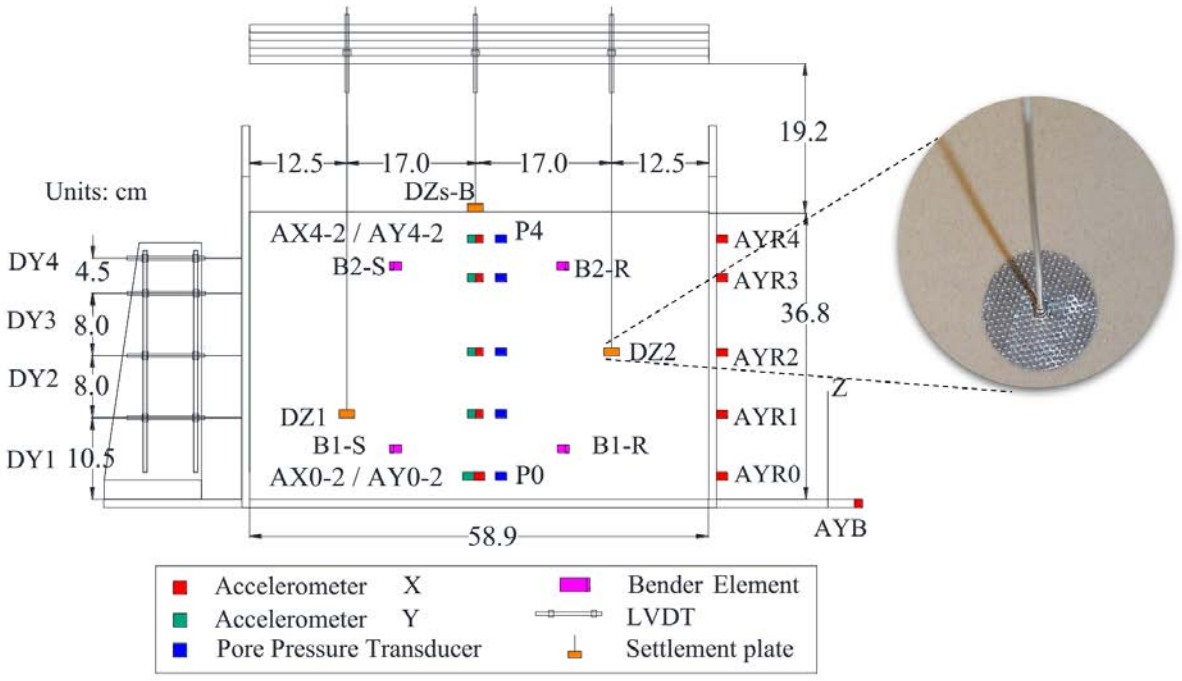

Figure 4-44. Detailed instrumentation layout for test Dr95FF.

Figure 4-45(a) shows changes in measured Vs during spin-up and after each shaking event, and Figure 4-45(b) Vs changes measured by bender elements in tests where $Vs_{,HH}$ and $Vs_{,HV}$ were recorded. Overall, each shaking event densified the sand and increased Vs. However, two high-intensity motions (M13-1DY at 60g and M5-1DX at 30g) induced a relatively small decrease in Vs at the shallow bender element location (B2). In contrast, the lower pair of bender elements (B1) exhibited increases in Vs after each event.

For comparison, Figure 4-45(a) includes Vs profiles for D_{Ro} = 95%, 100%, and 102% computed using the Menq (2003) correlation. Here, measured $Vs_{,HH}$ for D_{Ro}~ 95% were smaller than that computed using Menq (2003) for D_{Ro} = 95%. Interestingly, the measured $Vs_{,HH}$ at the end of all shaking events (at 60g) with D_{Rf} ~ 102% was much larger than that computed using Menq (2003) for D_R = 102%. In contrast, initial $Vs_{,HV}$ values agreed closely with values computed using Menq (2003) for D_R = 95%. After all shaking events, $Vs_{,HV}$ was slightly larger than that computed using Menq (2003) for D_R = 102%. This comparison suggests that the increase in Vs is influenced not only by the change in D_R but also by the change in effective mean stress (e.g., increase in effective horizontal stress) induced by shaking. This effect was also reported by Youd and Craven (1975), Zhu and Clark (1995), and Mesri and Vardhanabuthi (2007) in element tests. Figure 4-45 also illustrates that the change in measured Vs is larger at shallower depth. This result suggests that, as expected, volumetric strains were larger at lower effective vertical (or effective mean) stresses. Thus, as discussed subsequently, the average D_{Rf} ~ 102% is not constant throughout the profile. This result could also suggest that cyclic shear strains were larger at shallower depths.

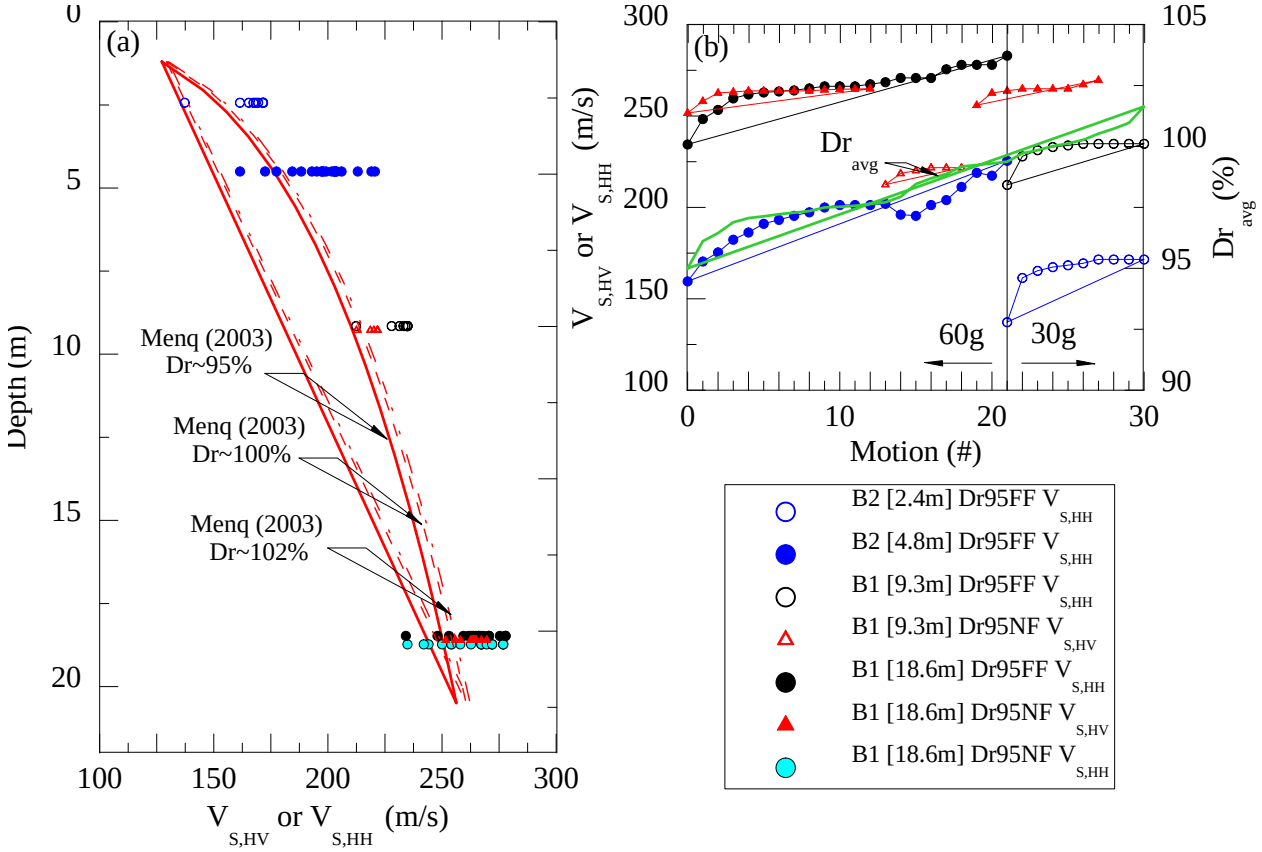

Figure 4-45. (a) Recorded Vs,HV and Vs,HH histories (with respect to depth) for 60g and 30g input motion series (depths are prototype scale; some depths are offset slightly for clarity); and (b) evolution of Vs at depths of 4.8 m and 18.6 m compared to evolution of average D_R.

4.7.7 Multi-directional factors for volumetric response

The r_u data from the centrifuge tests described above can be combined with laboratory 1D and 2D undrained cyclic direct simple shear (cDSS) test data to evaluate a multi-directionality factor for excess PWP ratio (MDF-r_u = $r_{u,2D}/r_{u,1D}$).Figure 4-46(a) presents MDF-r_u values computed from stress- and strain-controlled undrained cDSS performed on Monterey sand (D_{Ro} ~ 48-64%; Wu 2001; Kammerer 2002), Fuji river sand (D_{Ro} ~ 93%; Ishihara and Yoshimine 1992), and Ottawa 40/70 (D_{Ro} ~ 53-70%; Bhaumik 2017). Similarly, Figure 4-46(b) presents MDF-r_u values computed from centrifuge test Dr95FF and well as centrifuge tests performed by Su (2005) and El-Shafee (2016). For comparison, Figure 4-46(b) includes the approximate bounds of the laboratory element test data from Figure 4-46(a). These figures present MDF-r_u values as a function of excess PWP ratios generated during 1D shaking, and both data sets show similar trends. Generally, MDF-r_u values computed from both laboratory cyclic element tests and dynamic centrifuge tests ranged from 1 to 4, with MDF-r_u approaching unity as $r_{u,1D}$ approaches unity. The scatter in MDF-r_u from both laboratory element tests and dynamic centrifuge tests also decreases as $r_{u,1D}$ approaches unity. Essentially, as $r_{u,1D}$ approaches its limiting value of unity (i.e., the soil approaches level-ground liquefaction), the ratio of $r_{u,2D}/r_{u,1D}$ also must approach unity because the value of r_u cannot exceed unity.

This observation is illustrated further in Figure 4-46(c) which presents MDF-r_u as a function of factor of safety against triggering of liquefaction (FS_{liq}). The FS_{liq} for centrifuge cases was estimated by

computing the cyclic resistance ratio (from comparing the CRR and CSR) following Idriss and Boulanger (2008) procedure. The estimated CSR with depth used the near surface PGA measured during tests and propagated down via the r_d factor as proposed by Idriss and Boulanger (2008). Again, as the soil approaches liquefaction ($FS_{liq} \rightarrow 1$), MDF-r_u approaches unity and can be computed as follows.

$$\mathrm{MDF_{ru}} = 2\left(1 - e^{(1-1.7FS_{liq})}\right) \geq 1. \quad (4\text{-}93)$$

Using the same centrifuge test data sets as used in Figure 4-46(b), multidirectional factors for vertical strain (MDF-ε_v = $\varepsilon_{v,2D}$/ $\varepsilon_{v,1D}$) as a function of $r_{u,1D}$ and FS_{liq} are shown in Figure 4-47a and Figure 4-47b, respectivley. Again, available data suggest that MDF-ε_v tends to decrease as the soil approaches liquefaction ($r_{u,1D}$ and $FS_{liq} \rightarrow 1$), but MDF-ε_v remains > 1.0. While the soil has low r_u values (i.e., FS_{liq} > ~2), vertical strains from bidirectional shaking can be approximately superimposed, resulting in an average MDF-ε_v ~ 2. However, unlike MDF-r_u, as the soil approaches liquefaction, bidirectional shaking still influences the shear strains experienced by the soil. As shear strain closely relates to vertical strain (Ishihara and Yoshimine 1992), MDF-ε_v remains > 1.0 for all values of $r_{u,1D}$ and FS_{liq}. As shown for $FS_{liq} \leq 1.0$, MDF-ε_v is approximately 1.3, and increases as FS_{liq} increases, as:

$$\mathrm{MDF_{\varepsilon v}} = 2\left(1 - e^{(1-2FS_{liq}^{0.5})}\right) \geq 1.3 \quad (4\text{-}94)$$

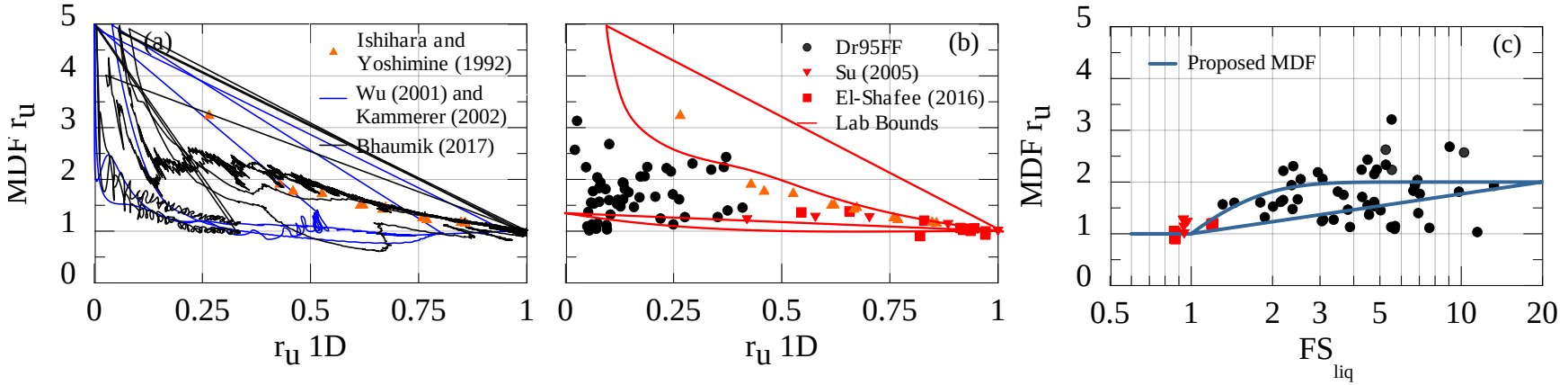

Figure 4-46. Multi-directional factors extracted from and laboratory and centrifuge tests as a function of $r_{u,1D}$ for: (a) strain and stress controlled undrained simple shear tests $r_{u,2D}/r_{u,1D}$ (b) Dr95FF (2015) and Su (2005) tests $r_{u,2D}/r_{u,1D}$; and (c) Dr95FF (2015) and Su (2003) tests $\varepsilon_{v,2D}/\varepsilon_{v,1D}$.

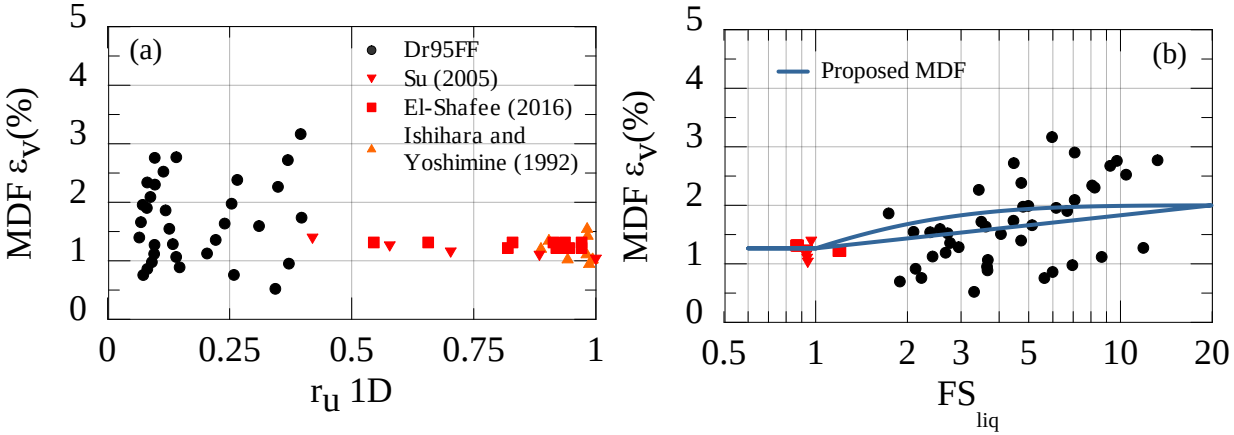

Figure 4-47. Multi-directional factor ε_v ($\varepsilon_{v,2D}/\varepsilon_{v,1D}$) extracted from centrifuge and laboratory tests. (a) Centrifuge tests from Dr95FF, Su (2005), El-Shafee (2016) and laboratory tests from Ishihara and Yoshimine (1992) in terms of $r_{u,1D}$; (b) centrifuge test Dr95FF and tests from Su (2005) and El-Shafee (2016) in terms FS_{liq}, respectively.

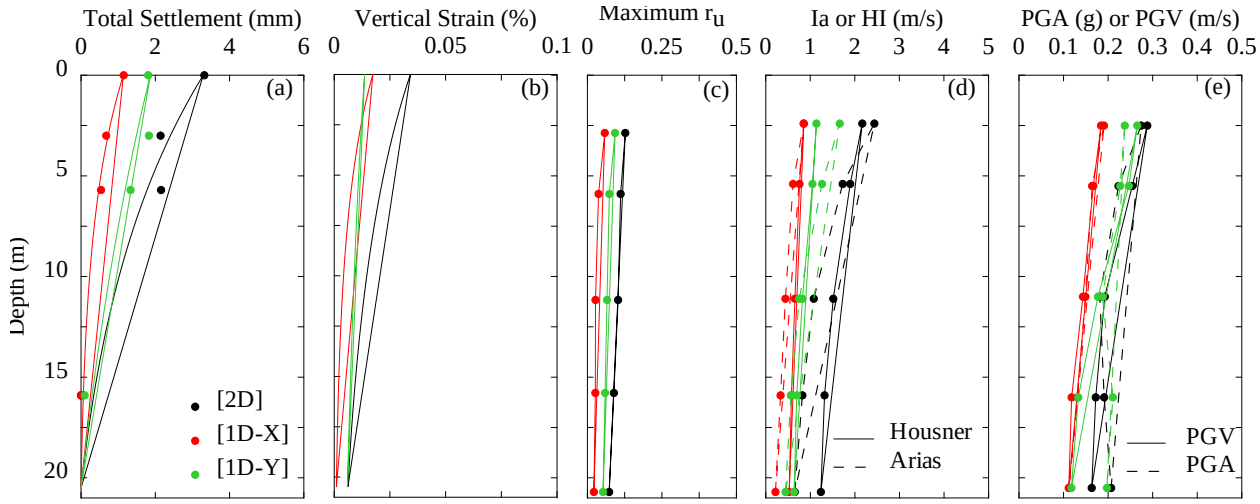

Figure 4-48. Recorded or computed profiles for input motion M12-X, Y, and 2D in test Dr95FF. (a) Settlement; (b) vertical strain;(c) excess pore water pressure ratio; (d) Arias and Housner intensities; and (e) PGA and PGV.

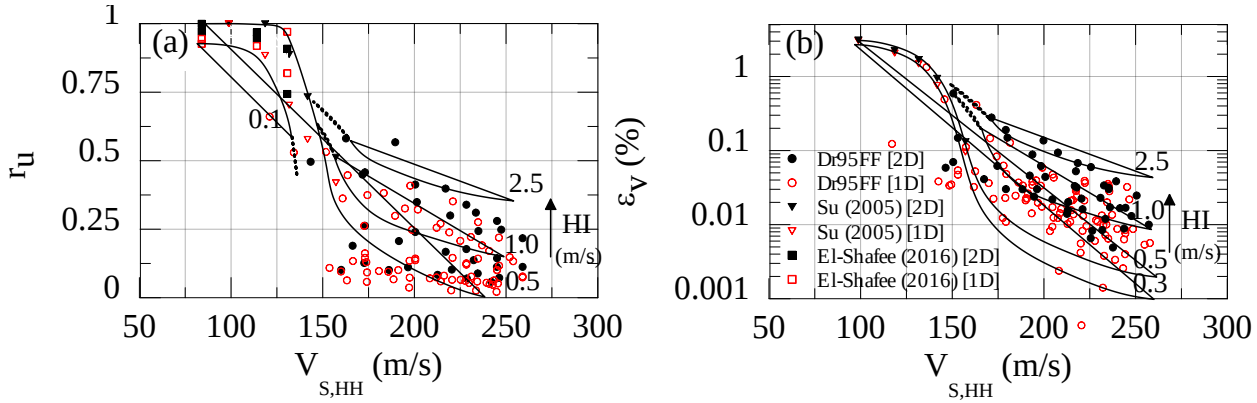

Figure 4-49. Cyclic response for 2D and 1D motions from Dr95FF test and Su (2005) test on Dr40% Toyoura sand in terms of (a) maximum excess PWP ratio and shear wave velocity; (b) shaking-induced volumetric strain and shear wave velocity.

4.7.8 Intensity measures (IM) to capture multi-directionality effects

Figure 4-49(a) summarizes the maximum r_u data from for all PPT and all 1D and 2D motions applied during test Dr95FF (20.5 m thick profile; D_{Ro} ~ 95%), during tests by Su (2005; 16 m thick profile; D_{Ro} ~ 40%), and during tests by El-Shafee (2016; 7 m thick profile; D_{Ro}~ 45%) in terms of $V_{S,HH}$ and HI. For Dr95FF, $V_{S,HH}$ were recorded throughout the test. In contrast, since $V_{S,HH}$ recordings were not available from Su (2005) and El-Shafee (2016), initial $V_{S,HH}$ for these cases were estimated using 90% of Menq (2003) $V_{S,VH}$ estimates. A difference of 10% between $V_{S,HH}$ and $V_{S,VH}$ (Menq's correlation) was found in Dr95FF tests as shown in Figure 4-45(a). Figure 4-49(a) includes approximate Housner intensity isolines to illustrate trends from the data. Several observations can be made from these data: (1) as $Vs_{,HH}$ increases and the soil becomes stiffer and denser (i.e., the resistance to PWP generation and liquefaction increases), the maximum r_u decreases; (2) as shaking intensity (i.e., seismic demand) increases, maximum r_u increases; (3) as $V_{S,HH}$ decreases and the soil becomes looser, only a small level of energy is needed to generate significant PWP; and (4) although there are limited 2D data for looser sands, it appears that the difference between 1D and 2D maximum r_u values are more evident for dense sands (where r_u values are lower) compared to loose sands (where r_u values are higher). Although these relations are illustrated in terms of HI, other intensity measures illustrate similar trends.

Similarly, Figure 4-49(b) summarizes sublayer vertical strains for all 1D and 2D motions applied during test Dr95FF, during tests by Su (2005) in terms of $V_{S,HH}$ and HI. Again, Figure 4-49(b) includes approximately Housner intensity isolines to illustrate trends from the data. Like the r_u data, these data highlight several key points: (1) as $V_{S,HH}$ increases and the soil becomes denser, the maximum ε_v decreases; (2) as shaking intensity (i.e., seismic demand) increases, maximum ε_v increases; (3) as $Vs_{,HH}$ decreases and the soil becomes looser, only a small level of energy is needed to generate significant ε_v; and (4) although there are limited 2D data for looser sands, it appears that the difference between 1D and 2D maximum ε_v values are more evident for dense sands (where ε_v values are lower) compared to loose sands (where ε_v values are higher). Again, although these relations are illustrated in terms of HI, other intensity measures illustrate similar trends.

To further explore the role of shaking intensity (and particular intensity measures) on multi-directionality, Figure 4-50 and Figure 4-51 summarize r_u and ε_v data, respectively, from test Dr95FF in terms of $V_{S,HH}$ and various IMs. To simplify the presentation of the data, V_S and the intensity measure (IM) are combined on the x-axis of the plots. Again, shear wave velocity is used to characterize soil density, stiffness, and resistance to PWP generation while seismic demand (i.e., shaking intensity) is characterized in terms of both vectored peak parameters (PGA and PGV) and energy based parameters (Arias and Housner intensities).

These figures demonstrate that energy-based IMs such as total Arias and Housner intensities (where the intensities are summed from the individual X- and Y-directions) reasonably capture multi-directional shaking effects, as there is a nearly unique relationships for the combined 1D and 2D r_u and ε_v data. In contrast, the vectored peak IMs (PGA and PGV) do not capture as well the multi-directional shaking effects, as there are larger differences between the trend lines for the 1D and 2D data for the vectored peak IMs than for the energy-based IMs. However, other than for ε_v and vectored peak PGA, the effects of multi-directional shaking are relatively small when evaluated in this format.

We note that some differences between the 1D and 2D relationships are expected even with energy-based IMs as the intensity measures do not capture the effects of stress path and principal stress rotation. For example, multi-directional cDSS tests performed by Kammerer (2002) and

Bhaumik et al. (2017) have shown that a figure-8 stress path causes greater PWP increase and vertical strain than an oval stress paths for the same maximum cyclic shear strain amplitude, specimen density, and consolidation stress. Despite this limitation, as shown in Figure 4-50 and Figure 4-51, the IMs with units of velocity (PGV and HI) provide dimensionless indices when normalized by V_S, and these relationships exhibit less scatter than their acceleration-based counterparts (PGA and Ia). As such, these dimensionless indices may be valuable for semi-empirical models to estimate r_u and vertical strain.

Figure 4-50 and Figure 4-51 summarize the effects of multi-directionality on maximum excess PWP ratios and volumetric strains, respectively. To simplify the presentation of the data, Vs and the intensity measure (IM) are combined on the x-axis of the plots. Shear wave velocity is used to characterize soil resistance to PWP generation (Figure 4-50) and soil stiffness (Figure 4-51) while seismic demand is characterized in terms of both vectored peak parameters (PGA and PGV) and energy based parameters (Arias and Housner intensities).

These analysis demonstrate that energy-based IMs such as Arias and Housner intensities capture multi-directionality effects, as there is a nearly unique relationship for the combined 1D and 2D data. In contrast, the vectored peak IMs (PGA and PGV) do not capture multidirectional loading effects as there are two distinct relationships for 1D and 2D data. However, we note that the differences between the 1D and 2D relationships are smaller for the vectored peak PGV and vectored peak PGA, and in both cases the 1D and 2D relationships are quite similar as Vs/PGA and Vs/PGV increases. These ratios increase as the soil becomes very stiff or as seismic demand becomes very small. Furthermore, some differences between the 1D and 2D relationships are expected even with energy-based IMs as the intensity measures do not necessarily capture the effects of stress path and principal stress rotation. Multi-directional cyclic direct simple shear (mc-DSS) tests performed by Kammerer (2002) and Bhaumik et al. (2017) have shown that figure-8 stress paths cause greater PWP increase and volumetric strain than oval stress paths at the same cyclic shear strain amplitude. Despite this limitation, as shown in Figure 4-50 and Figure 4-51, the IMs with units of velocity (PGV and HI) provide dimensionless indices with Vs and yield significantly less scatter in the correlations. As such, these formats may be valuable for semi-empirical models to estimate r_u and volumetric strain.

4.7.9 Summary

The section presents a unique series of dynamic centrifuge tests that examine the effects of multidirectional loading on shear and volumetric soil behavior of a saturated, dense, clean, uniformly-graded Ottawa sand. The centrifuge models were subjected to a suite of unidirectional (1D) and bidirectional (2D) motions under free-field conditions and exhibited significant ground motion amplification, non-uniform porewater pressure (PWP) generation, and non-uniform vertical strains with depth.

In general, only minor differences were observed between 1D and 2D response spectra for the X- and Y-directions, indicating that dynamic shear response of dense sands is not significantly affected by multi-directional earthquake loading. Response spectra computed using 1D nonlinear total (GQ/H) and effective (GQ/H+u) site response analyses reasonably agreed with recorded response spectra from 2D centrifuge data. Furthermore, GQ/H and GQ/H+u analysis yielded similar results for the dense sand tested here with a level of ru < 0.5. NL analyses yielded good agreement with several other intensity measures (IMs): peak ground acceleration (PGA), peak ground velocity (PGV), Arias intensity (Ia), and Housner intensity (HI). Therefore, this illustrates that 1D NL site response analysis can be used in practice to estimate shear response under multidirectional loading conditions for dense sands. Test results with model velocity based amplification (e.g., PGV and

Housner intensities) showed significantly less scatter and more consistent trends than shear amplification based on spectral accelerations at short periods (e.g., PGA and $Sa_{0.3}$).

Multi-directionality factors for both excess porewater pressure (MDF-r_u = $r_{u,2D}$/ $r_{u,1D}$) and vertical strains (MDF-ε_v = $\varepsilon_{v,2D}$/ $\varepsilon_{v,1D}$) ranged from 1 to 4. The multi-directionality factors observed in the dynamic centrifuge tests performed in this study were supported by limited dynamic centrifuge tests performed by others and by multi-directional cyclic direct simple shear tests under both drained and undrained conditions performed by other investigators. As expected, these multi-directionality factors are much larger than those proposed for loose sands by previous researchers. The differences result chiefly from loose sands reaching limiting values of both excess PWP and vertical strain at moderate strain amplitudes. When these limiting values are reached, the effects of multidirectional loading are eliminated. A relationship between multidirectional factors for PWP and vertical strains and FS_{liq} was proposed to be used in practice. A multidirectional factor for r_u and vertical strain of 2.0 is found to be reasonable for FS_{liq} > 2.0. In contrast, as soil approaches liquefaction FS_{liq} < 2.0.multidirectional factors for r_u and vertical strains tend to a value of 1.0, although higher for vertical strains.

Regression of 1D and 2D shaking data show that velocity-based IMs (PGV and HI) better predict r_u and ε_v compared to acceleration-based IMs (PGA and Ia). Further, when used with shear wave velocity, the velocity IMs can produce dimensionless resistance-to-demand ratios and are recommended for developing semi-empirical correlations for estimating r_u and volumetric strain.

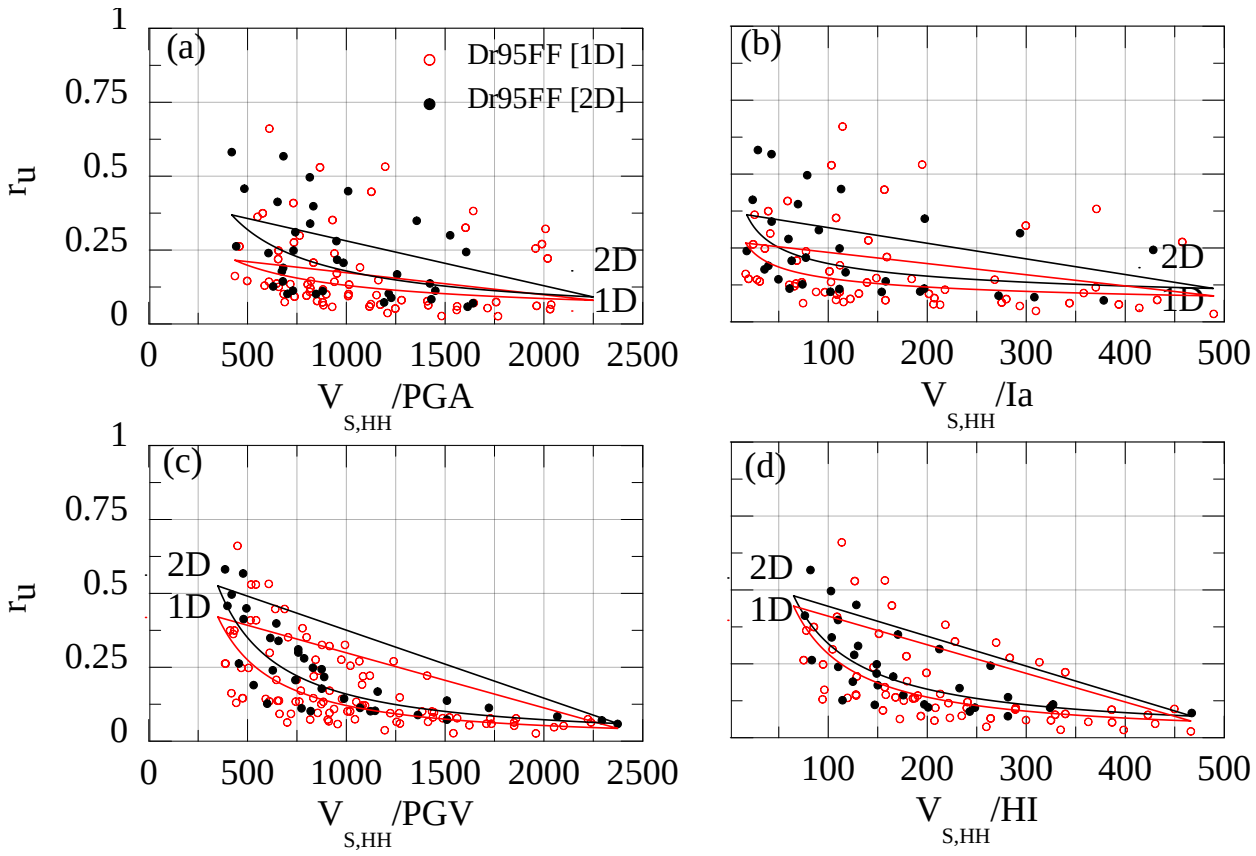

Figure 4-50. Maximum excess PWP ratio for 2D and 1D motions from Dr95FF test and normalized (a) Vs/PGA; (b) Vs/Ia; (c) Vs/PGV; and (d) Vs/HI

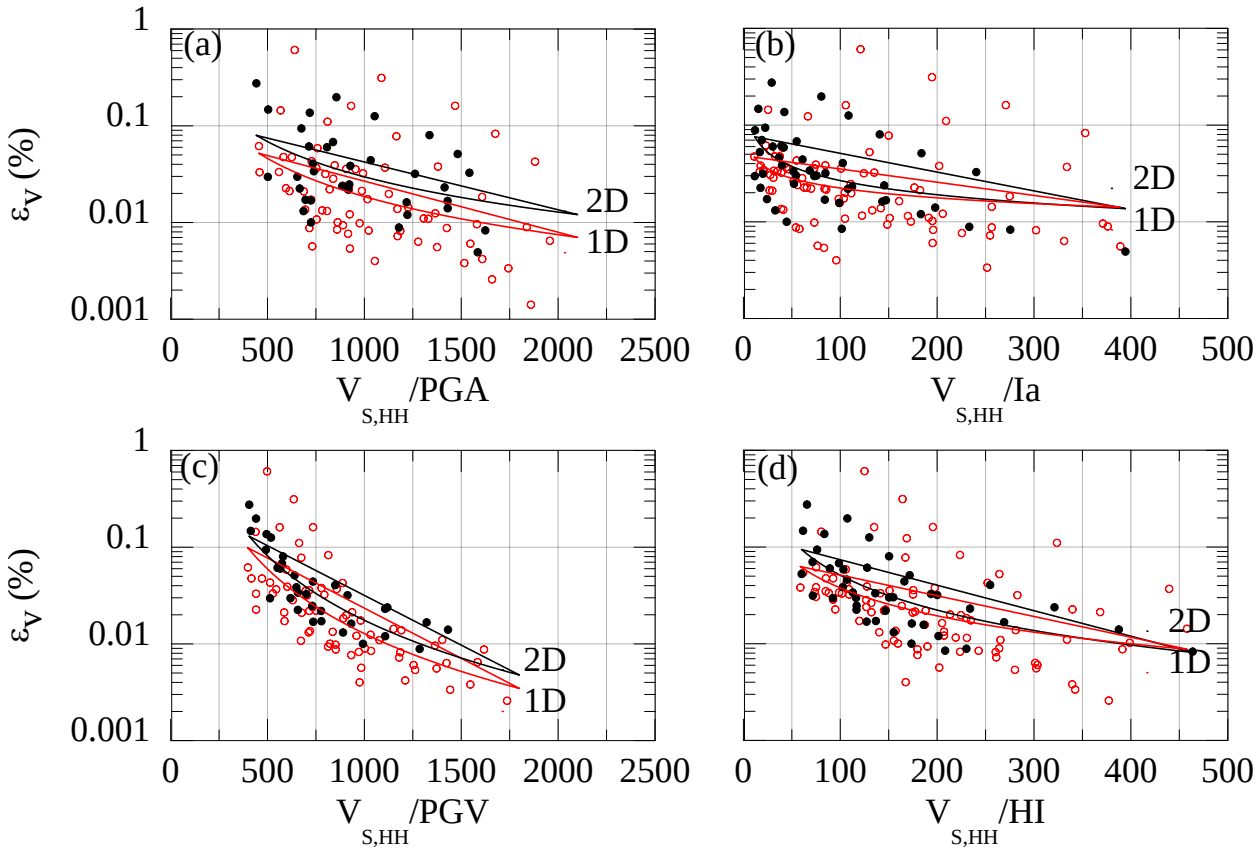

Figure 4-51. Volumetric cyclic response for 2D and 1D motions from Dr95FF test and normalized (a) Vs/PGA; (b) Vs/Ia; (c) Vs/PGV; and (d) Vs/HI

4.8 Near-field shear and volumetric response under unidirectional and bidirectional centrifuge tests

Due to the scarcity of case histories on seismic response on NPP structures in terms of shaking induced volumetric strains, a near-field test was proposed as a tool to validate the I-soil constitutive model in both shear and volumetric space. The collected near-field database is also currently used to develop simplified near-field settlements estimations for both loose and dense sands. This test involved a dense (D_{Ro} ~ 95%), saturated Ottawa sand at centrifugal accelerations of 60g and 30g. A high bearing pressure (q_b ~ 380 kPa) rigid structure was placed at the top of the model to represent a NPP structure. The following sections describes results from near-field (NF) centrifuge testing programs involving nearly rigid structures founded on dense sands deposits. The tests include a set of unidirectional (1D) and bidirectional (2D) dynamic centrifuge tests performed in this study on a thick layer (prototype thickness of 10.25 and 20.5 m) of saturated, dense (initial relative density, D_{Ro} ~ 95%), fine Ottawa sand. The testing data (see Table 4-1) also includes (1D) results from centrifuge tests performed by Montoya (2012) on dense Ottawa sand (D_{Ro} ~ 85%). The centrifuge models were excited using both broadband and sinusoidal motions with Arias intensities that ranged from 0.07 to 30 m/s. The results of the 1D and 2D dynamic centrifuge tests are discussed in terms of shear response, porewater pressure (PWP) generation and settlements. Multi-directionality factors for PWP generation and vertical strain are described based on the centrifuge data.

4.8.1 Structural loads and structure dimensions

Among NPP structures, a typical nuclear containment structure (Figure 4-52) exhibits high bearing pressures. The bearing pressure for this project was selected from those of major structures at the River Bend NPP (internal document provided by NRC). Table 4-1summarizes bearing pressures and structure dimensions for structures at the River Bend plant, with pressures ranging from 144 to 383 kPa (3 to 8 ksf). For comparison, Table 4-2 presents bearing pressures for Calvert Cliffs NPP structures, which range from 153 to 565 kPa (3.2 to 11.8 ksf) (http://pbadupws.nrc.gov/docs/ML1015/ML101580061.pdf).

The circular foundation shape typically employed for many containment structures represents an advantage for the centrifuge tests since it minimizes boundary effects when using it with the 2D circular laminar container. Furthermore, because the shape is axisymmetric, the structure will have an identical effect in both X and Y directions, so that earthquake-induced multidirectional effects can be better quantified. The physical dimensions of the model structure were limited by boundary locations. It was desired to allow settlement and bearing capacity mechanisms to develop freely within the model (both vertically and laterally). This consideration resulted in a solid steel structure (disk) with prototype dimensions of 9 m diameter by 4.85 m tall (including a depth of foundation, D_f, of 2.4m) for a centrifugal acceleration of 60g. Similarly, at 30g, prototype dimensions of 4.5 m diameter by 2.475 m tall with a foundation depth D_f of 1.2 m. Figure 4-53 shows the layout of the structure centrifuge model in prototype dimensions during 60g spinning. Also shown in Figure 4-53, structure dimensions in model scale (cm) in plan and profile view.

4.8.2 Intensity measures (IM) for unidirectional and bidirectional centrifuge tests

This model was subjected to the 27 motions (described in Section 3) calibrated during tests CTDr95FF and CTDr95NF and used in test Dr95FF, with 21 ground motions imposed at 60g and the remaining 6 imposed at 30g. Appendix C provides acceleration, velocity, displacement, relative displacement, Arias and Housner intensity time histories for each specific motion at each instrument location. Figure 4-54 summarizes the response spectra and Arias and Housner intensities for all 60g and 30g input motions, as measured within the model near the base (accelerometers AX0-2 and AY0-2). Input intensities ranged from 0.07 to 4.0 m/s for 60g and from 1.0 to 4.0 m/s for 30g motions.

As illustrated in Figure 4-55, good agreement was observed in the input ground motion intensities (i.e., Arias and Housner) of the otherwise identical free-field (Dr95FF) and near-field (Dr95NF) tests, with test Dr95FF exhibiting slightly higher input Arias intensities. During motion M1, overheating of the hydraulic actuator in the 2D-Y direction became noticeable and caused a moderate difference (~ 44%) in the input motion Arias intensity for test Dr95NF with respect to test Dr95FF. The mean error of Arias intensity for all input motions in Dr95NF (excluding M1) with respect to input motions in Dr95FF is 15%, with a range of 1.5% to 37%. This difference is within the variability of input motions typically reached for similar as built models in dynamic centrifuge testing. For example, Muszynski (2013) observed a difference up to 60% between Arias intensities of model input motions in soil centrifuge models, despite using identical input signals.

Table 4-1 Published centrifuge tests involving dense sands collected in this study

Reference	Prototype sand thickness (m)	Pre-shaking D_{Ro} (%)	Centrifugal acceleration (g)	Type of loading	Key details	Facility
Cerna-Diaz (2017)	20.5 and 10.25	95	60 and 30	1D and 2D	Structure mass (q_b~380 and 190 kPa) (28 shaking events)	RPI
Montoya (2012)	6	85	50	1D	free-field and structure mass (q_b~80 kPa) (7 shaking events)	UC-Davis

Table 4-2 Foundation bearing pressures for select structures at Calvert Cliffs and River Bend Nuclear Power Plants (Source: NRC - http://pbadupws.nrc.gov/docs/ML1015/ML101580061.pdf).

Calvert Cliffs NPP Structures	Foundation Pressure q_b (kPa)	River Bend NPP Structures	Foundation Pressure q_b (kPa)
NI Common Mat	565	Shield Building and Containment	382
Nuclear Auxiliary Building	464	Radwaste Building	287
Emergency Power Generation Building (EPGB)	153	Diesel Generator Building	192
Emergency Service Water Building (ESWB)	259	Turbine Building	144

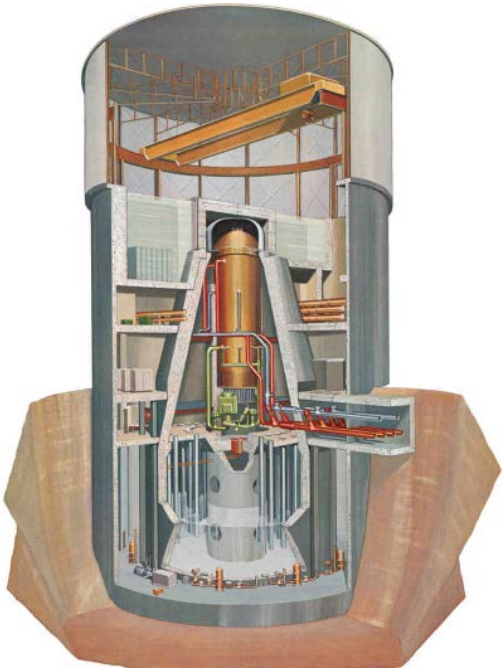

Figure 4-52. Illustration of typical nuclear power plant containment structure (Mark II Containment Structure; source: NRC - http://www.nrc.gov/reading-rm/basic-ref/teachers/03.pdf).

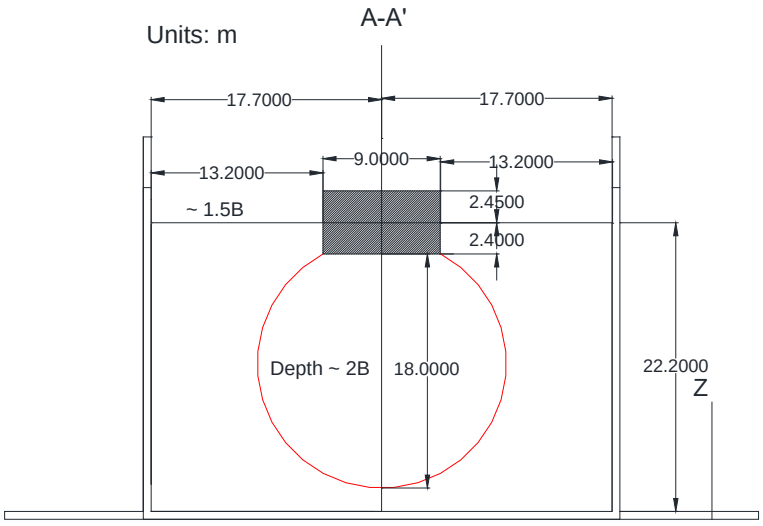

Figure 4-53. Prototype dimensions (in meters) of model cylindrical structure with a load pressure of 382 kPa (8ksf) with respect to soil model dimensions in centrifuge tests, illustrating approximate depth of Boussinesq stress distribution to where applied stress is 10% of stress applied at base of structure (2B = 2 x foundation diameter).

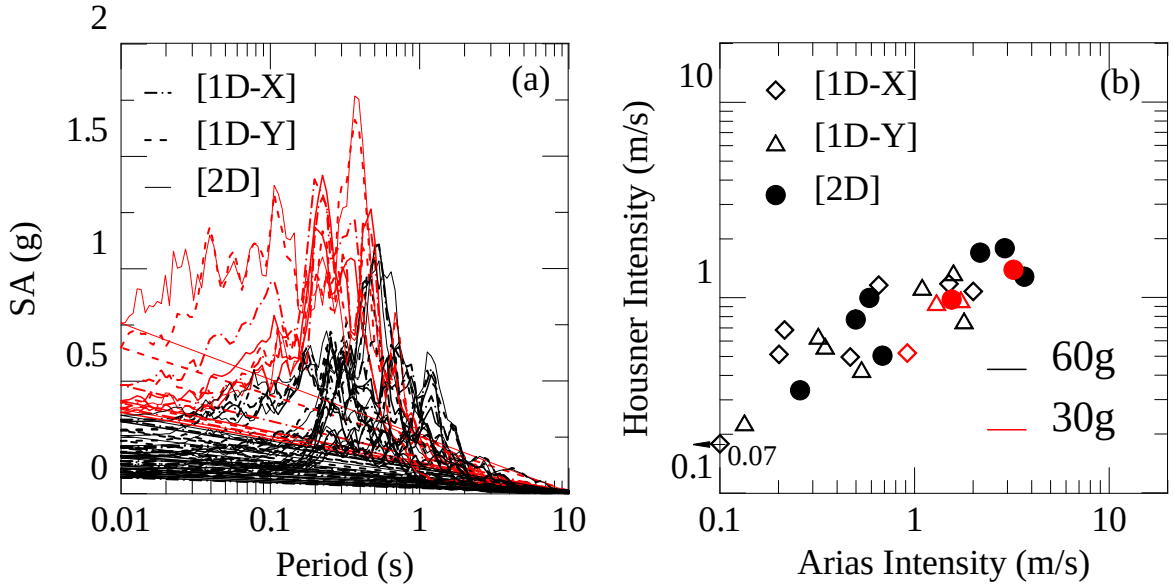

Figure 4-54. Input ground motions used in centrifuge testing program (black lines and symbols are 60g motions, red lines and symbols are 30g motions). (a) Response spectra; and (b) Arias and Housner intensities.

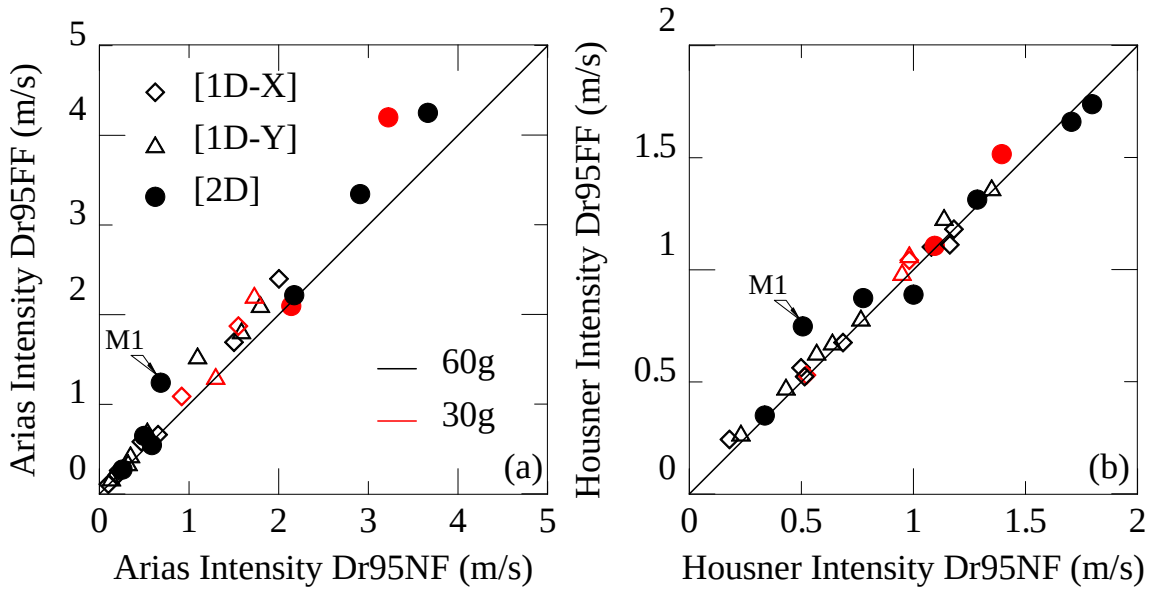

Figure 4-55. Comparison of input (AX0-2, AY0-2 in Figure 4-57 and Figure 4-43 in Section 4) ground motion intensities from tests Dr95FF (free-field) and Dr95NF (near-field): (a) Arias intensity; and (b) Housner intensity (black symbols are 60g motions, red symbols are 30g motions).

4.8.3 Changes in shear wave velocity

During test Dr95NF, excess PWP was allowed to dissipate after each shaking event and bender element readings were obtained (prior to starting the next shaking event) at the three locations shown in Figure 4-58: (1) immediately beneath the structure (~4.8 m and 2.4 m depths for 60g and 30g centrifugal accelerations, respectively); (2) at depths of 8.1 m (60g) and 4.05 m (30g); and (3) near the base of the model at depths of 18.6 m (60g) and 9.3 m (30g). The first and second locations involved horizontally propagating, horizontally polarized velocities ($Vs_{,HH}$), while the third location involved horizontally propagating, vertically polarized velocities ($Vs_{,HV}$).

Figure 4-58 shows the evolution of measured $Vs_{,HH}$ and $Vs_{,HV}$ after each shaking event at both 60g and 30g (corresponding to various prototype depths) for tests Dr95FF, Dr95NF, and CTDr95NF. The individual tests were discussed in Section 3. Figure 4-59 presents these changes in $Vs_{,HH}$ and $Vs_{,HV}$ with respect to depth for each of the bender element locations. Overall, each shaking event densified the sand and increased Vs, and as expected, a drop in Vs occurred when the centrifugal acceleration was decreased from 60g to 30g as a result of the significant decrease in effective vertical stress, σ'_v (despite the induced overconsolidation ratio of two).

As illustrated in Figure 4-59(a), at depths of 9.3 m and 18.6 m, the initial (pre-shaking) $Vs_{,HV}$ measurements agree closely with the Menq (2003) estimates for D_{Ro}~ 95%, while the initial $Vs_{,HV}$ are smaller than the Menq (2003) estimates for D_{Ro} ~ 95%. Interestingly, as shown in Figure 4-59(a), after all 60g and 30g shaking events (27 events), the measured $Vs_{,HH}$ at the end of all shaking events (at 60g and 30g) slightly exceed measured $Vs_{,HV}$ values at the same depths (9.3 m and 18.6 m), and all values of $Vs_{,HV}$ and $Vs_{,HH}$ exceed the Menq (2003) estimates for D_{Rf}~ 102%. And, similar to the free-field conditions discussed earlier in this section, the increase in Vs beyond the Menq (2003) estimates for a given D_R is likely due to an increase in lateral stresses resulting from shaking (i.e., preshearing effects).

As observed in Figure 4-59(b) and (c), initial $Vs_{,HH}$ measurements immediately beneath the structure (NF) for D_{Ro} ~ 95% were significantly larger than both the FF test measurements and the Menq (2003) estimates for D_R= 95% (FF conditions). This results from the significant increase in effective stress induced by the high-bearing-pressure structure compared to the free-field effective stress at the same depth. Figure 4-59(b) also shows that initial (pre-shaking) $Vs_{,HH}$ measurements at a depth of 8.1 m were essentially identical to the interpolated free-field $Vs_{,HH}$ measurements (Figure 4-59a), but were lower than the Menq (2003) estimates for D_R = 95% (free-field conditions). This suggests that the influence of the structure on relative density and effective stress was minimal at a depth of 8.1 m. For comparison, Figure 4-59(b) and (c) include initial Vs profiles for D_R = 95% (dashed blue lines) computed using the Menq (2003) correlation for the average increase in vertical stresses determined from the Boussinesq (1885) stress distribution for a circular foundation (Poulos and Davis 1974). As the increase in vertical stress decreases away from the center of a circular foundation, the authors computed the average increase in vertical stresses at a given depth using the average influence factor below the entire structure diameter because this distance corresponds to the distance between each pair of bender elements (receiver and sender). The measured initial $Vs_{,HH}$ are considerably smaller than Vs values estimated using Menq (2003) and the Boussinesq stress distribution, suggesting that the Boussineq stress distribution is conservative for dense sand, consistent with conclusions from Schmertmann et al. (1978) and Burland and Burbidge (1985).

Although the initial near-field $Vs_{,HH}$ measurements were smaller than estimates from Menq (2003) for D_R = 95%, the final (after shaking) $Vs_{,HH}$ increased to values equal to (at 30g) or higher than (at 60g) estimated using Menq (2003) for D_R = 102%. The increase in $Vs_{,HH}$ results from increases in both relative density and effective horizontal stress (σ'_h), although the increase in $Vs_{,HH}$ due to

increasing relative density is fairly insignificant (Figure 4-59a illustrates that the difference in Vs for D_R = 95 and 102% is small). Therefore, it appears that the increase in effective horizontal stress (σ'_h) with each shaking event is the primary source of increases in $Vs_{,HH}$ for both near- and free-field conditions.

In addition, the near-field $Vs_{,HH}$ measurements in Figure 4-59(b) and (c) provide some indication of the zone of influence of the foundation. Initial near-field $Vs_{,HH}$ measurements at depths of 8.1 m and 18.5 m (for 60g; Figure 4-59b) follow the free-field trend, while the near-field $Vs_{,HH}$ measurements at 4.8 m exceed the free-field trend. Similarly, initial near-field $Vs_{,HH}$ measurements at depths of 4.05 m and 9.25 m (for 30g; Figure 4-59c) follow the free-field trend, while the near-field $Vs_{,HH}$ measurements at 2.4 m exceed the free-field trend. At 60g, the depth to which final (post-shaking) near-field $Vs_{,HH}$ measurements exceed the free-field values appears to increase compared to the initial (pre-shaking) depth, while at 30g this depth remains nearly unchanged from initial to final conditions.

To better understand the zone of influence from the foundation, Figure 4-60 presents the influence depth (Z_I) with respect to foundation width (B) interpreted from $Vs_{,HH}$ measurements at 60g and 30g. The figure includes Z_I/B values inferred from settlement data collected by Burland and Burbidge (1985) from model tests, case histories, and finite element analyses of foundations and embankments founded on sands and gravels. Burland and Burbidge (1985) proposed an influence depth for foundation settlement of $Z_I = B^{0.75}$ (where B is in units of meters) for these cases. As illustrated in the figure, the influence depths inferred from the $Vs_{,HH}$ measurements at 60g and 30g are consistent with the Burland and Burbidge (1985) data. Therefore, this influence depth ($Z_I = B^{0.75}$) was adopted in this study to estimate vertical strains below the structure.

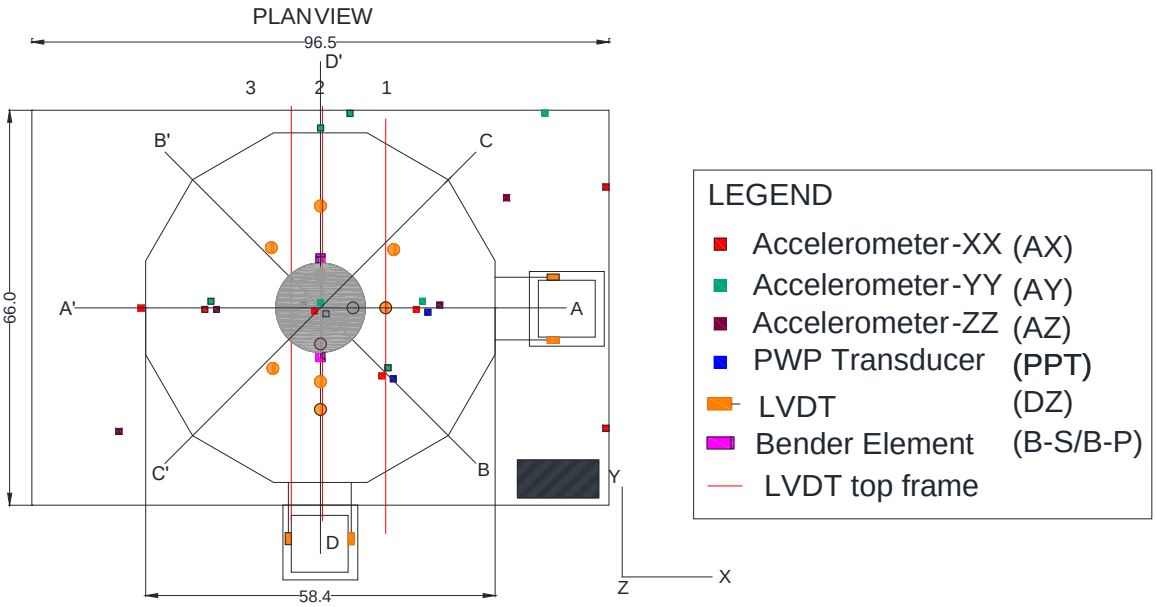

All dimensions are in centimeters (model scale)
Initial coordinates (X,Y)=(0,0) starts at the center of the circle
Initial coordinates Z=0 starts at the base of the model

Labeling of instrumentation
A B/C
A : type of instrument [e.g. A (AX,AY,AZ), DZ(LVDT), B-S or B-P (BE), ST (Structure)]
B : level considering the number of layer from 0 to 4 (see sections AA,BB.CC.DD)
C : column of array according to Plan View. From 1 to 3 (see plan view)

Figure 4-56. Detailed instrumentation layout for test Dr95NF.

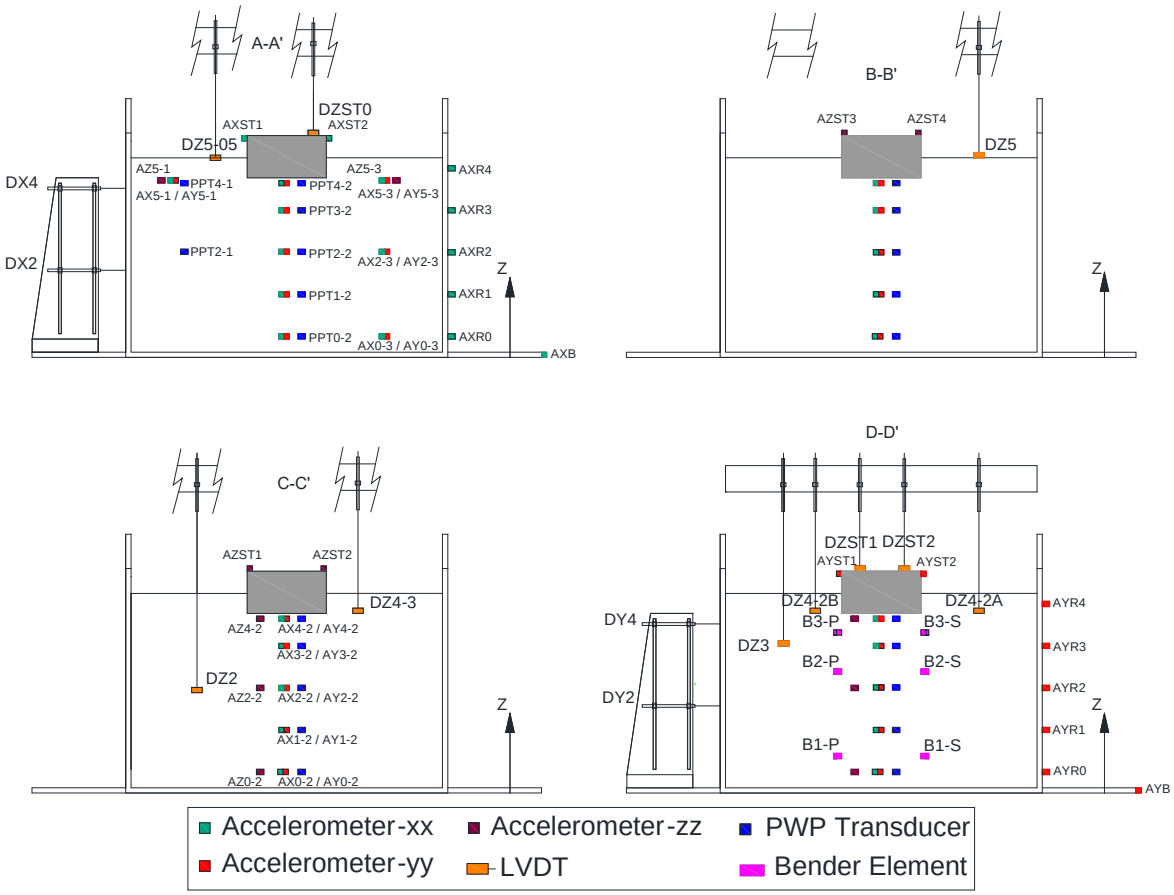

Figure 4-57. Detailed instrumentation layout for test Dr95NF.

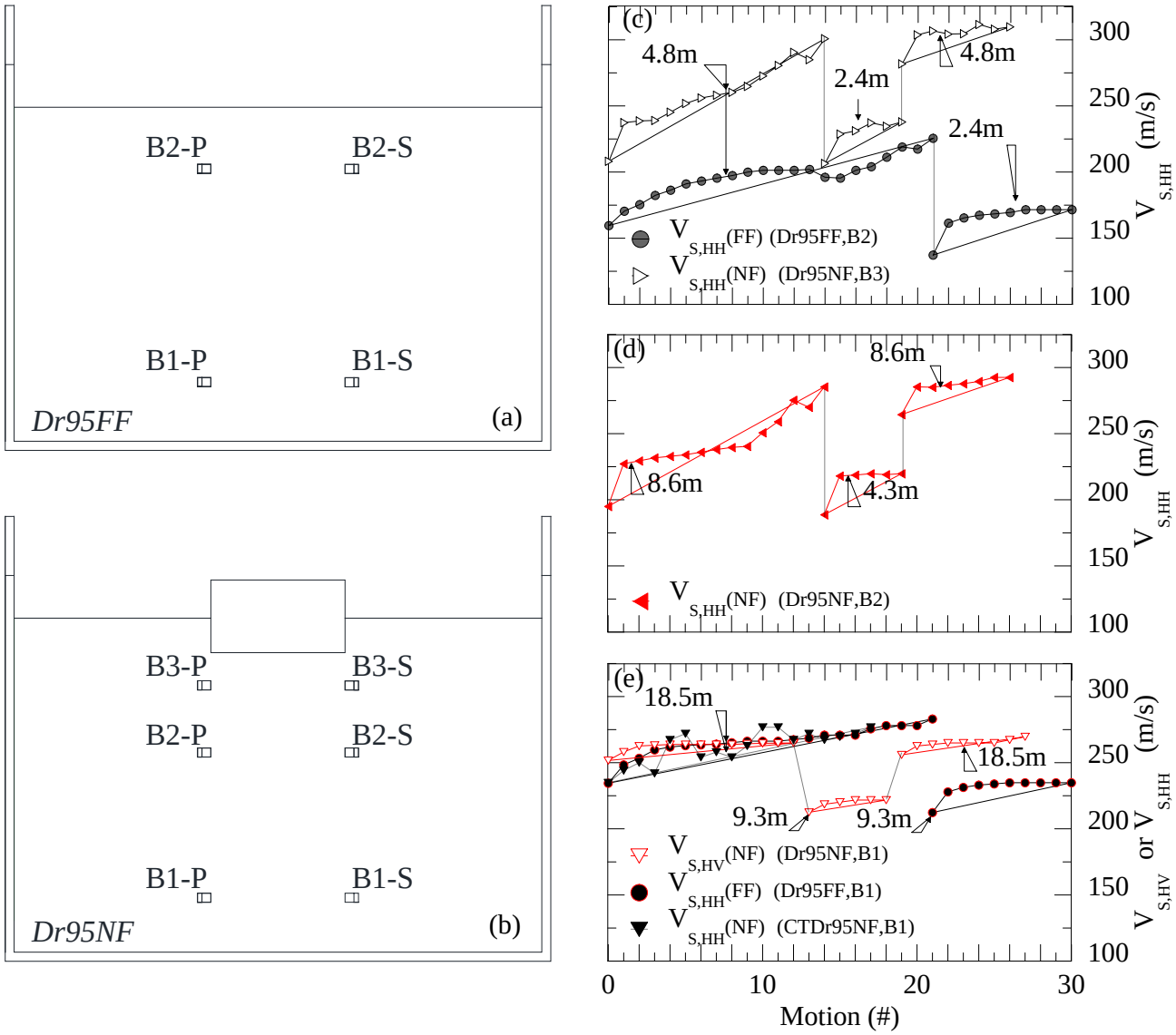

Figure 4-58. Bender elements positions in tests: (a) Dr95FF (free-field); and (b) Dr95NF and CTDr95NF (near-field). (c) Comparison of Vs at depths of 4.8 m (60g) and 2.4 m (30g) for NF and FF conditions; (d) Vs at depths of 8.6 m (60g) and 4.3 m (30g) for NF conditions; and (e) Vs at depths of 18.5 m (60g) and 9.3 m (30g) for NF and FF conditions.

•

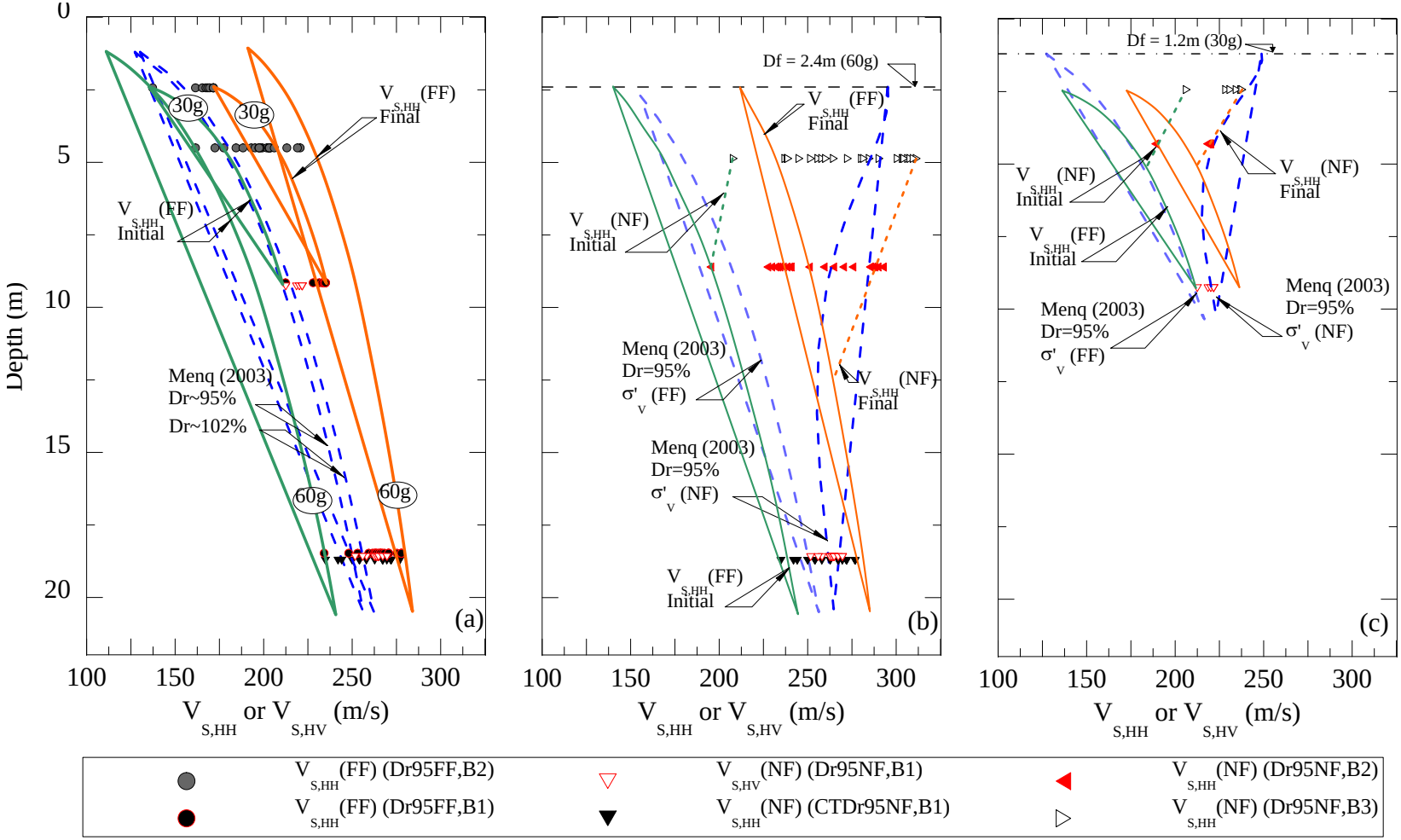

Figure 4-59. (a) Recorded $V_{S,HV}$ and $V_{S,HH}$ histories, and estimated initial and final $V_{S,HH}$ (with respect to depth) for 60g and 30g input motion series for free-field (FF) and near-field (NF) conditions; (b) recorded $V_{S,HH}$ histories and estimated initial $V_{S,HH}$ (with respect to depth) for 60g input motion series and NF conditions; and (c) recorded $V_{S,HH}$ histories and estimated initial $V_{S,HH}$ (with respect to depth) for 30g input motion series and NF conditions (depths are prototype scale; some depths are offset slightly for clarity).

Figure 4-57

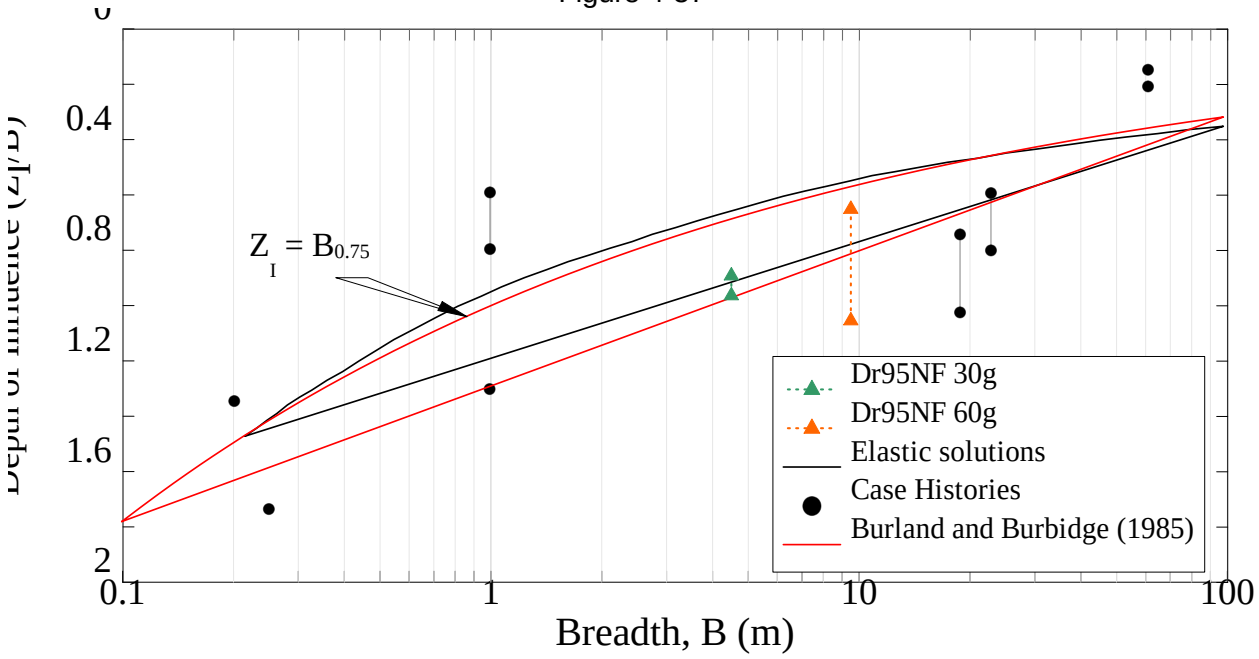

Figure 4-60. Influence depth (Z_I) contributing to settlement below structure foundation or embankment founded on sand or gravel. Data from Burland and Burbidge (1985) and free-field and near-field $Vs_{,HH}$ measurements made in this study.

4.8.4 Ground response (1D and 2D motions)

Figure 4-61 shows the 1D and 2D input and surface acceleration time histories for motion M12. The time histories correspond to accelerometers located beneath the structure (near-field; AXY4; depth ~3.5m; see Figure 4-57 for location) and in the free-field array (AXY5; depth ~2.5m; see Figure 4-57 for location). Ground motions were amplified in both the X- and Y-directions when applied as both 1D and 2D motions.

Figure 4-62(a) and (b) show response spectra for motion M12-X, Y, and 2D (see Figure 4-57 for accelerometer locations). In general, motion M12 exhibited only minor differences between the 1D and 2D response spectra for the X- and Y-directions, with significant amplification occurring at the elongated site period (T~0.6 sec) for both 1D and 2D motions. This finding was consistent for all of the input motions.

Figure 4-62(c) and (d) present residuals computed for free-field and near-field conditions between the 1D and 2D response spectra (in log-log space) for each X- and Y-directions acceleration time history as:

$$Residual\ S_a = \log\left(\frac{\mathrm{Sa,\ 2D-X\ or\ 2D-Y}}{\mathrm{Sa,\ 1D-X\ or\ 1D-Y}}\right) \quad (4\text{-}95)$$

where Sa is spectral acceleration. Positive residuals indicate that $Sa_{,1D}$ was less than $Sa_{,2D}$, while negative values indicate that $Sa_{,1D}$ was greater than $Sa_{,2D}$. Figure 4-62(c) and (d) show that the

mean residuals for all motions for both surface free-field and surface near-field conditions are essentially zero for periods less than 10 seconds. This result indicates that the dynamic shear behavior is not affected significantly by multidirectional shaking.

Figure 4-63 compares 2D response spectra in the free-field (recorded at 2.5 m depth) and in the near-field (recorded below the foundation at 3.5 m depth) for motion M12 (2D, X-direction). Figure 4-63(a) illustrates slightly larger spectral accelerations at periods (T) less than ~ 0.6s in the free-field location compared to the near-field location. These larger free-field spectral accelerations may be attributed to lower effective stress in the free-field compared to the near-field, where the presence of the high bearing pressure structure tended to suppress dilation spikes that were observed near the surface in the free-field. In contrast, Figure 4-63(b) shows essentially no difference between free-field and near-field response spectra at 11.0 m for motion M12 (2D, X-direction).

Figure 4-63(c) and (d) present residuals computed for the free-field (FF) and near-field (NF) response spectra (in log-log space) for each 1D and 2D X- and Y-direction acceleration time history as:

$$Residual\ S_a = \log\left(\frac{\mathrm{Sa, FF, X\ or\ Y}}{\mathrm{Sa, NF, X\ or\ Y}}\right) \tag{4-96}$$

Positive residuals indicate that $Sa_{,NF}$ was less than $Sa_{,FF}$, while negative values indicate that $Sa_{,NF}$ was greater than $Sa_{,FF}$. Figure 4-63(c) and (d) shows that the mean residuals for all near-surface free- to near-field motions were essentially zero for periods greater than 1 sec. However, for T < 1 sec, $Sa_{,NF}$ was consistently less than $Sa_{,FF}$. showing a mean residual up to +0.09. This difference, although small, appears to increase with shaking intensity (i.e., motions M6, M7 and M5) up to residuals of +0.25 at short periods (T < 0.2 sec). This response likely results from dilation spikes that occur in the free-field (at low σ'_v) with increasing amplitude as shaking intensity increases. Similar dilation spikes are not observed in the near-field locations because the high σ'_v related to the structure suppresses dilation in the soil.

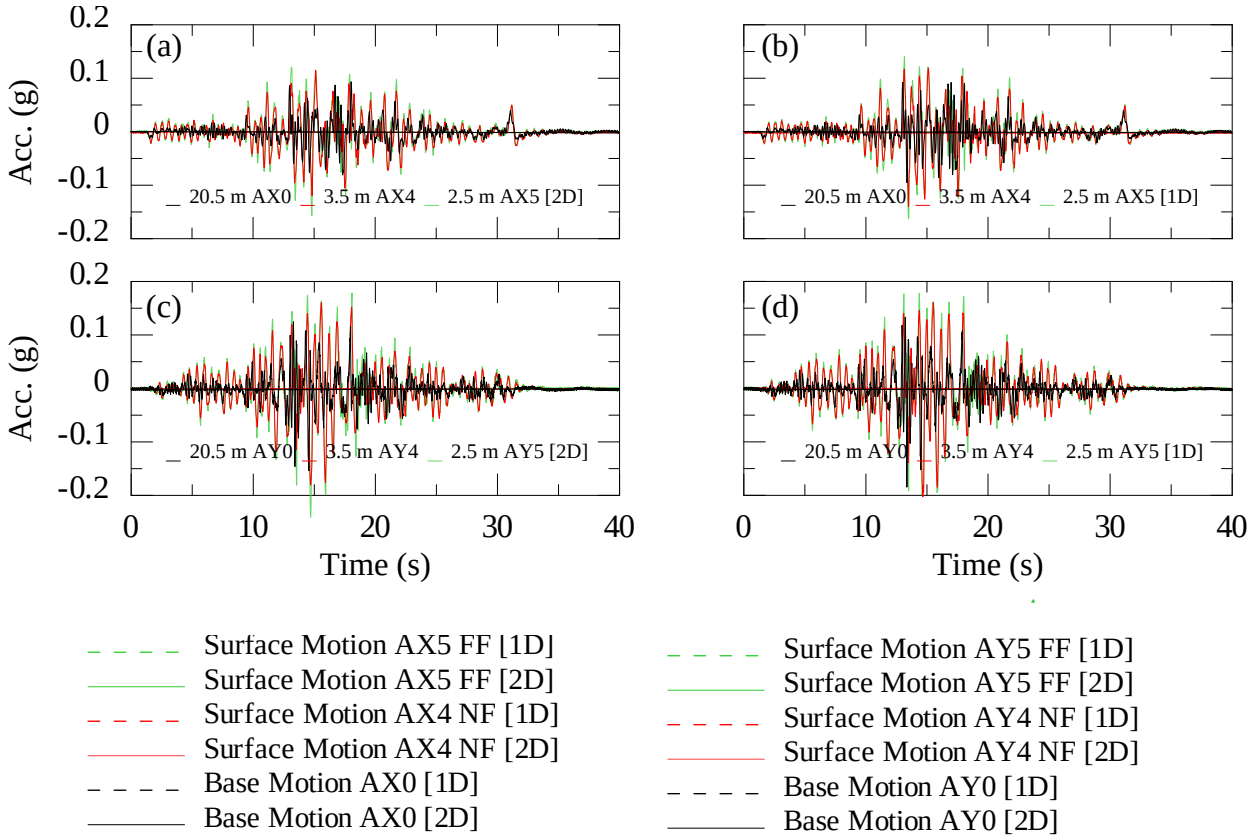

Figure 4-61. Recorded input and surface ground motion (a) M12-2D [X]; (b) M12-1D [X]; (c) M12-2D [Y]; and (d) M12-1D [Y].

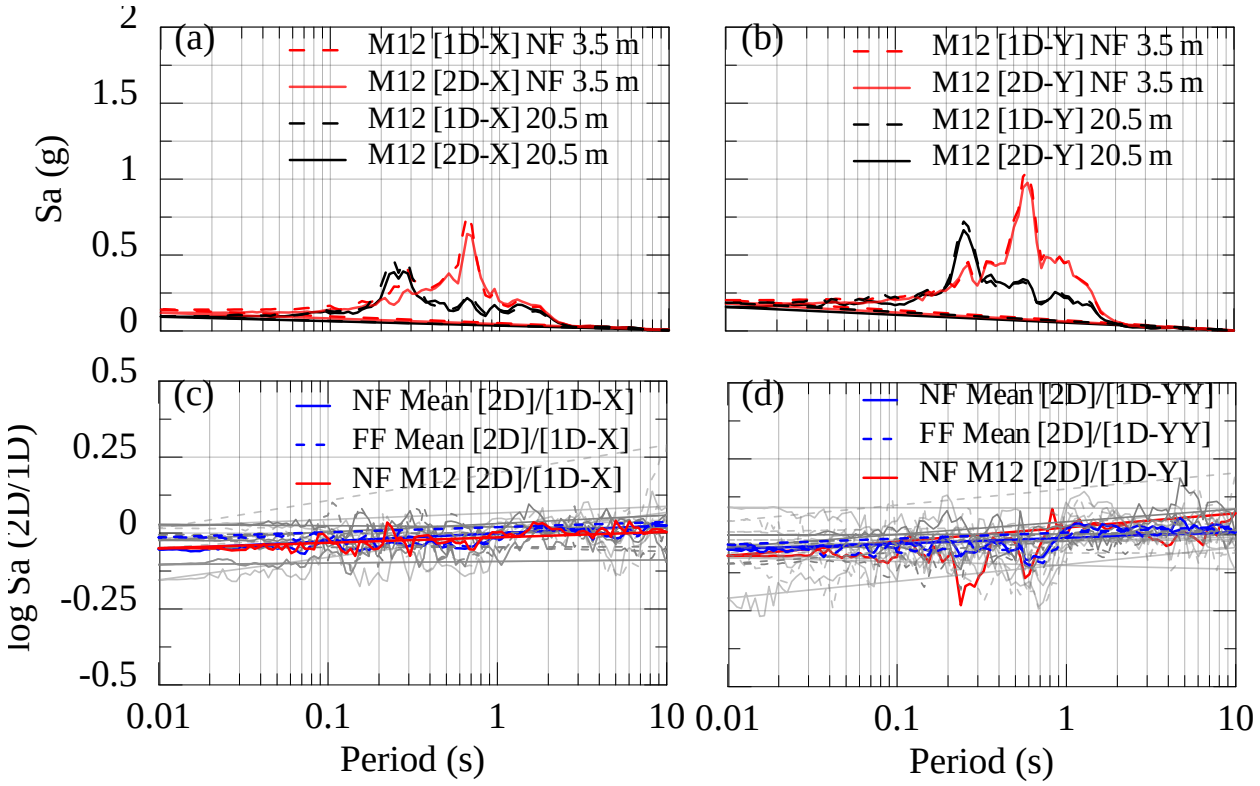

Figure 4-62. Comparison of response spectra for test Dr95NF, motion M12. (a) Input and surface response for M12, X-direction; (b) input and surface response M12, Y-direction; (c) ratio of spectral accelerations (2D to 1D, X-direction) for all 60g and 30g motions for both near-field (AX4-2) and free-field (AX5-3) locations, highlighting motion near-field (AX4-2) motion M12, X-direction; and (d) ratio of spectral accelerations (2D to 1D, Y-direction) for all 60g and 30g motions for both near-field (AX4-2) and free-field (AX5-3) locations, highlighting motion near-field (AX4-2) motion M12, Y-direction.

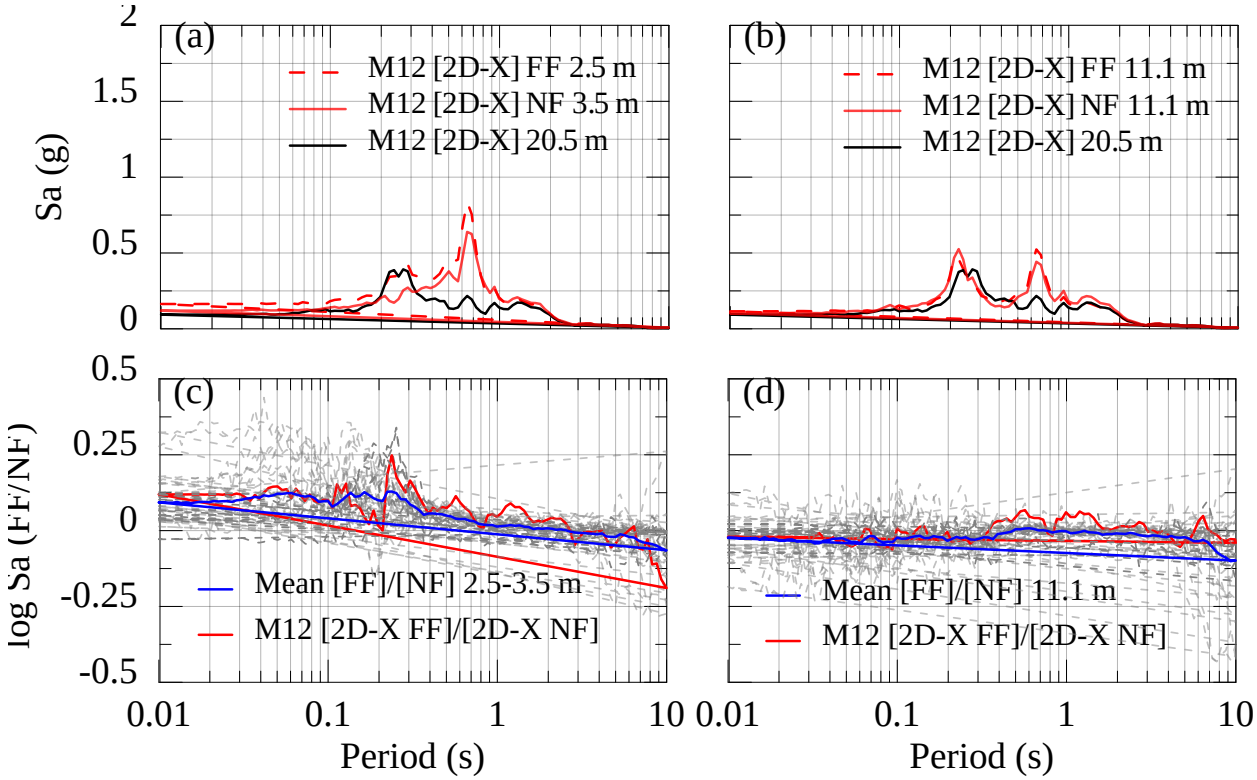

Figure 4-63. Response spectra comparisons for test Dr95NF. (a) Input, free-field and near-field surface response motion M12, X-direction; (b) input, free-field and near-field mid-depth (11.1 m) response motion M12, X-direction; (c) ratio of surface spectral accelerations (free field (AX4-2) to near field (AX5-3), X and Y direction) for all 60g and 30g motions, highlighting motion M12, X-direction; and (d) ratio of spectral accelerations at 11.1 m (free field (AX2-2) to near field (AX2-3), X and Y direction) for all 60g and 30g motions, highlighting motion M12, X-direction.

4.8.5 Excess PWP generation

Figure 4-64 presents instrument response measured in test Dr95NF for input motion M12. Specifically, the figure includes acceleration time histories in X- and Y-direction (AX4-2, AX4-0, AY4-2, and AY4-0; see Figure 4-57 for locations), excess PWP at 11.0 m (PPT2-2; see Figure 4-57 for locations), and Structure and free-field settlement time histories. Similar to free-field results described in Section 4, maximum excess PWP (Δu_{max}) measured at 11.0 m during 2D shaking was approximately 2 to 4 times larger than Δu_{max} values measured during the corresponding 1D [X and Y] shaking events.

Figure 4-65 compares near-field (below the structure) and free-field excess PWP generation at a depth of 3.5 m during motion M12. Ultimately, the increase in excess PWP under 2D shaking is approximately the same for both free- and near-field conditions; however, the rate of excess PWP generation differs greatly in the two locations. And, as illustrated in Figure 4-66(a), this similarity in ultimate maximum excess PWP was consistent in all shaking events (60g and 30g). However, the free-field location (PPT4-1) generated excess PWP during strong shaking (i.e., between 5% and 95% Ia) and excess PWP dissipation began near the end of strong shaking, while the near-field location (PPT4-2) experienced little generation of excess PWP during shaking. This is further illustrated in Figure 4-66(b), where the maximum near-surface, free-field excess PWPs measured

during strong shaking (PPT4-1) were larger than near-field values measured below the foundation (PPT4-2).

Figure 4-66(c) illustrates that as shaking-induced NF excess PWP increases, shaking-induced vertical strain below the structure ($\varepsilon_{v,Z(NF)}$) tends to increase. Interestingly, during weaker shaking events (i.e., excess PWP < 10 kPa) at both 60g and 30g, shaking-induced vertical strains below the structure were similar. However during stronger shaking events, vertical strains below the structure at 30g tended to be larger than vertical strains below the structure at 60g, despite the higher bearing pressure at 60g. This observation requires further investigation to explain.

Furthermore, significant downward (negative) PWP spikes before t ~ 16 sec were observed (e.g., M12 in Figure 4-65), despite the higher effective vertical stresses beneath the structure. These large downward excess PWP spikes likely are related to the significant static shear stresses imposed by the high bearing pressure structure and highly dilative tendency of the dense sand when subjected to cyclic shear stresses with a sustained static shear stress (e.g., Jefferies and Been 2016, among others). Toward the end of strong shaking (t > ~ 20 sec), positive excess PWP temporarily accumulates below the foundation as a result of upward PWP redistribution from greater depths before porewater flows around the foundation. In addition, shear stresses induced by vertical structural rocking also likely contribute to this observed behavior. This behavior was observed during the first four shaking events (M10, M11, M1, and M12 in Figure 4-67a). However, as observed in Figure 4-67(b), as shaking intensity increased for the subsequent motions (M5, M6 and M7), larger downward excess PWP spikes were observed in the FF location compared to beneath the structure (NF). This effect may be related primarily to the decrease in the structure-induced static bias under 30g conditions. In addition, as shaking intensity increases at low effective stress locations (FF locations), dilation effects may be more prominent. The shaking intensity in Figure 4-67(b) plotted in the x axis is defined as the acceleration at the time of minimum downward excess PWP spike during strong shaking (between t at 5% Arias intensity to t at 95% Arias intensity). Figure 4-67(c) also illustrates that dilation (negative excess PWP) induced during strong shaking beneath the structure (NF conditions) appears to be a function of both shaking intensity and shear wave velocity (Vs) for each data set (30g and 60g).

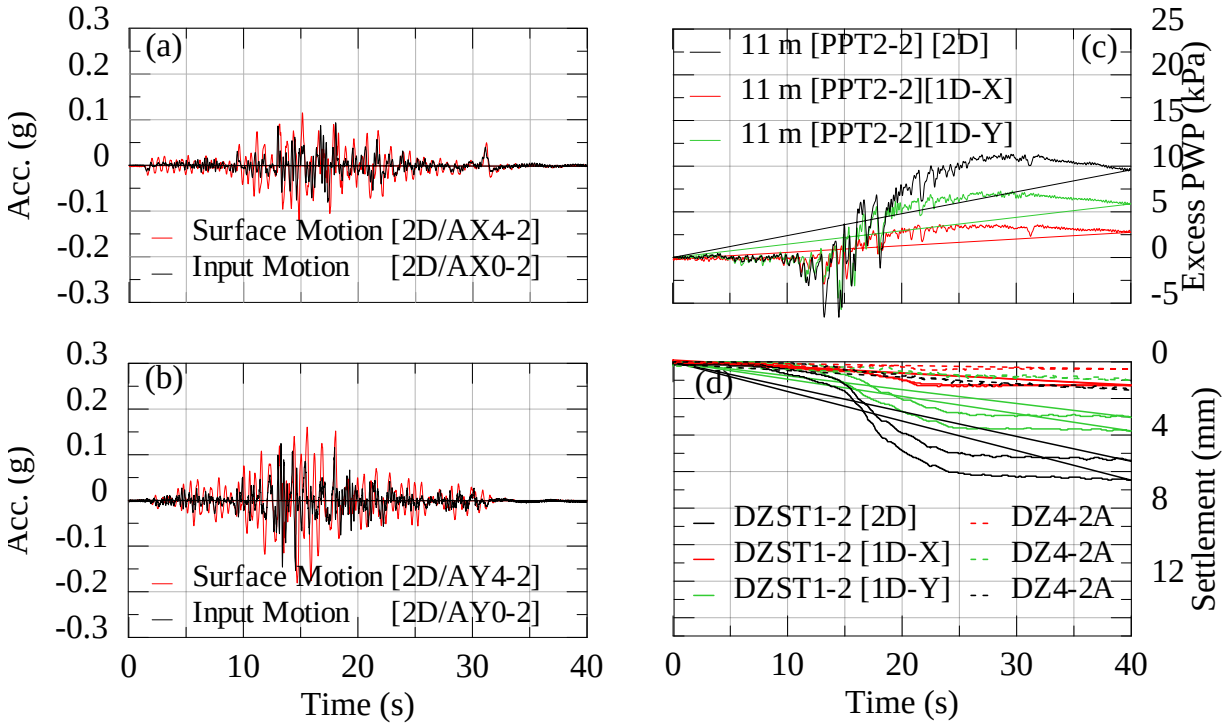

Figure 4-64. Instrument time histories for input motion M12-X, Y, and 2D from test Dr95NF. (a and b) Recorded input and surface acceleration time histories; (c) excess PWP at 11m depth; and (d) structure and free-field surface settlement, solid lines correspond to the two LVDTs located on the structure.

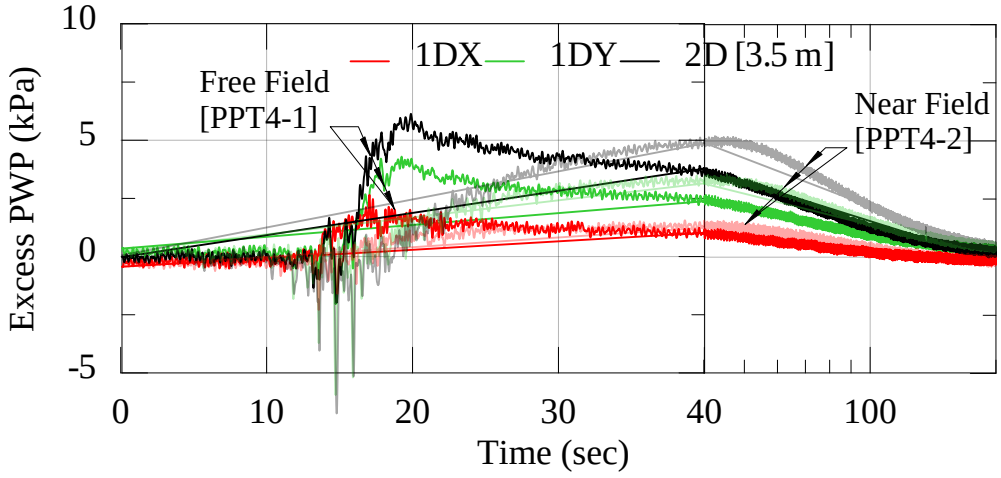

Figure 4-65. Excess PWP time histories for input motion M12-X, Y, and 2D from test Dr95NF at 3.5m depth for free-field and near-field locations (see Figure 5-4 for instrument locations).

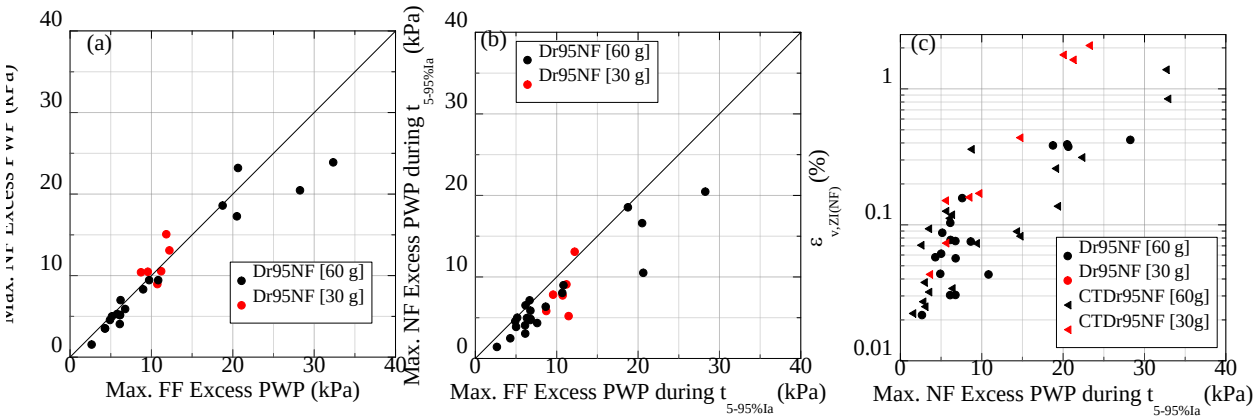

Figure 4-66. Results from test Dr95NF in terms of (a) Recorded maximum NF excess PWP at 3.5 m (60g) and 1.8 m (30g) versus recorded maximum FF excess PWP (at same depths); (b) recorded maximum NF excess PWP at 3.5 m (60g) and 1.8 m (30g) during strong shaking (i.e., between $t_{5\%}$ and $t_{95\%}$ of Arias intensity) versus recorded maximum FF excess PWP (at same depths); and (c) recorded maximum NF excess PWP at 3.5 m (60g) and 1.8 m (30g) during strong shaking ($t_{5\%}$ to $t_{95\%}$) versus shaking-induced vertical strain beneath the structure ($\varepsilon_{v,ZI(NF)}$).

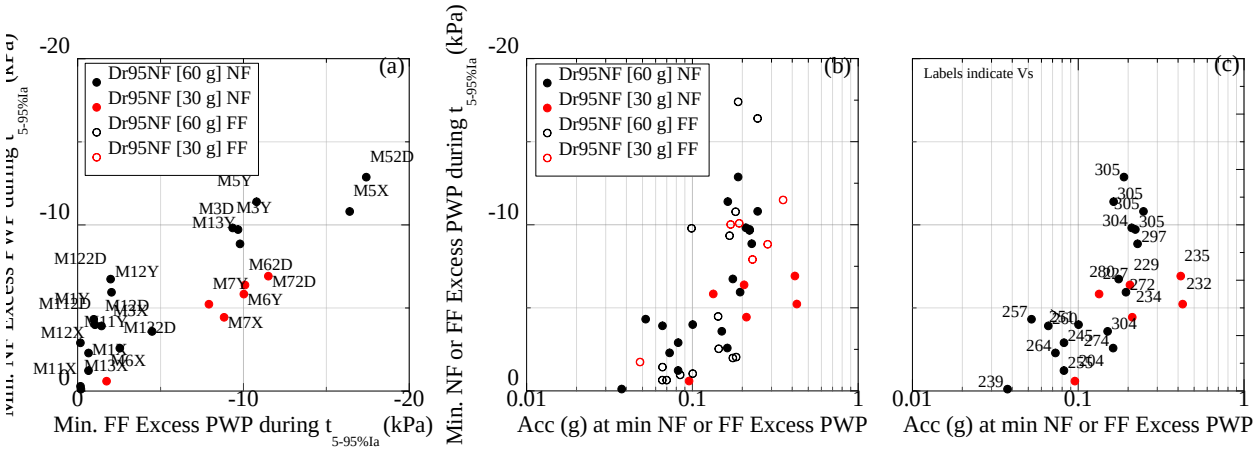

Figure 4-67. (a) Recorded minimum FF excess PWP versus recorded minimum NF excess PWP at 3.5 m (60g) and 1.8 m (30g) during strong shaking in test Dr95NF; (b) recorded minimum FF or NF excess PWP at 3.5 m (60g) and 1.8 m (30g) versus recorded acceleration at the time of minimum excess PWP measurement in test Dr95NF; and (c) recorded minimum NF excess PWP at 3.5 m (60g) and 1.8 m (30g) versus recorded acceleration at the time of minimum NF excess PWP at 3.5 m (60g) and 1.8 m (30g) in test Dr95NF for various shear wave velocities (V_S).

4.8.6 Settlements

Figure 4-68(a) shows measured near-field (i.e., on the structure) and free-field settlement plate displacements for input motion M12-2D, X and Y. Using these settlement measurements, shaking-induced vertical strains below the structure were calculated by estimating the total settlement of the structure within the influence depth (Z_I) as:

$$\varepsilon_{v,Z_I(NF)}(\%) = \frac{\delta_{ST} - \delta_{belowZ_I}}{Z_I}.100 \quad (4\text{-}97)$$

where $\varepsilon_{v,Z_I(NF)}$ = shaking-induced vertical strain below the structure (near-field vertical strain); δ_{ST} = cumulative settlement at structure foundation level (settlement plate reading); and δ_{belowZ_I} = cumulative settlement below the influence depth of the foundation (determined or interpolated from the free-field settlement plate array).

As illustrated in Figure 4-68, M12-2D shaking induced an increase in total structure settlements from 80% to 350% compared to M12-1D (X and Y direction) shaking. Figure 4-69 summarizes the structure settlements for all 30g and 60g motions. As illustrated in the figure, structure settlements during 2D shaking generally exceeded settlements during 1D (X- and Y-direction) shaking by a factor of 1.2 to 5.5.

Figure 4-70(a) and (b) highlight that structure (ST) settlements generally exceeded NF settlement by a factor from about 1.5 to 14, where both ST and NF settlements were compared at the foundation depth (D_f). The NF settlement was recorded at a distance of ~0.8 B from the structure side (LVDT DZ4-2A; Figure 4-57). Moreover, as shown in Figure 4-70(b) ST/NF settlement ratios under 2D shaking (average increase in settlements of 570%) was higher compared to 1D shaking (average increase in settlements of 270%). Interestingly, ST/NF settlement ratios (recorded at a distance of ~0.25 B from the structure side) were 0.9 to 6.7 (LVDT DZ4-2B; Figure 4-57). Figure 4-70(c) and (d) highlight that ST/NF settlement ratios were 0.7 to 8.6 for the surface FF settlements (LVDT DZ5; Figure 4-57). Moreover, the increase in structure settlements under 2D shaking (average increase of 340%) was higher compared to 1D shaking (average increase of 140%). Lastly, Figure 4-70(c) and (d) also show that ST/NF (LVDT DZ5-05; Figure 4-57) settlement ratios were 0.5 to 7.8.

Similar to the ST/NF (DZ5) comparison, the increase in structure settlement conditions under 2D shaking (average increase of 370%) was higher compared to 1D shaking (average increase of 170%). The ST/NF ratios (recorded at the surface by DZ5 or DZ5-05) also compare well with the increase in structure settlements observed by Dashti (2010), who found structure settlements were three to eight times higher than the NF settlements in liquefiable soils subjected to 1D shaking. Results from Montoya (2012), who performed a dynamic centrifuge test to explore structure settlements on dense Ottawa sand deposit (D_{Ro}~85%), indicated that structure settlements were 1.3 to 2.0 times greater than NF settlements (recorded at the surface) when subjected to 1D shaking. Note that the bearing pressure of the Montoya (2012) model structure (q_b ~ 100 kPa) was low compared to this study (q_b = 382 kPa for 60g).

Figure 4-71 summarizes the computed shaking-induced vertical strain below the structure (not including reconsolidation) (this study and Montoya 2012) against computed shaking-induced vertical strains for FF conditions for the recorded range of initial Vs for all shaking events. Consistent with previous researchers, these data illustrate that a well-calibrated 1D free-field predictive model cannot capture (underestimates) shaking-induced vertical strains beneath a structure. Figure 4-71 also shows relationships between IMs and calculated shaking-induced vertical strain below the structure (or Structure induced vertical strain) for increasing Vs for all 60g and 30g motions of test Dr95NF and Montoya (2012). In this context, it appears that as stiffness increases, the near-field vertical strain (for a given shaking intensity) decreases. Using this plot, Figure 4-72 compares the slopes of ε_v(%)/IM for a given Vs from a database on both loose liquefiable (Kim 2017) and dense

sands collected in this study. This comparison also shows an increase of vertical strains under NF conditions for a given intensity and stiffness.

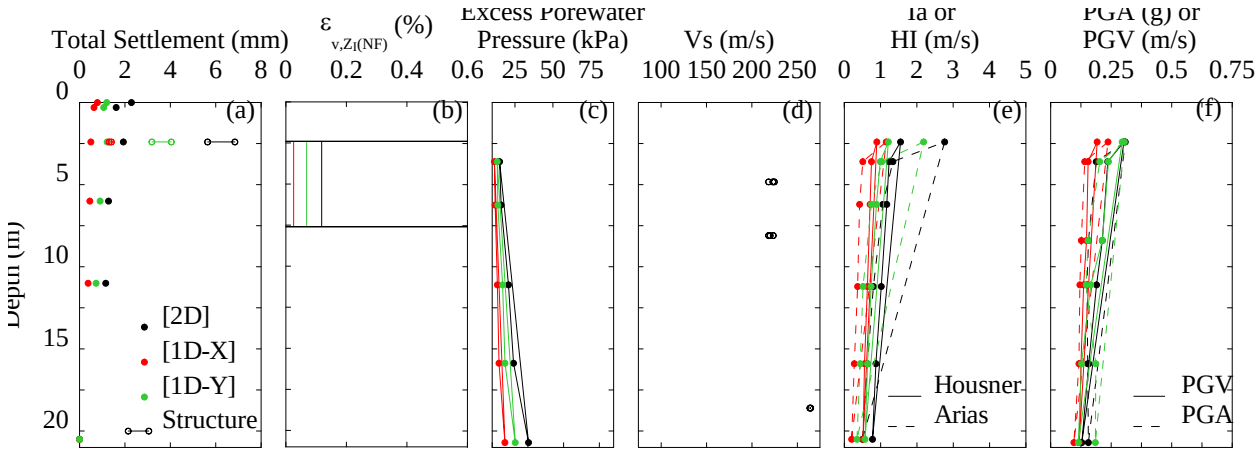

Figure 4-68. Recorded or computed profiles for input motion M12-X, Y, and 2D in test Dr95NF. (a) settlement; (b) shaking-induced vertical strain below the structure within Z_l ($\varepsilon_{v,Zl(NF)}$); (c) excess PWP ratio; (d) Vs; (e) Arias and Housner intensities; and (f) PGA and PGV.

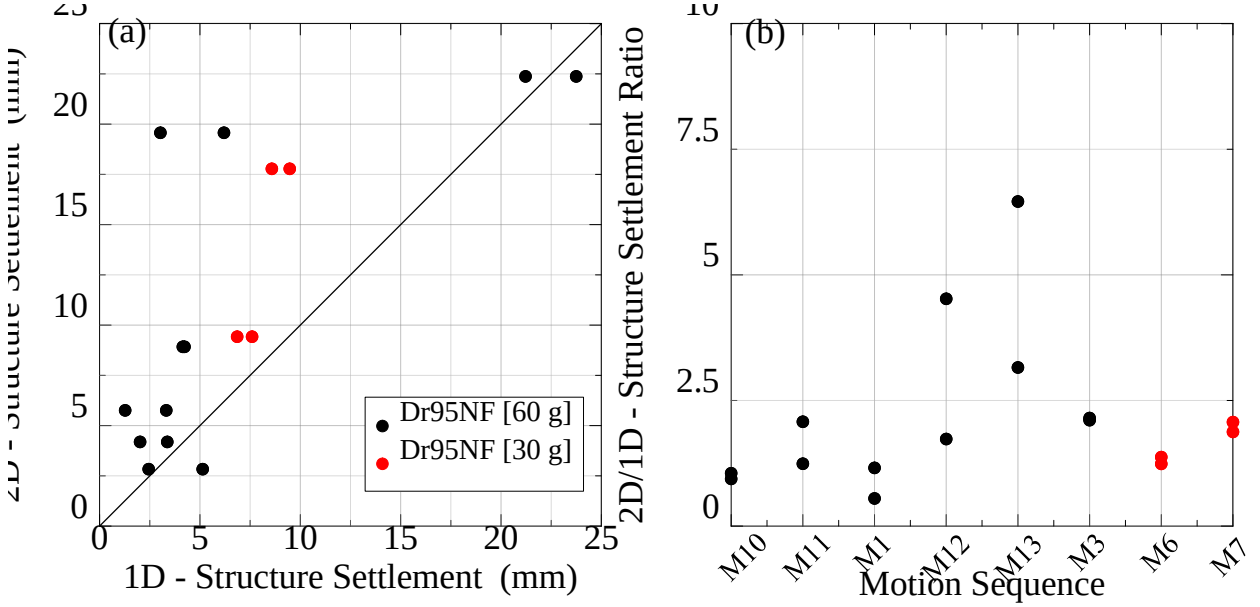

Figure 4-69. Results from test Dr95NF. (a) 1D and 2D recorded total structure (ST) settlement (60g and 30g); (b) ratio of 2D to 1D recorded total structure (NF) settlement (60g and 30g).

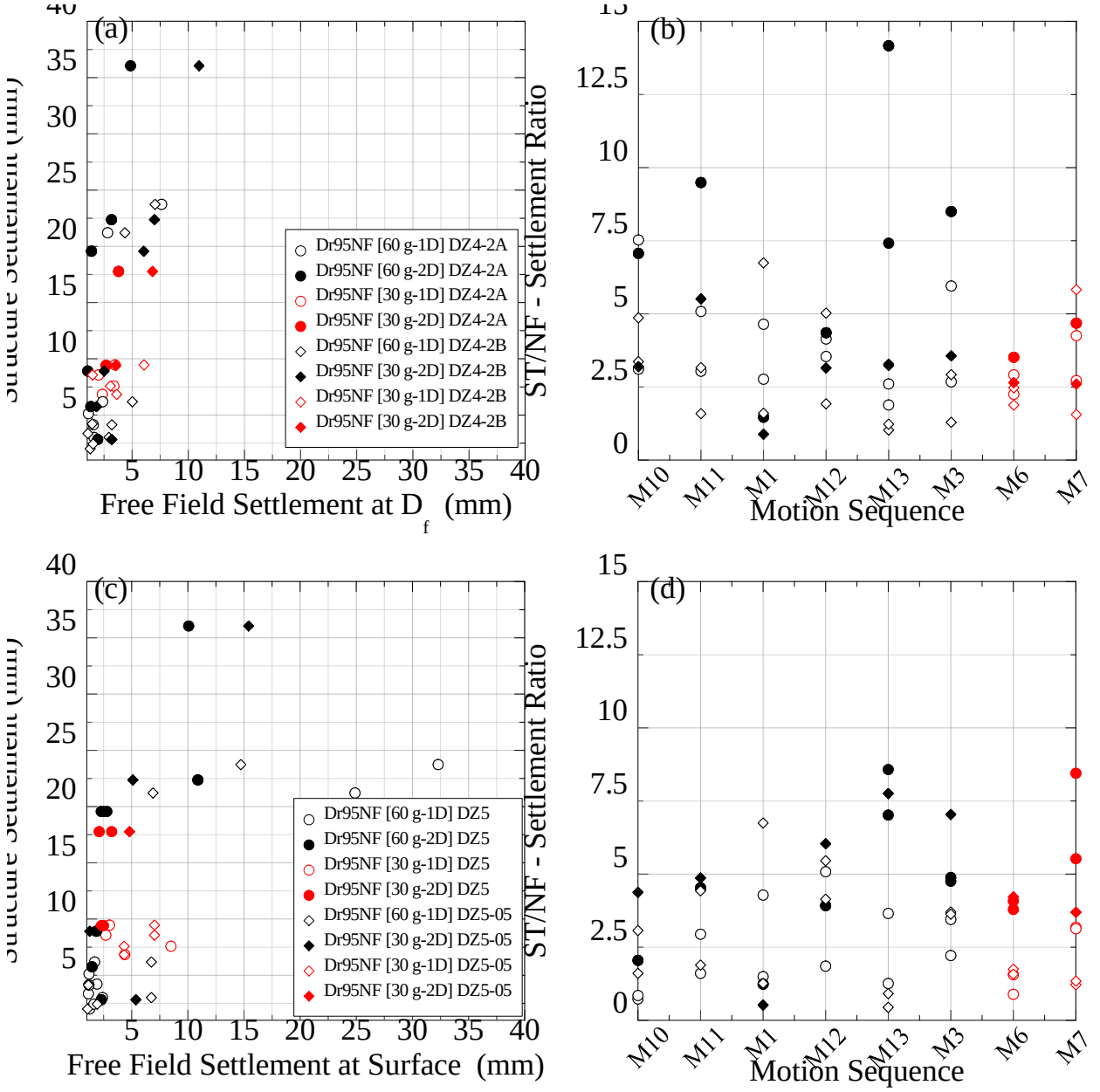

Figure 4-70. Results from test Dr95NF (60g and 30g). (a) NF settlement at depth D_f [locations DZ4-2B (0.25B from edge of structure) and DZ4-2A (0.8B from edge of structure)] compared to structure (ST) total settlement at depth D_f ; (b) ST to NF settlement ratios at depth D_f (locations DZ4-2B and DZ4-2A); (c) NF near-surface settlement (locations DZ5 and DZ5-05) compared to NF total settlement at a depth equal to D_f; and (d) ST/NF settlement ratios (locations DZ5 and DZ5-05).

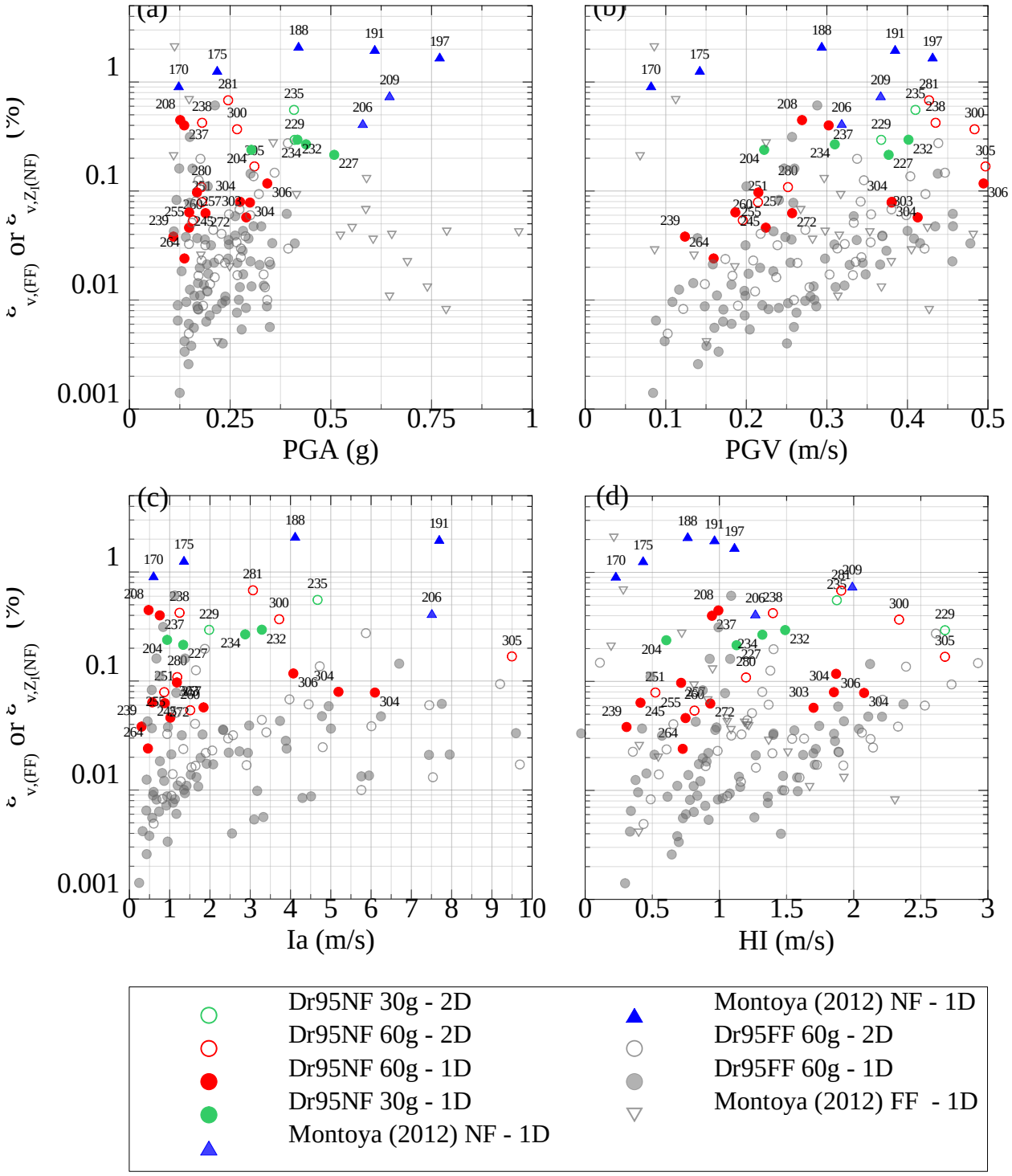

Figure 4-71. Recorded shaking-induced vertical strain below the structure ($\varepsilon_{v,Zi(NF)}$) compared to recorded free field vertical strains ($\varepsilon_{v,(FF)}$) compared for various IM (a) PGA;(b) PGV; (c) Ia; and (d) H. Numbers labels indicate Vs for NF data.

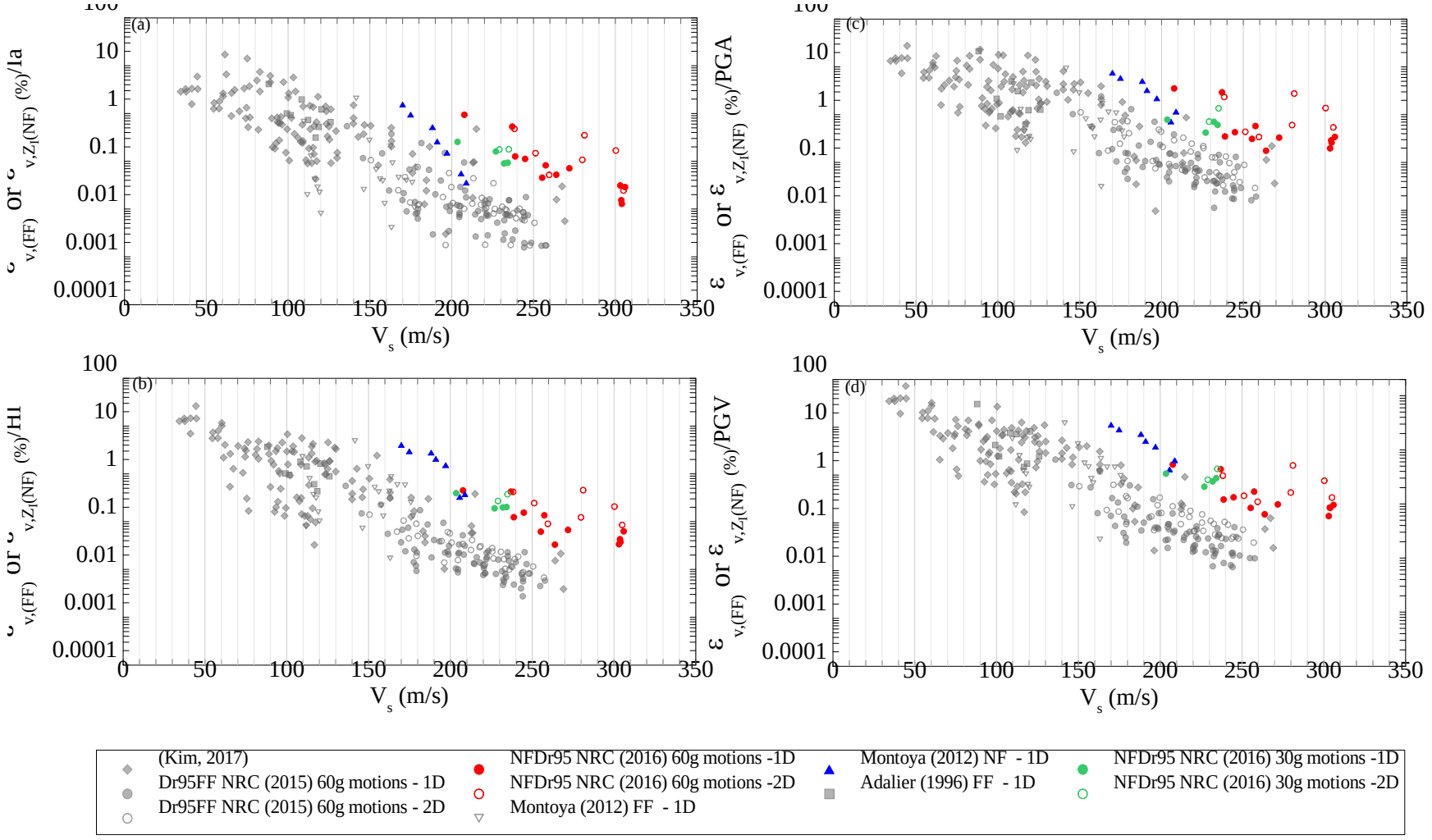

Figure 4-72. Relationship between $\varepsilon_{v,(FF)}$ or $\varepsilon_{v,Z_I(NF)}$ (%)/IM and Vs, illustrating change in slope of Vs trends for IM: (a) Ia; (b) HI; (c) PGA; and (d) PGV. All plots correspond to database collected from this study and Kim (2017).

4.8.7 Summary

This section presented a unique series of near-field dynamic centrifuge tests that examine the effects of multidirectional loading on shear and volumetric soil behavior of a saturated, dense, clean, uniformly-graded Ottawa sand. The centrifuge models were subjected a suite of unidirectional (1D) and bidirectional (2D) motions and exhibited significant ground motion amplification, non-uniform porewater pressure (PWP) generation, and near-field vertical strains larger than its corresponding free-field. These data were also combined with the limited dynamic centrifuge test data on dense sands available in the literature. The difference between the free-field vertical strains and the shaking induced vertical strains beneath a structure highlights the importance of performing a near-field settlement estimation analysis as this clearly is underestimated from free-field based estimations for a given stiffness.

Analysis of bender elements suggest that the influence depths (Z_I) inferred from the $Vs,_{HH}$ measurements at 60g and 30g are consistent with Burland and Burbidge (1985) who proposed an influence depth for foundation settlement of $Z_I = B^{0.75}$ (where B is in units of meters).

Recorded excess PWP and near-field vertical strains indicated multi-directionality factors ranging from 1.0 to 3 for PWP and 1.4 to 6 for vertical strains with an average of 2.5. In general, only minor differences were observed between 1D and 2D response spectra for the X- and Y-directions, indicating that dynamic shear response in each orthogonal component of dense sands is not significantly affected by multi-directional earthquake loading under near field-conditions. Furthermore, slight differences between free field ($Sa,_{NF}$) to near field ($Sa,_{NF}$) response spectra were observed with a mean residual of +0.09.

In summary, a new set of data have been developed for dense sand deposits, both under multidirectional earthquake loading and with a presence of a high-bearing pressure structure (i.e., q_b > 350kPa) that will be used for validation of advanced numerical models (e.g., I-soil) or development of semi-empirical approaches.

5 SEMI-EMPIRICAL MODELS FOR ESTIMATION OF SEISMIC VOLUMETRIC STRAIN UNDER FREE-FIELD AND NEAR-FIELD CONDITIONS

5.1 Introduction

In this Chapter, the authors describe semi-empirical models to estimate shaking induced volumetric strains on dense sands under cyclic loading. The models use both results from laboratory tests and free-field centrifuge tests. Both free-field and near-field (i.e., building settlement) semi-empirical models for dense sand are described below.

The centrifuge database includes a set of unidirectional (1D) and bidirectional (2D) dynamic centrifuge tests performed on a thick layer (prototype thicknesses of 10.25 and 20.5 m) of saturated dense (relative density, D_{R0} ~ 95%), fine Ottawa sand. The database also includes (1D) centrifuge tests performed by other researchers on dense Ottawa and Nevada sands (D_{R0} ~ 70-85%). The centrifuge models were excited using both broadband and sinusoidal motions with Arias intensities that ranged from 0.1 to 30 m/s. The proposed models include various ground motion intensity measures (e.g., PGA, PGV, Arias and Housner intensities) in conjunction with Vs, N_{60}, and q_c for models that could be used in a simplified manner (e.g., PGA) or by means of nonlinear site response analysis (e.g., PGA, PGV, Arias and Housner intensity). The proposed models reasonably capture settlements recorded in centrifuge tests on dense sands, whereas, undrained volumetric strain estimations generally overestimate recorded settlements.

5.2 Estimation of Volumetric Strain in Free-Field using Centrifuge Testing on Saturated Dense Sands

5.2.1 Introduction

Earthquake-induced vertical strains typically are estimated as “drained/seismic compression” for dry or partially saturated sands (e.g., Seed and Silver 1971; Youd et al. 1972; Shahien 1998; Pradel 1998; Duku et al 2008; Lasley et al. 2015) or “undrained/post-cyclic reconsolidation strains” for saturated sands (e.g., Ishihara and Yoshimine 1992; Tokimatsu and Seed 1984; Shamoto et al. 1998; Shahien 1998; Zhang et al. 2002; Idriss and Boulanger 2006, Cetin et al. 2009). The correlations that have been developed to estimate shaking-induced settlements for both dry and saturated sands are derived largely from drained and undrained, respectively, unidirectional cyclic direct simple shear tests with some cyclic triaxial tests. Multi-directional loading for both drained and undrained conditions is incorporated in these procedures using a “multi-directionality factor” that was largely derived from the work of Pyke et al. (1975) and Kammerer (2002)/Wu et al. (2003). Most of the data for these simplified models, however, have used results chiefly from loose to medium dense sands (Dr ~ 40-65%), and have not been validated for dense sands. As a result, significant differences exist in these models’ estimates of vertical strain for dense sands [i.e., $(N_1)_{60}$ > 30), as illustrated in (Figure 5-1). Although liquefaction at sites with dense or compacted coarse-grained soils typically is not a concern, even dense sands exhibit small to moderate vertical strain (contraction) when sheared cyclically (Youd 1972) and could lead to nontrivial settlement for thick soil deposits.

Despite the relatively large database of laboratory element tests, there are few dynamic centrifuge tests available to assess vertical strains in sand subjected to multi-directional loading under partially drained conditions, and the few available tests (Su and Li 2003; Su 2005; El-Shafee 2016) were performed on loose sands. Furthermore, while a significant number of 1D dynamic centrifuge tests

involving saturated loose sands are available in the literature, only a limited number of 1D dynamic centrifuge tests involving dense sands are available (Adalier 1996; Montoya 2012).

In this study, we examined the behavior of thick, saturated, dense sand profiles subjected to a suite of 1D and 2D broadband motions of varying intensities to assess both shear and volumetric response. Using this dynamic centrifuge testing database on dense sands, combined with centrifuge data from saturated loose sands, we propose a semi-empirical model to estimate shaking-induced vertical strains on dense saturated sands under multidirectional cyclic loading for partially-drained conditions. The proposed models utilize both energy-based intensity measures (i.e., Arias and Housner intensities) and vector peak shaking parameters (i.e., PGA, PGV) to capture vertical strains under multi-directional earthquake loading in conjunction with field soil indices Vs, cone penetration test (CPT) tip resistance (q_c), and standard penetration test (SPT) blow count (N_{60}). Lastly, the proposed shaking-induced vertical strain models are compared with existing correlations for volumetric strains under saturated conditions.

5.2.2 Proposed model database

5.2.2.1 Centrifuge case histories

To develop a free-field, shaking-induced vertical strain model for dense sands, a database of 1D and 2D dynamic centrifuge tests was used. The database, summarized in Table 5-1, includes tests performed in this study (as summarized in Chapter 3), as well as tests performed by Montoya (2012) and Adalier (1996).

The authors examined multi-directional earthquake loading response of dense Ottawa 40/70 saturated sand (D_{Ro}~95%) using 1D and 2D dynamic centrifuge tests with prototype depths of 20.5 m and 10.25 m at centrifugal accelerations of 60g and 30g, respectively. As shown in Figure 5-2, the FF model was instrumented using accelerometers (ACC), PWP transducers (PPT), and side and vertical linear voltage differential transformers (LVDTs) placed along the model profile. Pairs of bender elements were used to measure Vs within the model.

Montoya (2012) studied the effect of bio-mediated soil improvement on the dynamic response of sands that included FF experiments on a dense, untreated, saturated Ottawa 50/70 sand (D_{Ro}~85%). The model had a prototype depth of 6 m. As shown in Figure 5-3, the model instrumentation included ACCs, PPTs, and vertical LVDTs placed at the model surface. For this portion of this study, the author used data from the instrument array below vertical LVDT DV3.

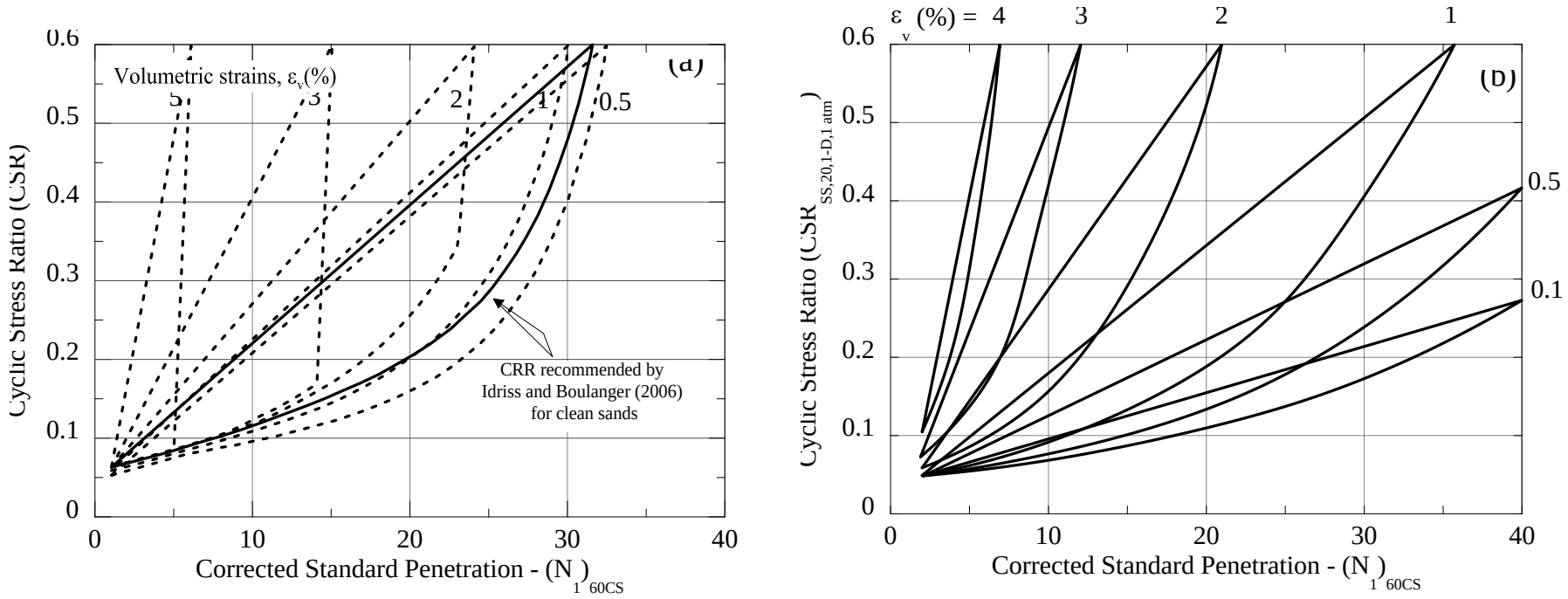

Figure 5-1. Deterministic relationships among post-cyclic volumetric strain, applied cyclic stress ratio, and equivalent clean sand stress-normalized standard penetration test blow count (a) Idriss and Boulanger (2006) and (b) Cetin et al (2009).

Similarly, Adalier (1996) studied liquefaction mitigation techniques of different soil improvement methods using centrifuge experiments that also included FF experiments on a saturated dense Nevada 120 sand (D_{Ro}~70%). The model had a prototype model depth of 2 m (Figure 5-4) and incorporated ACCs, PPTs, and LVDTs placed at the model surface. For this portion of this study, the author used data from the instrument array below vertical LVDT L1.

Table 5-1 ***Published centrifuge tests involving dense sands collected in this study***

No.	Reference	Prototype thickness (m)	Initial, D_{Ro} (%)	Centrifugal acceleration (g)	Type of loading	Purpose	Facility
1	Cerna-Diaz (2017)	20.5 and 10.25	95	60 and 30	1D-2D	free field mass (30 shaking events)	RPI
2	Montoya (2012)	6	85	50	1D	free field and structure mass (7 shaking events)	UC-Davis
3	Adalier (1996)	2	70	50	1D	free field mass (3 shaking events)	RPI

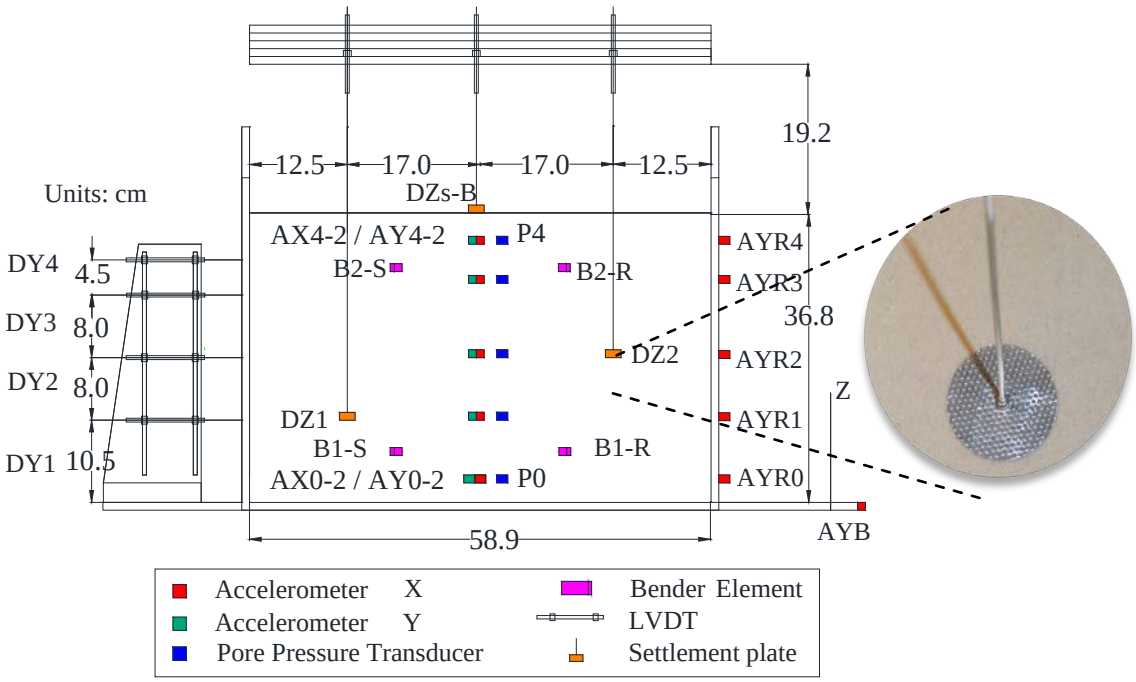

Figure 5-2. Detailed instrumentation layout for test Dr95FF (Cerna-Diaz 2017).

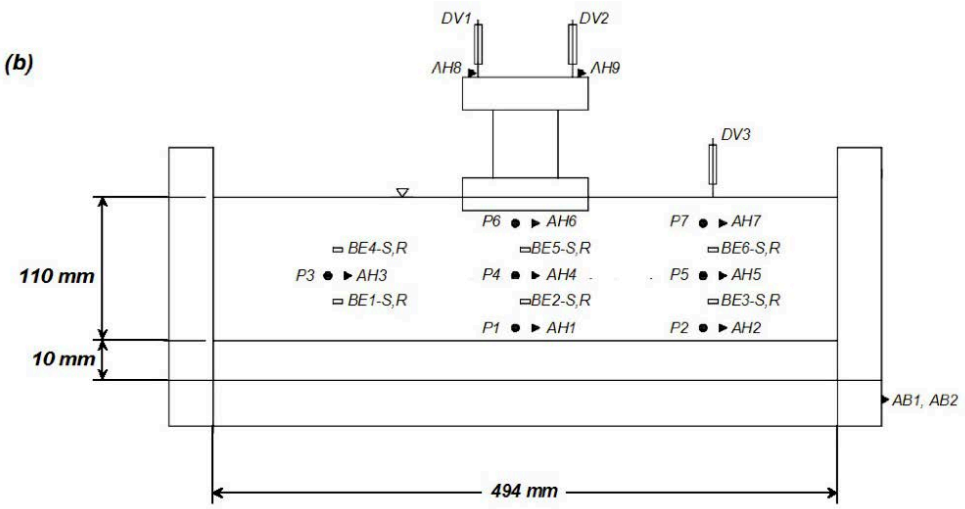

Figure 5-3. Schematic of instrumentation for a 6m centrifuge model D_{Ro}=85% (Montoya 2012)

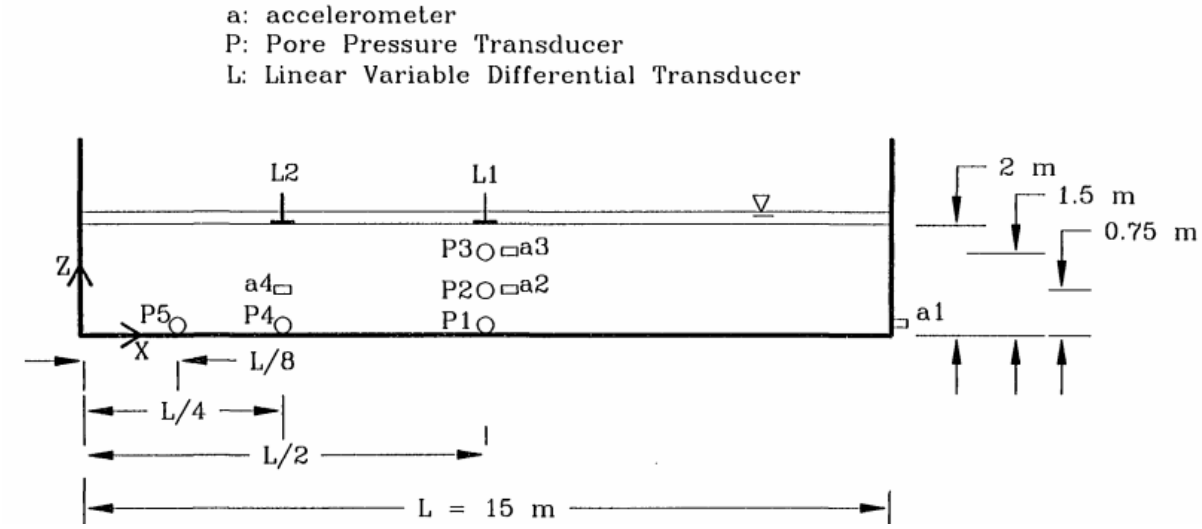

Figure 5-4. Schematic of instrumentation for a 2m centrifuge model D_{Ro}=70% (Adalier 1996)

5.2.2.2 Centrifuge model sands

The sands used in the dynamic centrifuge tests are summarized in Table 5-2. These tests involve fairly uniform clean sands: Ottawa 40/70 sand (this study), Ottawa 50/70 sand (Montoya 2012), and Nevada 120 sand (Adalier 1996). These poorly-graded, fine sands have sub-rounded grains with a median grain size (D_{50}) range of 0.15 to 0.28mm and uniformity coefficient range (C_U) of 1.36 to 1.83. Figure 5-5 presents the grain size distributions for these sands, as well as a scanning electron microscope image of the Ottawa 40/70 sand.

Table 5-2 summarizes minimum and maximum void ratios (e_{min} and e_{max}), grain size distribution characteristics, and specific gravities (Gs) for the sands used in the dynamic centrifuge tests listed in Table 6-1. As illustrated in Table 5-2, e_{min} ranged from 0.50 to 0.55, e_{max} ranged from 0.82 to 0.89, and Gs ranged from 2.65 to 2.67. All measurements were obtained following the procedures described in ASTM D4254, ASTM D4253, or Japanese method standards.

Table 5-2 ***Soil indices for clean sands***

Sand	USCS[a]	D_{50}[a] mm	C_U[a]	C_C[a]	G_s[b]	e_{max}[c]	e_{min}[d]	Reference
Ottawa 50/70	SP	0.28	1.36	0.99	2.67	0.82	0.50	Cerna-Diaz (2017)
Ottawa 40/70	SP	0.22	1.40	0.90	2.65	0.87	0.55	Montoya (2012)
Nevada 120	SP	0.15	1.83	1.28	2.67	0.89	0.51	Adalier (1996)

Note: USCS – Unified Soil Classification System; D_{50} – median particle size; C_U – coefficient of uniformity; C_C – coefficient of curvature; G_s – specific gravity; e_{max} – maximum void ratio; e_{min} – minimum void ratio; [a]ASTM D2487 (ASTM 2011) [b]ASTM D854 (ASTM 2014) [c]Dry tipping method equivalent to ASTM D4254 (ASTM 2006) [d]Japanese method equivalent to ASTM D4253 (ASTM 2016) for Ottawa sand 40/70 [e]ASTM D1557 (ASTM 2012)

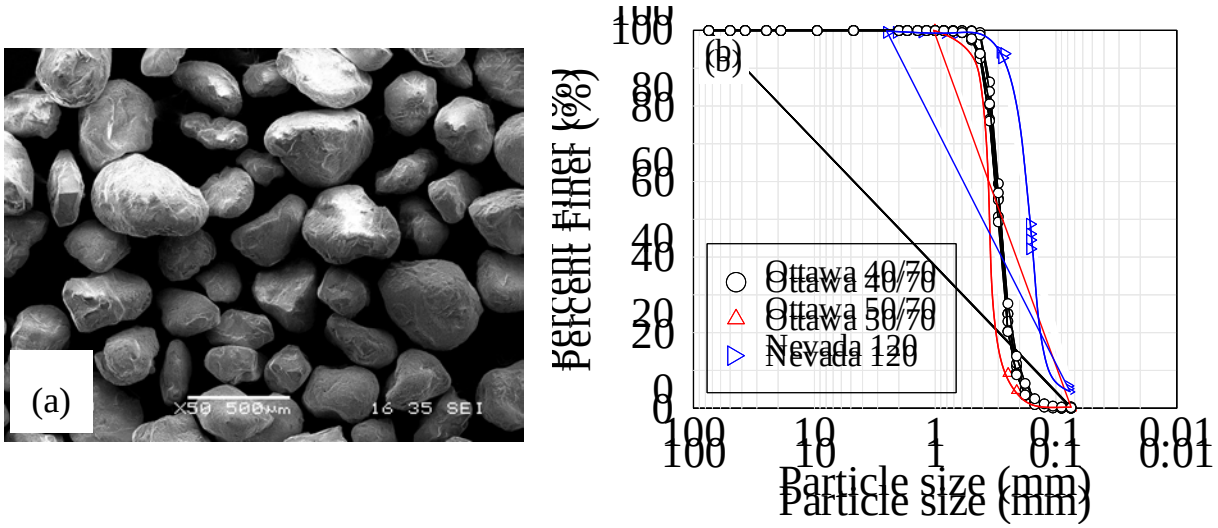

Figure 5-5. (a) Scanning electron microscope image of Ottawa sand used in testing program; and (b) grain size distributions of Ottawa and Nevada sand used from centrifuge database.

5.2.2.3 Shaking-induced vertical strains from database

In each of the dynamic centrifuge tests listed in Table 5-1, surface settlement time histories were available throughout each shaking event. As depicted in Figure 5-2, for the tests described in this research, settlements with depth were also available at specific locations via a vertical LVDT array which allowed a direct calculation of vertical strain with depth (i.e., effective vertical stress). For the Montoya (2012) and Adalier (1996) data, settlement recordings were measured only at the surface, therefore vertical strains with depth were estimated using the Kim (2017) model, which uses sublayer PWP recordings and compressibility estimates to properly distribute settlements and vertical strains with depth. Using the settlement profile derived from recorded LDVT data (this study) or estimated using the Kim (2017) model, vertical strains were calculated based on the post-shaking

thickness of the “tributary” layer as detailed in Chapter 4 and illustrated in Figure 5-6. Also, as the example in Figure 5-7 illustrates, vertical strain profiles were obtained for each specific motion (1D and 2D) applied during each centrifuge test.

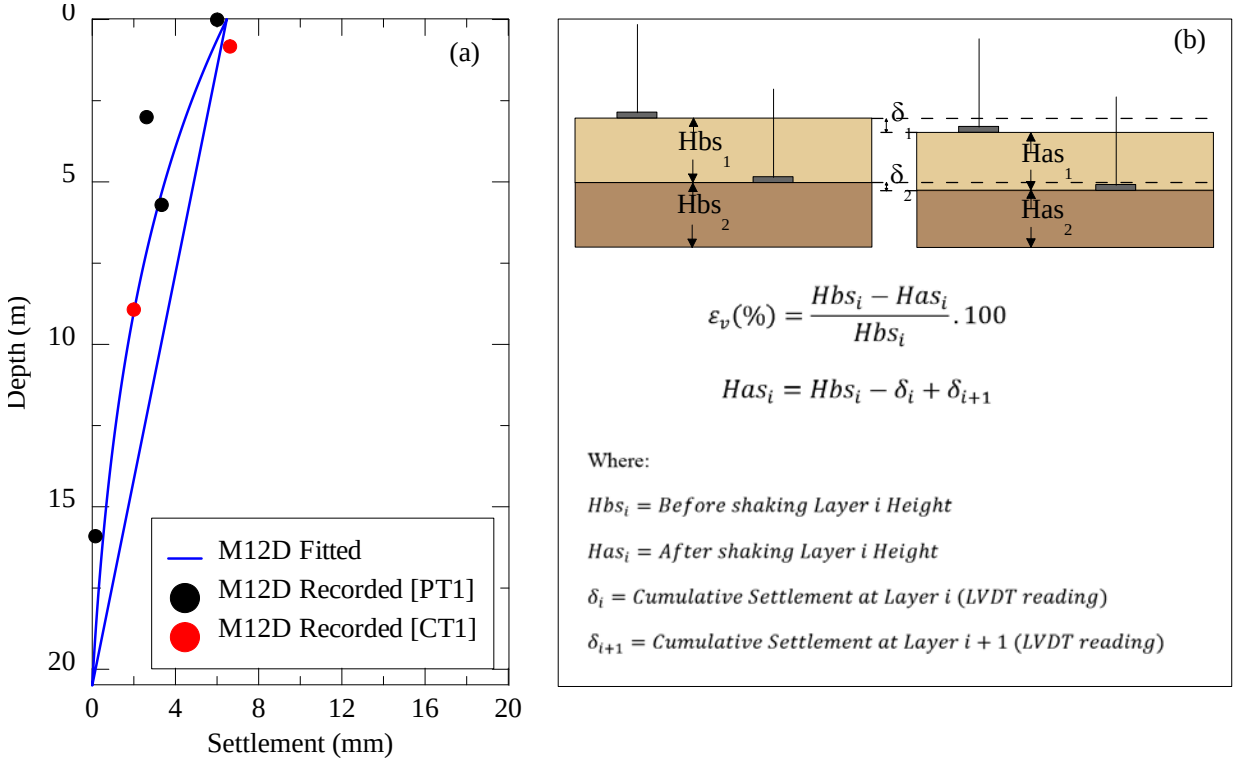

Figure 5-6. (a) Settlements recorded during motion M12D during centrifuge experiments PT1 and CT1, including nonlinear settlement profile; and (b) description of volumetric strain calculation for Sublayers 1 and 2 in typical centrifuge test using settlement plates located at the surface of Sublayers 1 and 2.

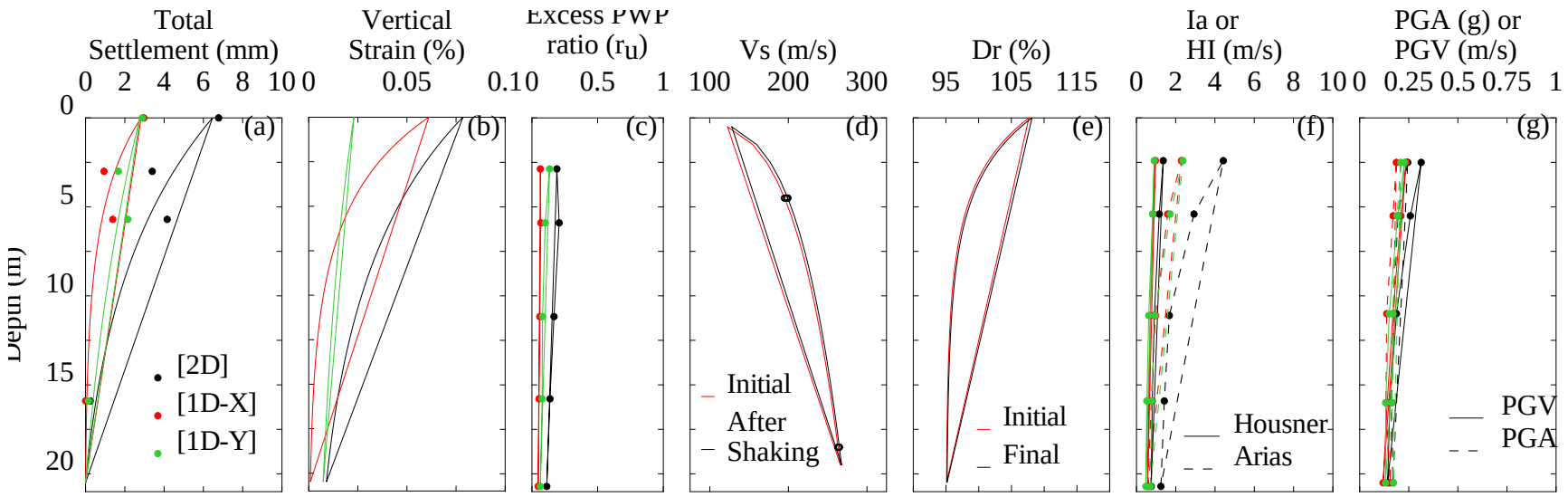

Figure 5-7. Recorded or computed profiles for input motion M1-X, Y, and 2D in test Dr95FF. (a) Settlement; (b) vertical strain;(c) excess PWP ratio; (d) shear wave velocity; (e) relative density; (f) Arias and Housner intensities; and (g) PGA and PGV.

5.2.2.4 Model capacity parameters from database

The database uses Vs values measured using bender elements (this study; Chapter 4) or Vs values estimated using the Brandenberg (2010) correlation for the Montoya (2012) and Adalier (1996) data. Each of the cases and the corresponding parameters are detailed in Appendices of this report.

5.2.2.5 Model intensity measures (IM) seismic demand parameters

The seismic demand in centrifuge models resulted from recorded seismic events and sinusoidal input motions applied at the base of centrifuge models. Figure 5-8 presents response spectra and input Arias and Housner intensities for all the motions. Seismic events used 1D (e.g. Montoya 2012, and Cerna-Diaz 2017) and 2D (e.g., Cerna-Diaz 2017) recorded motions, including both crustal and subduction rupture mechanisms in which two horizontal orthogonal components were available. Sinusoidal motions were used only on 1D experiments (e.g. Adalier 1996, and Montoya 2012) and used a constant amplitude acceleration. Furthermore, intensity measures (IM) at different depths were calculated to be used as seismic demand parameters for the volumetric semi-empirical models. This was done for both energy-based IM (Arias and Housner intensities) and vector peak shaking parameters (e.g., PGA, PGV).

The energy-based Housner intensity (HI) is defined as:

$$HI_{x,y} = \int_{0.1}^{2.5} S_{v_{x,y}}(\xi = 0.05, T)dT \tag{5-1}$$

where T = period (s); Sv = spectral velocity, ξ = damping. Energy-based IM Arias intensity (Ia) is defined as:

$$Ia_{x,y} = \frac{\pi}{2g}\int_{0}^{tmax} a(t)_{x,y}^{2}dt \tag{5-2}$$

where g = acceleration of gravity and a(t) is acceleration at time, t.

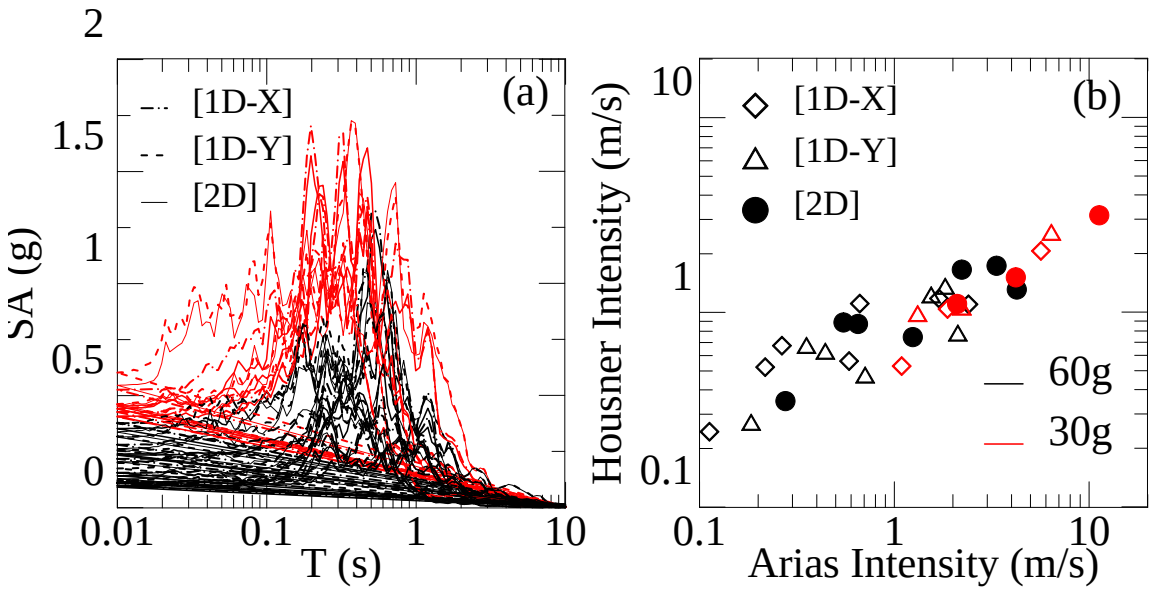

Figure 5-8. Input ground motions used in centrifuge testing program (black lines and symbols are 60g motions, red lines and symbols are 30g motions). (a) Response spectra; and (b) Arias and Housner intensities.

These IMs were computed for both 1D and 2D motions so that total energy from multi-directional shaking is considered. The selected database of ground motions exhibited a range of energy content (Arias intensity 0.11 to 30m/s) that induced nearly linear to nonlinear soil response along the depth within the centrifuge models.

5.2.3 Free-field semi-empirical model

The vertical strain profiles estimated from the centrifuge database were correlated with ground motion intensity measures (IM) and Vs measurements. Figure 5-9 catalogs FF shaking-induced vertical strain (not including reconsolidation) with respect to Vs and various IMs (PGA, PGV, Ia and HI). These plots illustrate that there is a slight trend of increasing vertical strain (ε_v) with 2D shaking for a given Vs, but when considering IMs, 2D shaking does not yield consistently larger values of ε_v for a given total intensity. As illustrated in Figure 5-9(a), ε_v tends to decrease with increasing Vs, and as illustrated in Figure 5-9(b) to (e), ε_v tends to increase with increasing PGA, PGV, HI, and Ia, respectively. When considering these variables alone, there is significant scatter in the trends. However as discussed below, the author combined these observations to develop a relationship between FF shaking-induced vertical strain, IMs, and soil resistance (e.g., Vs).

A multi-variate nonlinear regression of the collected database was performed adopting a hyperbolic functional form. Inspired by the Generalized Quadratic/Hyperbolic (GQ/H) functional form recently proposed by Groholski et al. (2016) for computing backbone stress-strain responses for site response analysis applications, a GQ/H function was utilized for the regression. This functional form was chosen due to its ability to capture physical characteristics of soil volumetric behavior, including: (1) predicting zero vertical strain for zero shaking intensity; (2) capturing vertical strain nonlinearity at small to moderate shaking intensity (or shear strain); (3) predicting decreasing rate of increase in vertical strains at moderate to large shaking intensity (or shear strain); and (4) reaching a limiting

(asymptotic) value of vertical strain at large shaking intensity (or shear strain). The resulting model is termed GQ/H-ε_v, and is presented below.

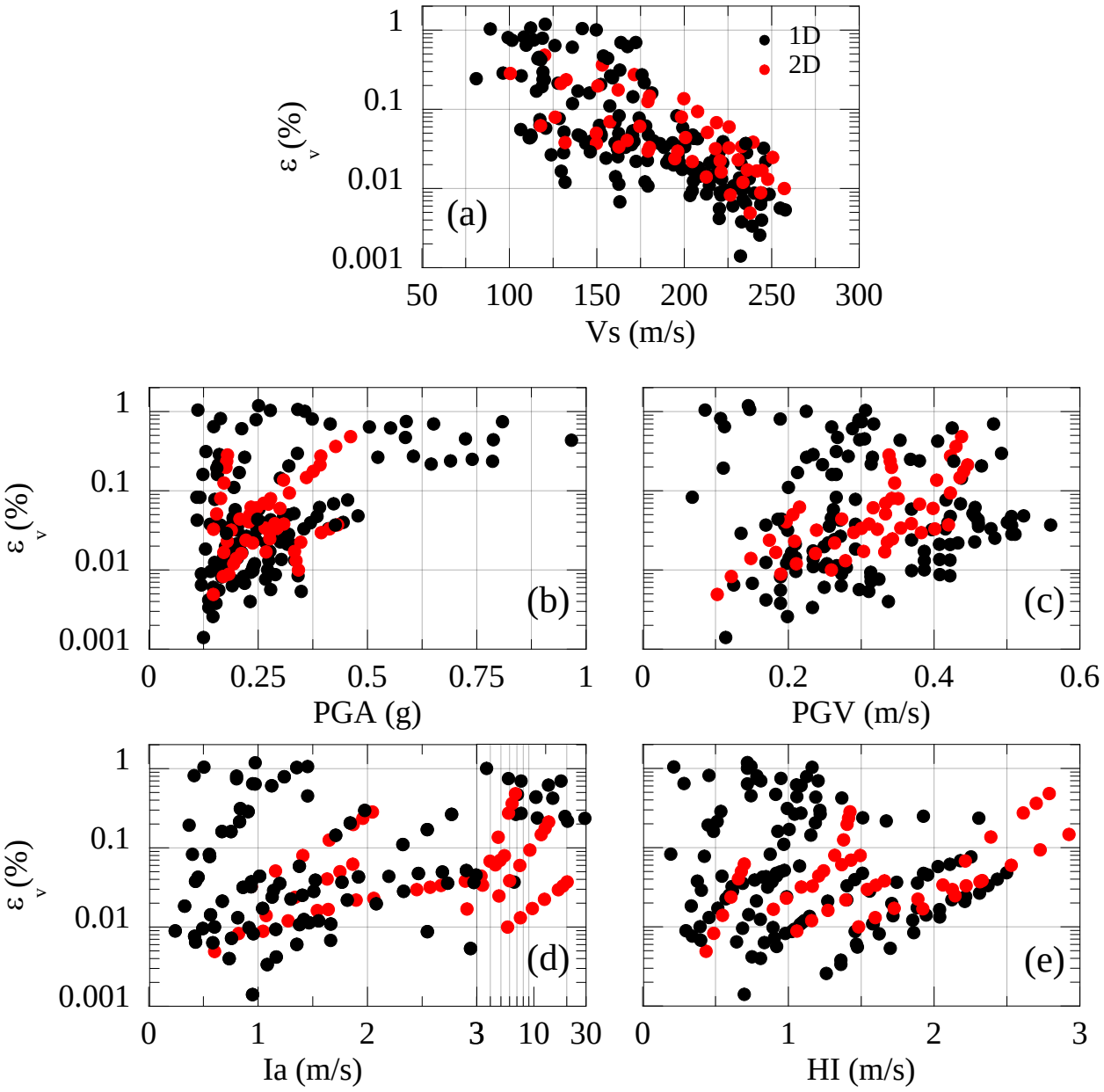

Figure 5-9. Relationship between shaking induced volumetric strain versus (a) Vs (m/s); (b) PGA; (c) PGV; (d) Ia; and (e) HI.

$$\varepsilon_{v_{1Dor2D}}(\%) = \frac{2 \cdot IM \cdot \theta_1}{(IM+1)\cdot\theta_2 + \sqrt{(IM+1)^2 \cdot {\theta_2}^2 - 4 \cdot IM}} \cdot \left(\frac{1}{e^{\theta_3 \cdot \left(\frac{\mathcal{R}}{100}\right)^{\theta_4}}} \right) \pm \varepsilon \qquad (5\text{-}3)$$

where IM = intensity measure; θ_i = model parameters; $\mathcal{R}$ = resistance index (i.e., Vs, in m/s, for this study); $\varepsilon_{v_{1D}}$ = vertical strain resulting from 1D shaking; $\varepsilon_{v_{2D}}$ = vertical strain resulting from 2D shaking; and ε is an error term. In Eqn. (5-3), vector PGA (percentage of g), vector PGV (m/s), Ia (m/s), and HI (m/s) can be utilized as the intensity measure (IM). Although not measured in this study, other field indices such as N_{60} or q_c can be utilized as the resistance index ($\mathcal{R}$). Each combination of IM and $\mathcal{R}$ results in different model parameters.

Table 5-3 summarizes the GQ/H-ε_v model parameters for vector PGA, vector PGV, Ia, and HI coupled with Vs. Note that θ_1 and θ_2 are constant for the Vs model summarized here, but would change if a different resistance index ($\mathcal{R}$) was used.

For the vector PGA and PGV models, only 1D cases were regressed as peak amplitudes do not capture multi-directional volumetric behavior (Chapter 4). Therefore, for PGA and PGV models, vertical strain ($\varepsilon_{v_{1D}}$) should be modified as follows to reflect 2D shaking using the multi-directionality factor (Eqn. (5-101)) for vertical strain (MDF-ε_v) described in Chapter 4.

$$\varepsilon_{v_{2D}} = \varepsilon_{v_{1D}} \mathrm{MDF}_{\varepsilon v} \tag{5-4}$$

As discussed in Chapter 4, MDF-ε_v appears to be strongly related to the factor of safety against liquefaction triggering, FS_{liq}. For FS_{liq} < 1.0, MDF-ε_v is approximately 1.3, and increases as FS_{liq} increases, as:

$$\mathrm{MDF}_{\varepsilon v} = 2\left(1 - e^{(1-2FS_{liq}^{0.5})}\right) \geq 1.3 \tag{5-5}$$

For the energy-based models (Arias and Housner intensities), 1D and 2D cases were included in the regression as these parameters are able to capture multi-directionality effects (Chapter 4). Hence, for the Ia and HI models, Eqn. (5-3) should be used alone as the procedure requires the computation of the total (2D) intensity for the site via selection of a suite of ground motions as explained in Section 6.3.3.

The model error, ε, is assumed to have a normal distribution and approximates the standard deviation of the residual error. This is defined as the square root of the mean square error (MSE) of the database as shown below.

$$\mathrm{MSE} = \frac{SSE}{n - p} \tag{5-6}$$

$$\mathrm{SSE} = \sum_{i=1}^{n} (y_i - \tilde{y}_i)^2 \tag{5-7}$$

where SSE = sum of squared errors of the database; n = number of database observations; p = number of model parameters; y_i = individual actual response variable (recorded vertical strain); and

$\tilde{y}_i$ = individual predicted response variable (computed vertical strain). The SSE is a measure of the variation in vertical strain that is not described by the proposed model and thus represents the term to be minimized by manipulating the model parameters.

Figure 5-10 compares vertical strains from the GQ/H-ε_v with respect to the ε_v database, including vertical strain data compiled by Kim (2017) for loose to medium dense, saturated sands. Each plot in Figure 5-10 corresponds to a different IM, and the ε_v database was binned using Vs values measured or estimated for the corresponding shaking event. The plots illustrate that the measured ε_v values generally fall within the range of GQ/H-ε_v estimates for the given Vs bin for each of the IM parameters.

Table 5-3 Model Parameters

Vertical strain model parameters					
	$\mathcal{R}$ (Resistance Factor) = Vs				Model error ±(ε)
IM	θ_1	θ_2	θ_3	θ_4	
Vector PGA (%g)	57.14	4.0	1.35	1.75	0.54
Vector PGV (m/s)	95.24	4.0	1.35	1.75	0.51
Ia (m/s)	30.3	4.0	1.25	1.80	0.44
HI (m/s)	42.0	4.5	1.26	1.82	0.43

5.2.4 Procedure to estimate free-field vertical strain using the GQ/H-ε_v model

The proposed GQ/H-ε_v model for dense sands can be used regardless of saturation, as shaking-induced settlements in the centrifuge tests occurred under partially drained conditions (small excess PWP). Consequently, GQ/H-ε_v model can be used to estimate free-field vertical strain in two forms (described below): (1) a simplified procedure using PGA; and (2) a procedure using PGA, PGV, Ia, or HI computed by total or effective stress nonlinear site response analysis. In dense sands, total stress site response analysis yields results nearly identical to effective stress analysis because excess PWP generation is minor (r_u < ~0.5) even when shaking is strong (Numanoglu 2017; see Chapter 4 for measured excess PWP values in dense sands).

The simplified procedure using PGA consists of three steps.

Step 1: Using the PGA at the ground surface defined from a seismic hazard analysis, estimate PGA throughout the sand layers within a soil profile using a depth reduction factor for PGA (r_d; e.g., Idriss and Boulanger 2008) as:

$$PGA_{depth} = PGA_{Surface}.r_d \quad (5\text{-}8)$$

Step 2: Compute shaking-induced vertical strains using the GQ/H-ε_{v1D} model (Eqn. 5-3) for shear wave velocities measured (or estimated) within sand layers along the profile (sand layers can be subdivided as appropriate). Apply a multi-directionality factor (MDF-ε_v) to adjust the 1D ε_v for 2D shaking (Eqn 5-4).

Step 3: Compute sublayer settlement as the product of the vertical strain per layer and the thickness of each sublayer. Sum the sublayer settlements to compute surface (total) shaking-induced settlement.

Alternatively, the GQ/H-ε_v model can be coupled with a nonlinear site response analysis as follows.

Step 1: Perform an appropriate total or effective stress site response analysis using appropriate software (e.g., DEEPSOIL), input parameters [i.e., measured Vs profile, Darendeli (2001) modulus reduction and damping curves with implied strength correction, etc.], and paired (e.g., EW and NS) ground motions to obtain the vectored PGA, vectored PGV, and total Ia or HI distribution with depth. The total Ia or HI for the two orthogonal-direction motions is estimated by summing the Arias intensity values as $Ia_{2D} = Ia_{EW} + Ia_{NS}$ or finding the resultant Housner intensity as $HI_{2D} = \sqrt{HI_{EW}^2 + HI_{NS}^2}$ based on the Arias or Housner intensities computed for each direction of shaking.

Step 2: Compute shaking-induced vertical strains using the GQ/H-ε_v model (Eqn. 5-3) for shear wave velocities measured (or estimated) within sand layers along the profile (sand layers can be subdivided as appropriate). For vectored PGA or PGV, apply the multi-directionality factor (MDF-ε_v) to the estimated vertical strains from the GQ/H-ε_{v1D} model as described above. The multi-directionality factor is not needed if the total Ia or HI are used to estimate ε_{v2D} directly.

Step 3: Compute sublayer settlement as the product of the vertical strain per layer and the thickness of each sublayer. Sum the sublayer settlements to compute surface (total) shaking-induced settlement.

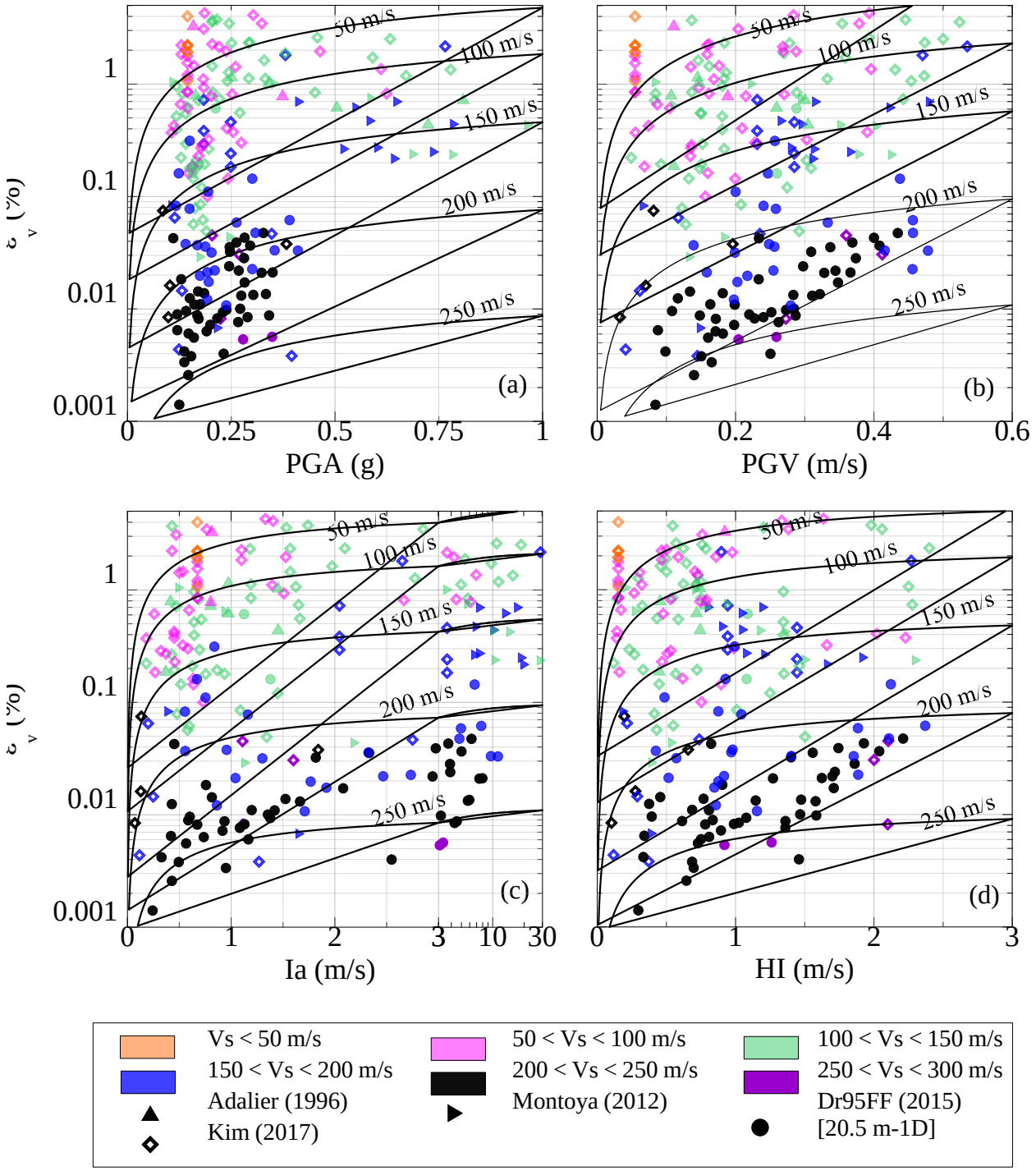

Figure 5-10. GQ/H-εv model compared to dense sands database against for a range of Vs for various IM: (a) PGA; (b) PGV; (c) Ia (in logarithmic scale for Ia > 3 m/s for clarity); and (d) HI. Kim (2017) database for loose sands is shown for comparison.

5.2.5 GQ/H-ε_v model accuracy

Figure 5-11 compares the settlements computed using the GQ/H-ε_v model (following the procedures in Section 6.3.3) to the surface settlements measured in the dynamic centrifuge tests summarized in Table 5-1. Specifically, Figure 5-11(a) presents settlements computed using the surface PGA and Idriss and Boulanger (2008) r_d factor as the IM, while Figure 5-11(b) to (d) presents settlements computed using PGV, Ia and HI as the IM computed from site response analysis. Settlements computed for 2D shaking using the simplified GQ/H-ε_v model generally agree reasonably with the measured surface settlements. And, settlement estimates are improved when using the GQ/H-ε_v model in conjunction with site response analysis results (see Figure 5-11(d) using HI).

For comparison, we also computed settlements for the dense sand profiles (summarized in in Table 5-1) using the Cetin et al. (2009) and Pradel (1998) methods, which are based on undrained and drained cyclic shear tests, respectively (see Chapter 2). As illustrated in Figure 5-11, the approach based on undrained cyclic shear tests consistently overpredicts the measured settlements in the dense sand profiles. In contrast, the approach based on drained cyclic shear tests reasonably agrees with both measured settlements and GQ/H-ε_v model. This result is expected in dense saturated sands as excess PWP generation and reconsolidation are minor, i.e., shaking occurs under nearly drained conditions.

While the proposed GQ/H-ε_v model clearly improves settlement estimates compared to conventional "undrained" methods, there is still considerable scatter in the predictions. To evaluate whether this level of scatter is acceptable, we compared the scatter graphically and in terms of residuals to the scatter that results from estimating the settlement of sands subjected to static (monotonic) loading. Terzaghi et al. (1996) summarized methods to estimate settlements of sands under static loading proposed by Burland and Burbidge (1985) and by Schmertmann (1970)/Schmertmann et al. (1978). Terzaghi et al. (1996) also compared settlement estimates using these two procedures to measured settlements in the combined "static settlement" database. Superimposed on Figure 5-11 is the range of computed-to-measured settlements for the Burland and Burbidge (1985) and Schmertmann (1970)/Schmertmann et al. (1978) methods, as computed by Terzaghi et al. (1996). As illustrated in the figure, the inherent scatter between computed and measured shaking-induced settlements is quite comparable to the inherent scatter between computed and measured static settlement of sands.

Figure 5-12 quantifies this scatter using residuals, computed as:

$$Residual\ \varepsilon_v(\%) = \log\left(\left(\frac{\varepsilon_v(\%), \text{recorded})}{\varepsilon_v(\%), \text{computed}}\right)\right) \quad (5\text{-}8)$$

Thus, positive residuals mean that the vertical strain is underestimated and negative values mean the vertical strain is overestimated.

To gain a broader perspective of the capabilities of the GQ/H-ε_v model, the data collected in this study was combined with the data for loose to medium-dense saturated sands collected and analyzed by Kim (2017). As illustrated in the Figure 5-12, when considering the entire database (i.e., from this study and from Kim 2017), the GQ/H-ε_v model results in nearly unbiased estimates of shaking-induced vertical strain when plotted against Vs for each of the IM (PGA, PGV, Ia, and HI) considered in this study. When considering residuals as a function of ε_v, the GQ/H-ε_v model

exhibited ε_v-residuals of less than ±0.5 for 90% of the database of dense sands (Dr > 70%) and less than ±0.8 for 90% of the entire database (Dr > 40%). For comparison, as computed by Terzaghi et al. (1996), the Burland and Burbidge (1985) model exhibited ε_v-residuals of less than ±0.6 for 90% of their database and the Schmertmann (1970)/Schmertmann et al. (1978) model exhibited ε_v-residuals of less than ±0.7 for 90% of the database. This comparison illustrates that the proposed GQ/H-ε_v model for estimating shaking-induced settlement of sands is nearly as reliable as methods developed to estimate static load-induced settlement of sands.

5.2.6 Summary

A semi-empirical vertical strain model (GQ/H-ε_v) was developed using a large database of dynamic centrifuge tests on saturated, dense, clean, uniformly-graded sands to estimate shaking-induced settlement under multidirectional loading. The model uses seismic intensity measures of PGA, PGV, Arias intensity, and Housner intensity coupled with shear wave velocity, but could be adapted for other resistance parameters such as SPT blow count or CPT tip resistance. The GQ/H-ε_v model can be implemented in both a simplified manner (using surface PGA and an r_d factor) or by means of nonlinear site response analysis (e.g., DEEPSOIL).

Model estimates of vertical strain for 1D and 2D shaking database show that in general the simplified GQ/H-ε_v model reasonably agrees with measured settlements of dense, saturated sands. However, estimated settlements improved when GQ/H-ε_v model was coupled with IMs computed by site response analysis. Furthermore, settlements computed using velocity-based IMs (PGV and HI) better agree with observed settlements compared to acceleration-based IMs (PGA and Ia). Lastly, when employed for dense sands (Dr>70%) the proposed model reasonably agrees with existing settlement methods based on drained cyclic shear tests (e.g., Pradel 1998), and the proposed model gives a nearly unbiased estimation of shaking-induced settlement for dense sands.

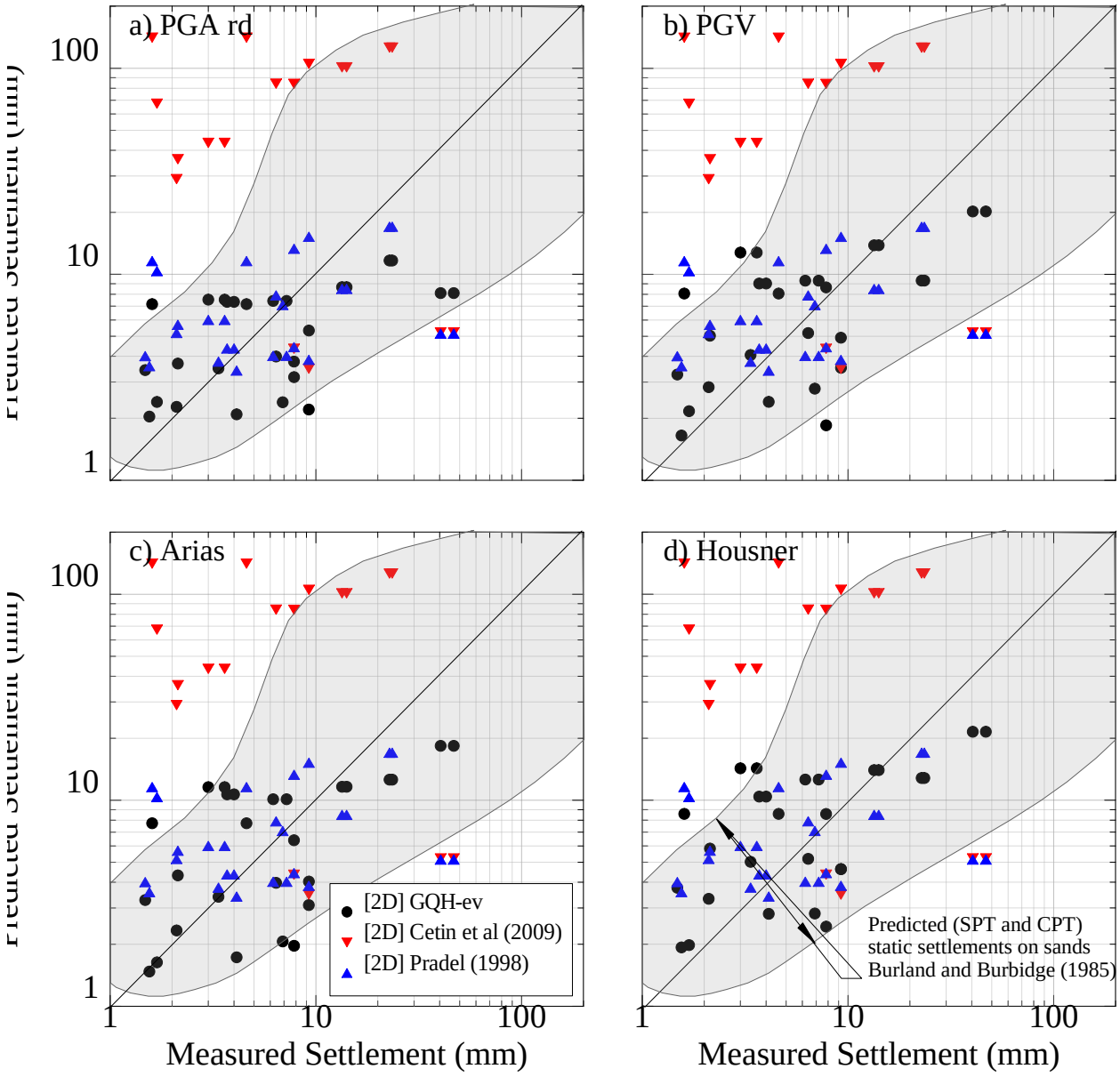

Figure 5-11. Comparison of shaking-induced settlements computed using the GQ/H-ε_v model and the Cetin et al. (2009) and Pradel (1998) models for: (a) surface PGA and Idriss and Boulanger (2008) r_d factor; (b) PGV using nonlinear site response analysis (DEEPSOIL); (c) Arias intensity using nonlinear site response analysis (DEEPSOIL) and; (d) Housner Intensity using nonlinear site response analysis (DEEPSOIL). Superimposed on the plots are the range of measured-to-computed settlements for static (monotonic) loading of sands computed by Terzaghi et al. (1996) using the Burland and Burbidge (1985) procedure.

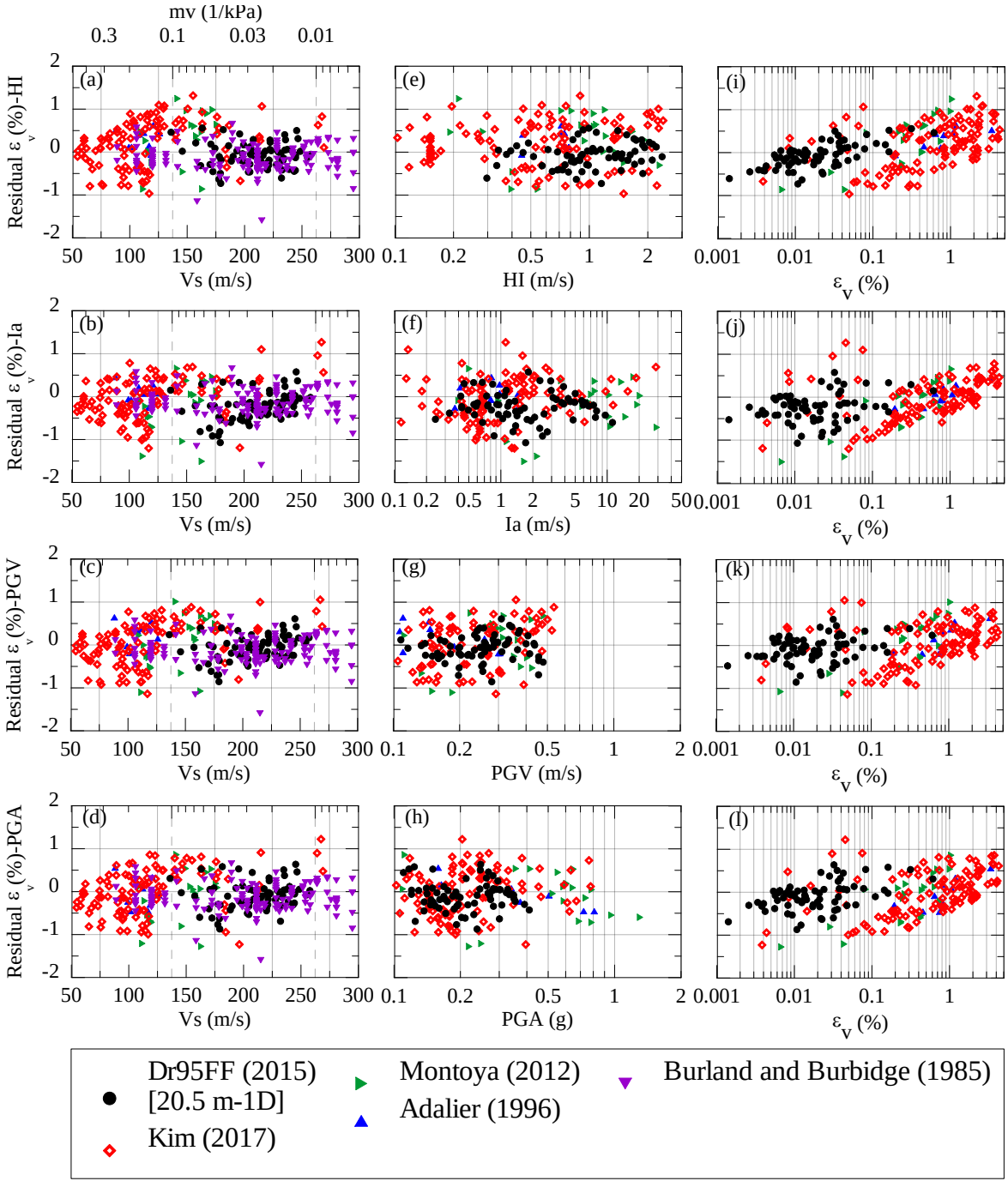

Figure 5-12. Residuals of vertical strain GQ/H-ε_v models compared to dense sands database against (a) to (d) Vs; (e) to (h) IM (PGA, PGV, Ia, and HI); and (i) to (l) ε_v. Kim (2017) database for loose sands is shown for comparison only. Superimposed on the plots (a) to (d) are the residuals-computed vertical strains for static (monotonic) loading of sands computed using the database from Burland and Burbidge (1985).

5.3 Estimation of Volumetric Strain under Structures using Centrifuge Testing on Saturated Dense Sands

In this Chapter, we describe a semi-empirical model to estimate shaking-induced vertical strains (ε_v) in dense sands in near-field (NF) conditions (i.e., near or below a structure) using centrifuge test data from dense sand models. The centrifuge tests include a set of unidirectional (1D) and bidirectional (2D) dynamic centrifuge tests performed in this study on a thick layer (prototype thickness of 10.25 and 20.5 m) of saturated, dense (relative density, D_{Ro} ~ 95%), fine Ottawa sand. The data also includes 1D results from centrifuge tests performed by Montoya (2012) on dense Ottawa sand (D_{Ro} ~ 85%). The centrifuge models were excited using both broadband and sinusoidal motions with Arias intensities that ranged from 0.07 to 30 m/s.

The proposed semi-empirical vertical strain model includes energy-based ground motion intensity measures to account for duration (e.g., Arias and Housner intensities) and a rocking stiffness parameter (originally proposed by Gazetas 1991) derived from shear wave velocity (V_S). The vertical strain model requires estimates of Arias or Housner intensity by means of site response analysis. The proposed vertical strain model reasonably captures settlements of structures founded on dense sands recorded in dynamic centrifuge tests.

5.4 Estimation of Near-field Vertical Strain of Dense Sands using Centrifuge Tests

5.4.1 Introduction

Vertical strains related to soil-structure interaction have been increasingly studied in the last twenty years using dynamic centrifuge tests. Based on Yoshimi and Tokimatsu (1977), Liu and Dobry (1997) normalized NF settlements by liquefiable soil thickness measured in a series of centrifuge tests (Figure 5-13a). While this normalized NF settlement tended to decrease with increasing structure width normalized by liquefiable soil thickness, Dashti et al (2010) later performed a series of centrifuge tests on loose Nevada sand and, as shown in Figure 5-13b, concluded that this trend may not apply to deposits with thin, near-surface liquefiable layers. Dashti et al. argued that the major source of NF settlement resulted from ratcheting of the structure into the softened, liquefied layer rather than solely shaking-induced vertical strains of the soil.

Dashti et al. (2010) describes this ratcheting as deviatoric strains and suggested that dynamic rocking of the structure increased vertical strains and total settlement. The NF settlements in Dashti et al. (2010) tests were three to eight times higher than the free-field (FF) settlements. Similarly, Montoya (2012) performed a dynamic centrifuge test to explore NF settlements. Although the bearing pressure of the structure was low (q_b ~ 80 kPa) compared to a typical nuclear power plant (NPP) structure, NF settlements were 30% to 100% greater than FF settlements. And, despite the settlement mechanisms inferred from centrifuge tests, there is no simplified procedure available to assess near-field vertical strain in sand under multi-directional loading.

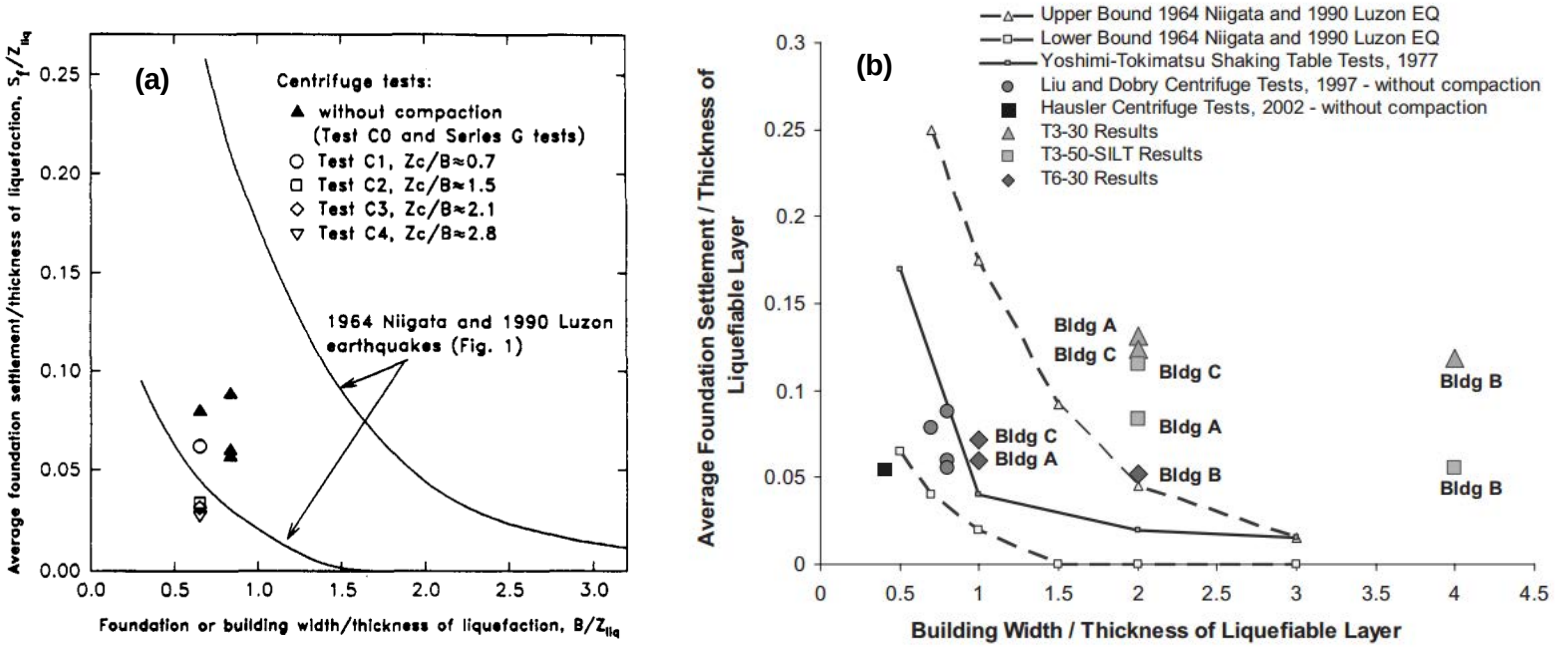

Figure 5-13. (a) Comparison between foundation width and foundation settlement, both normalized by liquefied layer thickness, observed in centrifuge test series with field observations made following 1964 Niigata, Japan and 1990 Luzon, Philippines earthquakes (Liu and Dobry 1997); and (b) comparison of Liu and Dobry (1997) summary with same parameters measured in more recent centrifuge test series reported by Dashti et al. (2010).

In this study, using near-field dynamic centrifuge tests on dense sands, we propose a semi-empirical rocking model to estimate shaking-induced NF vertical strains in dense saturated sands under multi-directional cyclic loading. The proposed model utilizes both foundation rocking stiffness (K_R) and energy-based intensity measures (e.g., Housner intensity) to capture vertical strains under multi-directional earthquake loading in conjunction with a local factor of safety against shear failure (FS_{local}).

5.4.2 Proposed model database

5.4.2.1 Centrifuge tests

For developing a semi-empirical model to estimate shaking-induced NF vertical strain in dense sands, a database of bidirectional (2D) and unidirectional (1D) dynamic centrifuge testing was collected. The database, summarized in Table 5-1, includes results from tests performed for this study and tests performed by Montoya (2012).

Table 5-4 Dynamic centrifuge tests involving dense sands and near-field conditions (i.e., with structures)

Reference	Prototype sand thickness (m)	Pre-shaking D_{Ro} (%)	Centrifugal acceleration (g)	Type of loading	Key details	Facility
This study	20.5 and 10.25	95	60 and 30	1D and 2D	Free-field and near-field (q_b~380 and 190 kPa) (28 shaking events)	RPI
Montoya (2012)	6	85	50	1D	Free-field and near-field (q_b~80 kPa) (7 shaking events)	UC-Davis

In this study, we examined the response of dense, saturated Ottawa 40/70 sand (D_{Ro} ~ 95%) with a high bearing pressure structure (q_b ~ 380 and 190 kPa) to multidirectional (2D and 1D) earthquake loading using dynamic centrifuge tests. The dense sand prototype thicknesses of 20.5 m and 10.25 m were achieved at centrifugal accelerations of 60g and 30g, respectively. As shown in Figure 5-14 and Figure 5-15, models were instrumented using accelerometers (ACC), porewater pressure (PWP) transducers (PPT), and lateral and vertical linear voltage differential transformers (LVDTs) placed on the structure and along the model depth. Two pairs of bender elements (BE) were used to measure horizontally propagating, horizontally polarized shear wave velocities ($V_{S,HH}$) underneath the structure and one pair of BE was used to measure horizontally propagating, vertically polarized velocity ($V_{S,HV}$) at the base of the model.

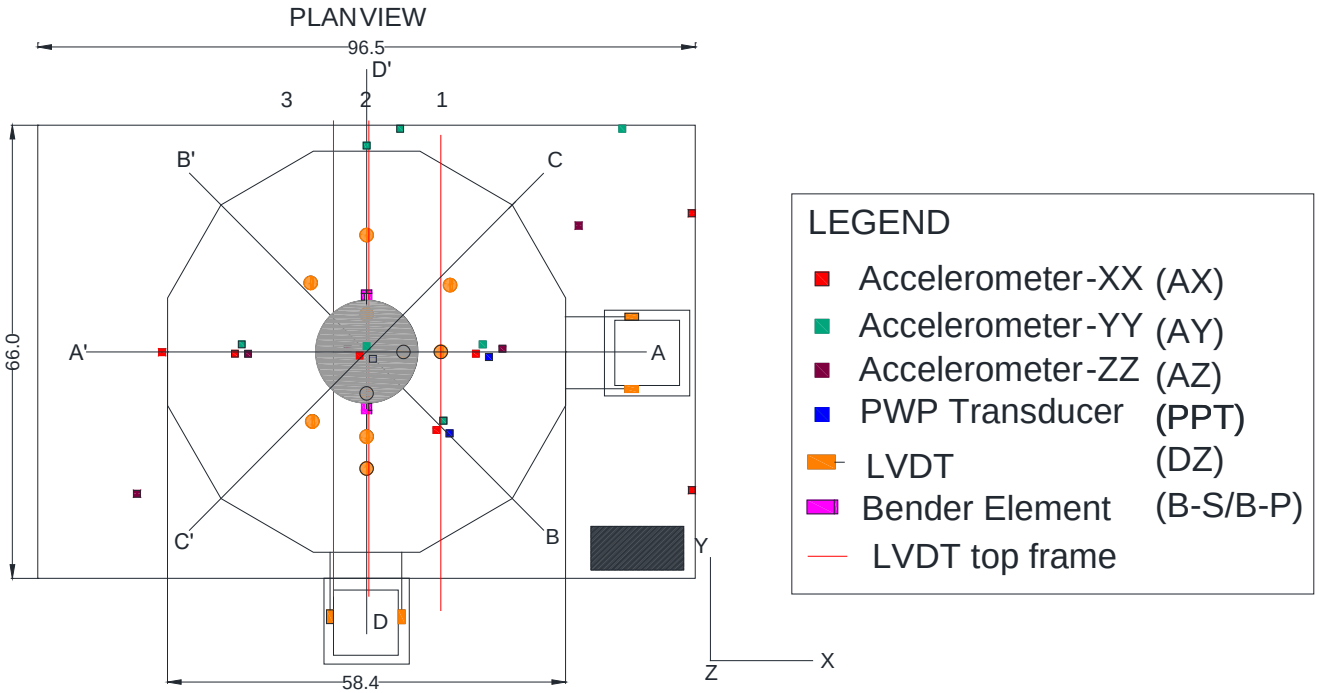

All dimensions are in centimeters (model scale)
Initial coordinates (X,Y)=(0,0) starts at the center of the circle
Initial coordinates Z=0 starts at the base of the model

Labeling of instrumentation
A B/C
A : type of instrument [e.g. A (AX,AY,AZ), DZ(LVDT), B-S or B-P (BE), ST (Structure)]
B : level considering the number of layer from 0 to 4 (see sections AA,BB.CC.DD)
C : column of array according to Plan View. From 1 to 3 (see plan view)

Figure 5-14. Plan view for test Dr95NF (Dr ~ 95%, Near-field) including instrumentation layout.

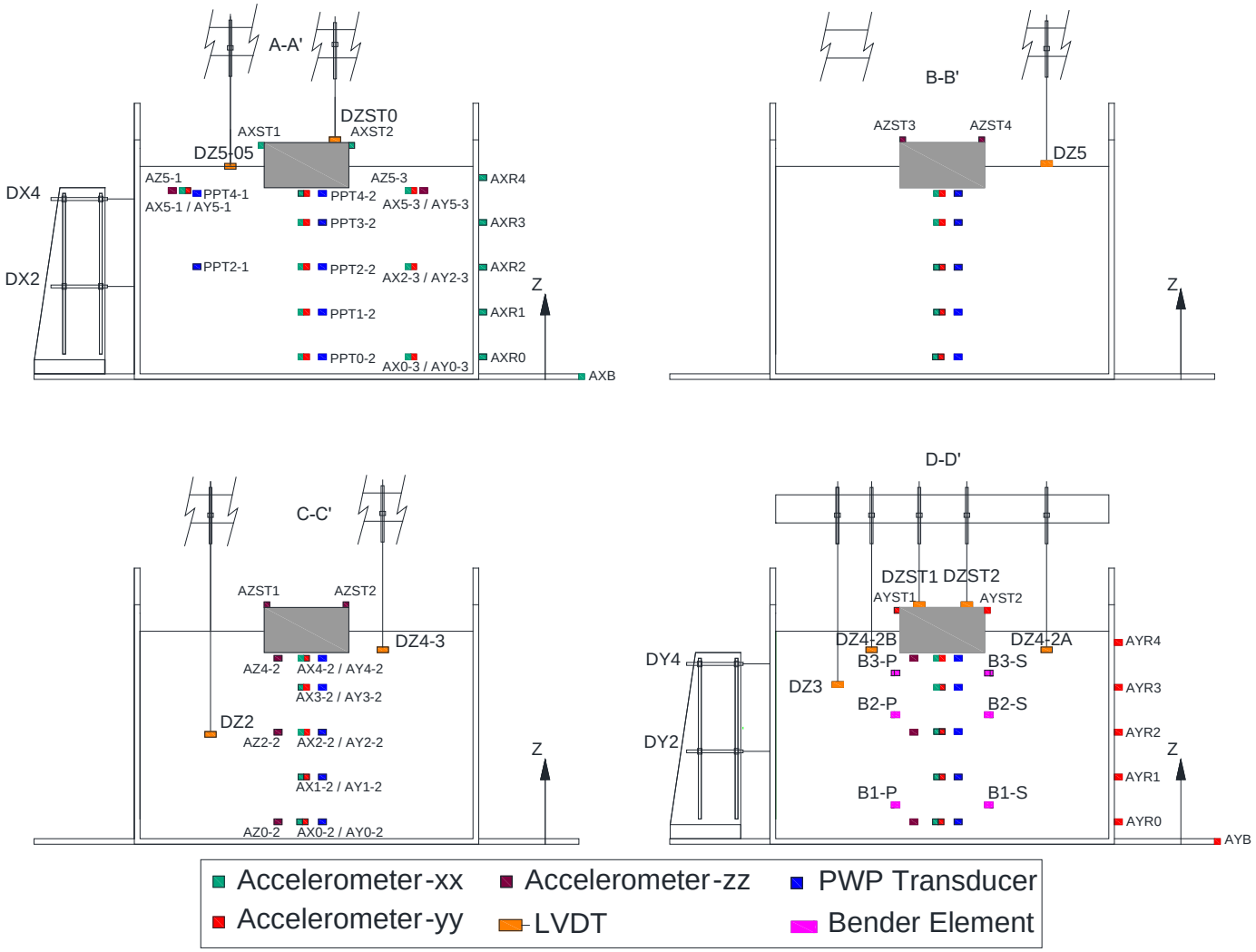

Figure 5-15. Detailed instrumentation layout for test Dr95NF. (a) Section A-A'; (b) section B-B'; (c) section C-C'; and (d) section D-D'. Section locations shown in

Figure 5-14..

Montoya (2012) studied the effect of bio-mediated soil improvement on the dynamic response of sands that included NF experiments that involved a structure with a bearing pressure of about 80 kPa founded on a dense, non-treated, saturated Ottawa 50/70 sand (D_{Ro} ~ 85%). The prototype sand thickness was 6 m at a 50g centrifugal acceleration. As shown in Figure 5-3, the model instrumentation included accelerometers (ACC), PWP transducers (PPT), bender elements (BE), and vertical linear voltage differential transformers (LVDTs) placed on the structure and at the model sand surface.

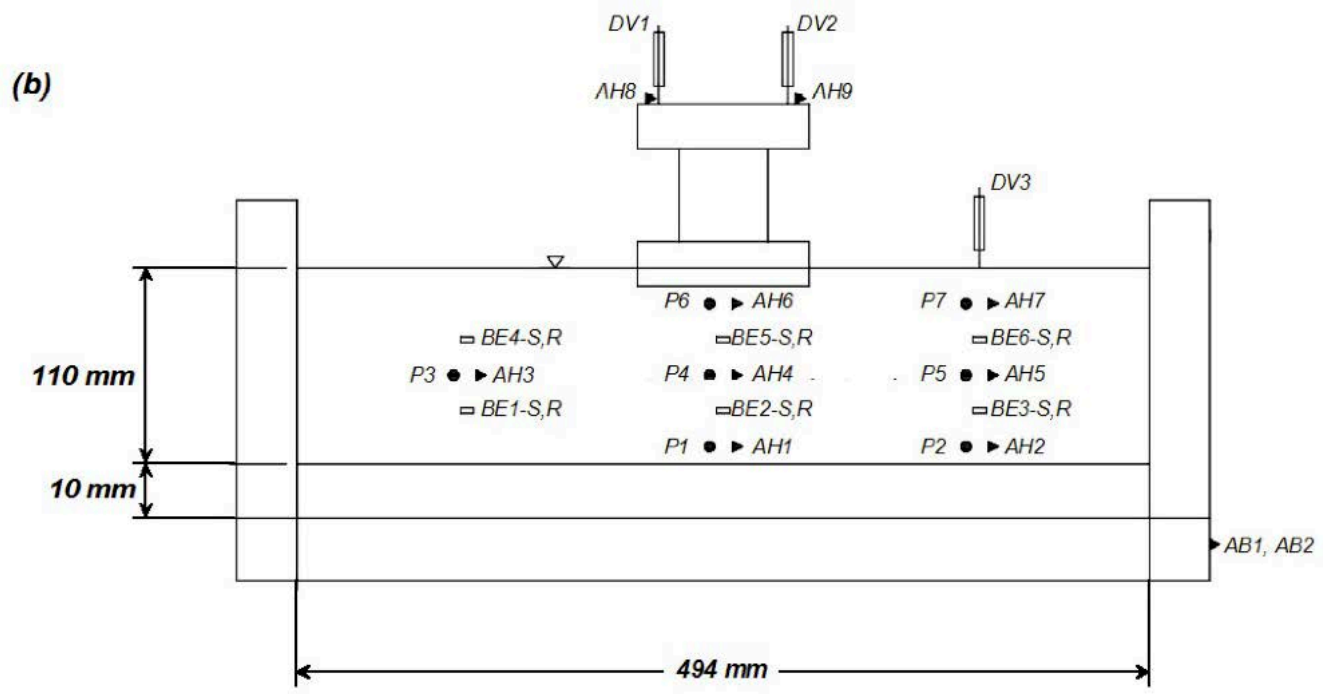

Figure 5-16. Schematic of instrumentation for a 6m (prototype) centrifuge model Dro=85% (Montoya 2012).

5.4.2.2 Test sands

The sands used in the tests listed in Table 5-1 are fairly uniform, fine, clean sands. This study used U.S. Silica Company Ottawa 40/70 sand while Montoya (2012) used Ottawa 50/70 sand. These sands have subrounded grains and are poorly-graded, with a median grain sizes (D_{50}) of about 0.15mm and 0.28mm, respectively, and uniformity coefficients (C_U) of 1.36 and 1.83, respectively. Figure 5-5 presents the grain size distributions of these sands and a scanning electron microscope image of the Ottawa 40/70 sand. Table 5-2 summarizes key parameters for these sands, including minimum void ratio (e_{min}), maximum void ratio (e_{max}), and specific gravity. All parameters were obtained following ASTM D4254, ASTM D4253, or Japanese method standards.

Table 5-5 Soil indices for clean sands

Sand	USCS[a]	D_{50}[a] mm	C_U[a]	C_C[a]	G_s[b]	e_{max}[c]	e_{min}[d]	Reference
Ottawa 50/70	SP	0.28	1.36	0.99	2.67	0.82	0.50	Cerna-Diaz (2017)
Ottawa 40/70	SP	0.22	1.40	0.90	2.65	0.87	0.55	Montoya (2012)
Nevada 120	SP	0.15	1.83	1.28	2.67	0.89	0.51	Adalier (1996)

Note: USCS – Unified Soil Classification System; D_{50} – median particle size; C_U – coefficient of uniformity; C_C – coefficient of curvature; G_s – specific gravity; e_{max} – maximum void ratio; e_{min} – minimum void ratio;

[a]ASTM D2487 (ASTM 2011)

[b]ASTM D854 (ASTM 2014)

[c]Dry tipping method equivalent to ASTM D4254 (ASTM 2006)

[d]Japanese method equivalent to ASTM D4253 (ASTM 2016) for Ottawa sand 40/70

[e]ASTM D1557 (ASTM 2012)

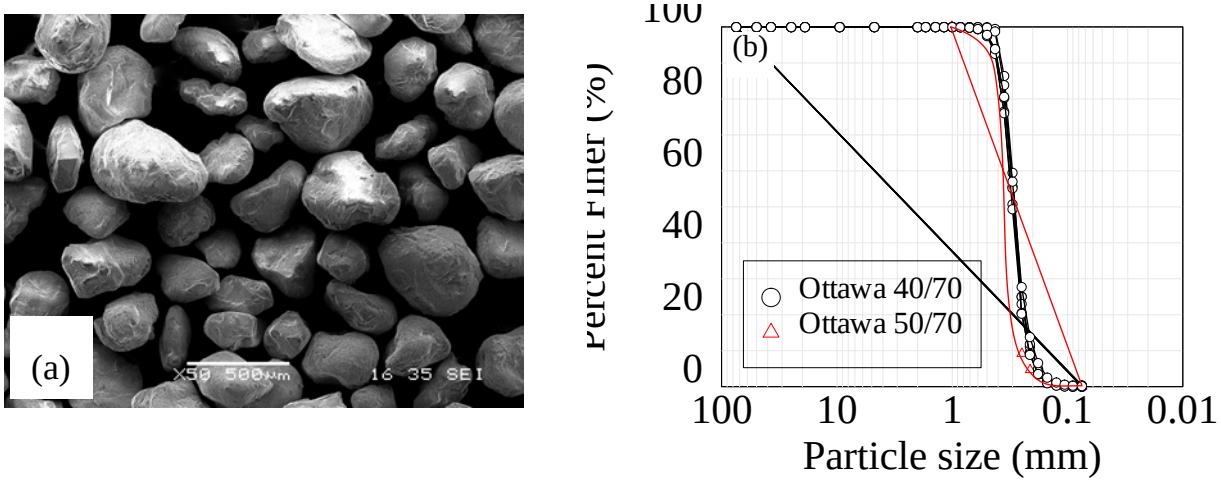

Figure 5-17. (a) Scanning electron microscope image of Ottawa 40/70 sand used in testing program; and (b) grain size distributions of Ottawa 40/70 and Ottawa 50/70 sand used from centrifuge database.

5.4.2.3 Model intensity measures (IM) seismic demand parameters

The centrifuge models listed in Table 5-1 were excited by both recorded seismic events (broadband motions) and sinusoidal motions input at the model bases. Figure 5-8 presents response spectra, input Arias and Housner intensities for seismic events used in this study. Individual input motions for Montoya (2012) can be found in Cerna-Diaz (2017). Broadband motions used in this study included both 1D recorded motions and 2D recorded motions in which two horizontal orthogonal components were available, induced by both crustal and subduction rupture mechanisms. Montoya (2012) used only 1D sinusoidal motions.

Arias intensity (Ia) and Housner intensity (HI) were computed beneath the structure as follows.

$$Ia_{x,y} = \frac{\pi}{2g}\int_0^{tmax} a(t)_{x,y}^2 dt \tag{5-9}$$

where g = acceleration of gravity and a(t) is acceleration at time, t.

$$HI_{x,y} = \int_{0.1}^{2.5} S_{v_{x,y}}(\xi = 0.05, T)dT \tag{5-10}$$

where T = period (s); Sv = spectral velocity, ξ = damping.

These intensities measures (IMs) were computed for both 1D and 2D motions so that total energy from multi-directional shaking could be considered. The input motions used in this study exhibited a fairly broad range of energy content (Arias intensity ranged from 0.07 m/s to 3.2 m/s) that induced nearly linear to nonlinear soil response in the sand models.

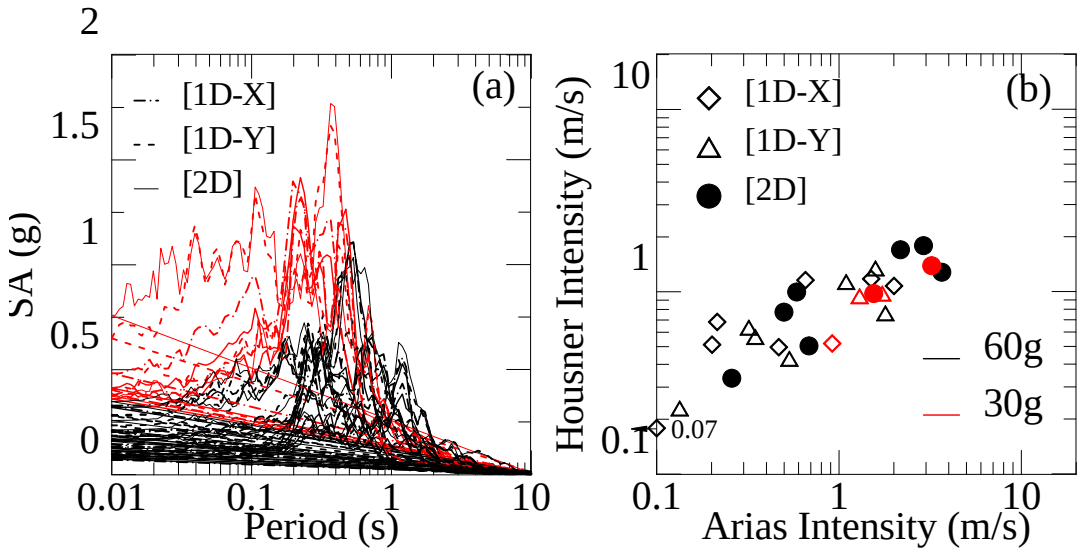

Figure 5-18. Input ground motions used in centrifuge testing program described in this study (black lines and symbols are 60g motions, red lines and symbols are 30g motions). (a) Response spectra; and (b) Arias and Housner intensities.

5.4.3 Near-field vertical strain conceptual model

5.4.3.1 Shaking-induced vertical strain mechanisms

Dashti et al. (2010) identified numerous potential mechanisms related to shaking-induced volumetric and deviatoric strains that result in FF and NF settlement. These potential mechanisms are summarized in Table 5-6. Dashti et al. also suggested that any of these mechanisms could dominate the observed settlements or these mechanics could combine depending on the soil, structural, and ground motions parameters. For instance, while deviatoric rocking-induced settlement (i.e., ratcheting) may dominate during shaking, reconsolidation-induced settlement also may act during and after shaking.

Table 5-6 Free-field and near-field volumetric and deviatoric displacement mechanisms (after Dashti et al 2010)

Displacement Type	Mechanisms of Displacement	Strain Abbrev.	Location
Volumetric	a) Localized volumetric strains due to partial drainage	$\varepsilon_{p\text{-}DR}$	All locations
	b) Sedimentation after liquefaction	$\varepsilon_{p\text{-}SED}$	
	c) Consolidation due to excess pore pressure dissipation	$\varepsilon_{p\text{-}CON}$	
	d) Volumetric expansion due to decrease in effective stresses	$\varepsilon_{p\text{-}EXP}$	
	e) Settlements due to the compression of air in a partially saturated soil or due to compliance errors	$\varepsilon_{p\text{-}COMP}$	
Deviatoric	a) Partial bearing failure due to strength loss in the foundation soil	$\varepsilon_{q\text{-}BC}$	Under & Adjacent to Structures
	b) SSI-induced building ratcheting due to cyclic loading of foundation	$\varepsilon_{q\text{-}SSI}$	

For predictive purposes, volumetric and deviatoric settlement mechanisms listed in Table 5-6 can be simplified to two primary components: (1) settlement resulting from excess porewater pressure (PWP) dissipation during and after shaking, termed S_{PWP}; and (2) settlement resulting from structure rocking, with or without soil softening and liquefaction, termed ($S_{Rocking}$). The PWP term, S_{PWP}, can be further subdivided into: (1) settlement resulting from excess PWP dissipation during shaking (i.e., intercycle partial drainage), termed S_{Sh}; and (2) settlement resulting from excess PWP dissipation after shaking (i.e., reconsolidation only), termed S_{Re}. This is expressed in Eqns. (5-109) and (5-110).

$$S_{\mathrm{NF}} = S_{Rocking} + S_{PWP} = S_{Rocking} + S_{Sh} + S_{Re} \tag{5-11}$$

$$S_{\mathrm{NF}} = \varepsilon_{v,Rocking} \cdot Z_I + \sum_{i=1}^{n} \left(\varepsilon_{v,Sh}\right)_i \cdot L_i + \sum_{i}^{n} \left(\varepsilon_{v,Re}\right)_i \cdot L_i \tag{5-12}$$

where S_{NF} = measured settlement resulting in near-field conditions (below a structure); $\varepsilon_{v,Rocking}$ = vertical strain resulting from structure rocking within zone of influence,Z_I; $\varepsilon_{v,Sh}$ = vertical strain resulting from excess PWP dissipation during strong shaking; $\varepsilon_{v,Re}$ = vertical strain resulting from excess PWP dissipation after strong shaking; Z_I= thickness of zone of influence below structure (as defined by Burland and Burbidge 1985, see Chapter 5); L_i = thickness of i^{th} sand sublayer; n = total number of sublayer.

5.4.3.2 Rocking-induced settlement estimates from centrifuge tests

Ground shaking below a structure supported on shallow foundations results in relative acceleration between the structure and the foundation soil. Relative accelerations at this interface can result in both structure sliding, rocking (local punching failure), and global bearing failure. Structure sliding is driven by the relative acceleration and structure mass and is resisted by both sliding along the base and passive resistance from the ground surface to the depth of foundation (D_f) in front of the structure. Structure rocking (or tilting) is related to local failure (punching) below the edge of the structure and is resisted by the shear strength of the soil on a vertical plane below D_f. Global bearing failure is resisted by global bearing capacity of the soil. Calculations for a limited combination of q_b, relative acceleration, structure width (B) and D_f, and soil strength suggest that rocking (local punching) failure occurs prior to sliding or global bearing failure, consistent with anecdotal evidence from centrifuge tests (e.g., Hausler 2002; Dashti 2010) and post-earthquake building damage surveys (Ashford et al. 2011; Bray et al. 2012; Tokimatsu and Katsumata 2012) where buildings are more likely to suffer settlement and tilting damage than sliding or global bearing failure. Therefore, the calculations described below are based on a rocking (local punching) mechanism.

A simplified mechanism for computing 1D shaking-induced structure settlements (S_{NF}) is depicted in Figure 5-19. Initially, the model structure (mimicking a building supported by a mat foundation or closely spaced footings at a depth, D_f) is in equilibrium under static loading (Figure 5-19a). As soon as shaking in the positive direction (+X) occurs, the shaking-induced inertial interaction between the foundation soil and the structure produces relative horizontal accelerations at their interface as depicted in the schematic time history in Figure 5-19a. Relative accelerations between the structure and foundation soil results in a moment-induced eccentricity in structure bearing pressure (q_b), resulting in an approximate trapezoidal distribution of bearing pressure with maximum and minimum values of $q_{b,max}$ and $q_{b,min}$, respectively, related to the current direction of relative acceleration (Figure 5-19b and c).

A relative yield acceleration ($a_{h,y}$) can be defined that corresponds to the relative acceleration at which $q_{b,max}$ is sufficiently large to cause local failure (punching), resulting in rocking of the structure. While the relative acceleration exceeds $a_{h,y}$, rocking-induced horizontal (D_H) and vertical (D_V) displacements, which are related as shown in Eq. (5-111) and Figure 5-19(b), accumulate.

$$D_{H-i} = 2D_{V-i}\frac{H}{B} \tag{5-13}$$

where D_{H-i} = rocking-induced horizontal displacement at the ith exceedance of $a_{h,y}$; D_{V-i}= rocking induced vertical displacements at the ith exceedance of $a_{h,y}$; and H = structure height.

Rocking-induced vertical strains occur until the relative acceleration no longer exceeds the relative yield acceleration ($a_{h,y}$).

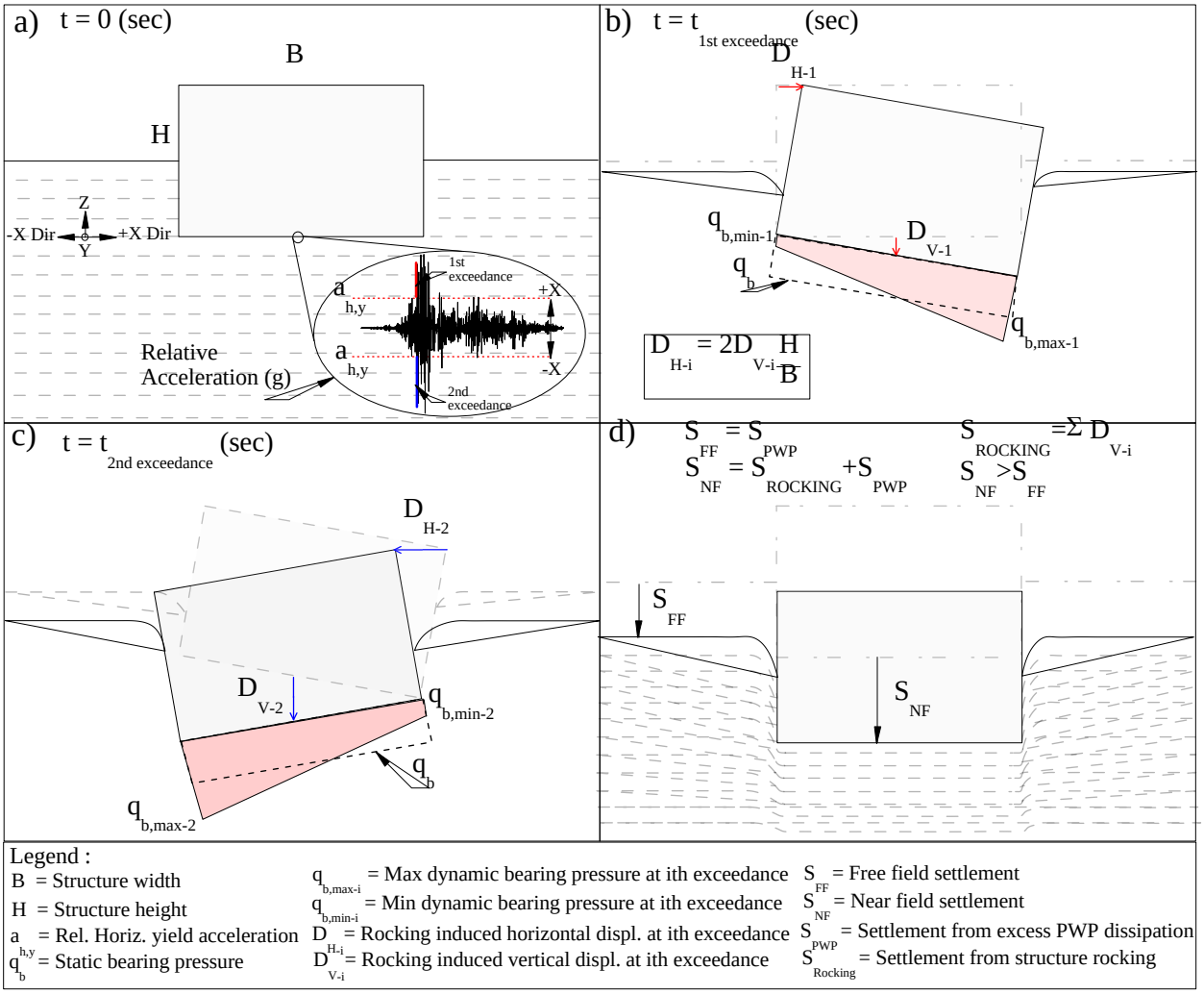

Figure 5-19. Schematic of a rocking rigid block and simplified mechanisms for structure settlements for (a) initial near-field conditions, relative horizontal acceleration between the structure and the foundation soil with the yield relative horizontal acceleration ($a_{h,y}$), and schematic illustration of first and second exceedances of $a_{h,y}$; (b) shaking in the positive direction (+X) and corresponding static and dynamic (seismic) bearing pressures on the foundation soil due to eccentric loading at the time (t) of 1st exceedance of $a_{h,y}$ and the relationship between horizontal and vertical displacement during rocking; (c) shaking in the negative direction (-X) and corresponding static and dynamic (seismic) bearing pressures on the foundation soil due to eccentric loading at the time (t) of 2nd exceedance of $a_{h,y}$; and (d) final structure (S_{NF}) and free-field (S_{FF}) settlements.

Total rocking-induced vertical settlements beneath the structure (Figure 5-19b and c), denoted as $S_{Rocking}$, then can be computed as:

$$S_{Rocking} = \sum_{i=1}^{n} D_{V-i} \tag{5-98}$$

where n = number of exceedance of $a_{h,y}$. Soon after shaking ceases, reconsolidation (only) take place under constant total stress conditions. The final equilibrium condition (Figure 5-19d) is reached when reconsolidation is complete.

In all of the collected cases, structure settlement time histories were available throughout each shaking event. Since rocking-induced settlement within the zone of influence cannot be measured directly, the rocking settlement can be estimated as the total measured structure settlement minus the S_{PWP} below the structure as:

$$S_{Rocking} = S_{\mathrm{NF}} - S_{PWP} \tag{5-99}$$

Kim (2017) proposed a model to estimate vertical settlement (or strain) with depth resulting from intercycle PWP dissipation during shaking (S_{PWP}). To accomplish this, the Kim (2017) model uses sublayer PWP recordings and updated compressibility estimates to compute settlements and vertical strains with depth during and after shaking resulting from intercycle PWP dissipation and reconsolidation as:

$$\sum_{i}^{n} \left(\epsilon_{v,Sh}\right)_i \cdot L_i = \sum_{i}^{n} \int_{First\ Threshold}^{Last\ Threshold} m_{v,t,i}\, \Delta u_{t,i} \cdot L_{t,i} \tag{5-100}$$

$$\sum_{i}^{n} \left(\epsilon_{v,Re}\right)_i \cdot L_i = \sum_{i}^{n} \int_{Last\ Threshold}^{\infty} m_{v,t,i}\, \Delta u_{t,i} \cdot L_{t,i} \tag{5-101}$$

where $\epsilon_{v,Sh}$= vertical strain resulting from excess PWP dissipation during strong shaking; $\epsilon_{v,Re}$= vertical strain resulting from excess PWP dissipation after strong shaking; $m_{v,t,i}$= shaking-induced compressibility at time t and sublayer i; $\Delta u_{t,i}$= shaking-induced excess PWP at time t and sublayer I; $L_{t,i}$ = i^{th} layer thickness at time t; and n = total number of sublayers.

For the cases listed in Table 5-1, settlements were measured on the structure, therefore, PWP-induced vertical strains beneath the structure (from D_f to the model base) were estimated using the Kim (2017) model (Eqns. 5.102 and 5.103). A rocking-induced structure settlement ($S_{Rocking}$) time history then was computed for each shaking event by deducting the computed S_{PWP} time history from the measured S_{NF} time history. Figure 5-20 shows an example of the computed rocking-induced ($S_{Rocking}$) and PWP-induced (S_{PWP}) settlement time histories for motion M1-1D-Y in Dr95NF test. As shown in Figure 5-20(c), the PWP-induced settlement was only about 10% of the structure settlement because of the very dense soil and heavy structure (q_b ~ 380 kPa).

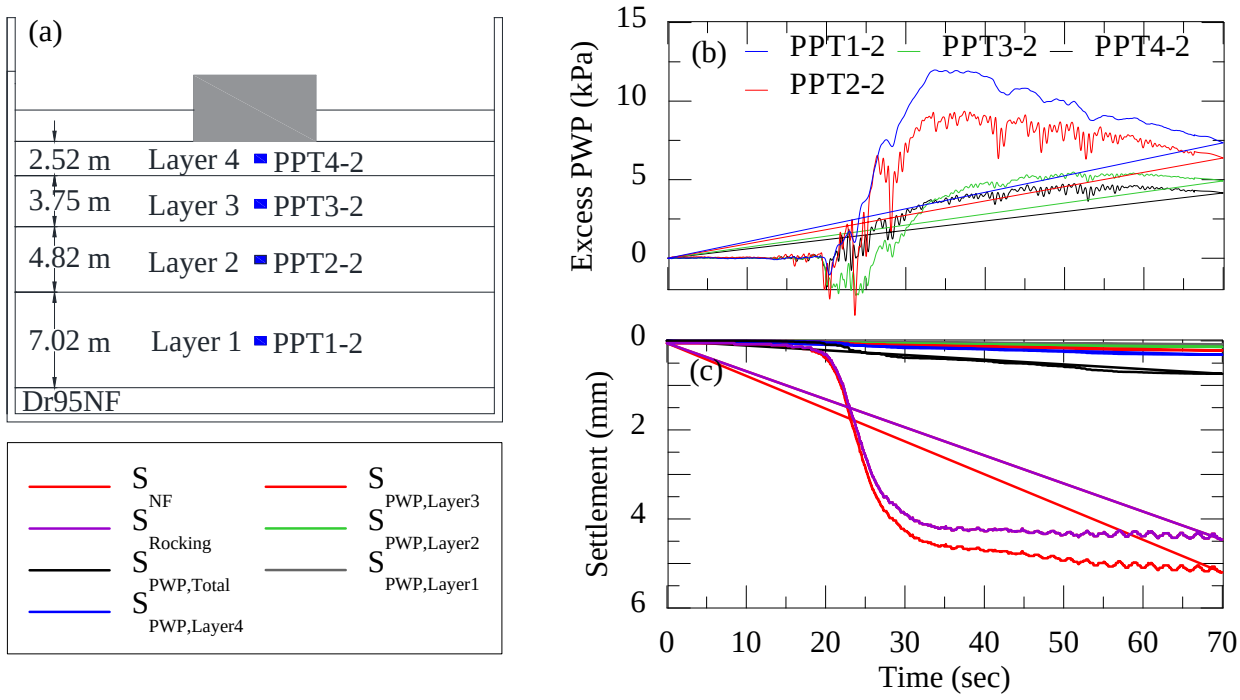

Figure 5-20. Method to estimate rocking-induced settlement beneath the structure for motion M1-1D-Y based on Kim (2017) model. (a) Cross-section of Dr95NF test including sublayers delineated by PWP transducers locations; (b) excess PWP time histories for sublayers below structure; and (c) total measured structure settlement time history (S_{NF}), calculated PWP induced settlement time histories beneath the structure ($S_{PWP,Total}$), and calculated rocking-induced settlement time histories beneath the structure ($S_{Rocking}$).

Figure 5-21(a) compares the computed total rocking vertical strains ($\varepsilon_{v,Rocking}$) from the near-field dynamic centrifuge tests with computed shaking-induced vertical strains for free-field conditions ($\varepsilon_{v,Sh,FF}$) for the recorded or estimated range of initial V_S in all shaking events for the centrifuge tests listed in Table 5-1. Consistent with previous researchers, it is shown that the well-calibrated 1D free-field GQ/H-ε_v model presented in Chapter 6 cannot capture (underestimates) shaking induced vertical strains beneath a structure. Figure 5-21(a) also shows relationships between HI and calculated NF shaking-induced vertical strain (not including reconsolidation) for increasing V_S for these cases. In this context, it appears that as stiffness increases, the NF vertical strain (for a given shaking intensity) decreases. Using the data in Figure 5-21(a), Figure 5-21(b) compares ratios of $\varepsilon_{v,Sh,FF}$ (%)/HI or $\varepsilon_{v,Rocking}$ (%)/HI to V_S. This comparison also shows that NF vertical strains exceed FF vertical strains for a given shaking intensity and soil stiffness.

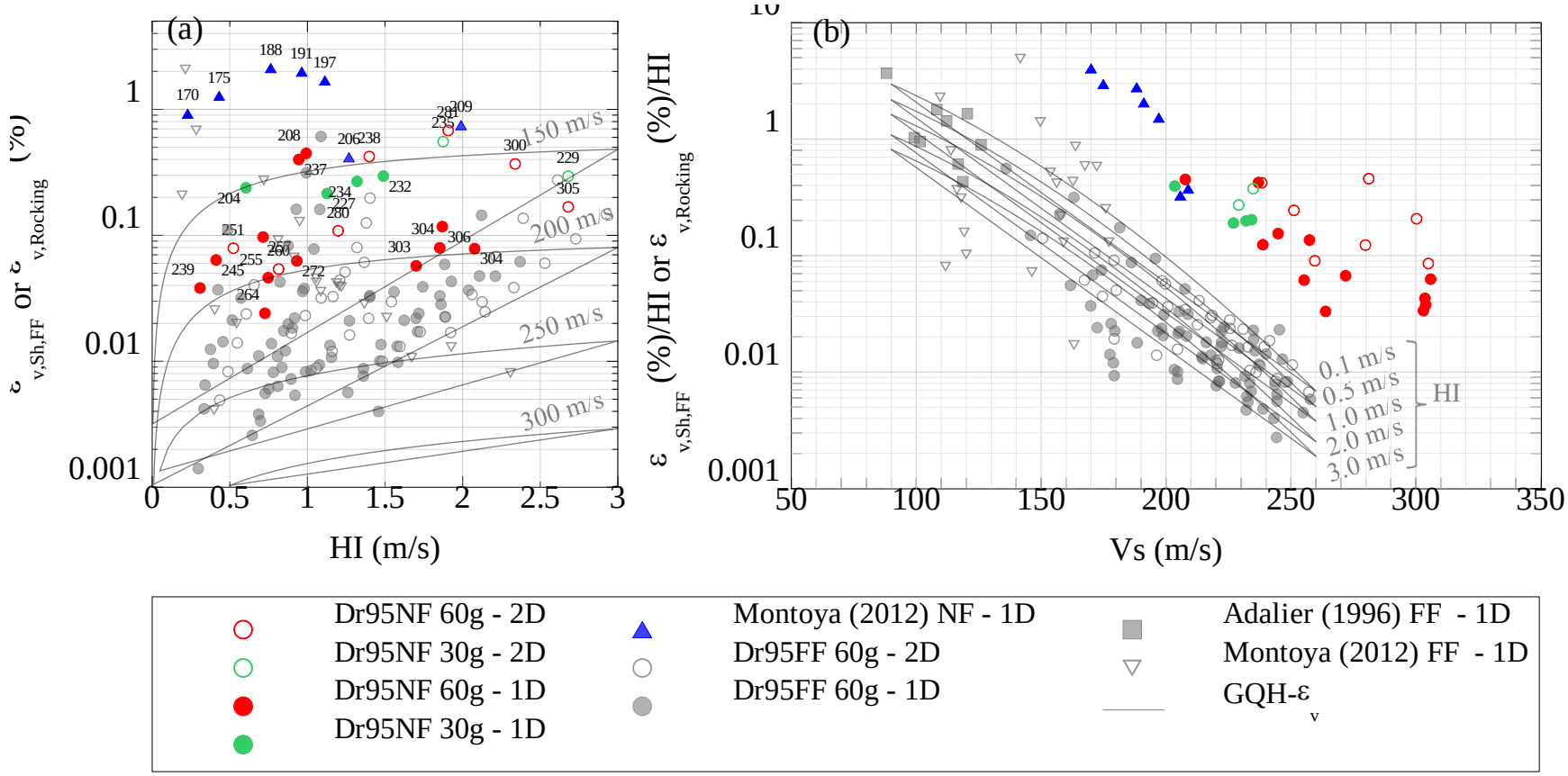

Figure 5-21. (a) Recorded near field (NF, $\varepsilon_{v,Rocking}$) compared to recorded and computed (GQ/H-ε_v model) free field (FF, $\varepsilon_{v,Sh,FF}$) vertical strains compared for Housner intensity (HI). Numbers next to symbols and lines indicate V_S for NF data and FF GQ/H-ε_v model, respectively; and (b) relationship between $\varepsilon_{v,Sh,FF}$ (%)/HI or $\varepsilon_{v,Rocking}$ (%)/HI and V_S, illustrating change in slope of V_S trend lines from (a). All plots correspond to database collected from this study, Adalier (1996) and Montoya (2012) and shown in Chapter 5.

5.4.3.3 Mobilized shear strength during rocking from centrifuge cases

As discussed above, depending upon the intensity of shaking and foundation soil strength, the trapezoidal distribution of seismic bearing pressures on the soil may produce localized soil yielding near the edge of the foundation, resulting in incremental structure rocking settlements. The relative horizontal acceleration that produces a factor safety for local shear (FS_{local}) of unity is denoted as the yield acceleration ($a_{h,y}$). Local (punching) shear occurs along a vertical plane extended from the edge of the foundation. To consider average conditions for local shear, the shear strength and shear stress are compared at the mid-depth of the zone of foundation influence (Z_I; determined in Chapter 5), at a depth of $D_f + Z_I/2$. The FS_{local} then is computed as:

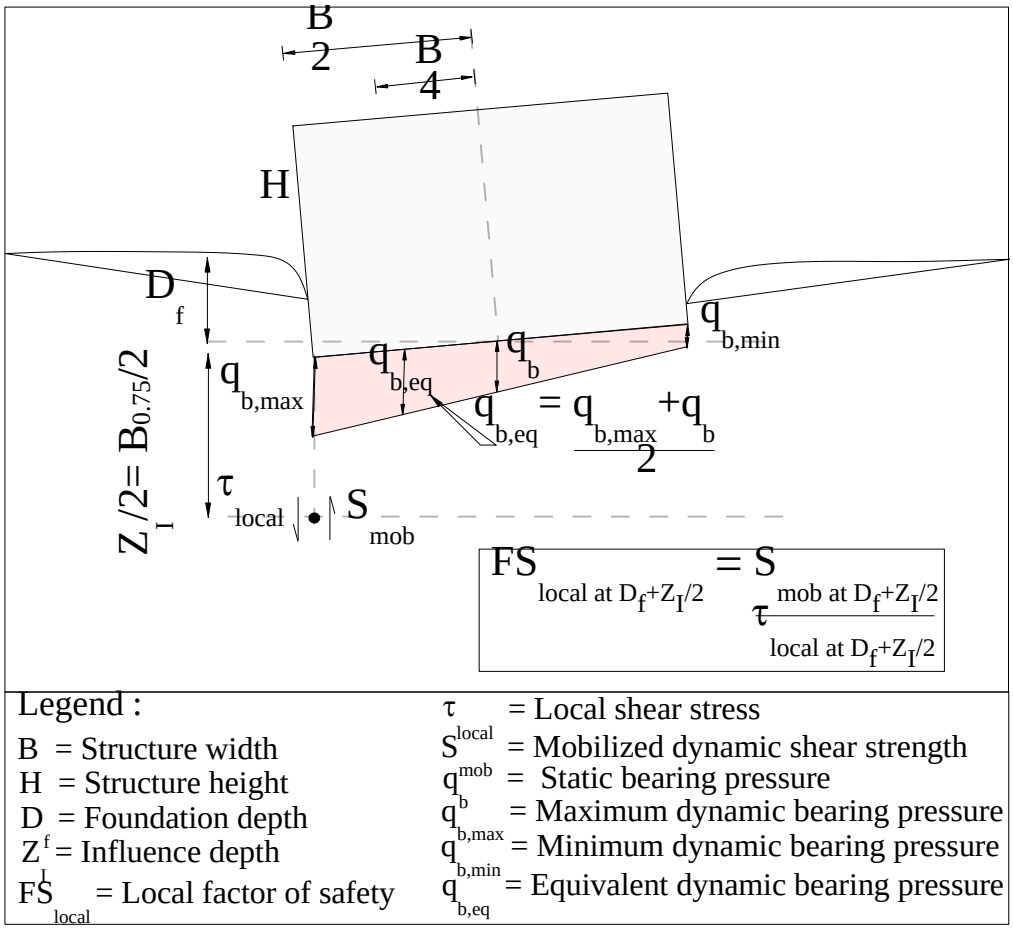

Figure 5-22. Schematic of FS_{local} computation at the mid-depth of the influence depth ($D_f + Z_I/2$) on a vertical plane extended from the foundation edge along with an equivalent dynamic bearing pressure used to estimate induced local shear stress (τ_{local}) at the depth of interest.

$$FS_{local\ at\ \mathrm{Df} + Z_I/2} = \frac{s_{mob\ @\ \mathrm{Df} + Z_I/2}}{\tau_{local\ @\ \mathrm{Df} + Z_I/2}} \quad (5\text{-}104)$$

$$Z_I = B^{0.75} \quad (5\text{-}105)$$

where $s_{mob\ @\ \mathrm{Df} + Z_I/2}$= mobilized shear strength on the vertical plane along the edge of the foundation at a depth of $D_f + Z_I/2$; and $\tau_{local\ @\ \mathrm{Df} + Z_I/2}$ = rocking-induced shear stresses on the same vertical plane at the same depth.

The vertical-plane shear stresses (τ_{local}) transmitted at a depth of $D_f + Z_I/2$ can be estimated from elastic theory (Ahlvin and Ulery 1962 solution reported by Poulos and Davis 1974) using a stress distribution factor denoted as G_1 for a rectangular or circular foundation as:

$$\tau_{local\ at\ \mathrm{Df}} = q_{b,\max at\ \mathrm{Df}} = \left(\frac{\mathrm{Q}}{BL} + \frac{6M_{(x\ or\ y)/CM}}{B^2 L}\right) \quad (5\text{-}106)$$

$$\tau_{local\ at\ \mathrm{Df}} = q_{b,\max at\ \mathrm{Df}} = \frac{Q}{\pi r^2}\left(1 + \frac{4M_{(x\ or\ y)/CM}}{Qr}\right) \quad (5\text{-}107)$$

where $q_{b,max}$ = maximum dynamic bearing pressure transmitted on the vertical plane along the edge of the foundation at a depth of D_f ; Q = total vertical load; $M_{(x\ or\ y)/CM}$ = rocking-induced moment at the center of mass of the structure; B and L = foundation width and length; r = foundation radius for circular shape.

Rocking-induced moments at the center of mass (CM) of the cylindrical structure used in this study is computed as:

$$M_{x\ or\ y/CM} = (\mathrm{m})(\mathrm{H}/2)(a_h/2) + (I_{x\ or\ y})(\frac{a_h}{H}) \quad (5\text{-}108)$$

$$I_{x\ or\ y} = \frac{\mathrm{m}r^2}{4} + \frac{\mathrm{m}H^2}{12} + m(r^2 + \left(\frac{H}{2}\right)^2) \quad (5\text{-}109)$$

where m = structure mass; a_h = relative horizontal acceleration between the top of the structure and the foundation soil; $I_{x\ or\ y}$ = rotational structure moment of inertia for a solid cylinder at the axis parallel to X or Y at the edge of the structure.

$$\tau_{local\ at\ \mathrm{Df} + Z_I/2} = q_{b,\max at\ \mathrm{Df} + Z_I/2} = q_{b,\mathrm{eq}\ at\ \mathrm{Df}}(G_1) \quad (5\text{-}110)$$

$$q_{b,\mathrm{eq}\ at\ \mathrm{Df}} = \frac{q_{b,\max at\ \mathrm{Df}} + q_b}{2} \quad (5\text{-}111)$$

where $q_{b,\max at\ \mathrm{Df} + Z_I/2}$ = maximum dynamic bearing pressure transmitted on the vertical plane along the edge of the foundation at a depth of $D_f + Z_I/2$; Q = total vertical load; $M_{(x\ or\ y)/CM}$ = rocking-induced moment at the center of mass of the structure; B and L = foundation width and length; r = foundation radius for circular shape.

and G_1 = shear stress distribution factor for the vertical plane along the edge of a foundation. Since an elastic solution is not available for shear stress on a vertical plane below a trapezoidal pressure distribution, an equivalent dynamic bearing pressure ($q_{b,eq}$) (uniform pressure distribution) was computed for use in the elastic solution. The uniform $q_{b,eq}$ is computed as the average of $q_{b,max}$ and q_b (Figure 5-22), where $q_{b,eq}$= equivalent dynamic bearing pressure.

While the local shear stress (τ_{local}) can be estimated readily, assigning a mobilized shear strength is more difficult, as it is not evident whether conditions are drained, undrained, or partially drained during shaking. Therefore, the author back-calculated mobilized shear strengths for each centrifuge shaking event by determining the $a_{h,y}$ required such that the rocking settlement computed equals the rocking settlement defined by the measured structure settlement, and used this required $a_{h,y}$ to compute a mobilized shear strength.

For each centrifuge shaking event, $a_{h,y}$ required to match computed and measured rocking settlements was determined by iteration using a Newmark-style displacement calculation for the relative acceleration time history between the structure (instrument AXYST) and the foundation soil (instrument AXY4-2). Figure 5-23 presents an example back-calculation of horizontal relative yield acceleration ($a_{h,y}$) using input motion M1Y and the relative acceleration time history computed between the top of the structure (instrument AYST) and the foundation soil (instrument AY4). Here, displacements are calculated for both positive and negative Y-directions, as rocking about the X-axis occurs in both Y-directions. Figure 5-23(c) compares the computed and measured rocking settlement time histories. It can be observed that the computed rocking settlements match the measured rocking settlement at the end of shaking.

Figure 5-24 presents the back-calculated $a_{h,y}$ for all 1D shaking events in test Dr95NF. As shown in the figure, $a_{h,y}$ generally increases with increasing SPT penetration resistance, N_{60}, i.e., as soil strength and stiffness increase. Here, N_{60} values were estimated by averaging N_{60} values derived from the Andrus and Stokoe (2004) and Brandenberg (2010) empirical correlations with V_S for the effective vertical stress under near field conditions at a depth of $D_f + Z_l/2$ located under the center of the structure.

As most correlations between drained or undrained shear strength and SPT penetration resistance are based on effective stress-normalized penetration resistance $(N_1)_{60}$, Figure 5-25 presents the mobilized shear strengths back-calculated from the Newmark-style analyses as a function of $(N_1)_{60}$. For comparison, Figure 5-25(a) includes yield strength ratios [s_u(yield)/σ'_{vo}; Olson and Stark 2003] from Olson (2009) and Idriss and Boulanger (2008) for the corresponding structure induced initial static shear stresses ratios (e.g., e.g $\tau_{static}/\sigma'_{vo}$ = 0.22 for Montoya 2012 cases, 0.47 for 30g and 0.49 for 60g). The Idriss and Boulanger (2008) yield strength ratios were estimated assuming the following relation:

$$\frac{s_u(yield)}{\sigma'_{vo}} = \frac{\tau_{static}}{\sigma'_{vo}} + (K_\alpha)(CRR) \qquad (5\text{-}112)$$

where $\tau_{static}/\sigma'_{vo}$, the initial static shear stress ratio; K_α and CRR are the static shear stress correction factor and the cyclic resistance ratio (Idriss and Boulanger 2008).

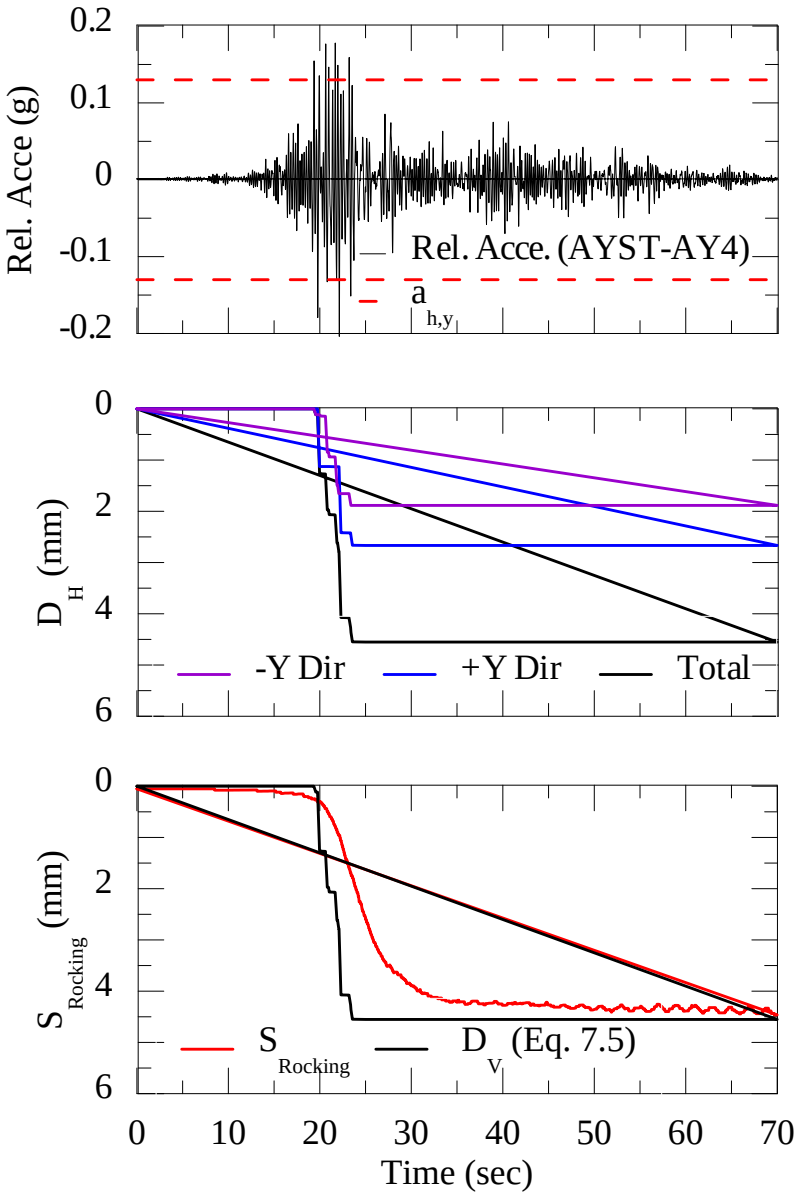

Figure 5-23. Back calculation of horizontal relative yield acceleration (ah,y) from motion M1Y (a) relative acceleration between the top of the structure (AYST) and foundation soil (AY4); (b) calculated lateral displacements (D_H) time histories for both +Y and –Y direction of M1Y from a Newmark-style approach using the relative acceleration between the top of the structure and surrounding soil; and (c) estimated settlement resulting from structure rocking ($S_{Rocking}$) and rocking settlement computed from lateral displacements (D_H; in mm).

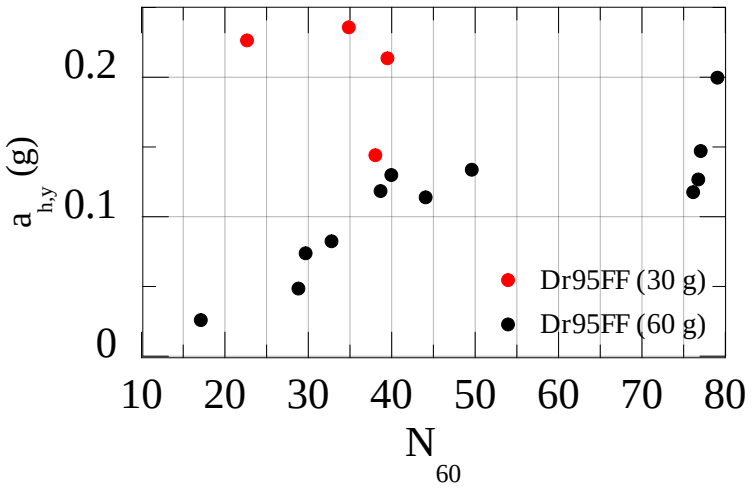

Figure 5-24. Back-calculated relative yield acceleration versus SPT penetration resistance N_{60} calculated from centrifuge tests.

Olson (2009) proposed a relationship among $(N_1)_{60}$, yield strength ratio, and static shear stress ratio as:

$$\frac{s_u(yield)}{\sigma'_{vo}} = \frac{\tau_{static}}{\sigma'_{vo}} + \left(\frac{0.0020}{\frac{\tau_{static}}{\sigma'_{vo}}} \right) (N_1)_{60} \qquad (5\text{-}113)$$

The comparisons indicate that the mobilized shear strength ratios are larger than yield strength ratios for [$(N_1)_{60}$ < 20] and smaller than shear strength ratios derived from ϕ' correlations for $(N_1)_{60}$ > 20. In summary, for the dense to very dense sands analyzed in this study, the mobilized shear strength appears to correspond to a significant fraction of the drained strength available before shaking.

5.4.3.4 Simplified model to capture rocking induced settlements from centrifuge cases

Although a few correlations have been proposed to estimate shaking-induced structure settlement (e.g., Liu and Dobry 1997), these methods have focused solely on liquefiable soils and have been shown to be inaccurate for thin liquefiable layers (Dashti 2010). However, for structures supported on dense sands in which liquefaction is unlikely, the application of these methods is limited and has not been validated.

To incorporate soil-foundation stiffness in soil-structure interaction analysis, Gazetas (1991) defined dynamic stiffness functions for various rigid foundations shapes and modes of vibration. In particular, for a rocking mode of vibration, the dynamic stiffness is controlled by both the shear modulus of the soil and the foundation width as shown in Eqs. (5-28) and (5-29) for a rigid circular and rectangular shapes, respectively (Gazetas et al 2013).

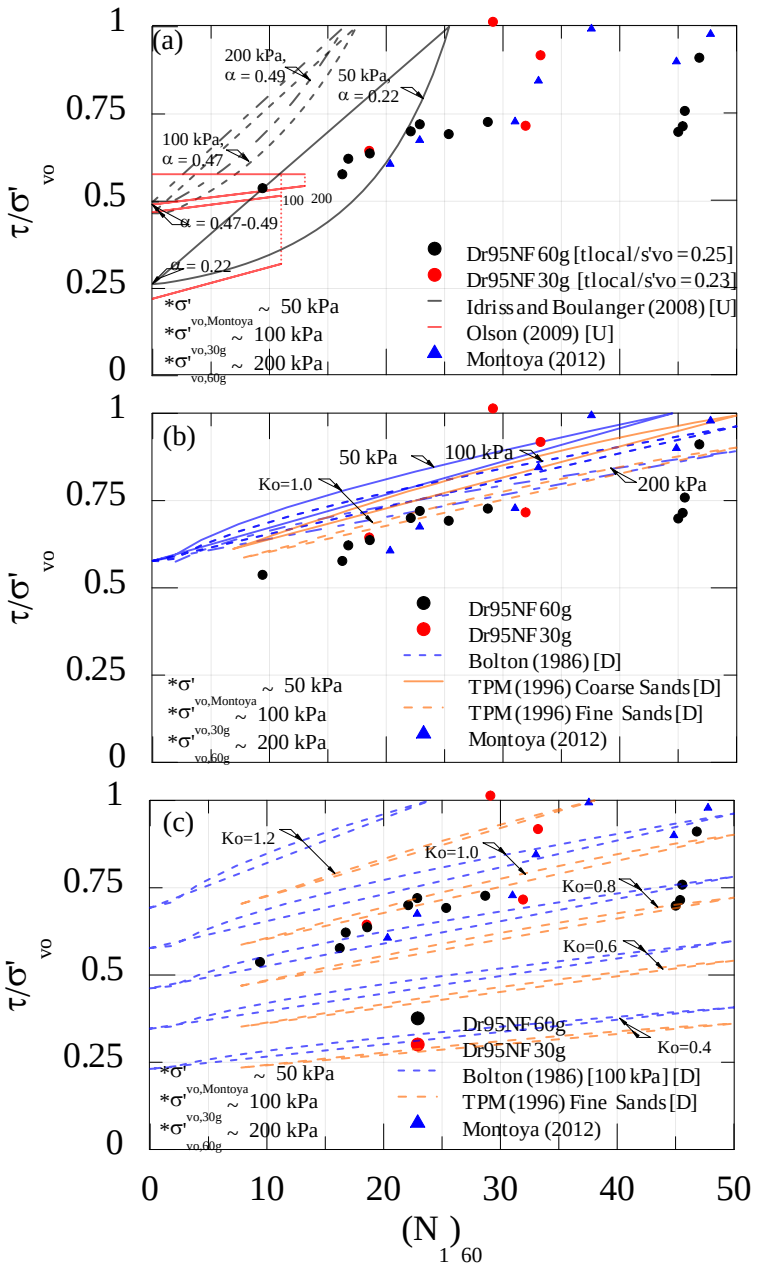

Figure 5-25. Mobilized dynamic strengths ratios at the mid influence depth of the foundation corner ($D_f+Z_l/2$) versus corrected SPT penetration resistance $(N_1)_{60}$ at the mid influence depth of the center of the foundation ($D_f+Z_l/2$) back-calculated from centrifuge tests compared along with (a) undrained empirical correlations from Olson (2009) and Idriss and Boulanger (2008) for $\alpha=\tau_{local}/\sigma'_{vo}$=0.47 (30g), 0.49 (60g); and 0.22 (Montoya 2012) (b) drained empirical correlations from Bolton (1986) for 50 kPa (Montoya 2012), 100 kPa (30g) and 200 kPa (60g) and Terzaghi, Peck and Mesri (1996) for fine and coarse sand gradations; (c) Bolton (1986).

$$K_{R,elastic} = \frac{8}{3}\frac{GR^3}{1-\nu} \tag{5-114}$$

$$K_{R,elastic} = 3.65\frac{Gb^3}{1-\nu} \tag{5-115}$$

where G = soil shear modulus; R = circular foundation radius; b = B/2; ν = Poisson's ratio. The shear modulus used here corresponds to an effective shear modulus which is a function of both shear strain and initial small-strain shear modulus (G_{max}). Here, as the Housner intensity is used as a proxy of shear strain and G_{max} is used in place of G for the centrifuge case histories.

Based on the collected NF centrifuge data (30g and 60g), Figure 5-26 illustrates the relationship between rocking-induced vertical strains ($\varepsilon_{v,Rocking}$) and the ratio of the computed rocking dynamic foundation stiffness, $K_{R,elastic}$, to Housner intensity. The correlation appears to be related to the local (punching mechanism) factor of safety (FS_{local}; described above), with lower FS_{local} values yielding larger rocking strains for a given $K_{R,elastic}$/HI ratio. For the cases shown in Figure 5-26, the number beside each data point is the FS_{local} computed using the Bolton (1986) correlation for drained strengths and the shear stress on the vertical plane as described above. As illustrated in the figure, the FS_{local} data are reasonably consistent with the proposed relationships.

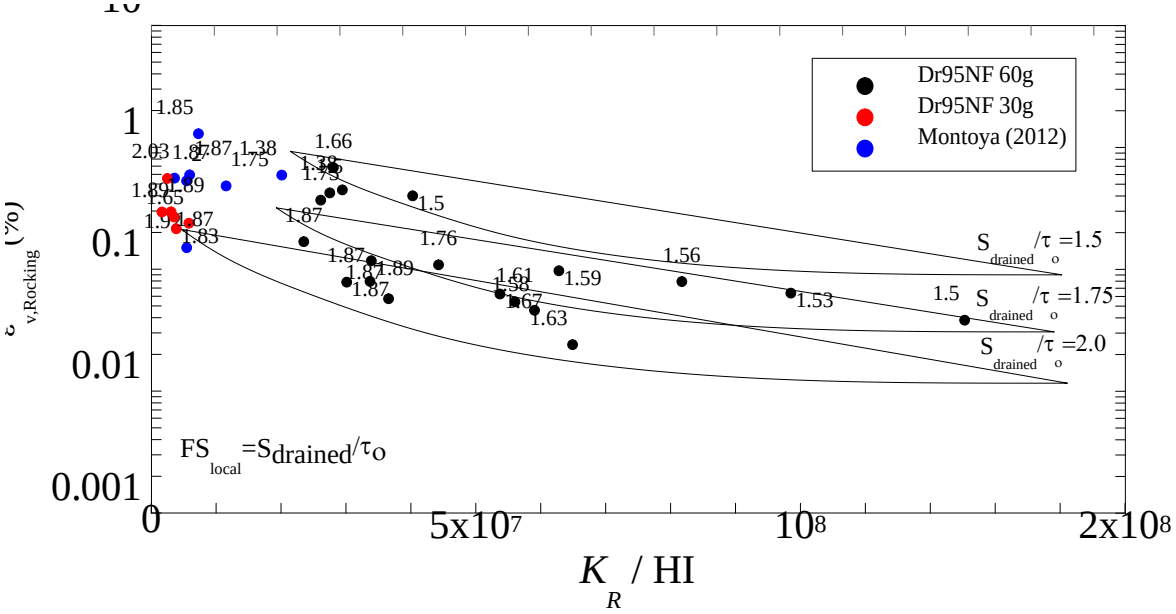

Figure 5-26. Simplified rocking induced vertical strain model from centrifuge tests for various local factor of safety (FS_{local})

The proposed rocking model could be used as follows to estimate structure settlement during earthquake shaking.

Step 1: Select a suite of paired (e.g., EW and NS) ground motions compatible with target rock or input response spectrum of the project.

Step 2: Subdivide the soil profile based on geology and soil characterization and perform a total-stress nonlinear site response analysis using appropriate tools and correlations (see Chapters 4

and 6) to obtain Housner intensity (HI) at a depth of $D_f + Z_l/2$. The total Housner intensity for two orthogonal directions of shaking is computed as $HI_{2D} = \sqrt{HI_{EW}^2 + HI_{NS}^2}$. As illustrated in Chapter 5, the use of 1D site response analysis to estimate NF seismic demand in a presence of a structure is supported as the structure has a minor effect on the computed Housner intensities.

Step 3: Estimate dynamic rocking stiffness for the specific foundation shape using Eq. (5-28; circular foundation) and Eq. (5-29; rectangular foundation) as proposed by Gazetas (1991) using a shear wave velocity that accounts for the presence of the structure to compute G_{max}.

Step 4: Compute FS_{local} using Eq. (5-29) and the procedures described above at a depth of $D_f + Z_l/2$ on a vertical plane extended from the edge of the foundation, assuming a coefficient of earth pressure at rest (K_o) of 1.0

Step 5: Estimate the rocking-induced vertical strain using Figure 5-26. Estimate the rocking-induced settlement as the product of the rocking-induced vertical strain and the influence zone thickness, Z_l [Eq.(5-11)]. Note that no multidirectional factor is used as the vertical strain is estimated using HI_{2D}.

Step 6: Add PWP-induced settlement (estimated using GQ/H-ε_v model) to rocking-induced settlement from Step 5 to compute total structure settlement. In using the GQ/H-ε_v model, the shear wave velocity should incorporate the building stresses.

5.5 Summary

A semi-empirical vertical strain model (GQ/H-ε_v) was developed using a large database of dynamic centrifuge tests on saturated, dense, clean, uniformly-graded sands to estimate shaking-induced settlement under multidirectional loading. The model uses seismic intensity measures of PGA, PGV, Arias intensity, and Housner intensity coupled with shear wave velocity, but could be adapted for other resistance parameters such as SPT blow count or CPT tip resistance. The GQ/H-ε_v model can be implemented in both a simplified manner (using surface PGA and an r_d factor) or by means of site response analysis (e.g., DEEPSOIL).

Model estimates of vertical strain for the 1D and 2D shaking database show that in general the simplified GQ/H-ε_v model reasonably agrees with measured settlements of dense, saturated sands. However, estimated settlements improved when GQ/H-ε_v model was coupled with IMs computed by site response analysis. Furthermore, settlements computed using velocity-based IMs (PGV and HI) better agree with observed settlements compared to acceleration-based IMs (PGA and Ia). Lastly, when employed for dense sands (Dr > 70%) the proposed model reasonably agrees with existing settlement methods based on drained cyclic shear tests (e.g., Pradel 1998), and the proposed model gives a nearly unbiased estimation of shaking-induced settlement for dense sands.

A semi-empirical seismic rocking-induced vertical strain model was proposed using a database of near-field dynamic centrifuge tests on saturated, dense, clean uniformly-graded sands as a component needed to estimate near-field, shaking-induced vertical strains under multidirectional loading conditions. The model uses the dynamic rocking stiffness (Gazetas 1991) as a soil-structure interaction parameter that can be estimated from shear wave velocity (V_S), and uses Housner intensity as a seismic demand parameter that can be computed by means of site response analysis (e.g., DEEPSOIL).

When used in combination with free-field PWP-induced vertical strain model presented elsewhere, the combined model can be used to estimate total settlements of structures founded on sandy soils and subjected to multidirectional earthquake loading.

6 A NEW SOIL CONSTITUTIVE MODEL FOR SAND PLASTICITY

6.1 Introduction

Reliable modeling of soil behavior via constitutive equations is essential to solve practical geotechnical problems reliably. The complexity of soil behavior observed from laboratory tests and field observations is challenging to represent in such constitutive models. Significant effort has been made to describe soil behavior via generalized models using a theoretical framework of rate-independent elasto-plasticity (Drucker et al. 1957) and effective stress change – deformation relations (Terzaghi 1925). A variety of models have been developed to simulate soil behavior in monotonic loading via a single yield surface concept (e.g., Tresca 1864; von Mises 1913; Mohr-Coulomb 1773; Drucker and Prager 1952). A significant departure from this concept was achieved through the formulation of the Cam Clay (Roscoe et al. 1963) and Modified Cam Clay (MCC; Roscoe and Burland 1968) models, which use a Critical State Soil Mechanics (Schofield and Wroth 1968) framework to model idealized soil behavior.

Single yield surface type models reasonably explain the stress-strain behavior of soils during monotonically increasing load (without unloading). However, such models suffer from two main shortcomings: (1) the elastic domain in these models generally is too large and a single yield surface causes a sudden change from elastic to plastic which is not observed in laboratory tests; (2) the kinematic (Prager 1955; Ziegler 1959) and isotropic hardening rules used in the single surface models cannot capture cyclic behavior observed in laboratory experiments. These limitations provided impetus for the significant research efforts over the last thirty years on developing constitutive models to describe cyclic soil behavior. Multi-yield surface plasticity and bounding surface plasticity are two widely used theories in modelling soil (e.g., Prevost 1985; Manzari and Dafalias 1997) despite the complex implementation and calibration procedures.

This chapter presents a new constitutive model, termed I-soil, developed using a DEP (Distributed Element Plasticity) framework. Section 6.2 describes the framework within which the constitutive model is built, and Section 6.3 introduces the I-soil constitutive model formulation. Section 6.4 details model implementation in the finite element analysis software LS-DYNA. Section 6.5 presents some examples to verify the model's ability to simulate cyclic soil behavior via comparing simulations to laboratory element tests. Finally, Section 6.6 discusses and draws conclusions related to I-soil.

6.2 Distributed Element Plasticity (DEP) Framework for Cyclic Loading

Chiang and Beck (1994) proposed a class of 3D DEP models for constitutive modeling in cyclic plasticity. The model formulation is based on the one dimensional parallel-series distributed element plasticity model proposed by Iwan (1966; Figure 6-1), where N number of components are connected in *parallel*, and each component has a linear spring with stiffness "E_i" and a slip element of yield strength σ_i^* arranged in *series* so that the model is classified as *parallel-series*.

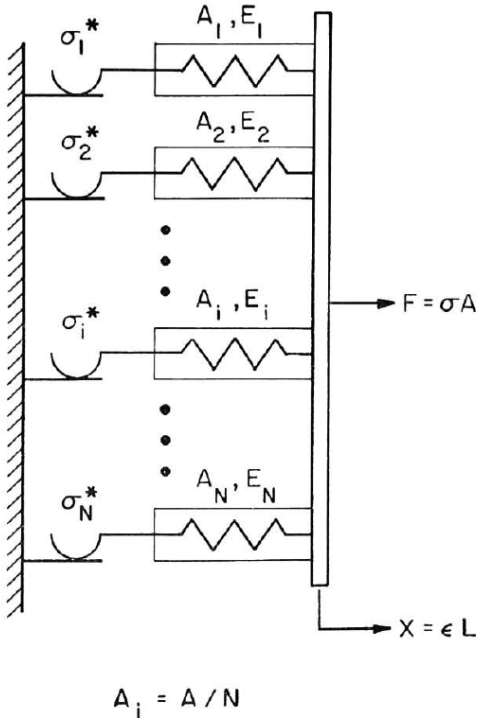

Figure 6-1 The Iwan distributed element plasticity model for one-dimensional uniaxial loading (from Iwan 1967)

Each component in the model represents an elasto-plastic material that has a stress-strain behavior as shown in Figure 6-2.

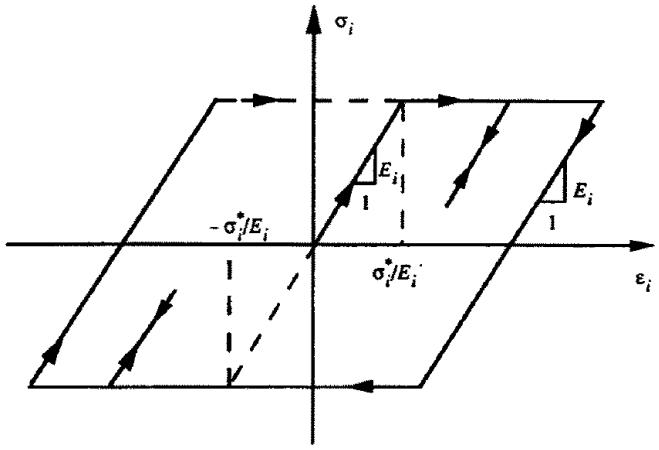

Figure 6-2 Hysteretic behavior of an elasto-plastic component (from Chiang and Beck, 1994)

Each component of the model is exposed to the same incremental strain, and the stress obtained from the initial loading part of the model is defined as:

$$\sigma = \frac{F}{A} = \sum_{i=1}^{n} \frac{E_i}{N} \varepsilon + \sum_{i=n+1}^{N} \frac{\sigma_i^*}{N} \tag{6-1}$$

where the sum from i = 1 to n represents the components that are still in the elastic domain whereas the sum from i = n+1 to N represents the components that have yielded.

Extension of the 1D DEP models to 3D was achieved by Iwan (1967) by introducing nested 3D yield surfaces for each model component, along with kinematic hardening rules applied to the *series-parallel* (N number of components distributed in series where the elastic spring and slip elements are arranged in parallel) DEP model rather than *parallel-series* model to simulate Masing-type hysteresis. This model formulation successfully simulated the cyclic behavior of metals under multi-directional loadings (Iwan 1967). However, numerical implementation of this concept is complex and inefficient due to the need to track each yield surface. Chiang and Beck (1994) adopted the parallel-series DEP model and provided a formulation in the invariant yield surface domain where the components experience the same strain increment and have different yield stresses. The core idea of the formulation is that the yield surfaces defined for the components are invariant and do not move in stress space. This model characteristic provides a straightforward and efficient numerical implementation without any kinematic hardening rules required to simulate cyclic behavior. The discretized model (i.e., a discrete number of components, N, rather than an infinite number of components) can be used with very few components to solve practical problems related to cyclic loading. The theoretical formulation of the discretized model is summarized by Iwan (1967) stating the following rules:

(1) Each nested component in the model is subjected to the same total strain response as experienced by the model itself.

(2) Each component exhibits an ideal elasto-plastic response to the applied strains. This provides the characteristics of invariant yield surfaces.

(3) All the components have the same stiffness and the yield functions have the same form with different yield constants.

(4) The model stress is computed by averaging the sum of stresses in each component by the total number of components.

The formulation details for a nested component closely follows a general elasto-plastic model formulation and is broadly explained for the I-soil model below.

6.3 I-soil Constitutive Model Formulation

The I-soil model is based on the work of Iwan (1966) and Chiang and Beck (1994) and provides an efficient way to model cyclic nonlinear soil behavior in 3D stress space. The constitutive model captures key mechanical aspects of cyclic soil behavior within the strain levels of interests, such as: (1) small strain nonlinearity; (2) hysteretic damping behavior; (3) shear induced volumetric contraction-dilation; and (4) modulus degradation due to excess pore pressure generation. It is assumed that the soil behavior is rate independent, and the model does not consider creep and other viscous effects.

Monotonic shear behavior closely follows the MAT_79 constitutive model (LSTC 2009) and is modelled by extending the concepts introduced in the previous section to shear space. This is achieved by idealizing a shear model similar to the uniaxial model presented in Figure 6-1. Figure 6-3 demonstrates the model setup in shear space.

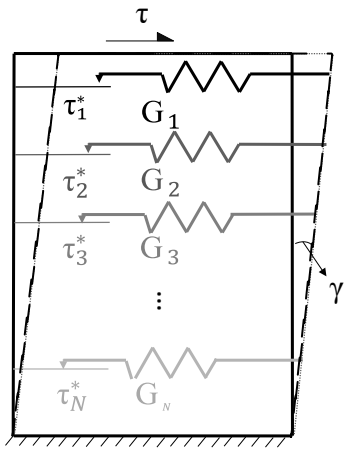

Figure 6-3 I-soil model setup for one-dimensional shear

The one-dimensional shear model uses N number of nested components. Each component is subjected to the same shear strain, and each component has a yield strength of τ_i and shear modulus of G_i. The shear stress experienced by the model due to monotonic shear loading is defined as:

$$\tau = \sum_{i=1}^{n} G_i \gamma + \sum_{i=n+1}^{n} \tau_i^* \tag{6-2}$$

where the sum from i = 1 to n represents the components that are still in the elastic domain, whereas the sum from i = n+1 to N represents the components that are yielded. Figure 6-4 shows an example of a four component model to simulate 1D shear behavior. Each component has a different shear modulus and yield strength, and the model backbone is obtained by summing the component responses. Thus, a nonlinear backbone curve is obtained in a piecewise linear fashion. A smoother response is obtained by increasing the number of model components.

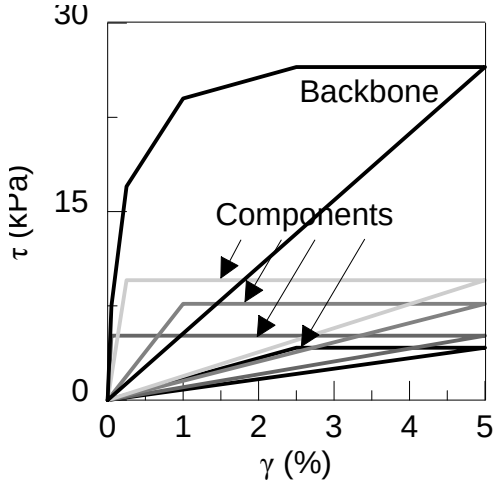

Figure 6-4 Piecewise linear backbone curve and corresponding nested components for one dimensional monotonic shear response

The theoretical framework for I-soil can be summarized as follows:

(1) Each nested component in the model is subjected to the same total shear strain response as experienced by the model itself.

(2) Each component responds to the applied shear strains in an ideal elasto-plastic way. This provides the characteristics of invariant yield surfaces.

(3) All the components have different stiffness and the yield functions have the same form with different yield constants.

(4) The model stress is computed by summing the stresses.

Upon unloading, components regain their stiffness and yield strengths. This inherently incorporates Masing-type unloading-reloading rules during cyclic loading. Figure 6-5 presents the behavior of I-soil under one full cyclic loading loop with 5% cyclic shear strain amplitude.

Upon unloading, components regain their stiffness and yield strengths. This inherently incorporates Masing-type unloading-reloading rules during cyclic loading. Figure 6-5 presents the behavior of I-soil under one full cyclic loading loop with 5% cyclic shear strain amplitude.

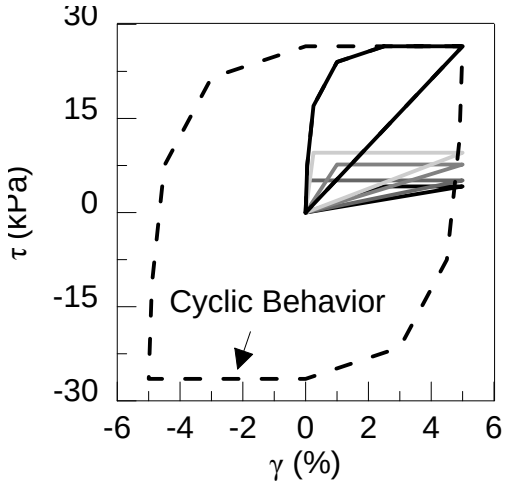

Figure 6-5 Masing type un/reloading behavior of backbone curve presented in Figure 6-4 under cyclic loading

The 3D generalization of the model is achieved by introducing yield surfaces that operate in 3D stress space. I-soil can handle both pressure independency and pressure dependency by using yield functions that resemble von Mises type cylindrical or Drucker-Prager type conical yield surfaces. The pressure dependency operates as:

$$\frac{\tau_i^*(p,\gamma)}{\tau_i^*(p_{ref},\gamma)} = \sqrt{\frac{a_0 + a_1(p-p_0) + a_2(p-p_0)^2}{a_0 + a_1(p-p_0) + a_2\left(p_{ref}\right)^2}} \tag{6-3}$$

where τ_i^* is the yield strength of the i[th] component; $p = -\frac{\sigma_{ii}}{3}$; p_{ref} is the reference pressure (mean effective stress for which the input parameters are defined) where the input backbone is defined; p_0 is the cut-off pressure below which strength is set to zero (e.g., no strength in tension); and a_0, a_1, and a_2 are flags for pressure dependency. That is, for example, if $a_0 = 1$, $a_1 = 0$, and $a_2 = 0$ then the model is a von Mises type and is pressure independent. If $a_0 = 0$, $a_1 = 0$, and $a_2 = 1$ the model is a Drucker-Prager type and linearly pressure dependent. In addition, the shear and bulk modulus also are pressure dependent via:

$$G_i = G_{0i} * \left(\frac{p - p_0}{p_{ref}}\right)^b \tag{6-4}$$

and

$$K_i = K_{0i} * \left(\frac{p - p_0}{p_{ref}}\right)^b \tag{6-5}$$

where b is the pressure dependency coefficient for stiffness. Stiffness also vanishes if the current pressure, p, goes below p_0.

Both yield strength and stiffness formulations operate in nested component stress states and are superposed to obtain model response. Reference values for nested components (values that are valid for the input reference pressure) are determined by decomposing the input reference backbone curve provided by user. Then yield strength and stiffness dependencies are applied. Appendix E is provided to determine the strength and stiffness parameters for each nested component that constructs the input backbone curve upon superposition. I-soil automatically executes an algorithm to obtain nested component parameters from a given backbone curve. Effective mean stress dependency of mobilized strength as well as shear/bulk moduli are demonstrated in Figure 6-6 for an undrained single element test.

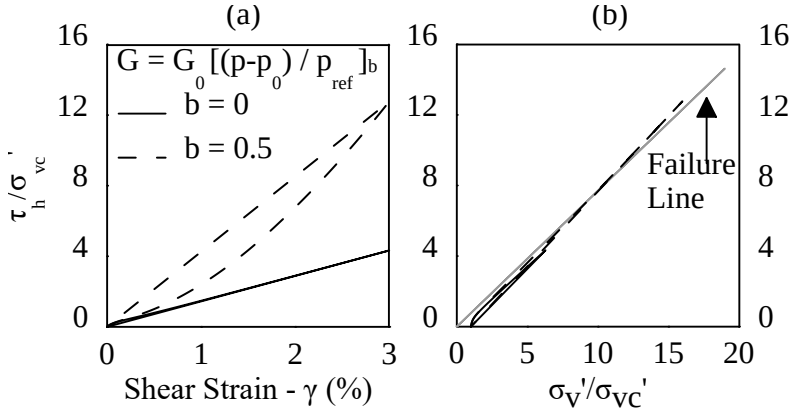

Figure 6-6 Effective mean stress dependent undrained monotonic response in a single element test: (a) normalized shear stress – shear strain; (b) normalized shear stress – normalized vertical stress.

Direct extension of the uniaxial Iwan type parallel series distributed model to modeling shear behavior inherently incorporates Masing type unloading-reloading behavior, and hysteretic damping (ξ) can be calculated as the area enclosed by the stress-strain loop. Several studies have demonstrated that Masing rules overestimate hysteretic damping (Figure 6-7) observed in laboratory cyclic tests (Darendeli 2001; Phillips and Hashash 2009).

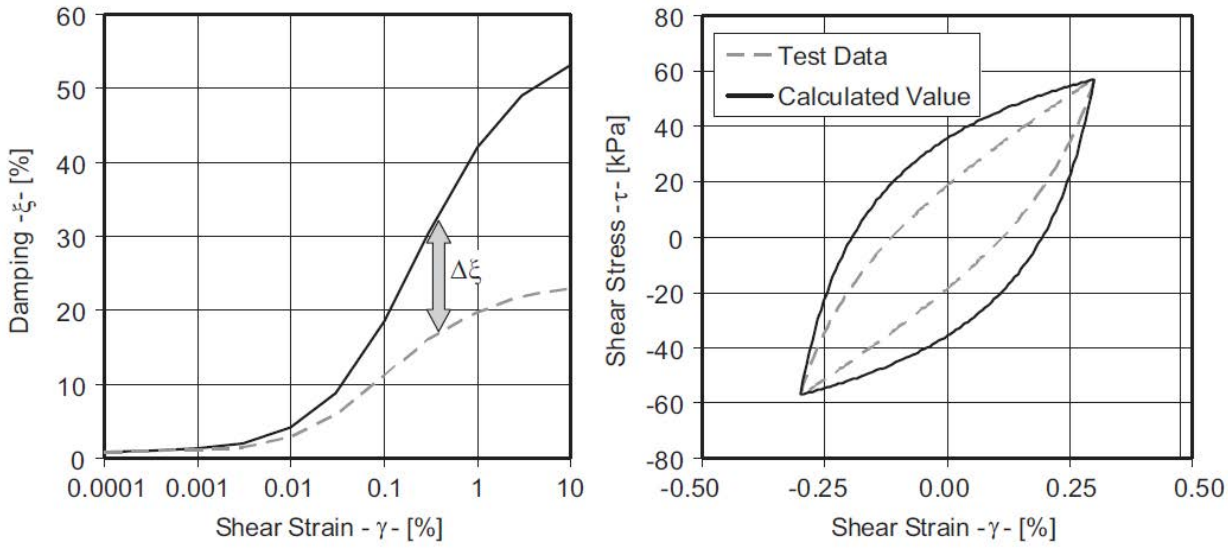

Figure 6-7 Overestimation of hysteretic damping using Masing rules in a 1D hyperbolic model. (a) Damping curve. (b) Hysteretic loop (from Phillips and Hashash 2009)

Phillips and Hashash (2009) solved this problem by introducing a reduction factor applied to the 1D Masing unloading-reloading rules. The original Masing rule provides unloading-reloading as:

$$\tau = \left[\frac{2G_0\left(\frac{\gamma-\gamma_{rev}}{2}\right)}{1+\beta\left(\frac{\gamma-\gamma_{rev}}{2\gamma_r}\right)^s}\right] + \tau_{rev} \tag{6-6}$$

Upon applying the reduction factor from Phillips and Hashash (2009), the unloading-reloading rule becomes:

$$\tau = F(\gamma_m)\left[2\frac{G_0\left(\frac{\gamma-\gamma_{rev}}{2}\right)}{1+\beta\left(\frac{\gamma-\gamma_{rev}}{2\gamma_r}\right)^s} - \frac{G_0(\gamma-\gamma_{rev})}{1+\beta\left(\frac{\gamma_m}{\gamma_r}\right)^s}\right] + \frac{G_0(\gamma-\gamma_{rev})}{1+\beta(\gamma_m-\gamma_r)^s} + \tau_{rev} \tag{6-7}$$

where β and s are 1D hyperbolic function coefficients, γ_{rev} is reversal shear strain, γ_m is maximum shear strain, τ_{rev} is reversal shear stress, and $F(\gamma_m)$ is a reduction factor calculated as:

$$F(\gamma_m) = P_1 - P_2(1 - G(\gamma_m)/G_0)^{P_3} \quad (6\text{-}8)$$

where P_1, P_2, and P_3 are non-dimensional parameters selected to obtain the best fit to the target damping curve.

The 1D formulation provided by Phillips and Hashash (2009) was extended to 3D and incorporated in I-soil to capture hysteretic damping at moderate to large shear strains. With this, the complete 3D deviatoric behavior of I-soil is defined. Details of the formulation can be found in Numanoglu et al. (2017) as well as Appendix E.

Monotonic or cyclic shear loads cause a sand to undergo complex behavior due to the shear – volumetric coupling. Multidimensional deformation characteristics can be achieved by establishing a link between shear and volumetric coupling. In addition, sand behavior is significantly affected by its relative density and effective stress, as well as the magnitude of applied shear stress. This is because a given sand may be contractive when effective stresses are large or the particles are loosely packed. On the other hand, a dense sand at a low effective stress will tend to dilate during shear. This pressure dependent behavior significantly affects shear deformation characteristics during undrained and/or partially drained loading. Thus it is important for a constitutive model to define the stress-strain dilatancy behavior.

I-soil incorporates a volumetric model resembling Rowe's stress-dilatancy theory and follows the simplified version of Manzari and Dafalias (1997) where the relation between deviatoric strain and volumetric strain is defined by a non-associative flow rule as:

$$d\varepsilon_v^p = D|d\varepsilon_q^p| \quad (6\text{-}9)$$

where

$$D = A_0(\eta_{pt} - \eta) \quad (6\text{-}10)$$

where η_{pt} is the phase transformation stress ratio and η is the current stress ratio.

This model effectively captures the contractive-dilative behavior of sands depending on the stress ratio being less than (contractive) or greater than (dilation) the phase transformation stress ratio. Single element simulation results that demonstrate the physical meaning of both A_0 and η_{pt} are presented in Figure 6-8.

I-soil is available both in the LS-DYNA and MASTODON (Coleman et al. 2017) dynamic finite element analyses frameworks.

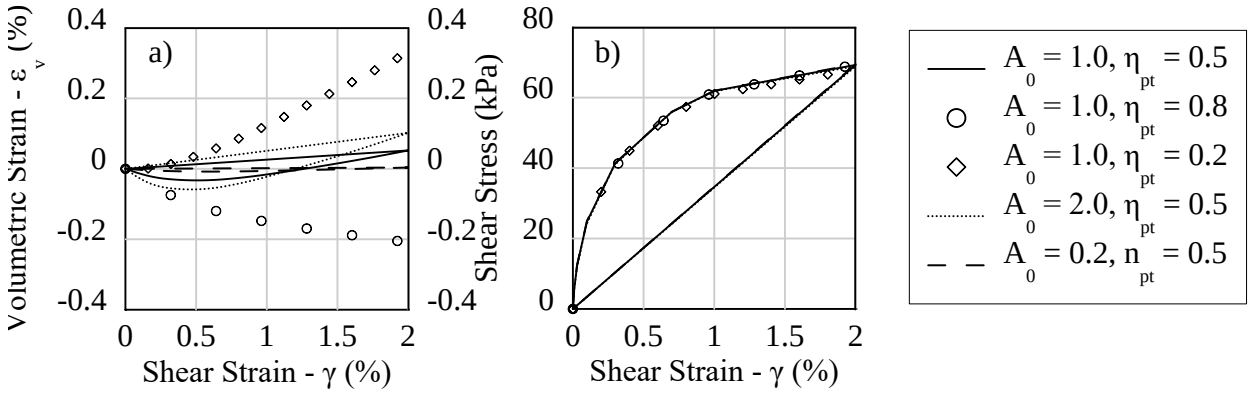

Figure 6-8 Single element drained monotonic DSS simulations using different values for A_0 and η_{pt}: (a) shear strain – volumetric strain behavior; and (b) shear stress – shear strain behavior.

6.4 Constitutive Model Implementation in LS-DYNA

The LS-DYNA finite element code can incorporate generalized effective (or total) stress soil models through a user material subroutine. This study implements I-soil in effective stress space to describe soil response within the finite element (FE) analysis platform.

Reference shear behavior (e.g., monotonic and cyclic behavior at the reference pressure) only requires $F_{bb}^{p_{ref}}(\gamma)$ and p_{ref}. Once the component properties are determined, stresses are integrated in components stress space and superposed to obtain model behavior. I-soil is a rate independent model and its stress integration follows classical elastic predictor – plastic corrector whereby first an elastic prediction is made with a given strain increment and then a one step, forward Euler type return mapping algorithm characterizing the solution as the closest point projection of the trial stress state onto Drucker – Prager and/or von Mises yield surface is executed to correct the initial elastic prediction (Simo and Hughes 2006). A numerical implementation flow chart is presented in Figure 6-9 which describes the steps required to implement I-soil in a strain driven plasticity algorithm where ε (strain) is an independent variable. The radial return algorithm is separately presented in Appendix E.

Establishing the initial, in-situ state of stress is an integral part of simulating geotechnical earthquake engineering related problems. In general, FE software performs an initial analysis where the stresses due to gravity loading are computed. Strains created due to this procedure are reset to zero prior to primary load application (i.e., dynamic excitation). LS-DYNA, however, does not require any separate analysis for initial stress conditions; initial stresses can be input to the domain by the user. The user defined material model can be implemented in a way to be compatible with such input to satisfy equilibrium and bring the constitutive model and its stress dependent parameters to an initial state. The implemented I-soil model in LS-DYNA achieves such compatibility.

The initial stress inputs can be used to achieve in-situ conditions for free-field ground response analyses. In case of having structures on top of soil domain, before applying base excitation, first equilibrium is established by the user with free-field conditions. Then the structure is added. Addition of structure induces shock waves in the dynamic analysis. There should be enough analysis time provided by the user to damp out the artificially induced shock waves due to structural loads.

Coupled analysis for dynamic problems involving a soil-structure system can be achieved using the solid-fluid coupling formulation of LS-DYNA. This allows excess porewater pressure generation and dissipation during ground shaking. LS-DYNA uses Terzaghi's effective stress principle to model soils with excess porewater pressures. The coupling is broadly explained in LSTC (2009) as:

> *The pore fluid and soil skeleton are assumed to occupy the same volume and to carry loads in parallel. Thus, the total stress in an element is the sum of the "effective stress" in the soil skeleton, plus the hydrostatic stress in the pore fluid. LS-DYNA calculates the "effective stress" with standard material models. The pore fluid treatment, then, is independent of material model. The pore pressure is calculated at nodes, and interpolated onto the elements. The pore fluid's hydrostatic stress is equal to the negative of the element pore pressure.*

An effective stress analysis in LS-DYNA can be utilized with no excess porewater pressure generation, excess porewater pressure generation, and both excess porewater pressure generation

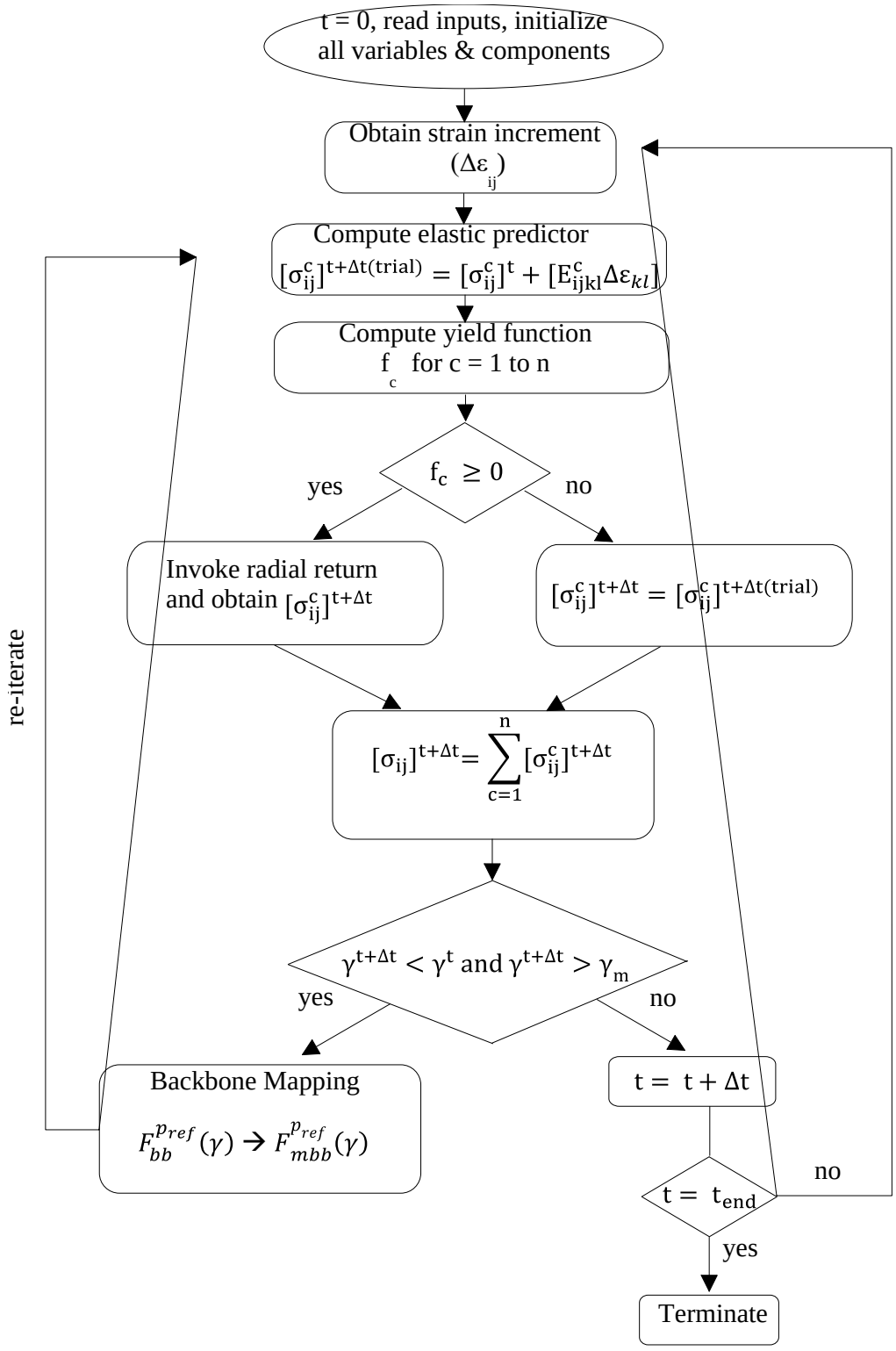

Figure 6-9 Numerical implementation flow diagram for I-soil with n number of components (modified from Chiang and Beck 1994)

and dissipation options. Excess porewater pressure dissipation is achieved by activating the time dependent consolidation option in the software. For time-dependent consolidation, Darcy's law is used to describe the flow of fluid through the material due to the pressure gradient as:

$$v = \kappa \nabla (p + z) \tag{6-11}$$

where v is the fluid velocity, κ is permeability, p is pressure head, and z is the z-coordinate of the node. Porewater pressure coupling and the effect of the flow is described in LSTC (2009) as:

> *Net inflow or outflow at a node leads to a theoretical volume gain or loss. The analysis is coupled, i.e. any difference between actual and theoretical volume leads to pore pressure change, which in turn affects the fluid flow. The result is a prediction of response-versus-time.*

6.5 Constitutive Model Calibration using I-mcDSS Tests

Seismic loading can be approximated in the laboratory most accurated by cyclic direct simple shear tests (cDSS). In the cDSS test, a short cylindrical specimen is laterally constrained by either stacked metal rings or a wire-reinforced membrane. By applying shear force or displacement to the soil specimen, the specimen is deformed in a way that mimics vertically propagating shear waves (Figure 6-10).

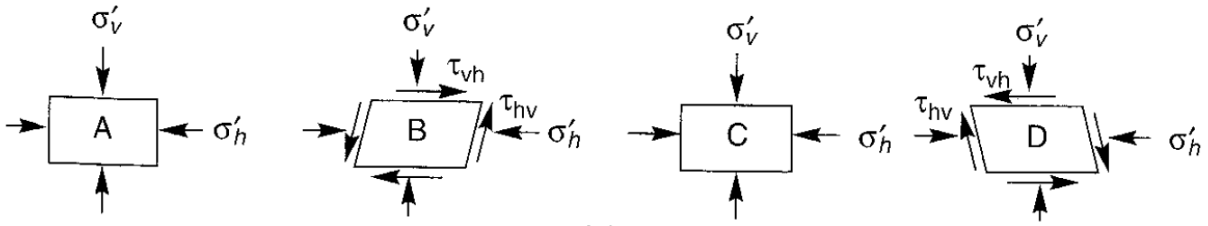

Figure 6-10 Stress and strain conditions imposed in an ideal element of soil below level ground surface by s- waves (Kramer, 1996)

The one drawback of cDSS is that the shear stresses are imposed on the horizontal plane and no complementary shear stress are imposed on the vertical planes. This causes non-uniform stress distribution within the specimen.

Element-scale simulations of cDSS results were used to validate the I-soil constitutive model under different loading conditions. The simulations in this section are restricted to single integration point 3D brick elements. Figure 6-11 presents the simulated and measured response of a D_R = 68% Ottawa sand specimen under strain-controlled, monotonic, drained and undrained conditions and demonstrates that I-soil is able to reproduce the soil response measured in laboratory tests under both drained and undrained conditions.

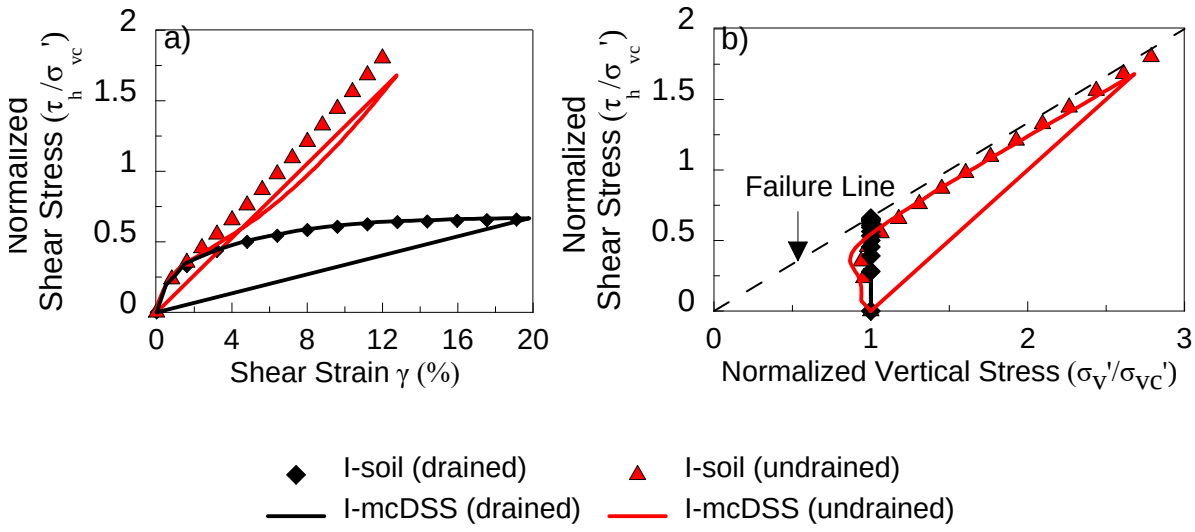

Figure 6-11 Strain controlled monotonic test on Ottawa sand with D_R = 68% and σ'_{vc} = 100 kPa. (a) Stress-strain behavior; (b) stress path to failure.

The same numerical model was subjected to strain controlled cyclic loading where the cyclic shear strain amplitude was 1%. The simulation results are presented in Figure 6-12. It is observed that I-soil is able to produce the cyclic shear stress degradation due to excess pore pressure generation under cyclic loading as well as the tendency to dilate (butterfly shapes in the stress path plot).

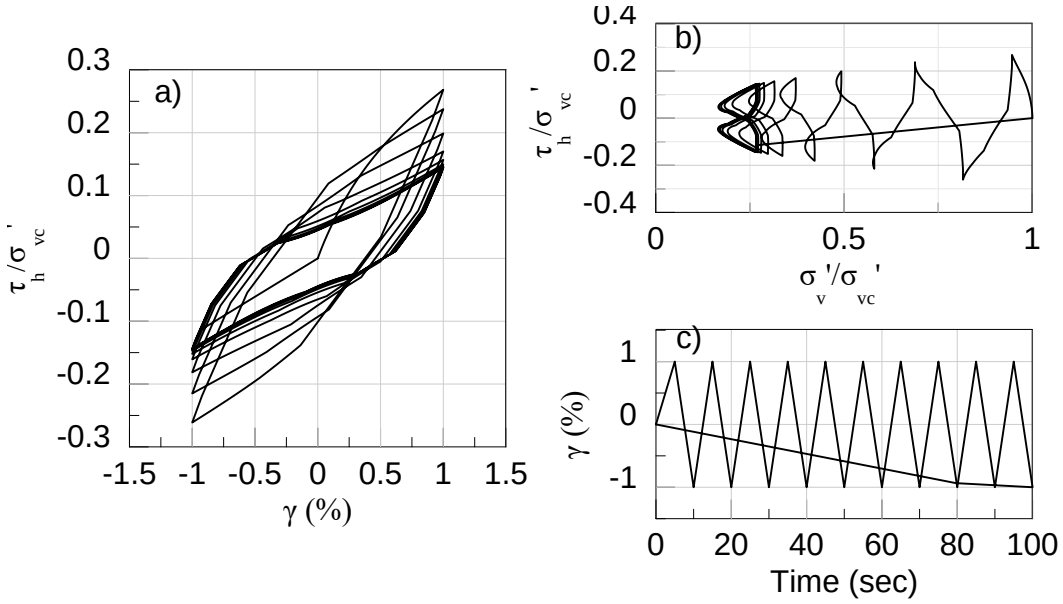

Figure 6-12 Strain controlled cyclic test on Ottawa sand with D_R = 68% and σ'_{vc} = 100 kPa. (a) Stress-strain behavior in simulations. (b) Stress path to failure in simulations. (c) Applied shear strain – time history.

The results of another set of simulations and I-mcDSS experiment (D_R = 95% Ottawa sand under strain controlled, cyclic, drained conditions) are plotted on Figure 6-13. It is demonstrated that the non-Masing rules implemented in I-soil captures the measured hysteretic loop response (hysteretic damping) of the sand in laboratory experiments.

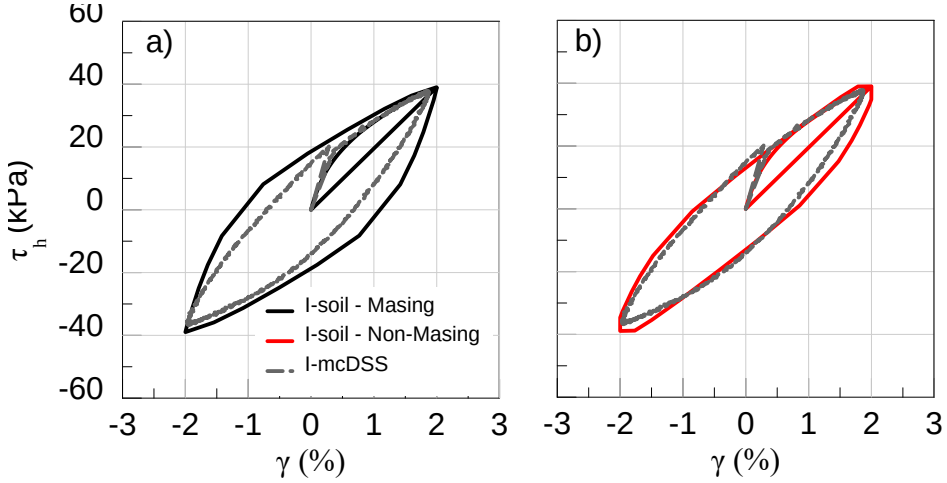

Figure 6-13 Strain controlled cyclic test on Ottawa sand with D_R = 95% and σ'_{vc} = 94 kPa. (a) Measured response vs I-soil simulation with Masing rules. (b) Measured response vs I-soil simulation with Non-Masing rules.

6.6 Summary

This chapter described I-soil, a simple constitutive model for sands to be utilized in multi-directional seismic site response and soil-structure interaction analyses. In summary, the chapter described the following main points.

1. The distributed element modeling concept was reviewed and mechanics behind the framework were briefly explained. Its application to monotonic and cyclic shear behavior was demonstrated via monotonic and cyclic response simulations in 1D stress space.
2. The distributed element framework was extended via I-soil to 3D stress space by use of von Mises and Drucker Prager yield surfaces. A damping factor type formulation that achieves non-Masing type hysteretic behavior was extended from 1D to 3D and included in the I-soil constitutive model. The model coupled shear and volumetric behavior using Rowe (1962) volumetric response theory via a non-associative flow rule, and is capable of simulating shear induced volumetric behavior.
3. I-soil was implemented in LS-DYNA, explicit dynamic finite element code, and is able to operate in effective stress space. The implementation details were presented in a flow chart, and further details are presented in Appendix E.
4. Monotonic undrained tests obtained from direct simple shear tests were simulated using I-soil in a single element test. Simulated results were close to the measured response In addition, drained response under cyclic loading was demonstrated and compared to a direct simple shear test, and results show that I-soil captures the hysteretic damping observed in laboratory tests. In addition, theoretical a single element simulation was demonstrated and showed that the model is capable of simulating stiffness degradation due to excess porewater pressure generation.

7 FINITE ELEMENT MODELING OF WAVE PROPAGATION THROUGH FREE-FIELD SOIL AND SOIL-STRUCTURE SYSTEMS

7.1 Introduction

Theoretical modeling of site response requires performing wave propagation analysis to simulate ground response effects. Conventional practice for wave propagation utilizes 1D equivalent linear or nonlinear analysis. The equivalent linear method is the most common procedure in practice (Kramer and Paulsen 2004), since the required input parameters are well-established and the parameters are physically meaningful. Nonlinear ground response analyses better represent nonlinear soil behavior; however, until recently such analyses were limited due to poor documentation and unclear parameter selection and code usage protocols. Stewart et al. (2008) and Matasovic and Hashash (2012) highlighted such problems related to nonlinear site response analyses and clarified a number of items related to proper utilization of ground response analysis using theoretical models in both 1D site response analysis and in a finite element platform.

One-dimensional nonlinear site response software (e.g., DEEPSOIL, D-Mod2) are widely used to analyze wave propagation through a horizontally layered soil domain with a level ground surface. However, such methods cannot be used to conduct multi-dimensional analyses due to their 1D nature. Therefore, other methods such as the finite element method (FEM) where the domain is idealized as a discretized continuum with distributed mass becomes a useful tool to model the dynamic response of sites in a 3D domain under multi-directional seismic loading. The FEM can incorporate factors such as: (1) soil layer and property details; (2) structural components and properties; and (3) soil-structure interaction. Both the predictive capabilities and computational power have improved significantly in recent years that allow for conducting such analyses on readily accessible computing platforms. Table 7-1 summarizes some finite element programs along with their capabilities and the soil models that are implemented within each program.

Table 7-1 Finite Element Programs for Wave Propagation Analysis

Program Name	Fluid Coupling	Soil Models	Integration of EOM*	Multi-core run****
SUMDES	Yes	Wang (1990)	?	?
OpenSees	Yes	PIMYM**,PDMYM***, Manzari Dafalias	Implicit	Yes
Plaxis	Yes	UBCSand	Implicit	Yes
ABAQUS	Yes	UMAT	Implicit/Explicit	Yes
MASTODON	No	I-soil	Implicit	Yes
LS-DYNA	Yes	I-soil,MAT79	Implicit/Explicit	Yes

* Equation of motion
** Pressure independent multi-yield material model
*** Pressure dependent multi-yield material model
****Parallel computing using multiple cores for a given analysis

In this report, LS-DYNA software and the I-soil material model were used to simulate wave propagation through free-field and soil-structure systems. In addition, I-soil is also available in

MASTODON and has been successfully utilized for single element, shear beam and SSI analyses (e.g. Baltaji et al. 2017).

7.2 Numerical Modeling Issues and Procedures in LS-DYNA

Two- and three-dimensional dynamic response analysis of soil-structure systems can be performed using a dynamic finite element analysis platform. LS-DYNA is an explicit dynamic finite element analysis program that allows 3D simulations to be utilized for dynamic systems. The same considerations related to discretization and incorporation of viscous damping, etc., in 1D nonlinear site response analysis are valid for 2D and 3D dynamic response analysis of soil-structure systems. This section discusses various additional procedures and issues related to use of FEM in simulation of wave propagation through free-field and soil-structure systems.

7.2.1 Free-field modeling

Modeling of wave propagation can simulate free-field conditions whereby the ground motion at the surface is not expected to be affected from the presence of a structure. In these conditions, a 3D analysis can be approximated by a shear beam analysis. A shear beam analysis is based on the assumption of simple shear-type deformation. In addition, shear stresses and strain are assumed to be uniform across horizontal planes. Extensive evaluation of the approach was presented in Gazetas (1987). Although the application of such an approach is restricted to certain conditions, for 3D large scale problems, a large system of equations solved in many time steps can be reduced to a couple dozen elements (where applicable) and run times can be reduced by one or more orders of magnitude. The shear beam type analysis with a uni-directional base excitation is analogous to 1D site response analyses in software such as DEEPSOIL.

Figure 7-1 illustrates the simplification of a full 3D free-field model to a shear beam model. Figure 7-1a shows the 3D geometry of a centrifuge model using approximately 20,000 elements. The nodes at the outer edge that are at the same elevation, are constrained to move together (EqualDOF), and the excitation is applied to the entire bottom surface (all nodes). Figure 7-1b shows a shear beam approach where the stack of brick elements creates a shear beam model that can represent any vertical column within the 3D geometry. The shear beam model reduces the degrees of freedom by approximately three orders of magnitude in this example.

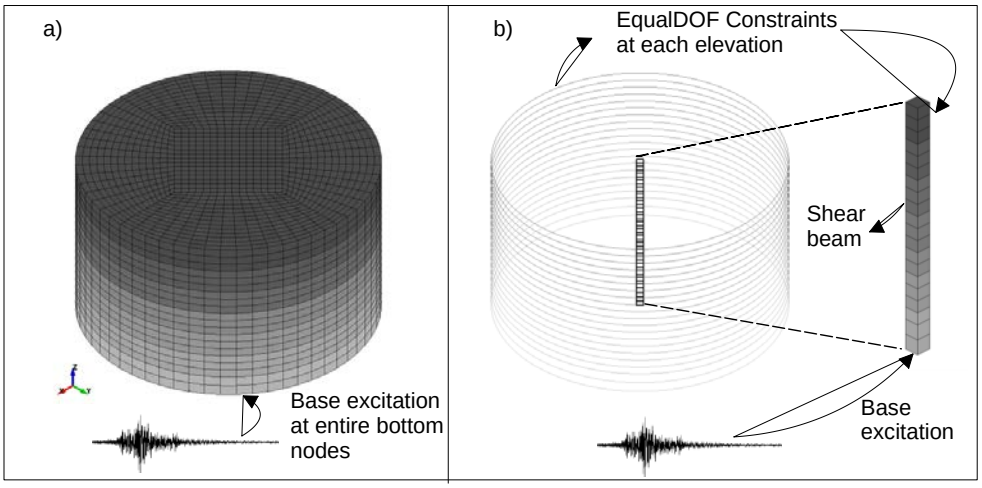

Figure 7-1 Simplification of 3D free-field in a shear beam approach. (a) 3D free-field model. (b) Shear beam model extracted from middle of 3D model

Surface spectral accelerations obtained from a simulation of an approximately 20 m deep soil profile with 3D free-field and shear beam numerical models (using the I-soil constitutive model) presented in Figure 7-2 demonstrate that the surface response in 3D and shear beam models are identical.

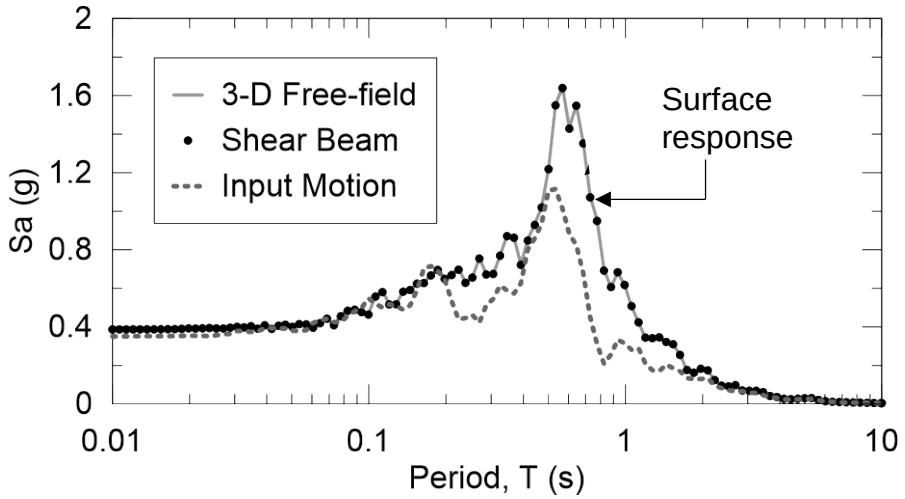

Figure 7-2 Surface responses obtained from 3D free-field and shear beam analyses.

Thus, shear beam analyses can be conveniently used to simulate level ground or gently sloped free-field conditions where there is not a significant 3D stratigraphy and topography change.

7.2.2 Soil-structure interaction modeling

Heavy structures founded on top of a soil domain may alter the characteristics of the ground motions at the base of the structure. In such cases, the response of the structure affects the response of the soil and vice versa. This process is coupled and such coupling may not be represented by free-field numerical models. Thus, in soil-structure interaction (SSI) analyses it becomes necessary to simulate the coupling process and its effect on both the soil and structural components. Two methods commonly are used to analyze SSI problems: (1) a multistep method; and (2) a direct method. The multistep method uses superposition to simplify SSI analyses by isolating the kinematic and inertial interactions. Kinematic and inertial interactions are treated separately and then superposition is used to combine the effects. This method is restricted to linear and equivalent linear analyses because it relies on the principle of superposition. To remove this restriction, the entire soil-structure system can be modeled using a direct method where the soil-structure system is modeled together (Figure 7-3) and the equation of motion is solved for the system response without differentiating the structure and the soil. In this study, dynamic simulations of SSI systems are conducted using direct methods.

7.2.3 Soil modeling

The LS-DYNA explicit dynamic finite element code can incorporate generalized effective stress analysis with and without excess porewater pressure generation and dissipation via fluid-solid coupling. The program allows user-defined material model codes to be implemented and utilized. This study uses the I-soil material model to describe soil response.

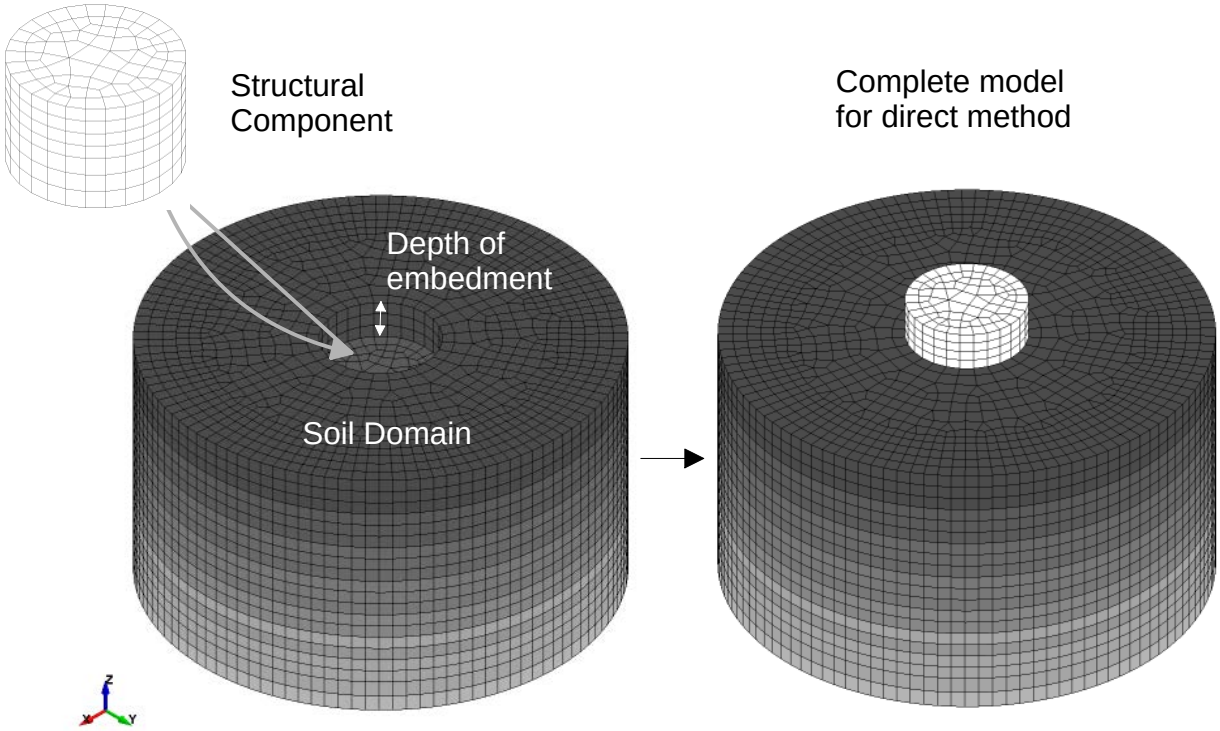

Figure 7-3 Soil-structure system geometry for direct method SSI analysis.

7.2.4 Simulation of the Structural Component

The simulation of the structural component in an SSI problem involves: (1) modeling the structural material; and (2) modeling soil-structure interaction. The structural component used in dynamic soil-structure centrifuge testing presented in this report is solid steel with a cylindrical shape. Since the stiffness of this solid is much higher than the underlying soil, it is assumed that the structural component behaves rigidly on top of the soil domain. This assumption was tested by comparing the spectral acceleration responses assuming an elastic structure and a rigid structure. The preliminary results showed insignificant differences between the rigid and elastic structures, whereas run time decreased by an order of magnitude when modeling the structure as rigid. The factor of safety against sliding was found to be between 4.8 and 6.8 (Cerna-Diaz 2018). In addition, preliminary numerical simulations conducted with interface elements showed very small (on the order of fraction of mm) sliding of the structure. Thus, we did not take into account the sliding between soil elements and structure elements on simulations presented herein. The boundary between soil and structure is set to be impermeable so that no fluid can flow through the structural component.

7.2.5 Base excitation inputs

In finite element analysis, both unidirectional and bidirectional input motions can be specified at the base of shear beam and SSI numerical models. Two types of base motions can be used in such analyses: (1) outcrop motion; and (2) within motion. A recorded motion is called an outcrop motion when the recording is obtained from the surface of a rock site (outcropping condition). If the motion is obtained at depth within the site (i.e., from a downhole array), it is called a within motion. Stewart et al. (2008) recommends that if the motion is an outcrop motion, an elastic base should be used for the base excitation conditions. If the motion is a within motion, then it should be used without any modification with a rigid base condition.

In the centrifuge tests presented in this report, excitation time histories were recorded on the base plate and along the depths of soil sample. To minimize potential uncertainty related to interaction between the base plate and the soil model, the authors used the acceleration recorded at the deepest level of the soil sample and input motions were treated as a within motion in the simulations. Thus a rigid base was used in the numerical models and the recorded input motions were applied at the base of the numerical models without any modifications. In case of modeling outcrop motions, the finite element analysis method allows an elastic layer introduction at the base of the model and/or dampers at the degrees of freedom to represent damping due to interaction between bedrock and soil. Further information regarding the overall computation times and application of early versions of I-soil in SSI analyses can be found in (Numanoglu et al. 2017)

7.3 Summary

This chapter briefly described the finite element analysis method used to simulate free-field and SSI problems. The following items summarize the main points achieved by the chapter.

1. Several different finite element modeling platforms were tabulated. Their solution characteristics were presented. Further details were provided on fluid-solid coupling, available soil models and multi-core run capabilities of each platform.
2. Validity of shear beam type modeling in level surface seismic problems was verified within the LS-DYNA dynamic finite element analysis platform. This was achieved by simulating both shear beam and three dimensional free-field models. Results showed that shear beam solution provides identical results compared to three dimensional model and thus can be conveniently used to simplify three dimensional free-field seismic problems whereby the ground is level, and stratigraphy and topography are uniform.
3. Several simplification on modeling structural component and soil-structure interaction were presented for stiff structure and dense sand cases. These simplifications are related to modeling the structure as a rigid material rather than an elastic material as well as the interaction at the interface elements.
4. Base excitation characteristics for outcrop and within conditions were briefly summarized.

8 FINITE ELEMENT SIMULATION OF DYNAMIC CENTRIFUGE TESTS

8.1 Introduction

For nuclear power plants founded on top of dense natural or compacted coarse-grained soils, the soil is not expected to liquefy during an earthquake. However, cyclic loading causes an accumulation of small volumetric strains. If the deposit is thick, the resulting total and differential settlements may impair operations at the plant. To assess this problem, a seismic deformation analysis can be conducted to estimate settlements induced by earthquake loading. In the last 50 years, researchers have developed empirical correlations and advanced constitutive models to estimate the cyclic response of coarse-grained soils. Most of these studies focused on loose to medium dense sands (liquefiable soils) to estimate both cyclic shear and volumetric behavior under drained, partially drained, and undrained conditions. In addition, these studies generally investigated soil behavior under uni-directional loading using laboratory element tests and harmonic cyclic motions (e.g., sinusoidal motion; Elgamal et al. 2002, 2005, 2008; Yang et al. 2003; Byrne et al. 2004; Dafalias and Manzari 1997, 2004; Lai et al. 2004; Choi et al. 2005; Gutierrez et al. 2009; Boulanger et al. 2013; Armstrong et al. 2012; Daftari et al. 2014; Karimi and Dashti 2015; Armstrong et al. 2015; Jefferies et al. 2015; Dafalias and Teibat 2016; Ziotopoulou 2017; Ghofrani et al. 2017).

In contrast, few studies have considered broadband motions, or multi-directional loading because: (1) there are insufficient data available to validate models with multi-directional broadband loading; and (2) some constitutive models are limited to plane strain conditions and cannot properly capture 3D effects.

8.2 Scope of Validation Study

The chief aim of this study was to evaluate multi-directional loading effects on soil behavior and to estimate the deformations resulting from such loading. A compilation of laboratory and centrifuge data presented in Chapter 4 illustrates that multi-directionality cyclic loading clearly affects soil deformations. Thus, any numerical analysis conducted to estimate cyclic soil response and soil-structure interaction should be 3D. This chapter presents numerical simulations and comparisons of computed and measured soil response. Bi-directional centrifuge test results were used to validate the I-soil constitutive model for both free-field and SSI conditions. The analyses include the following details.

1. 3D free-field simulations utilize a shear beam approach. This assumption was verified by comparing 3D and shear beam model simulations. The results were identical as shown in Figure 7-2.
2. The simulations were conducted under saturated conditions with the soil free to drain. Both excess porewater pressure generation and dissipation were allowed via fluid-solid coupling. A zero pore pressure boundary condition was applied at the foundation depth elevation (i.e., the water table was slightly below the ground surface) to prevent numerical instabilities at low effective stresses. The structure was defined as impermeable.
3. Effective stress-strain soil behavior was characterized by I-soil and corresponds to the response of a uniformly graded, subrounded Ottawa sand with Dr ~ 95%. I-soil is capable of capturing important aspects of soil behavior, such as: (a) small strain nonlinearity; (b) non-Masing type hysteretic behavior; and (c) shear induced contraction-dilation.
4. The 60g centrifuge tests were modeled. These tests correspond to an approximately 20 m deep sand profile. Base excitations are applied as within motions using within recordings measured near the bottom of the centrifuge model (see Chapter 4 for more details). Figure

8-1 shows the meshed numerical model geometry, components used to model the soil-structure system and the location of input motions. Simulations of 30g tests require more detailed investigation of effects of shaking history and overconsolidation on the response of sands and this work is still ongoing.

5. Constant-stress solid elements (default element for solids with a single integration point) were used to discretize the domain. Such solid elements are under-integrated (single integration point rather than eight) and very efficient in dynamic applications. However, under-integrated characteristics of elements may cause hourglassing (whereby the deformations do not produce any strain energy, thus the deformation is a zero energy mode – LSTC Theory Manual, 2009). LS-DYNA includes control options to minimize the hourglass effect. The defaults options provided by LS-DYNA are used in this study to minimize potential effects of the hourglass problem.

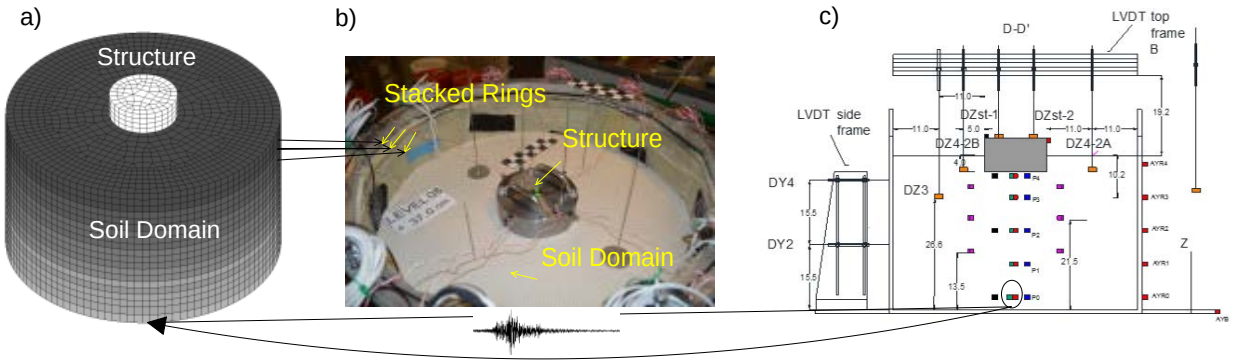

Figure 8-1 3D soil-structure system details. (a) Model geometry and mesh used in the simulations; (b) photograph of soil-structure system modeled in centrifuge; (c) the instrumentation layout of the centrifuge sample.

Free-field and soil-structure centrifuge tests were conducted at RPI using the 2D shaker and laminar soil container. Table 8-1 summarizes key aspects of these tests.

Table 8-1 Summary of centrifuge simulations run in this section

Test type	Prototype Thickness (m)	Centrifugal Acceleration (g)	Type of Loading
Production Test 95-FF-60g [PT1]	20.5	60	1D, 2D
Production Test 95-SSI-60g [PT2]	20.5	60	1D, 2D

Twenty-one bi-directional and uni-directional motions were used as base excitations of the numerical models. These input motions are summarized in Table 8-2.

Table 8-2 Input motions for simulations

No.*	Event	M_w	Station	HypD (km)	PGA (g)		Arias Intensity (m/s)			Sig. duration
					x	y	I_x (m/s)	I_y (m/s)	I_{total} (m/s)	(s)
M10	Kobe 1995/01/16	6.9	OSAJ	21.4	0.097	0.115	0.207	0.342	0.549	43.9
M11	Northridge19 94/01/17	6.7	87	64.4	0.091	0.127	0.093	0.181	0.274	19.2
M1	Chi-Chi 1999/09/20	6.1	TCU-087	60.74	0.142	0.154	0.589	0.653	1.242	36
M12	Loma Prieta 1989/10/18	6.9	58393	18	0.109	0.201	0.216	0.435	0.651	16.02
M13	Lotung 1986/11/14	7.3	Smart1 006	54	0.238	0.328	0.663	1.558	2.221	15.5
M3	Landers 1992/06/28	7.3	Joshua Tree	15.36	0.234	0.259	1.532	1.812	3.344	27.9
M5	Chile 2010/02/27	8.8	Maipu	100	0.35	0.308	2.219	2.01	4.229	50.8

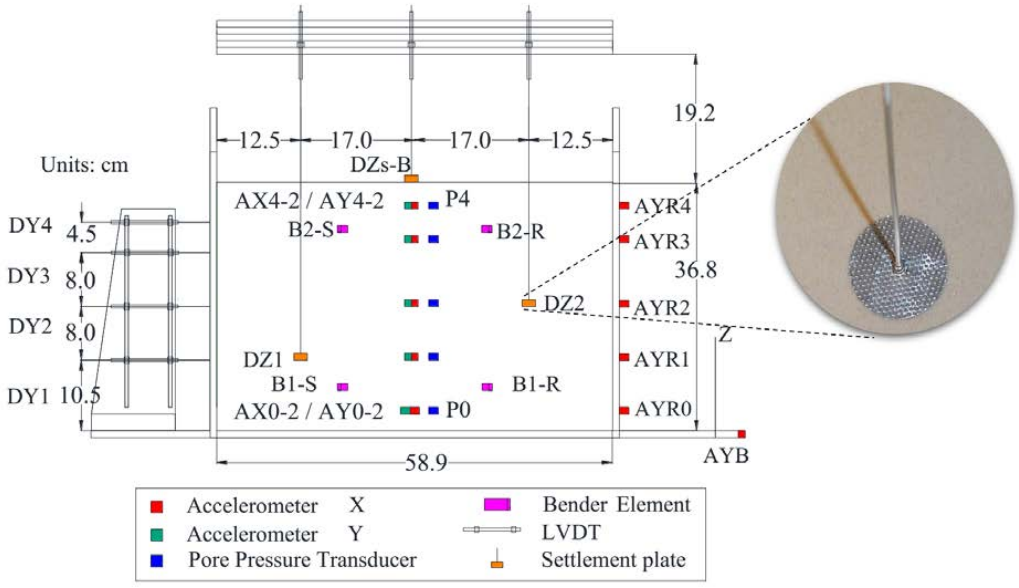

Figure 8-2 Detailed instrumentation of D_R 95% FF centrifuge test.

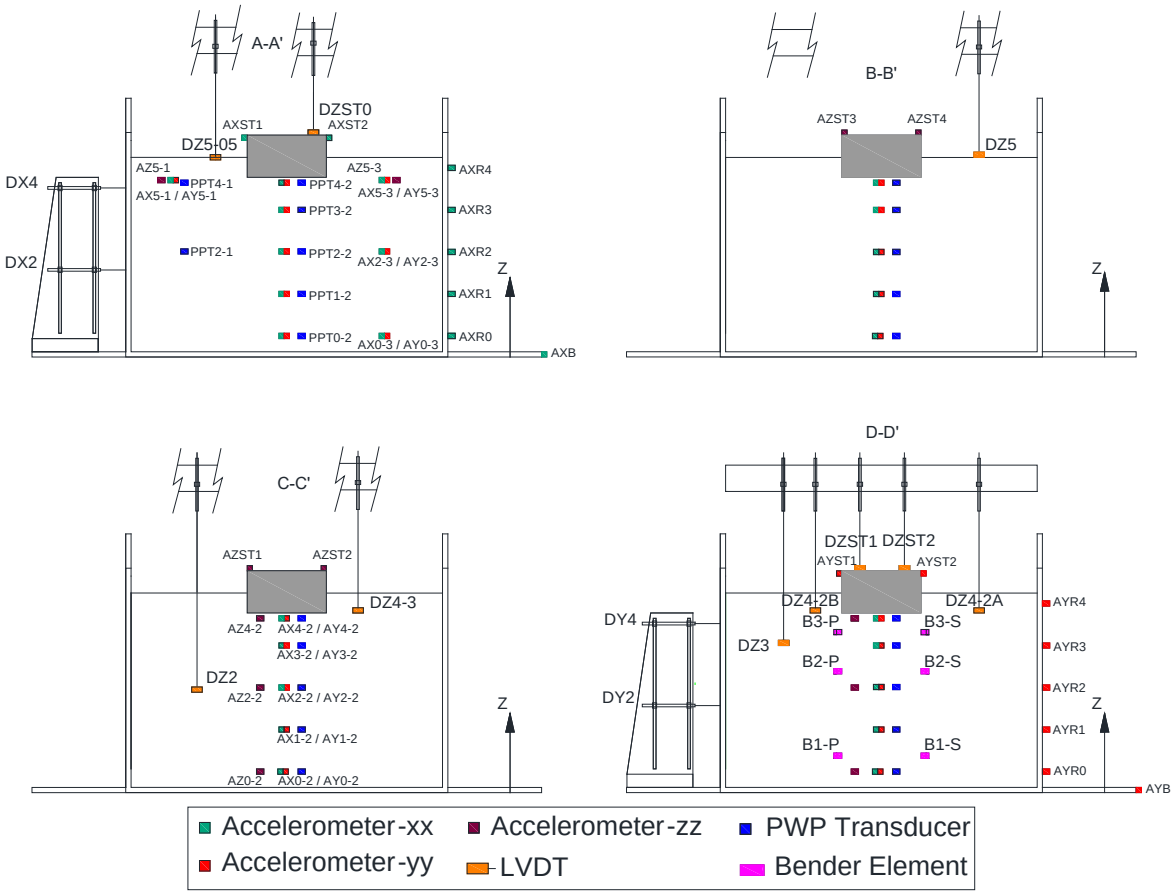

Figure 8-3 Detailed instrumentation of D_R 95% SSI centrifuge test.

8.3 I-soil Input Parameters

The primary input that I-soil requires is a backbone curve. The backbone curve defines soil behavior under monotonically increasing strains and can be constructed using the following four items: (1) shear wave velocity (V_s); (2) normalized modulus reduction curve (G_{sec}/G_{max}); (3) large-strain shear strength; and (4) density (ρ), where backbone shear stress (τ) and backbone shear strain (γ) are related as:

$$\tau = G_{sec}\gamma \tag{8-1}$$

where G_{sec} is secant shear modulus. Equation (8-1) can be written as:

$$\tau = \frac{G_{sec}}{G_{max}} G_{max}\gamma \tag{8-2}$$

where $G_{max} = \ maximum\ shear\ modulus = \rho V_s^2$. Therefore,

$$\tau = \frac{G_{sec}}{G_{max}} \rho V_s^2 \Upsilon \quad (8\text{-}3)$$

Equation (8-3) shows that the backbone curve can be constructed using normalized shear modulus at a given strain, shear wave velocity and density.

There are numerous correlations available in the literature to estimate shear wave velocity. This study uses the correlation proposed by Menq (2003) to estimate the shear wave velocity profile of the 20 m deep sand column. The V_s measurements from the centrifuge tests agreed well with the Menq (2003) correlation (see Figure 8-4c). The G_{sec}/G_{max} curve represents the decrease in soil stiffness due to an increase in cyclic shear strain amplitude. Several empirical studies are available to determine the normalized modulus reduction curves of sands (e.g., EPRI, 1993; Vucetic and Dobry 1991; Darendeli 2001; Menq 2003). The Darendeli (2001) study includes uniformly graded sand (PI = 0) similar to the Ottawa sand used in this study. Therefore, the Darendeli (2001) curves were used to construct the backbone curves for the soil profile. Finally, the shear strength mobilized at large shear strain was determined using Bolton (1986) considering interparticle sliding and geometrical interference components of friction via $\varphi' = \varphi'_{cv} + \psi$ where φ' is the mobilized shear strength, φ'_{cv} is the constant volume friction angle, and ψ dilative component of the mobilized friction angle. Bolton (1986) proposes the following empirical form for the dilative component of the mobilized friction angle:

$$\psi = 3 * \{D_R[10 - \ln(p')] - 1\} \quad (8\text{-}4)$$

where D_R is relative density and, p' is effective mean stress.

Figure 8-4 presents the soil profile information including the discretization, effective vertical stresses, shear wave velocity, and large-strain effective friction angles. Figure 8-5 presents the modulus reduction and damping curves used for the construction of backbone curves input to I-soil. The mobilized friction angle profile presented in Figure 8-4d is based on constant volume friction angle of 30 degrees and dilative component of the mobilized friction angle ranging between 12 and 20 from higher confining stresses to lower confining stresses for Ottawa Sand.

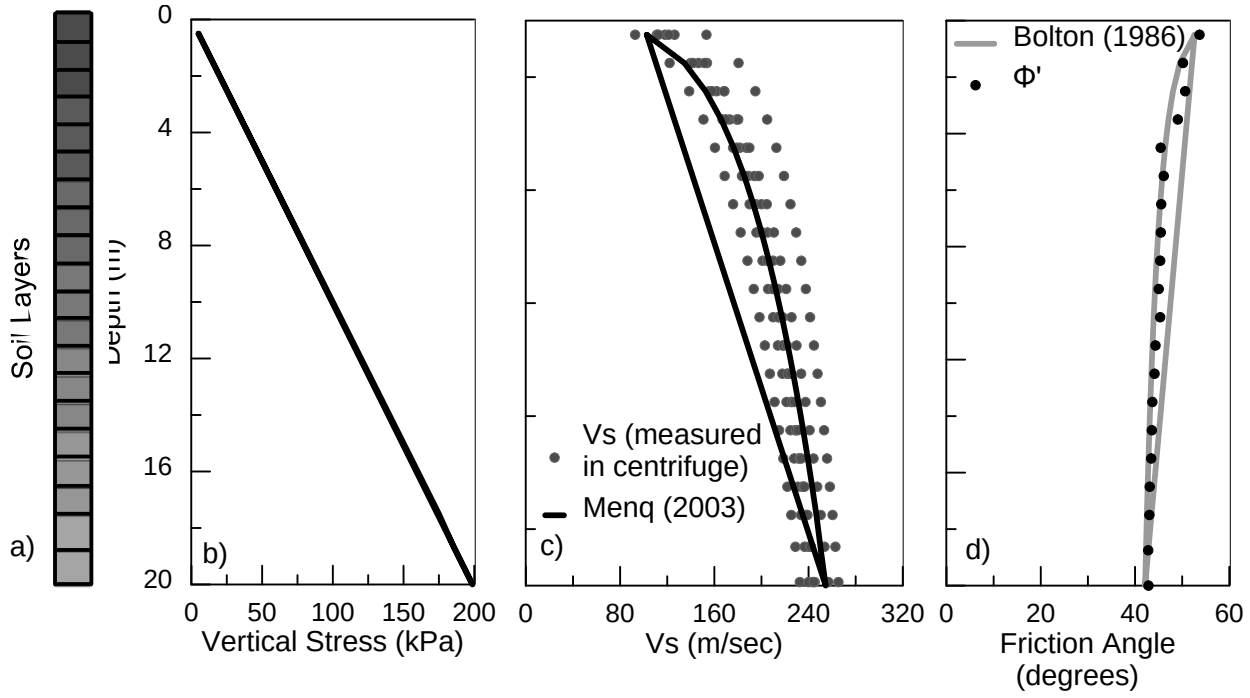

Figure 8-4 Shear beam soil profile constructed for 60g centrifuge tests; (a) Layered soil domain; (b) initial effective vertical stresses; (c) comparison of V_s measured in the centrifuge and calculated from Menq (2003); (d) Bolton (1986) and achieved friction angles at large shear strains.

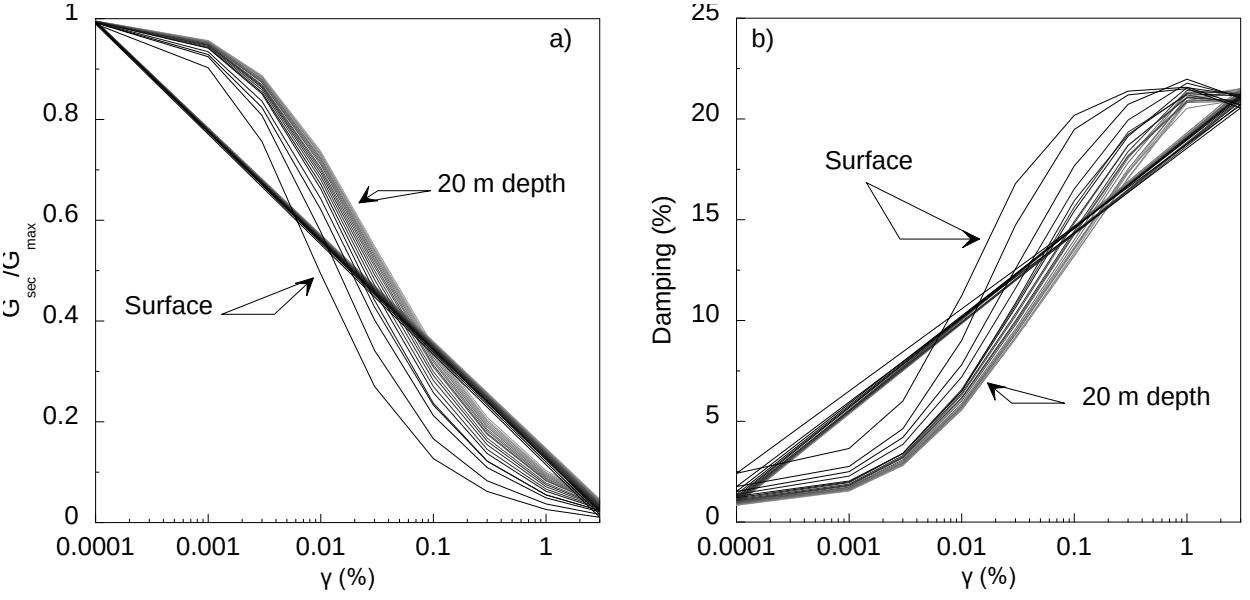

Figure 8-5 Soil profile inputs: (a) normalized modulus reduction curves; and (b) damping curves for the 60g centrifuge test simulations.

8.4 Simulation of Free-field Centrifuge Tests using 1D Effective Stress Site Response Analysis from DEEPSOIL

1D nonlinear effective stress site response analysis is an essential first step before utilizing more complex 3D finite element analyses. Thus, the soil profile constructed for simulating the 60g centrifuge tests using I-soil were first simulated in DEEPSOIL v6.1, and 1D nonlinear effective stress site response analyses without excess porewater pressure generation were conducted. Each component of the bi-directional input motions was used separately due to the 1D nature of the site response analysis. The generalized quadratic hyperbolic constitutive model (GQ/H; Groholski et al. 2016) was used to represent the backbone stress-strain response of the sand. Frequency independent damping formulated by Phillips and Hashash (2009) was used for viscous small-strain damping. The MRDF type (Phillips and Hashash 2009) non-Masing unloading-reloading rules were used to properly model hysteretic damping behavior.

Near-surface spectral responses from recorded and computed accelerations for motion M12 (Table 8-2) are plotted in Figure 8-6. This example compares the x and y direction motions from separate analyses performed using the individual components of the bi-directional input motions. Analyses capture the near-surface response in the corresponding direction. This example illustrates that 1D site response provides a reasonable approximation by separating the components of multi-directional input motions.

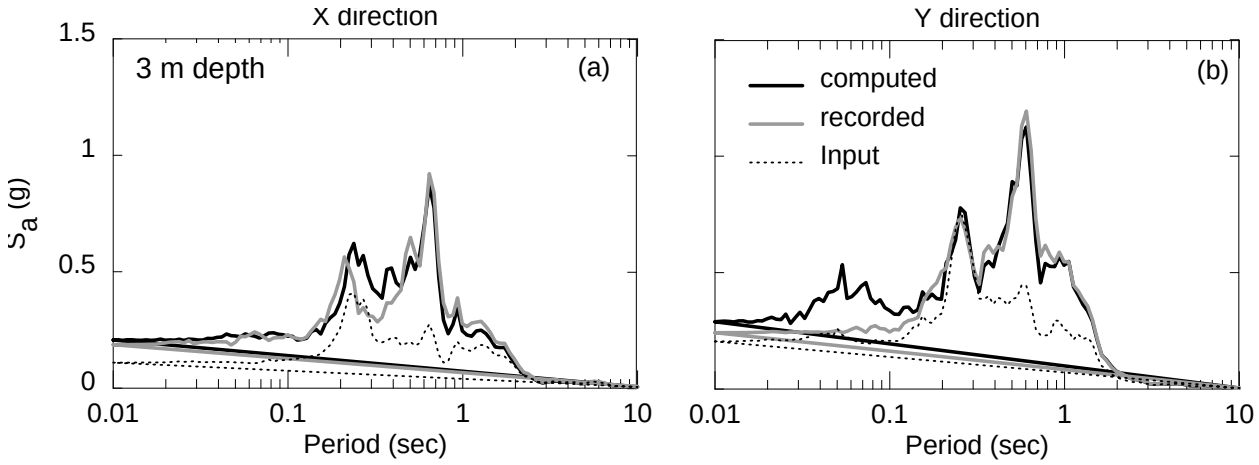

Figure 8-6 Computed (DEEPSOIL) and measured 5% damped spectral response at 3 m depth for M12 motion modeled in centrifuge test: (a) x direction; (b) y direction.

Figure 8-7 plots the residuals of spectral accelerations for every motion used in the simulations. Also the mean residuals (μ_r) computed by averaging the residuals of all the motions are presented. The residuals are computed as log (S_{ar} / S_{ac}) where S_{ar} is spectral response of the recorded motion and S_{ac} is the spectral response of the computed motion. Thus, positive residuals mean that the response is underestimated and negative values mean the response is overestimated.

While the mean residual spectral accelerations for an individual motion between periods of 0.03 – 0.1 sec reach -0.3, the average residual value was -0.14 between these periods. Within an 80% confidence interval, the residual ranges between -0.1 to -0.17. In addition, at shorter periods (near PGA) the mean residual decreases to -0.08 and the 80% confidence interval is between -0.06 and -0.09. These results imply that 80 % of the simulations will overestimate the measured PGA by only

15 to 20%. At periods longer than 0.1 sec, the residuals decrease significantly and approach zero, implying an agreement between computed and recorded accelerations.

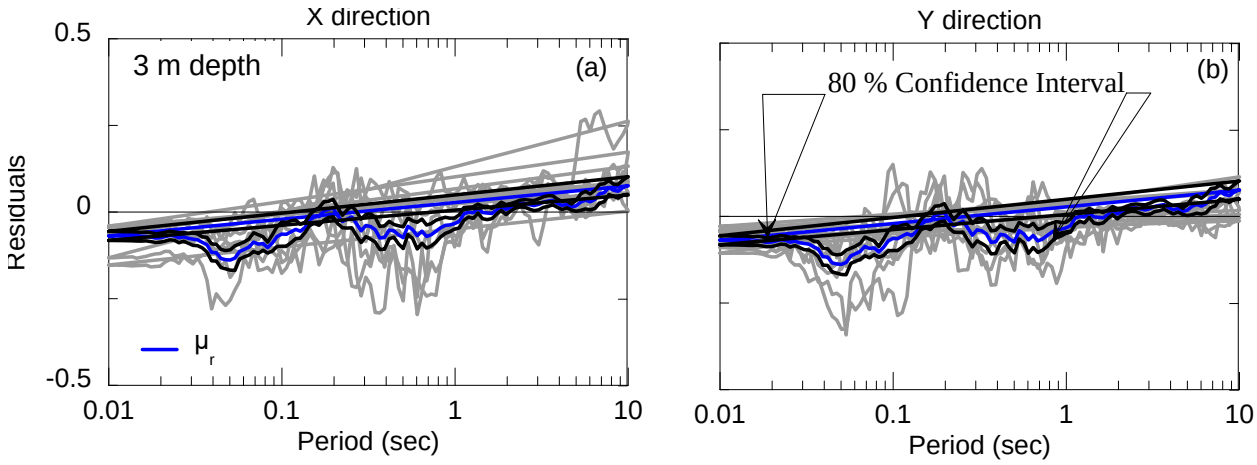

Figure 8-7 Residuals of 5% damped spectral accelerations at 3 m depth corresponding to one dimensional analyses that uses directional component of bi-directional motions. and mean residuals (μ_r) calculated by averaging all residuals from all the components: (a) x direction; (b) y direction.

Figure 8-8 presents residuals computed for Arias intensity, Housner intensity, PGA, and PGV for all the motions where the residual for each parameter is computed as log(measured/computed). In addition, mean residual profiles are presented. Although for some parameters and individual motions the residuals approach ±0.25, mean residuals for all of the parameters are within -0.1 and 0.0, indicating that the 1D nonlinear effective stress site response without excess porewater pressure simulations reasonably captured the measured response. Further details of the time histories and spectral accelerations can be found in Appendix D.

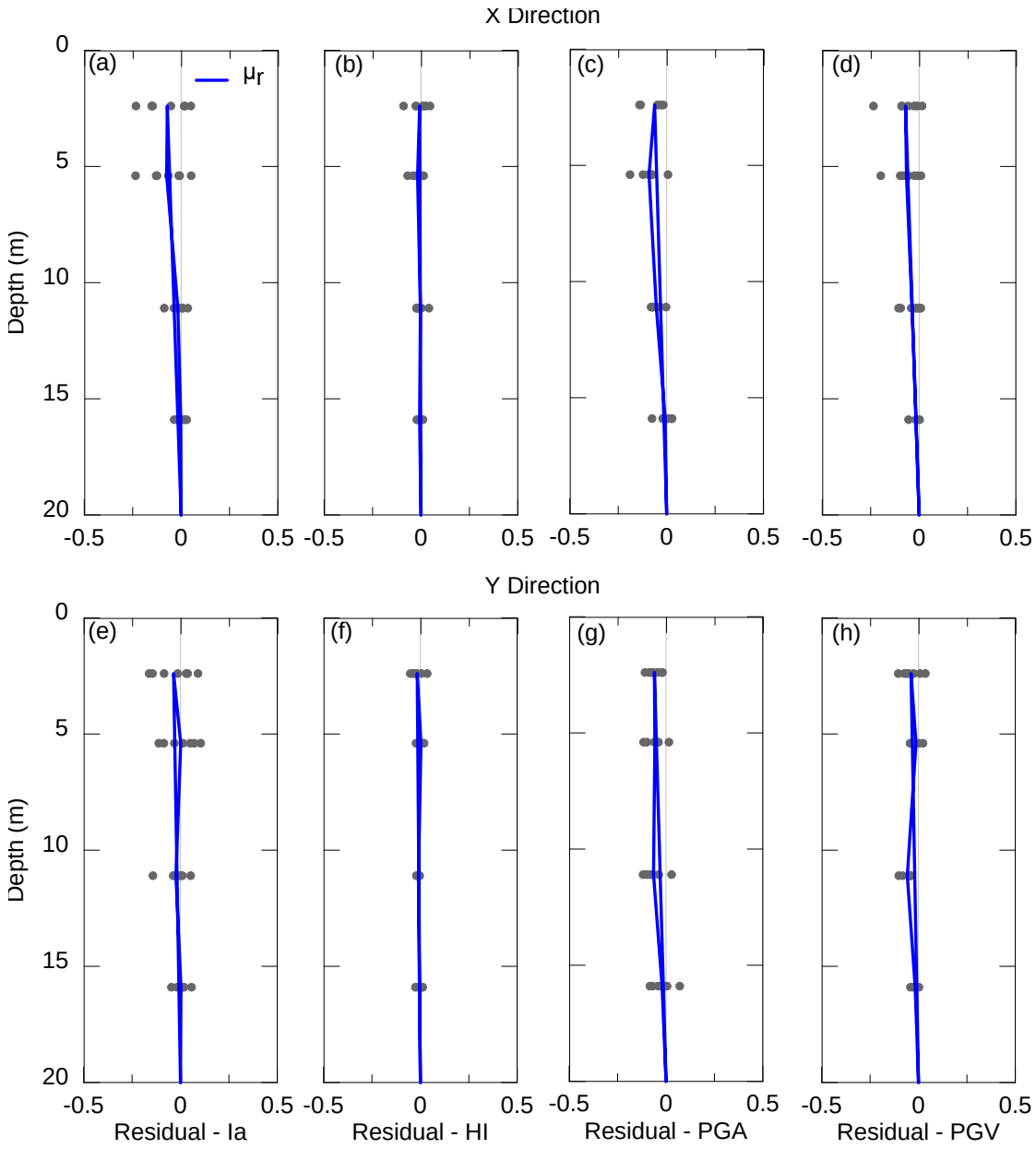

Figure 8-8 Residuals of (a) Arias intensity - x direction; (b) Housner intensity - x direction; (c) PGA - x direction; (d) PGV - x direction; (e) Arias intensity - y direction; (f) Housner intensity - y direction; (g) PGA - y direction; (h) PGV -y direction for all the motions and mean residuals (μr) calculated by averaging the residuals from all the motions corresponding to the same direction.

8.5 Shear Beam Simulations of Free-field Centrifuge Tests

A shear beam approach is an idealization of the 3D free-field behavior using a smaller numerical model where the degrees of freedom are reduced by orders of magnitude. The shear beam yields results identical to the full 3D domain if: (1) the 3D stratigraphy is not significantly heterogeneous; and (2) the surface is either level or slightly inclined. The shear beam model used in this study is solved using a finite element platform, and the soil column is modeled as stacked brick elements.

The discretization used in the finite element analyses is identical to that used in 1D site response analysis. One advantage of the shear beam models over the 1D nonlinear site response models is that the bi-directional motions can be applied simultaneously because: (1) the finite element method is able to solve 3D wave propagation problems; and (2) the I-soil model is a 3D model. This section compares the computed shear beam responses to centrifuge measurements. The shear beam analyses include the following details:

1. Shear strength and stiffness in I-soil is effective stress-dependent and unloading-reloading rules are non-Masing type.
2. Volumetric model parameters were selected based on the laboratory I-mcDSS tests. The phase transformation stress ratio was determined to be 0.55 from a monotonic test shown in Figure 8-9. The parameter A_0 used in the ideal monotonic test is equal to 1.0. Several broadband motions successively applied on a D_R 65% specimen showed a significant decrease on accumulated volumetric strains after the first shaking event (Figure 8-10). In addition, the corresponding element test simulations using I-soil demonstrated that although the first and second shaking events have similar shear stress–shear strain response, A_0 = 0.7 reasonably captures the accumulated volumetric strains at the end of the first shaking event whereas a reduction in A_0 (A_0 = 0.15) was necessary to capture the pre-shearing effect on accumulated volumetric strains (after the first shaking event). This reduction in shear-induced volumetric strain continues with successive broadband shaking evens with less difference compared to the difference in first and second shaking. Thus, for the centrifuge tests, an average value of 0.15 was used for A_0.
3. Since a viscous fluid was used in the centrifuge tests, realistic permeability (k) required to simulate porewater flow was determined using Hazen (1918) as:

$$k\ (m/s) = C_e D_e^2 \tag{8-5}$$

where D_e is effective grain diameter (D_{10}) and C_e represents the effects of grain shape and gradation on the pore channels in the direction of flow. Louden (1952) showed that the permeability value for silty sands to gravel can be estimated by:

$$k\ (m/s) = 0.01 D_{10}^2 \tag{8-6}$$

where D_{10} is in [mm]. Based on these studies, the permeability value for subrounded Ottawa sand was estimated to be 5 x 10^{-4} m/s.

4. Frequency independent viscous damping was added to represent the small strain hysteretic damping. The viscous damping values along the depth of the profile were determined from Darendeli (2001) which is indirectly presented in Figure 8-5 at 0.0001% shear strains.

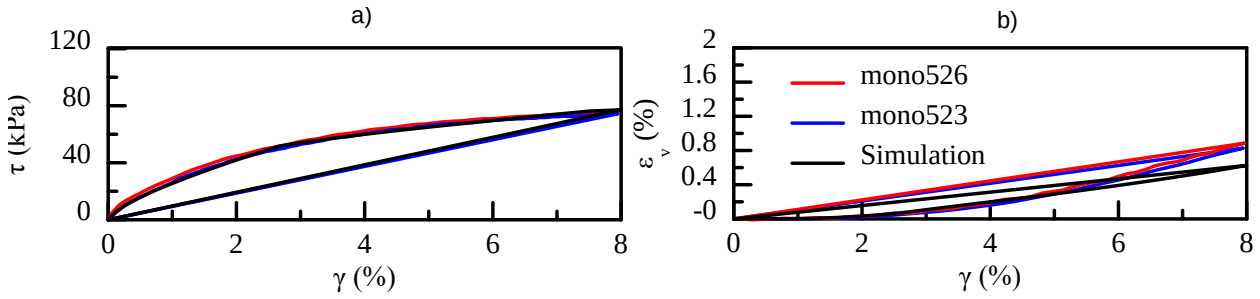

Figure 8-9 Determination of phase transformation stress ratio from monotonic test: (a) monotonic stress strain response; (b) volumetric strain – shear strain response from laboratory tests and simulation.

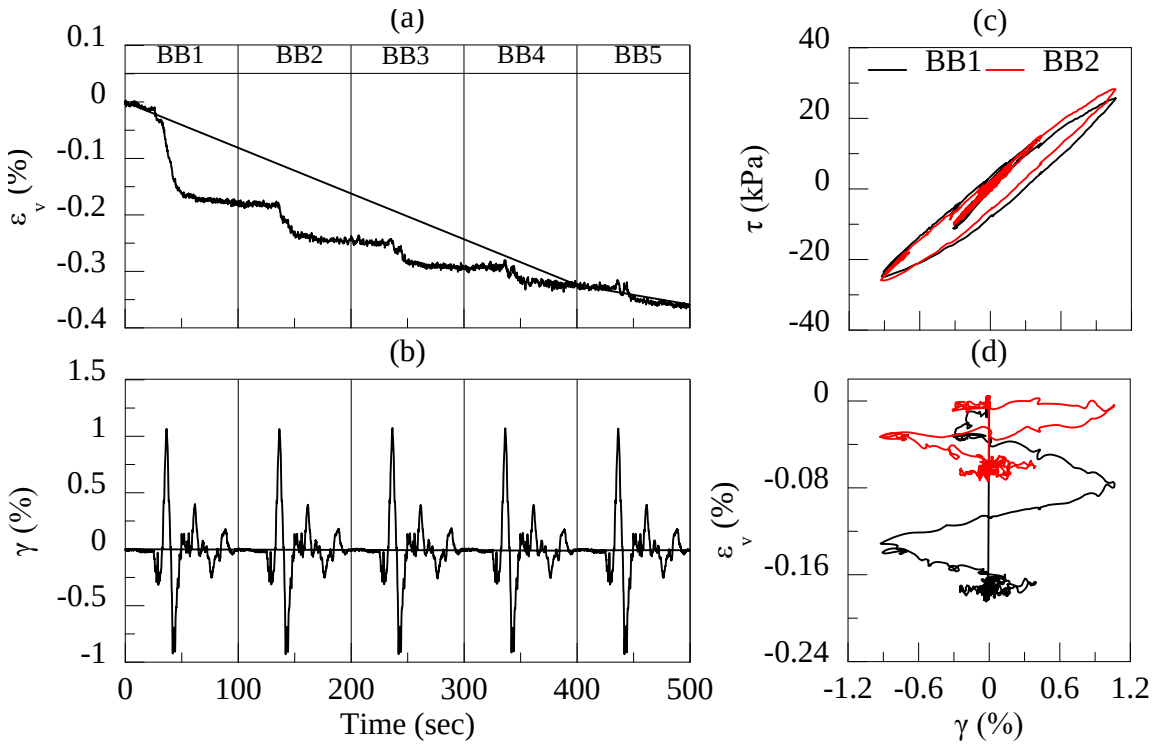

Figure 8-10 Five broad band motion applied successively on D_R 65% Ottawa Sand: (a) shear induced volumetric strain time history; (b) applied shear strain time history; (c) stress strain behavior of first two broad band motion; (d) shear induced volumetric strains vs. applied shear strain time history.

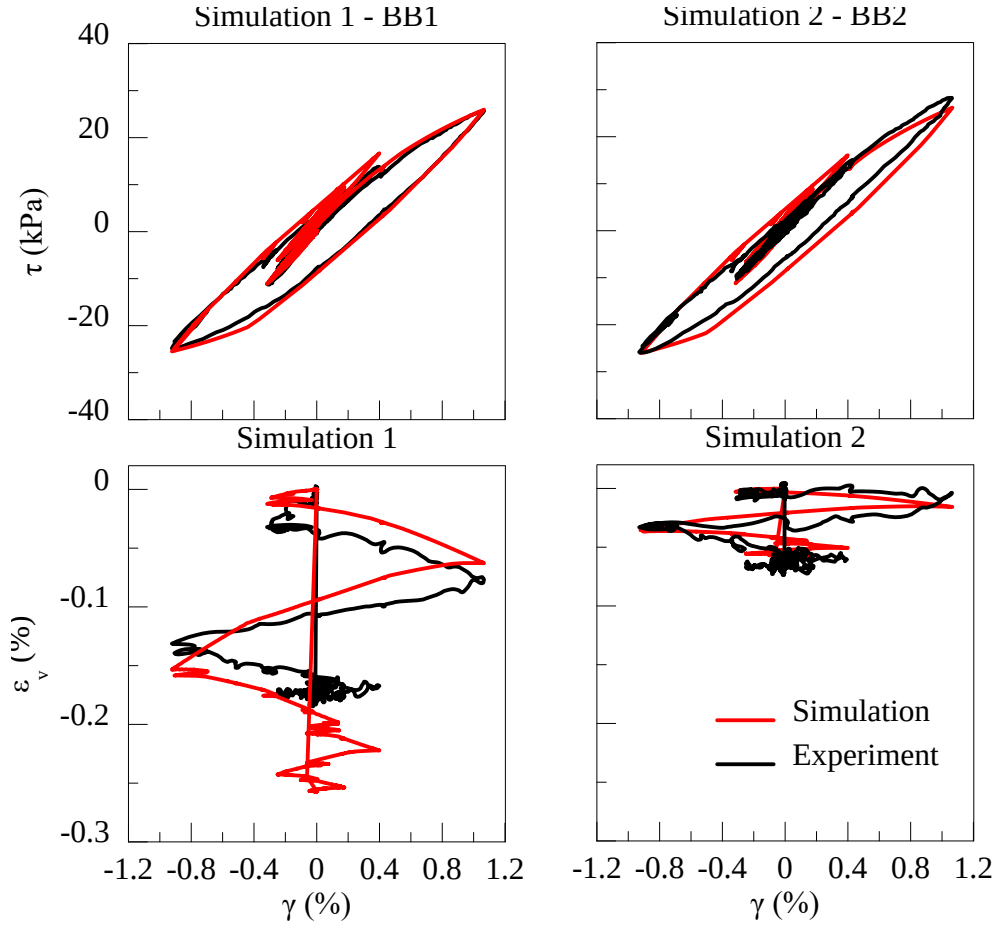

Figure 8-11 Comparison of simulation and experimental results for first and second broadband motion presented in Figure 8-10

Sample near-surface spectral responses calculated from recorded and computed accelerations at 3 m depth are plotted in Figure 8-12. Comparison based on motion M12 shows that the shear beam model with bi-directional input motions reasonably captures the measured acceleration response. This observation is overall valid for the entire simulation set. Appendix D includes a complete comparison of measured and computed spectral accelerations for each motion at each depth.

Figure 8-13 presents the residuals of near-surface spectral responses for all simulated motions as well as the mean residuals (μ_r) obtained from averaging all the spectral acceleration components. While the mean residual accelerations for an individual motion between periods of 0.03 – 0.1 sec reach -0.3, the average residual value was -0.14 between these periods. Within an 80% confidence interval, the residual ranges between -0.1 to -0.17. In addition, at shorter periods (near PGA) the mean residual decreases to -0.1 and the 80% confidence interval is between -0.08 and -0.12 which implies there is an 80 percent chance a simulation will only overestimate the measured PGA measurements by 20 to 25%. The residuals decrease significantly after 0.1 sec and reach near zero values implying an excellent agreement between computed and recorded values. There are slight differences between mean residuals computed for results obtained from I-soil (LS-DYNA) and GQ/H (DEEPSOIL). This is because, although, the same backbone curves and damping values are used for each model, I-soil has a shear induced volumetric component whereas GQ/H is a solely shear model.

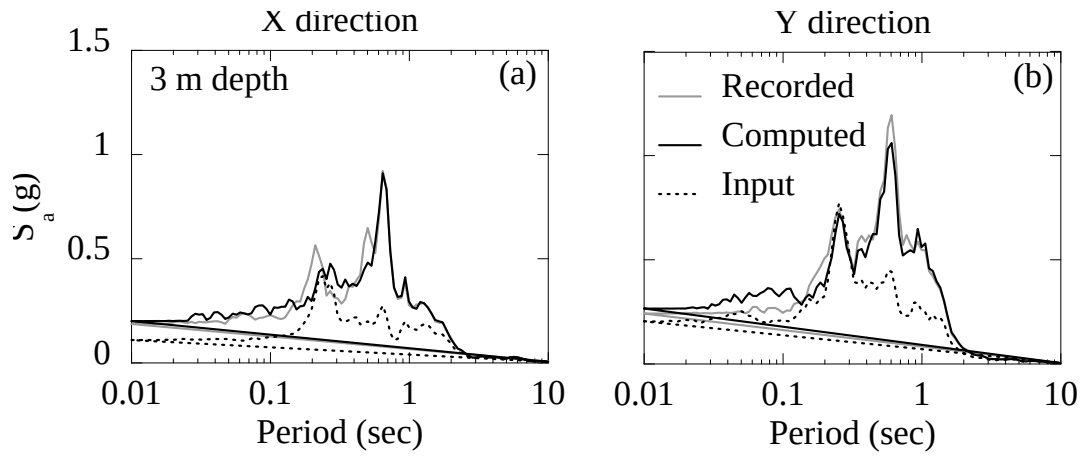

Figure 8-12 Computed (LS-DYNA) vs measured 5% damped spectral response at 3 m depth for motion M12 modeled in centrifuge test.

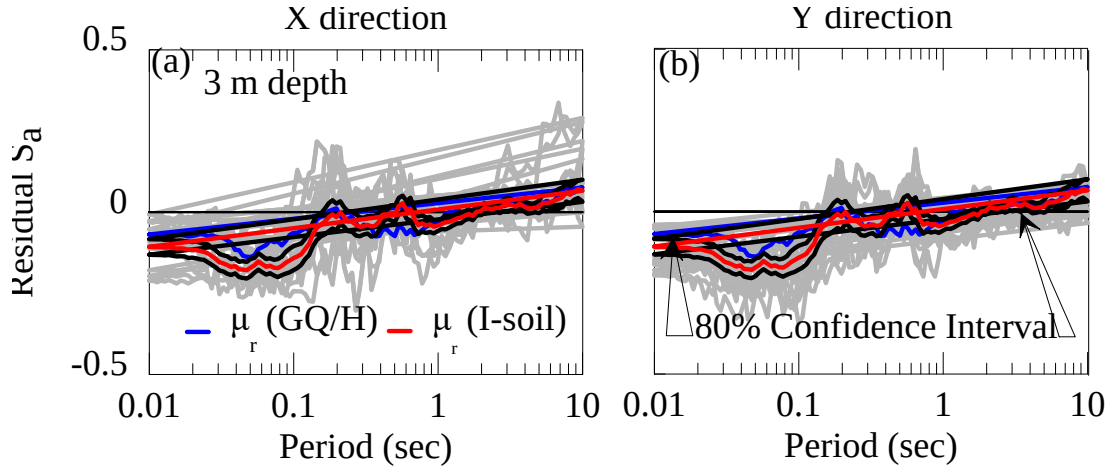

Figure 8-13 Residuals of spectral accelerations at 3 m depth for all the motions and mean residuals (μ_r) calculated by averaging the residuals from all motions including both directional components: (a) shaded grey lines are x component residuals; (b) shaded grey lines are y component residuals.

Figure 8-14 shows that small accumulated surface settlement at the end of shaking in the centrifuge test was estimated reasonably. The fluctuation in the centrifuge settlement recordings may result from a combination of small up and down movements of the LVDT plates, electronic interference with the data acquisition, and contraction – dilation cycles. Small vibration of LVDT plates or high frequency interference in model scale may amplify in prototype and contribute to the fluctuations. We used raw recording data to compare to simulation results. Normalized excess porewater pressures measured in the centrifuge tests were overestimated by the numerical model. This amount of overestimation of r_u was not consistently observed at all depths for each test (see Appendix D) and since $r_u < 0.6$, the r_u difference between the computed and recorded results has minimal effect on the observed shear behavior. Finally, a good agreement was observed between computed and recorded acceleration time histories and this was also observed in computed vs measured energy intensities reached at the end of the shaking.

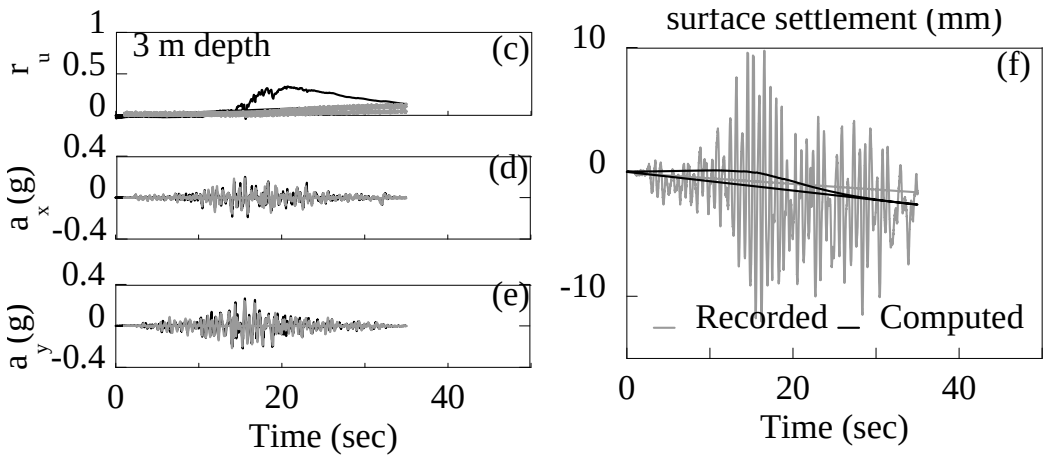

Figure 8-14 Computed vs recorded time histories of: (a) excess pore pressure at 3 m depth; (b) acceleration in x direction at 3 m depth; (c) acceleration in y direction at 3 m depth; and (d) settlement at surface for M12 motion modeled in centrifuge test

Figure 8-15 compares measured and computed values for both unidirectional and bidirectional shaking events and illustrates the agreement between computed and measured maximum settlements at the end of each shaking for surface to ~6 m depth. Since the settlement plate near 10 m depth malfunctioned, and measurements at ~15 m depth are very small, they are not included in the comparisons. Comparisons of maximum settlements showed that most of the values are bounded within the 1:2 and 2:1 ratio except the first shaking (M10) and last shaking (M5) events. The M10 motions are the first set of motions and M5 motions are the last set of motions applied during the centrifuge test. The overall trend indicates that starting from M10, the comparisons qualitatively shifts from 1:2 line to 2:1 line with most of the data clustered around 1:1 line.

The main reason of the shift from 1:2 to 2:1 line is (1) the simulations do not take into account any pre-shearing effects as the motions progress, (2) the initial shear wave velocity profile is the average of the entire data set, which means that the soil profile is stiffer during initial shakings and softer for shaking sets at the end. The effect of shaking history is demonstrated in Figure 8-16(a) and (b). Figure 8-16(a) shows that there is a significant reduction in the final settlements for each shaking event after the first couple of motions were applied. The overall trend in later motions is that the maximum settlement at the end of each shaking event mildly decreases as the sequence progress. There are some motions exhibiting larger settlements at the intermediate shaking levels and these are mostly because although the motion history progresses, there are some high intensity motions that again increases the settlements.

Figure 8-16(b) normalizes the settlements at the end of shaking with Arias intensity and shows a correlation between shaking intensity and normalized settlements. Normalized excess porewater pressure comparisons demonstrate similar trends, with most of the data clustered between the 1:1 and 2:1 lines, indicating an overall overestimation of the measurements. However, since the excess PWPs are small (< 0.6), the difference between the computed and measured values have a minor effect on the overall response. A qualitative comparison of settlement estimates in this study for the FF dynamic case with empirical estiamtes of settlement for static (monotonic) loading (Figure 8-17) illustrates that the dynamic FF settlement estiamtes are nearly as accurate as the static settlement estimates. Finally, excellent agreement was observed in maximum intensity measures (Arias and Housner intensities). This excellent agreement also allows simple shear beam simulations to be utilized in semi-empirical dynamic settlement correlations.

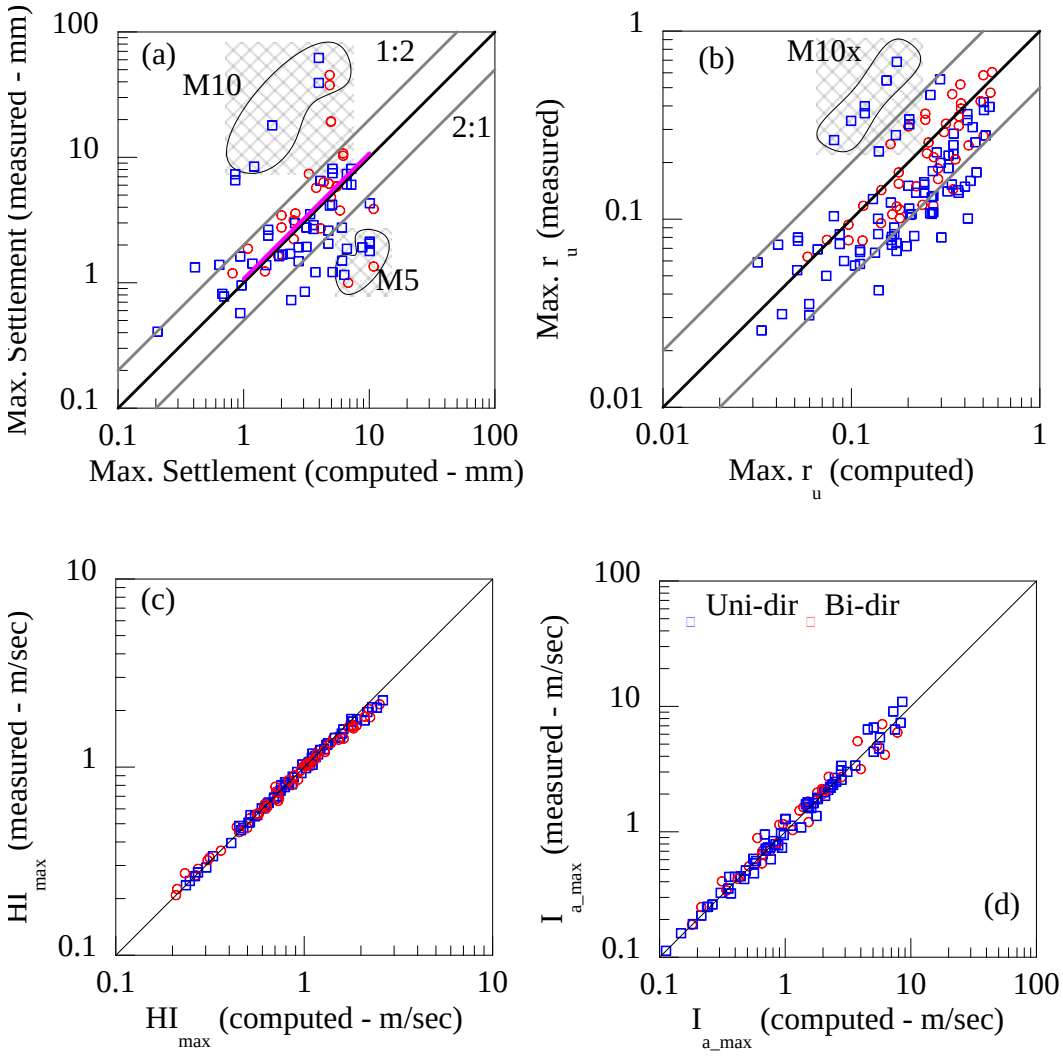

Figure 8-15 Computed vs measured maximum values for (a) final settlements (shown as absolute values) at depths up to 6 m; (b) maximum normalized excess pore water pressures throughout the central array; (c) Housner intensities throughout the central array; and (d) Arias intensities throughout the central array.

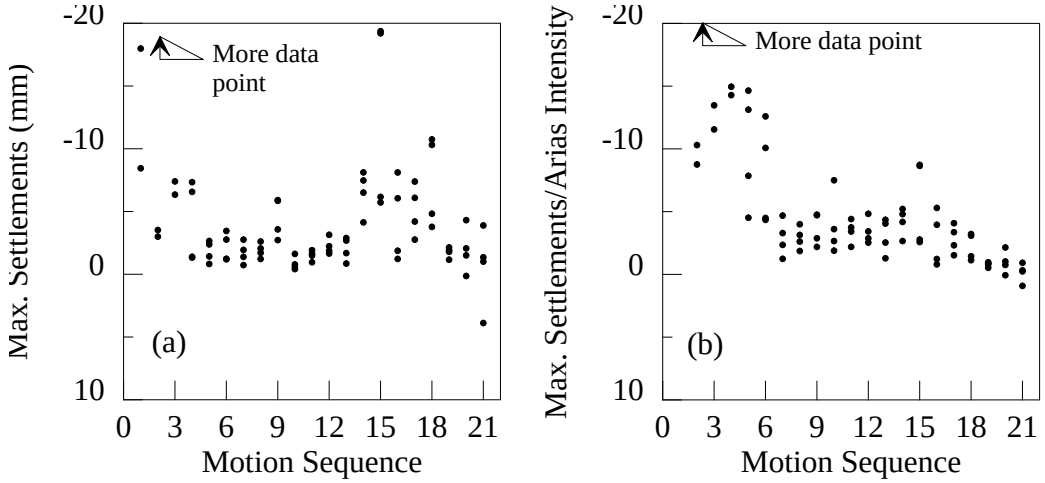

Figure 8-16 Maximum settlements for each shaking at surface to 6 m depth (a) motion sequence vs settlement; (b) motion sequence vs. settlements normalized by Arias Intensity.

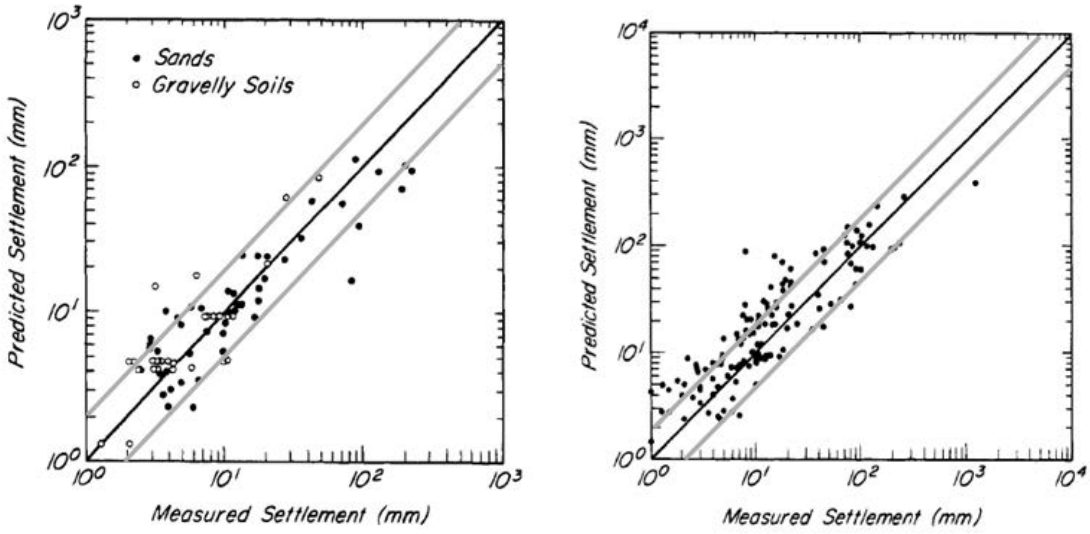

Figure 8-17 Comparison of measured and empirical estimation of static settlements of footings on sands by (a) cone penetration tests, (b) standard penetration tests. (from Terzaghi et al. 1996)

8.6 Effective Stress Space 3D Simulations of Soil-Structure System Centrifuge Tests

Soil-structure interaction analyses described in this section were conducted using the direct method (see Chapter 1). The full 3D system geometry was created based on the 3D soil-structure centrifuge model developed and presented in previous sections. The structural component was embedded in the numerical soil model similar to the structure in the dynamic centrifuge tests. The modeling details reported in previous section still apply, with the following additional details.

1. Structure boundaries are impermeable. Fluid cannot flow inside or at the surface of the structural component.

2. The water table was specified at the foundation embedment elevation to prevent numerical instability at low effective stresses.
3. The structural component was represented with a rigid material model. To validate this assumption, elastic material simulations were conducted, and no significant difference was observed. Representing the structural component as a rigid material significantly reduced computation times because the time step used in the explicit integration scheme is controlled by the stiffness of the materials. The presence of stiff (but elastic) components reduces the time step size, which in turn, increases the computation time by at least an order of magnitude.
4. Frictional interaction between soil and structure at the base of the foundation was not modeled. This approach was justified because no sliding occurred in the centrifuge tests or in simulations considering frictional interaction. However, frictional interaction that may occur on the sides of the structure cannot be simulated with the model presented here because the element degrees of freedom on the sides of the structure are tied to the degrees of freedom of the soil surface elements facing the structure.

Sample spectral responses calculated from recorded and computed accelerations under the structure are presented in Figure 8-18. The comparison in the x and y directions for the Loma Prieta earthquake motion (M12) shows that the 3D SSI numerical simulation with a bi-directional input motion captures the acceleration response well for this particular motion.

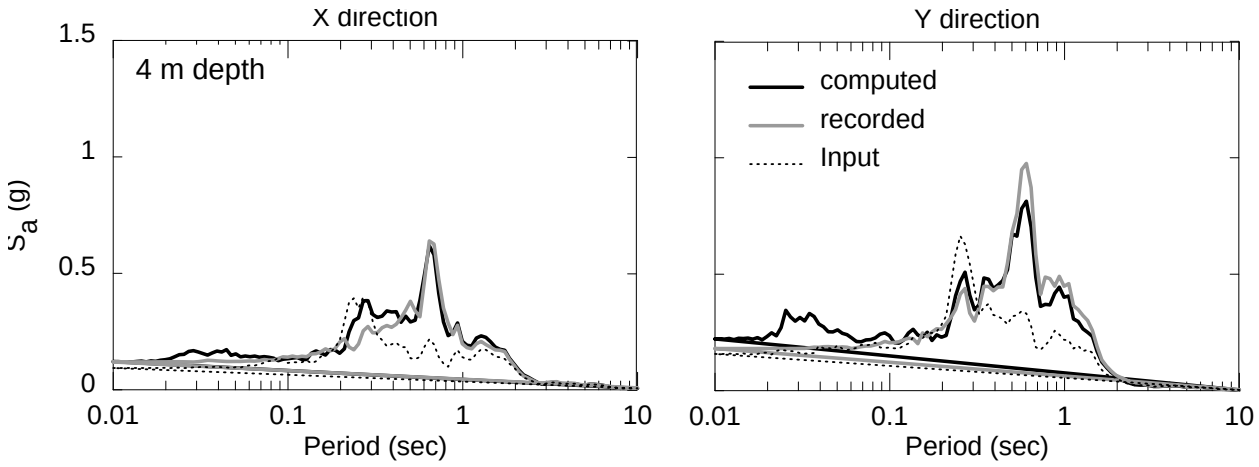

Figure 8-18 Computed vs measured spectral response at 4 m depth (~ 1 m under the structure) for M12 motion modeled in centrifuge test.

Moreover as shown in Appendix D, the spectral response calculated from accelerations recorded along the central array under the structure were captured in all of the analyses. Figure 8-19 presents the residuals of spectral responses ~1 m below the structure foundation for all the simulated motions. Residuals calculated for PGA show that the mean residual is -0.085 with the 80% confidence interval ranging from -0.062 to -0.11. This indicates that, on average, the spectral responses are overestimated by 18%, and that 80% of the simulations yielded PGA values within 14% to 20 % of the values measured under the structure.

Between periods of 0.1 sec to 10 sec, the mean residuals are within 0.033 and -0.077, with 80% confidence interval bounds of 0.064 to -0.115. This means that the spectral accelerations calculated using measured values were reasonably captured by the simulations within about an

8% underestimation and 14% overestimation. Furthermore, 80 % of the simulations fall within 16% underestimation to a 23% overestimation.

In contrast, at periods between 0.03 – 0.1 sec the simulations overestimated the measured values by 50%. This rather large overestimation is somewhat consistent with the overestimation observed at the same periods for free-field analyses. We are currently investigating the potential reasons for the overestimation observed in these periods. Baltaji et al. (2017) demonstrated that the time step and backbone discretization (number of points on a piecewise linear backbone curve) have an impact on the high frequency response observed in the spectral accelerations. The work presented in this report uses Vs/4H > 25 - 60Hz discretization which is larger than the minimum values suggested by Hashash et al. (2010). However, Chopra (2007) and Hashash et al. (2010) state that mesh discretization should be increased based on the frequency of interest. Chopra (2007) sets the limit as Vs/10H > (10 x frequency of interest). Further investigation is ongoing to explore the high frequency response overestimation.

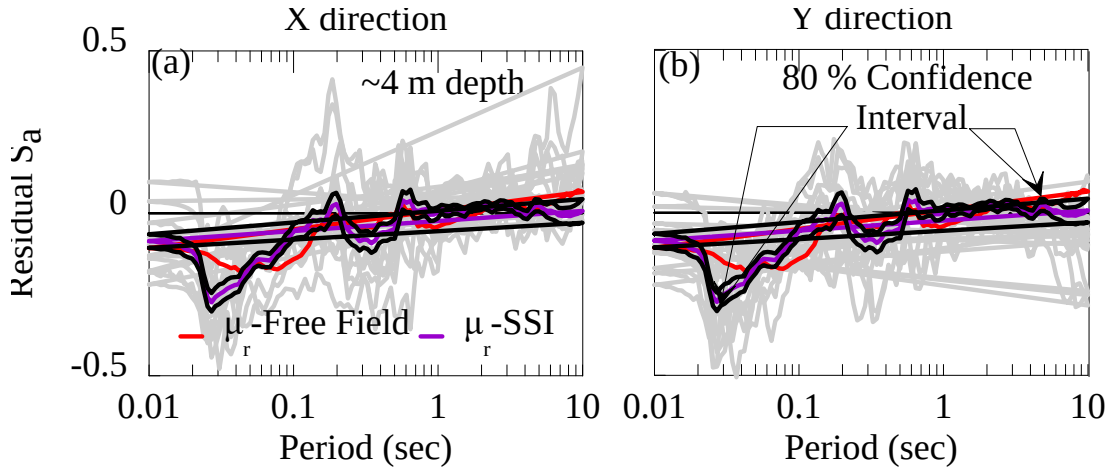

Figure 8-19 Residuals of 5% damped spectral accelerations at 4 m depth (under the structure) for all the motions and mean residuals (μ_r) calculated by averaging the residuals from all motions and including both components: (a) shaded grey lines are x component residuals; (b) shaded grey lines are y component residuals.

Figure 8-20 (a magnified version of Figure 8-21c and d) presents measured and computed acceleration time histories during motion M12. The comparison shows that the agreement between measured and computed values are very good. This is further demonstrated in Figure 8-22 c and d where the recorded vs. measured intensity measures are compared. The maximum r_u reached during the event was estimated by the simulation (Figure 8-21a). Although it is not observed in every motion, the maximum value of excess porewater pressure during the simulation was reached earlier than the measured counterpart. Downward spikes of excess porewater pressure and maximum values were captured by the model, especially for M3, M5, and M11 (see Appendix D). For the M12 event, settlements were low in magnitude and the simulations underestimated accumulated structural settlements reached at the end of the event. This under-estimation of structural settlements were not consistently observed in all of the analyses and detailed response of each motion can be found in Appendix D.

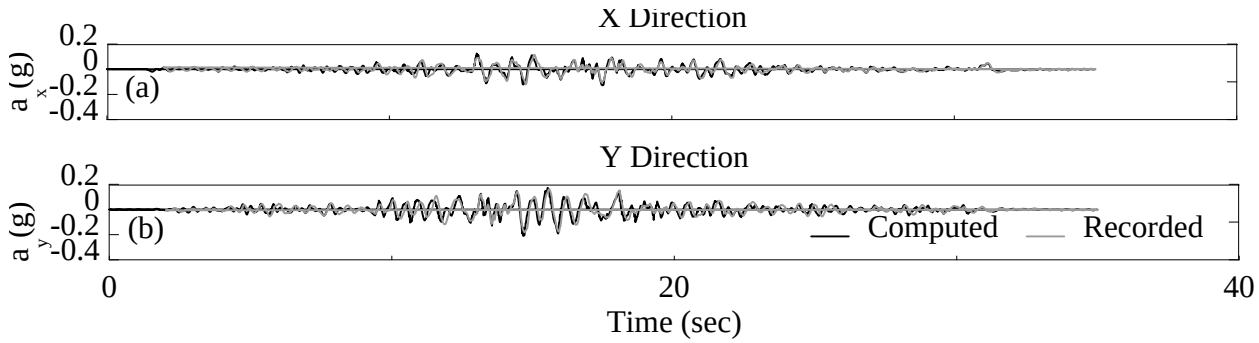

Figure 8-20 Computed vs recorded acceleration time histories (same as Figure 8-21 b and c) ~ 1 m below structure: (a) x direction, (b) y direction.

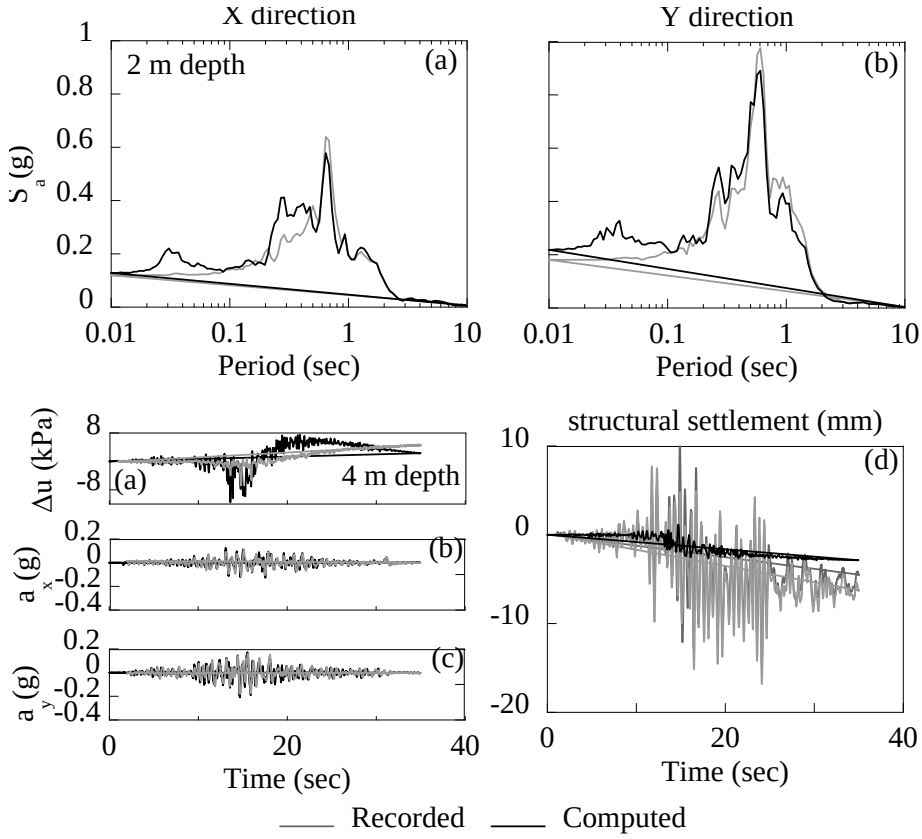

Figure 8-21 Computed vs recorded time histories of: (a) excess pore pressure at 4 m depth (from free surface, ~1 m under the structure); (b) acceleration time history in x direction at 4 m depth; (c) acceleration time history in y direction at 4 m depth; and (d) structural settlement for M12 motion modeled in centrifuge test

Figure 8-22 compares measured and computed intensity, final settlement, and maximum excess porewater pressure values for both unidirectional and bidirectional cases. Figure 8-22a demonstrates the computed vs measured accumulated structural settlements at the end of each

shaking. Comparisons of maximum settlements showed that most of the values are bounded within the 1:2 and 2:1 ratio except the first shaking (M10). The M10 motions are the first set of motions and M5 motions are the last set of motions applied on the centrifuge test. The overall trend indicates that starting from M10, the comparisons qualitatively shifts from the 1:2 line to the 2:1 line with most of the data clustered around the 1:1 line.

The main reasons for underestimation of settlements at the beginning compared to overestimation towards the end of the test are: (1) the simulations do not take into account any shaking history effects as the motions are applied (14 unidirection + 7 bidirectional motions), (2) the initial shear wave velocity profile is an average of the entire data set which does not take into account any densification effect on the stiffness of the profile, thus the response may be stiffer for the initial shakings and softer for shaking sets at the end (see Figure 8-4). This observation is consistent with the observations made for the free-field case.

Figure 8-23a shows that there is a significant reduction in settlement right after the 3rd shaking event (M10-XY). In contrast to the FF cases, settlement increases slightly as the shaking sequence progresses. This is because each new shaking event in the sequence has a larger intensity than the previous one. In the SSI case, this leads to a slight increase in settlement. However, Figure 8-23a shows a consistent decrease in the settlement potential based on the total settlement normalized by intensity measure (Arias Intensity). Excess PWP comparisons demonstrate similar trends with most of the data, on average, clustered around the 1:1 line which demonstrates decent agreement between computed and measured values. Qualitative comparison of settlement estimations in this study for the SSI case vs empirical correlations that enables calculation of footing settlements under static conditions (Figure 8-22) shows that accuracy of dynamic calculations for SSI simulations are as good as the accuracy of empirical static settlement estimations under footings. Finally, excellent agreement was observed in maximum intensity measures in term of Arias and Housner intensities (except the M5-2D event where the accelerometer in the test malfunctioned). This excellent agreement also allows the simulations to be utilized with existing energy intensity based semi-empirical correlations to estimate settlements.

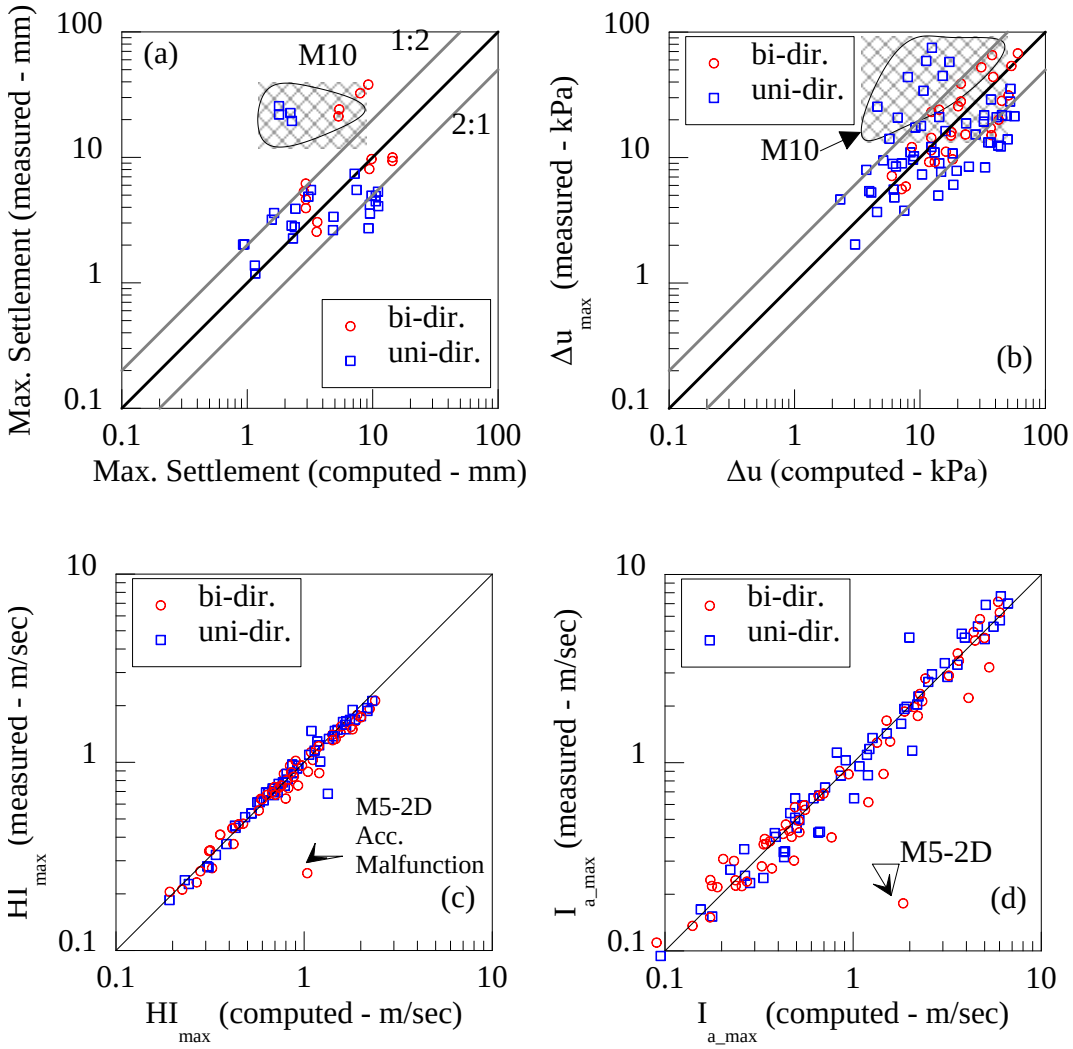

Figure 8-22 Computed vs measured maximum values for (a) final structural settlements; (b) maximum excess pore water pressures throughout the central array; (c) Housner intensities throughout the central array; and (d) Arias intensities throughout the central array.

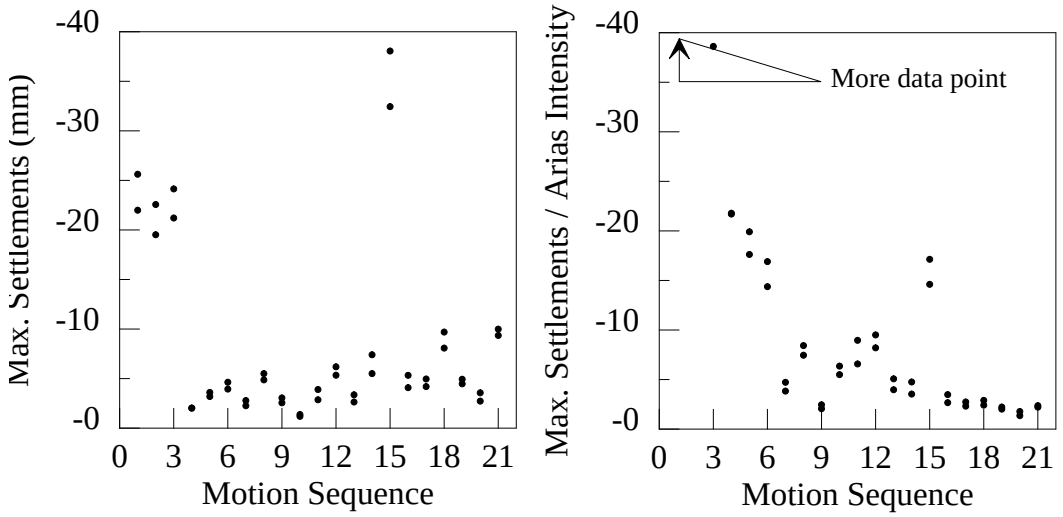

Figure 8-23 Maximum structural settlements for each shaking: (a) motion sequence vs settlement; (b) motion sequence vs. settlements normalized by Arias Intensity.

Further comparisons were done to evaluate the performance of the numerical simulations by comparing the settlements away from the structure using the measurements obtained from DZ 4-3, DZ 4-2B and DZ 4-2A, DZ3 shown in Figure 8-3. The comparison shows that centrifuge tests show very small settlements or heave away from the structure, whereas simulations still have a finite amount of settlement with magnitudes comparable to the free-field case. Further research is ongoing to investigate the cause of this mismatch between measured and computed values.

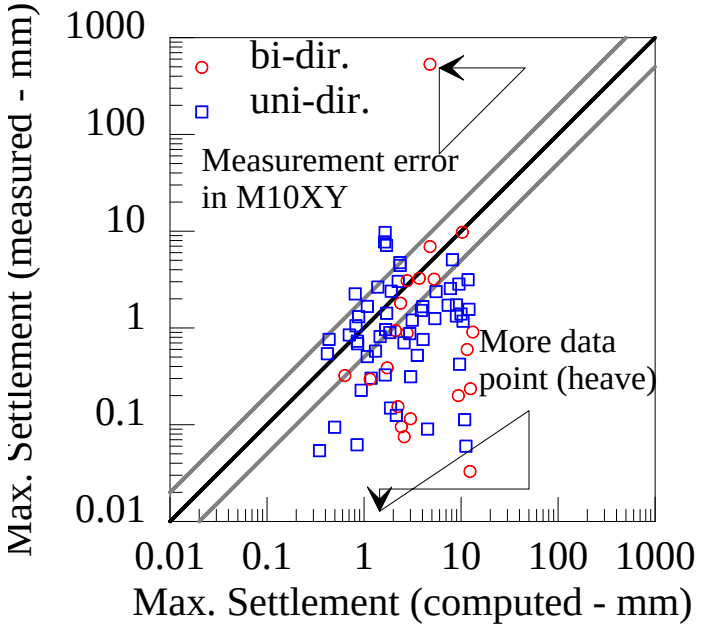

Figure 8-24 Computed vs measured final settlements (contraction is shown positive) away from structure (at DZ 4-3, DZ 4-2B and DZ 4-2A, DZ3).

8.7 Summary

This chapter presented numerical simulations of free-field conditions and soil-structure interaction (SSI) and compared the computed and measured soil response for these cases. Uni-directional and bi-directional centrifuge test results were used to validate the I-soil constitutive model for both free-field and SSI conditions. The following observations resulted from these comparisons.

1. Orthogonal components of the 2D base excitations used as a uni-directional input in 1D nonlinear site response analyses captures the shear behavior observed in the corresponding direction for dense sands. This observation allows 1D nonlinear site response analyses to be utilized to estimate the directional shear behavior observed in multi-directional centrifuge tests.
2. Free-field simulations show that shear response in terms of average 5% damped spectral accelerations were estimated reasonably well within the periods of 0.1 sec to 10 sec. PGA values were slightly overestimated by the numerical simulations. These overestimations are, on average, between 20-25 %. However, between 0.02 – 0.1 sec, ~35 % overestimation was observed. Further study is required to identify the potential reasons for overestimation of shear response in terms of spectral accelerations at these high periods. Intensity measures (Arias intensity and Housner intensity) calculated from recorded and computed acceleration time histories were observed to agree in terms of final accumulated energy. Within these two energy measures, Housner intensity comparisons showed better agreement. On average, volumetric response in terms of settlements and normalized excess porewater pressures demonstrated decent agreement, although detailed response for each shaking demonstrates consistent overestimation of measured behavior for the initial shaking event, whereas underestimation was observed through the final events among 21 uni and bi-directional shaking events. Several sources, such as densification and shaking history, contributes to this trend. Significant underestimation of volumetric response for first shakings whereas requires further study.
3. SSI simulations show that shear response in terms of average 5% damped spectral accelerations were estimated reasonably well within the periods of 0.1 sec to 10 sec. PGA values were slightly overestimated by the numerical simulations. These overestimations are, on average, between 15-20 % with an 80 percent confidence interval assuming the residuals are normally distributed. However, between 0.02 – 0.1 sec, ~50 % overestimation was observed. This behavior also was observed in the the free-field case and further study is required to identify the potential reasons for overestimation of shear response in terms of spectral accelerations at these high periods. Overall acceleration time histories as well as cumulative intensity measures (Arias intensity and Housner intensity) calculated from recorded and computed acceleration time histories were observed to agree very well. Within these two energy measures, Housner intensity comparisons showed better agreement. On average, volumetric response in terms of settlements and excess porewater pressures demonstrated decent agreement, although detailed response for each shaking demonstrated consistent overestimation of measured behavior for the initial shakings and underestimation through the final events (21 uni and bi-directional shaking events). Several sources such as densification and shaking history contributes to this trend. Significant underestimation of volumetric response for the first shaking requires further study.

9 SUMMARY, CONCLUSIONS, AND RECOMMENDATIONS

This report describes the following contributions:

1. Development of a database of drained and undrained element tests subjected to unidirectional and bidirectional cyclic shearing to study volumetric strains in medium dense to dense sands;
2. Development of unidirectional and bidirectional centrifuge "case histories" on dense sands with and without a structure to investigate and quantify dynamic soil response in the field;
3. Development of multidirectionality factors for volumetric strains and porewater pressure generation;
4. Development of new semi-empirical correlations for estimating bidirectional volumetric strains and porewater pressures under natural drainage conditions; and
5. Development of a new 3D soil constitutive model to characterize shear and volumetric behavior of sand with and without the presence of structures (SSI analyses).

The practical problem of the effects of multidirectional earthquake shaking on dense coarse-grained soil motivates this research. The study includes the following tasks:

1. Evaluation of currently available semi-empirical and constitutive models for estimating volumetric strain under drained and undrained loading;
2. Element and centrifuge cyclic testing to investigate the soil behavior under multidirectional loading conditions;
3. Semi-empirical model formulation to capture the volumetric behavior observed in element and centrifuge cyclic tests;
4. Constitutive model development to characterize soil behavior under monotonic and cyclic loads;
5. Description of numerical issues and procedures to utilize finite element methods to simulate dynamic sand behavior and SSI; and
6. Finite element analyses to simulate the dynamic centrifuge tests to evaluate the developed constitutive model and validate its ability to evaluate cyclic soil behavior.

9.1 Unidirectional and Bidirectional Simple Shear Testing Database

9.1.1 Summary

Four different sands tested in the element-level experimental program include: (1) a clean uniformly graded sand, Ottawa 40/70 (OT), commercially available from U.S. Silica (classified as SP); (2) a well-graded sand-silt mixture prepared by mixing portions of commercially obtained sands and natural silts sieved from a Mississippi river silty sand (classified as SW-SM); (3) a natural Mississippi River (MR) silty sand obtained from Cape Girardeau, Missouri (classified as SM); and (4) a Mississippi River – Gulf of Mexico (MRGM) clayey sand mixture (classified as SC). A total of 400 tests were performed.

9.1.1.1 Drained direct simple shear tests

Unidirectional (sinusoidal, broadband) and bidirectional (circular, figure-8 and broadband) strain-controlled, drained cyclic direct simple shear tests were conducted at shear strains of 0.1% to 10%. For comparison, cyclic shear strain amplitude in unidirectional tests is considered equivalent to the resultant shear strain amplitude in bidirectional tests. Loading frequencies for these tests were 0.1 and 1Hz, and 150 to 450 loading cycles were applied. Duku et al. (2008) and Yee et al. (2013) illustrated that volumetric strain in clean sands and sands with non-plastic fines are negligibly

influenced by degree of saturation ranging from 0 to 90%. Thus, the OT-SP, SW-SM and MR-SM specimens in this study were tested dry. The MRGM-SC specimens were saturated before testing.

9.1.1.2 Constant volume direct simple shear tests

Constant volume direct simple shear tests on dry specimens are commonly used for replicating undrained tests on saturated specimens because: (1) a shorter time is required; and (2) simpler experimental setup is required for preparing dry specimens. In constant volume simple shear testing, it is assumed that the change in the vertical stress during shear is equivalent to the porewater pressure generation in an undrained test with constant total vertical stress (Bjerrum and Landva 1966; Iversen 1977; Dyvik et al. 1987). For this project, unidirectional (sinusoidal) and bidirectional (circular, figure-8) strain controlled constant volume cyclic simple shear tests were conducted at shear strains of 0.1% to 2%. The OT-SP, SW-SM and MR-SM sands were tested dry, while the MRGM-SC was tested saturated. Fifteen undrained loading cycles were applied to represent an M = 7.5 earthquake (as suggested by Seed et al. 1971).

9.1.2 Recommendations for future work

Future element experimental work on volumetric deformation of sands can include the following.

1. Evaluating the effect of initial static shear due to the presence of a slope or a structure on bidirectional settlement. The initial static shear can be a unidirectional or bidirectional.
2. Extending the bidirectional testing database to loose "liquefiable" sands with relative density less than 50%. Currently there are no drained bidirectional tests available on these loose sands.
3. Systematic inclusion of fines in sand (e.g., 10%, 20%, 30% and so on) to explicitly study the effect of fines content in bidirectional shear. Similarly, varying the plasticity of clayey sands to capture the effect of PI on volumetric compression in bidirectional loading conditions.
4. Conducting tests with shear in all three directions to incorporate the effect of the vertical component of ground motions.

9.2 Dynamic Response from Element Testing of Coarse-grained Soil

9.2.1 Summary and conclusions

To quantify drained volumetric strain under multidirectional loading, the effect of different loading, initial state and soil-related parameters were studied separately. The shear stress – shear strain – volumetric strain response of dry clean sands was observed to be frequency independent for frequencies ranging from 0.1 – 10.0Hz, consistent with Youd (1972) and Duku et al. (2008). The average ratio $\varepsilon_v/\varepsilon_{v,N=15}$ was independent of loading direction (unidirectional and bidirectional), and was similar to ratios obtained by Duku et al. (2008) in unidirectional simple shear tests on 16 sands. Based on these results, we observed that the commonly-used Tokimatsu and Seed (1987) relationship tends to overestimate volumetric strains for more than 25 cycles because the rate of change of volumetric strain with number of cycles decreases too slowly. When this rate of change is extrapolated to a large number of cycles, volumetric strains are overestimated.

To study the effect of shear strain amplitude on soil behavior, unidirectional tests first were conducted with γ_{cs} ranging from 0.30 to 10 %. As the shear strain increases, volumetric strain increases in unidirectional, figure-8 and circular tests. At a given shear strain, volumetric strains were smallest in the unidirectional tests and largest in the figure-8 tests. The multidirectionality factor at a shear strain of 5.5 % approaches unity and bidirectional loading does not have a significant effect on volumetric strain for shear strains exceeding 3.5 %.

The presence of non-plastic fines in the SW-SM (FC = 9 %), in addition to the wider range of particle size with respect to the clean OT-SP, causes the SW-SM to be more contractive at the same relative density. This observation agrees with the findings of Belkhatir et al. (2014) for porewater pressure generation in sands of relative density 20 to 91%. For a sand with D_R = 50%, Singh (1994) also observed that increasing the fines content results in higher positive porewater pressures.

9.2.2 Recommendations for future work

Future work in assessing the dynamic response of dense coarse-grained soil under bidirectional element testing could consider the following.

1. Comparing unidirectional and bidirectional constant volume and truly undrained tests to confirm that these are identical. This work is currently under way.
2. Performing some stress-controlled tests on the same soils to validate the use of parameters such as dissipated energy, rather than a single shear strain or cyclic stress ratio, to estimate shaking-induced volumetric strains.

9.3 Dynamic Centrifuge Testing Database

9.3.1 Summary

Dynamic centrifuge tests were performed to start developing a database for dense sand (Dr_o=95%) under unidirectional and multidirectional earthquake loading. The database includes experiments under free field and near field conditions for profile thicknesses of 20.5 m and 10.25 m. The near field experiment involves a rigid circular structure with a bearing pressure of 380 kPa (20.5 m model) and 190 kPa (10.25 m model). The input motions included historical motions obtained from the PEER and the Chilean strong motion databases. The database also includes dynamic centrifuge tests performed by Montoya (2012) and Adalier (1996) on dense sands (Dro = 70-85 %).

9.3.2 Recommendations for future work

Future dynamic centrifuge testing could consider the following.

1. Expand the database to loose liquefiable sands (e.g., Dro < 50 %) to evaluate shaking-induced volumetric strains across densities. Current work by Kim (2017) will, in part, address this shortcoming.
2. Expand the database by performing centrifuge tests with varying structural properties such as bearing pressure, structure dimensions, and structural stiffness.

9.4 Dynamic Centrifuge Test Soil Response

9.4.1 Summary and conclusions

9.4.1.1 Free-field response

The free-field centrifuge experiments illustrated that dynamic shear response in each orthogonal direction (represented as response spectra) is not affected significantly by multidirectional shaking, as mean residuals computed between 1D and 2D response spectra were less than ±0.125 for periods up to 10 seconds. Also, comparing the recorded response with the shear response computed in a suite of 1D nonlinear total stress site response analyses illustrates that site amplification factors can be estimated reasonably irrespective of multidirectionality (residuals < ~0.25). Site amplification factors computed from the centrifuge tests exhibited considerable scatter, and only marginally agreed with code-based amplification factors. In contrast, energy-based (e.g., Arias and Housner intensities) site amplification factors showed significantly less scatter and more

consistent trends than amplification factors based on spectral accelerations. Centrifuge test multidirectionality factors for both excess PWP and volumetric strains (ε_v) ranged from 1 to 4, and approached unity as the soil approached liquefaction. Therefore, a multidirectional factor of 2 is found to be reasonable for dense saturated sands. Energy-based intensity measures (Arias and Housner intensities) provided nearly unique estimates of excess PWP and ε_v for both 1D and 2D motions, indicating that they capture multi-directionality effects, while vectored peak accelerations and velocities (PGA and PGV) yielded different relationships for 1D and 2D motions.

9.4.1.2 Near field response

The centrifuge near-field models exhibited significant ground motion amplification, non-uniform porewater pressure (PWP) generation, and near-field volumetric strains larger than the corresponding free-field strains. These data were combined with the limited dynamic centrifuge test data on dense sands available in the literature for near-field conditions (e.g., Montoya 2012).

Recorded excess PWP and volumetric strains indicated multi-directionality factors ranging from 1 to 3 for PWP and 1.4 to 6 for volumetric strains with an average of 2.5. In general, only minor differences were observed between 1D and 2D response spectra for the X- and Y-directions, indicating that dynamic shear response in each orthogonal component of dense sands is not significantly affected by multi-directional earthquake loading under near-field conditions. In summary, a new set of data have been developed for dense sand deposits, both under multidirectional earthquake loading and with the presence of a high-bearing pressure structure (i.e., q_b > 350kPa) that will be used for validating advanced numerical models (e.g., I-soil) or development of more simplified approaches.

9.4.2 Recommendations for future work

A multidirectional factor of 2 for volumetric strains estimated from saturated centrifuge tests is reasonable for dense sands and results from this study are consistent with the work by Pyke (1975). However, a wider range of multidirectional factor (up to 6) was found for near-field conditions. Further research could assess ratcheting effects under multidirectional loading and its effects on volumetric strains under 2D loading. Future simplified models could use higher multidirectional factors for volumetric strains when estimating building settlements.

9.5 Development of GQ/H-ε_v Semi-empirical Free-field Model

9.5.1 Summary and conclusions

A semi-empirical hyperbolic model (GQ/H-ε_v) model was developed to estimate shaking-induced volumetric strains on dense sands under cyclic loading. The model uses results from free-field unidirectional (1D) and bidirectional (2D) dynamic centrifuge tests performed on a thick layer (prototype thicknesses of 10.25 and 20.5 m) of saturated dense (relative density, Dro~95%), fine Ottawa sand. The database also includes (1D) centrifuge tests performed by other researchers on dense Ottawa and Nevada sands (Dro~70-85%). The sand centrifuge models were excited using both broadband and sinusoidal motions with Arias intensities that ranged from 0.1 to 30 m/s. The proposed models include various ground motion intensity measures (e.g., PGA, PGV, Arias and Housner intensity) in conjunction with shear wave velocity. To validate the proposed model, the database was compared with estimates of undrained volumetric strain calculated utilizing the most-commonly used reconsolidation volumetric strain methods (Cetin et al., 2009). The implementation of the (GQ/H-ε_v) model can be performed in both a simplified way or by means of a site response analysis (e.g., DEEPSOIL).

Model predictions for the 1D and 2D shaking database shows that, in general, the simplified version of the model gives reasonable results. However, predictions were improved when using the model in conjunction with site response analysis results. Furthermore, the use of velocity-based IMs (HI) in the model equations better predicts observed settlements compared to use of acceleration-based IMs (PGA).

9.5.2 Recommendations for future work

The GQ/H-ε_v model was developed to estimate free-field shaking-induced volumetric strains for dense coarse-grained soils (Dro>70%) that typically undergo small to moderate strains.

Future work on this semi-empirical model is ongoing and could include the following.

1. Expand the database to loose liquefiable sands (e.g., Dro<40%) to be able to estimate shaking-induced volumetric strains across densities. Current work by Kim (2017) and Cerna-Diaz (2017) will incorporate a unified database for loose and dense sands that will be used for the GQ/H-ε_v model. The model will also consider reconsolidation volumetric strains that are more significant for loose liquefiable soils.
2. A simplified near field volumetric model is required to estimate seismic settlements for buildings. The current work by Cerna-Diaz (2017) and Kim (2017) aim to quantify structure settlements via a simplified framework.

9.6 Development of Sand Plasticity Model

9.6.1 Summary and conclusions

Significant research efforts over the last thirty years have attempted to develop constitutive models to describe monotonic and cyclic soil behavior. Multi-yield surface plasticity and bounding surface plasticity models have been proposed to model cyclic soil behavior despite the complex implementation procedures of such models. This study presents a new constitutive model (I-soil) that can be used to model cyclic behavior of sands. The model is capable of capturing: (1) small strain nonlinearity; (2) hysteretic damping; (3) shear-induced volumetric contraction-dilation; and (4) modulus degradation due to excess porewater pressure generation. The model is implemented in LS-DYNA and is capable of simulating 3D geotechnical earthquake engineering problems.

9.6.2 Recommendations for future work

I-soil is capable of simulating the dynamic response of medium dense to dense coarse-grained soils at small to moderate strains. The model is an effective stress model and can be utilized to estimate deformation characteristics of soils under cyclic loading. The model can be coupled with fluid to estimate the excess porewater pressure generation and dissipation characteristics under dynamic loadings. Although the model is very efficient to simulate the behavior of medium dense to dense coarse-grained soil at small to moderate strain, to apply it to medium to loose coarse-grained soils in large-strain problems, the following capabilities should be added.

1. Moderate cyclic shear strains may cause coarse-grained soils to undergo cyclic mobility. Such problems occur incrementally and have a significant effect on the shear stress – shear strain – volumetric strain soil behavior. Cyclic mobility can cause large permanent deformations even though the soil is not liquefied. Incremental and cumulative changes in soil fabric are not incorporated in I-soil. Thus, the model should be used with caution in problems related to lateral spreading. Current work by Numanoglu (2017) focuses on extending the model to cyclic mobility problems.

2. Liquefaction-related phenomena cause significant instabilities in coarse-grained soils. The problem is large strain in nature and has multiple consequences (e.g., flow liquefaction failure, post-liquefaction reconsolidation strains). The current version of I-soil should be used with caution for simulating sand behavior during or after liquefaction. Current work by Numanoglu (2017) also focuses on addressing this limitation.

9.7 Simulations of Bidirectional Dynamic Centrifuge Tests

9.7.1 Summary and conclusions

The effects of multidirectional earthquake loading can be incorporated in simulations by utilizing 3D numerical models. This report presents numerical methods, issues and procedures to model wave propagation through free-field and soil-structure systems within the finite element method. The details of the numerical modeling procedure demonstrated in this report include the following.

1. A shear beam approach is demonstrated and used to simplify free-field problems where the ground is level or slightly sloping. This simplification greatly reduces the degrees of freedom and run times.
2. LS-DYNA, a dynamic explicit finite element analysis software, was used to simulate SSI problems using the direct method where the soil and structure are modeled together. The stiffness of structural component material (steel) is significantly larger than soil and the deformation modes of the structure are not significant (e.g., solid box type structural component). Thus, the structural component is assumed to be rigid to reduce the run times. The run times decreased because the time step in an explicit analysis is controlled by the stiffer element in the numerical model.
3. Input motions applied at the base of the numerical model were 'within' motions that were obtained from near the bottom of the centrifuge soil model. Since the motion is within, rigid base conditions were applied.

3D numerical modeling procedures were followed by simulations of bidirectional dynamic centrifuge tests of free-field and soil-structure system. The details of the finite element simulations included the following.

1. The modeled soil domain is saturated with soil free to drain. Solid-fluid coupling capability of LS-DYNA was used to evaluate excess porewater pressure generation and dissipation characteristics. The water table was defined at the foundation base elevation to prevent near-surface numerical instabilities.
2. I-soil was used to characterize the effective stress-strain behavior of the soil.
3. A 20 m soil profile (corresponding to 60g centrifuge tests) was modeled. The mesh of the numerical model consisted of constant stress (single integration point) elements with hourglass controlling options suggested by LS-DYNA.
4. The backbone curves used as an input in I-soil and were obtained using the shear wave velocity profile of Menq (2003), normalized modulus reduction curves of Darendeli (2001), and shear strength mobilized at large strains obtained from Bolton (1986).

A systematic set of analyses were conducted starting from 1D nonlinear site response analyses towards SSI simulations. The details about the inputs and findings related to a particular set of analyses are as follows.

1. DEEPSOIL was used to conduct 1D nonlinear effective stress site response analyses (with no porewater pressure generation/dissipation). Each component of bidirectional input motions was simulated separately. The GQ/H model was used to characterize the 1D shear

stress-strain behavior. The simulations showed that the 1D nonlinear site response analysis is capable of capturing the behavior related to simulated component.

2. Free-field analyses were simplified to a shear beam approach and bidirectional simulations were conducted using LS-DYNA. The input motions were applied simultaneously and I-soil was used to simulate constitutive behavior. Input parameters for I-soil are obtained from the parameters used in 1D nonlinear site response analysis as well as laboratory tests. The simulations reasonably estimated both shear and volumetric behavior for most of the cases. Some discrepancies were observed in terms of settlements for the first and last shaking events (M10 and M5). Settlements in motion M10 were overestimated, which is attributed to M10 being the first shaking event that induced larger settlements than the other motions. The computed settlements for motion M5 overestimated measured settlements because motion M5 was the last shaking event after significant densification had occurred (and was not simulated). However, in average, measured and computed response are in good agreement.
3. SSI analyses were conducted using the direct method where the soil and structure were modeled together. Sliding and gapping between soil and structure were not modeled explicitly. This assumption is valid for base sliding because no sliding was observed in centrifuge tests. In addition, an analysis conducted considering the sliding of the base did not affect the results compared to the simulations where no sliding was allowed.
4. SSI analyses captured the shear behavior observed in the dynamic centrifuge tests. Volumetric behavior in terms of excess pore pressures were captured reasonably well. The settlements under the structure were also captured reasonably well. However, it was observed that the near-field settlements were significantly overestimated, potentially because of localization of settlements under the structure. Further study is ongoing on this issue.

9.7.2 Recommendations for future work

The I-soil model, overall, captured the behavior observed in the dynamic centrifuge tests conducted in free-field and SSI conditions. Some particular behavior observed in the centrifuge tests were not properly captured by the model due to: (1) experimental setup and procedures; and (2) numerical and constitutive model assumptions and simplifications. Recommendations to improve the simulation performance include the following.

1. Incorporation of volumetric behavior in 1D nonlinear site response analysis via simplified algorithms.
2. Incorporation of sequential simulation dependent soil profiles whereby the input parameters are updated based on soil densification and fabric change observed in the centrifuge tests.
3. Incorporation of sliding and gapping between soil-structure to capture the potential effects of rocking and ratcheting of the structural component.

Numanoglu (2017) focuses on the first two items presented above and item 3 is under consideration.

10 REFERENCES

[1] Abdoun, T., Gonzalez, M. A., Thevanayagam, S., Dobry, R., Elgamal, A., Zeghal, M., Mercado, V. M., and El Shamy, U. (2013). “Centrifuge and Large Scale Modeling of Seismic Pore Pressures in Sands: a Cyclic Strain Interpretation”. J. of Geotechnical and Geoenvironmental Engineering, ASCE, 139(8), 1215-1234.

[2] Adalier, K. (1996). “Mitigation of Earthquake Induced Liquefaction Hazards”. Doctoral dissertation, Rensselaer Polytechnic Institute, Troy, New York.

[3] Amini, F., and Qi, G. Z. (2000). “Liquefaction testing of stratified silty sands.” J. Geotech. Geoenviron. Engr., 126(3), 208-217.

[4] Ancheta T.D., Darragh R.B., Stewart J.P., Seyhan E., Silva W.J., Chiou B.S.-J., Wooddell K.E., Graves R.W., Kottke A.R., Boore D.M., Kishida T., Donahue J.L. (2013). “PEER NGAWest2 database”, PEER Report No. 2013/03, Pacific Earthquake Engineering Research Center, University of California, Berkeley, CA

[5] Andrus, D.A., P. Piratheepan, B.S. Ellis, J. Zhang, and C.H. Juang. (2004). “Comparing liquefaction evaluation methods using penetration-Vs relationships.” *Soil Dynamics Earthquake Engr.*, 24 (9-10), 713-721.

[6] Arias, A. (1970). “A measure of earthquake intensity”. Seismic Design for Nuclear Power Plants, MIT Press, Cambridge, Massachusetts, pp. 438-483.

[7] Armstrong, R. J., and Boulanger, R. W. (2015). “Numerical Simulations of Liquefaction Effects on Piled Bridge Abutments”.

[8] Armstrong, R. J., Boulanger, R. W., and Beaty, M. H. (2012). “Liquefaction effects on piled bridge abutments: Centrifuge tests and numerical analyses”. J. of Geotechnical and Geoenvironmental Engineering, 139(3), 433-443.

[9] Assimaki, D., and Kausel, E. (2002). “An equivalent linear algorithm with frequency-and pressure-dependent moduli and damping for the seismic analysis of deep sites”. Soil Dynamics and Earthquake Engineering, 22(9), 959-965.

[10] Assimaki, D., Kausel, E., and Whittle, A. (2000). “Model for dynamic shear modulus and damping for granular soils”. J. of Geotechnical and Geoenvironmental Engineering, 126(10), 859-869.

[11] ASTM, Standard D1557 (2001). “Standard test methods for laboratory compaction characteristics of soil using modified effort”. Annual book of ASTM standards, 4(8), ASTM International, West Conshohocken, PA.

[12] ASTM, Standard D4254 (2000). “Standard test methods for minimum index density and unit weights of soils and calculation of relative density”. Annual book of ASTM standards, 4(8), ASTM International, West Conshohocken, PA.

[13] ASTM, Standard D854 (2000). “Standard test method for specific gravity of soil solids by water Pycnometer”, Annual book of ASTM standards, 4(8), ASTM International, West Conshohocken, PA.

[14] Baltaji, O., Numanoglu, O. A., Veeraraghavan, S., Hashash, Y. M., Coleman, J. L., & Bolisetti, C. NON-LINEAR TIME DOMAIN SITE RESPONSE AND SOIL STRUCTURE ANALYSES FOR NUCLEAR FACILITIES USING MASTODON.

[15] Been, K., and Jefferies, M. G. (1985). A state parameter for sands. *Géotechnique*, *35*(2), 99-112.

[16] Bhaumik, L. (2017). PhD thesis in progress, University of Illinois at Urbana-Champaign.

[17] Bhaumik, L., Rutherford, C.J.R., Cerna-Diaz, A., Olson, S. M., Numanoglu, O. A., Hashash, Y.M.A., and Weaver, T. (2017). “Volumetric strain in non-plastic silty sand subjected to multidirectional cyclic loading”. *Proc. Geotech. Frontiers*, Orlando, Florida.

[18] Bolton, M. D. (1986). “Strength and dilatancy of sands” *Geotechnique*, 36(1): 65-78.

[19]Boroschek R., Soto P., Leon R., (2010). “RENADIC Report 10/08 Rev.2, 2010/10”, Faculty of Mathematics and Physical Sciences – Civil Engineering Department, University of Chile, Santiago, Chile
[20]Boulanger, R. W. (2003). Relating K α to relative state parameter index. *J. of geotechnical and geoenvironmental engineering*, *129*(8), 770-773.
[21]Boulanger, R. W., and Ziotopoulou, K. (2012). “PM4Sand (Version 2): a sand plasticity model for earthquake engineering applications”. Department of Civil and Environmental Engineering, University of California at Davis.
[22]Boulanger, R. W., Montgomery, J., and Ziotopoulou, K. (2015). Nonlinear deformation analyses of liquefaction effects on embankment dams. In *Perspectives on Earthquake Geotechnical Engineering* (pp. 247-283). Springer International Publishing. Boulanger, R., Chan, C., Seed, H., Seed, R., and Sousa, J. (1993). "A Low-Compliance Bi-Directional Cyclic Simple Shear Apparatus," *Geotech. Testing J.*, 16, (1), 36-45, https://doi.org/ 10.1520/GTJ10265J. ISSN 0149-6115.
[23]Boulanger, R., Chan, C., Seed, H., Seed, R., and Sousa, J. (1993). "A Low-Compliance Bi-Directional Cyclic Simple Shear Apparatus," *Geotech. Testing J.*, 16, (1), 36-45, https://doi.org/ 10.1520/GTJ10265J. ISSN 0149-6115.
[24]Burland, J. B. and M. A. Burbidge (1985). "Settlement of Foundations on Sand and Gravel," Proceedings of Institute of Civil Engineering and Ground Engineering Group, Part I, Dec., 1325-1381.
[25]Byrne, P. (1991). “A cyclic shear-volume coupling and pore pressure model for sand.” *Proc., 2nd Int. Conf. Recent Advances Geotech. Earthquake Engr. Soil Dynamics*, Missouri Univ. of Science and Technology, Rolla, Missouri, 47–55.
[26]Byrne, P. M., S. S. Park, M. Beaty, M. Sharp, L. Gonzales and T. Abdoun (2004). “Numerical modeling of liquefaction and comparison with centrifuge tests”.Canadian Geotechnical J., 41(2): 193-211.
[27]CEES-RPI (2016). “2D Laminar Box”. < http://www.nees.rpi.edu/equipment/laminar-boxes/> (Dec. 5, 2016).
[28]Cerna-Diaz, A., Olson, S. M., Numanoglu, O. A., Hashash, Y.M.A., Bhaumik, L., Rutherford, C.J.R., and Weaver, T. (2017). “Free-field cyclic response of dense sands in dynamic centrifuge tests with 1D and 2D shakings”. Proceedings of GeoFrontiers.
[29]Cerna-Diaz, A.A. (2017). PhD thesis in progress, University of Illinois at Urbana-Champaign.
[30]Cetin, K. O., Bilge, H. T., Wu, J., Kammerer, A. M., and Seed, R. B. (2009). “Probabilistic model for the assessment of cyclically induced reconsolidation (volumetric) settlements.” *J. Geotech. Geoenviron. Engr.*, 135(3), 387-398.
[31]Cetin, K. O., Seed, R. B., Der Kiureghian, A., Tokimatsu, K., Harder, L. F., Jr., Kayen, R. E., and Moss, R. E. S. (2004). “SPT-based probabilistic and deterministic assessment of seismic soil liquefaction potential.” *J. Geotech. Geoenviron. Eng.*, 130(12), 1314–1340.
[32]Chang, C. Y., and Duncan, J. M. (1970). “Analysis of soil movement around a deep excavation”. J. of Soil Mechanics and Foundations Div.
[33]Chiang, D. Y., and Beck, J. L. (1994). “A new class of distributed-element models for cyclic plasticity—I. Theory and application”. International J. of solids and structures, 31(4), 469-484.
[34]Choi, C., P. Arduino and M. D. Harney (2005). “Two-surface soil constitutive model calibration for coarse granular materials”. Geo-Frontiers Congress 2005, Austin,Texas, United States, American Society of Civil Engineers.
[35]Coleman, J., Slaughter, A., Veeraraghavan, S., Bolisetti, C., Numanoglu, O. A., Spears, R., ... & Hurt, E. (2017). *MASTODON Theory Manual* (No. INL/EXT-17-41930). Idaho National Laboratory, Idaho Falls, ID (United States).
[36]Dafalias, Y. F. and M. T. Manzari (2004). “Simple plasticity sand model accounting for fabric change effects”. J. of Engineering Mechanics, 130(Special Issue: Constitutive Modeling of Geomaterials).

[37]Dafalias, Y. F., and Popov, E. P. (1975). “A model of nonlinearly hardening materials for complex loading”. Acta mechanica, 21(3), 173-192.
[38]Dafalias, Y. F., and Taiebat, M. (2016). “SANISAND-Z: zero elastic range sand plasticity model”. Géotechnique, 66(12), 999-1013.
[39]Daftari, A., and Kudla, W. (2014). “Prediction of Soil Liquefaction by Using UBC3D-PLM Model in PLAXIS”. International J. of Environmental, Ecological, Geological and Mining Engineering.
[40]Darendeli, M. B. (2001). “Development of a new family of normalized modulus reduction and material damping curves”. Ph. D., University of Texas at Austin.
[41]Davis, R. O., and Selvadurai, A. P. S. (2002). “Plasticity and Geomechanics”, 287 pp., doi: 10.1017/CBO9780511614958.
[42]De Alba, P., Chan, C. K., and Seed, H. B. (1975). " Determination of soil liquefaction characteristics by large-scale laboratory tests." Earthquake Engineering Research Center, University of California, Berkeley, Report No. EERC 75-14.
[43]DeGroot, D., Germaine, J., and Ladd, C. (1993). "The Multidirectional Direct Simple Shear Apparatus." *Geotech. Testing J.*, 16(3), 283-295, https://doi.org/10.1520/GTJ10049J. ISSN 0149-6115.
[44]Dobry, R., Ladd, R. S., Yokel, F. Y., Chung, R. M., and Powell, D. (1982). “Prediction of pore water pressure buildup and liquefaction of sands during earthquakes by the cyclic strain method”, National Bureau of Standards 138, Gaithersburg, MD.
[45]Dobry, R., Yokel, F. Y., and Ladd, R. S. (1981). “Liquefaction potential of over-consolidated sands in moderately seismic areas.” In *Proc. Conference Earthquakes and Earthquake Engr. in Eastern US*, 2, 643-64.
[46]Drucker, D. C. (1957). “A definition of stable inelastic material (No. TR-2)”. BROWN UNIV PROVIDENCE RI.
[47]Drucker, D. C., and Prager, W. (1952). “Soil mechanics and plastic analysis or limit design”. Quarterly of applied mathematics, 10(2), 157-165.
[48]Duku, P. M., Stewart, J. P., and Whang, D. H. (2006). “Effect of post compaction ageing on seismic compression of fine-grained soils.” *Geotech. Special Pub. 152: Ground Modification and Seismic Mitigation*, ASCE, 152, 411.
[49]Duku, P. M., Stewart, J. P., Whang, D. H., and Yee, E. (2008). “Volumetric strains of clean sands subject to cyclic loads.” *J. Geotech. Geoenviron. Eng.*, 134(8), 1073-1085.
[50]Duncan, J. M., G. W. Williams, A. L. Sehn, and Raymond B. Seed. (1991). "Estimation earth pressures due to compaction." *J. Geotech. Engr.*, 117(12), 1833-1847.
[51]Einav, I., and Collins, I. (2008). “A thermomechanical framework of plasticity based on probabilistic micromechanics”. J. of Mechanics of Materials and Structures, 3(5), 867-892.
[52]Elgamal, A., L. Yan, Z. Yang and J. P. Conte (2008). “Three dimensional seismic response of Humboldt Bay bridge-foundation-ground system”. J. of Structural Engineering, 134(7): 1165-1176.
[53]Elgamal, A., Yang, Z., Parra, E., and Ragheb, A. (2003). “Modeling of cyclic mobility in saturated cohesionless soils”. International J. of Plasticity, 19(6), 883-905.
[54]Elgamal, A., Z. Yang and E. Parra (2002). “Computational modeling of cyclic mobility and post-liquefaction site response”. Soil Dynamics and Earthquake Engineering, 22(4): 259-271.
[55]Elgamal, A., Z. Yang, T. Lai, B. Kutter and D. Wilson (2005). “Dynamic response of saturated dense sand in laminated centrifuge container”. J. of Geotechnical and Geoenvironmental Engineering, 131(5): 598-609.
[56]Franke, E., Kiekbusch, M., and Schuppener, B. (1979). “A new direct simple shear device.” *Geotech. Testing J.*, 2(4), 190-199.
[57]Fukutake, K. and Matsuoka, H. (1989). “A unified law for dilatancy under multi-directional simple shearing.” *J. of JSCE Div. C*, (412), 143–151(In Japanese).
[58]Gazetas, G. (1987). “Seismic response of earth dams: some recent developments”. Soil dynamics and earthquake engineering, 6(1), 2-47.

[59]Ghayoomi, M., Ko, H.-Y., and McCartney, J. S. (2011). “Measurement of seismically induced settlement in unsaturated sands.” ASTM Geotech. Test. J., 34(4), 1–11.
[60]Ghayoomi, M., McCartney, J. S., and Ko, H. Y. (2012). “Empirical methodology to estimate seismically induced settlement of partially saturated sand.” *J. of Geotechnical and Geoenvironmental Engineering*, 139(3), 367-376.
[61]Ghofrani, A., and Arduino, P. (2017). “Prediction of LEAP centrifuge test results using a pressure-dependent bounding surface constitutive model”. Soil Dynamics and Earthquake Engineering.
[62]Groholski, D. R., Hashash, Y. M., Kim, B., Musgrove, M., Harmon, J., and Stewart, J. P. (2016). “Simplified Model for Small-Strain Nonlinearity and Strength in 1D Seismic Site Response Analysis”. J. of Geotechnical and Geoenvironmental Engineering, 04016042.
[63]Gutierrez, M., Wang, J., and Yoshimine, M. (2009). “Modeling of the simple shear deformation of sand: effects of principal stress rotation”. Acta Geotechnica, 4(3), 193-201.
[64]Hardin, B. O., and Drnevich, V. P. (1972). “Shear modulus and damping in soils: Design equations and curves.” J. Soil Mech. Found., 98(7), 667–692.
[65]Hardin, B. O., and Richart, F. E. (1963). “Elastic wave velocities in granular soils.” J. Soil Mech. Found., 89(1), 33–65.
[66]Hashash, Y. M. A., C. Phillips and D. R. Groholski (2010). “Recent advances in non-linear site response analysis”. Fifth International Conference in Recent Advances in Geotechnical Eartqhuake Engineering and Soil Dynamics. San Diego, CA. CD-Volume: OSP 4.
[67]Hashash, Y. M. A., M. I. Musgrove, J. A. Harmon, D. R. Groholski, C. A. Phillips and D. Park (2016). DEEPSOIL 6.1, User Manual: 114.
[68]Hashash, Y. M., and Park, D. (2001). “Non-linear one-dimensional seismic ground motion propagation in the Mississippi embayment”. Engineering Geology, 62(1), 185-206.
[69]Housner, GW (1952). “Intensity of ground motion during strong earthquakes”. Second technical report. August 1952, California Institute of Technology, Pasedena, California.
[70]Hsu, C.-C., and Vucetic, M. (2004). “Volumetric threshold shear strain for cyclic settlement.” *J. Geotech. Geoenviron. Engr.*, ASCE, 130(1), 58-70.
[71]Hughes, T. J. R., and Simo, J. C. (1998). “Computational inelasticity”. New York.
[72]Ishihara, K. and M. Yoshimine (1992). “Evaluation of settlements in sand deposits following liquefaction during earthquakes.” *Soils Found.*, 32(1), 173-188.
[73]Ishihara, K. and Yamazaki, F. (1980). “Cyclic simple shear tests on saturated sand in multi-directional loading.” *Soils Found.*, 20(1), 45-59.
[74]Itasca. 2009. Dynamic Analysis, FLAC3D Fast Lagrangian Analysis of Continua in 3 Dimensions. Itasca Consulting Group, Minneapolis, Minn
[75]Iwan, W. D. (1966). “A distributed-element model for hysteresis and its steady-state dynamic response”. ASME.
[76]Iwan, W. D. (1967). “On a Class of Models for the Yielding Behavior of Continuous and Composite Systems”. J. of Applied Mechanics, 34(3): 612-617.
[77]Iwasaki, T., Arakawa, T., and Tokida, K. (1982). “Standard penetration test and liquefaction potential evaluation.” Proc., Int. Conf. of Soil Dynamics and Earthquake Engineering, Vol. 2, 925–941.
[78]Iwasaki, T., Tatsuoka, F., and Takagi, Y. (1978). "Shear modulus of sands under cyclic torsional shear loading." *Soils Found.,* 18(1), 39-50.
[79]Jaky, J. (1948). “Pressure in silos.” *Proc. 2nd Int. Conf. Soil Mech.*, Vol. 1, 103-107.
[80]Jefferies, M. G. (1993). “Nor-Sand: a simple critical state model for sand”. Geotechnique, 43(1), 91-103.
[81]Jefferies, M., Shuttle, D., and Been, K. (2015). Principal stress rotation as cause of cyclic mobility. Geotechnical Research, 2(2), 66-96.
[82]Kammerer, A. (2002). "Undrained Response of Monterey 0/30 Sand Under Multidirectional Cyclic Simple Shear Loading Conditions." Ph.D. Dissertation, University of California, Berkeley.

[83]Kammerer, A. M., Seed, R.B., Wu J., Riemer M. F., and Pestana J. M. (2004). “Pore Pressure Development in Liquefiable Soils Under Bi-Directional Loading Conditions”, Proceedings, 11th Int. Conf. on Soil Dynamics and Earthquake Engineering and 3rd Intl. Conf. On Earthquake Geotechnical Engineering, Vol.2 P.697.
[84]Karimi, Z., and Dashti, S. (2015). “Numerical and centrifuge modeling of seismic soil–foundation–structure interaction on liquefiable ground”. J. of Geotechnical and Geoenvironmental Engineering, 142(1), 04015061.
[85]Kim, J.H. (2017). “Prediction of earthquake-induced free-field and shallow foundation settlement on saturated, coarse grained soils using centrifuge and shaking table tests analysis.” PhD Dissertation, Univ. of Illinois at Urbana-Champaign.
[86]Kondner, R. L., and Zelasko, J. S. (1963). “Proceedings of the 2nd Panamerican Conference on Soil Mechanics and Foundations Engineering”.
[87]Kramer S. L. (1996). *Geotechnical Earthquake Engineering*, Prentice Hall, Englewood Cliffs, N.J., 653.
[88]Kramer, S. L., and Paulsen, S. B. (2004). “Practical use of geotechnical site response models”. In Proc. Int. Workshop on Uncertainties in Nonlinear Soil Properties and their Impact on Modeling Dynamic Soil Response (p. 10). Berkeley: Univ. of California.
[89]Krieg, R. D. (1975). “A practical two surface plasticity theory”. J. of applied mechanics, 42(3), 641-646.
[90]Kutter, B. L., Carey, T. J., Hashimoto, T., Zeghal, M., Abdoun, T., Kokkali, P., ... and Hung, W. Y. (2017). LEAP-GWU-2015 experiment specifications, results, and comparisons. *Soil Dynamics and Earthquake Engineering*.
[91]Ladd, R. S. (1974). “Specimen Preparation and Liquefaction of Sands,” *J. Soil Mech. Found. Div.*, 100(10), 1180–1184.
[92]Lai, T., A. Elgamal, Z. Yang, D. W. Wilson and B. L. Kutter (2004). “Numerical modeling of dynamic centrifuge experiments on a saturated dense stratum”. 11th Int. Conference on Soil Dynamics and Earthquake Engineering and 3rd Int. Conference on Earthquake Geotechnical Engineering. University of California, Berkeley.
[93]Lasley, S. J. (2015). “Application of fatigue theories to seismic compression estimation and the evaluation of liquefaction potential.” Ph.D. Dissertation, Virginia Tech, Blacksburg, VA.
[94]Lasley, S., Green, R., Chen, Q., and Rodriguez-Marek, A. (2016). "Approach for Estimating Seismic Compression Using Site Response Analyses." *J. Geotech. Geoenviron. Eng.*, 10.1061/(ASCE)GT. 1943-5606.0001478, 04016015.
[95]Lee, K. L., and A. Albaisa (1974). "Earthquake induced settlements in saturated sands." Journal of Geotechnical Engineering, ASCE, 100(4), 387-406.
[96]Liquefaction Effects on Embankment Dams”. In Perspectives on Earthquake Geotechnical Engineering (pp. 247-283). Springer International Publishing.
[97]Loudon, A. G. (1952). “The computation of permeability from simple soil tests”. Geotechnique, 3(4), 165-183.
[98]LSTC (2009). “LS DYNA Keyword User's Manual” - Release 971 R4. L. Corporation. Livermore, California.
[99]Lu, N., Godt, J. W., and Wu, D. T. (2010). “A closed form equation for effective stress in unsaturated soil.” Water Resources Res., 46, W05515.
[100] Manzari, M. T., and Dafalias, Y. F. (1997). “A critical state two-surface plasticity model for sands”. Geotechnique, 47(2), 255-272.
[101] Martin, G. R., Finn, W. D. L., and Seed, H. B. (1975). “Fundamentals of liquefaction under cyclic loading.” *J. Geotech. Eng. Div.*, 101(5), 423–438.
[102] Masing G. Eignespannungen und verfestigung beim messing. In: Second International Congress on Applied Mechanics, Zurich, Switzerland, 1926, pp. 332–335
[103] Matasovic, N. (1993). “Seismic response of composite horizontally-layered soil deposits” (Doctoral dissertation, UCLA).

[104] Matasovic, N. (2006). D-MOD_2: a computer program for seismic response analysis of horizontally layered soil deposits, earthfill dams, and solid waste landfills. *Users's manual. GeoMotions, LLC*.
[105] Matasović, N., and Vucetic, M. (1993). Cyclic characterization of liquefiable sands. *J. of Geotechnical Engineering*, *119*(11), 1805-1822.
[106] Matsuda, H., Hendrawan, A. P., Ishikura, R., and Kawahara, S. (2011). "Effective stress change and post-earthquake settlement properties of granular materials subjected to multi-directional cyclic simple shear." *Soils Found.*, 51(5), 873–884.
[107] Mayne, P. W., and Kulhawy, F. H. (1982). "Ko-OCR Relationships in Soil." *J. Soil Mech. Found. Div.*, 108(6), 851-872.
[108] Mayne, P.W., B. Christopher, R. Berg, and J. DeJong. (2002). *Subsurface investigations – geotechnical site characterization*, FHWA-NHI-01-031, FHWA, Washington, D.C., 301 pages.
[109] Mazzoni, S., McKenna, F., Scott, M. H., and Fenves, G. L. (2006). The Open System for Earthquake Engineering Simulation (OpenSEES) User Command-Language Manual.
[110] Mei, X. (2017). "Porewater pressure generation and liquefaction analysis using nonlinear, effective stress-based site response analysis." PhD Dissertation, Univ. of Illinois at Urbana-Champaign.
[111] Mei, X., Olson, S.M., and Hashash, Y.M.A. (2017)." Empirical porewater pressure generation model parameters in 1-D seismic site response analysis." Soil Dynamics Earthquake Engineering, *In review*.
[112] Menq, F. Y. (2003). "Dynamic Properties of Sandy and Gravelly Soils" Ph.D, University of Texas at Austin.
[113] Mesri, G. (1973). "One-dimensional consolidation of a clay layer with impeded drainage boundaries," American Geophysical Union, Water Resources Research, 9(4), 1090-1093.
[114] Mojtaba, E. K., and Taiebat, H. A. (2014). On implementation of bounding surface plasticity models with no overshooting effect in solving boundary value problems. *Computers and Geotechnics*, *55*, 103-116.
[115] Montoya, B. M. (2012). "Bio-mediated soil improvement and the effect of cementation on the behavior, improvement", and performance of sand. Doctoral dissertation, University of California, Davis, CA, USA
[116] Mroz, Z. (1967). "On the description of anisotropic work hardening". J. of the Mechanics and Physics of Solids, 15(3), 163-175.
[117] Mulilis, J. P., Arulanandan, K., Mitchell, J. K., Chan, C. K., and Seed, H. B., (1977). "Effects of Sample Preparation on Sand Liquefaction," *J. Geotech. Engr. Div.*, 103(2), 91–108.
[118] Nagase, H., and Ishihara, K. (1988). "Liquefaction-induced compaction and settlement of sand during earthquakes." *Soils Found.*, 28(1), 65-76.
[119] NEHRP (2009) "Recommended Seismic Provisions for Seismic Regulations for New Buildings and Other Structures." FEMA 2009 Edition.
[120] Nemat-Nasser, S., and Tobita, Y. (1982). "Influence of fabric on liquefaction and densification potential of cohesionless sand". Mechanics of Materials, 1(1), 43-62.
[121] Numanoglu, O.A. (2017). PhD thesis in progress, University of Illinois at Urbana-Champaign.
[122] Numanoglu, O. A., Musgrove, M., Harmon, J. A., & Hashash, Y. M. (2017). Generalized Non-Masing Hysteresis Model for Cyclic Loading. *Journal of Geotechnical and Geoenvironmental Engineering*, *144*(1), 06017015.
[123] Numanoglu, O. A., Hashash, Y. M., Cerna-Diaz, A., Olson, S. M., Bhaumik, L., Rutherford, C. J., & Weaver, T. Nonlinear 3-D Modeling of Dense Sand and the Simulation of a Soil-Structure System under Multi-Directional Loading. In *Geotechnical Frontiers 2017* (pp. 379-388).
[124] Oda, M., (1972). "Initial Fabric and Their Relations to Mechanical Properties of Granular Material," *Soils Found.*, 12(1), 17–36.

[125] Ohta, Y., and N. Goto (1978). “Empirical shear wave velocity equations in terms of characteristic soil indexes,” Earthquake Engineering and Structural Dynamics, Vol. 6, pp. 167-187.
[126] Olson, S. M., Hashash, Y. M. A., Rutherford, C. J., Cerna-Diaz, A., Numanoglu, O. A., Bhaumik, L., and Weaver, T. (2015). “Experimental and Numerical Investigation of Cyclic Response of Dense Sand under Multidirectional Shaking.” *Proc., 6th Int. Conf. on Earthquake Geotech. Eng.*, Christchurch, New Zealand.
[127] Parra-Colmenares, E. J. (1996). “Numerical modeling of liquefaction and lateral ground deformation including cyclic mobility and dilation response in soil systems” (Doctoral dissertation, [Sl: sn]).
[128] Pestana, J. M. (1994). “A unified constitutive model for clays and sands”, Doctoral dissertation, Massachusetts Institute of Technology.
[129] Pestana, J. M., Whittle, A. J., and Salvati, L. A. (2002). “Evaluation of a constitutive model for clays and sands: Part I–sand behavior”. International J. for numerical and analytical methods in geomechanics, 26(11), 1097-1121.
[130] Phillips, C. and Y. M. A. Hashash (2009). “Damping formulation for non-linear 1D site response analyses”. Soil Dynamics and Earthquake Engineering, 29(7): Pages 1143-1158.
[131] Pradel, D. (1998). “Procedure to evaluate earthquake-induced settlements in dry sandy soils.” *J. Geotech. Geoenviron. Eng*., 124(4), 364-368.
[132] Prager, W. (1955). “The theory of plasticity: a survey of recent achievements”. Proceedings of the Institution of Mechanical Engineers, 169(1), 41-57.
[133] Prevost, J. H. (1978). “Plasticity theory for soil stress-strain behavior”. J. of the Engineering Mechanics Division, 104(5), 1177-1194.
[134] Prevost, J. H. (1985). “A simple plasticity theory for frictional cohesionless soils”. International J. of Soil Dynamics and Earthquake Engineering, 4(1), 9-17.
[135] Puebla, H., Byrne, P. M., and Phillips, R. (1997). “Analysis of CANLEX liquefaction embankments: prototype and centrifuge models”. Canadian Geotechnical J., 34(5), 641-657.
[136] Pyke, R., Seed, H. B., and Chan, C. K. (1975). “Settlement of sands under multidirectional shaking.” *J. Geotech. Engr. Div*., 101(4), 379-398.
[137] Randolph, M. F. and Wroth, C. P. (1981). “Application of the failure state in undrained simple shear to the shaft capacity of driven piles.” *Geotechnique*, 31(1), 143-157.
[138] Richard, R. E., Woods, R. D. and Hall, J. R. H. (1970). “Vibrations of Soils and Foundations”, Prentice-Hall, N.J.
[139] Richart, F. E. and Newmark, N. M. (1948). “A hypothesis for determination of cumulative damage in fatigue,” *ASTM Proc.*, 48: 767-800.
[140] Robertson, P.K., and Wride (Fear), C.E. 1998. Evaluating cyclic liquefaction potential using the cone penetration test. Canadian Geotechnical Journal, 35(3): 442–459.
[141] Roscoe, K. H., Schofield, A., and Thurairajah, A. (1963). “Yielding of clays in states wetter than critical”. Geotechnique, 13(3), 211-240.
[142] Roscoe, K. H., Schofield, A., and Wroth, C. P. (1958). “On the yielding of soils”. Geotechnique, 8(1), 22-53.
[143] Roscoe, K., and Burland, J. B. (1968). “On the generalized stress-strain behaviour of wet clay”.
[144] Rowe, P. W. (1962, October). “The stress-dilatancy relation for static equilibrium of an assembly of particles” in contact. In Proceedings of the royal society of London a: mathematical, physical and engineering sciences (Vol. 269, No. 1339, pp. 500-527). The Royal Society.
[145] Rudolph, C., Grabe, J., and Albrecht, I. (2014). “Simple shear tests with a varying shearing direction during cyclic shearing.” *Géotechnique Letters*, 4(2), 102-107.
[146] Rutherford, C. J. (2012). “Development of a multi-directional simple shear testing device for characterization of the cyclic shear response of marine clay." Ph.D. Dissertation, Texas AandM University.

[147] Sadrekarimi, A. and Olson, S. M. (2012). "Effect of Sample-Preparation Method on Critical-State Behavior of Sands," *Geotech. Testing J.*, 35(4), 548-562, https://doi.org/10.1520/GTJ104317. ISSN 0149-6115.
[148] Schofield, A., and Wroth, P. (1968). Critical state soil mechanics.
[149] Seed, H. B., and Idriss, I. M. (1971). "Simplified procedure for evaluating soil liquefaction potential." *J. Soil Mech. Found. Div.*, 97(9), 1249-1273.
[150] Seed, H. B., and Lee, K. L. (1965). "Studies of liquefaction of sands under cyclic loading conditions." Rep. TE-65-65, Dept. of Civil Engineering, Univ. of California, Berkeley, CA.
[151] Seed, H. B., and Silver, M. L. (1972). "Settlement of dry sands during earthquakes." *J. Soil Mech. Found. Div*., 98(SM4), 381-397.
[152] Seed, H. B., Mori, K., and Chan, C.K. (1977). "Influence of Seismic History on Liquefaction of Sands," *J. Geotech. Engr. Div.*, ASCE, 103(4), 257-270.
[153] Seed, H. B., Pyke, R. M., and Martin, G. R. (1978). "Effect of multi-directional shaking on pore-pressure development in sands". J. Geotechnical Engineering Division, ASCE, 104(GT1), 27-44.
[154] Seed, R. B., Cetin, K. O., Moss, R. E. S., Kammerer, A. M., Wu, J., Pestana, J. M., and Riemer, M. F. (2001). "Recent Advances in Soil Liquefaction Engineering and Seismic Site Response Evaluation." International Conference and Symposium on Recent Advances in Geotechnical Earthquake Engineering and Soil Dynamics, San Diego, CA.
[155] Seed, R. B., Cetin, K. O., Moss, R. E. S., Kammerer, A. M., Wu, J., Pestana, J. M., and Riemer, M. F. (2001). "Recent Advances in Soil Liquefaction Engineering and Seismic Site Response Evaluation." *Int. Conf. Sym. Recent Advances Geotech. Earthquake Engr. Soil Dynamics*, San Diego, CA.
[156] Shahien, M. M. (1998). *Settlement of structures on granular soils subjected to static and earthquake loads*, Doctoral dissertation, University of Illinois at Urbana-Champaign.
[157] Shamoto, Y., M. Sato and J.-M. Zhang (1996). "Simplified estimation of earthquake-induced settlements in saturated sand deposits," Soils and Foundations, Japanese Society of Soil Mechanics and Foundation Engineering, 36(1), 39-50.
[158] Shamoto, Y., Zhang, J. M., and Tokimatsu, K. (1998). "Methods for evaluating residual post-liquefaction ground settlement and horizontal displacement." *Soils Found.*, 22, 69–83.
[159] Shaw, P. and Brown, S. F. (1986). "Cyclic simple shear testing of granular materials." *Geotech. Test. J.*, 9 (4), 213-220.
[160] Silver, M. L., and Seed, H. B. (1969). *The behavior of sands under seismic loading conditions* (No. EERC-69-16). Univ. California Berkeley, Earthquake Engineering Research Center.
[161] Silver, M. L., and Seed, H. B. (1971). "Volume changes in sands during cyclic loading." *J. Soil Mech. Found. Div*., 97(9), 1171-1182.
[162] Simo, J. C., and Hughes, T. J. (2006). *Computational inelasticity* (Vol. 7). Springer Science and Business Media.
[163] Stewart, J. P., Kwok, A. O., Hashash, Y. M. A., Matasovic, N., Pyke, R., Wang, Z., and Yang, Z. (2008). "Benchmarking of nonlinear geotechnical ground response analysis procedures", Report PEER 2008/04, Pacific Earthquake Engineering Research Center. University of California, Berkeley.
[164] Su, D. (2005). "Centrifuge Investigation on Responses of Sand Deposit and Sand–Pile System Under Multi-directional" Earthquake Loading. Ph.D. Dissertation. The Hong Kong University of Science and Technology, Hong Kong.
[165] Su, D. and X. Li (2003). "Centrifuge tests on earthquake response of sand deposit subjected to multi-directional shaking". In The 16th ASCE Engineering Mechanics Conference, University of Washington, Seattle. ASCE.
[166] Sze, H. Y., and Yang, J. (2013). "Failure modes of sand in undrained cyclic loading: impact of sample preparation." *J. Geotech. Geoenviron. Engr.*, 140(1), 152-169.

[167] Tatsuoka, F., Iwasaki, T., Yoshida, S., Fukushima, S., and Sudo, H. (1979). “Shear modulus and damping by drained tests on clean sand specimens reconstituted by various methods.” *Soils Found.*, 19(1), 39-54.
[168] Tatsuoka, F., Ochi, K., Fujii, S., and Okamoto, M. (1986). “Cyclic undrained triaxial and torsional shear strength of sands for different sample preparation methods.” *Soils Found.*, 26(3), 23–41.
[169] Tatsuoka, F., Zhou, S., Sato, T., and Shibuya, S. 1990. Method of evaluating liquefaction potential and its application. In Report on seismic hazards on the ground in urban areas, Ministry of Education of Japan, Tokyo. (in Japanese.)
[170] Terzaghi, K. (1925). Principles of soil mechanics, IV - “Settlement and consolidation of clay”. Engineering News-Record, 95(3), 874-878.
[171] Terzaghi, K., Peck, R. B., and Mesri, G. (1996). *Soil mechanics in engineering practice*. John Wiley and Sons.
[172] Tessari, A. (2007). "Measuring Primary and Secondary Wave Velocities on a Geotechnical Centrifuge Using Bender Elements". Masters of Science Dissertation. Rensselaer Polytechnic Institute, Troy, NY.
[173] Thevanayagam, S., and Mohan, S. (2000). “Intergranular state variables and stress–strain behaviour of silty sands.” *Geotechnique*, 50(1), 1-23.
[174] Tokimatsu, K. and Seed, H. B. (1987). “Evaluation of settlements in sands due to earthquake shaking.” *J. Geotech. Eng. Div.*, 113(8), 861-878.
[175] Tokimatsu, K., and Yoshimi, Y. (1983). “Empirical correlation of soil liquefaction based on SPT N-value and fines content.” Soils Found., 23(4), 56–74.
[176] Tresca, H. (1864). “On the flow of solid bodies subjected to high pressures”. CR Acad Sci Paris, 59, 754.
[177] U.S. Nuclear Regulatory Commission. (2008). “NRC Seismic Research Program” Plan FY 2008-2011. Retrieved from: http://www.nrc.gov/docs/ML0729/ML072960792.pdf.
[178] Vaid, Y. P. and Negussey, D. (1988). “Preparation of Reconstituted Sand Specimens.” Advanced Triaxial Testing of Soils and Rock, ASTM STP977, ASTM International, West Conshohocken, PA, 405–417.
[179] Vaid, Y. P., Sivathayalan, S., and Stedman, D. (1999). “Influence of specimen reconstituting method on the undrained response of sand.” *Geotech. Test. J.*, 22(3), 187–195.
[180] van Genuchten, M. (1980). “A closed form equation for predicting the hydraulic conductivity of unsaturated soils.” Soil Sci. Soc. Am. J., 44(5), 892–898.
[181] Von Mises, R. (1913). “Mechanics of solid bodies in the plastically - deformable state”. German. Nachr. Ges. Wiss. Goettingen, Math.-Phys. Kl, 1, 582-592.
[182] Vucetic, M. (1994). “Cyclic threshold shear strains in soils.” *J. Geotech. Engr.*, 120(12), 2208-2228.
[183] Vucetic, M., and Dobry, R. (1991). “Effect of soil plasticity on cyclic response”. J. of geotechnical engineering, 117(1), 89-107.
[184] Vucetic, M., and Mortezaie, A. (2015). “Cyclic secant shear modulus versus pore water pressure in sands at small cyclic strains.” *Soil Dynamics Earthquake Engr.*, 70, 60-72.
[185] Whang, D. H., Moyneur, M. S., Duku, P., and Stewart, J. P. (2005). “Seismic compression behavior of nonplastic silty sands.” *Proc., Int. Symp. Advanced Experimental Unsaturated Soil Mech.*, Netherlands, 257-263.
[186] Whang, D. H., Stewart, J. P., and Bray, J. D. (2004). “Effect of compaction conditions on the seismic compression of compacted fill soils.” *Geotech. Testing J.*, 27(4), 371-379.
[187] Whitman, R. V., and Ortigosa, P. O. (1969). “Densifcation of sand by vertical vibrations.” *Proc. 4th World Conf. Earthquake Engr.*, Santiago, Chile, 29–37.
[188] Wood, F. M., Yamamuro, J. A., and Lade, P. V. (2008). “Effect of depositional method on the undrained response of silty sand.” *Canadian Geotech. J.*, 45(11), 1525–1537.

[189] Wu, J. (2002). “Liquefaction triggering and post-liquefaction deformation of Monterey 0/30 sand under uni-directional cyclic simple shear loading”. Ph.D. Dissertation, University of California, Berkeley.
[190] Wu, J., and Seed, R. B. (2004). “Estimating of liquefaction-induced ground settlement case studies.” *Proc., 5th Int. Conf. Case Histories Geotech. Engr.*, Paper 3.09, New York.
[191] Wu, J., Seed, R.B. and Pestana, J.M. (2003). “Liquefaction Triggering and Post Liquefaction Deformations of Monterey 0/30 Sand under Uni-Directional Cyclic Simple Shear Loading”. Geotechnical Engineering Report No. UCB/GE-2003/01, April 2003, Univ. of California, Berkeley.
[192] Yamamuro, J. A. and Wood, F. M. (2004). “Effect of Depositional Method on the Undrained Behavior and Microstructure of Sand with Silt.” *Soil Dynamic Earthquake Engr.*, 24(9), 751–760.
[193] Yang, Z. (2000). “Numerical modeling of earthquake site response including dilation and liquefaction” (Doctoral dissertation, Columbia University).
[194] Yang, Z., and Elgamal, A. W. M. (2000). “Numerical modeling of earthquake site response including dilation and liquefaction” (Doctoral dissertation, Columbia University).
[195] Yang, Z., Elgamal, A., and Parra, E. (2003). Computational model for cyclic mobility and associated shear deformation. *J. of Geotechnical and Geoenvironmental Engineering*, *129*(12), 1119-1127.
[196] Yee, E., Duku, P. M., and Stewart, J. P. (2013). “Cyclic volumetric strain behavior of sands with fines of low plasticity.” *J. Geotech. Geoenviron. Eng.*, 10.1061/(ASCE)GT.1943-5606.0001041, 04013042.
[197] Yi, F. (2010). “Procedure to evaluate seismic settlement in dry sand based on shear wave velocity.” *Proc. 9th U.S. National 10th Canadian Conf. Earthquake Engr. (9USN/10CCEE)*, Toronto, Canada. Paper No. 760.
[198] Yoshimi, Y. and Tokimatsu, K. (1977). “Settlement of Buildings on Saturated Sand During Earthquakes”. Soils and Foundations, Vol. 17, No. 1, pp. 23-38.
[199] Yoshimi, Y., Tanaka, K., and Tokimatsu, K. (1989). “Liquefaction resistance of a partially saturated sand.” Soil Found., 29(3), 157–162.
[200] Youd, T. L. (1972a). “Compaction of sands by repeated shear straining.” *J. Soil Mech. Found. Div.*, 98(7), 709-725.
[201] Youd, T. L. (1972b). “Volume changes in sands during cyclic loading,” Discussion, *J. Soil Mech. Found. Div.*, 98(12), 1422-1425.
[202] Youd, T. L. et al. (2001). “Liquefaction resistance of soils: summary report from the 1996 NCEER and 1998 NCEER/NSF workshops on evaluation of liquefaction resistance of soils.” *J. Geotech. Geoenviron. Engr.*, 127(4), 817-833.
[203] Youd, T. L., Hansen, C. M., and Bartlett, S. F. (2002). "Revised MLR equations for prediction of lateral spread displacement." *J. Geotech. Geoenviron. Engr.*, 128(12), 1007-1017.
[204] Zhang, G., Robertson, P.K., and Brachman, R.W.I. (2002). “Estimating Liquefaction induced ground settlements from CPT for level ground”. Canadian Geotechnical J., 39(5): 1168–1180. doi:10.1139/t02-047.
[205] Ziegler, H. (1959). “A modification of Prager’s hardening rule”. Quarterly of Applied mathematics, 17(1), 55-65.
[206] Ziotopoulou, K. (2017). “Seismic response of liquefiable sloping ground: Class A and C numerical predictions of centrifuge model responses”. Soil Dynamics and Earthquake Engineering.